NASA Reference Publication 1292, Vol. III

1993

The Atmospheric Effects of Stratospheric Aircraft: Report of the 1992 Models and Measurements Workshop

Volume III—Special Diagnostic Studies

Edited by
Michael J. Prather
NASA Office of Space Science and Applications
Washington, D.C.

Ellis E. Remsberg
Langley Research Center
Hampton, Virginia

NASA
National Aeronautics and Space Administration
Office of Management
Scientific and Technical Information Program

Contributing Authors:

G. Anderson
C. Bruhl
B. Connor
A. Douglass
R. Eckman
D. Fahey
D. Fisher
I. Folkins
R. Garcia
C. Granier
W. Grose
M. Hitchman
C. Jackman
R. Kawa
J. Kaye
J. Kinnersley
D. Kinnison
M. Ko
M. Kurylo
R. McPeters
C. Miller
R. Nagatani
P. Newman
G. Pitari
C. Rinsland
R. Rood
J. Rosenfield
T. Sasaki
U. Schmidt
R. Seals
M. A. Smith
R. Stolarski
K.-K. Tung
D. Weisenstein
H. Wesoky
D. Wuebbles
G. Yue
Y. Yung
J. Zawodny

TABLE OF CONTENTS

VOLUME I

VOLUME II

VOLUME III

Key to Model Data in Plots

H: Simultaneous Observations of Long-Lived Species

H: Simultaneous Observations of Long-Lived Species

S. R. Kawa
National Oceanic and Atmospheric Administration

R. A. Plumb
Massachusetts Institute of Technology

U. Schmidt
Institut fur Atmospharische Chemie

INTRODUCTION

Correlation plots provide a useful framework for analyzing several important aspects of model performance. The characteristics of the correlation plot between two species reflect the relative efficiency of transport and mixing versus photochemistry and also the relative distribution of the net source/sink terms for the species. The advantage of this comparison is the ability to exploit the high resolution sampling of normal stratospheric species fluctuations in the aircraft and balloon measurements. By expressing the various species as a function of a nearly conservative tracer like N_2O, we can map measurements over a limited altitude and latitude range to a much broader range of space in the two-dimensional zonal mean representation, thereby greatly increasing the value of the comparison between the models and measurements. Furthermore, the balloon and aircraft data sets include a fairly extensive number of long-lived species with varying lifetimes and loss/production mechanisms, thus providing a variety of points of contact to model processes.

In addition to the comparison of species correlations, this section also directly compares latitude profiles of O_3, NO_y, and simultaneously measured NO_y/O_3 from the ER-2 aircraft with the corresponding quantities from the models near aircraft altitudes (about 20 km). These measurements represent the most extensive in situ data available for these quantities, covering nearly all latitudes of both hemispheres.

The primary goal of this experiment is to provide a framework and the data with which to analyze model performance. The theoretical basis for interpreting correlation characteristics in terms of specific model processes is briefly reviewed in the next section, Theory, and includes guidance on the limits of this approach. The data used for this comparison are discussed under Measurements. In some cases, uncertainties in the measurements severely limit the value of the comparison to the models. In Comparison and Model Correlation the general features of the comparison of correlations from measurements and models are discussed and some specific examples are presented. Examples of the comparison of latitude profiles of NO_y, O_3, and NO_y/O_3 are presented next followed by a brief summary.

THEORY

A theory for the existence and significance of species correlations has been proposed by Plumb and Ko (1992). Stratospheric transport may be viewed as being represented by two components: mixing along isentropic surfaces associated primarily with breaking planetary waves and the planetary scale "Brewer-Dobson" circulation. The approach follows the "equilibrium slopes" hypothesis of Mahlman et al. (1986) and Holton (1986). A species whose stratospheric lifetime is long compared with the time scale of the isentropic mixing will become well mixed, not along the isentropic surfaces but along "rapid exchange" surfaces that dip poleward and downward relative to the isentropic surfaces because of the effects of the mean circulation. The location of such a surface can be defined by the (single) value of the mixing ratio of any long-lived reference species

such as N_2O; for this value of N_2O, the mixing ratio of any other long-lived species will also have a single value. Therefore, a correlation plot of these two species will be compact, i.e., the plot will not be scattered (though it may not be a straight line). Using a two-dimensional transport formulation Plumb and Ko (1992) argue that the slope of this compact curve is equal to the ratio of the globally integrated, vertical fluxes of the two species through the rapid exchange surfaces. In regions where the lifetimes of the two species are *very* long – compared with the time scale of (relatively slow) quasi-vertical transport – both fluxes will be constant and therefore the slope of the correlation will be linear.

For a species to be long lived requires a lifetime of maybe a year in winter middle latitudes where mixing times are short, but much longer in summer and in the tropics. In the latter case, there may be few if any species whose chemical lifetime in the tropics is long enough to satisfy this criterion.

These concepts suggest the following interpretations of the correlation diagrams. The *compactness* (or noncompactness) of the correlation indicates that the transport rates within the rapid exchange surfaces are short compared with the local chemical lifetime. The *curvature* of the relationship is indicative of nonconstant net flux and thus of differing quasi-vertical distributions of integrated sources and sinks for the two species. In correlations that are linear in the lower stratosphere, the value of the *slope* of the relationship can be used to determine the ratio of upward fluxes into the stratosphere and thence the ratio of species *lifetimes* in the stratosphere.

MEASUREMENTS

Table H-1 lists the long-lived species considered here and their approximate stratospheric lifetimes, as provided by the World Meteorological Organization (WMO) (1992). The CFC species and N_2O have no known losses in the troposphere, so their stratospheric lifetimes are equal to their total atmospheric lifetimes. These lifetimes are derived empirically and from model calculations. The stratospheric lifetimes for CH_4 and the hydrochlorofluorocarbons are estimated from model calculations (e.g., Prather and Spivakovsky, 1990; Fung et al., 1991).

Several issues must be considered when interpreting the comparison between atmospheric measurements and two-dimensional steady-state, zonal mean model representations. Clearly, measurement uncertainties limit the degree to which agreement can be expected. The major sources of uncertainty in measurements of long-lived species are variations in calibration standards, instrument precision, and sampling efficiency. Variations in calibration standards include uncertainty in the absolute accuracy of the standards and possible drift of the standards with time. These uncertainties are manifest in systematic calibration differences between different measurement groups (WMO, 1992). The model uncertainties that limit the value of comparisons to data are generally questions of the representativeness of the model formulation. For example, comparison with steady-state stratospheric models is limited by the effects of annual increases in the tropospheric abundances of long-lived species. Systematic meridional variations, model boundary conditions, and parameterization of processes such as heterogeneous reactions should also be considered. The magnitudes of some of these uncertainties are listed in Table H-1. Their effects will be discussed below for each of the individual correlations.

The data for this comparison come mainly from balloon-borne cryogenic samples (Schmidt et al., 1987, 1991) and whole-air samples from the NASA ER-2 stratospheric aircraft (Heidt et al., 1989; Kawa et al., 1992). Note that the balloon and aircraft data sets are complementary in giving high-resolution vertical and horizontal sampling, respectively. Simultaneous measurements of N_2O and CH_4 and measurements of several other long-lived chlorine species are also available from the ATMOS experiment (Gunson et al., 1990; Zander et al., 1987). Table H-2 lists the specific sampling details for these main data sources. None of the correlation data shown here are

from tropical latitudes. The raw data from the balloon samples, ATMOS, and the average NO_y, O_3, and NO_y/O_3 from the ER-2 are available from the UADP (see Volume I, chap. 3). The aircraft data are on CDROM for the Airborne Antarctic Ozone Expedition (AAOE) and Airborne Arctic Stratospheric Expedition (AASE) (Winkler and Gaines, 1989; Hipskind and Gaines, 1990). Fits to preliminary data for $CFCl_3$ and $C_2F_3Cl_3$ from the Airborne Chromatograph for Atmospheric Trace Species (ACATS) experiment on the ER-2 during the AASE-II are also included (J. W. Elkins and D. W. Fahey, personal communication, 1992).

Table H-1. Measured Species, Stratospheric Lifetimes, and Uncertainties (from WMO, 1992)

Species	Stratospheric Lifetime (yr)	Accuracy of Standards (%)	Precision		Annual Increase (%)
			Balloon (%)	Aircraft (%)	
N_2O	130	5	5	5	0.2
CH_4	150	5	1	2	1
CF_2Cl_2	120	5	5	5	4
$CFCl_3$	55	10	5	1	4
$C_2F_3Cl_3$	110	20-40*	5-10	1	10
CHF_2Cl	240	5-10		15	7
CCl_4	50	20	5-10	15	1.5
CH_3CCl_3	50	10-25	5-10	15	4
CH_3Cl	50	20-30	5-10	15	0
Cl_y		20#			3
NO_y		15#			0
O_3		5#			0

* Data scaled to remove the systematic difference.
\# Estimated total uncertainty.

As indicated in Table H-2 the measurement data span about 9 years, so that interannual increases in the abundance of many of the species are significant. To attain a more representative comparison to the models that were run for 1990 steady-state conditions, we have scaled the data by the amount of the annual increase for each species in the troposphere, i.e., (scaled data) = (raw data) (1+ fractional increase)(1990-year of measurement). The fractional annual increases are derived from the Ozone Trends Panel and WMO reports (Watson et al., 1988; WMO, 1990,1992) and are shown in Table H-1. Thus, assuming that transport is similar from year to year, the scaled data simulate an ensemble of samples all taken with tracer values at 1990 levels. Although stratospheric transport is not exactly the same interannually (Schmidt and Khedim, 1991), this procedure greatly reduces the variability in correlations with species with significant growth rates. N_2O values have

not been scaled because the annual increase is negligible compared with other uncertainties in this comparison. No attempt has been made to account for different ages of air in samples (at different altitudes, for example) for a given year.

Table H-2. Measurement Sampling

	Balloon	Aircraft	ATMOS
N samples	204	337	19
Year	1982-1990	1987, 1989	1985
Season	fall, winter*	winter	spring
Latitude	44N, 68N	55-80	48S, 28N
Altitude (km)	10-35	16-20	22-62

*Also includes a few spring and summer samples

The measurement correlations shown in this section use N_2O as the independent variable for correlation plots because of its long lifetime, small annual increase, relatively simple photochemistry, and accurate measurements (Table H-1). A long lifetime for N_2O has been corroborated by Ko et al. (1991) in comparison with Stratospheric and Mesospheric Sounder (SAMS) measurements although their lifetime estimate is somewhat lower (110 years) than that from WMO (1992). In many cases the data are fit to a line that serves as a reference for comparison to model correlations. The examples shown here are only a small sample of those possible from current data sets for models and measurements. Numerous other correlations are possible and may be used to examine processes specific to those species (e.g., Solomon et al. [1992]).

N_2O-CH_4

Figure H-1 shows the correlation plot for N_2O and CH_4 and a linear least-squares fit to the balloon and aircraft data for $N_2O > 20$ ppbv. ATMOS data are also plotted but are not included in the fit. The correlation is tightly distributed and nearly linear with a correlation coefficient (r value) of 0.983. The high degree of linear correlation between these species verifies that the lifetime of CH_4 is long in the lower stratosphere. Although N_2O is primarily lost via photolysis and CH_4 through reaction with OH, two processes that may have different spatial distributions, both lifetimes are sufficiently long in the lower stratosphere to satisfy the conditions for a compact, linear slope. Also, the measurement accuracy is very good. With N_2O less than about 30 ppbv the correlation becomes distinctly nonlinear. Measurements in this regime are from altitudes above about 33 km where losses of one or both species become significant. Note that the slope of the correlation plot in the linear region yields a ratio of about 1.4 for the lifetime of CH_4 relative to N_2O.

N_2O-CF_2Cl_2

Figure H-2 shows the correlation plot for N_2O and CF_2Cl_2 (CFC-12). The data distribution is fairly compact, and a linear fit to the data for $N_2O > 20$ ppbv gives a correlation coefficient of

0.980. A second-order polynomial fit to the data (not shown) is within 10 pptv CF_2Cl_2 of the linear fit for $50<N_2O<320$ ppbv. Thus, within the regime of N_2O values greater than about 50 ppbv, the CF_2Cl_2 lifetime is long relative to transport, in agreement with the estimates of Table H-1. Values of N_2O less than 50 ppbv are generally from samples taken above 30 km. Note that the CF_2Cl_2 fit to the tropospheric N_2O mixing ratio (308 ppbv) is 407 pptv, which is significantly lower than measured tropospheric CF_2Cl_2 for 1990 (about 470 pptv) (WMO, 1991). This may reflect systematic uncertainty in the measurements; however, CF_2Cl_2 is not expected to be lost in the grab samples (Knapska et al., 1985). The compactness of the correlation also suggests that the mixing time scale is short compared with that for changing CF_2Cl_2 in the stratosphere due to the moderate rate of increase of CF_2Cl_2 in the troposphere. The CF_2Cl_2 values from the AASE used for this report are slightly different from those published on the mission CD-ROM as a result of a post-mission calibration comparison (L. E. Heidt, personal communication, 1992).

N_2O-$CFCl_3$

Figure H-3 shows the balloon and whole-air aircraft data for $CFCl_3$ (CFC-11) and the best polynomial fit to that data. Also shown is a fit to $CFCl_3$ data from the ACATS instrument (J. W. Elkins and D. W. Fahey, personal communication, 1992) with simultaneous N_2O (M. Loewenstein, personal communication, 1992) from the ATLAS instrument (Loewenstein et al., 1990) aboard the ER-2 during AASE-II in 1991-1992 (the $CFCl_3$ and N_2O from AASE-II are preliminary data subject to revision). The ACATS curve is fit to 1654 data points, and the data are scaled back 2 years to 1990. The ACATS data generally agree closely with the balloon and whole-air sample data, within the measurement uncertainties of about 10%. The variability of the data is comparable in both sets. All of the data show a fairly compact distribution with distinct curvature in the correlation relationship over nearly the entire range of N_2O values. This compactness indicates that compared with mixing, the local $CFCl_3$ lifetime is long in the measurement regime while the curvature reflects the greater loss of $CFCl_3$, and hence shorter lifetime, compared to N_2O. The $CFCl_3$ loss is expected to occur mainly in the tropical lower and middle stratosphere. The ACATS fit (which most nearly represents in situ sampling) extrapolates more closely to the tropospheric measured value for $CFCl_3$ in 1990 (265 to 278 pptv [WMO, 1991]) at tropospheric N_2O.

N_2O-$C_2F_3Cl_3$

Figure H-4 shows the balloon and whole-air aircraft data, the polynomial fit to that data, and the fit to the ACATS/ATLAS data for $C_2F_3Cl_3$ (CFC-113). The raw balloon data are analyzed relative to the OGIST standard (Schmidt et al., 1991), which is 37% lower than the NOAA-CMDL standard used by the whole air and ACATS groups (WMO, 1992). Consequently, we have scaled the balloon data by 1.37 for this comparison. The balloon and whole-air data show considerable scatter even after scaling to remove calibration standard differences and annual increases. Given the fairly long lifetime of $C_2F_3Cl_3$, this scatter is most likely due to measurement uncertainty in combination with the effect of the rapid annual increase of $C_2F_3Cl_3$ rather than local photochemistry. The fit to the ACATS data is from 2034 points, which show substantially less scatter than that shown in Figure H-4. The fit lines are very similar, however, and both indicate definite curvature to the correlation relationship. Similar to $CFCl_3$, this curvature reflects a shorter lifetime for $C_2F_3Cl_3$ relative to N_2O. Both curves extrapolate to a value somewhat lower than the tropospheric $C_2F_3Cl_3$ value of 70 pptv for 1990 (WMO, 1992) at N_2O = 308 ppbv, but the measurement uncertainties are fairly large. The rapid annual increase for $C_2F_3Cl_3$ probably contributes to this discrepancy since the age of the lower stratospheric air is not precisely known.

N_2O-CHF_2Cl

Data for CHF_2Cl (HCFC-22) are only available from the whole-air samples during the AASE and are shown in Figure H-5. A line is fit to the data to serve as a reference for comparison to the

models, but the fit does not explain much of the variance (r=0.58). The large scatter in the data is a result of measurement uncertainty derived from imprecision in the analysis (Table H-1) and the possible lack of conservation of CHF_2Cl in the sampling containers. Furthermore, CHF_2Cl is thought to have a significant interhemispheric gradient between the north and the south, while N_2O is much more uniformly distributed. This difference may contribute to variability in the stratospheric measurements since air entering the stratosphere will have different amounts of CHF_2Cl for the same value of N_2O depending on the hemisphere from which the air enters. The long stratospheric lifetime calculated for CHF_2Cl suggests that the variability of the measurements is not the result of local photochemistry. Based on Figure H-5, the CHF_2Cl measurements are only of limited value in comparison to the models.

N_2O-CH_3CCl_3

Figure H-6 shows data for CH_3CCl_3 (methyl chloroform) and the best polynomial fit to that data for $N_2O > 90$ ppbv. The data definitely indicate curvature in the correlation relation at nearly all N_2O values, but the scatter about the fit is fairly large. The scatter in the data reflects the shorter lifetime of CH_3CCl_3 in combination with measurement uncertainties (Table H-1) and the fact that some CH_3CCl_3 is probably lost in sampling (Knapska et al., 1985). Tropospheric CH_3CCl_3 in 1990 is about 140 pptv, which is significantly higher than the measurement fit at 308 ppbv N_2O but well within the range of the data.

N_2O-CCl_4

Data for CCl_4 (carbon tetrachloride) and the polynomial fit are shown in Figure H-7. Again the scatter about the curve is large, reflecting the difficulty of the measurement and the relatively short lifetime of CCl_4 (Table H-1). The annual increase of CCl_4 is small, and the fit value at $N_2O = 308$ ppbv is in good agreement with tropospheric CCl_4 (108 pptv) for 1990.

N_2O-CH_3Cl

Figure H-8 shows data for CH_3Cl (methyl chloride). The data are very scattered and suggest the possibility of a systematic difference between the aircraft and balloon data sets. No reference line has been fit for CH_3Cl. Tropospheric CH_3Cl is about 600 pptv. Although this is a major component of organic chlorine and the only known chlorocarbon with a significant natural source, the difficulty of the measurement limits its usefulness for comparison to models (Schmidt et al., 1985; Knapska et al., 1985)

N_2O-Cl_y

Cl_y is defined as the sum of inorganic chlorine and is important to evaluating chlorine budget studies using measured data. The major species are HCl, $ClONO_2$, ClO, HOCl, Cl_2O_2, and atomic Cl. The origin of Cl_y in the stratosphere is decomposed organic chlorine molecules, the CFCs, whose source is near the Earth's surface. Figure H-9a shows the correlation plot for the sum of measured organic chlorine (CCl_y) from the AAOE and AASE (Kawa et al., 1992). The polynomial (curved) fits have been chosen for estimating Cl_y from N_2O. Cl_y for a given value of N_2O is obtained by subtracting CCl_y for that N_2O from the estimated total chlorine for the air parcel. Total chlorine is expected to be a conserved quantity in the stratosphere. The value for total chlorine is determined by the organic chlorine abundance of the tropospheric air that is transported into the stratosphere. Measurements of organic chlorine in the troposphere show an increase of about 3% per year (WMO, 1992). An average age of 3 years has been used to determine total chlorine for the time of the AAOE and AASE data. Figure H-9b shows the correlation plot for Cl_y based on the CCl_y measurements of AAOE and AASE scaled up to 1990. The estimated uncertainty in the Cl_y values is ±20% (Kawa et al., 1992).

N_2O-NO_y

NO_y is defined as the sum of reactive nitrogen species (Fahey et al., 1989). NO_y is directly measured on the ER-2 aircraft and the principle NO_y species are all measured by ATMOS. The NO_y-N_2O correlation has been used extensively as a diagnostic for processes related to polar stratospheric clouds (e.g., Fahey et al., 1990). An example of the strong anticorrelation of NO_y with N_2O is shown in Figure H-10. The relationship is tight and linear for $N_2O > 120$ ppbv. The fits to the AAOE and AASE data, obtained from thousands of measurements during tens of flights, are $NO_y = -0.065(N_2O)+20.6$ ppbv in the Arctic and $NO_y = -0.074(N_2O)+21.8$ ppbv in the Antarctic, for $(N_2O) > 150$ ppbv. The ATMOS data also fit these correlations well and indicate that the linearity of the correlation extends down to N_2O values of about 50 ppbv. The compactness and linearity of this correlation suggest that the lifetime of NO_y is at least several years in the middle and high latitude lower stratosphere (in the absence of polar stratospheric clouds). The estimated uncertainty in the correlation slope, derived from the individual measurement uncertainties and the standard deviation of the fit is ±16% at the 1 σ level (Fahey et al., 1990).

NO_y/O_3

Latitude profiles of ER-2 measurements of NO_y, O_3, and simultaneously measured NO_y/O_3 are shown in Figure H-11. These data are from the STEP, AAOE, and AASE measurement campaigns. Measurement uncertainties are ±15% for NOy and ±5% for ozone (Fahey et al., 1989; Proffitt et al., 1989). The averages and standard deviations are calculated over 5 degree latitude intervals from 120-s average data points as presented in Murphy et al. (1992) with additional data from 870823, 870916, 870921, 890112, 890116, 890120, and 890124 (dates are read YYMMDD). Extratropical data are from the winter season in either hemisphere (except for 870929, 871001, 871003, and 881015). Data are from potential temperatures between 430 and 520 K, which corresponds to 45 to 65 mb in the tropics and 50 to 80 mb at middle and high latitudes. The advantage of using NO_y/O_3 for comparison of horizontal gradients can be seen in the lower variability of NO_y/O_3 relative to the mean which is lower than that for either species individually. With respect to the correlation figures shown above, the NO_y/O_3 plots represent a cut across latitude of the slope of the NO_y-O_3 correlation in the lower stratosphere. The ratio will have variations with latitude (approximately isentropically) where the local production/loss processes of these species become significant relative to mixing transport. For further discussion see Murphy et al. (1992).

COMPARISON WITH MODEL CORRELATIONS

The model scenario specified for comparison of tracer correlations is shown in Table H-3. Note that the tropospheric boundary conditions for the tracer mixing ratios are fixed at values representative of approximately 2.5 years prior to 1990. Since the measurements are scaled by annual increases to be representative of 1990, measured values for air with a residence time of 2.5 years in the stratosphere are expected to give the best agreement with the steady-state model results. These should be values in the middle of the N_2O range of the correlation plots. Species with small annual increases are expected to give closer comparisons than those with large increases.

The model groups participating in this comparison are CAMED, DUPONT, GSFC, ITALY, LLNL, MRI, NCAR, and WASH; AER and NOCAR provided a partial set of results. Model abbreviations are defined in chapter 3. The large number of plots generated for this comparison cannot totally be accommodated in the final report. We have tried to select a representative subset of examples to demonstrate the features discussed below.

Table H-3. Bulk Tropospheric Mixing Ratios for 'Current' Stratosphere Runs

yearSS	F11	F12	F113	F114	F115	1211	1301	H22	CCl_4	CH_3CCl_3	CO_2	N_2O	CH_4
1980SS	149	250	11	3	2	0.4	0.4	41	93	85	334	300	1538
1990SS	253	434	44	7	5	2.0	2.6	92	103	145	350	308	1685
	ppt----------								---------->	ppt	ppm	ppb	ppb

also fixed: CH_3Cl=600 ppt, CH_3Br=15 ppt, N_2=78%, O_2=21%

These steady-state scenarios use tropospheric boundary conditions from 2.5 years previous and are identical to the UNEP scenarios. Total Cl=3.3 ppbv

General Features

Most general features of the model results are consistent with expectations for long-lived species. Very slight seasonal differences are found between the model correlations from December and March, and differences between gas phase and heterogeneous chemistry results are negligible (including species lost in reaction with OH). Also, the hemispheric asymmetry is small for most comparisons; the primary latitude dependence is the difference of the tropical points from those at higher latitudes, consistent with expectations from theory outlined above and by Plumb and Ko (1992). These general features can be observed in Figure H-12. Because of the similarity of the March and December models and also the gas phase and heterogeneous cases of each model, only correlations for December, gas phase simulations will be shown in the comparisons that follow.

When comparing the data for most cases, the differences between models are not much greater than the variability in the data. Although differences exist, the data are often not precise enough to indicate which models are more accurate. The models differ substantially in the compactness of their tropical points, but little tropical data are available for comparison. All the models seem to have weak poleward-downward circulation at high latitudes compared with the data. Steady-state models are not very useful for comparison to species with significant growth rates. These features are consistent with the results of the model-model comparison of idealized tracers in section O.

CH_4

All of the models do reasonably well in simulating the N_2O-CH_4 correlation in absolute value and slope in the linear region of N_2O greater than about 50 ppbv (Figure H-13). The agreement is consistent with the long stratospheric lifetime and small annual rate of increase for CH_4 (Table H-1). The models differ chiefly in the amount of scatter in the correlation but, except for the tropical points, almost all the model points are within the envelope of the measured data points. The tropical points are expected to form a more scattered correlation as discussed above. The models also appear to do well in simulating the nonlinear decrease of CH_4 at N_2O less than 50 ppbv in comparison with the few measured points. Comparison of N_2O and CH_4 latitude-height cross sections and vertical profiles along with correlation plots from SAMS data are found in section E.

CF_2Cl_2

With reference to the N_2O-CF_2Cl_2 correlation, the models all differ from the measurements in predicting higher CF_2Cl_2 values for N_2O greater than about 200 ppbv (Figure H-14). This difference follows from the difference between the extrapolation of the measured correlation and CF_2Cl_2 values measured in the troposphere as discussed in the measurement section above. The

models all predict a relatively tight, nearly linear relationship similar to the measurements, as expected for the long lifetime of CF_2Cl_2.

$CFCl_3$

The model correlations for $CFCl_3$ exhibit significant curvature and scatter, in general agreement with the measurements, with the tropical points deviating furthest from the reference lines (Figure H-15). The models are all similar in this respect except for ITALY, which has most points below the reference lines and greater scatter, indicative of slower horizontal transport relative to the photochemical $CFCl_3$ sink. The relatively high amount of scatter is a consistent feature of the ITALY model.

$C_2F_3Cl_3$

The comparison for $C_2F_3Cl_3$ is dominated by the effect of the rapid annual increase in the troposphere for this species (e.g., Figure H-16). The model values all lie below the reference curve for N_2O greater than about 100 ppbv, because their steady state tropospheric boundary condition of 44 pptv is much less than that of ambient $C_2F_3Cl_3$ in 1990, i.e., 70 pptv. The model correlation slopes are all less steep than the measurements, as expected for comparison of steady-state versus increasing tropospheric abundances. $C_2F_3Cl_3$ is clearly not a good point of comparison for models using steady state tropospheric input, but could be of considerable value in testing models with varying tropospheric input.

CHF_2Cl

The correlation comparison for CHF_2Cl is not constrained very closely because of the large scatter in the measurements, much of which is attributed to measurement uncertainty. Among the models, however, the differences for this correlation are large. Figure H-17 shows the range of values and scatter for the models. These differences indicate significant differences in the models' transport versus loss due to OH reaction, the primary loss for CHF_2Cl. Such large differences do not appear in the correlations for CH_4 or CH_3CCl_3, other species lost in reaction with OH. CHF_2Cl is an important CFC replacement compound, so a better measurement data base and careful analysis of model loss processes for this compound are very important.

CH_3CCl_3

CH_3CCl_3 is lost both through photolysis and reaction with OH but its lifetime is much shorter than CHF_2Cl. This leads to greater scatter in the correlation relationship for CH_3CCl_3 compared with CHF_2Cl in the models, but in this case the model results are all rather similar to one another (e.g., Figure H-18), more like $CFCl_3$. Most model values (outside the tropics) are higher than the reference curve, consistent with the possible sampling loss of CH_3CCl_3 in the measurements; however, comparison with Figure H-6 shows that the model points fall within the range of the measured data.

CCl_4

The correlation for CCl_4 shows a large amount of scatter in all the models (e.g., Figure H-19), especially in the tropical points, which is indicative of its relatively short photolytic lifetime. The measurements are also highly scattered, but even more so than the models, due in part to measurement errors. CCl_4 is increasing slowly in the atmosphere but the model slopes are all steeper than the measurements, with most points below the reference line. This difference is probably not significant in light of the measurement uncertainties.

CH_3Cl

Comparison with CH_3Cl is difficult because of the large measurement uncertainty. The models all show a very tight correlation relationship (e.g., Figure H-20) in contrast to the highly scattered measurements. There is a significant degree of curvature, indicating a difference in the distributions of loss rates for N_2O photolysis versus reaction of CH_3Cl with OH. The degree of curvature differs somewhat among the models but not as much as for CHF_2Cl.

Cl_y

The model results show generally good agreement compared with Cl_y derived from measurements (Figure H-21). Some models have slightly more curvature than the reference line and differ in the amount of scatter in the correlation, but most extratropical points fall within the scatter of the measurements (Figure H-9). The reason that the CAMED model at low N_2O does not approach the total chlorine amount specified by the boundary conditions (Table H-3) is not presently apparent.

NO_y

Most models simulate the N_2O–NO_y correlation fairly well (Figure H-22); the CAMED model does exceptionally well. All the models show a nearly linear, fairly compact relationship for N_2O greater than 100 ppbv, away from the tropics. However, several have higher NO_y values than the reference, suggesting a problem in simulating the NO_y sources and sinks. In the NCAR model, for example, the net amount of NO_y entering the stratosphere from the troposphere appears to be too large. Another possible reason for overestimation of NO_y in the models is loss of NO_y in the stratosphere due to sedimentation of polar stratospheric cloud particles; this process is not represented in the models. The global magnitude of NO_y loss on cloud particles is not well known. The models all show a change in slope at N_2O less than about 50 ppbv, a feature also seen in the ATMOS measurements at high altitudes. At altitudes above about 30 km, the loss of NO_y from both the photolysis of NO and the reaction of NO with N becomes significantly rapid (Fahey et al., 1990).

NO_y, O_3, and NO_y/O_3 LATITUDE PROFILES

Among the models a wide range of differences can be seen with respect to NO_y, O_3, and simultaneously measured NO_y/O_3 as functions of latitude (Figure H-23). For NO_y and O_3, the upper set of three model curves (20 km) corresponds more closely to the data in tropical latitudes while the lower set (18 km) more closely corresponds to the high latitude data. For NO_y/O_3, the lower set of model curves in the tropics is at 20 km. The December to March curves are most representative of the data in the northern hemisphere, while the September curves are more representative of the southern hemisphere data.

Within the large differences between models some general features appear. In contrast to the correlation plots, seasonal variations and hemispheric asymmetries are observable in most models. These variations arise mainly from O_3 changes, as expected from the greater photochemical activity of O_3 relative to the longer-lived species. Also, differences are noticeable between the gas phase and heterogeneous simulations, especially in O_3. For most models these differences are small, with slightly increased O_3 at high latitudes in the heterogeneous runs (not shown) and a negligible change in NO_y (DUPONT is an exception showing removal of NO_y and a larger increase in O_3 than the others, with a corresponding decrease in NO_y/O_3, in the heterogeneous case).

All of the models, except DUPONT gas phase, tend to predict NO_y mixing ratios that are too low at high latitudes in comparison to the measurements (see also the comparison to LIMS data in section F on NO_y absolute stratospheric abundance and distribution). Presumably, this feature is

due to the models' weakness in simulating the polar vortex. Low modeled NO_y at high latitudes is consistent with comparisons for other tracers in zonal mean cross sections which show that the poleward, downward slope of the isolines is not steep enough, a feature that seems to indicate that the model meridional circulation versus isentropic mixing is not strong enough. Comparison to O_3 data at high latitudes is closer for most models, as it is at all latitudes. This leads to underestimation of NO_y/O_3 at high latitudes for most models.

The models generally fail to simulate well the steep NO_y/O_3 gradient between the tropics and middle latitudes. The ITALY model is unique in simulating this gradient, consistent with weaker horizontal diffusion which seems to be characteristic of the ITALY model. However, the magnitudes of the NO_y/O_3 values from the ITALY model are too low at tropical and subtropical latitudes. Many of the models underpredict NO_y/O_3 at middle latitudes. In the tropics all models either are in agreement with NO_y/O_3 or overestimate the observed values (mostly due to overestimated NO_y), except ITALY as mentioned and MRI which underestimates NO_y almost everywhere. The general difficulty in simulating the NO_y, O_3, and NO_y/O_3 data with latitude, and the wide disagreement between models, indicates that the two-dimensional models have serious problems with transport in the lower stratosphere.

SUMMARY

We have attempted to provide a method to analyze model performance in comparison with measured data. The theoretical framework and observational data have been put forth along with some example comparisons. We expect that the main value of this section will come in detailed analysis by the individual modeling groups studying their model characteristics compared with the measurements. In this way improved model representations of transport and chemical loss/production will enhance confidence in the model assessments of the atmospheric effects of perturbations such as stratospheric aircraft.

An equally important aspect of this comparison has been identification of the need for improvement of the measurement data base. In some cases the measurement uncertainties are too large to rigorously constrain the model results. This situation should be improved by intercomparison of calibration standards among the measurement groups and new, more precise instrument techniques. Additional data, especially in the tropical regions where almost no data are available, will also increase the value of these comparisons.

REFERENCES

Fahey, D. W., D. M. Murphy, K. K. Kelly, M. K. W. Ko, M. H. Proffitt, C. S. Eubank, G. V. Ferry, M. Loewenstein, and K. R. Chan, Measurements of nitric oxide and total reactive nitrogen in the Antarctic stratosphere: observations and chemical implications, *J. Geophys. Res., 94,* 16665-16681, 1989.

Fahey, D. W., S. Solomon, S. R. Kawa, M. Loewenstein, J. R. Podolske, S. E. Strahan, and K. R. Chan, A diagnostic for denitrification in the winter polar stratospheres, *Nature, 345*, 698-702, 1990.

Fung, I., J. John, J. Lerner, E. Matthews, M. Prather, L. P. Steele, and P. J. Fraser, Three-dimensional model synthesis of the global methane cycle, *J. Geophys. Res, 96*, 13033-13065, 1991.

Gunson, M. R., C. B. Farmer, R. H. Norton, R. Zander, C. P. Rinsland, J. H. Shaw, and B.-C. Gao, Measurements of CH_4, N_2O, CO, H_2O, and O_3 in the middle atmosphere by the

Atmospheric Trace Molecule Spectroscopy Experiment on Spacelab 3, *J. Geophys. Res., 95,* 13867-13882, 1990.

Heidt, L. E., J. F. Vedder, W. H. Pollock, R. A. Lueb, and B. E. Henry, Trace gases in the Antarctic atmosphere, *J. Geophys. Res., 94,* 11599-11611, 1989.

Hipskind, S., and S. Gaines (eds.), Airborne Arctic Stratospheric Expedition, NASA ER-2 and DC-8 aircraft measurements and related data, Compact disc NASA/UARP-003, edition 2, NASA, Moffett Field, CA, 1990.

Holton, J. R., A dynamically based transport parameterization for one-dimensional photochemical models of the stratosphere, *J. Geophys. Res., 91,* 2681-2686, 1986.

Kawa, S. R., D. W. Fahey, L. E. Heidt, W. H. Pollock, S. Solomon, D. E. Anderson, M. Loewenstein, M. H. Proffitt, J. J. Margitan, K. R. Chan, Photochemical partitioning of the reactive nitrogen and chlorine reservoirs in the high latitude stratosphere, *J. Geophys. Res. 97,* 7905-7923, 1992.

Knapska, D., U. Schmidt, C. Jebsen, F. J. Johnen, A. Khedim, and G. Kulessa, A laboratory test of cryogenic sampling of longlived trace gases under simulated stratospheric conditions, *Atmospheric Ozone,* Proc. Quadrennial Ozone Symposium, Halkidiki, Greece, 1984, 122-128, D. Reidel, Dordrecht, Netherlands, 1985.

Ko, M. K. W., N. D. Sze, and D. K. Weisenstein, Use of satellite data to constrain the model-calculated atmospheric lifetime for N_2O: Implications for other trace gases, *J. Geophys. Res., 96,* 7547-7552, 1991.

Loewenstein, M., J. R. Podolske, K. R. Chan, and S. E. Strahan, Atlas instrument characterization: Accuracy of the AASE and AAOE nitrous oxide data sets, *Geophys. Res. Lett.,* 17, 481-484, 1990.

Mahlman, J. D., H. Levy II, and W. J. Moxim, Three-dimensional simulations of stratospheric N_2O: Predictions for other trace constituents, *J. Geophys. Res., 91,* 2687-2707, 1986.

Murphy, D. M., D. W. Fahey, M. H. Proffitt, S. C. Liu, C. S. Eubank, S. R. Kawa, and K. K. Kelly, Reactive nitrogen and its correlation with ozone in the lower stratosphere and upper troposphere, *J. Geophys. Res.,* in press, 1992.

Plumb, R. A., and M. K. W. Ko, Interrelationships between mixing ratios of long-lived stratospheric constituents, *J. Geophys. Res., 97,* 10145-10156, 1992.

Prather, M. J., and C. M. Spivakovsky, Tropospheric OH and the lifetime of hydrochlorofluorocarbons, *J. Geophys. Res., 95,* 18723-18729, 1990.

Proffitt, M. H., M. J. Steinkamp, J. A. Powell, R. J. McLaughlin, O. A. Mills, A. L. Schmeltekopf, T. L. Thompson, A. F. Tuck, T. Tyler, R. H. Winkler and K. R. Chan, In situ ozone measurements within the 1987 Antarctic ozone hole from a high-altitude ER-2 aircraft, *J. Geophys. Res., 94,* 16547-16556, 1989.

Schmidt, U., and A. Khedim, In situ measurements of carbon dioxide in the winter Arctic vortex and at mid-latitudes: An indicator of the 'age' of stratospheric air, *Geophys. Res. Lett.,* 18, 763-766, 1991.

Schmidt, U., D. Knapska, and S. A. Penkett, A study of the vertical distribution of methyl

chloride (CH_3Cl) in the midlatitude stratosphere, *J. Atmos. Chem., 3*, 363-376, 1985.

Schmidt, U., G. Kulessa, E. Klein, E.-P. Röth, P. Fabian, and R. Borchers, Intercomparison of balloon-borne cryogenic whole air samplers during the MAP/GLOBUS 1983 campaign, *Planet. Space Sci., 35*, 647-656, 1987.

Schmidt, U., R. Bauer, A. Khedim, E. Klein, G. Kulessa and C. Schiller, Profile observations of long-lived trace species in the Arctic vortex, *Geophys. Res. Lett., 18*, 767-770, 1991.

Solomon, S., M. Mills, L. E. Heidt, W. H. Pollock, and A. F. Tuck, On the evaluation of ozone depletion potentials, *J. Geophys. Res., 97*, 825-842, 1992.

Watson, R. T., M. J. Prather, and M. J. Kurylo, Present state of knowledge of the upper atmosphere 1988: An assessment report, *NASA Ref. Publ., NASA RP 1208*, 1988.

Winkler, R., and S. Gaines (eds.), Airborne Antarctic Ozone Experiment, NASA ER-2 and DC-8 aircraft measurements and Antarctic ozonesondes, Compact disc NASA/UARP-002, NASA, Moffett Field, CA, 1989.

World Meteorological Organization (WMO), *Scientific Assessment of Stratospheric Ozone: 1989*, Global Ozone Res. and Monitor. Proj. Rep. 20, WMO, Geneva, Switzerland, 1990.

World Meteorological Organization (WMO), *Scientific Assessment of Ozone Depletion: 1991*, Global Ozone Res. and Monitor. Proj. Rep., WMO, Geneva, Switzerland, 1992.

Zander, R., C. P. Rinsland, C. B. Farmer, and R. H. Norton, Infrared spectroscopic measurements of halogenated source gases in the stratosphere with the ATMOS instrument, *J. Geophys. Res., 92*, 9836-9850, 1987.

FIGURE CAPTIONS

Figure H-1. Correlation plot for N_2O and CH_4 and a linear least-squares fit to the data for N_2O > 20 ppbv. The equation of the reference line is $CH_4 = 3.82(10^{-3})(N_2O) + 0.5$ ppmv where N_2O is in units of ppbv. The standard deviations of the slope and intercept are $3.12(10^{-5})$ and $5.9(10^{3})$, respectively.

Figure H-2. Correlation plot for N_2O and CF_2Cl_2. The equation of the reference line is $CF_2Cl_2 = 1.5(N_2O) - 55.5$ pptv where N_2O is in units of ppbv. The standard deviations of the slope and intercept are 0.013 and 2.4, respectively.

Figure H-3. Correlation plot for N_2O and $CFCl_3$. The equation of the reference curve for the balloon and whole-air data is $CFCl_3 = 3.36(10^{-3})(N_2O)^2 - 0.218(N_2O) - 10.4$ pptv where N_2O is in units of ppbv. The standard deviations of the coefficients are $1.6(10^{-4})$, 0.06, and 5.8, respectively.

Figure H-4. Correlation plot for N_2O and $C_2F_3Cl_3$. The balloon $C_2F_3Cl_3$ data are multiplied by 1.37 to account for the different calibration standards used by the different measurement groups. The equation of the reference curve for the balloon and whole-air data is $C_2F_3Cl_3 = 3.93(10^{-4})(N_2O)^2 + 0.10(N_2O) - 5.25$ pptv where N_2O is in units of ppbv. The standard deviations of the coefficients are $4.9(10^{-5})$, 0.02, and 1.7, respectively.

Figure H-5. Correlation plot for N_2O and CHF_2Cl. The equation of the reference line is $CHF_2Cl = 0.166(N_2O) + 42.3$ pptv where N_2O is in units of ppbv. The standard deviations of the slope and intercept are 0.02 and 2.94, respectively.

Figure H-6. Correlation plot for N_2O and CH_3CCl_3. The equation of the reference curve is $CH_3CCl_3 = 2.87(10^{-3})(N_2O)^2 - 0.63(N_2O) + 35.3$ pptv for N_2O > 90 ppbv. The standard deviations of the coefficients are $1.4(10^{-4})$, 0.06, and 5.4, respectively.

Figure H-7. Correlation plot for N_2O and CCl_4. The equation of the reference curve is $CCl_4 = 1.02(10^{-3})(N_2O)^2 + 0.054(N_2O) - 15.0$ pptv where N_2O is in units of ppbv. The standard deviations of the coefficients are $1.4(10^{-4})$, 0.05, and 5.0, respectively.

Figure H-8. Correlation plot for N_2O and CH_3Cl.

Figure H-9. (a) The organic chlorine (CCl_y) sum versus N_2O from whole-air sample measurements in the Arctic and the Antarctic from *Kawa et al.* (1992). The solid and dashed curves are fit to the data by regression for a second degree polynomial and a line, respectively. The equations of the polynomial fits used to predict CCl_y from continuous N_2O measurements are $(CCl_y) = 2.79(10^{-5})\ (N_2O)^2 + 1.73(10^{-3})\ (N_2O) + 0.137$ in the Arctic and $(CCl_y) = 3.19(10^{-5})\ (N_2O)^2 + 0.76(10^{-3})\ (N_2O) + 0.013$ in the Antarctic, where (CCl_y) and (N_2O) are in ppbv. (b) Correlation plot for N_2O and Cl_y derived from the measurements of CCl_y and estimates for total chlorine appropriate to the measurement regime. The equations of the reference curves are $Cl_y = 3.3-(2.98(10^{-5})(N_2O)^2 + 1.65(10^{-3})(N_2O) + 0.13)$ pptv for the AASE and $3.3-(3.57(10^{-5})(N_2O)^2 + 0.85(10^{-3})(N_2O) + 0.02)$ pptv for the AAOE.

Figure H-10. Example correlation plot for N_2O and NO_y from the flight of 12 January 1989 in the AASE. Data are 10-s averages from a latitude range of 59 to 79° and a potential temperature of 460 ±10 K. From *Fahey et al.* (1990).

Figure H-11. Latitude profiles of (a) O_3, (b) NO_y , and simultaneously measured (c) NO_y/O_3

from the NASA ER-2 aircraft. Points are 120-s averages of 1-s data. Averages (triangles) and standard deviations (bars) are calculated over 5° latitude intervals.

Figure H-12. N_2O versus CH_4 for the DUPONT model. Model results are interpolated onto the standard UADP grid and species values are plotted at every second latitude grid point for each altitude level. The different symbols represent different latitude ranges. Triangles are for 90 to 30S, squares are for 20S to 20N, and circles are for 30 to 90N. Correlations at approximately the solstice and equinox are shown. The plots labeled het are for the model including heterogeneous reactions of N_2O_5 and $ClONO_2$ with H_2O on background sulfate aerosol particles. The reference line is a fit to the measured data as discussed in the measurements section above.

Figure H-13. N_2O versus CH_4 for the December gas phase simulation of each model as in Figure H-12. N_2O values greater than 308 ppbv in the GSFC model are a numerical artifact occurring near the north pole.

Figure H-14. N_2O versus CF_2Cl_2 (CFC-12) for each model as in Figure H-13.

Figure H-15. N_2O versus $CFCl_3$ (CFC-11) for each model as in Figure H-13.

Figure H-16. An example of N_2O versus $C_2F_3Cl_3$ (CFC-113) from the CAMED model as in Figure H-13.

Figure H-17. N_2O versus CHF_2Cl (HCFC-22) for each model as in Figure H-13.

Figure H-18. An example of N_2O versus CH_3CCl_3 from the LLNL model as in Figure H-13.

Figure H-19. An example of N_2O versus CCl_4 from the NCAR model as in Figure H-13.

Figure H-20. An example of N_2O versus CH_3Cl from the NOCAR model for January.

Figure H-21. N_2O versus Cl_y for each model as in Figure H-13.

Figure H-22. N_2O versus NO_y for each model as in Figure H-13.

Figure H-23. O_3, NO_y, and simultaneously sampled NO_y/O_3 as functions of latitude for the contributing models. Circles with error bars are measured averages as discussed in the measurements section. Lines are model results from March (dotted), September (dashed), and December (solid). Upper set of 3 lines for O_3 and NO_y is at $z^* = 20$ km and lower set is at $z^* = 18$ km. The measurements correspond most closely to the lower dashed curve south of about 30S, to the upper solid curve between about 30S and 30N, and between the lower solid and dotted curves north of about 30N. For NO_y/O_3 the lower set of lines in the tropics is for 20 km and the curves should bracket the observations.

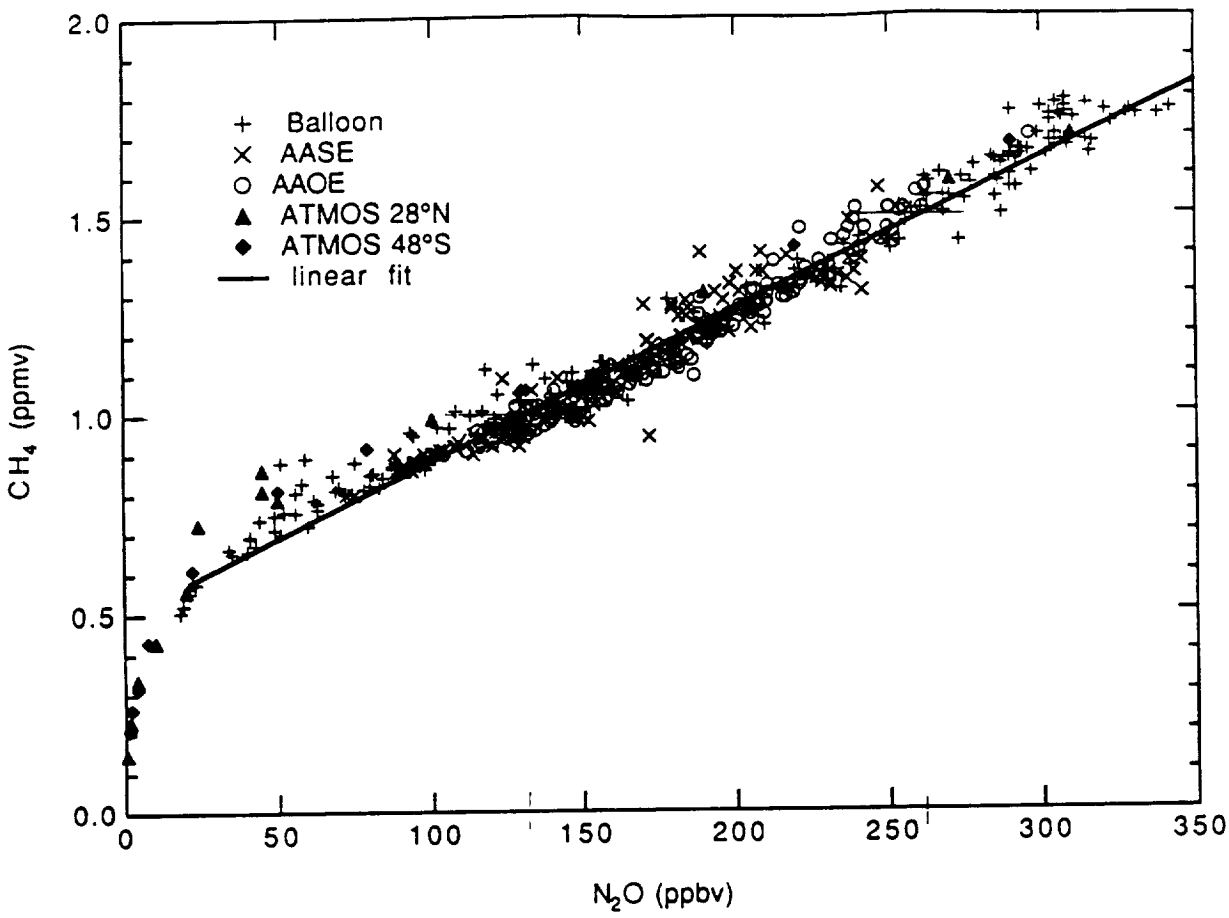
2.0
1.5
1.0
0.5
0.0
0
50
100
150
200
250
300
350
+ Balloon
× AASE
○ AAOE
▲ ATMOS 28°N
◆ ATMOS 48°S
— linear fit
CH4 (ppmv)
N2O (ppbv)

Figure H-1

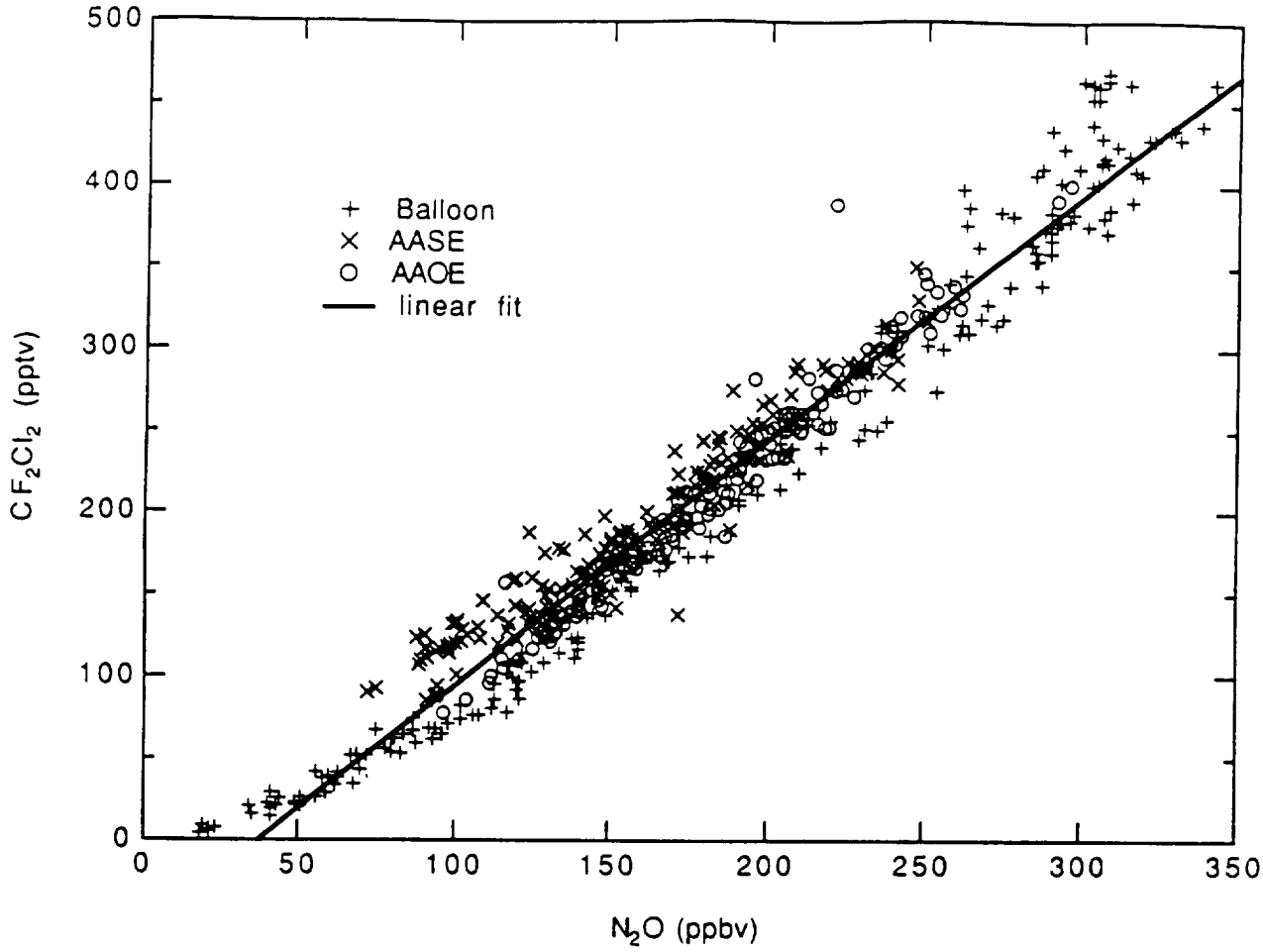
500
400
300
200
100
0
0
50
100
150
200
250
300
350
+ Balloon
× AASE
○ AAOE
linear fit
CF_2Cl_2 (pptv)
N_2O (ppbv)

Figure H-2

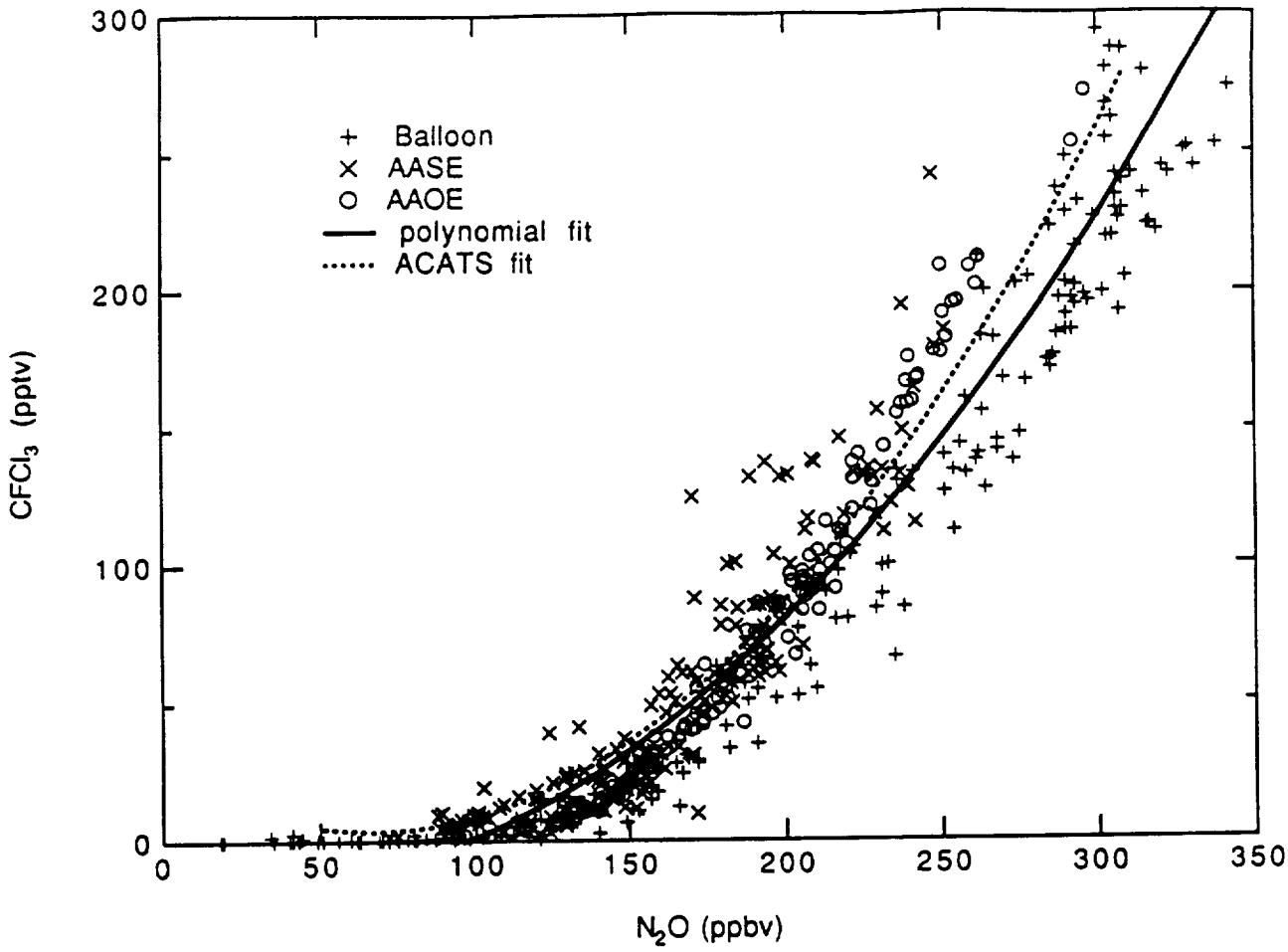
300
200
100
0
0
50
100
150
200
250
300
350
+ Balloon
× AASE
○ AAOE
polynomial fit
ACATS fit
CFCl3 (pptv)
N2O (ppbv)

Figure H-3

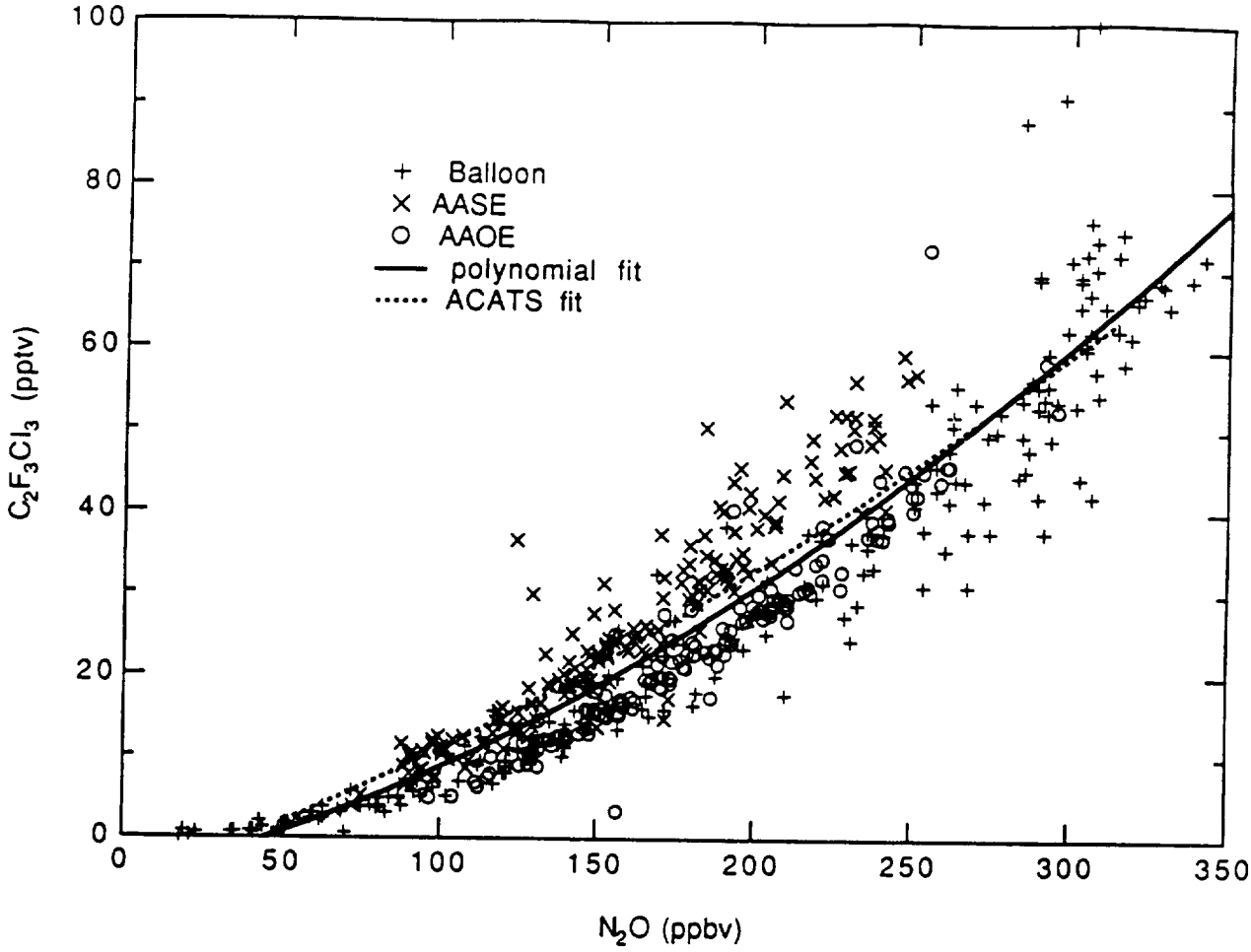
100
80
60
40
20
0
0
50
100
150
200
250
300
350
+ Balloon
× AASE
○ AAOE
polynomial fit
ACATS fit
$C_2F_3Cl_3$ (pptv)
N_2O (ppbv)

Figure H-4

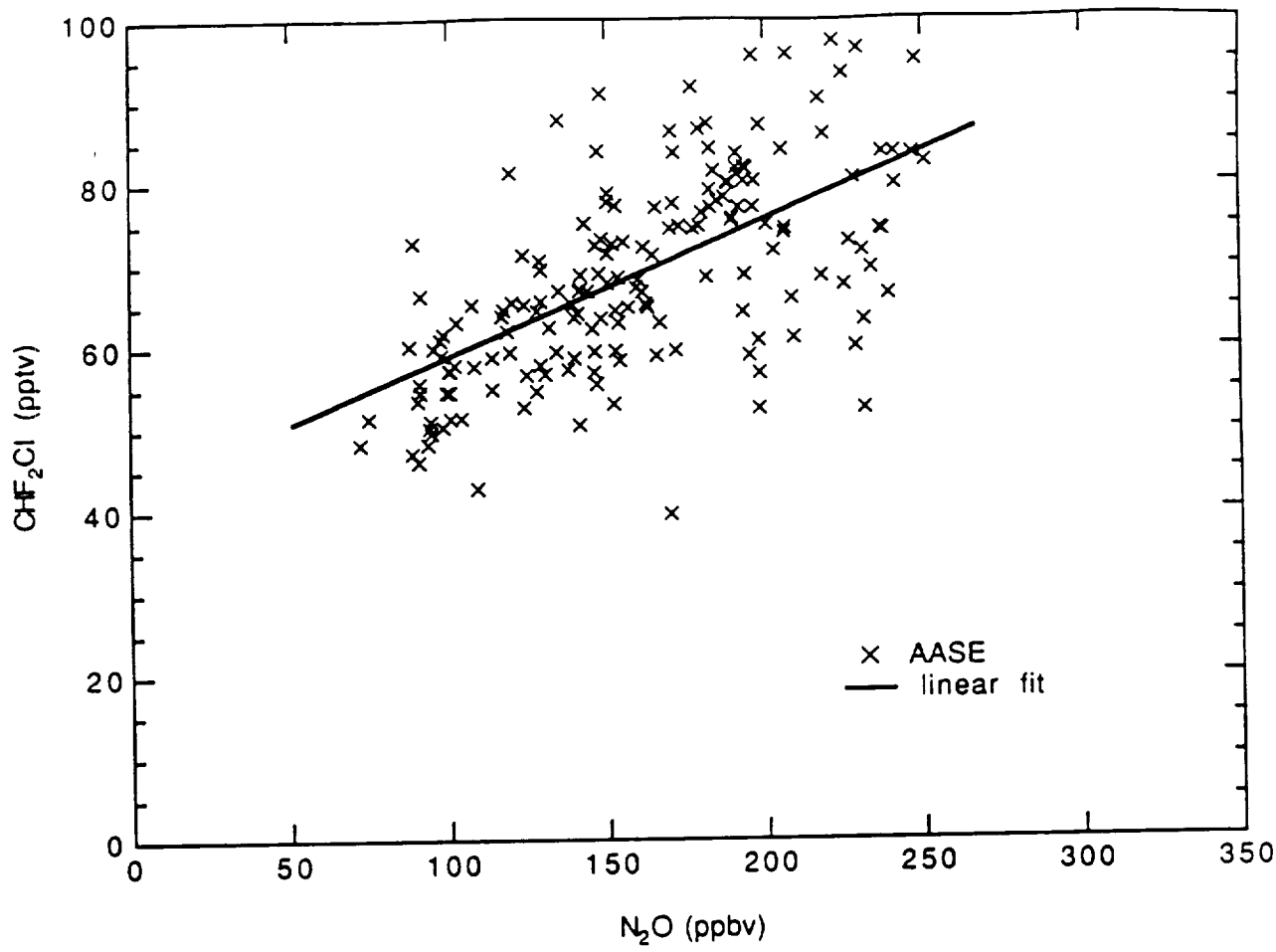
100
80
60
40
20
0
0
50
100
150
200
250
300
350
CHF_2Cl (pptv)
N_2O (ppbv)
AASE
linear fit

Figure H-5

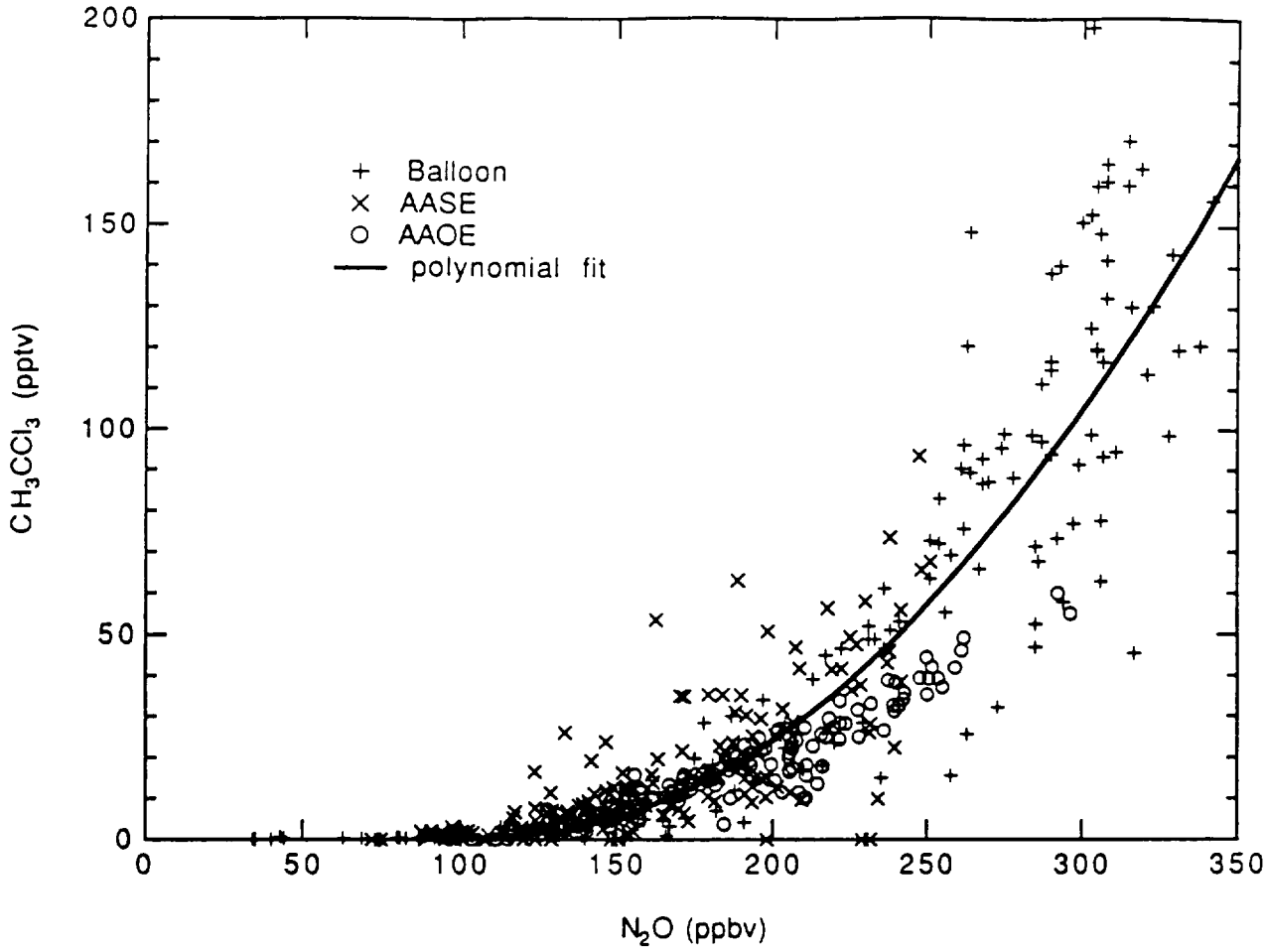
200
150
100
50
0
0
50
100
150
200
250
300
350
+ Balloon
× AASE
○ AAOE
polynomial fit
CH_3CCl_3 (pptv)
N_2O (ppbv)

Figure H-6

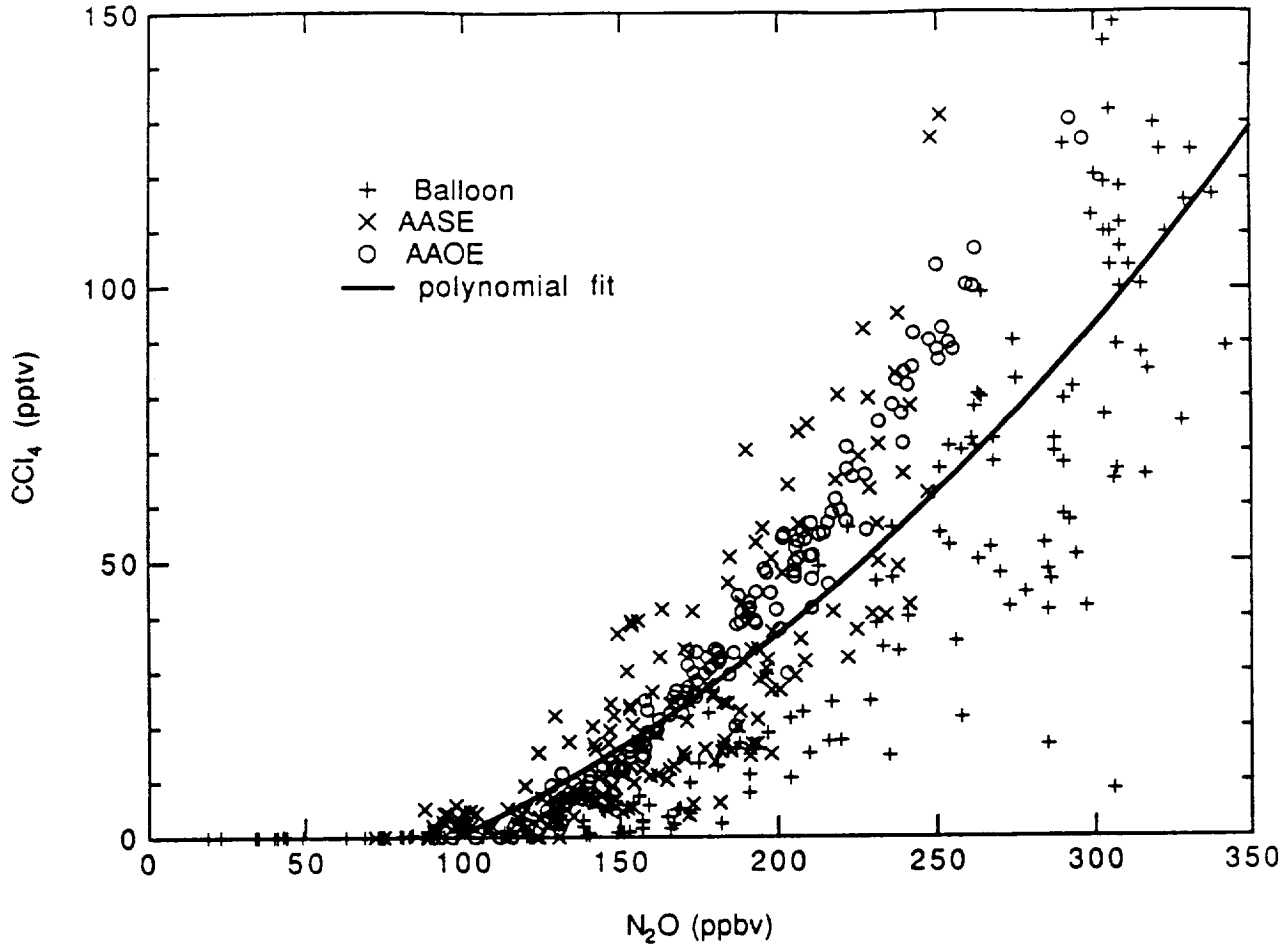
150
100
50
0
0
50
100
150
200
250
300
350
+ Balloon
× AASE
○ AAOE
polynomial fit
CCl_4 (pptv)
N_2O (ppbv)

Figure H-7

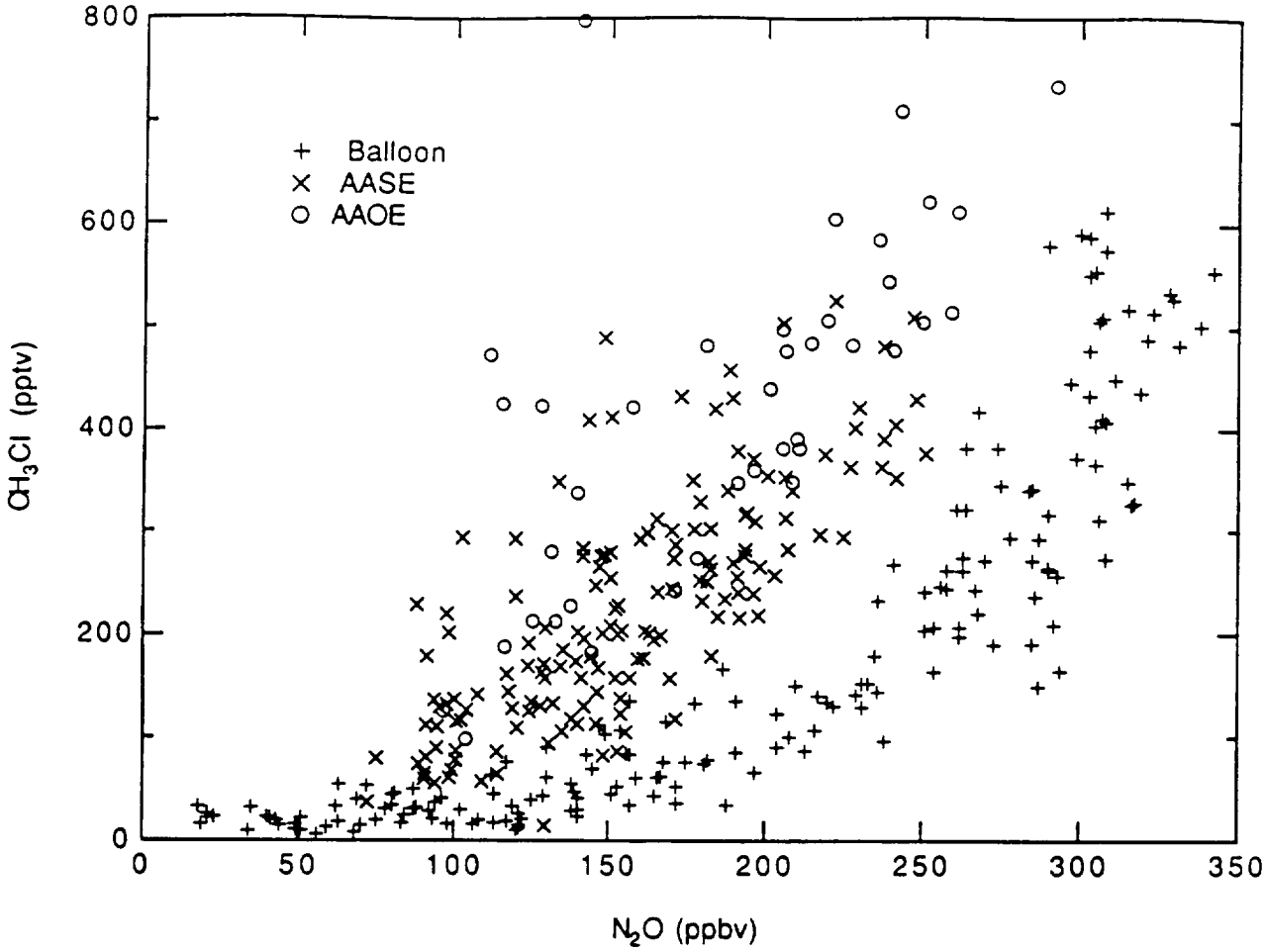
800
600
400
200
0
0
50
100
150
200
250
300
350
+ Balloon
× AASE
○ AAOE
CH3Cl (pptv)
N2O (ppbv)

Figure H-8

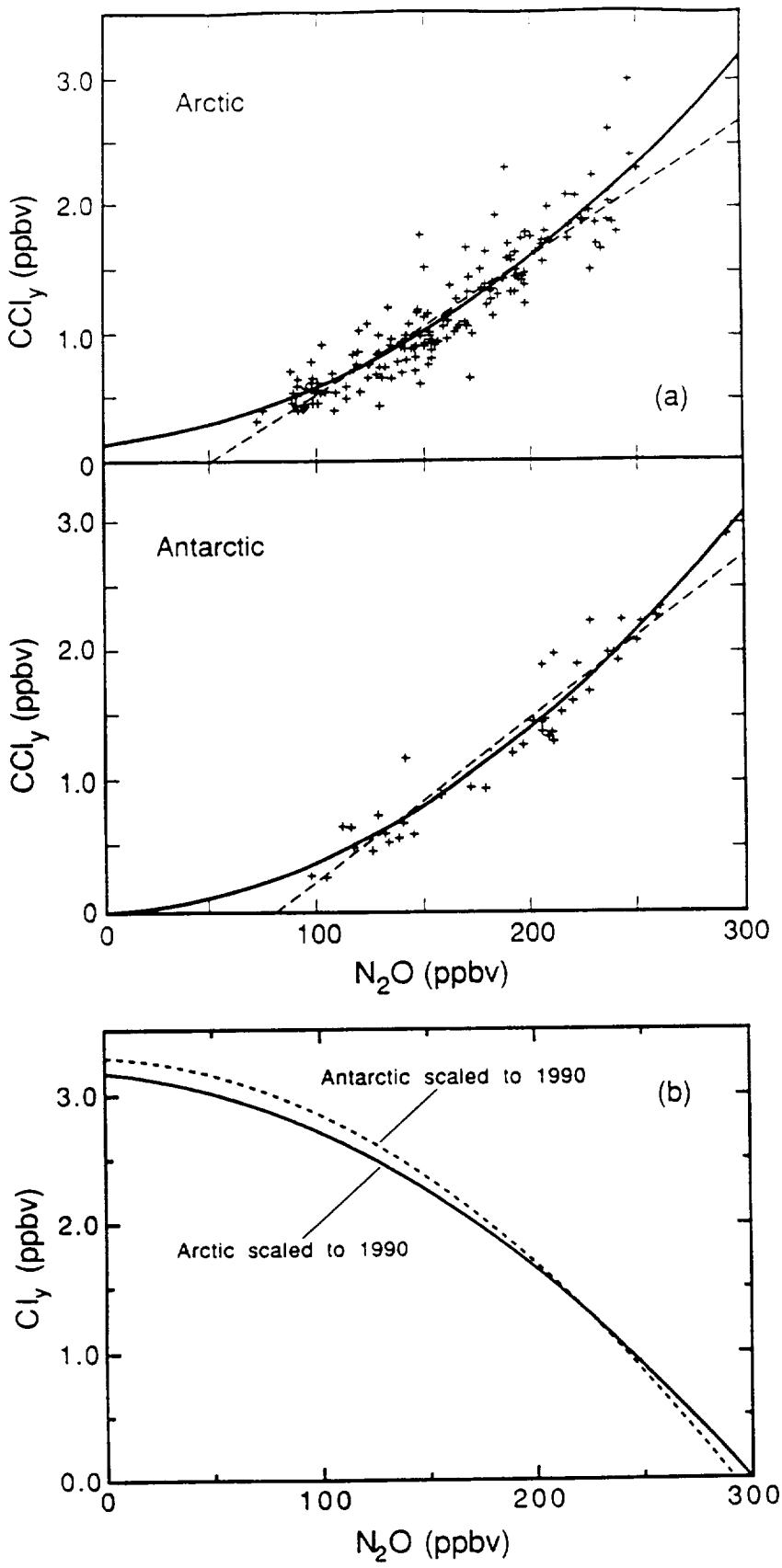
Arctic
(a)
Antarctic
CCl_y (ppbv)
N_2O (ppbv)
0
1.0
2.0
3.0
100
200
300
Antarctic scaled to 1990
Arctic scaled to 1990
(b)
Cl_y (ppbv)
0.0

Figure H-9

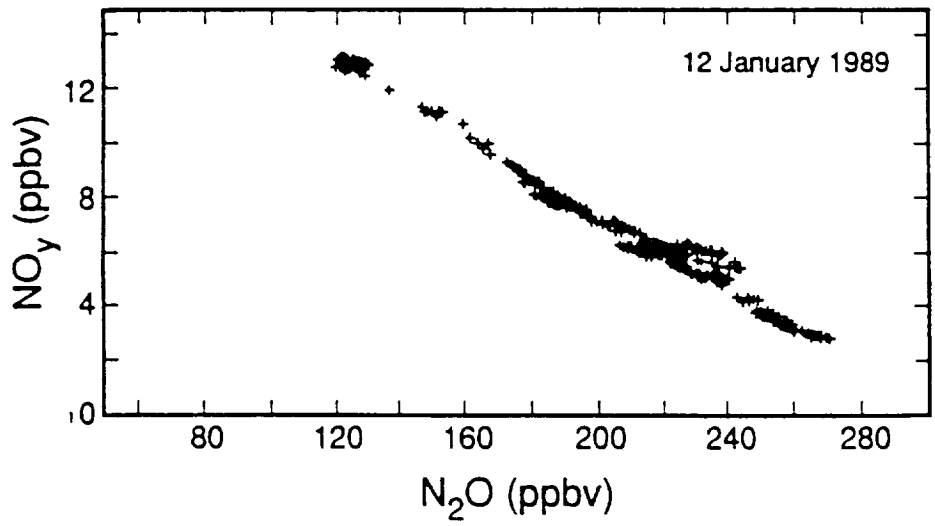

Figure H-10

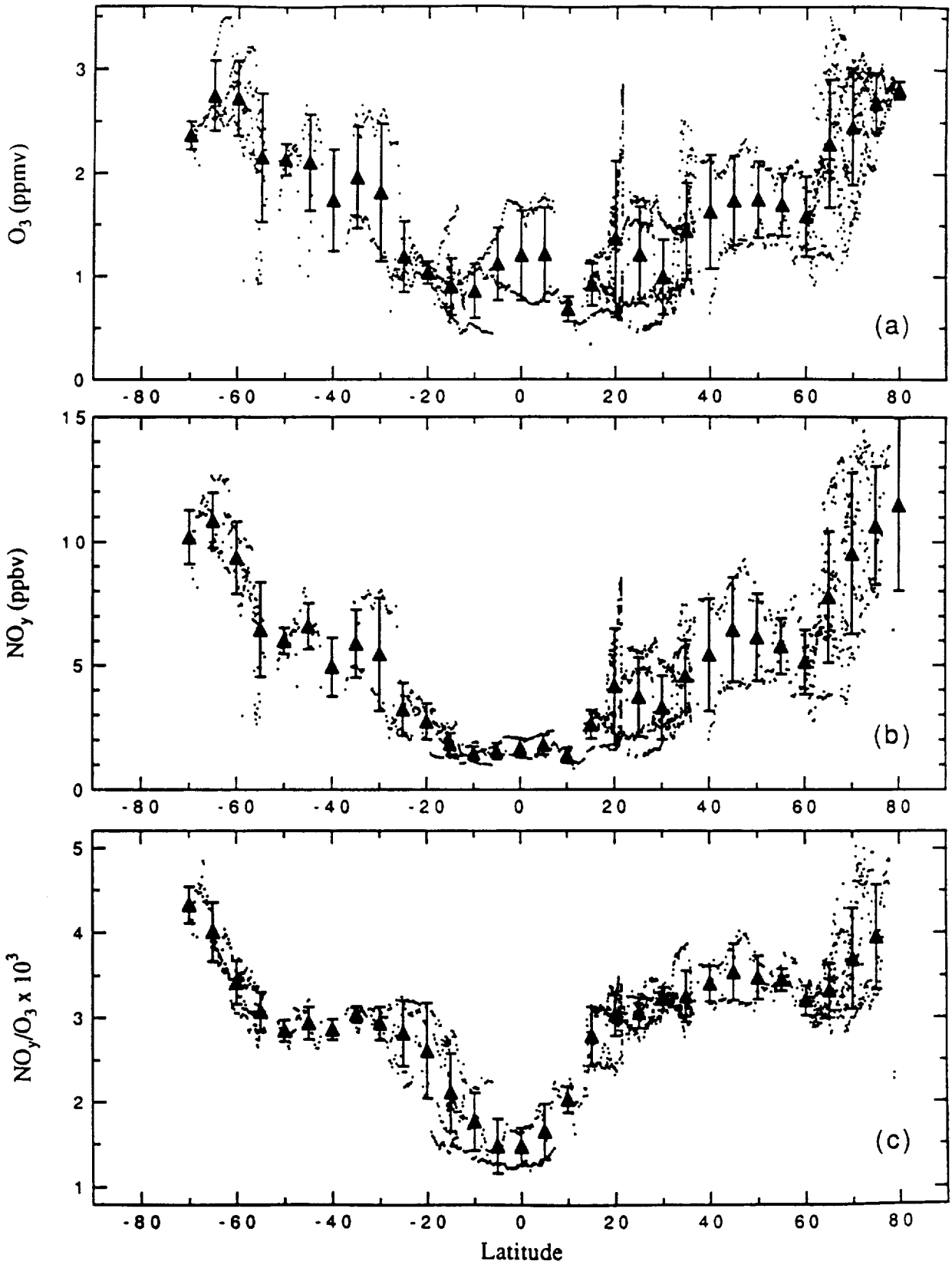

Figure H-11

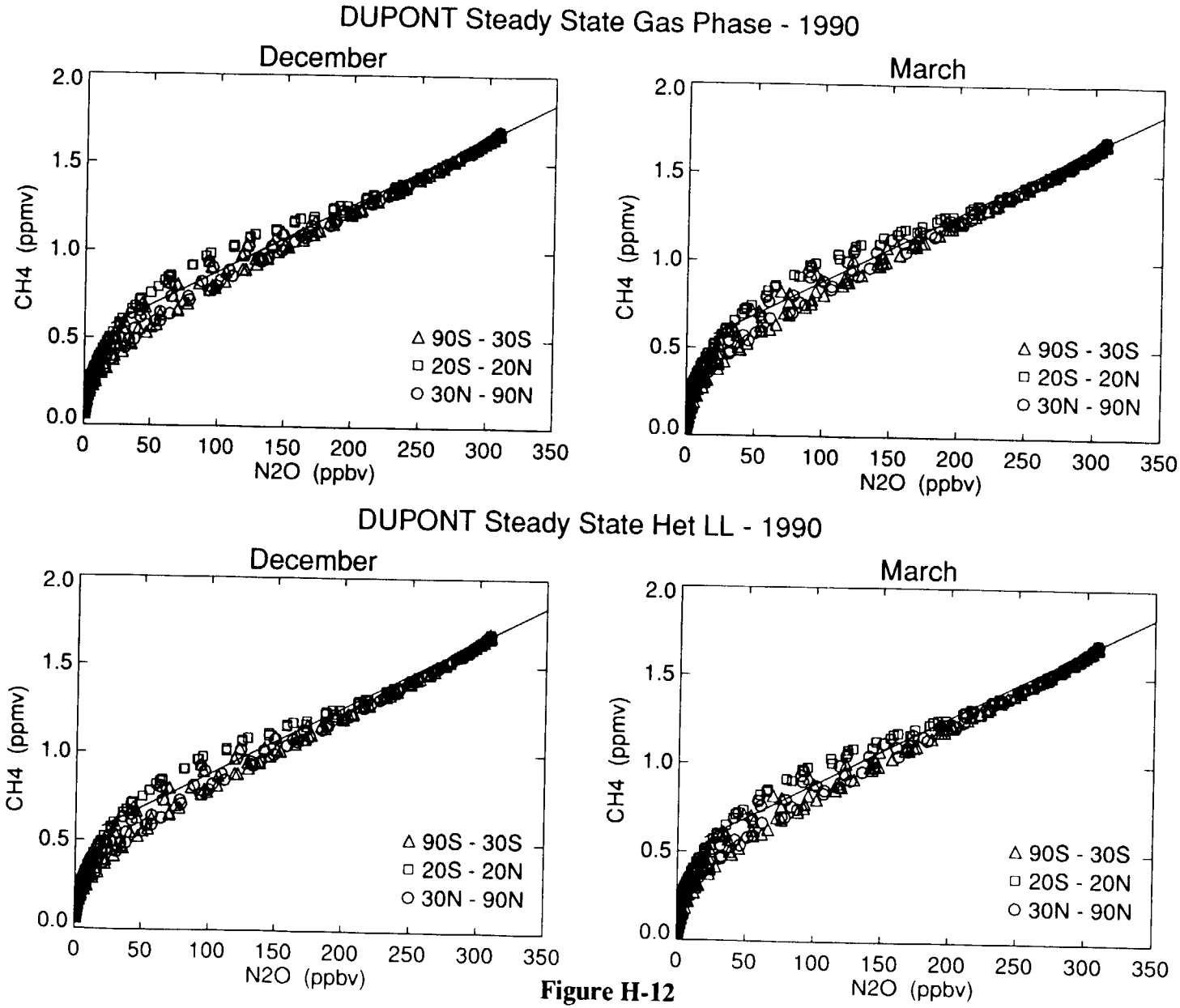
DUPONT Steady State Gas Phase - 1990
December
March
DUPONT Steady State Het LL - 1990
December
March
CH4 (ppmv)
N2O (ppbv)
0.0
0.5
1.0
1.5
2.0
0
50
100
150
200
250
300
350
△ 90S - 30S
□ 20S - 20N
○ 30N - 90N

Figure H-12

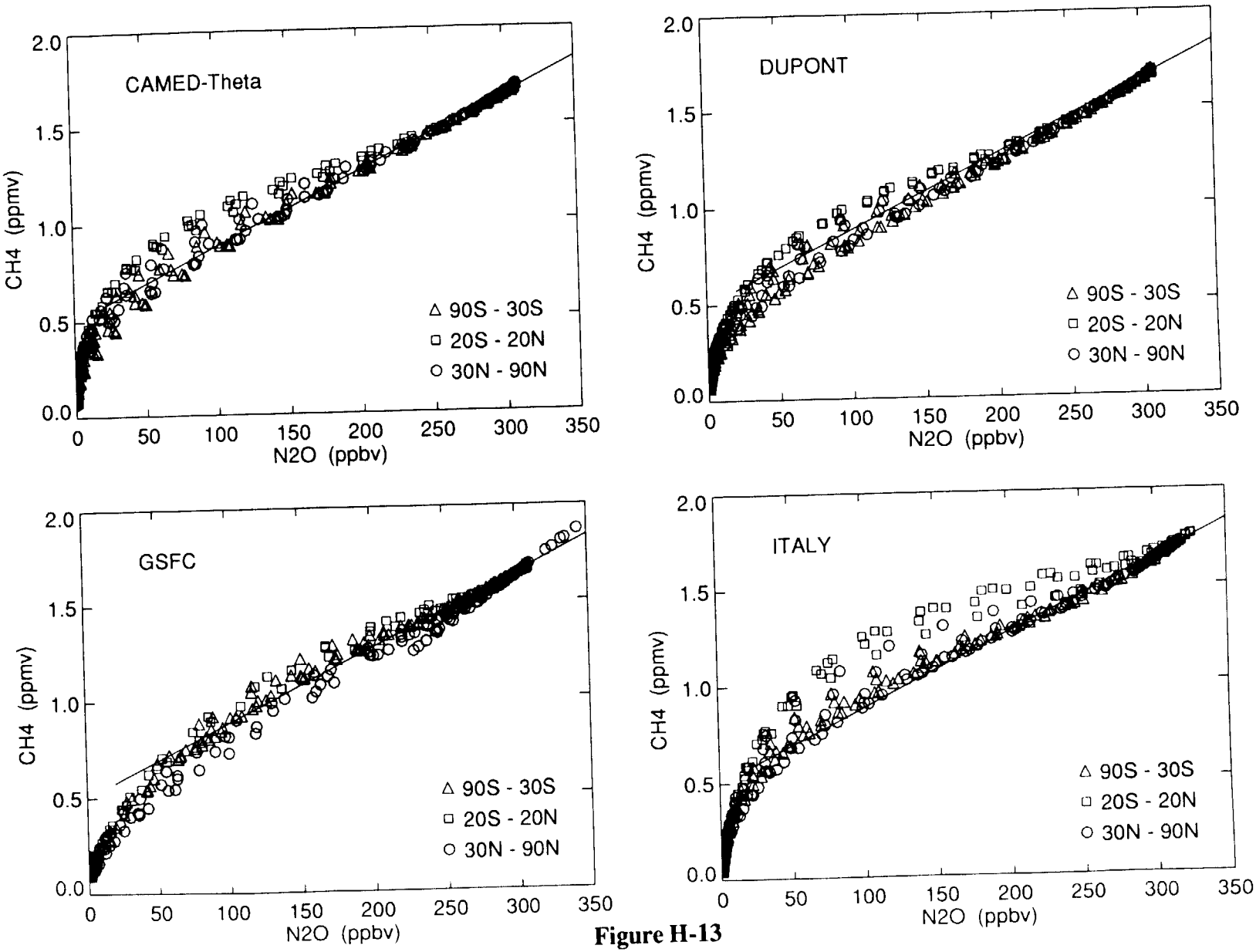
CAMED-Theta
DUPONT
GSFC
ITALY
CH4 (ppmv)
N2O (ppbv)
0.0
0.5
1.0
1.5
2.0
0
50
100
150
200
250
300
350
△ 90S - 30S
□ 20S - 20N
○ 30N - 90N

Figure H-13

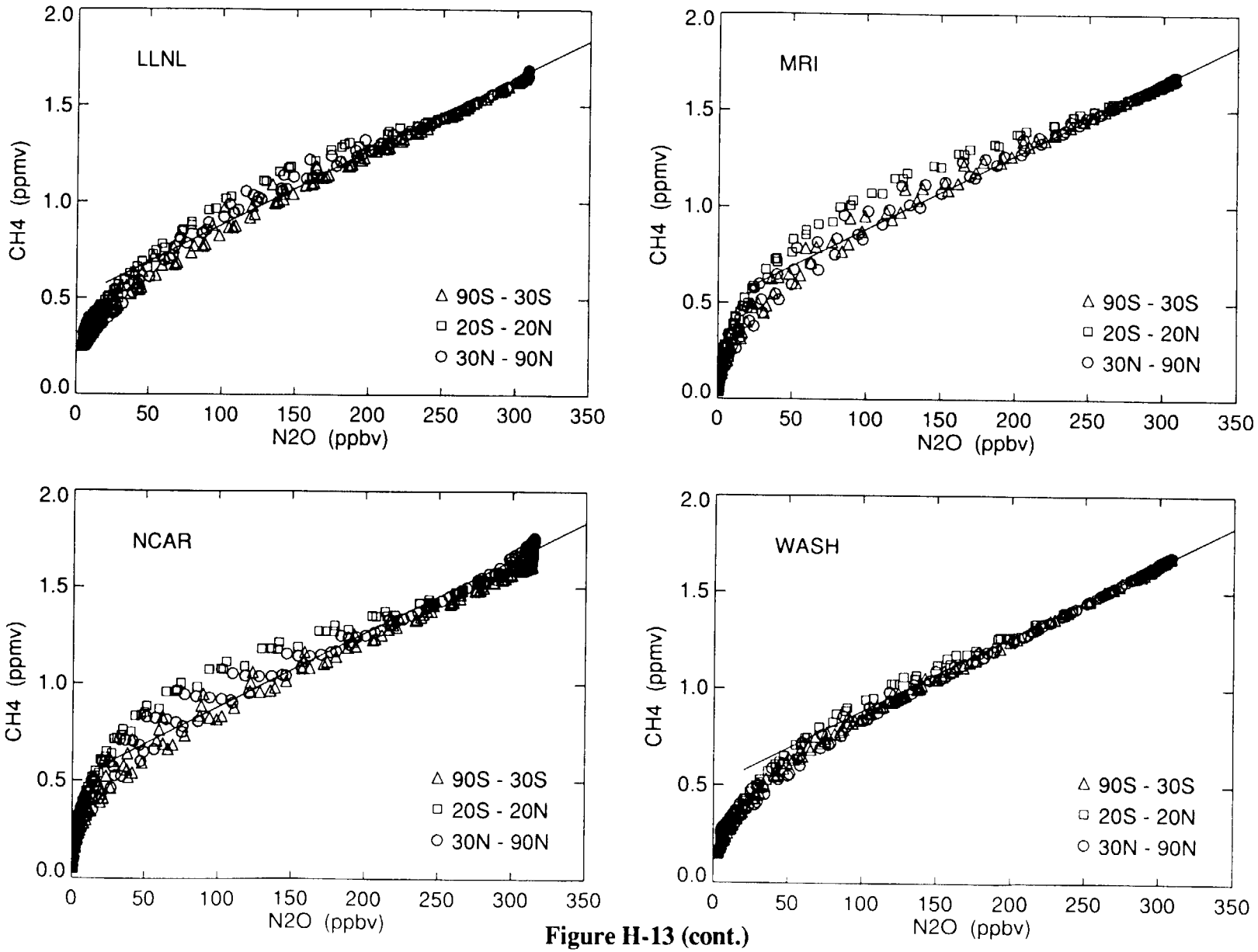

Figure H-13 (cont.)

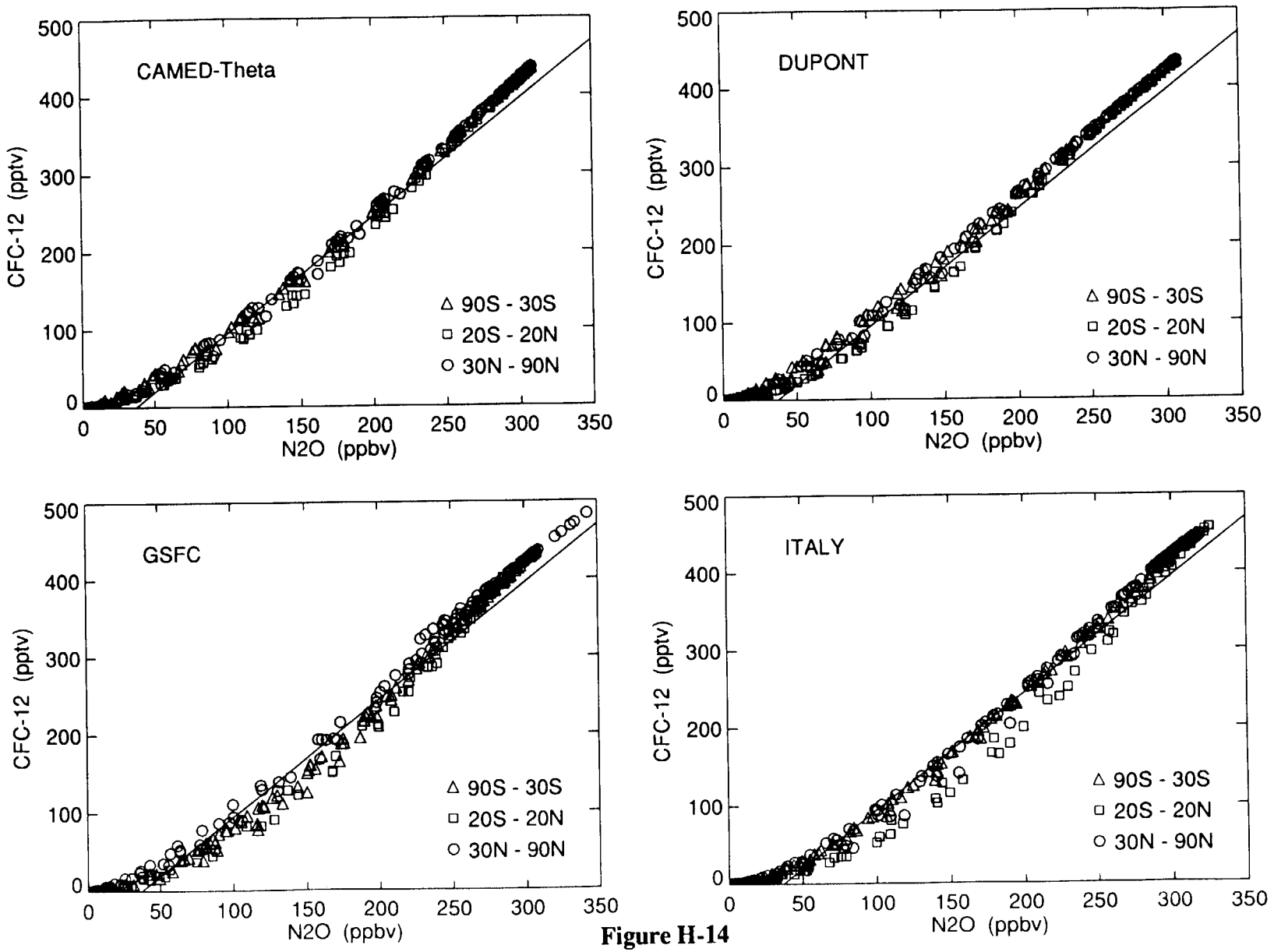
CAMED-Theta
DUPONT
GSFC
ITALY
CFC-12 (pptv)
N2O (ppbv)
0
50
100
150
200
250
300
350
100
200
300
400
500
△ 90S - 30S
□ 20S - 20N
○ 30N - 90N

Figure H-14

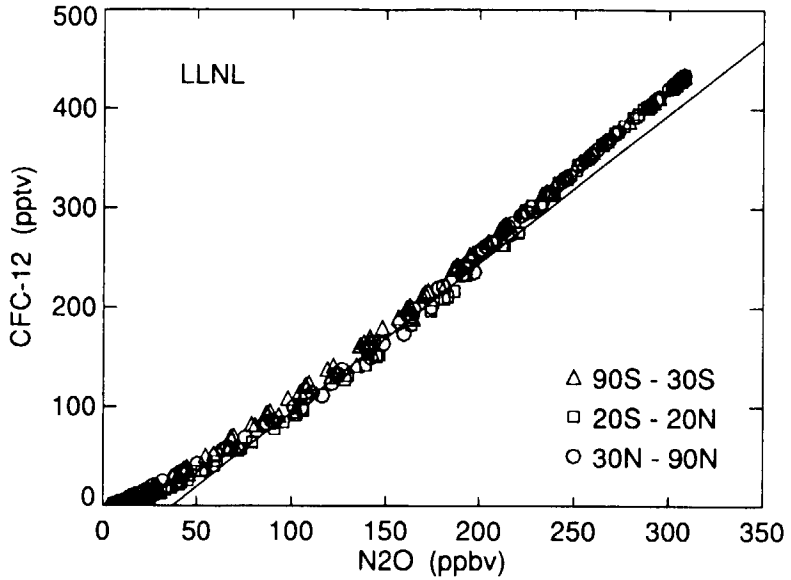

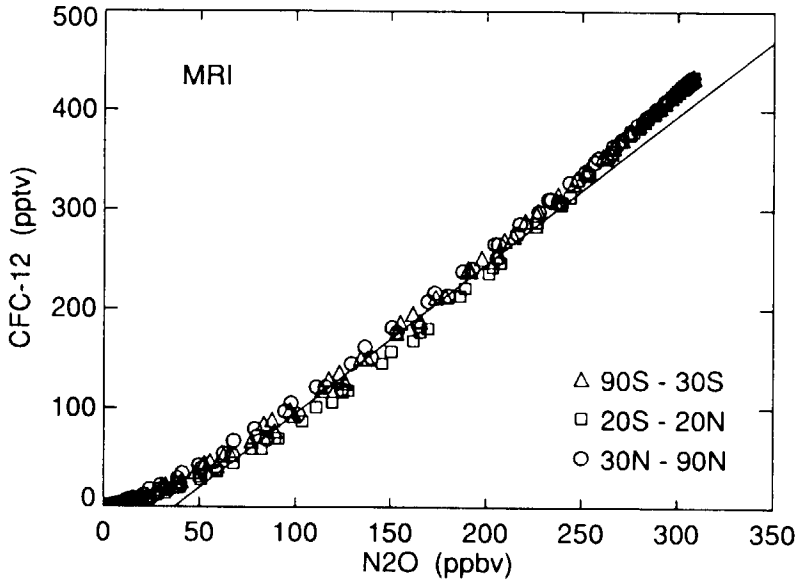

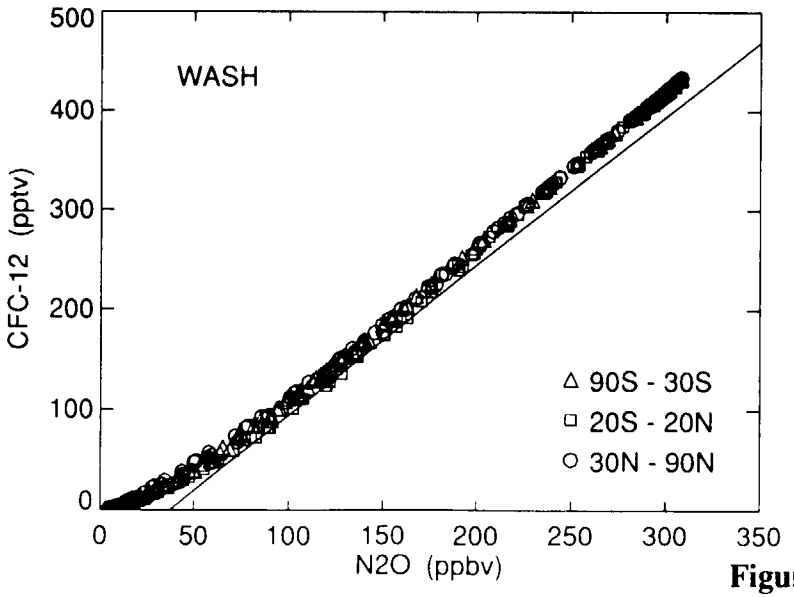

Figure H-14 (cont.)

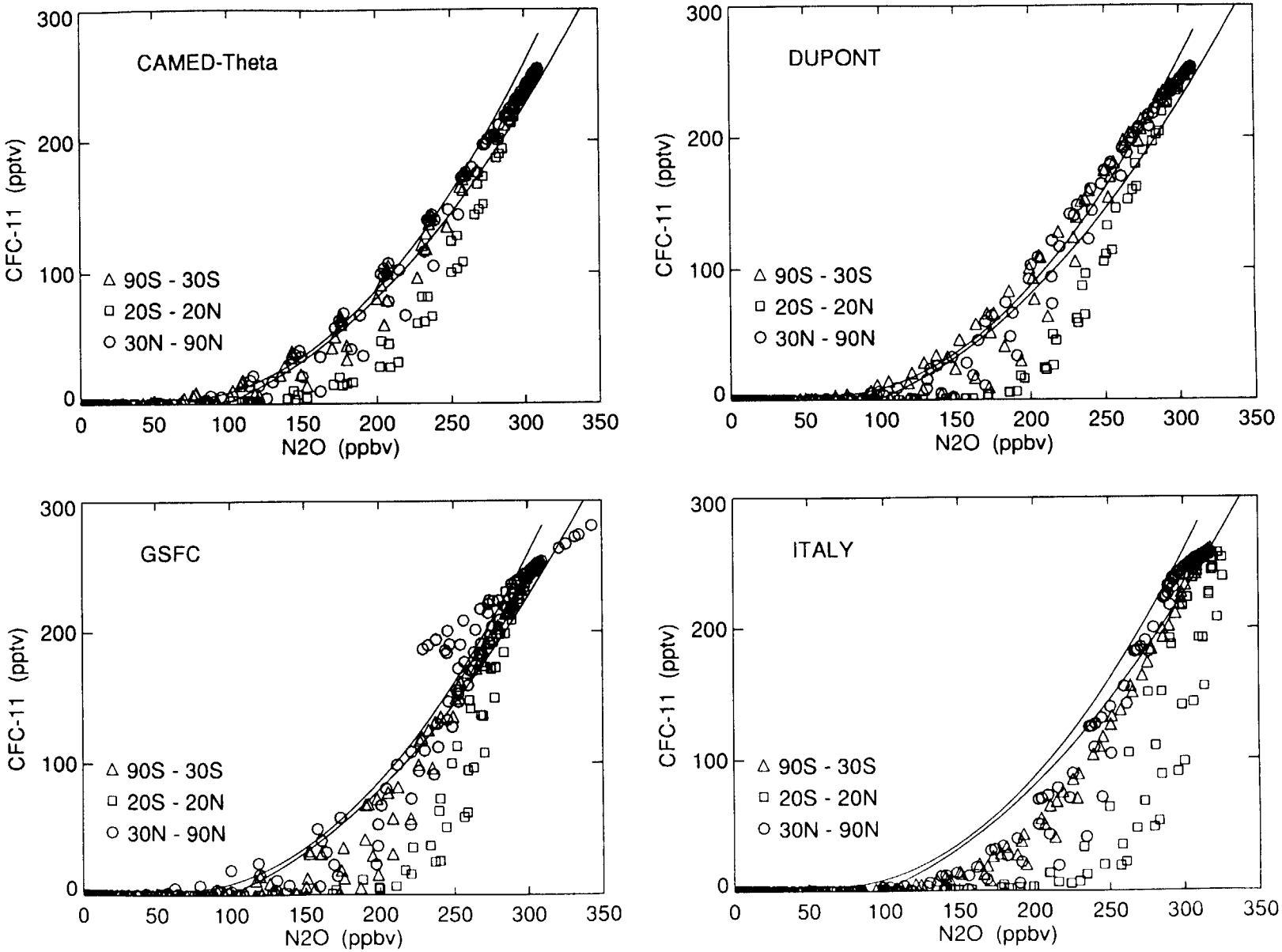
CAMED-Theta
DUPONT
GSFC
ITALY
CFC-11 (pptv)
N2O (ppbv)
90S - 30S
20S - 20N
30N - 90N
0
50
100
150
200
250
300
350

Figure H-15

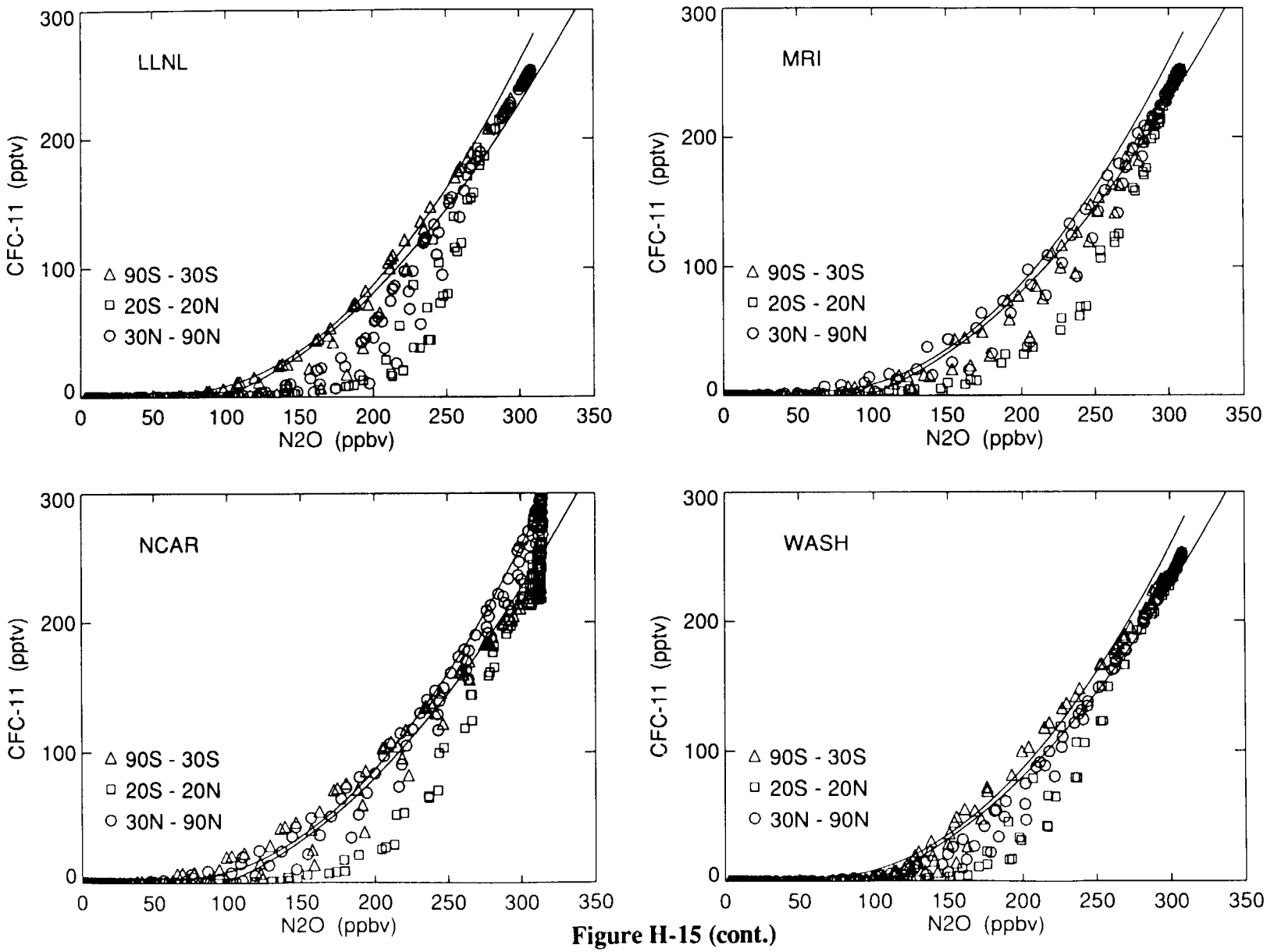

Figure H-15 (cont.)

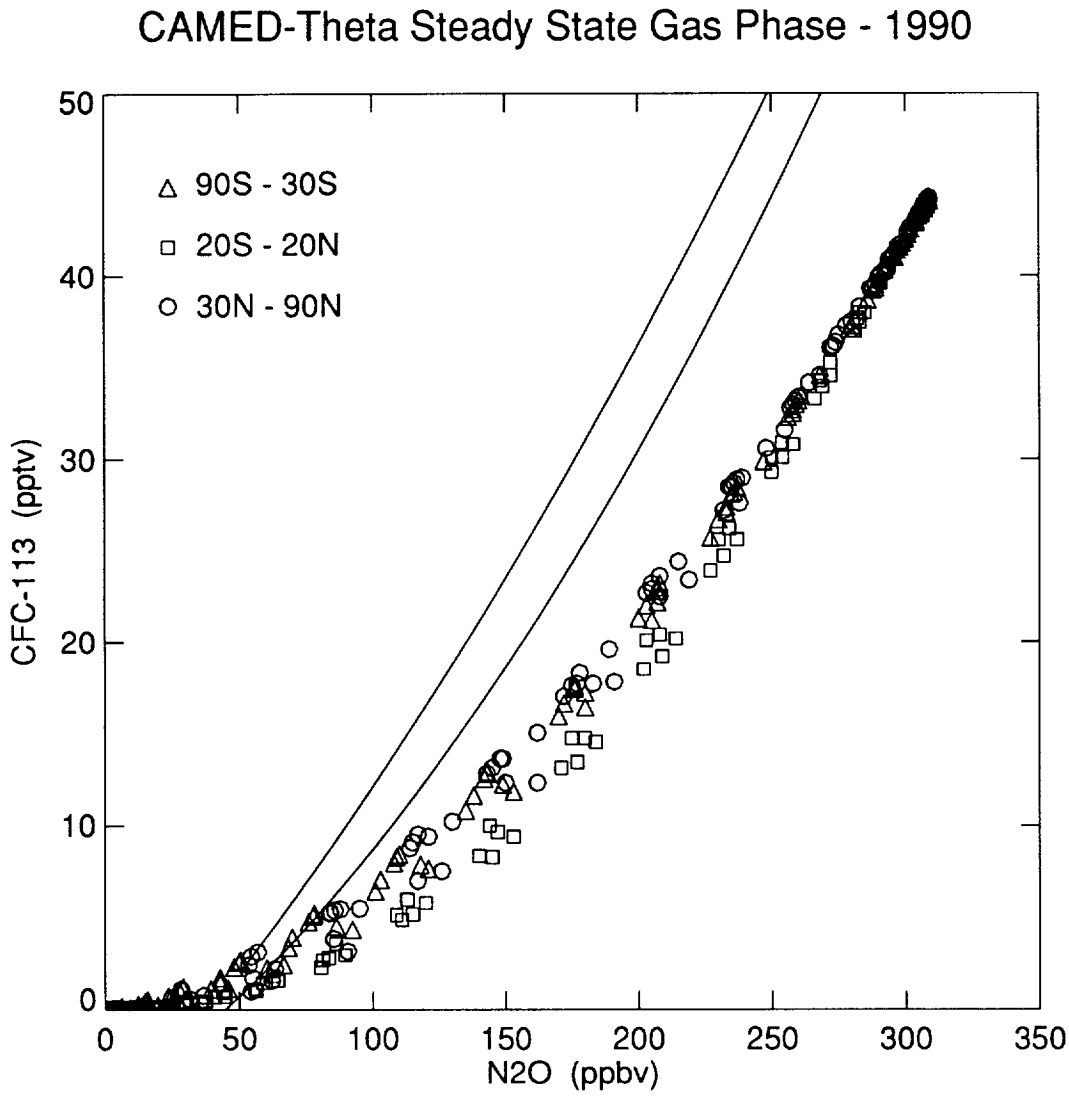
CAMED-Theta Steady State Gas Phase - 1990
90S - 30S
20S - 20N
30N - 90N
CFC-113 (pptv)
N2O (ppbv)
0
10
20
30
40
50
0
50
100
150
200
250
300
350

Figure H-16

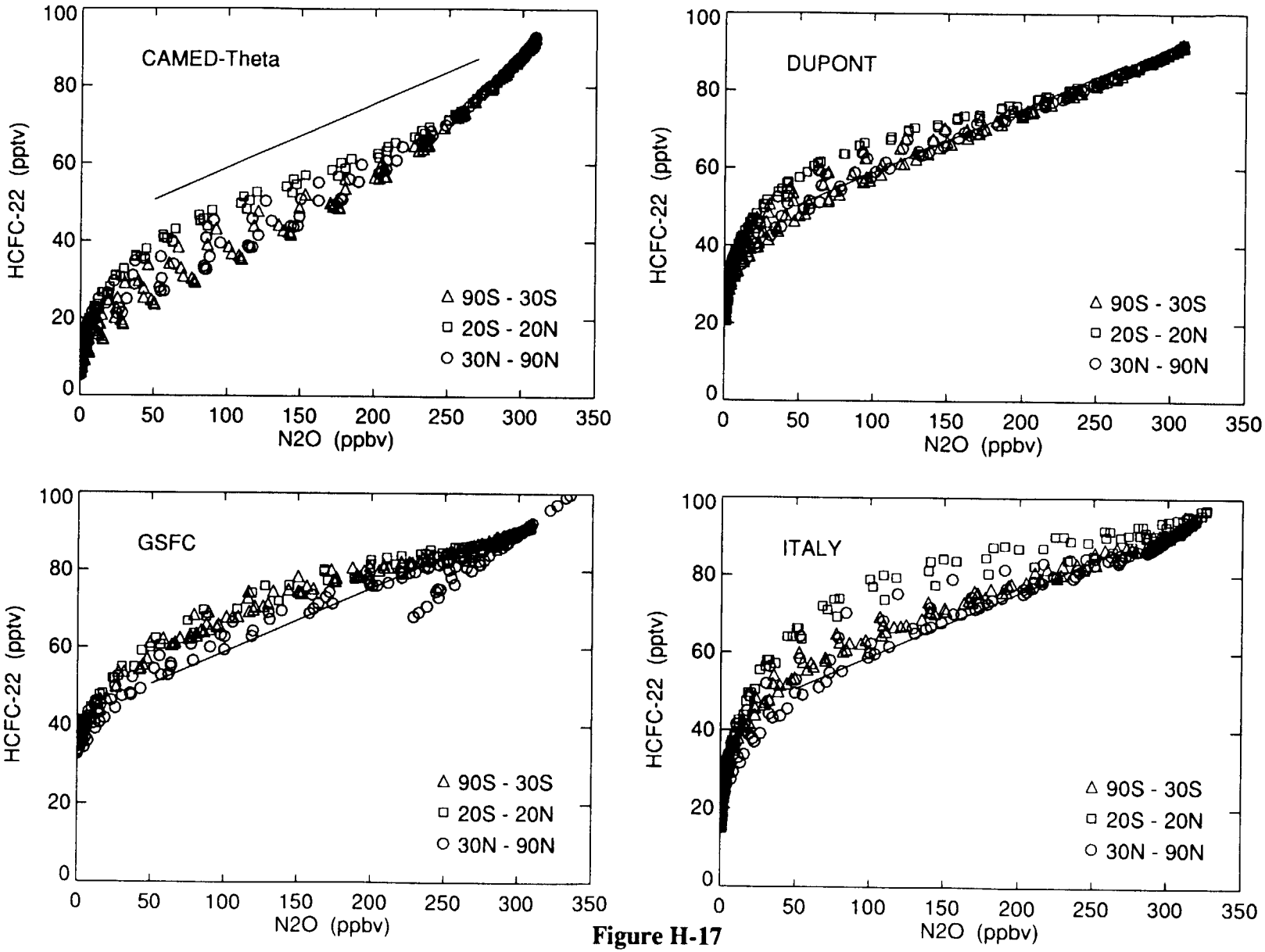
CAMED-Theta
DUPONT
GSFC
ITALY
HCFC-22 (pptv)
N2O (ppbv)
0
20
40
60
80
100
0
50
100
150
200
250
300
350
△ 90S - 30S
□ 20S - 20N
○ 30N - 90N

Figure H-17

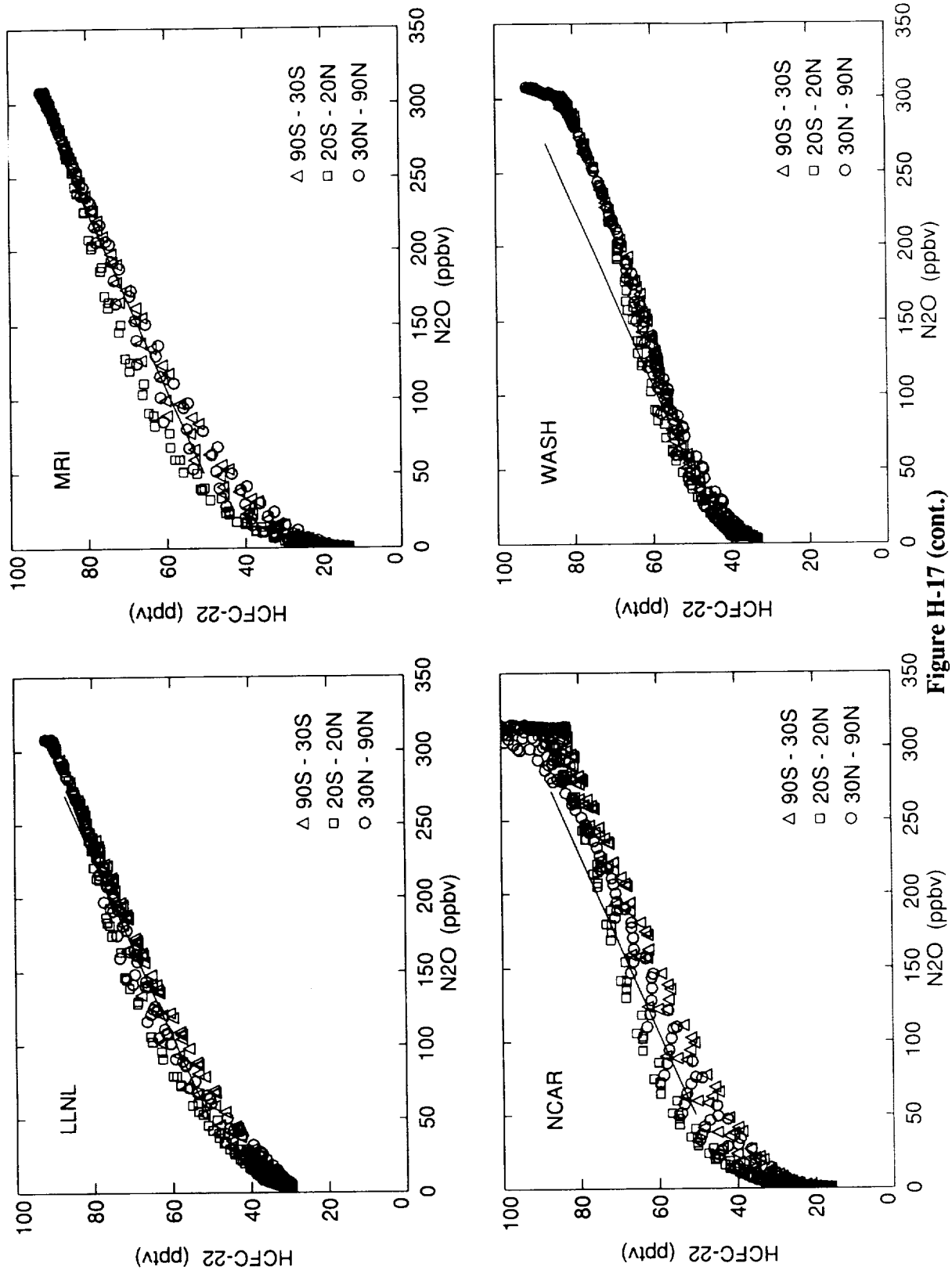

Figure H-17 (cont.)

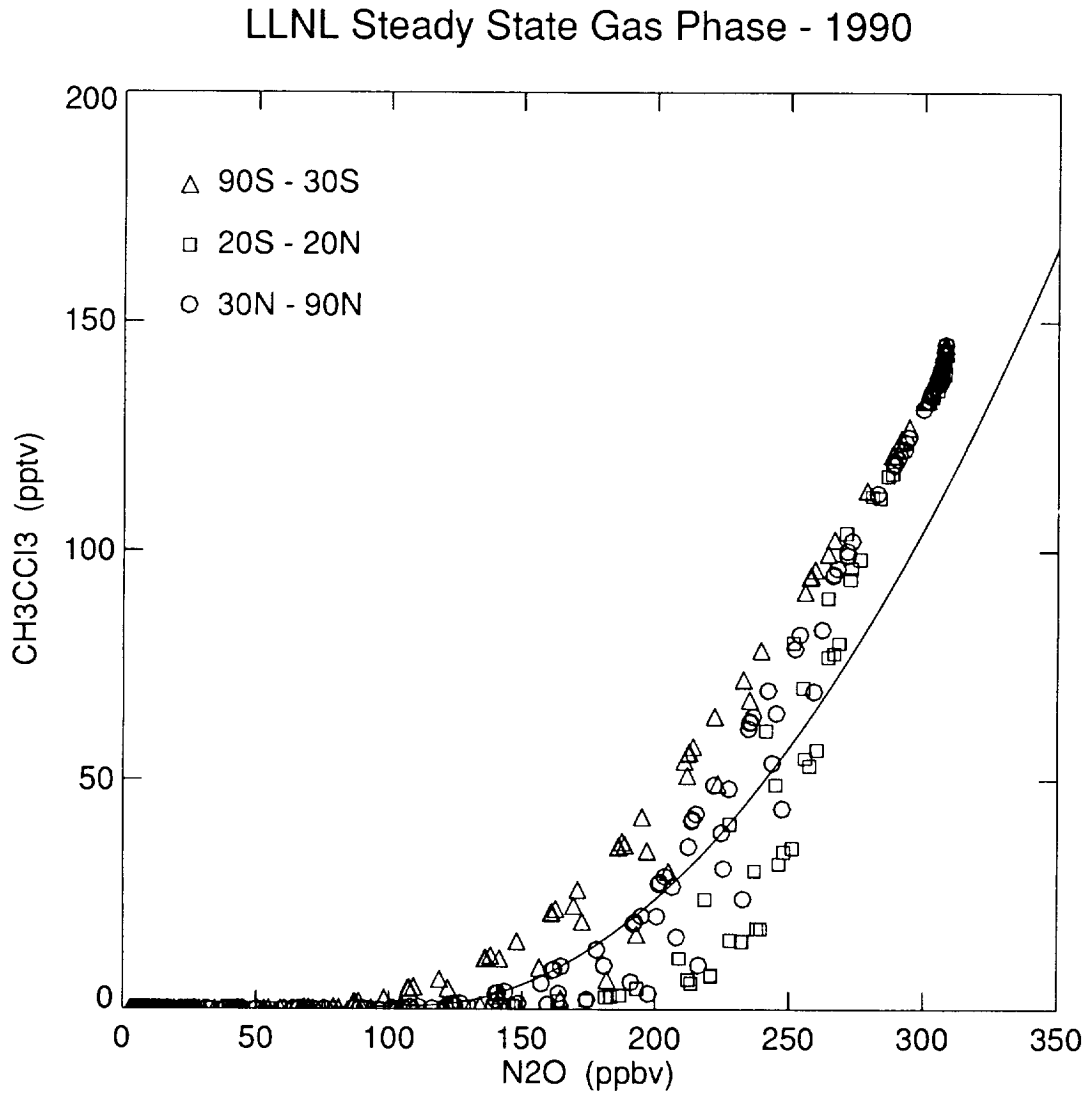
LLNL Steady State Gas Phase - 1990
90S - 30S
20S - 20N
30N - 90N
CH3CCl3 (pptv)
N2O (ppbv)
0
50
100
150
200
250
300
350

Figure H-18

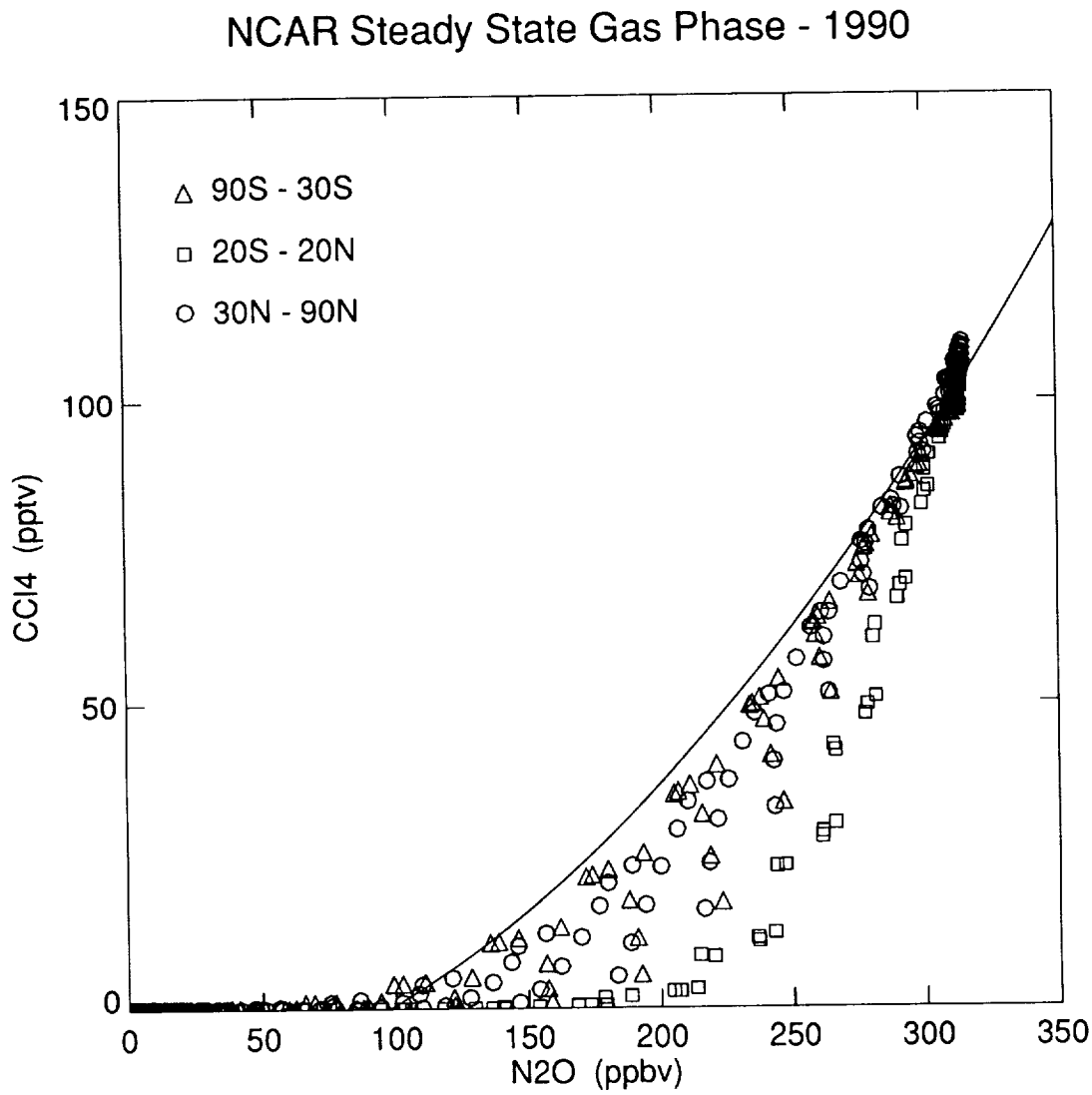
NCAR Steady State Gas Phase - 1990
90S - 30S
20S - 20N
30N - 90N
CCl4 (pptv)
N2O (ppbv)
0
50
100
150
200
250
300
350

Figure H-19

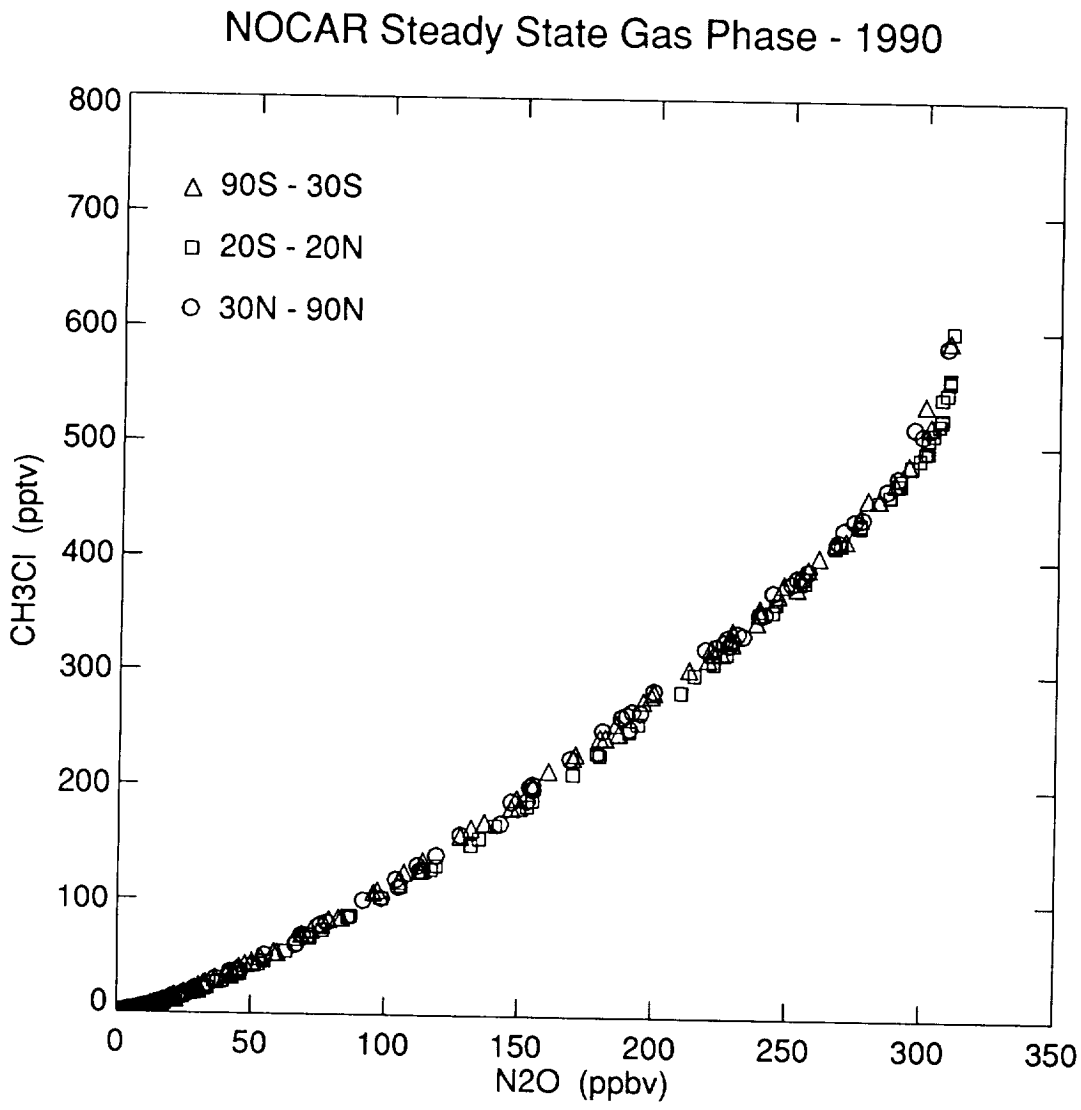
NOCAR Steady State Gas Phase - 1990
90S - 30S
20S - 20N
30N - 90N
CH3Cl (pptv)
N2O (ppbv)
0
100
200
300
400
500
600
700
800
0
50
100
150
200
250
300
350

Figure H-20

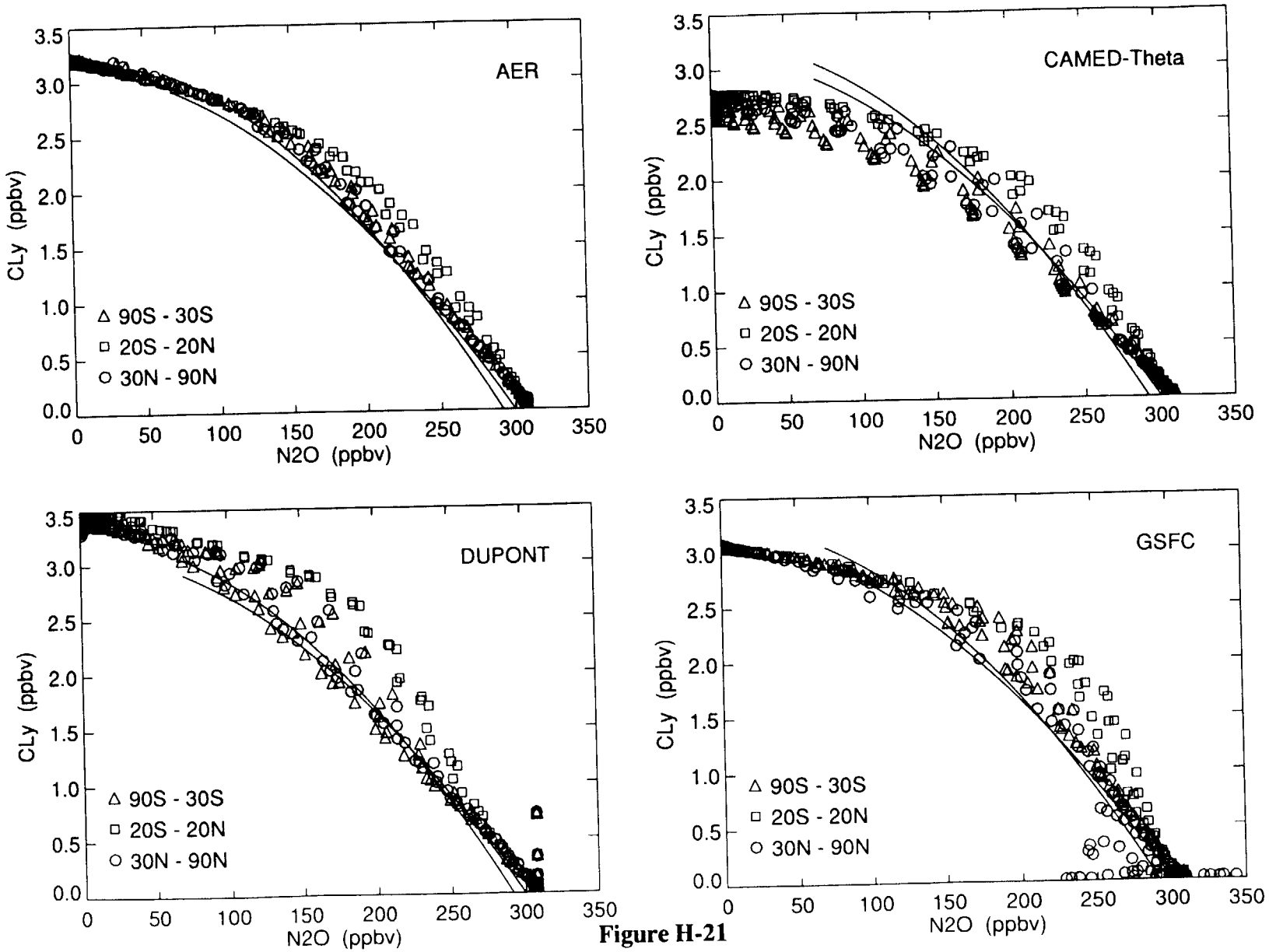
AER
CAMED-Theta
DUPONT
GSFC
CLy (ppbv)
N2O (ppbv)
90S - 30S
20S - 20N
30N - 90N
0.0
0.5
1.0
1.5
2.0
2.5
3.0
3.5
0
50
100
150
200
250
300
350

Figure H-21

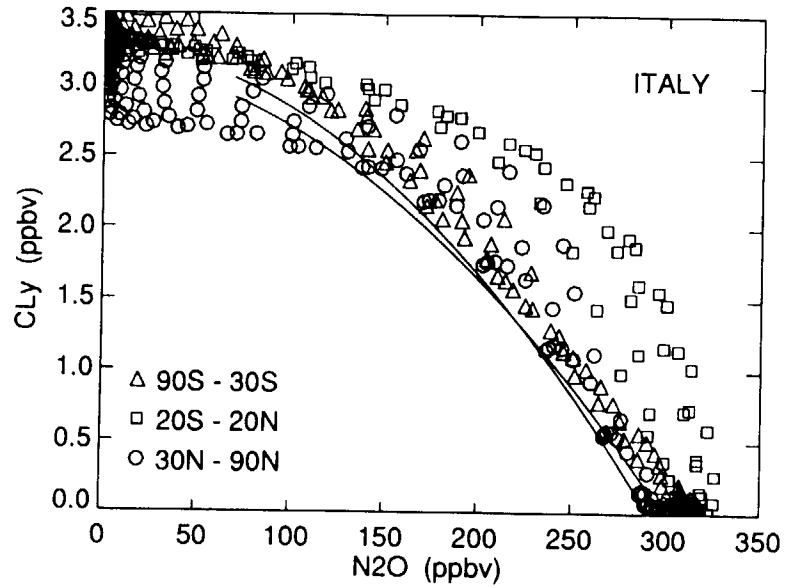

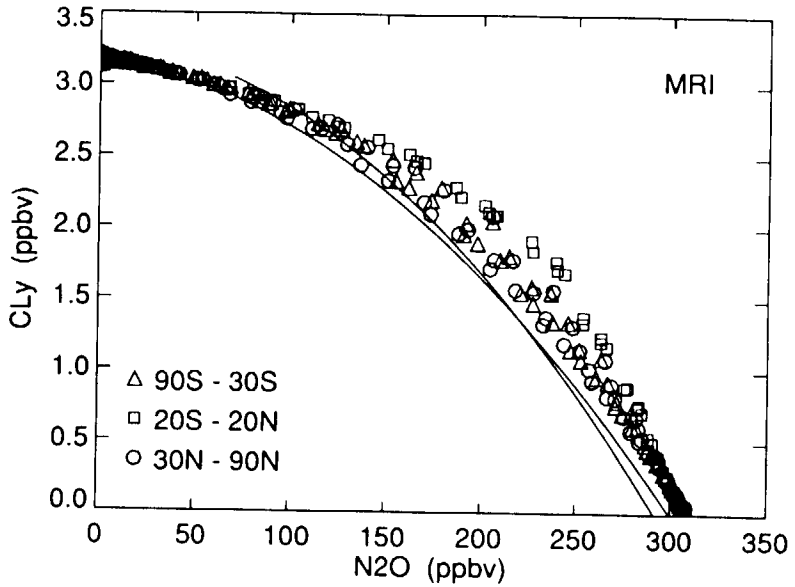

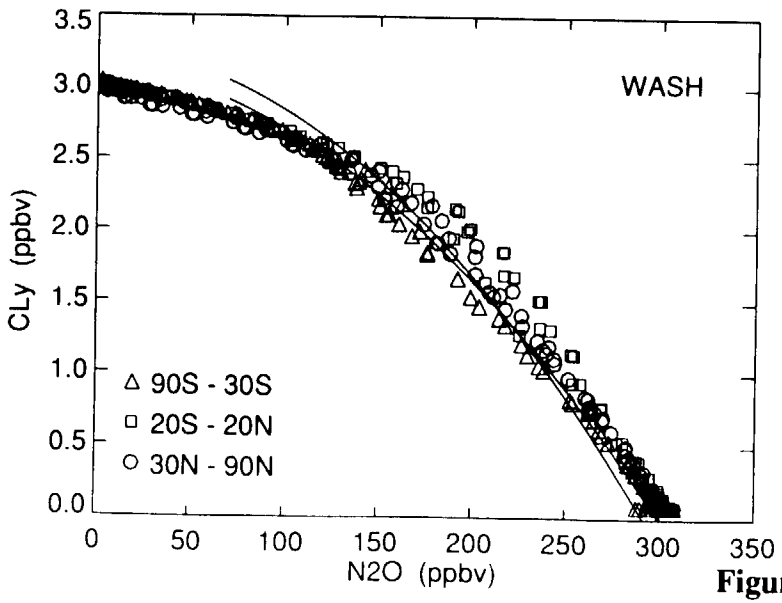

Figure H-21 (cont.)

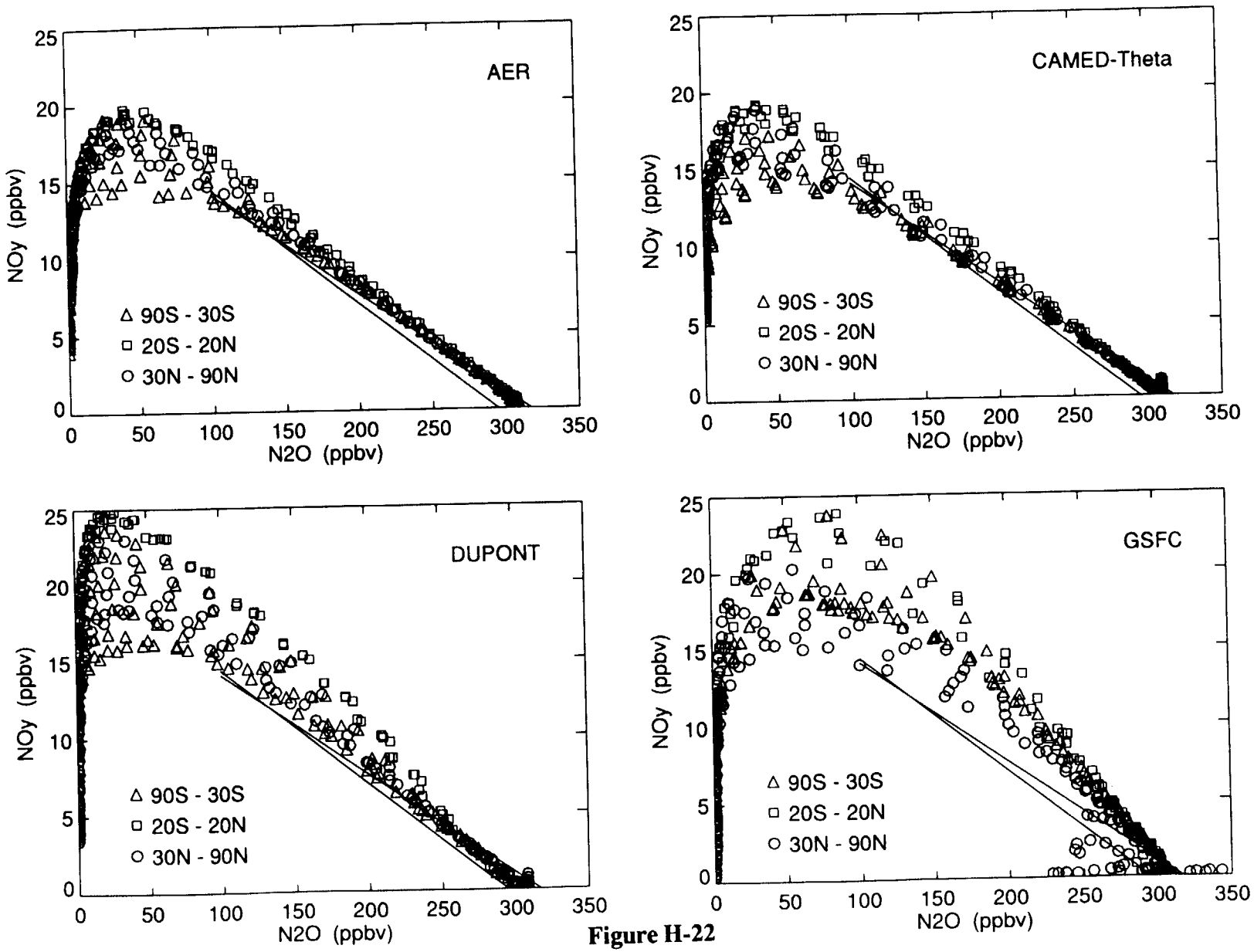
AER
CAMED-Theta
DUPONT
GSFC
NOy (ppbv)
N2O (ppbv)
90S - 30S
20S - 20N
30N - 90N
0
5
10
15
20
25
0
50
100
150
200
250
300
350

Figure H-22

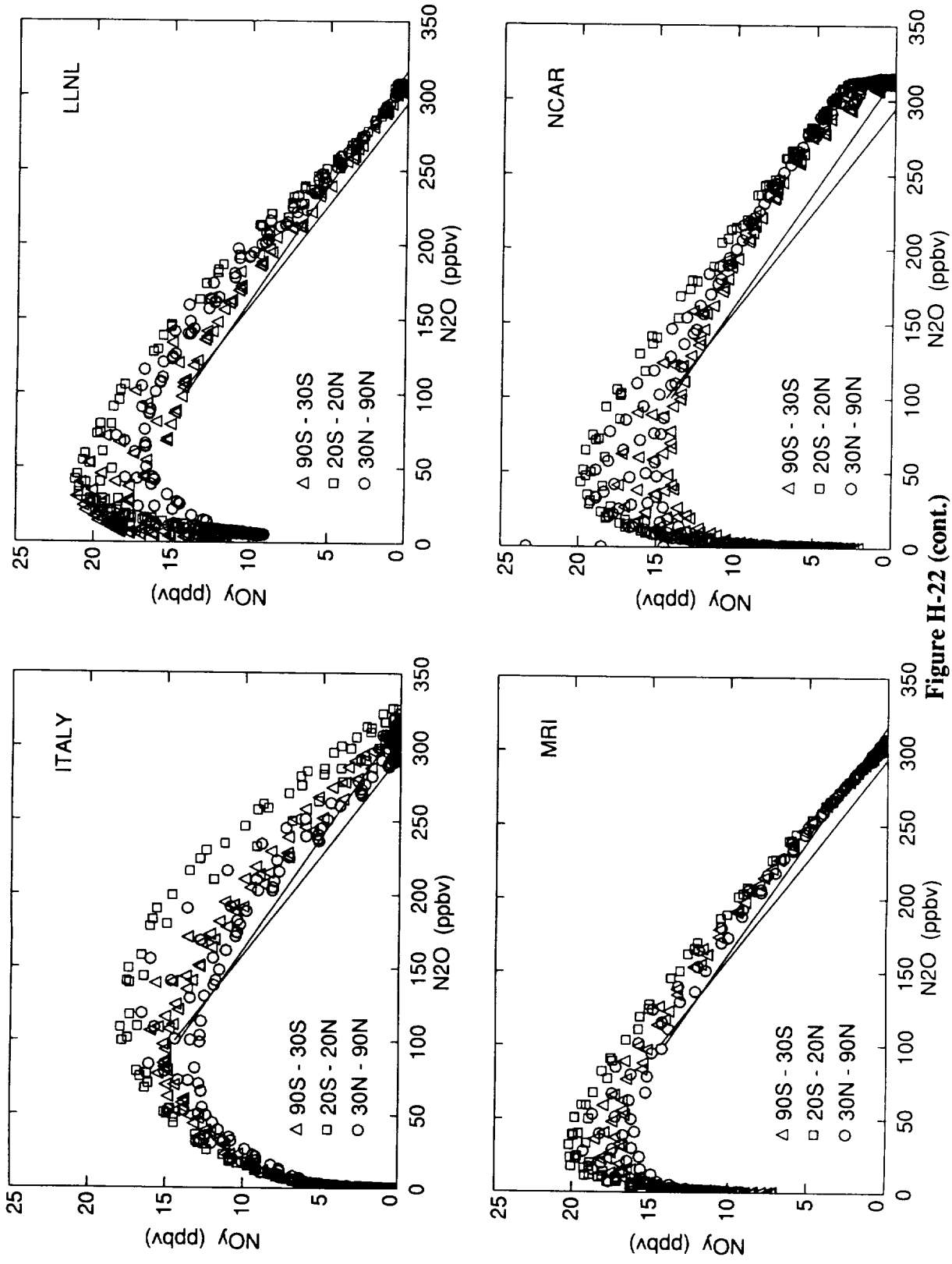

Figure H-22 (cont.)

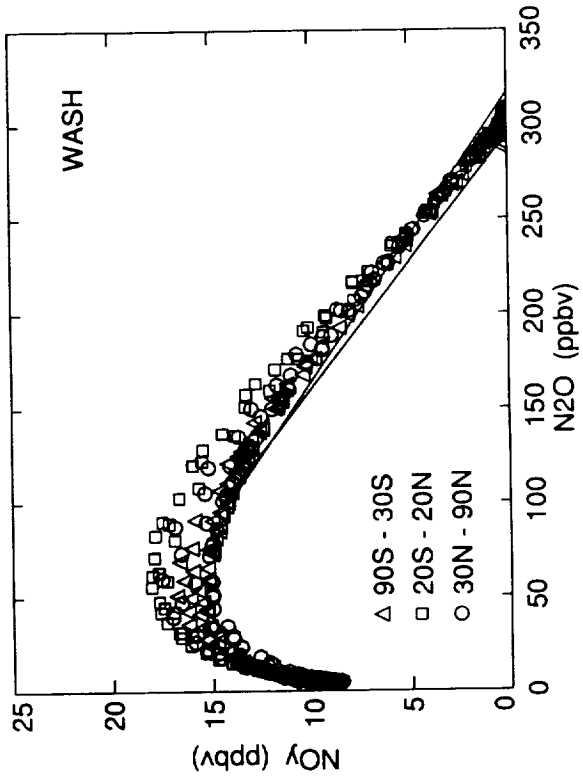

Figure H-22 (cont.)

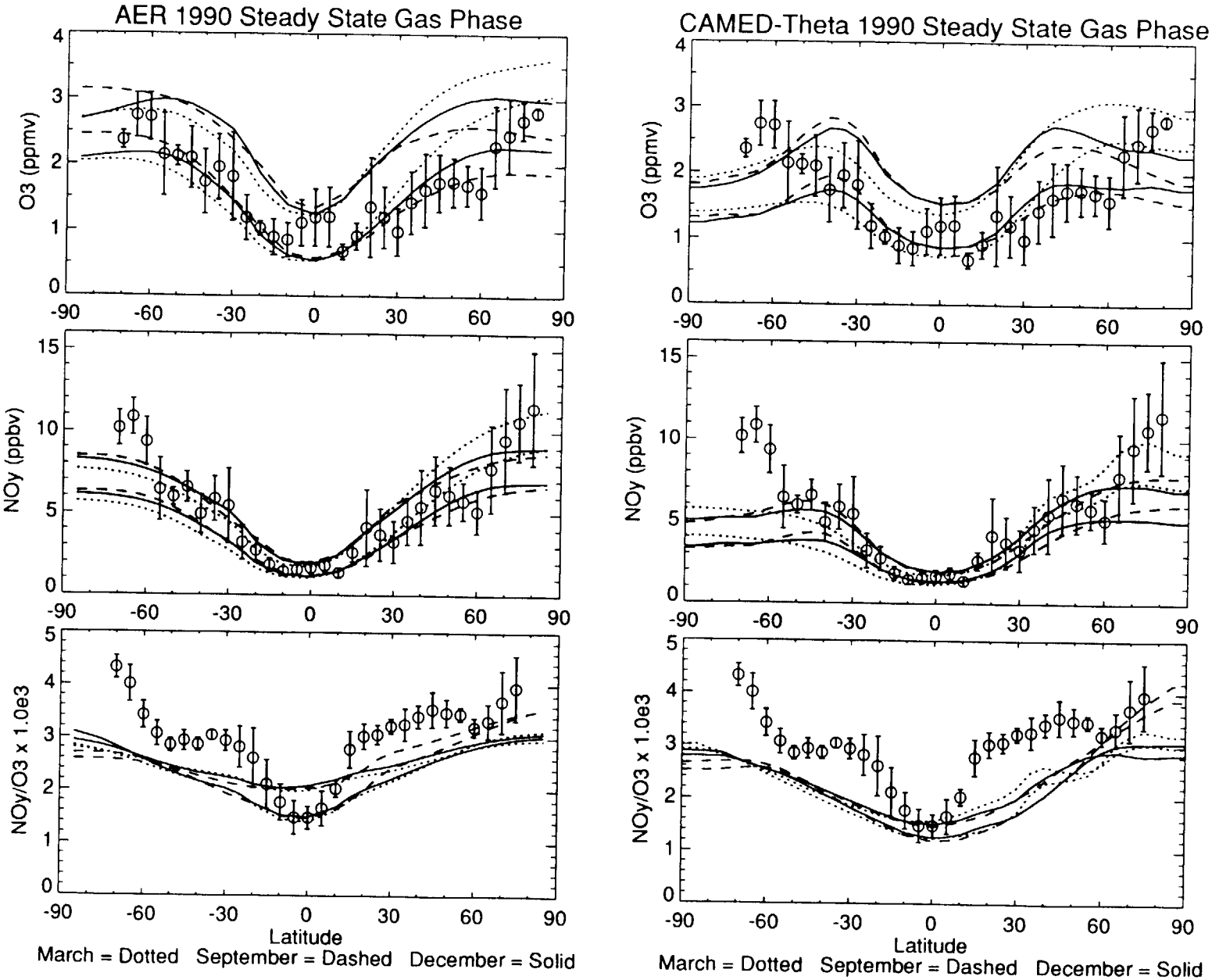
AER 1990 Steady State Gas Phase
CAMED-Theta 1990 Steady State Gas Phase
O3 (ppmv)
NOy (ppbv)
NOy/O3 x 1.0e3
Latitude
March = Dotted September = Dashed December = Solid

Figure H-23

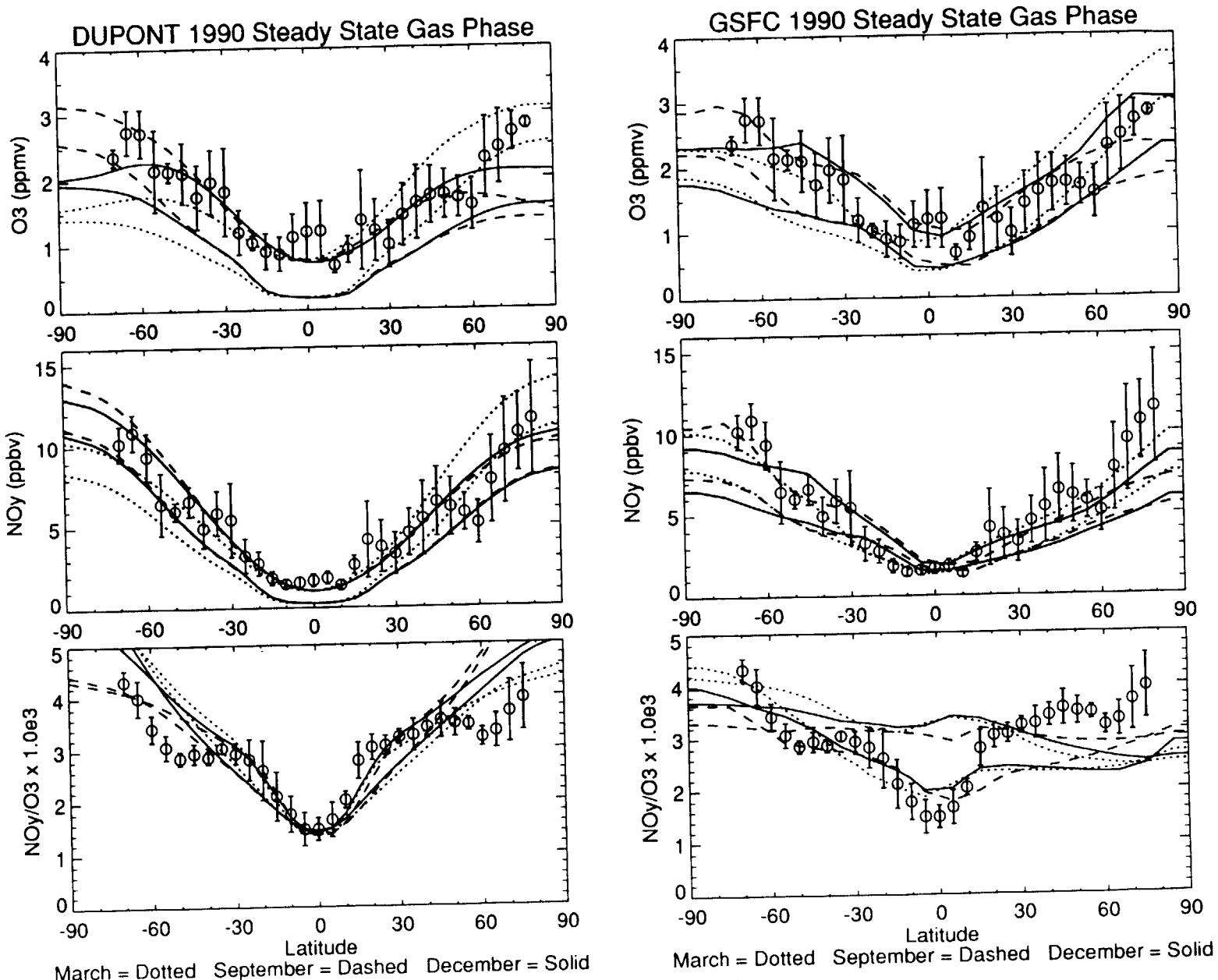

Figure H-23 (cont.)

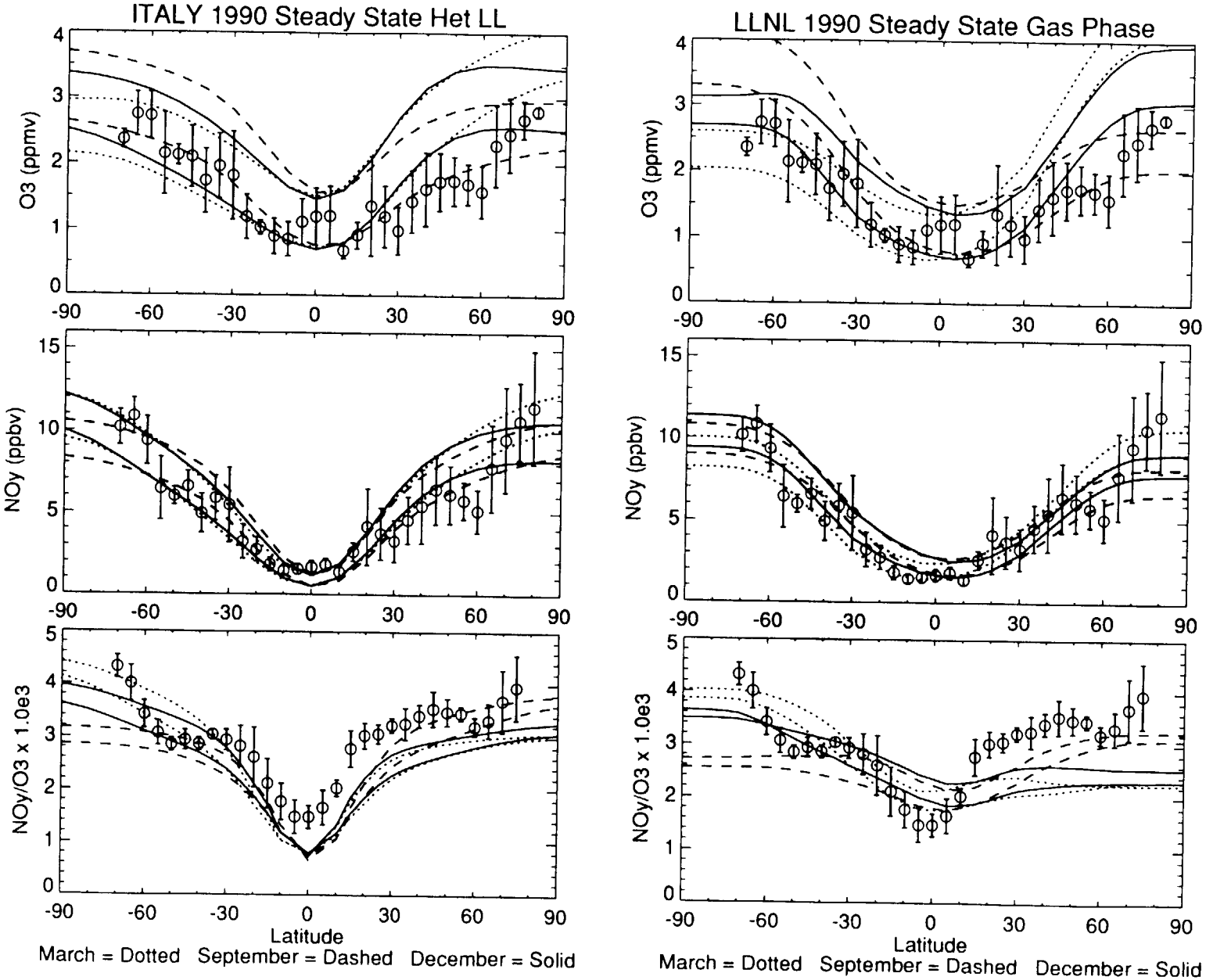

Figure H-23 (cont.)

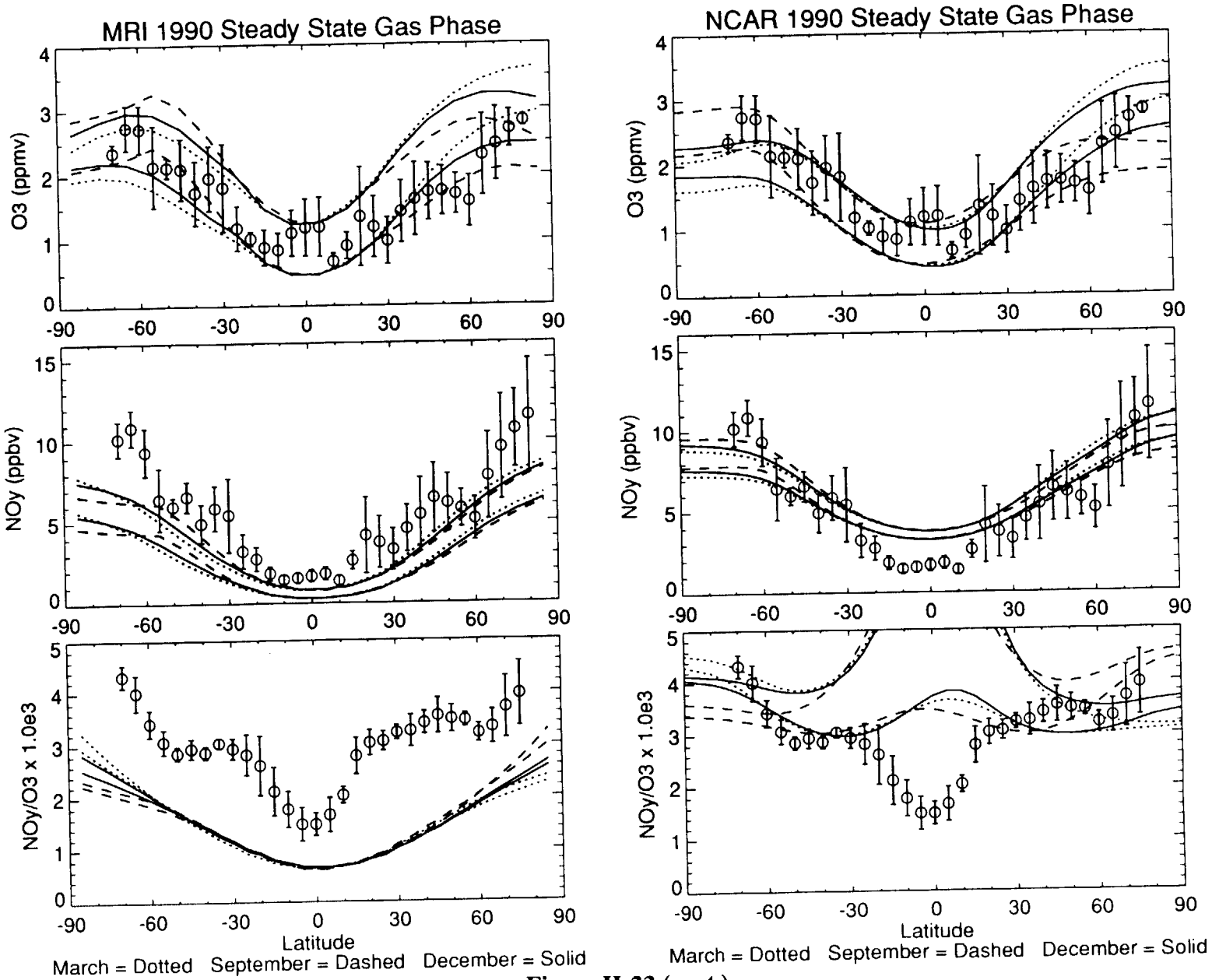

Figure H-23 (cont.)

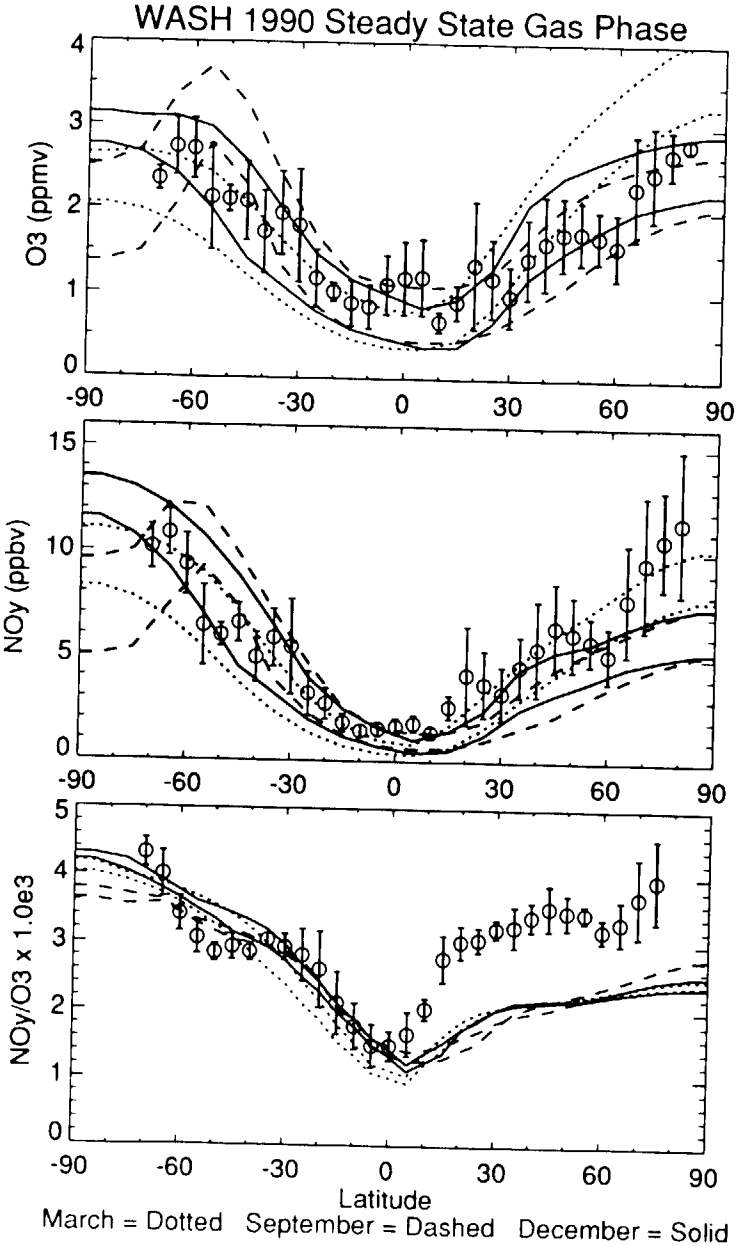

Figure H-23 (cont.)

I: Radionuclides as Exotic Tracers

I: Radionuclides as Exotic Tracers

D. E. Kinnison
Lawrence Livermore National Laboratory

H. S. Johnston
University of California, Berkeley

D. Weisenstein
Atmospheric and Environmental Research, Inc.

G. K. Yue
NASA-Langley Research Center

INTRODUCTION AND BACKGROUND

The goals of the carbon-14 and strontium-90 radionuclide experiments are to conduct fundamental tests of dynamical transport in the models that are independent of chemistry. Previous studies have used carbon-14 (Johnston et al., 1976; Kinnison, 1989; Shia et al., 1989; Jackman et al., 1991) and strontium-90 (Kinnison, 1989) as tracers in one- and two-dimensional models. These tracers were produced by the aboveground nuclear tests of the late 1950s and early 1960s. Carbon-14 is produced by fission and fusion nuclear processes, while strontium-90 is produced only by fission processes. The atmospheric nuclear test moratorium between the United States and the U.S.S.R. ended aboveground nuclear tests in December 1962. After January 1, 1963, the distribution of these tracers became dependent only on the transport processes in the stratosphere. After June 1967, the French and Chinese performed a small number of atmospheric nuclear detonations in which the bomb-rise height was primarily below 20 km altitude. The injection of these radioactive species into the lower stratosphere is somewhat similar to the proposed high-speed civil transport (HSCT) emissions, and the time scales for removal of these radionuclides is a suitable test of the models.

This section is divided into two parts: Modeling Carbon-14, which is in the form of CO_2 and acts as a passive gaseous tracer; and Modeling Strontium-90, which sticks to aerosols and therefore must include a settling velocity to calculate its spatial and temporal variation. Throughout this section the comparison of model-derived tracers is compared to observed distributions. All altitudes reported in this chapter are pressure altitudes (z^*-coordinates). In addition, model intercomparisons are examined.

MODELING CARBON-14

Extensive measurements of excess carbon-14 from nuclear weapons testing were conducted aboard U.S. aircraft and balloonsondes in the troposphere and stratosphere (see Hagemann et al., 1965, 1966; Telegadas, 1971; Telegadas et al., 1972) as a function of time, latitude, and altitude. Typically, there were four latitudes (70N, 31N, 9N, and 42S) where carbon-14 data were measured. Measurements were observed at altitudes greater than 20 km only at latitude 31N.

Telegadas (1971) reported the measured, atmospheric, excess carbon-14 data from March 1955 through July 1969. Using these data, his experience with other radioactive isotopes (Sr, Cs, Zr, etc.), and his aircraft-based observations of early stage bomb clouds, Telegadas constructed contour plots of carbon-14 mixing ratios (that is, units proportional to mixing ratios) for each quarter year over the 15 years. Each plot represents an average of all aircraft and balloon data

for a 3-month period (e.g., October is an average over September, October, and November). In Figure I-1a, the altitude-latitude distribution of carbon-14 for October 1963 is shown, including numerical values of measurements at four latitudes, crosses where measurements were made at other latitudes, and contour lines drawn by Telegadas. Johnston (1989) concluded that October 1963 provided good initial conditions for testing the dynamical representation of two-dimensional models and used Telegadas' contour plot for this purpose. October 1963 was 9 months after the conclusion of the nuclear bomb test series and was the first time at 31N that the local carbon-14 mixing ratios at all measured altitudes passed through their maximum value. Since the nuclear tests were in the northern hemisphere and in the tropics, there were large spatial gradients of carbon-14 at that time. Values outside the range of Telegadas' contour lines for October 1963 were extrapolated by Johnston (1989), largely on the basis of observed trends during the period 1958 to 1961. Using the observed carbon-14 distribution for January 1960 as initial conditions and two models for nuclear bomb-cloud rise, Kinnison (1989) calculated the carbon-14 distribution as a function of time during and after the 1961-1962 nuclear bomb-test period, having each bomb contribute at its appropriate latitude and time. The model results using the bomb-rise model of Seitz et al. (1968) agreed very well with Johnston's initial conditions for October 1963 at 70N, agreed fairly well at 31N, but gave substantially larger carbon-14 mixing ratios in the tropics and southern hemisphere, especially at altitudes above 25 km. On this basis Johnston (1989) prepared a second set of extrapolated values (Figure I-1b), having larger carbon-14 mixing ratios than the first set but still having values substantially lower than Kinnison's (Figure I-1c) in the region of extrapolation. For this study, Johnston's higher values (Figure I-1b) were used at altitudes above Telegadas' contour lines. Inspection of Figure I-1a shows that the data for the initial conditions (October 1963) are extremely sparse, but they are reinforced to some extent by Telegadas' experience and by Kinnison's modeling (1989).

The time-dependent lower boundary values specified by the models for the northern and southern hemispheres were obtained from Johnston (1989) and are given by the following functions:

$$^{14}C\ (N\text{-}Hem.) = 73.0 - 0.27823\ t - 3.45648\times10^{-3}\ t^2 + 4.21159\times10^{-5}\ t^3$$
$$^{14}C\ (S\text{-}Hem.) = 44.5 + 1.02535\ t - 2.13565\times10^{-2}\ t^2 + 8.61853\times10^{-5}\ t^3$$

where t is the time in months after 15 October 1963. These functions are based on observed data during this time period. For all times after 15 June 1968, the lower boundary values for the southern hemisphere were set equal to the calculated values from the northern hemisphere. The upper boundary conditions were specified as zero flux. The observed distributions are reported in units of 10^5 atoms of excess carbon-14 per gram of dry air, which is proportional to the mixing ratio, and these units are referred to as "mixing ratio units" or at times simply as "mixing ratios."

The models were used to derive the distribution of carbon-14 between October 1963 and January 1971. The three-dimensional GISS model was integrated only from October 1963 to October 1968. Comparisons are made between observed profiles at the four latitudes during the period from 15 October 1963 to 15 July 1966. Recall that each observed profile is an average of numerous aircraft and balloonsondes over a 3-month period. The variability of carbon-14 in a selected number of observed profiles at 31N is represented in Figure I-2. Four different times are included in this plot; the individual measurements along with the profile derived by Johnston (1989) from Telegadas' contours are shown. There is low variability in the troposphere but significant variability in the stratosphere.

Observed carbon-14 profiles are available (Johnston, 1989) for the four latitudes every 3 months through July 1966. There are additional profiles between July 1966 and July 1969, which have no data above 20 km altitude and are not discussed in this section. Figures I-3, I-4, I-5, and I-6 give observed and calculated carbon-14 mixing ratio vertical profiles, respectively, at

70N, 31N, 9N, and 42S. In Figure I-7, altitude-latitude contour plots of carbon-14 are shown for each model one and two years after the initial condition (October 1964 and October 1965). A final measurement campaign with balloon flights above 20 km at five latitudes was carried out in 1970-71 (Figures I-8 and I-9) (Telegadas et al., 1972).

Inter-model Comparisons

Global Stratospheric Residence Times

The global inventory of excess carbon-14 molecules was calculated for each 3-month period, and the global stratospheric residence times were found by a least-squares fit of *ln(inventory)* vs *time*. In Table I-1, the global stratospheric residence times (between 16 and 60 km) are shown for different time intervals. In Table I-2, for each interval, the models are grouped according to their relative stratospheric residence time: short, medium, and long. Between October 1963 and October 1964 (Table I-2a), there are eight models in the *short* stratospheric residence time section, and the range of residence times among all the models is 1.3 to 3.2 years. When the stratospheric residence time for the same models are compared between January 1965 and July 1966, three models—GISS, GSFC, and NCAR—have a relatively short stratospheric residence time, and the range for all the models is 2.9 to 4.9 years. In Table I-2c, the period between October 1963 and July 1966 is shown, and the range in stratospheric residence times is from 2.3 years (GISS) to 4.1 years (ITALY). Table I-2d spans the full time, October 1963 through January 1971, and the residence times range from 3.8 to 4.9 years. For the time interval January 1965 through January 1971, the range of calculated residence times is 4.3 to 5.4 years. In general, ITALY, DUPONT, and WASH have the longest stratospheric lifetimes. LLNLND and WASH have short lifetimes over the first year but show considerably longer carbon-14 removal times at longer times after the October 1963 initial conditions. As can be seen from the figures, the models remove carbon-14 relatively rapidly from the lower stratosphere, but the middle to upper stratospheric removal rates are much slower.

Altitude-Latitude Contour Maps

Figure I-1b gives the altitude-latitude contour plot of carbon-14 mixing ratio units used by all models as initial conditions for October 1963. Figures I-7 give altitude-latitude contour plots calculated by 12 models for October 1964 and for October 1965. A rough measure of the agreement and disagreement among the models for October 1964 was carried out by superimposing all lines for contour 200, contour 300, contour 400, and contour 500, each on a separate page. The superimposed lines for contour 200 spread from pole to pole with maximum altitude at tropical latitudes, and at each latitude there is a vertical spread, among the 12 models, of about 4 km. The 300 contours appear at both low altitudes and at high altitudes. The low altitude band was similar in shape to the band of 200 contours, and its vertical spread was about 5 km. The upper altitude 300 contours appear as a random tangle from 30 to 60 km in middle and high latitudes and from 40 to 60 km in tropical latitudes. The superimposed 400 contours stretch from the North Pole to southern midlatitudes, show a lower altitude band of about 7 km vertical spread and an upper altitude band of about 15 km vertical spread. One model has a 400 contour line as high as 50 km and another has no 400 contour line above 30 km. The 500 contours more or less uniformly fill an envelope with a 15 to 20 km vertical spread and stretching from the North Pole to about 15S. This rough preview of the model calculations indicates large differences among their results.

Comparisons Between Calculated and Observed Excess Carbon-14

Lower Stratosphere

The boundary values at the Earth's surface are the time-dependent observed carbon-14, which implicitly gives a flux into the surface, and there is no significance to the agreement between models and data in the troposphere. The altitude at which carbon-14 begins its sharp increase is a measure of the tropopause height, both for the data and for the models. At 70N, 9N, and 42S, the measurements were made only from aircraft, and the maximum altitude was 20 km. The observed data at 70N, Figure I-3, appear in some cases to reach the maximum carbon-14 mixing ratio and give a good comparison of models and data in the lowest stratosphere, but the tropopause is so high at 9N and 42S that the comparison between models and data is of limited value at these latitudes (Figures I-5 and I-6). From about April 1964 to April 1965, the altitude of the calculated carbon-14 tropopause is lower (-), about the same (0), or higher (+) than that observed, as follows:

Lat.	Model		Lat.	Model	
70N	NCAR	-	31N	ITALY	-
	CAMED	-		CAMED	-
	DUPONT	0		DUPONT	0
	ITALY	0		LLNLND	0
	AER	0		AER	0
	LLNL	0		LLNL	0
	WASH	+		WASH	+
	GSFC	+		GSFC	+
	CALJPL	+		CALJPL	+
	GISS	+		GISS	+
	LLNLND	+		NCAR	+
	MPI	+		MPI	+

A quantitative comparison of the data and the models is given by Table I-3, where the ratio of calculated carbon-14 to observed carbon-14 at 31N latitude and 20 km altitude (the altitude of the observed maximum carbon-14 mixing ratio) is given from January 1964 through October 1965. On October 1963, all models agreed with each other and with the data, and at January 1964, three months later, most models have a calculated/observed ratio slightly below one, with the range of values being 0.57 to 1.00. During the next 2 years, this ratio decreases to about 0.35 for MPI; 0.5 for GISS, NCAR, and GSFC; 0.6 for CALJPL and WASH; and 0.7 for AER, LLNL, and DUPONT. For three models the ratio, calculated/observed, remained fairly constant for 2 years: LLNLND averaging 0.90, CAMED averaging 0.97, and ITALY averaging 1.25. For all the models, the average ratio varies from 0.36 to 1.23. A similar comparison is given for 70N latitude and 16 km altitude in Table I-4, but these data show greater irregularities than those at 20 km. GISS, CALJPL, and GSFC decrease to about 0.6. Within the large scatter, AER, LLNLND, and WASH show a tendency for the ratio to decrease with time; the ratio averages about 0.9 for these three models. The ratio, calculated/observed, averages about 1.1 for NCAR, CAMED, and LLNL, and it is 1.2 for ITALY and 1.4 for DUPONT. For all the models, the average ratio varies from 0.56 to 1.4. At (16 km, 70N) and at (20 km, 31N), the 2-year average model results are higher than the data for some models and lower for others. The model predictions, involving only atmospheric motions and no chemistry, show a factor of two spread among the 2-year average, lower stratosphere, sweep-out times (Tables I-3 and I-4).

Middle Stratosphere

At 31N latitude, the observed carbon-14 data show a bell-shaped vertical profile, skewed toward the vertical, whose altitude of maximum mixing ratio increased from 21 km in January 1964 to 25 km in January 1966 (Table I-5). The model-calculated vertical profiles show quite different behavior; in all cases the altitude of maximum carbon-14 mixing ratio increased from about 22 km in January 1964 to altitudes greater than 40 km by April 1966 (Table I-5). It is instructive to examine sequences of vertical profiles in Figure I-4, for example April 1964, October 1964, and April 1965. By April 1965, the maximum calculated carbon-14 mixing ratio for AER and NCAR is above 40 km, the upper border of Figure I-4, but the carbon-14 data profile has its maximum at 23 km. By July 1965, all models but LLNLND and ITALY have their mixing ratio maxima above 40 km, and by April 1966 these two models also have their maxima above 40 km.

Another representation of this effect is shown in Table I-6. The ITALY model most nearly resembles the carbon-14 data with respect to the rise of its altitude of maximum mixing ratio, and the CALJPL model is an average of the other models in this respect (Table I-5). The slopes of the carbon-14 mixing ratio with altitude, ($d\mu/dz$), between 25 and 33 km are presented for the observed data, the ITALY model, and the CALJPL model in Table I-6 from January 1964 to July 1966. The two models and the observed data all have a decrease of 32 mixing ratio units per km in January 1964, and a year later the carbon-14 data have the same vertical slope. During this year, January 1964 to January 1965, the upper arm of the CALJPL mixing ratio profile opened up from a slope of -32 units to -18 to -11 to -2, which is almost straight up. The ITALY model gives results that are intermediate between the observed data and the results of the CALJPL model; it remained strongly negative until October 1964 and then rotated upwardly, passing the vertical by October 1965. This feature had been noted in the LLNL model (Kinnison, 1989); it is a universal feature of the 12 models studied here. Two reviewers of this section offer suggestions as to the possible cause of this strong qualitative discrepancy between the observations and all of the models, and the authors of this section give a discussion of its possible cause. These three suggestions are given as the next three paragraphs.

Reviewer A. "With the initial conditions all models used, there is no way the values above the peak can be kept as low as that observed–no matter what K_{zz} profile one uses. One could get lower values above the peak and hence have the profiles not open as much if the initial conditions are such that the equatorial values are lower than Johnston's initial conditions. These low values can then be transported poleward and downward. I think it is subsidence of low carbon-14 values from the top that is keeping the profiles from opening up. . ."

Reviewer B. "I do not believe that any of the models include a proper treatment of tropical dynamics as diagnosed by say Trepte and Hitchman (1992, Nature, 626-628). This may [also] be important to an understanding of Figure I-10."

The source of disagreement between the observed carbon-14 data and all the models may be based, in part, on too fast transfer to the troposphere by the models, as can be seen from examination of the actual mixing ratios at 31N instead of the ratios of Table I-4 (where JPL is equivalent to CALJPL):

Date	**4/64**	**7/64**	**10/64**	**1/65**	**4/65**	**7/65**	**10/65**	**1/66**	**4/66**	**7/66**
Obs (20 km)	580	520	500	520	400	340	340	300	300	280
JPL (20 km)	560	380	330	300	280	200	190	200	185	150
Obs (32 km)	325	340	300	400	340	320	340	330	300	280
JPL (32 km)	450	520	500	460	420	390	360	325	305	290
JPL (40 km)	350	410	460	440	420	410	390	360	340	305

At 32 km altitude, the observed mixing ratios are essentially constant at 350±50 from April 1964 to April 1966, falling to 280 units by July 1966. At 32 km, the calculated mixing ratios are larger than the observed values, increase slightly (450 to 520) between April 1964 and July 1964, and decrease during the next 2 years to 290 units in July 1966. At 40 km altitude, the calculated mixing ratios increase slightly (350 to 460) from April 1964 to October 1964, and then decrease slowly to 305 over the remainder of the period. The differences between 30 and 40 km of observed and calculated values are not large. The principal action that determines the features of Tables I-5 and I-6 occurs at 20 km altitude. The observed carbon-14 mixing ratios fall slowly, with some seasonal irregularity, from 580 units in April 1964 to 280 units in July 1966; over the same period the calculated mixing ratios started with essentially the same value (560 units) and fell to 150 units, a value of 54% of that observed. Relative to observations, the too rapidly rising altitude of the calculated maximum mixing ratio maximum on the vertical profile at 31N latitude (Table I-5) and the large differences between the vertical gradient of mixing ratio with altitude (Table I-6) have a small component due to too rapid calculated increase of carbon-14 in the middle stratosphere and a large component of too rapid calculated depletion of carbon-14 at the 20 km altitude. In a one-dimensional model, these differences would be ascribed to too large a vertical eddy diffusion function in the models. In a two- or three-dimensional model, these differences could be ascribed to vertical mixing or to differential horizontal transport or to both. Table I-4 and Figure I-3 show that CALJPL mixing ratios at 70N latitude and 16 km altitude decreased almost twice as fast as the observed carbon-14. The data at 9N (Figure I-5) and 42S (Figure I-6) give relatively little information. At the highest altitude of the observed data, about 20 km, the qualitative relation between calculated and observed carbon-14 for the CALJPL results at various times is as follows:

	Calc > Obs	Calc ≈ Obs	Calc < Obs
9N	1/64	4/64 - 10/64, 4/65	1/65, 7 /65, 10/65
42S	1/64 - 1/65	4/65, 7/65	10/65 - 7/66

Thus at all four latitudes, carbon-14 decreased at 16 or 20 km altitude faster in the models than that observed. Since the carbon-14 data for the 1963 to 1966 period were measured above 20 km only at 31N latitude, it cannot be said whether the faster loss at low altitudes at 70N, 9N, and 42S was caused by transport to higher altitudes or to removal from the stratosphere. However, the next paragraph discusses one period of high altitude sampling at five latitudes, which indicates faster loss from the stratosphere.

Long-time Observations

At the conclusion of atmospheric carbon-14 monitoring by the Atomic Energy Commission(AEC), a special investigation was carried out in the fall of 1970, almost 8 years after the conclusion of atmospheric nuclear bomb testing. Balloons captured samples of air for carbon-14 analysis at five latitudes (65N, 42N, 30N, 9N and 34S) and from 20 km to at least 30 km and up to 36 km at 30N (Telegadas et al., 1972).

In this comparison of the long-term observed and modeled carbon-14 in the stratosphere, we review briefly the nature of the carbon-14 measurements that were made. The AEC, Department of Defense (DoD), and National Oceanographic and Atmospheric Administration (NOAA) carried out extensive measurements of radioactive products of atmospheric nuclear bomb tests as a high-priority, high-technology activity. Beginning in 1953, whole air samples were collected in the atmosphere and the samples were brought back to laboratories for analysis of carbon-14 and several other radioactive species, zirconium, strontium, cesium, etc. From 1953 to July 1969, aircraft collected whole air samples at many latitudes and up to pressure altitudes of 20 km. Balloons collected air samples from 20 km to about 35 km at several latitudes from 1953 to 1959 but only at 31N from 1959 to July 1966. After termination of the high-altitude collection

of carbon-14 in whole air samples, the AEC developed a molecular sieve collector specific for carbon-14 in carbon dioxide. This detector was tested in the AEC high altitude test chamber under realistic stratospheric conditions and tested in the stratosphere with a series of balloon launches at 31N latitude in 1968 and 1969. Molecular sieve instruments gave carbon-14 values in agreement with values found by whole air sampling. AEC conducted an atmospheric research program during 1970-1971 with 84 balloon launches from six latitudes, 65N, 42N, 31N, 9N, 23S, and 34S. Carbon dioxide collected by the molecular sieve absorbers had specific carbon-14 two to four times greater than that of carbon dioxide derived from pre-nuclear age standards. In multiples of 10^5 atoms of carbon-14 per gram of dry air, the natural background of stratospheric carbon-14 was 74 units, and the values observed between 20 and 36 km in 1970-1971 varied between 75 and 158 units after the background of 74 units was subtracted (Telegadas, 1971; Telegadas et al., 1972). This procedure of subtracting 74 units from the total measure of carbon-14 is correct only in the troposphere. Jackman et al., 1991, derived the pre-bomb background carbon-14 using a galactic cosmic ray production function peaking in the stratosphere. This study used the magnitude of carbon-14 produced per year from Lingenfelter and Ramaty (1970), but with the altitude distribution correlated with the beryllium-7 production function. Their preliminary results suggest that the maximum carbon-14 produced between 20 and 30 km was 76 to 82 units (Jackman, personal communication). If this is accurate, subtracting a constant amount for pre-bomb or background carbon-14, at all altitudes and latitudes, would not significantly affect the shape of the excess carbon-14 vertical profiles. Further work should be conducted using a production function explicitly for carbon-14.

Telegadas et al. (1972) discussed whether the Chinese and French atmospheric nuclear-bomb tests of 1967-1970 are adequately included in the 1970 observations. During the period of 1953 to 1959 the nuclear bombs that were exploded in the atmosphere were equivalent in energy to 90 megatons (MT) of TNT, almost every bomb was less than 10 MT. During 1961-1962, the bombs tested were equivalent to 337 MT, including 15 bombs greater than 10 MT, 7 greater than 20 MT, and one of about 60 MT. The bombs having energy equivalents greater than 10 MT rise well into the stratosphere. After December 1962, atmospheric bomb tests were made as follows: Chinese, 40N, 3 MT in 1967, 3 MT in 1968, and in October 1970; French, 22S, 2.5 and 1.0 MT in 1968 and tests in summer 1970. For 3-MT bombs at these latitudes the top of the initial bomb cloud is about 22 km. Telegadas compared the atmospheric records of zirconium-95 having 65-day half-life with respect to radioactive decomposition and cesium-137 having a 30-year half-life, and he concluded that the debris of nuclear bomb tests of 1967 to 1970 deposited above 20 km was one or two orders of magnitude less than that deposited below that altitude. In 1970-1971, the maximum mixing ratio of carbon-14 was observed at altitudes of 24 to 28 km, and the maximum mixing ratio of zirconium-95 and cesium-137 was between 14 and 18 km in the northern hemisphere and between 15 and 19 km in the southern hemisphere. Telegadas cautiously concluded that almost all excess carbon-14 observed above about 21 km in 1970-71 was from pre-1963 nuclear bomb tests. The results are reproduced in Table I-7; the calculated and observed vertical profiles are given in Figure I-8; Telegadas' contour plot is shown in Figure I-10. The observed vertical profiles are quantitatively different from all the calculated profiles. Each observed vertical profile shows a broad maximum carbon-14 mixing ratio at more-or-less 25 km and a distinct decrease with altitude above the maximum; but except for ITALY at 70N, each calculated profile increases with altitude up to 40 km (Figure I-8). In the 22- to 28-km range, NCAR, MPI, GSFC, AER, CALJPL, LLNL, and LLNLND calculate carbon-14 to be much less than the observed values. For example, the observed and calculated values at 26 km altitude are listed in Table I-8. The excess carbon-14 in the troposphere was 50 units, and the merit of a model in predicting long-term stratospheric carbon-14 is the difference between the stratospheric value and the tropospheric value. These differences range from 18 for the NCAR model to 77 for the ITALY model, compared with 90 observed at 26 km. The DUPONT and ITALY models agree with the magnitude of the 26-km data to 75% or better. The LLNLND, WASH, and CAMED models account for better than 50% of the long-term carbon-14. The

NCAR, MPI, GSFC, AER CALJPL, and LLNL models account for 40% or less of the long-term carbon-14. The data show far greater persistence of carbon-14 in the 20- to 25-km range than shown by any model except ITALY and DUPONT.

The LLNLND two-dimensional model was used to investigate Telegadas's conclusion that the French and Chinese tests did not enhance the middle stratosphere observed carbon-14 profiles in November 1970. The model was integrated from October 1963 (using Johnston initial conditions) through November 1970 including the effects of the French and Chinese tests. The amount of carbon-14 from these tests was derived by knowing the time, latitude, bomb cloud stabilization height, magnitude of each nuclear test, distribution within the cloud [Bauer, 1979], and the amount of carbon-14 produced per MT–2.0 x 10^{26} atoms/MT [Telegadas, 1971]. The results of this study are shown in Figure I-9. The additional carbon-14 produced from the French and Chinese tests increased the carbon-14 mixing ratio in the northern hemisphere below 20 km. The LLNLND model with the additional carbon-14 compares better to the observed data in the lower stratosphere. It does not explain the observed carbon-14 profile between 25 and 35 km. Including the French and Chinese nuclear tests has a small impact on the vertical profile of carbon-14 in the southern hemisphere.

Figure I-10 is a latitude-altitude contour map of carbon-14 mixing ratio units during November 1970. It is transcribed from Telegadas' (1972), with a different vertical scale, and it is based on the data in Table I-7. The data for the southern hemisphere are sparse; the northern hemisphere data include four vertical profiles. In the 23- to 30-km altitude band, the data show a minimum with respect to latitude above the tropics. This minimum above the tropics can be rationalized in terms of the Brewer model of stratospheric circulation, in that tropospheric air of relatively low carbon-14 mixing ratio rises from the tropics into the stratosphere. At each latitude on the contour plot, the vertical profile of carbon-14 mixing ratios goes through a broad maximum, spanning approximately the 24- to 28-km range. Unlike all the models, the reported carbon-14 mixing ratios decrease above about 28 km, and the decrease continues to the topmost observation altitude, 36 km at 30N. The explanation for this decrease of carbon-14 mixing ratios with altitude is unknown to the authors of this chapter. However, see quotations from Reviewers A and B in the previous section.

MODELING STRONTIUM-90

As with carbon-14, strontium-90 data were measured by balloonsondes and a very large number of aircraft flights. Telegadas (1967) averaged the data over a 3-month period and produced altitude-latitude contour plots. Johnston (1989) used these plots to produce the October 1964 initial conditions for this study. Strontium-90 data, like carbon-14, are proportional to mixing ratios and were modeled in this manner. Typically, four latitudes (64N, 31N, 9N, and 34S) were measured from October 1964 to January 1967 with an altitude range from the surface to 30 to 36 km.

Since strontium-90 rapidly coalesces on aerosol particles, and the settling velocity of aerosol particles is proportional to the square of their radius, the removal of strontium-90 is dependent on the size of aerosol particles in the atmosphere. In situ measurements of aerosol size from the early 1960s are sporadic. Mossop (1964) reported the size distribution of aerosol particles at 20 km from early 1963 to July 1964. Measurements show that although large size particles with diameters equal to 8 μm were collected in early 1963, the median diameters of aerosol particles gradually reduced to 0.2 μm by July 1964. Volcanic dust from the eruption of Mt. Agung on March 17, 1963, may have settled to the lower stratosphere by the end of 1964. After 1963, no major volcanic eruptions were reported until the eruption of Mt. Fuego in October 1974. Since this radionuclides study is to simulate the concentration of strontium-90 from October 1964 to

January 1971, we can assume that in this period there are only background aerosol particles in the stratosphere.

The Stratospheric Aerosol and Gas Experiment (SAGE) II provides global coverage of the properties of aerosols and some tracer gases. It was demonstrated that the multi-wavelength aerosol extinction measured by SAGE II can be used to deduce aerosol size (Yue et al., 1986). Analysis of SAGE II data shows the loading of aerosol particles in the stratosphere has gradually decreased since the eruption of Ruiz in November 1985. In this study, we assume the aerosol particles have returned to background levels by 1989. We used the January and February 1989 SAGE II data to deduce the global distribution of aerosol size. The settling velocities were then calculated as a function of altitude and latitude. The settling velocities were derived from the mass mean radii that conserve the total mass of aerosols in a size distribution. Since aerosol size decreases with height due to an increase of ambient temperature, this model comparison project assumes that the aerosol becomes small enough to act like a gas at altitudes above 30 km (Table I-9).

In Figures I-11 through I-14, the strontium-90 profiles derived by the models are compared with the observed profiles cataloged by Johnston (1989). For each time period, results are shown for strontium-90 treated as a gas and as an aerosol particle for the seven models that participated in this study. As previous work (Johnston et al., 1976; Kinnison, 1989) suggested, the strontium-90 profiles derived by the models do not represent the observed data when a settling velocity is not incorporated into the scenario. Large deviations between the model and data in the middle to upper stratosphere are observed (e.g., Figure I-11, April 1966). When the settling velocity is used, the agreement between model-derived and observed distributions of strontium-90 is comparable to that between the models and carbon-14 data.

In Table I-10, the global stratospheric residence times (between 16-60 km) for strontium-90 are shown for the time period of October 1964 through October 1966. Observed global stratospheric residence times are not available; however, in Johnston (1989) local residence times were calculated for the four latitudes in the lower stratosphere. These values ranged from 1.0 to 1.6 years. Most of the models derived global stratospheric residence times in this range when settling velocities were included. Without settling velocities, the range of global stratospheric residence times was from 1.8 (AER and GSFC) to 3.9 years (ITALY).

With only model results that include particle settling, the ratios of calculated strontium-90 to observed strontium-90 are presented in Table I-11 for each of seven models, for each of four latitudes, and for each of eight times (when high-altitude data were reported). At each latitude, the altitude is that of the observed maximum strontium-90 mixing ratios, which are 17 km at 64N, 20 km at 30N and 34S, and 24 km at 9N. In the discussion of carbon-14, it was found that a systematic decrease of this ratio with time indicates model removal of tracer gas faster than that observed. Since high altitude (above 20 km) carbon-14 data were only taken at one latitude, such a faster local removal of tracer could be due to removal from the stratosphere or it could be redistribution of tracer within the stratosphere. With the availability of four latitudes with high altitude strontium-90 measurements, and since particulate settling prevents any significant transfer of strontium to the upper stratosphere, a better estimate is available of which of these alternatives is more likely to be correct. The individual models are discussed below.

The AER model shows the ratio, Sr-90(calc)/Sr-90(obs), to decrease strongly with time at all four latitudes (Table I-10). The interpretation is that this model sweeps strontium-90 out of the lower stratosphere much faster than that observed. To a less extreme extent, the GSFC model shows the same pattern. The CALJPL model shows the calc/obs ratio to decrease at 30N and 9N and to remain about constant at 64N and in the southern hemisphere. On balance, the evidence is that these three models remove strontium-90 from the stratosphere faster than that observed.

The WASH and LLNL models show a similar pattern: a systematic decrease of the calc/obs ratio at 30N; weak or no trends at 64N, 9N, and 34S. At the three latitudes with no distinct trends, the average value of the calc/obs ratio is close to one.

The CAMED model shows no trend of the calc/obs ratio with time, and the average value of this ratio is close to one at all three latitudes. The interpretation is that this model removes strontium-90 from the stratosphere at the same rate as that observed.

The ITALY model shows an increasing trend of the calc/obs ratio at all four latitudes. The interpretation is that this model removes strontium-90 from the lower stratosphere more slowly than the measured values.

The strontium-90 data test two things at once: the model for settling velocity and the model of stratospheric air motions. If the model for settling velocity is correct, the test gives fairly well-focused information about removal of material from the lower stratosphere. Although this stratospheric-tropospheric exchange is important to the HSCT problem, the lower stratosphere to middle stratospheric exchange is equally important, and the strontium data do not apply to that problem. The three models that agree well with the strontium-90 data, CAMED, WASH, and LLNL, do not agree nearly so well with the carbon-14 data, especially the long-term and middle stratospheric tests. These differences may arise from features that control exchange between the lower and middle stratosphere.

CONCLUSIONS

The observed excess carbon-14 in the atmosphere from 1963 to 1970 provide useful, but limited, data for testing the air motions calculated by multidimensional atmospheric models up to an altitude of about 35 km. The observed strontium-90 in the atmosphere from 1964 to mid-1967 provide data, more extensive than those of carbon-14, useful for testing combined models of air motions and aerosol settling.

The models all give stratospheric residence times of excess carbon-14 that increase with time after the conclusion of the nuclear bomb tests: among the models, the average residence time is 2.2 years and the range is 1.3 to 3.2 years between 1963 and 1964; between 1965 and 1971, the average residence time is 4.9 years and the range is 4.3 to 5.4 years.

If the ratio of C-14(calc)/C-14(obs) is less than one, it could mean any of several calibration errors or real differences between model and observations; but when this ratio decreases systematically with time, it means that the model is removing carbon-14 from the area in question more rapidly than that observed. Most, but not all, models in this study remove carbon-14 from the lower stratosphere at a rate distinctly faster than that observed. Most, but not all, models remove strontium-90 from the stratosphere at a rate distinctly faster than that observed.

Over an 8-year time period, all models but two remove carbon-14 from 20 to 30 km altitude in the stratosphere much more rapidly than observed.

The long-term vertical profiles of all models at all latitudes are in strong qualitative disagreement with the observed vertical profiles. Experts in fundamental stratospheric dynamics should consider this problem and decide whether the fault is in the carbon-14 data or in all the two-dimensional models

REFERENCES

Bauer, E., A catalog of perturbing influences on stratospheric ozone, 1955-1975, *J. Geophys. Res.*, *84*, 6929-6940, 1979.

Hagemann, F. T., J. Gray, and L. Machta, "Carbon-14 Measurements in the Atmosphere - 1953 to 1964," Rep. 159, Health and Safety Laboratory, U.S. Atomic Energy Commission, Washington, D. C., 1965.

Hagemann, F. T., J. Gray, and L. Machta, "Carbon-14 Measurements in the Atmosphere - 1953 to 1964," Rep. 166, Health and Safety Laboratory, U.S. Atomic Energy Commission, Washington, D. C., 1966.

Jackman, C. H., A. R. Douglass, K. F. Brueske, and S. A. Klein, The influence of dynamics on two-dimensional model results: Simulations of ^{14}C and stratospheric aircraft NO_x injections, *J. Geophys. Res.*, *96*, 22559-22572, 1991.

Johnston, H. S., D. Kattenhorn, and G. Whitten, Use of excess carbon 14 data to calibrate models of stratospheric ozone depletion by supersonic transports, *J. Geophys. Res.*, *81*, 368-380, 1976.

Johnston, H. S., Evaluation of excess carbon-14 and strontium-90 data for suitability to test two-dimensional stratospheric models, *J. Geophys. Res.*, *94*, 18485-18493, 1989.

Kinnison, D.E., "The Effect of Trace Gases on Global Atmospheric Chemical and Physical Processes," University of California at Berkeley, Ph.D. Thesis (Also LLNL Report UCRL-53903), 1989.

Lingenfelter, R. E., and R. Ramaty, Astrophysical and geophysical variations in ^{14}C production, in *Radiocarbon Variations and Absolute Chronology* (I. U. Olsson, ed.), pp. 513-537, Wiley Interscience, New York, 1970.

Mossop, S. C., Volcanic dust collected at an altitude of 20 km, *Nature*, *203*, 824-827, 1964.

Shia, R., Y. L. Yung, M. Allen, R. W. Zurek, and D. Crisp, Sensitivity study of advection and diffusion coefficients in a two-dimensional stratospheric model using excess carbon 14 data, *J. Geophys. Res.*, *94*, 18467-18484, 1989.

Seitz, H. et al., "Final Report on Project Streak: Numerical Models of Transport, Diffusion and Fallout of Stratospheric Radioactive Material," Rep. NYO-3654-4, Atomic Energy Commission, Washington, D. C., May 1968.

Telegadas, K., "The Seasonal Stratospheric Distribution and Inventories of Cadmium-109, Plutonium-238, and Strontium-90," Rep. 184, pp. 53-118, Health and Safety Laboratory, U.S. Atomic Energy Commission, Washington, D. C., 1967.

Telegadas, K. "The Seasonal Atmospheric Distribution and Inventories of Excess Carbon-14 from March 1955 to July 1969," Rep. 243, pp. 3-86, Health and Safety Laboratory, U.S. Atomic Energy Commission, Washington, D. C., July 1, 1971.

Telegadas, K., J. Gray, Jr., R. E. Sowl, and T. E. Ashenfelter, "Carbon-14 Measurements in the Stratosphere from a Balloon-borne Molecular Sieve Sampler," Rep. 246, pp. 69-106, Health and Safety Laboratory, U.S. Atomic Energy Commission, Washington, D. C., 1972.

Yue, G. K., M. P. McCormick, and W. P. Chu, Retrieval of composition and size distribution of stratospheric aerosols with the SAGE II satellite experiment, *J. Atmos. Oceanic Technology*, *3*, 371-380, 1986.

ACKNOWLEDGMENTS

The authors would like to thank Robert Leifer, Environmental Studies Division, Environmental Measurements Laboratory, Department of Energy, and Lester Machta, Air Resources Laboratory, National Oceanic and Atmospheric Administration for their help in retrieving the individual carbon-14 data measurements used in this section. For Doug Kinnison, this work was performed under the auspices of the U.S. Department of Energy by the Lawrence Livermore National Laboratory under contract W-7405-Eng-48 and supported in part by the NASA High Speed Research Program. For Harold S. Johnston, this work was conducted at the University of California, Berkeley, and at the Lawrence Berkeley Laboratory and was supported by the Director, Office of Energy Research, Office of Basic Energy Sciences, Chemical Sciences Division of the U. S. Department of Energy under Contract No.DE-AC03-76SF00098.

Table I-1. Carbon-14 stratospheric residence times in years based on linear least squares regression analysis. For each period the model derived burden was integrated globally between 16 and 60 km.

Model	Oct 63-Oct 64	Jan 65-Jul 66	Oct 63-Jul 66	Oct 63-Jan 71	Jan 65-Jan 71
AER	1.7	3.5	2.7	3.9	4.5
CALJPL	1.7	3.9	2.8	4.2	4.8
CAMED	2.4	3.4	3.4	4.5	5.0
DUPONT	2.7	4.9	3.6	4.9	5.4
GISS	1.3	3.2	2.3	NA	NA
GSFC	1.7	2.9	2.4	3.8	4.3
ITALY	3.2	4.4	4.1	4.9	5.1
LLNL	2.7	3.5	3.1	4.1	4.7
LLNLND	2.0	3.6	2.9	4.6	5.3
MPI	1.3	3.5	2.4	4.3	5.3
NCAR	1.9	3.0	2.5	3.8	4.4
WASH	2.0	3.7	3.4	4.9	5.4

Table I-2a. Grouping of global stratospheric residence times (between 16-60 km) for October 1963 through October 1964

Short	Medium	Long
AER	CAMED-theta	ITALY
CALJPL	LLNL	
GISS	DUPONT	
GSFC		
LLNLND		
MPI		
NCAR		
WASH		
1.3 -- 2.0	2.4 -- 2.7	3.2

Table I-2b. Grouping of global stratospheric residence times (between 16-60 km) for January 1965 through July 1966

Short	Medium	Long
GISS	AER	DUPONT
GSFC	CALJPL	ITALY
NCAR	CAMED-theta	
	LLNL	
	LLNLND	
	MPI	
	WASH	
2.9 -- 3.2	3.4 -- 3.9	4.4 -- 4.9

Table I-2c. Grouping of global stratospheric residence times (between 16-60 km) for October 1963 through July 1966

Short	Medium	Long
AER CALJPL GISS GSFC LLNLND MPI NCAR	CAMED-theta DUPONT LLNL WASH	ITALY
2.3 -- 2.9	3.1 -- 3.6	4.1

Table I-2d. Grouping of global stratospheric residence times (between 16-60 km) for October 1963 through January 1971

Short	Medium	Long
AER CALJPL GSFC LLNL NCAR	CAMED-theta LLNLND MPI	DUPONT ITALY WASH
3.8 -- 4.2	4.3 -- 4.6	4.9

Table I-2e. Grouping of global stratospheric residence times (between 16-60 km) for January 1965 through January 1971

Short	Medium	Long
AER GSFC NCAR	CALJPL CAMED-theta LLNL	DUPONT ITALY LLNLND MPI WASH
4.3 -- 4.5	4.7 -- 5.0	5.1 -- 5.4

Table I-3. The ratio ^{14}C (calc)/^{14}C (obs) at 31N latitude and 20 km altitude

DATE	OBS	MPI	GISS	NCAR	GSFC	CALJPL	WASH	AER	LLNL	DUPONT	LLNLND	CAMED	ITALY
1/64	900	0.57	0.78	0.83	0.78	0.78	0.97	0.89	0.90	0.92	0.91	1.00	0.98
4/64	580	0.53	0.81	0.86	0.84	0.95	1.07	1.00	1.12	1.14	1.14	1.16	1.29
7/64	520	0.42	0.65	0.72	0.72	0.73	0.75	0.96	0.94	0.94	1.00	1.06	1.33
10/64	420	0.44	0.51	0.60	0.63	0.65	0.70	0.86	0.76	0.90	0.84	0.90	1.28
1/65	520	0.34	0.46	0.50	0.50	0.60	0.65	0.63	0.60	0.67	0.72	0.79	1.06
4/65	400	0.31	0.48	0.55	0.60	0.70	0.75	0.65	0.75	0.78	0.83	0.83	1.20
7/65	340	0.32	0.49	0.56	0.59	0.60	0.62	0.75	0.76	0.76	0.82	1.03	1.32
10/65	325	0.31	0.46	0.52	0.55	0.62	0.62	0.69	0.68	0.68	0.77	0.80	1.26
Average		0.36	0.58	0.64	0.65	0.70	0.77	0.80	0.81	0.83	0.88	0.95	1.23

Table I-4. The ratio ^{14}C (calc)/^{14}C (obs) at 70N latitude and 16 km altitude

DATE	OBS	MPI	GISS	CALJPL	GSFC	AER	LLNLND	WASH	NCAR	CAMED	LLNL	ITALY	DUPONT
1/64	830	0.90	0.82	1.03	0.97	1.04	1.07	1.16	1.10	0.83	1.19	0.88	1.20
4/64	600	0.83	0.83	1.07	0.93	1.32	1.28	1.13	1.27	1.17	1.38	1.08	1.48
7/64	400	0.65	0.98	0.84	0.99	1.33	0.74	1.00	1.54	1.40	1.43	1.38	1.88
10/64	450	0.42	0.57	0.55	0.67	0.73	0.55	0.81	1.13	1.09	0.83	1.13	1.33
1/65	430	0.42	0.53	0.65	0.65	0.77	0.87	0.91	0.93	0.80	1.00	1.12	1.21
4/65	310	0.56	0.79	0.82	0.87	1.16	1.26	1.06	1.13	1.26	1.39	1.45	1.45
7/65	250	0.50	0.72	0.66	0.83	1.00	0.68	0.83	1.18	1.32	1.20	1.52	1.52
10/65	270	0.39	0.56	0.56	0.63	0.74	0.59	0.74	0.96	1.07	0.83	1.33	1.19
1/66	305	0.39	0.49	0.59	0.56	0.66	0.75	0.75	0.75	0.79	0.90	1.16	0.98
Average		0.56	0.70	0.75	0.79	0.97	0.87	0.93	1.11	1.08	1.13	1.23	1.36

Table I-5. Altitude/km of maximum carbon-14 mixing ratio from January 1964 to July 1966

DATE	OBS	AER	NCAR	MPI	DUPONT	GSFC	LLNL	CALJPL	WASH	GISS	CAMED	LLNLND	ITALY
1/64	21	22	22	24	22	22	22	22	20	22	20	22	21
4/64	20	21	24	26	22	24	21	22	22	24	22	22	22
7/64	22	21	27	28	24	26	24	25	24	26	24	23	23
10/64	24	22	30	30	26	30	28	27	27	28	24	25	24
1/65	21	33	32	31	32	30	30	30	28	30	27	25	24
4/65	23	>40	>40	34	34	34	34	34	30	30	30	25	25
7/65	25	>40	>40	>40	>40	>40	>40	>40	>40	>40	>40	30	25
10/65	25	>40	>40	>40	>40	>40	>40	>40	>40	>40	>40	35	32
1/66	25	>40	>40	>40	>40	>40	>40	>40	>40	>40	>40	>40	36
4/66	>33	>40	>40	>40	>40	>40	>40	>40	>40	>40	>40	>40	>40
7/66	25	>40	>40	>40	>40	>40	>40	>40	>40	>40	>40	>40	>40

Table I-6. Change of carbon-14 mixing ratio with altitude between 25 and 33 km, ($d\mu/dz$), expressed in carbon-14 mixing ratio units per kilometer, 31 north latitude

DATE	OBS	ITALY	CALJPL
1/64	-32	-32	-32
4/64	-40	-44	-18
7/64	-40	-44	-11
10/64	-32	-22	-2
1/65	-24	-12	+2
4/65	-11	-5	+4
7/65	-12	-6	+6
10/65	-10	+4	+7
1/66	-6	+8	+6
4/66	+5	+9	+5
7/66	-2	+9	+5

Table I-7. Excess carbon-14 mixing-ratio units measured as a function of latitude and altitude for November 1970 [Telegadas et al., 1972]

65N		42N		30N		9N		34S	
z	C	z	C	z	C	z	C	z	C
31.0	120	36.0	125	36.3	96	31.5	106	32.3	120
30.0	130	31.5	130	35.5	110	30.6	110	27.3	120
27.0	140	30.8	134	34.0	120	27.2	111	27.2	130
26.9	141	27.4	138	33.0	130	23.7	120	27.0	134
24.0	139	27.2	140	32.8	128	23.0	110	24.2	135
22.3	140	24.0	143	32.5	116	22.0	100	23.9	130
20.3	130	23.3	140	31.2	130	21.4	90	21.7	120
		21.3	130	27.6	142	21.0	80	21.1	128
		20.9	125	27.2	131	20.8	77	20.9	119
		19.6	120	26.5	140			20.0	120
				24.4	139				
				24.3	140				
				23.9	142				
				22.2	130				
				21.2	128				
				21.0	135				
				20.3	120				
				19.6	110				

Table I-8. Excess carbon-14 mixing ratio measurements at 30N latitude, 26 km altitude, during November 1970 (almost 8 years after cessation of atmospheric nuclear bomb tests of 1961-62 series). At this latitude and altitude, the observed carbon-14 mixing ratio was a maximum.

	OBS	NCAR	MPI	GSFC	AER	LLNL	CALJPL	LLNLND	CAMED	WASH	DUPONT	ITALY
Value	140	68	72	72	76	82	86	96	102	110	118	127
Ratio	1.00	0.49	0.51	0.51	0.54	0.59	0.61	0.69	0.73	0.79	0.84	0.91

Subtract tropospheric value (50) from stratospheric value

Value	90	18	22	22	26	32	36	46	52	60	68	77
Ratio	1.00	0.20	0.24	0.24	0.29	0.36	0.40	0.51	0.58	0.67	0.76	0.86

Table I-9. Settling velocities (x 10^{-4} cm s^{-1}) of aerosol particles used in the strontium-90 simulation

Southern Hemisphere Latitude Zones in Degrees

km	90-85	85-80	80-75	75-70	70-65	65-60	60-55	55-50	50-45	45-40	40-35	35-30	30-25	25-20	20-15	15-10	10-5	5-0
0-2	6.9	6.9	6.9	6.9	6.9	6.9	6.9	7.3	9.0	9.9	8.9	8.0	9.9	10.3	6.7	13.1	17.5	3.8
2-4	7.1	7.1	7.1	7.1	7.1	7.1	7.1	7.4	9.1	9.9	9.0	8.1	10.0	10.4	6.8	13.2	17.4	4.0
4-6	8.9	8.9	8.9	8.9	8.9	8.9	8.9	9.4	12.1	13.1	12.1	11.2	13.4	13.2	10.9	16.3	21.3	6.5
6-8	10.9	10.9	10.9	10.9	10.9	10.9	10.9	10.3	11.4	11.2	12.0	11.9	13.0	13.2	14.4	19.3	35.2	11.5
8-10	13.9	13.9	13.9	13.9	13.9	13.9	13.9	14.3	14.9	17.5	18.2	15.5	12.9	19.4	17.9	19.3	35.2	20.8
10-12	25.1	25.1	25.1	25.1	25.1	25.1	25.1	24.4	24.4	25.6	22.5	21.4	22.9	27.0	21.1	24.4	35.2	29.6
12-14	32.7	32.7	32.7	32.7	32.7	32.7	32.7	32.6	32.6	32.1	29.0	29.9	31.2	34.0	34.1	29.7	43.0	25.2
14-16	47.6	47.6	47.6	47.6	47.6	47.6	47.6	49.7	46.1	44.8	44.3	44.3	43.5	42.5	42.3	41.4	45.5	42.5
16-18	64.4	64.4	64.4	64.4	64.4	64.4	64.4	65.2	62.6	61.5	56.7	56.6	54.4	53.5	54.0	47.3	40.5	54.4
18-20	82.4	82.4	82.4	82.4	82.4	82.4	82.4	82.1	81.1	79.6	77.2	74.8	73.8	75.9	72.1	66.2	63.5	65.7
20-22	100.7	100.7	100.7	100.7	100.7	100.7	100.7	102.1	100.0	100.7	101.5	100.7	99.4	103.4	102.3	97.7	97.6	91.9
22-24	118.5	118.5	118.5	118.5	118.5	118.5	118.5	123.4	120.7	123.3	125.7	128.0	133.7	142.8	146.9	143.3	139.5	126.9
24-26	132.4	132.4	132.4	132.4	132.4	132.4	132.4	143.6	142.1	148.0	152.0	161.9	170.8	189.9	199.6	197.7	197.8	186.3
26-28	143.4	143.4	143.4	143.4	143.4	143.4	143.4	170.1	166.6	175.2	189.1	202.2	220.5	240.9	261.7	269.7	268.5	263.6
28-30	184.2	184.2	184.2	184.2	184.2	184.2	184.2	213.6	202.3	203.9	220.6	239.8	268.0	288.5	328.9	346.4	349.2	341.2
30-32	209.9	209.9	209.9	209.9	209.9	209.9	209.9	281.6	251.6	269.2	266.1	273.9	299.7	315.0	368.2	394.0	383.9	402.7

Northern Hemisphere Latitude Zones in Degrees

km	0-5	5-10	10-15	15-20	20-25	25-30	30-35	35-40	40-45	45-50	50-55	55-60	60-65	65-70	70-75	75-80	80-85	85-90
0-2	11.5	9.3	11.1	10.4	9.7	10.5	13.4	8.6	6.5	9.7	8.4	10.2	10.2	10.2	10.2	10.2	10.2	10.2
2-4	11.6	9.4	11.1	10.5	9.8	10.6	13.5	8.7	6.7	9.8	8.5	10.2	10.2	10.2	10.2	10.2	10.2	10.2
4-6	15.4	13.8	14.6	13.1	13.6	13.7	16.6	12.1	9.7	13.1	10.6	13.6	13.6	13.6	13.6	13.6	13.6	13.6
6-8	16.9	13.6	15.2	13.6	14.7	13.8	13.1	14.3	13.2	13.2	13.1	13.1	13.1	13.1	13.1	13.1	13.1	13.1
8-10	20.8	19.2	22.6	21.4	20.9	20.6	16.8	19.0	16.4	17.0	13.7	14.8	14.8	14.8	14.8	14.8	14.8	14.8
10-12	25.8	27.6	30.3	24.2	25.1	27.7	23.6	26.7	25.7	27.1	21.9	24.3	24.3	24.3	24.3	24.3	24.3	24.3
12-14	30.3	34.5	35.4	34.8	31.7	32.4	33.6	31.9	32.4	34.9	33.3	32.1	32.1	32.1	32.1	32.1	32.1	32.1
14-16	39.1	44.3	45.0	45.5	47.1	43.4	44.6	44.3	42.3	50.5	44.7	43.3	43.3	43.3	43.3	43.3	43.3	43.3
16-18	54.2	45.9	49.1	50.4	54.3	55.9	58.2	58.0	59.4	59.5	58.8	57.2	57.2	57.2	57.2	57.2	57.2	57.2
18-20	69.6	70.5	61.9	66.6	68.6	72.6	76.2	77.2	79.7	77.6	78.6	77.3	77.3	77.3	77.3	77.3	77.3	77.3
20-22	92.4	94.3	93.7	98.3	94.0	98.2	99.1	99.8	100.9	98.7	98.8	99.1	99.1	99.1	99.1	99.1	99.1	99.1
22-24	123.1	131.8	136.5	140.4	128.3	131.2	126.6	127.2	127.1	126.7	126.5	126.8	126.8	126.8	126.8	126.8	126.8	126.8
24-26	179.8	192.7	198.7	192.6	174.4	174.0	155.5	154.2	155.0	157.0	160.2	155.6	155.6	155.6	155.6	155.6	155.6	155.6
26-28	265.1	270.2	264.7	251.8	225.2	220.2	178.9	173.6	186.9	179.3	176.2	183.2	183.2	183.2	183.2	183.2	183.2	183.2
28-30	352.9	353.7	339.7	318.2	297.8	267.9	223.8	211.5	202.1	234.5	239.7	234.1	234.1	234.1	234.1	234.1	234.1	234.1
30-32	394.9	385.7	379.3	348.3	322.8	291.9	302.2	272.0	265.1	284.0	273.9	282.5	282.5	282.5	282.5	282.5	282.5	282.5

Table I-10: Strontium-90 global stratospheric residence times in years based on linear least squares regression analysis. For each case the model derived burden was integrated globally from 16 to 60 km.

Models	Stratospheric Residence Time (years) With Settling Velocities	Without Settling Velocities
AER	0.9	1.8
CALJPL	1.4	NA
CAMED-theta	1.6	2.9
GSFC	1.1	1.8
ITALY	2.1	3.9
LLNL	1.5	2.3
WASH	1.6	2.3

Table I-11. The ratio ^{90}Sr (calc)/^{90}Sr (obs) at four latitudes and at the altitude of maximum observed ^{90}Sr at each latitude for calculations that included settling velocities of stratospheric Junge particles

AER

DATE	64N 17km	31N 20km	9N 24km	34S 20km
10/64	1.00	1.00	1.00	1.00
1/65		0.86		
4/65	0.97	0.83	0.43	1.00
7/65	0.78	0.53		0.78
10/65	0.56	0.51	0.29	0.62
1/66		0.46	0.25	
4/66	0.57	0.39	0.22	0.72
7/66	0.38	0.31		0.30
10/66		0.30	0.22	0.44

CAMED-theta

DATE	64N 17km	31N 20km	9N 24km	34S 20km
10/64	1.00	1.00	1.00	1.00
1/65		1.06		
4/65	1.03	1.17	0.77	1.08
7/65	0.95	0.87		1.08
10/65	0.85	0.93	0.76	0.97
1/66		1.00	0.80	
4/66	1.14	1.00	0.87	1.26
7/66	0.95	1.00		0.74
10/66		0.94	1.00	1.40

GSFC

DATE	64N 17km	31N 20km	9N 24km	34S 20km
10/64	1.00	1.00	1.00	1.00
1/65		0.77		
4/65	0.68	0.75	0.69	0.95
7/65	0.65	0.52		0.90
10/65	0.50	0.53	0.59	0.72
1/66		0.54	0.55	
4/66	0.54	0.51	0.53	0.84
7/66	0.46	0.48		0.42
10/66		0.42	0.53	0.60

ITALY

DATE	64N 17km	31N 20km	9N 24km	34S 20km
10/64	1.00	1.00	1.00	1.00
1/65		0.92		
4/65	0.86	1.17	0.82	1.19
7/65	0.91	0.67		1.10
10/65	0.75	1.08	0.96	1.00
1/66		1.13	0.96	
4/66	0.98	1.20	1.12	1.80
7/66	0.94	1.28		0.87
10/66		1.29	1.42	1.46

CAL-JPL

DATE	64N 17km	31N 20km	9N 24km	34S 20km
10/64	1.00	1.00	1.00	1.00
1/65		0.80		
4/65	1.36	0.93	0.41	1.08
7/65	0.95	0.54		1.08
10/65	0.70	0.63	0.32	0.97
1/66		0.75	0.34	
4/66	1.45	0.83	0.39	
7/66	0.87	0.63		0.74
10/66		0.60	0.43	1.20

WASH

DATE	64N 17km	31N 20km	9N 24km	34S 20km
10/64	1.00	1.00	1.00	1.00
1/65		0.91		
4/65	0.87	0.93	0.94	1.18
7/65	0.80	0.58		1.10
10/65	0.66	0.64	1.08	1.05
1/66		0.73	1.15	
4/66	0.91	0.75	0.93	1.04
7/66	0.69	0.60		0.67
10/66		0.64	1.08	1.40

LLNL

DATE	64N 17km	31N 20km	9N 24km	34S 20km
10/64	1.00	1.00	1.00	1.00
1/65		1.02		
4/65	0.98	1.12	0.71	1.00
7/65	0.86	0.95		1.12
10/65	0.69	0.66	0.70	1.05
1/66		0.80	0.69	
4/66	1.08	0.86	0.71	1.24
7/66	0.82	0.77		0.72
10/66		0.64	0.84	1.20

FIGURE CAPTIONS

Figure I-1. Carbon-14 altitude-latitude initial conditions for October 1963: a) Telegadas (1971) constructed contours for October 1963 (which is an average of September, October, and November data); b) Johnston (1989) initial conditions for October 1963 (used in this study); and c) Kinnison (1989) model-derived October 1963 data. Contours are in units of 10^5 atoms of carbon-14 per gram of dry air as obtained from a total air sampler. These units are proportional to mixing ratio.

Figure I-2. Individual measurements at 31N of carbon-14 over a three-month time period centered on October 1963, January 1964, October 1964, and October 1965. The solid line for each time period is the profile derived by Johnston (1989) from Telegadas' contours.

Figure I-3. Comparison of model-derived carbon-14 and observed data at 70N between January 1964 and July 1966. Profiles are in units of 10^5 atoms of carbon-14 per gram of dry air as obtained from a total air sampler. These units are proportional to mixing ratio.

Figure I-4. Comparison of model-derived carbon-14 and observed data at 31N between January 1964 and July 1966. Profiles are in units of 10^5 atoms of carbon-14 per gram of dry air as obtained from a total air sampler. These units are proportional to mixing ratio.

Figure I-5. Comparison of model-derived carbon-14 and observed data at 9N between January 1964 and July 1966. Profiles are in units of 10^5 atoms of carbon-14 per gram of dry air as obtained from a total air sampler. These units are proportional to mixing ratio.

Figure I-6. Comparison of model-derived carbon-14 and observed data at 42S between January 1964 and July 1966. Profiles are in units of 10^5 atoms of carbon-14 per gram of dry air as obtained from a total air sampler. These units are proportional to mixing ratio.

Figure I-7. Model-derived carbon-14 altitude-latitude contour plots for October 1964 and October 1965. Contours are in units of 10^5 atoms of carbon-14 per gram of dry air as obtained from a total air sampler. These units are proportional to mixing ratio.

Figure I-8. Comparison of model-derived carbon-14 and observed data at 70N, 42N, 30N, 9N, and 34S for November 1970. Profiles are in units of 10^5 atoms of carbon-14 per gram of dry air as obtained from a total air sampler. These units are proportional to mixing ratio.

Figure I-9. Comparison of LLNLND model-derived carbon-14 with and without additional carbon-14 from the French and Chinese nuclear tests (November 1970). Profiles are in units of 10^5 atoms of carbon-14 per gram of dry air as obtained from a total air sampler. These units are proportional to mixing ratio.

Figure I-10. Contour plot of mixing ratio of carbon-14 in November 1970. Equal distance along the horizontal scale corresponds to equal surface area on the three-dimensional globe, and equal distance along the vertical scale corresponds approximately to equal mass of air. The dashed line represents a standard tropopause.

Figure I-11. Comparison of model-derived strontium-90 and observed data at 64N between April 1965 and July 1966. For each time period, results are shown for strontium-90 treated as a gas and as an aerosol particle. Profiles are in units of disintegrations per minute per 1000 cubic feet (28 m^3) of standard air. These units are proportional to mixing ratio.

Figure I-12. Comparison of model-derived strontium-90 and observed data at 31N between January 1965 and January 1967. For each time period, results are shown for strontium-90 treated as a gas and as an aerosol particle. Profiles are in units of disintegrations per minute per 1000 cubic feet (28 m^3) of standard air. These units are proportional to mixing ratio.

Figure I-13. Comparison of model-derived strontium-90 and observed data at 9N between January 1965 and January 1967. For each time period, results are shown for strontium-90 treated as a gas and as an aerosol particle. Profiles are in units of disintegrations per minute per 1000 cubic feet (28 m^3) of standard air. These units are proportional to mixing ratio.

Figure I-14. Comparison of model-derived strontium-90 and observed data at 30S for January 1965 and 34S for April 1965 through January 1967. For each time period, results are shown for strontium-90 treated as a gas and as an aerosol particle. Profiles are in units of disintegrations per minute per 1000 cubic feet (28 m^3) of standard air. These units are proportional to mixing ratio.

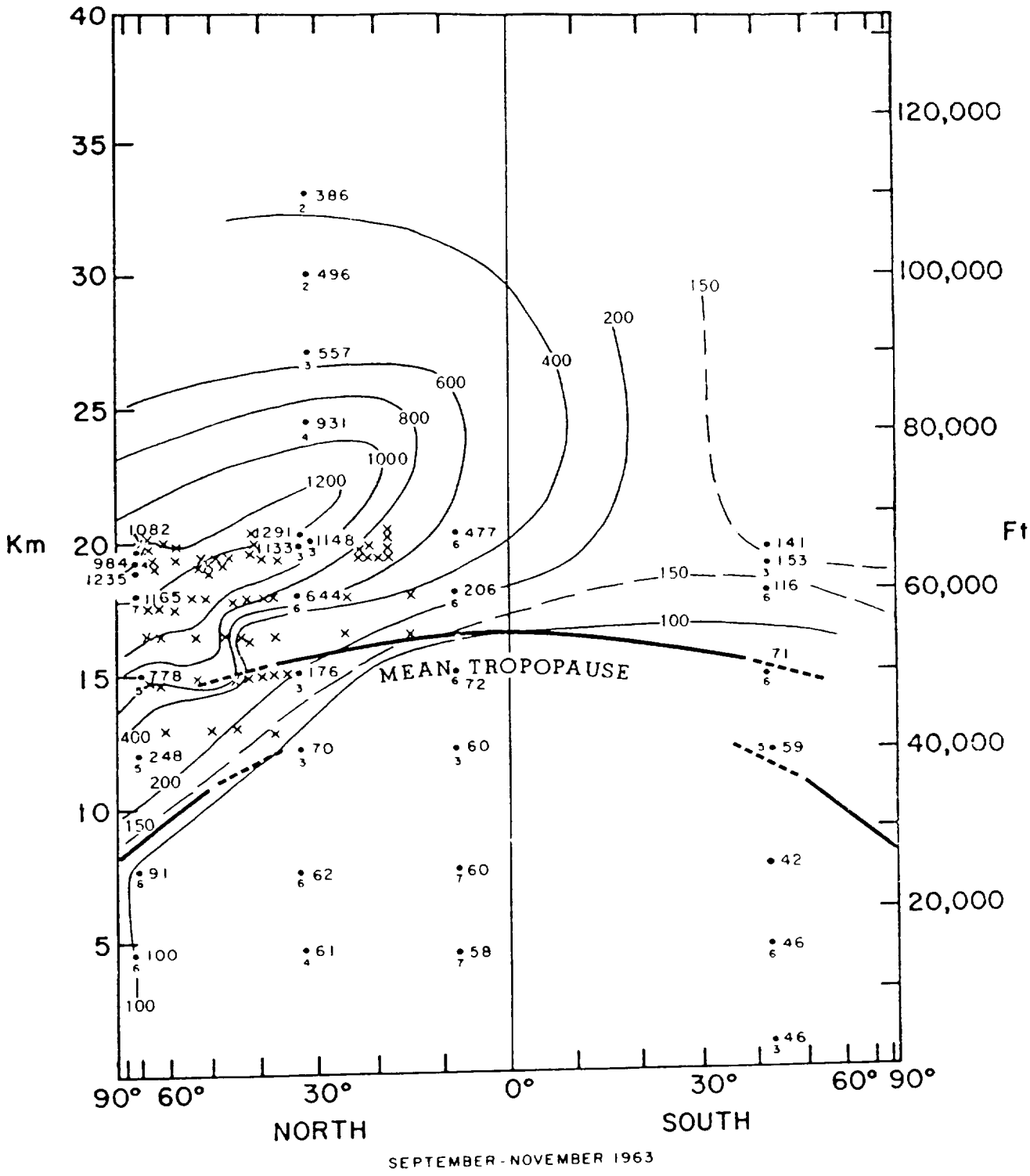
40
35
30
25
20
15
10
5
Km
120,000
100,000
80,000
60,000
40,000
20,000
Ft
MEAN TROPOPAUSE
90° 60° 30° 0° 30° 60° 90°
NORTH
SOUTH
SEPTEMBER - NOVEMBER 1963

Figure I-1 a

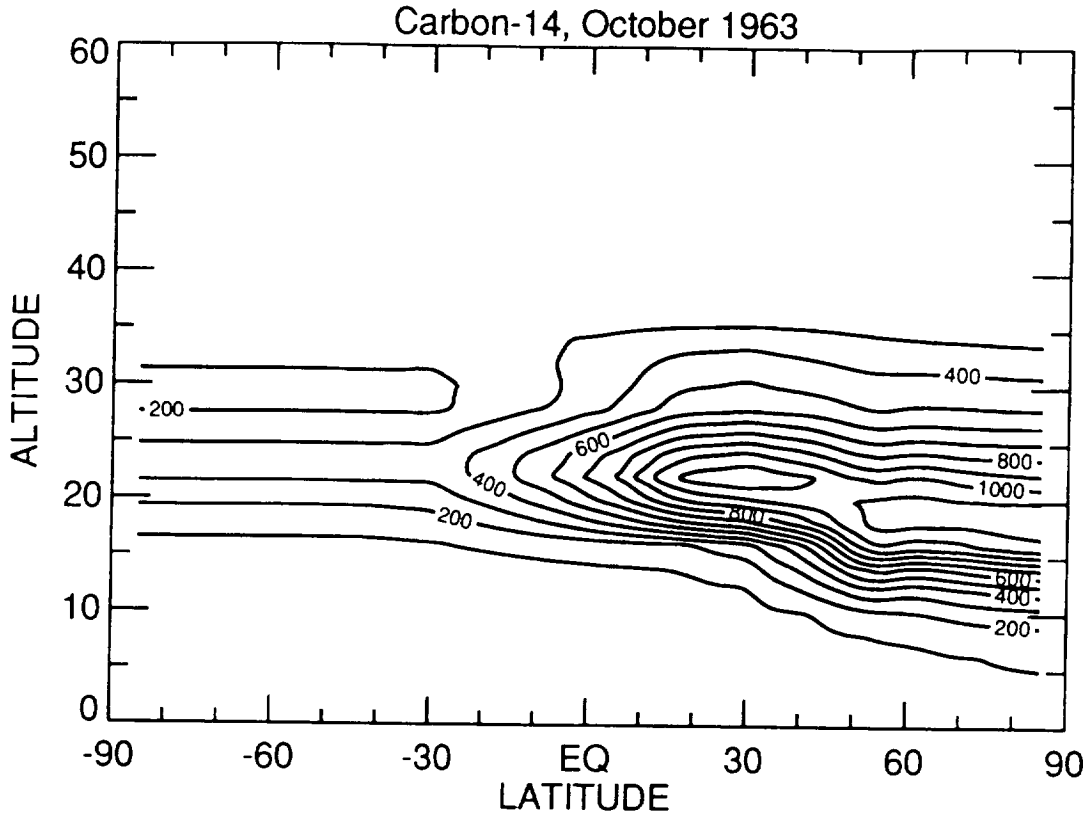

Figure I-1 b

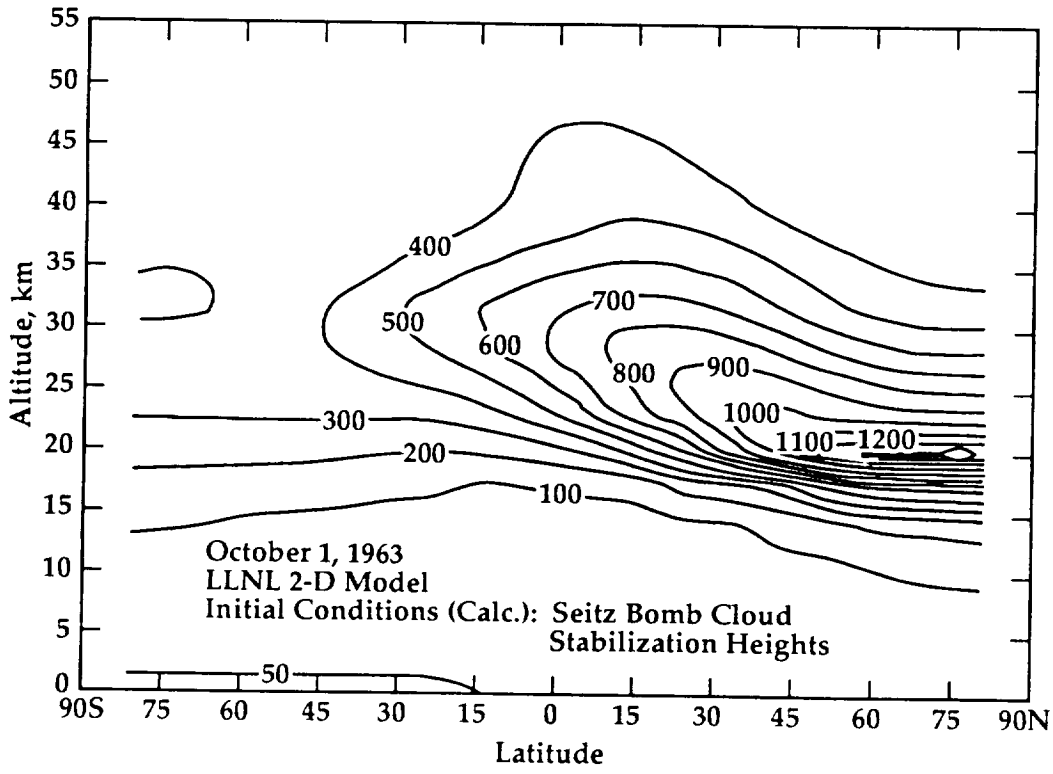

Figure I-1 c

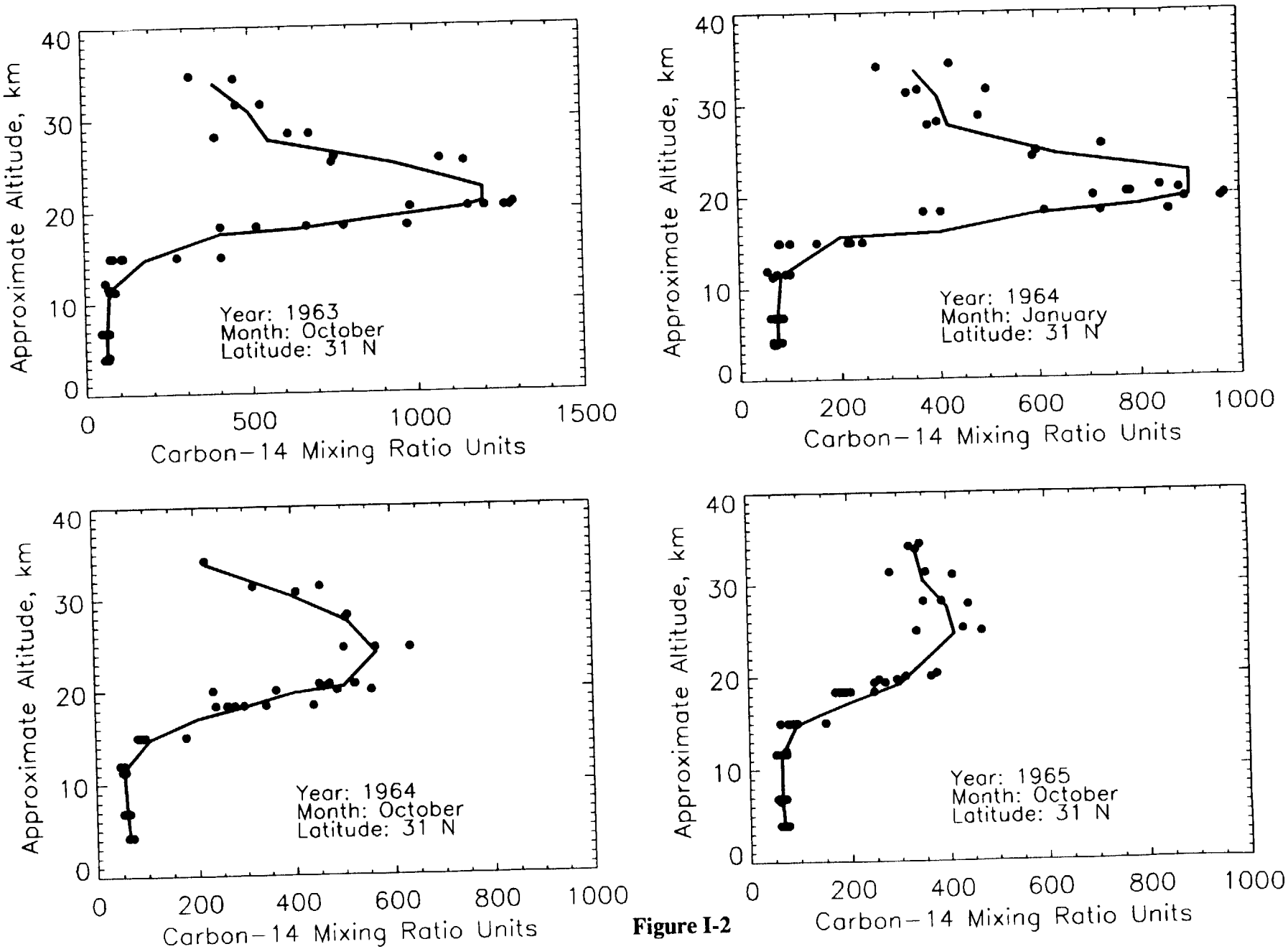
Approximate Altitude, km
Carbon–14 Mixing Ratio Units
Year: 1963
Month: October
Latitude: 31 N
Year: 1964
Month: January
Latitude: 31 N
Year: 1964
Month: October
Latitude: 31 N
Year: 1965
Month: October
Latitude: 31 N

Figure I-2

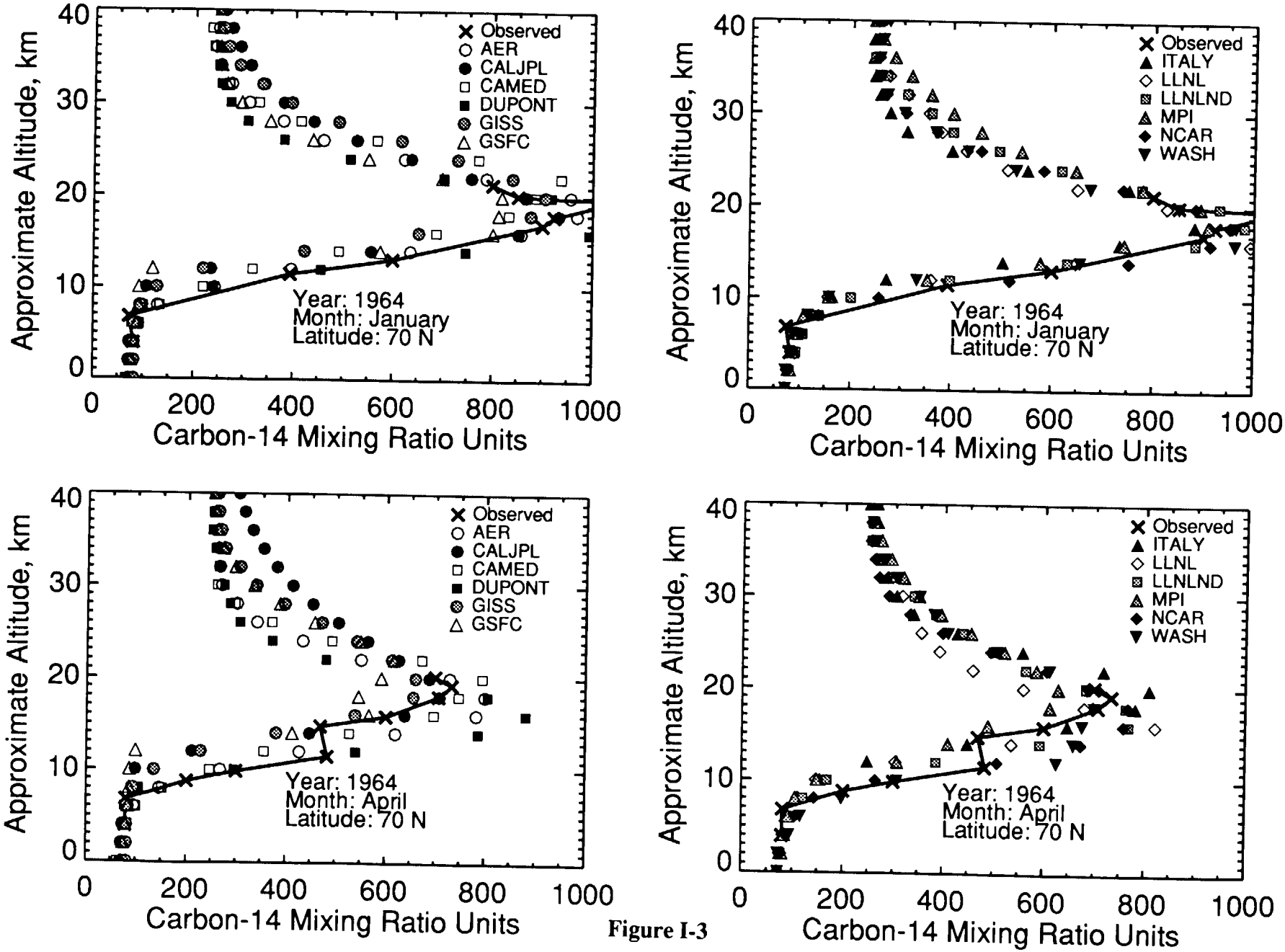
Approximate Altitude, km
Carbon-14 Mixing Ratio Units
Observed
AER
CALJPL
CAMED
DUPONT
GISS
GSFC
Year: 1964
Month: January
Latitude: 70 N
Observed
ITALY
LLNL
LLNLND
MPI
NCAR
WASH
Year: 1964
Month: January
Latitude: 70 N
Year: 1964
Month: April
Latitude: 70 N
Year: 1964
Month: April
Latitude: 70 N

Figure I-3

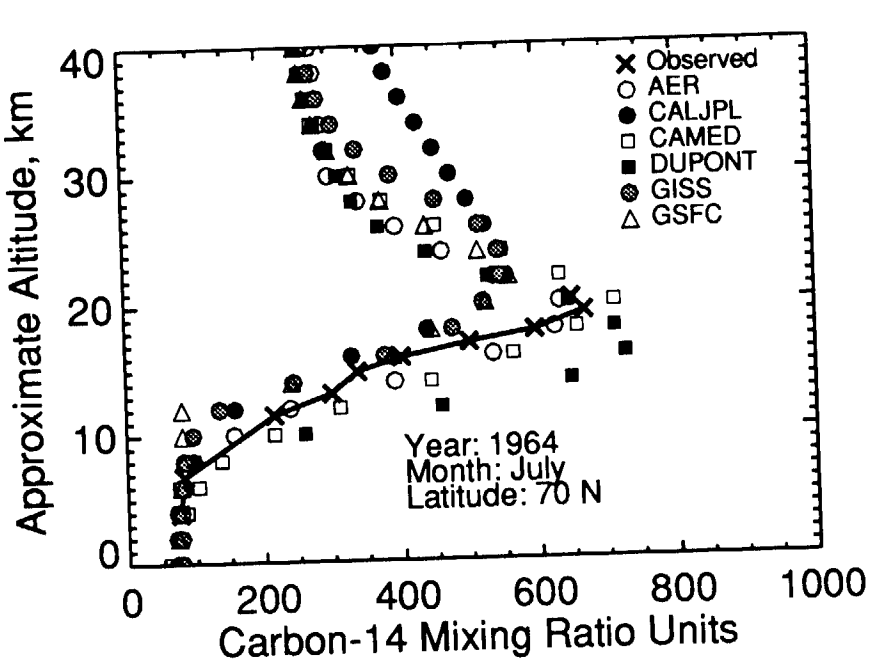

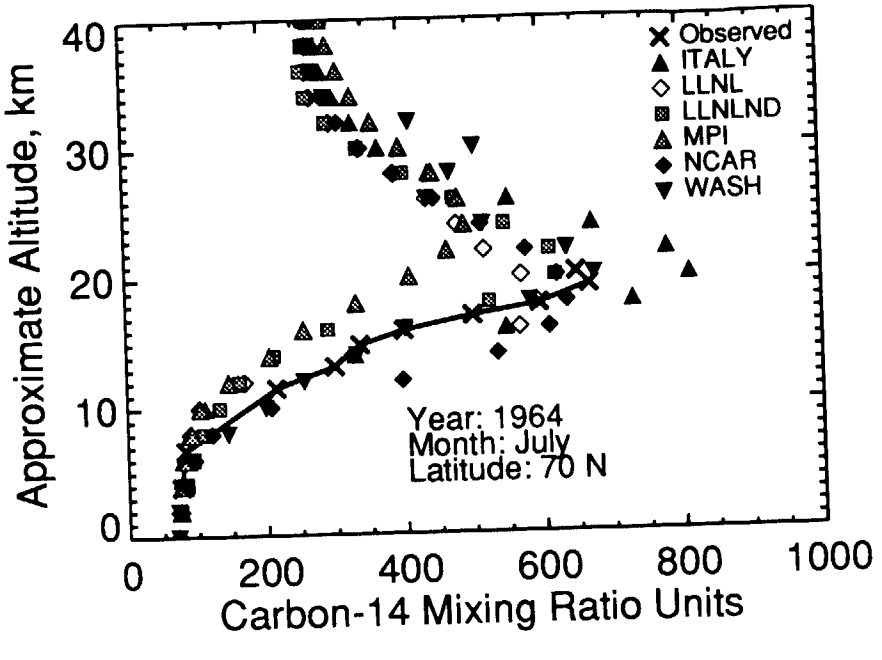

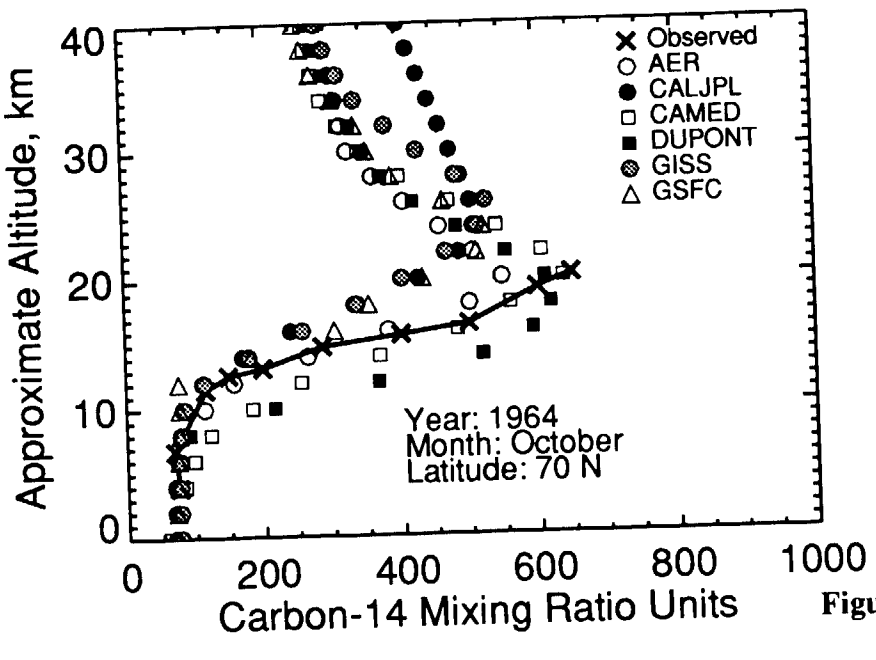

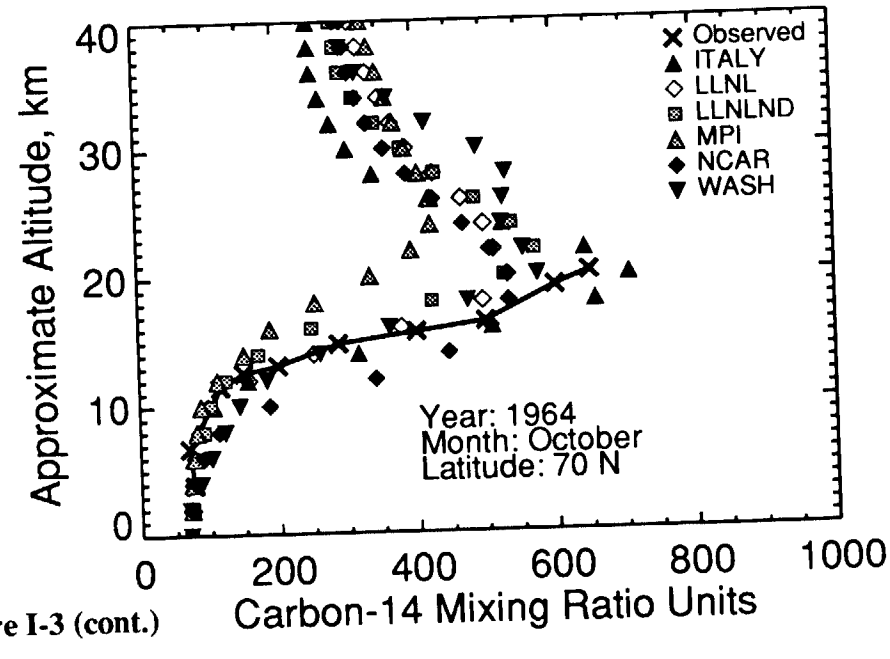

Figure I-3 (cont.)

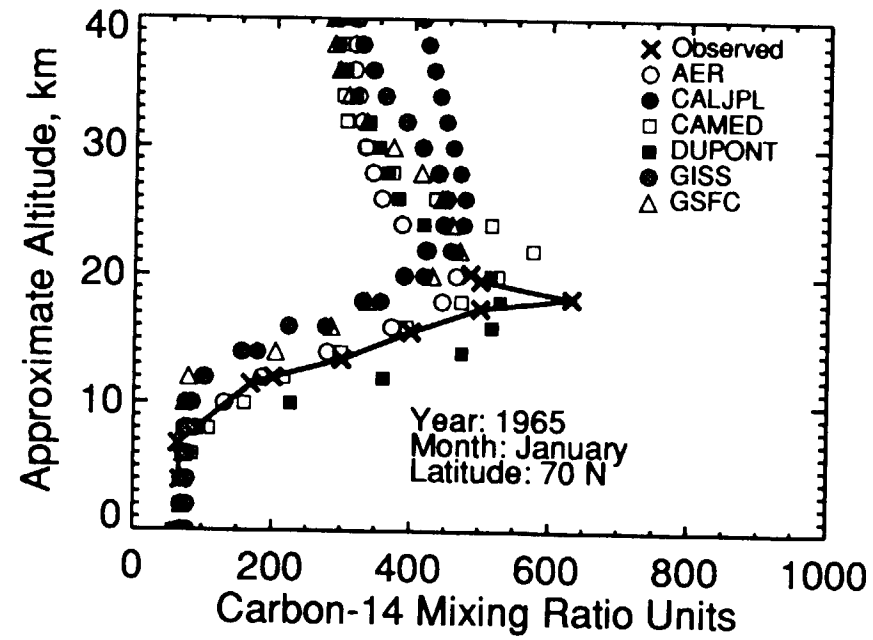

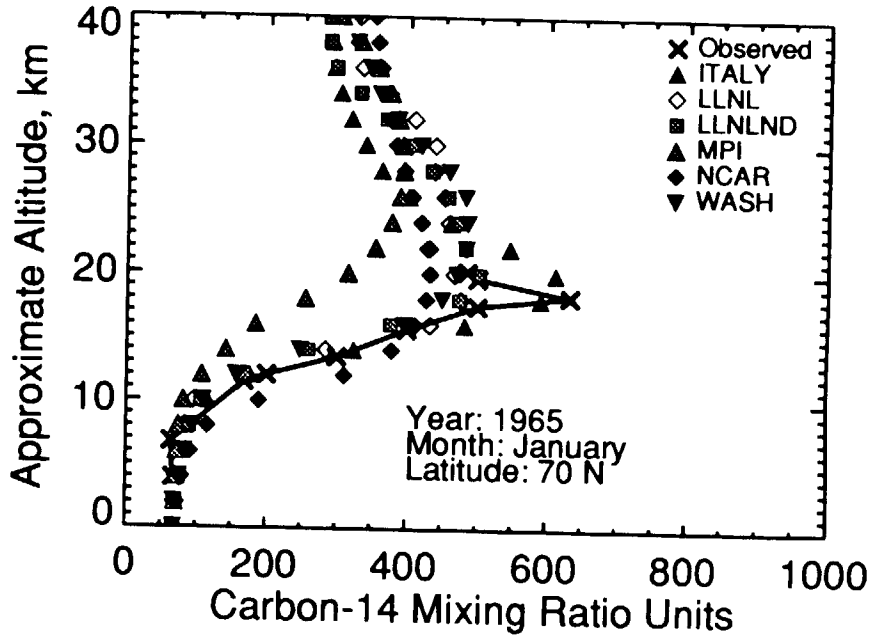

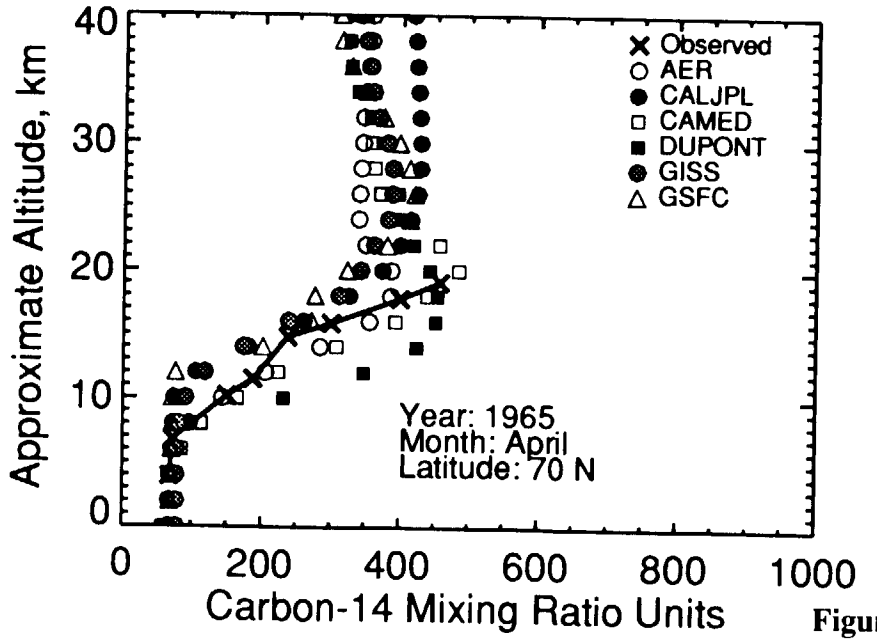

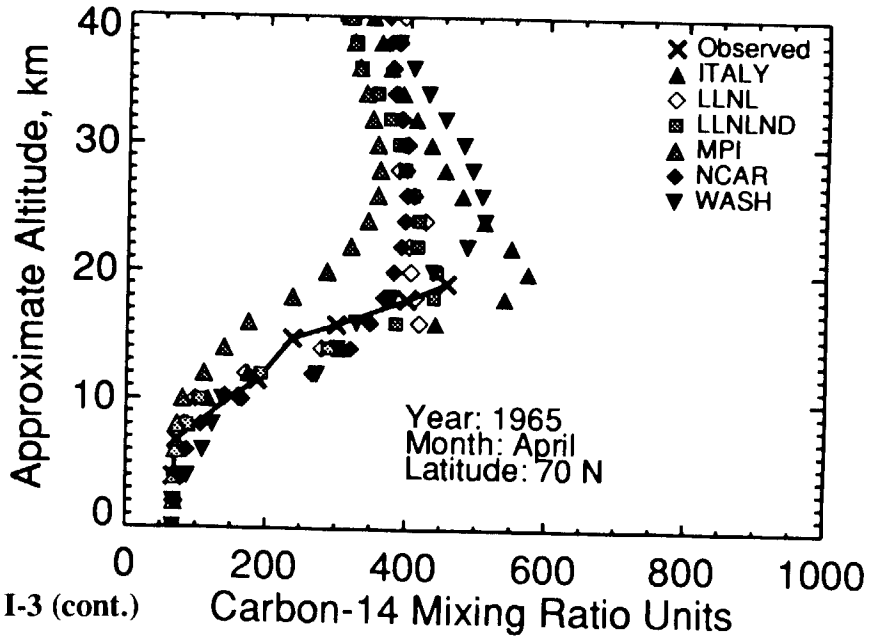

Figure I-3 (cont.)

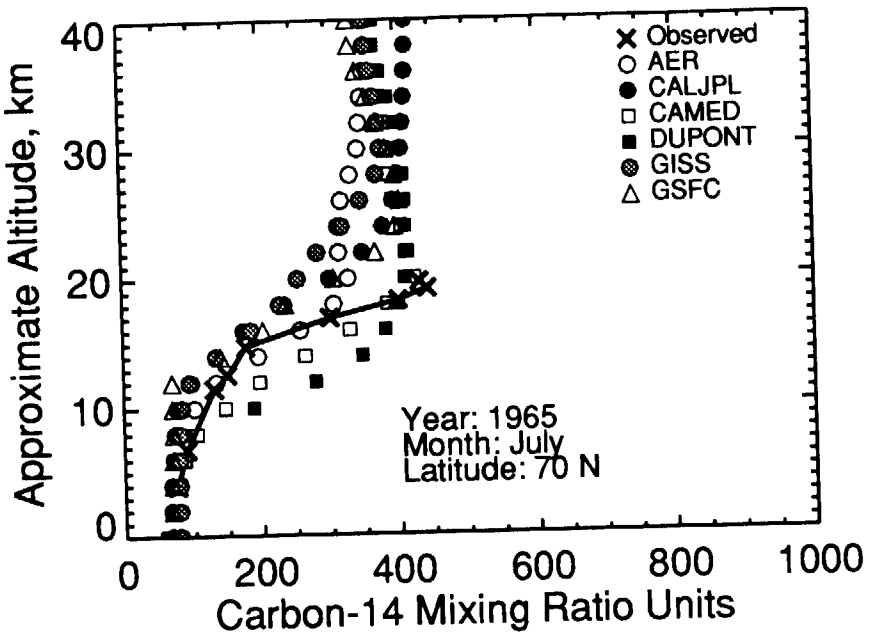

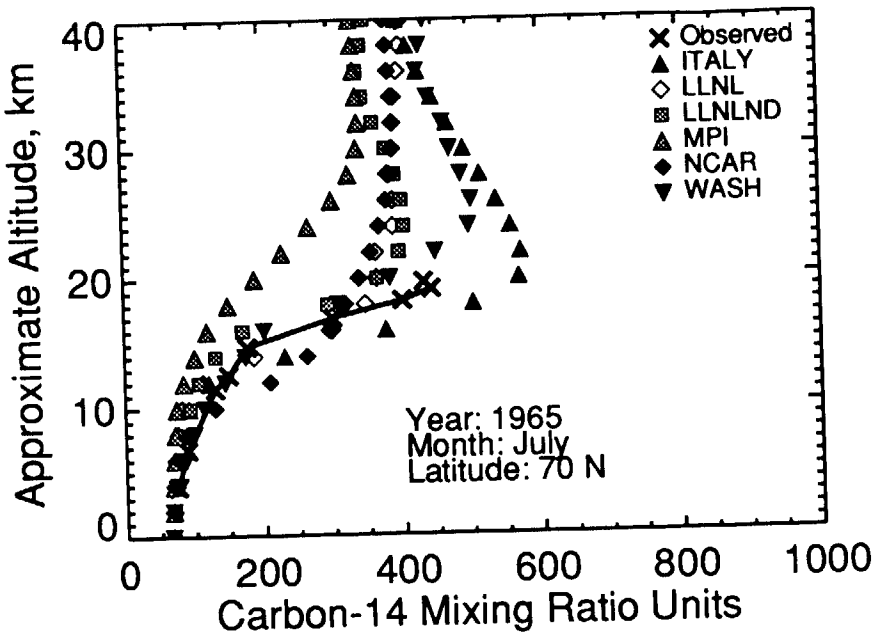

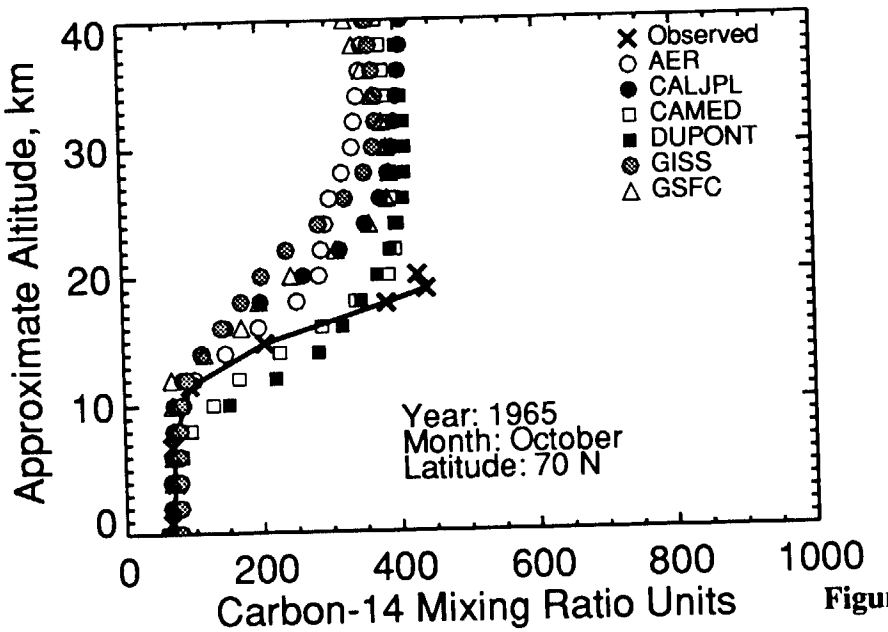

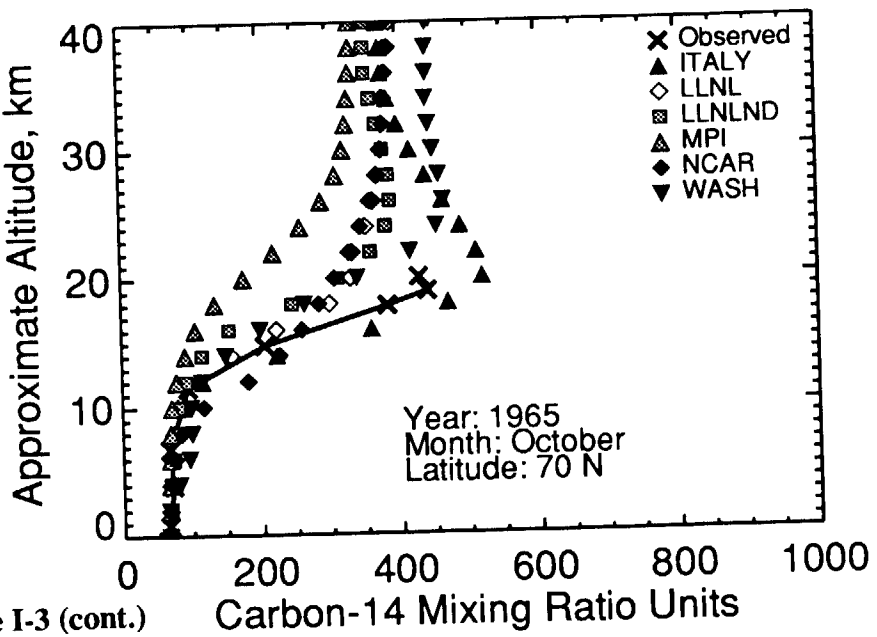

Figure I-3 (cont.)

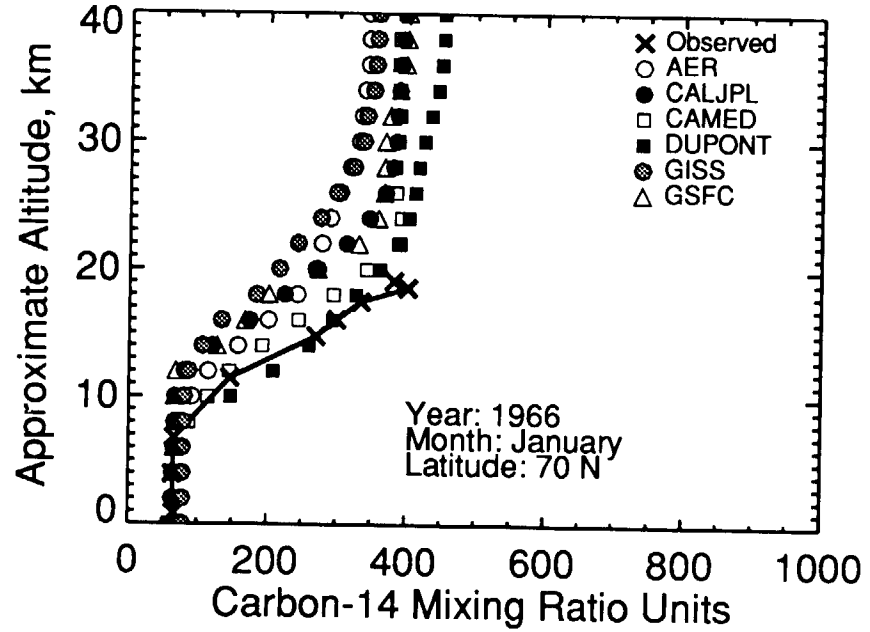

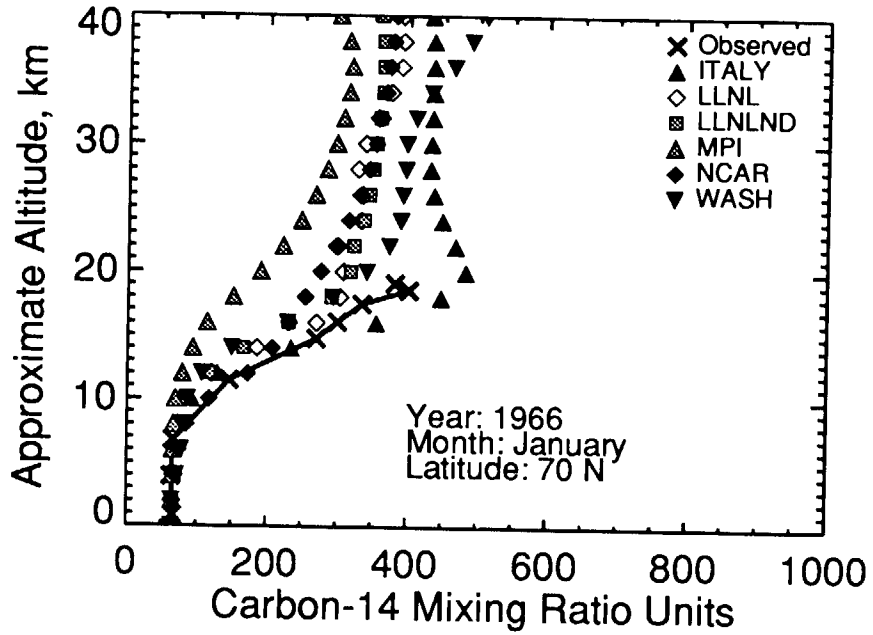

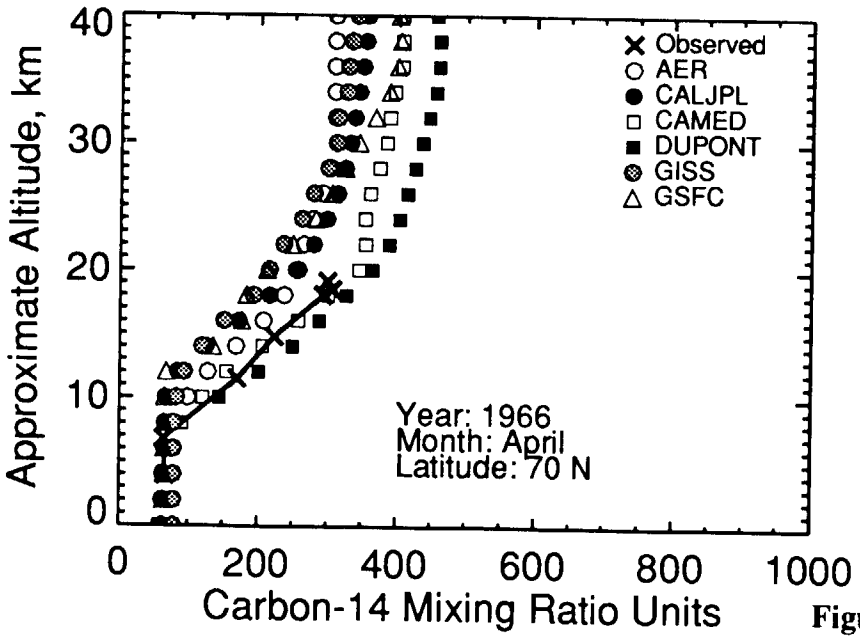

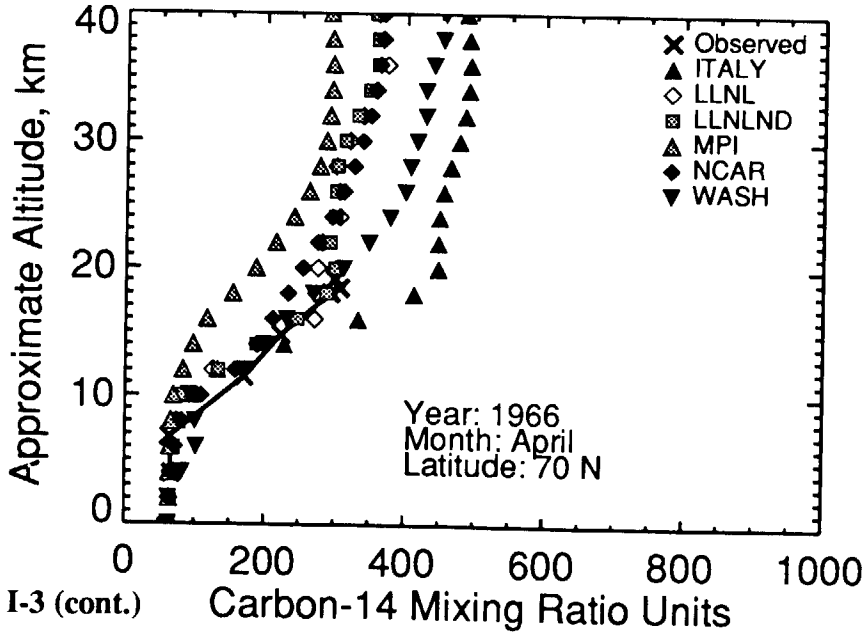

Figure I-3 (cont.)

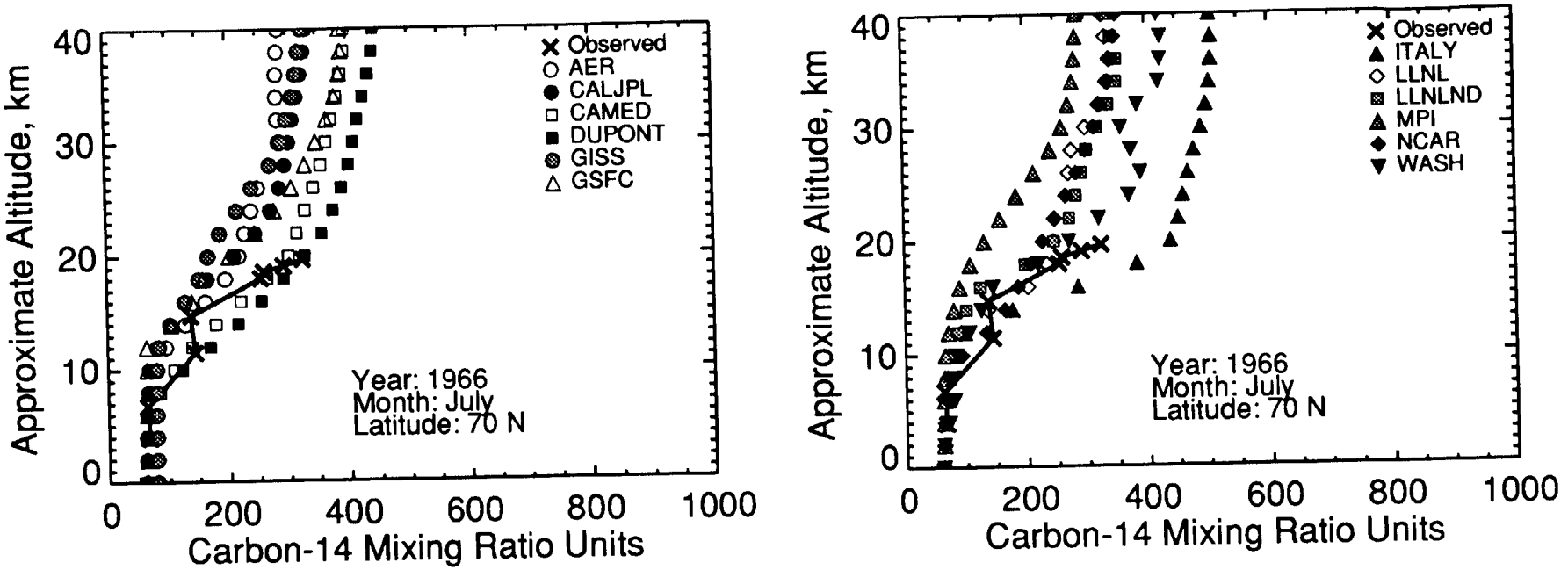

Figure I-3 (cont.)

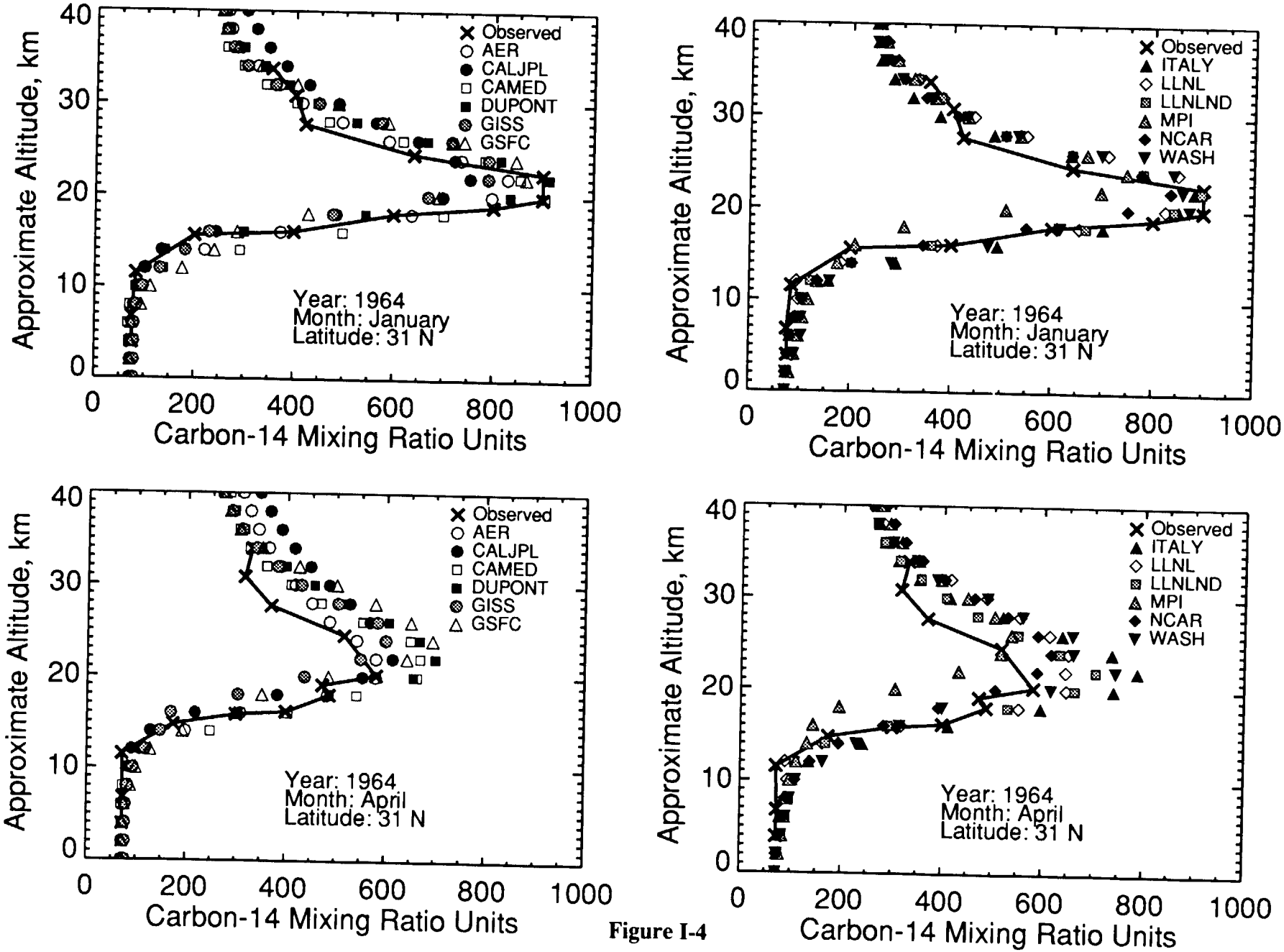
Approximate Altitude, km
Carbon-14 Mixing Ratio Units
Observed
AER
CALJPL
CAMED
DUPONT
GISS
GSFC
Year: 1964
Month: January
Latitude: 31 N
Observed
ITALY
LLNL
LLNLND
MPI
NCAR
WASH
Year: 1964
Month: January
Latitude: 31 N
Year: 1964
Month: April
Latitude: 31 N
Year: 1964
Month: April
Latitude: 31 N

Figure I-4

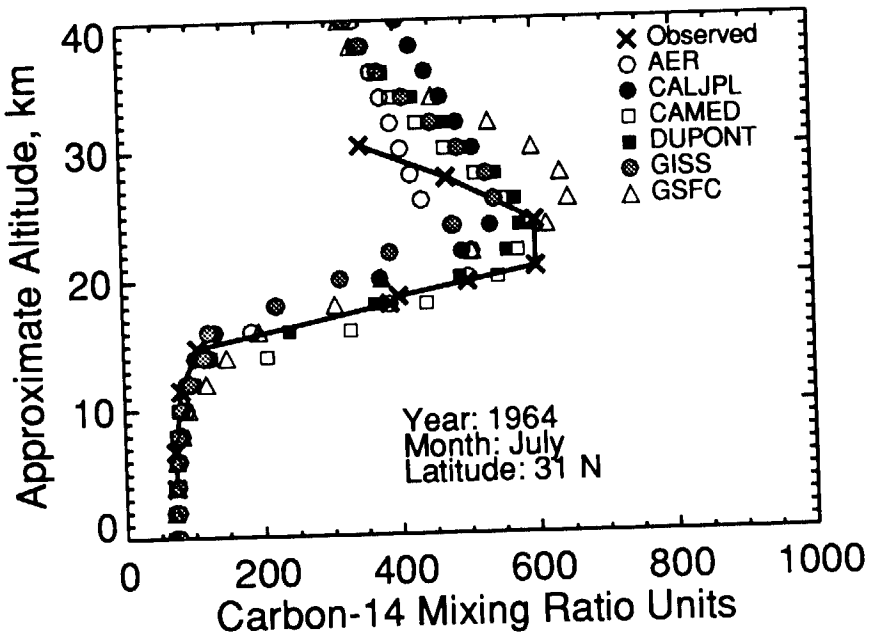

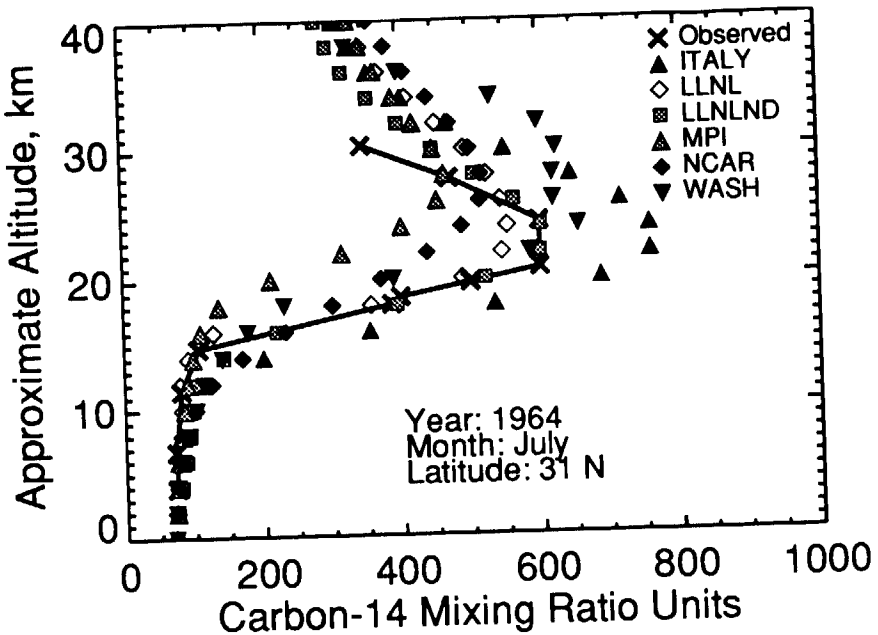

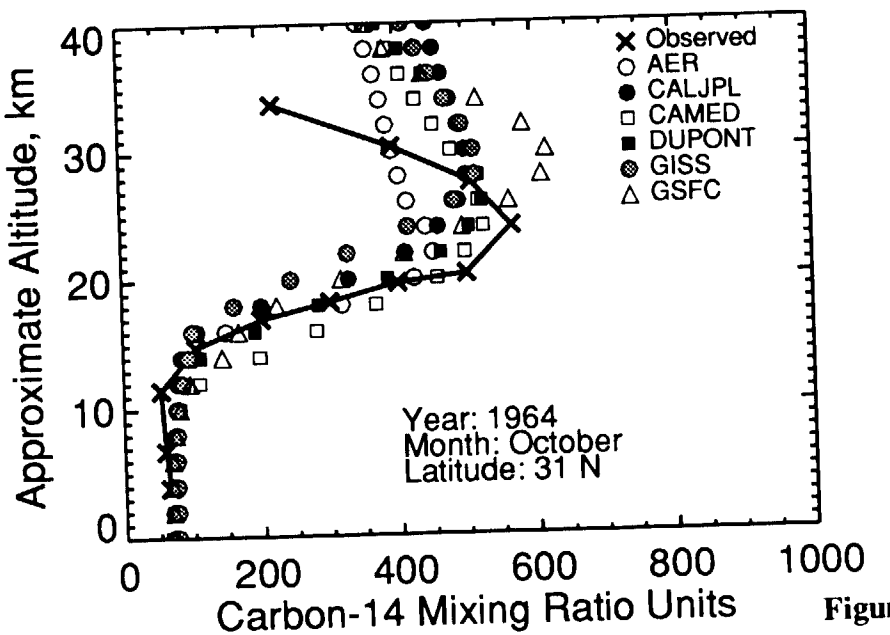

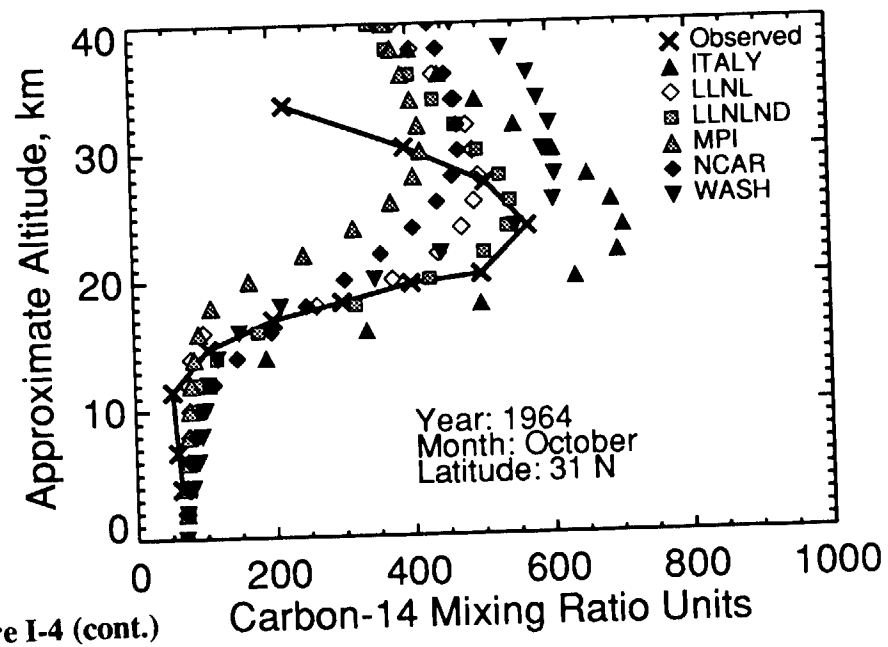

Figure I-4 (cont.)

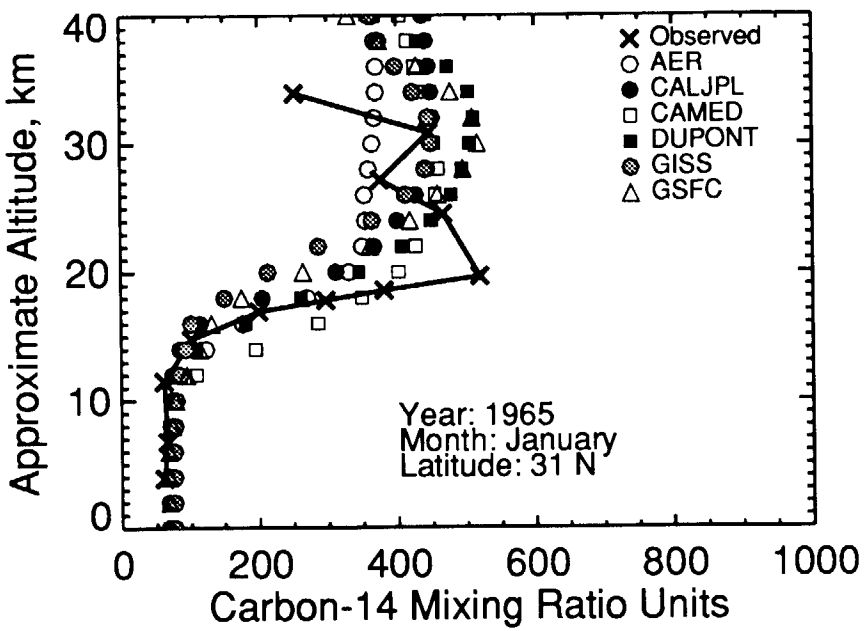

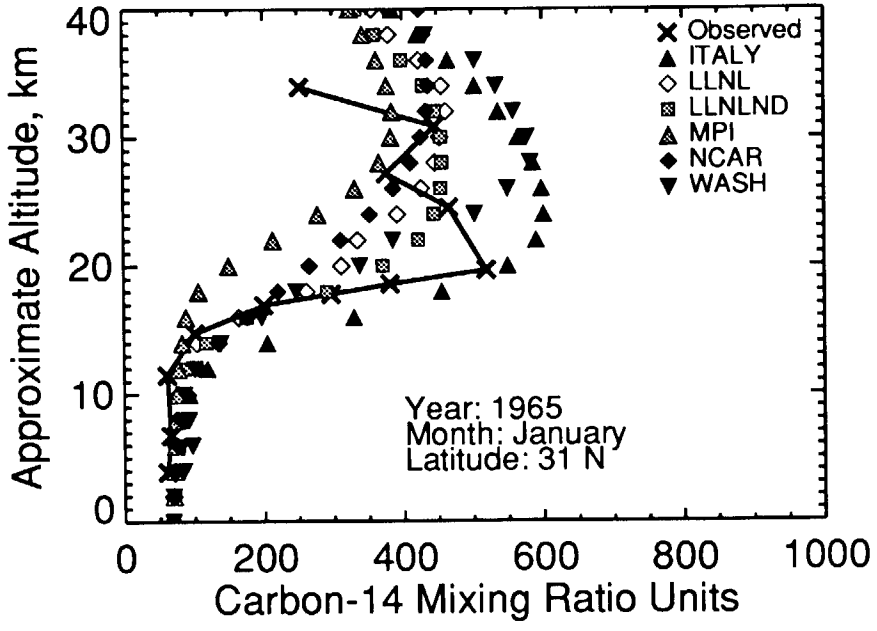

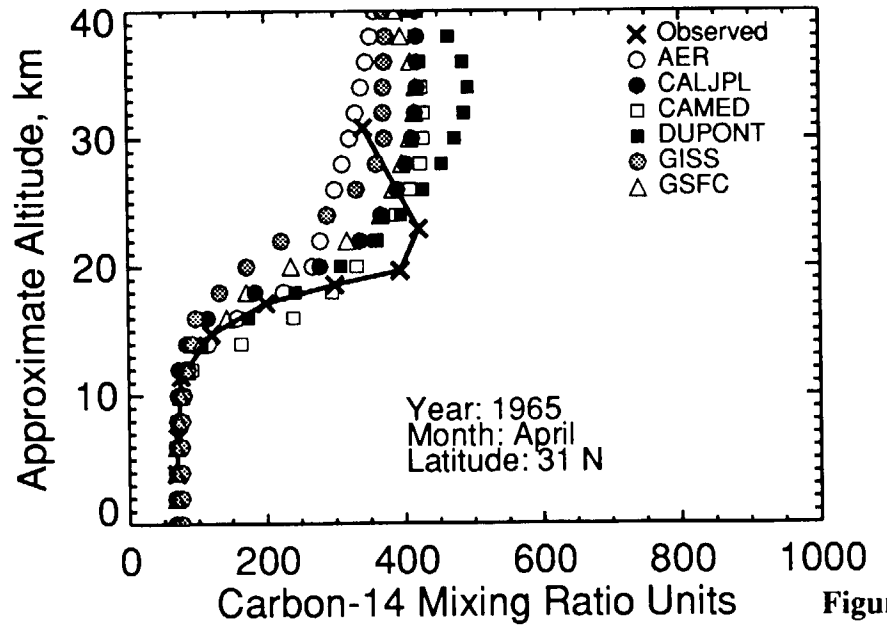

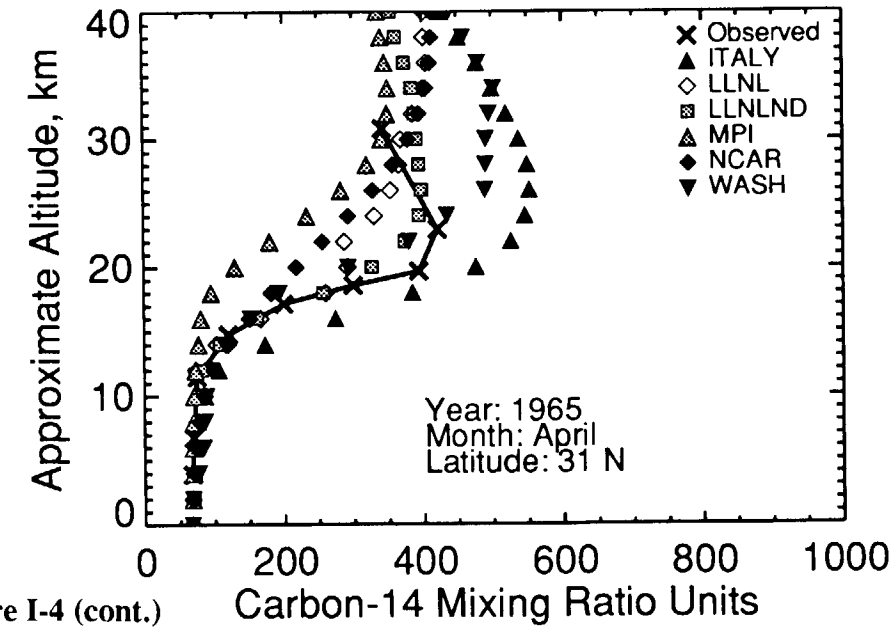

Figure I-4 (cont.)

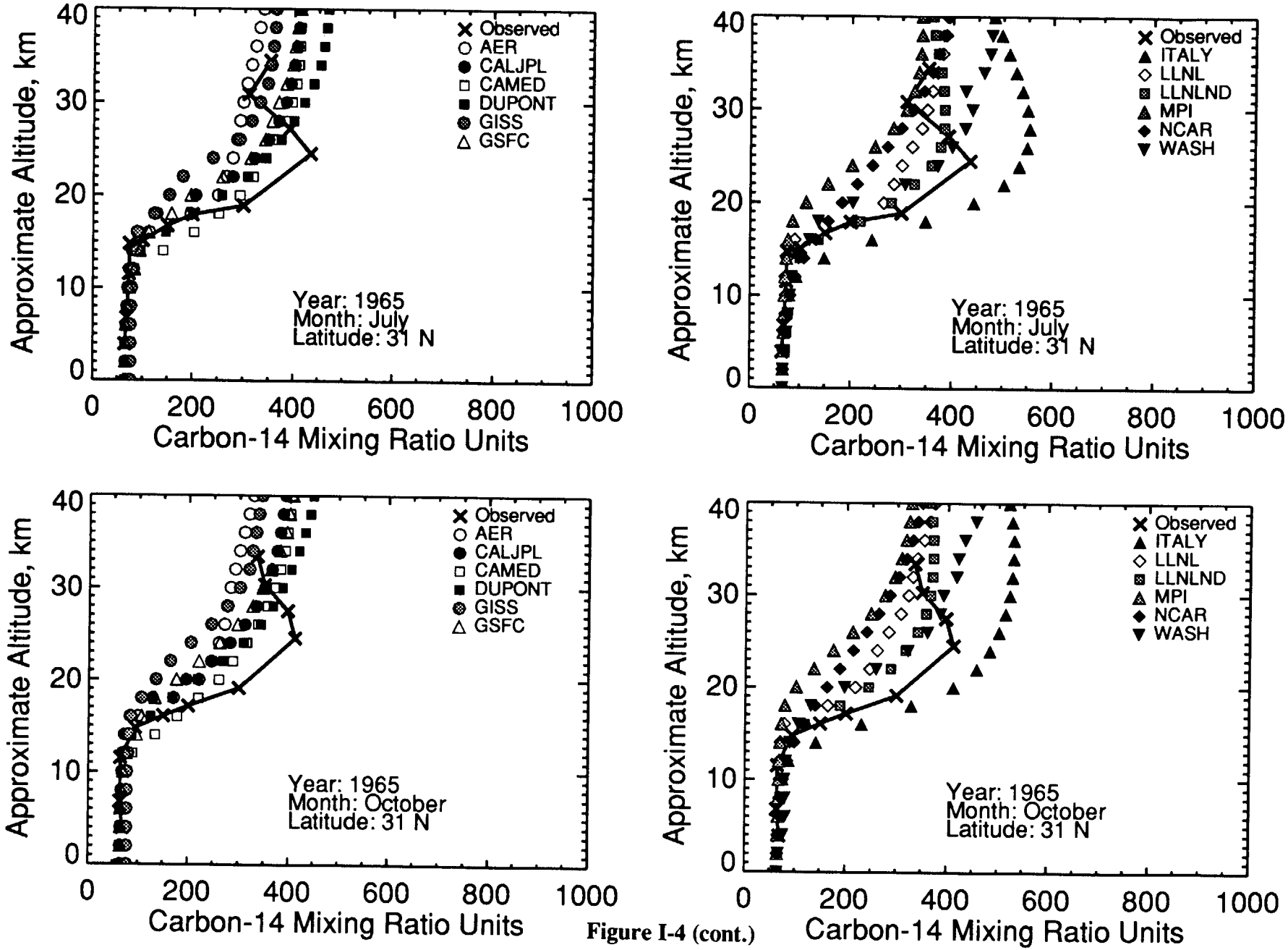

Figure I-4 (cont.)

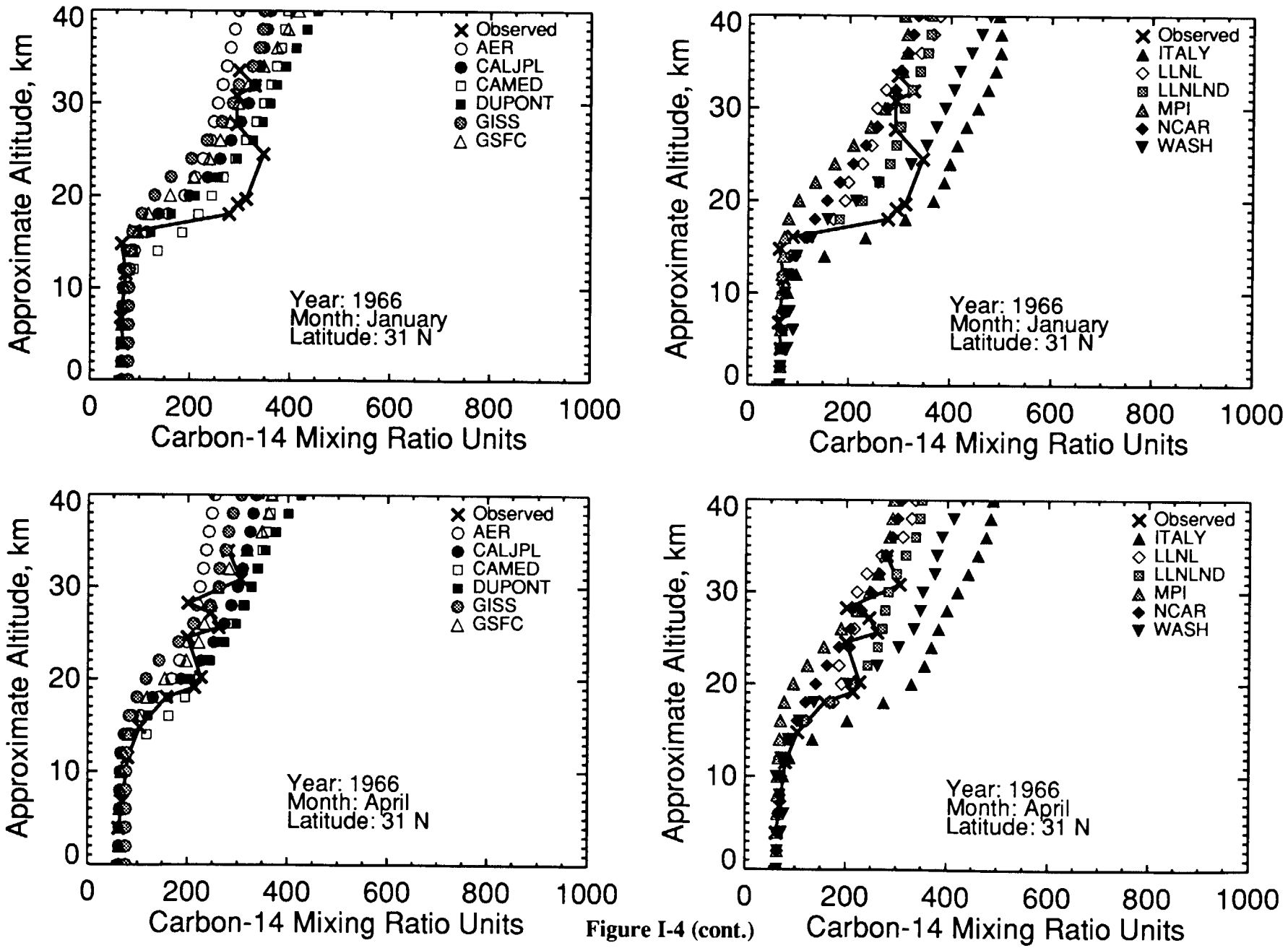

Figure I-4 (cont.)

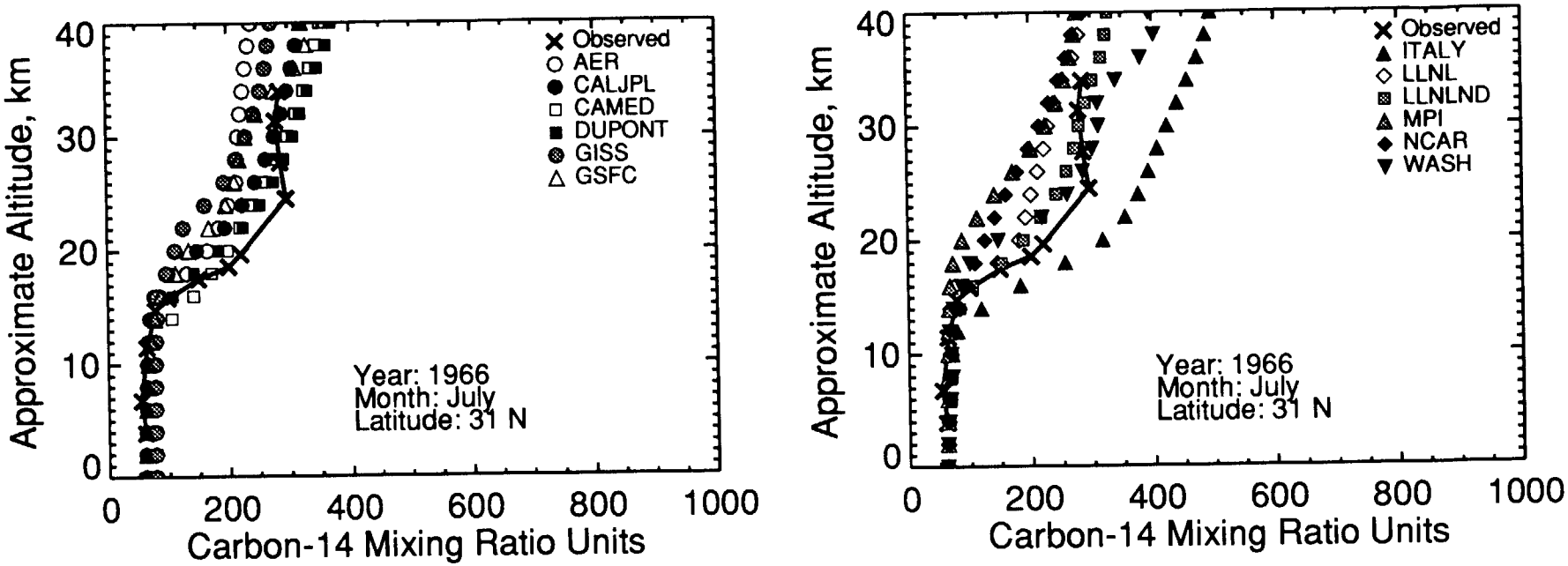

Figure I-4 (cont.)

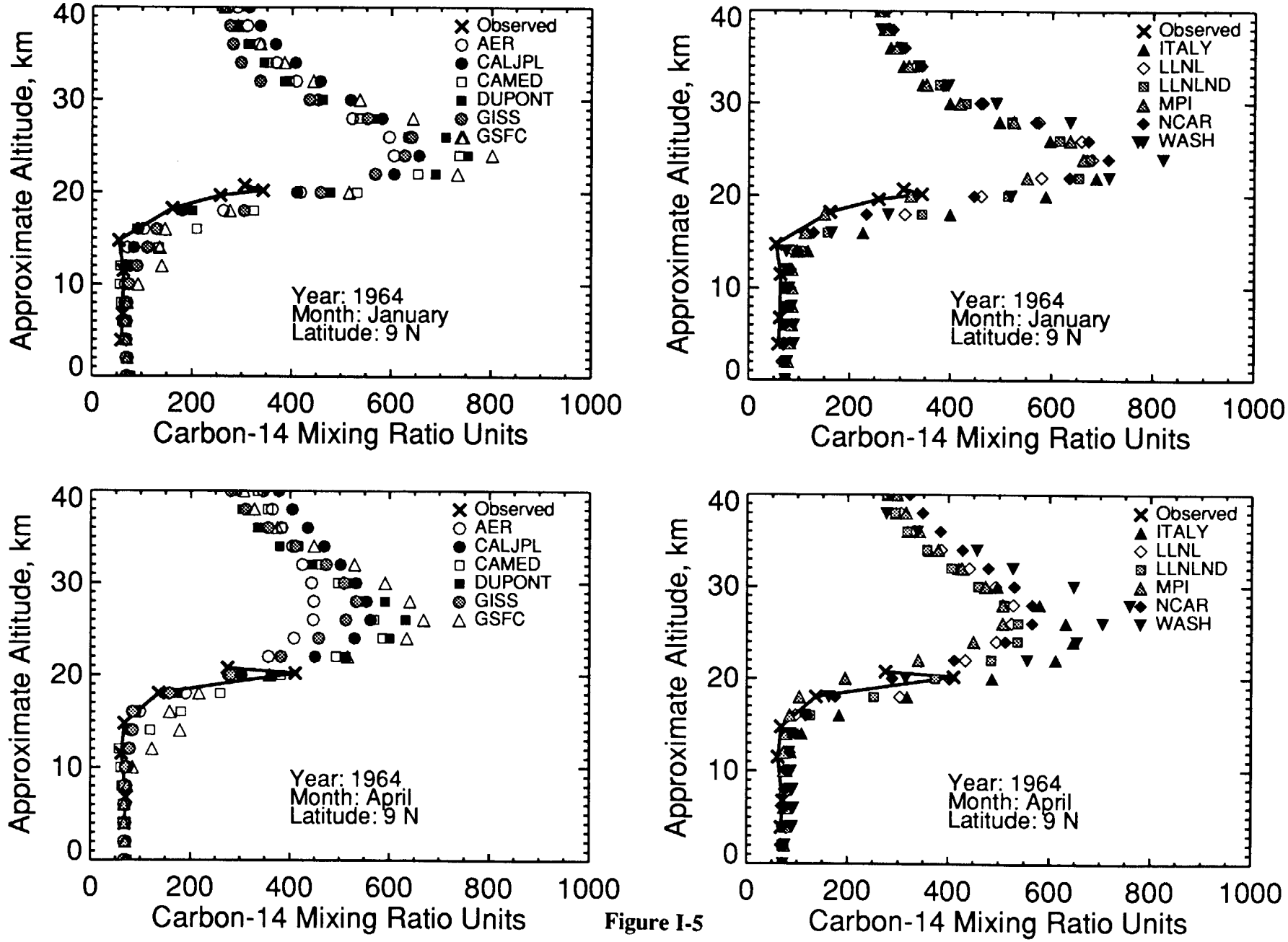
Approximate Altitude, km
Carbon-14 Mixing Ratio Units
Observed
AER
CALJPL
CAMED
DUPONT
GISS
GSFC
ITALY
LLNL
LLNLND
MPI
NCAR
WASH
Year: 1964
Month: January
Latitude: 9 N
Year: 1964
Month: April
Latitude: 9 N

Figure I-5

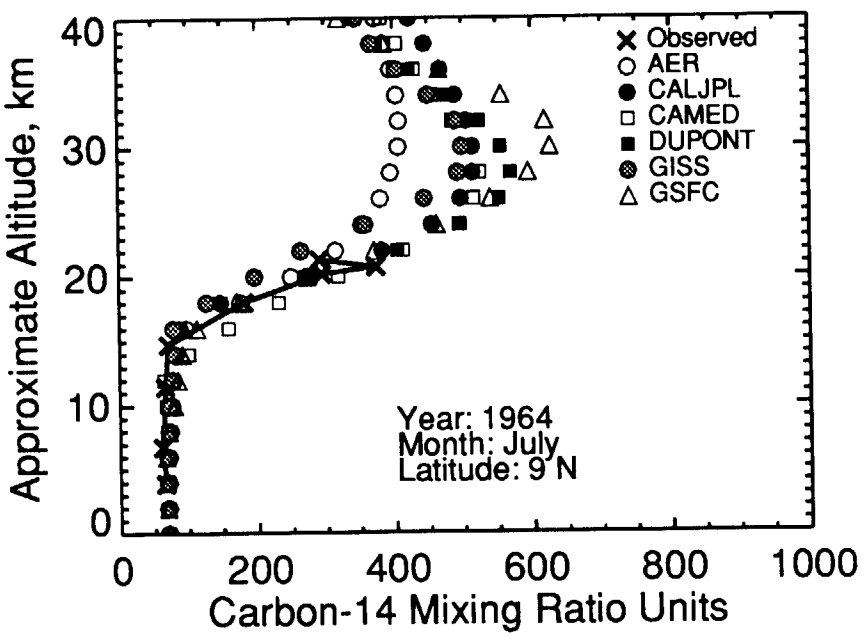

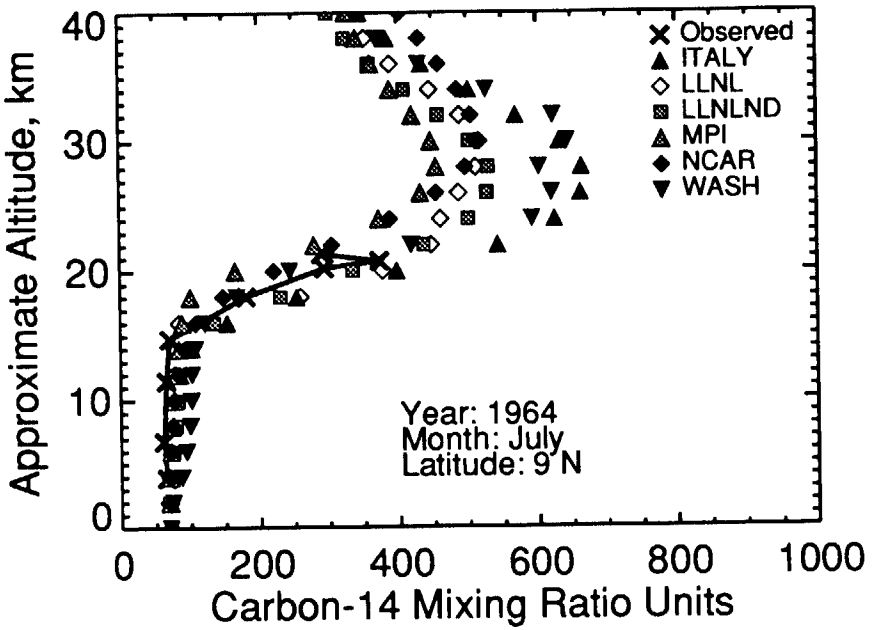

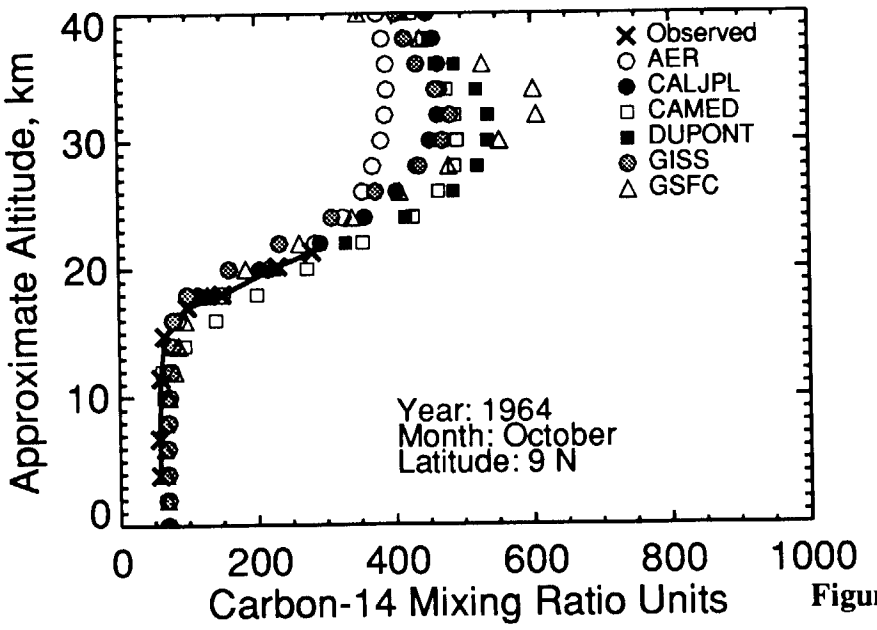

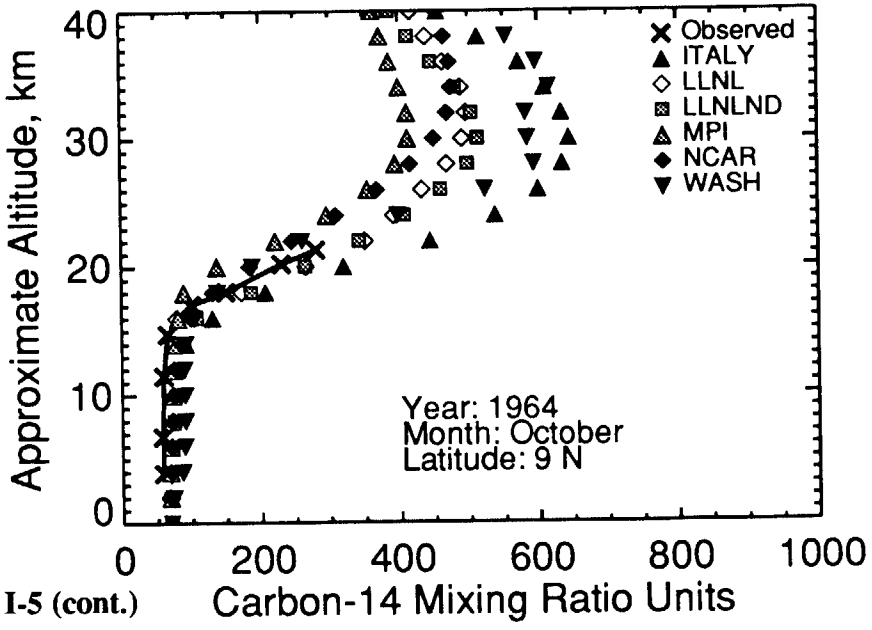

Figure I-5 (cont.)

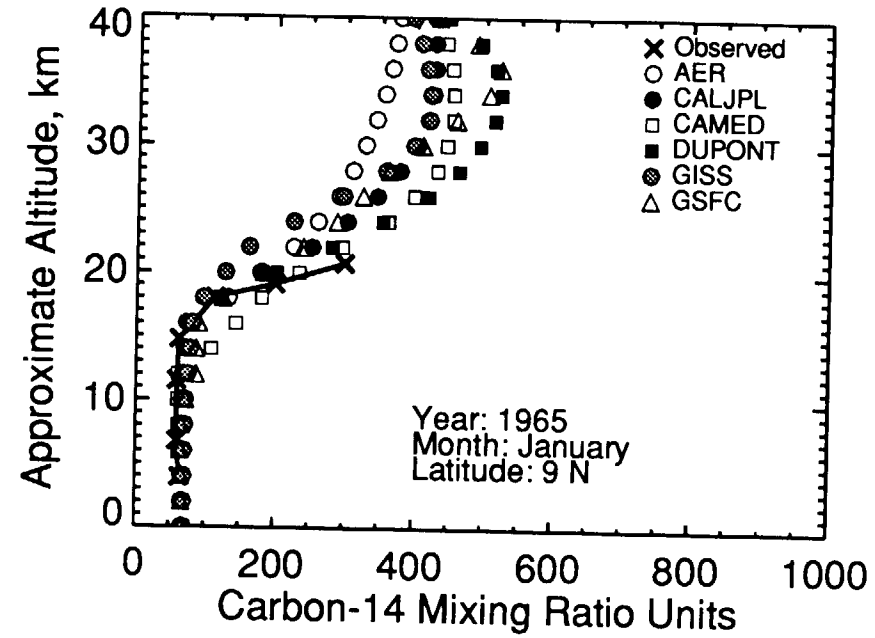

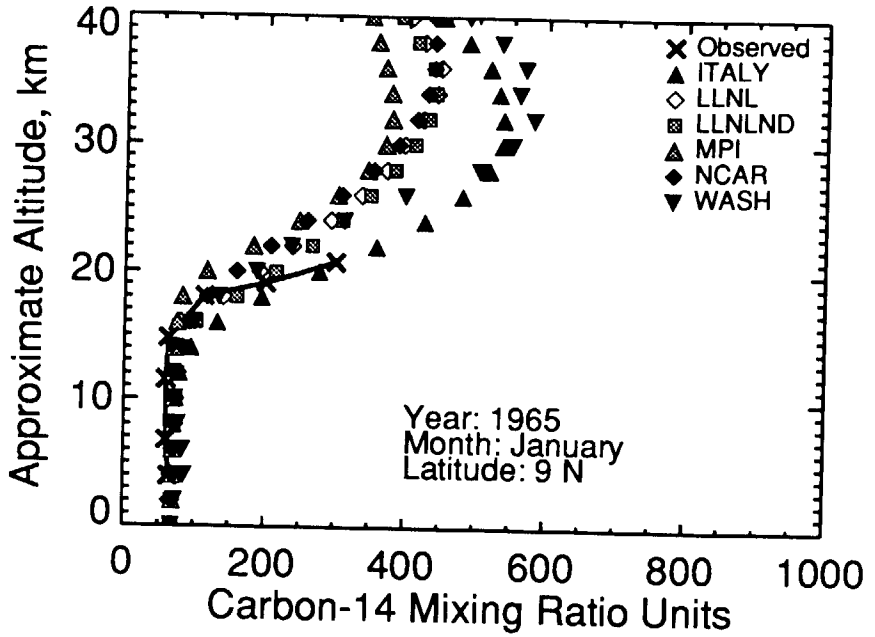

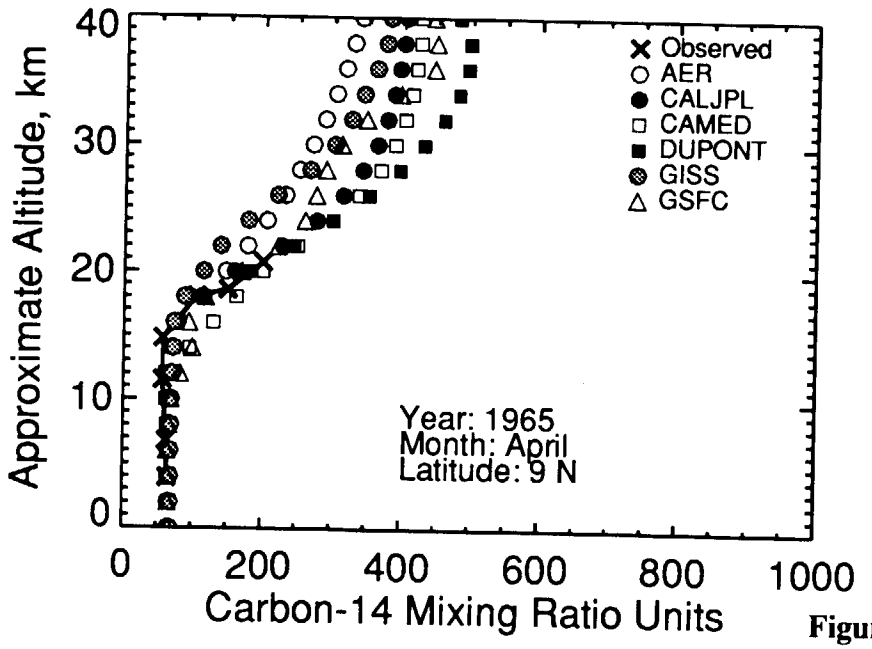

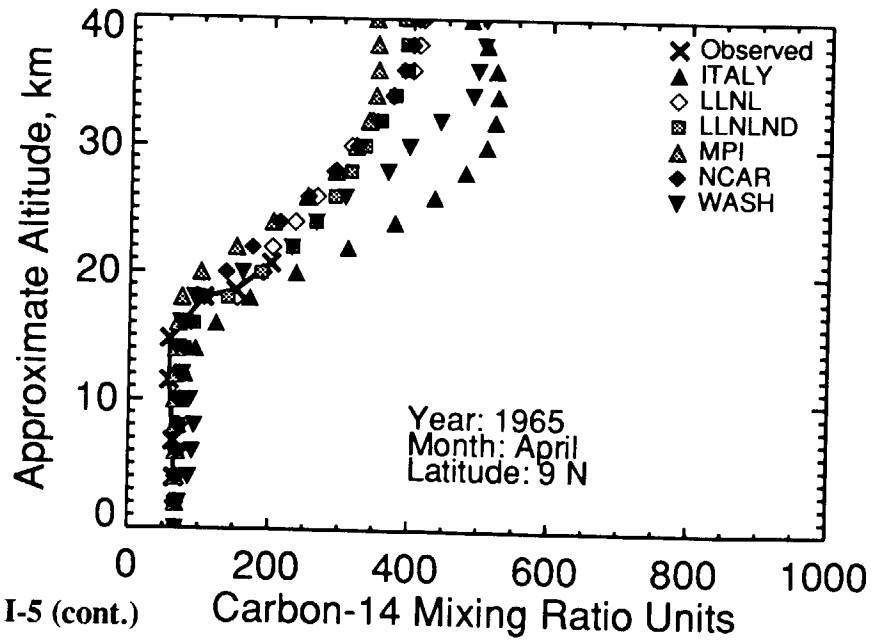

Figure I-5 (cont.)

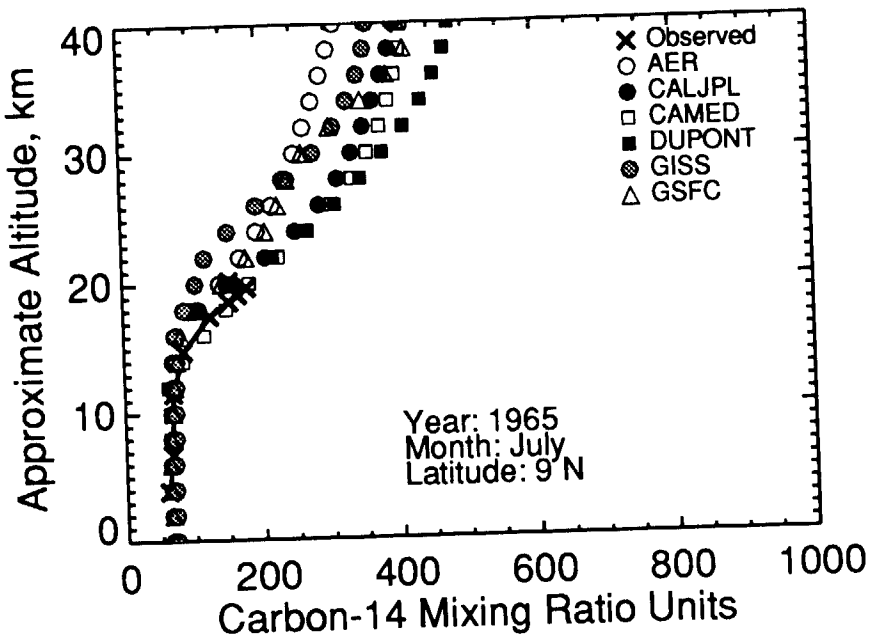

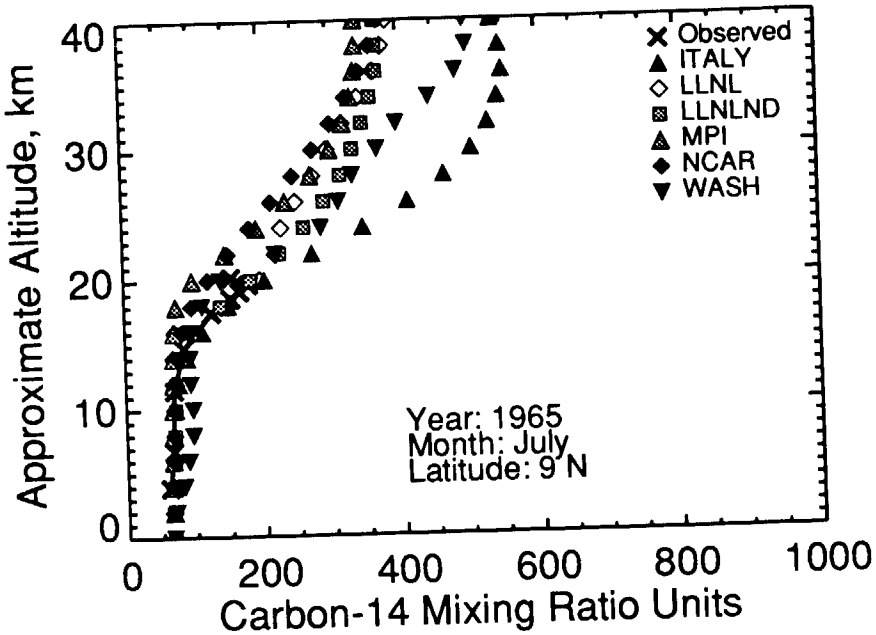

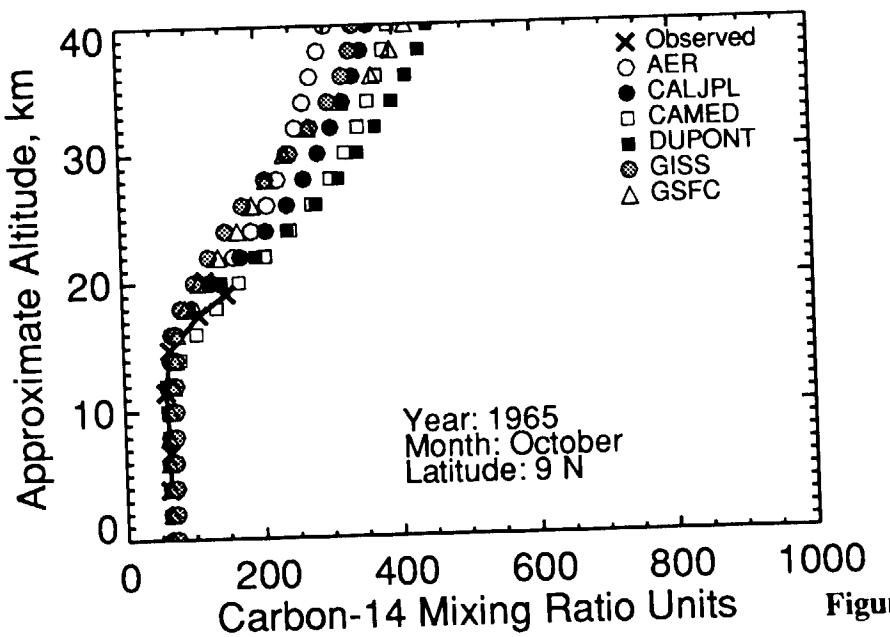

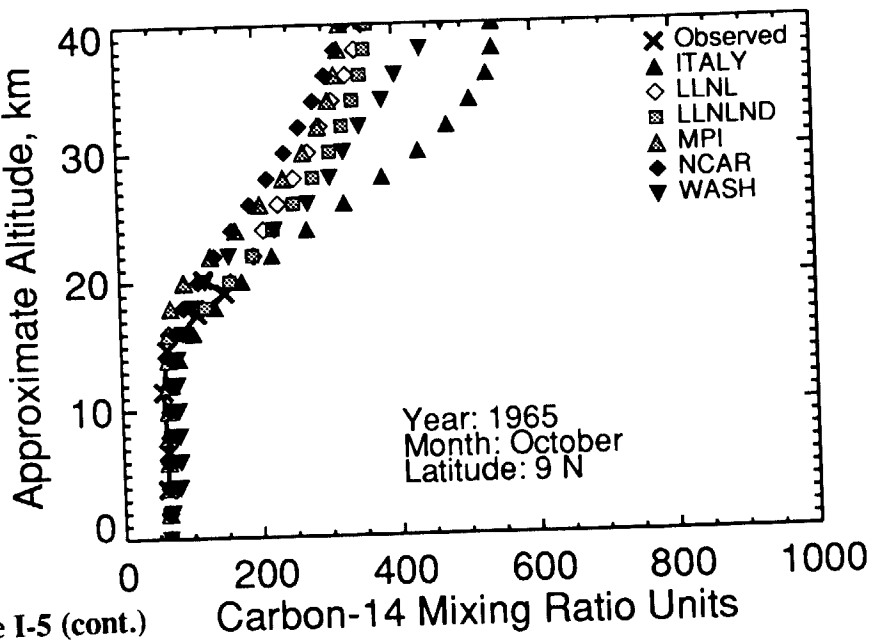

Figure I-5 (cont.)

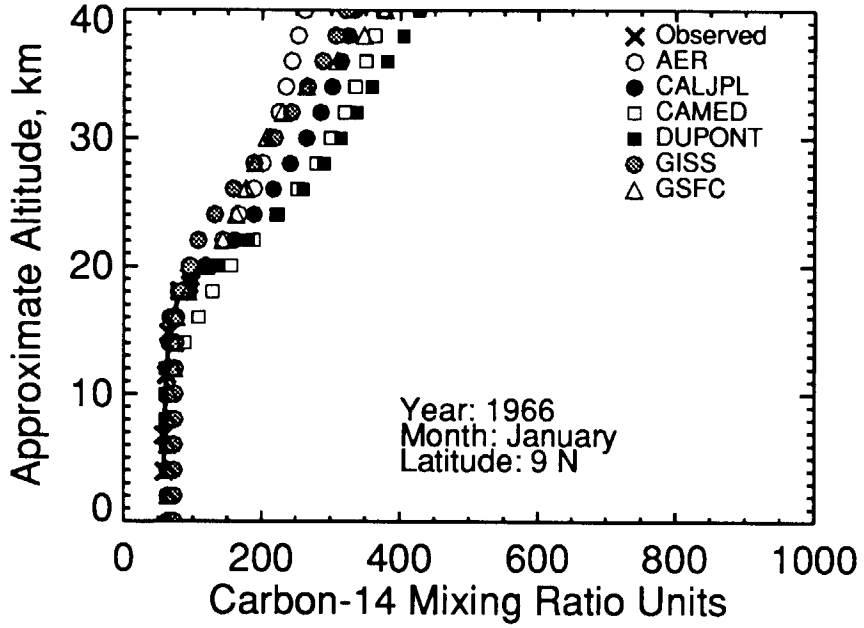

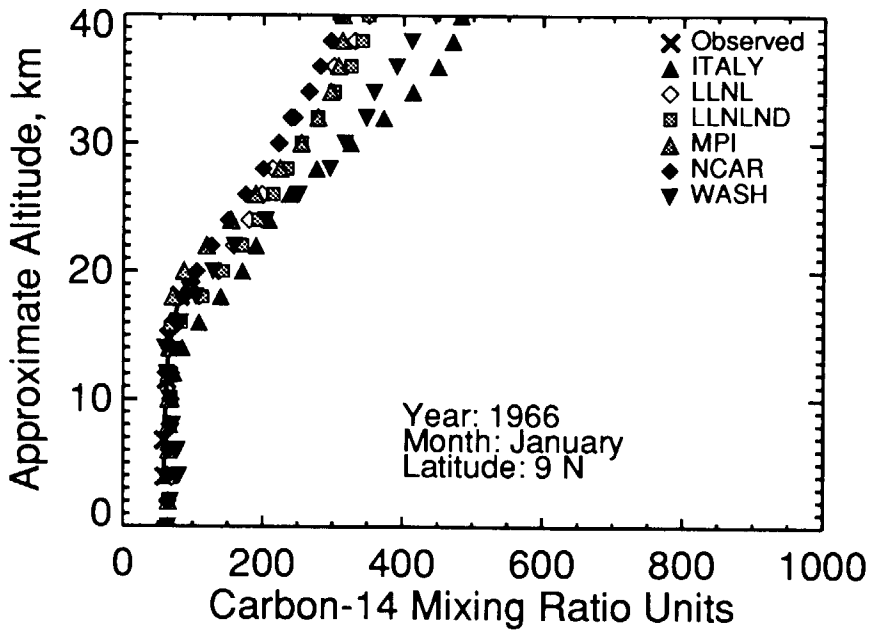

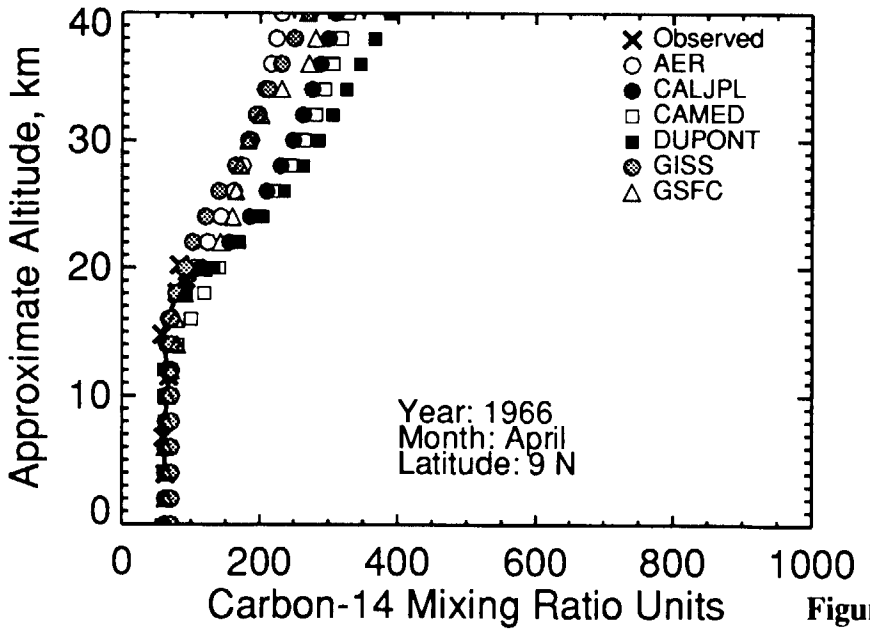

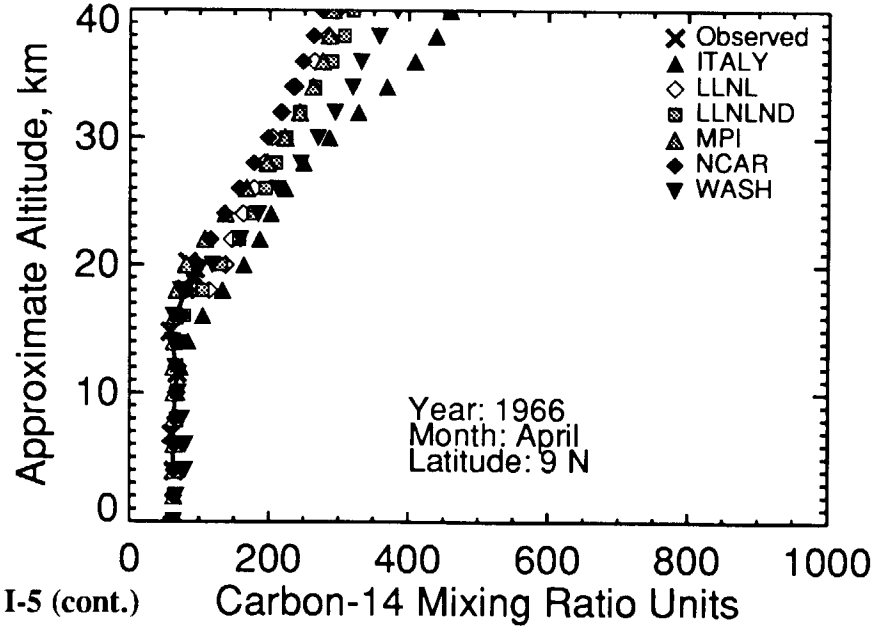

Figure I-5 (cont.)

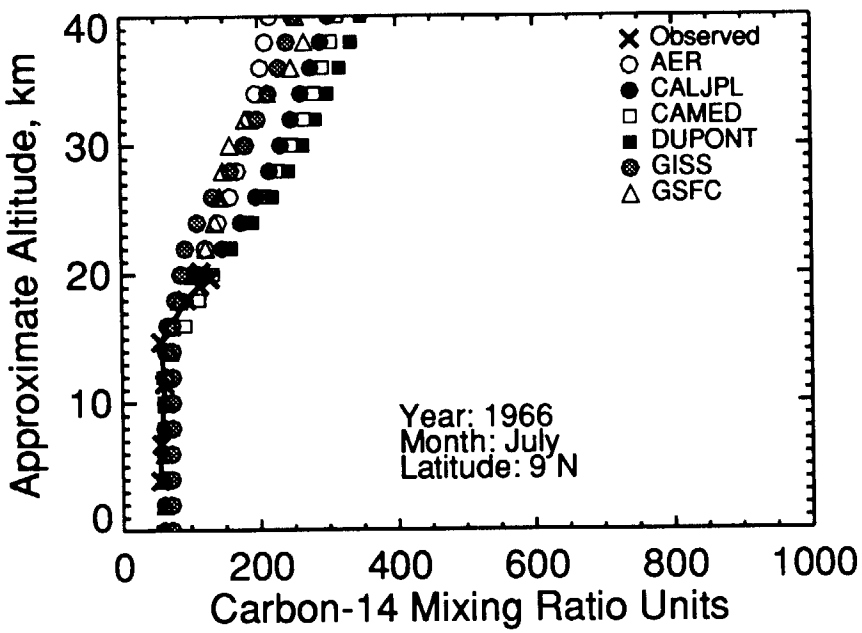

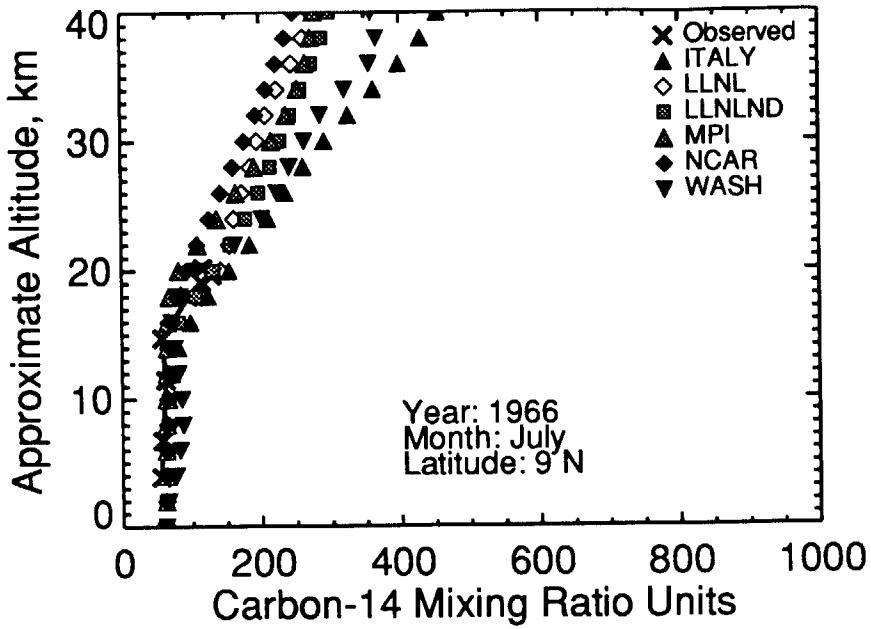

Figure I-5 (cont.)

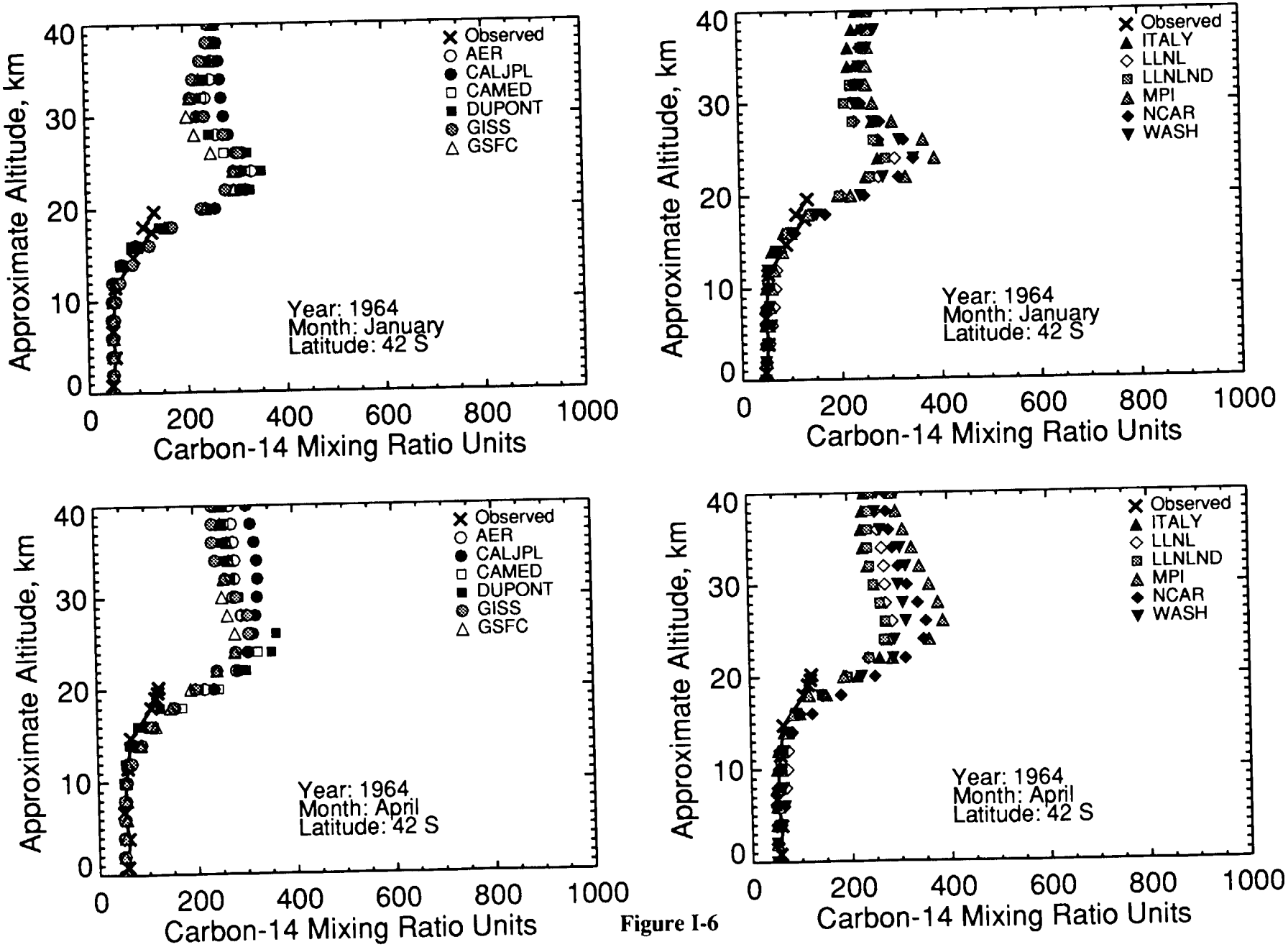
Approximate Altitude, km
Carbon-14 Mixing Ratio Units
Observed
AER
CALJPL
CAMED
DUPONT
GISS
GSFC
Year: 1964
Month: January
Latitude: 42 S
Observed
ITALY
LLNL
LLNLND
MPI
NCAR
WASH
Year: 1964
Month: January
Latitude: 42 S
Year: 1964
Month: April
Latitude: 42 S
Year: 1964
Month: April
Latitude: 42 S

Figure I-6

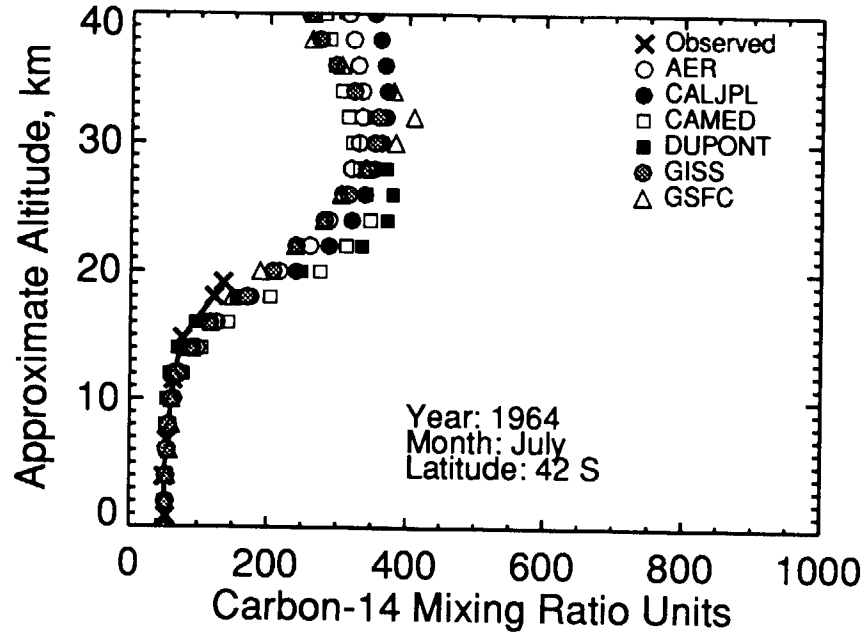

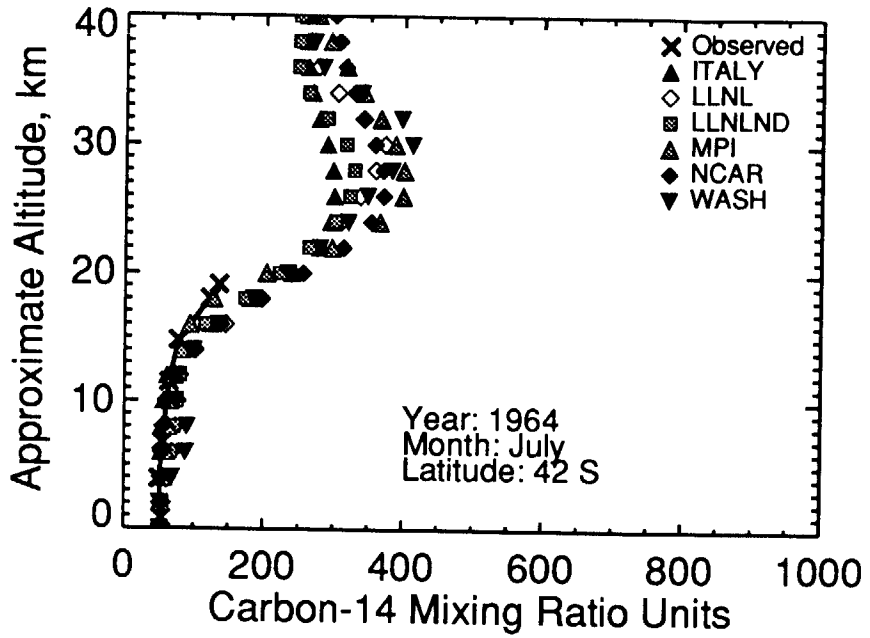

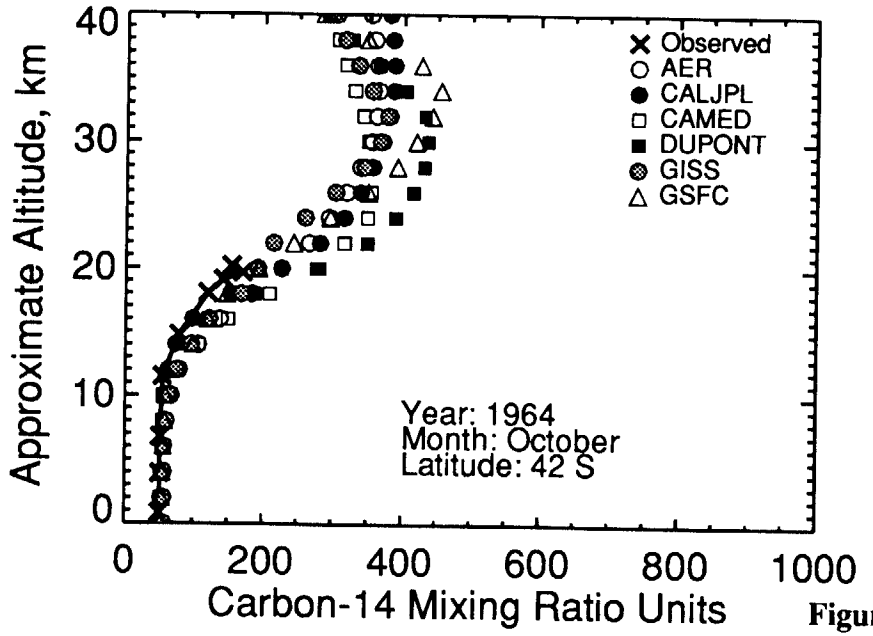

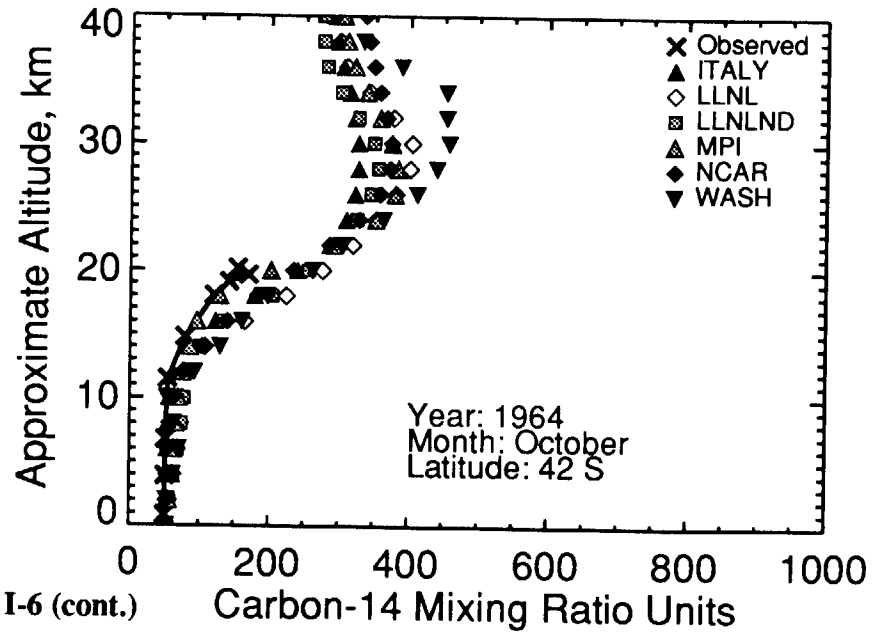

Figure I-6 (cont.)

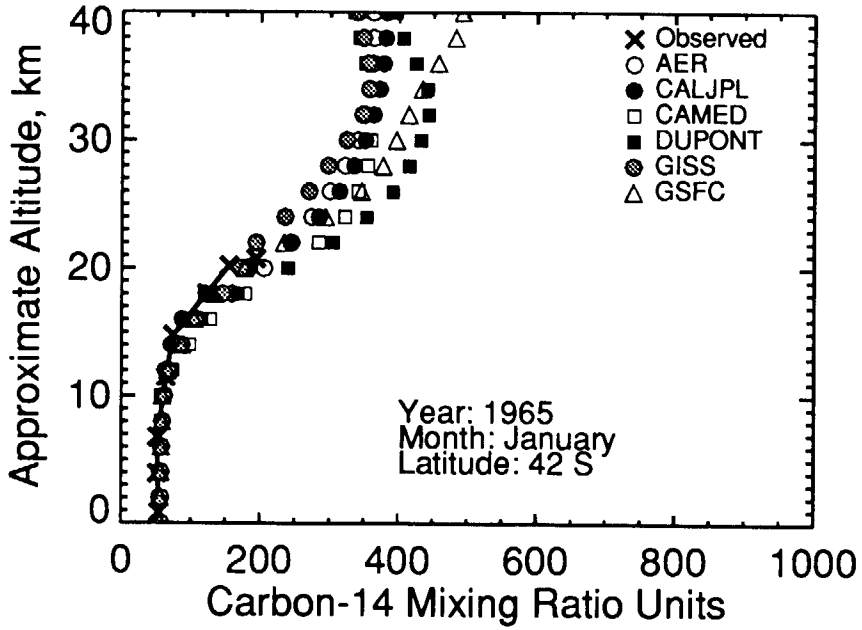

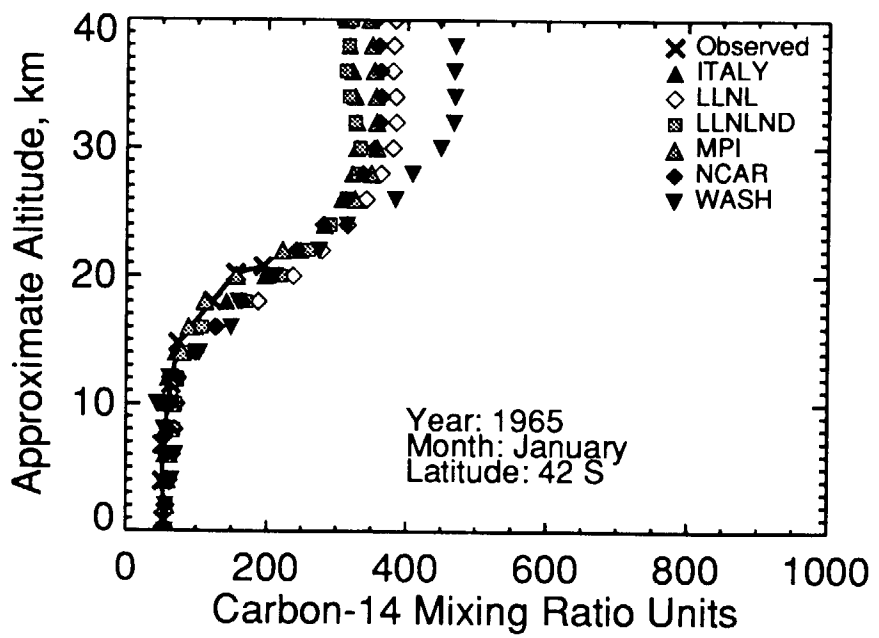

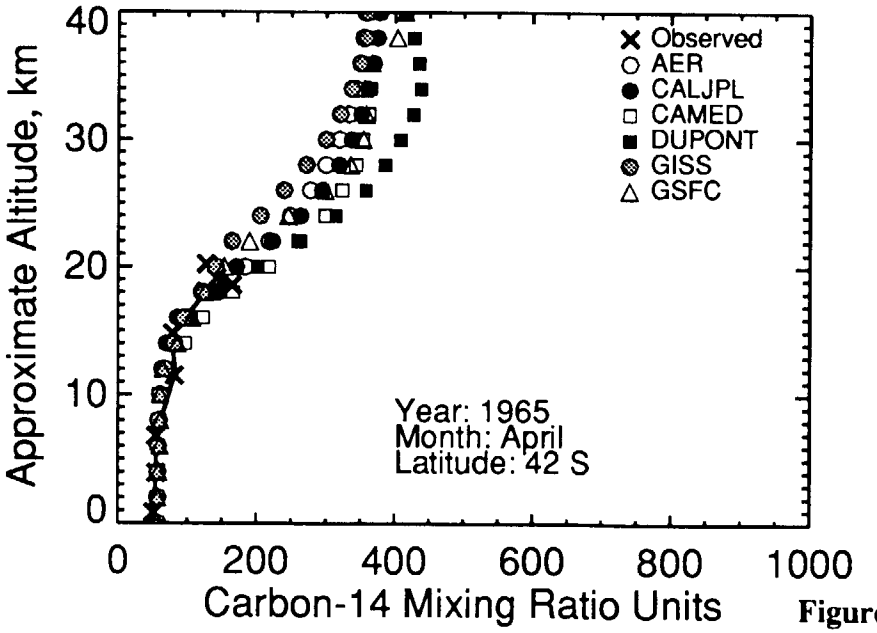

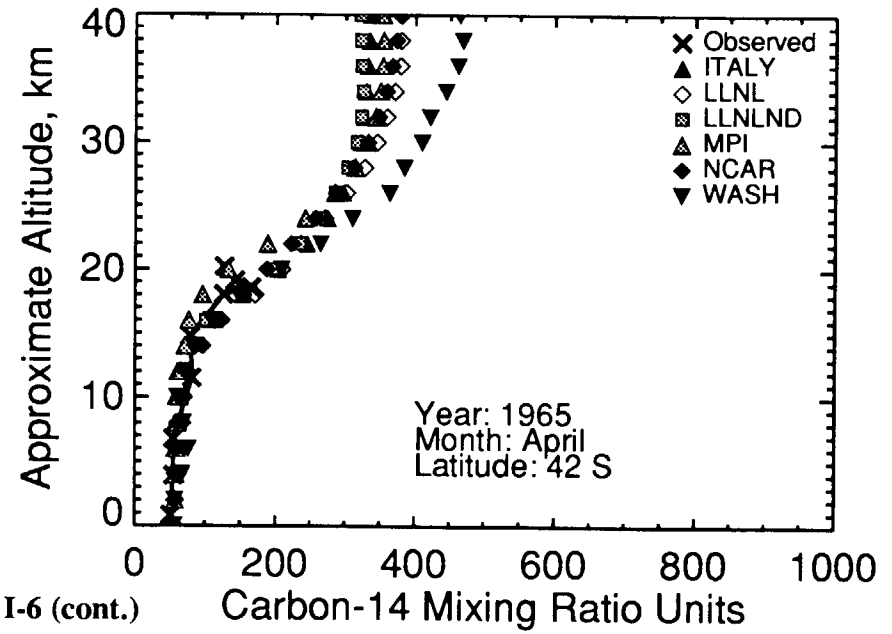

Figure I-6 (cont.)

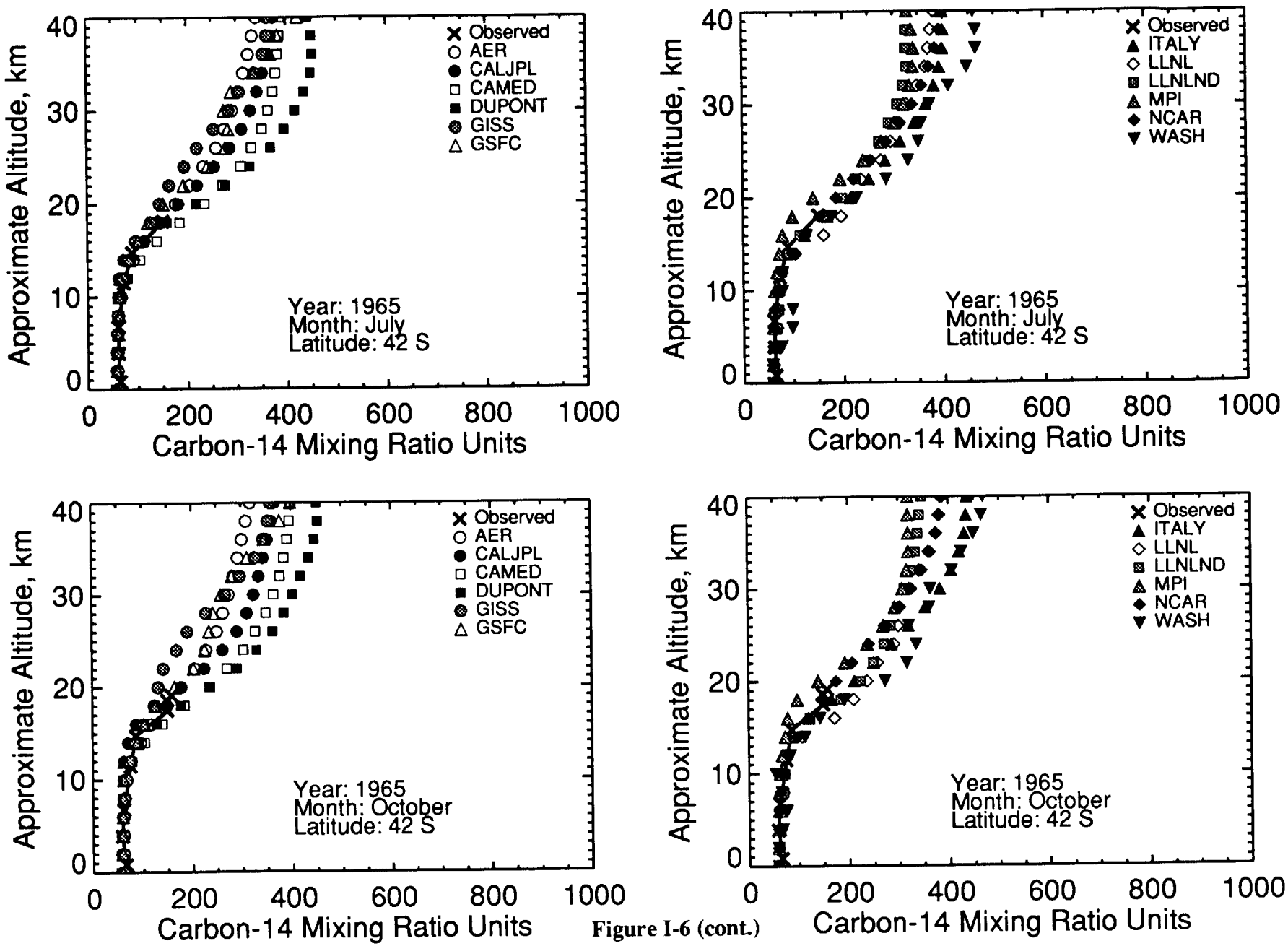

Figure I-6 (cont.)

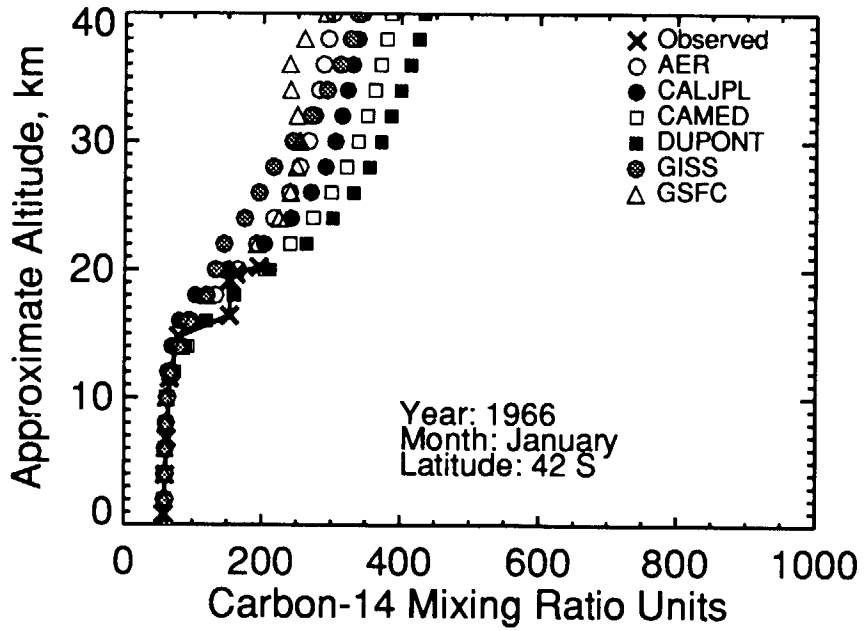

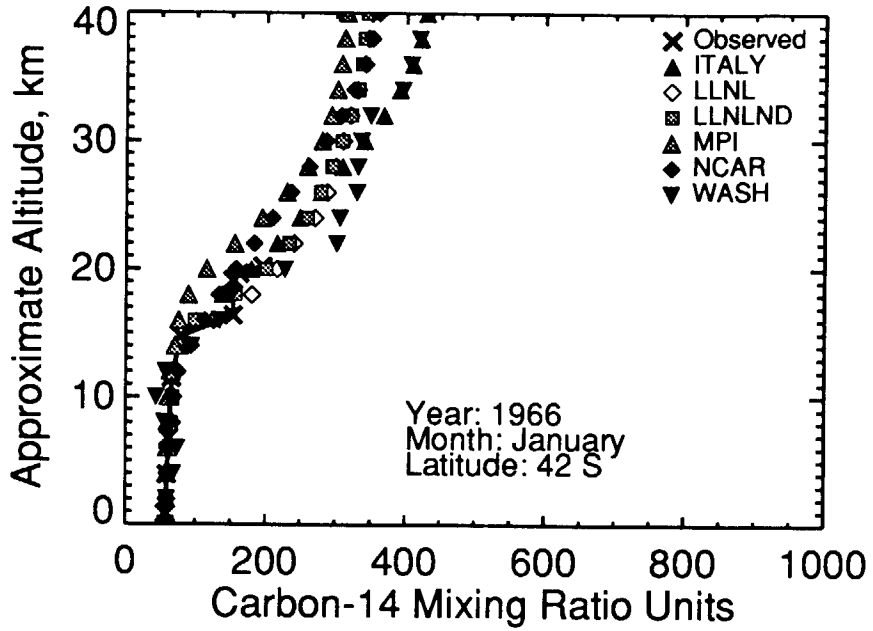

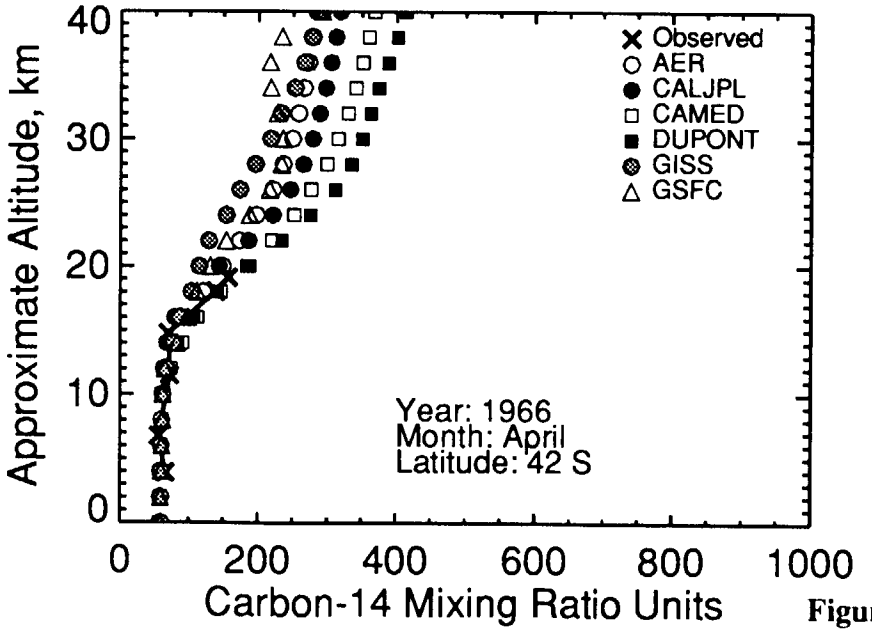

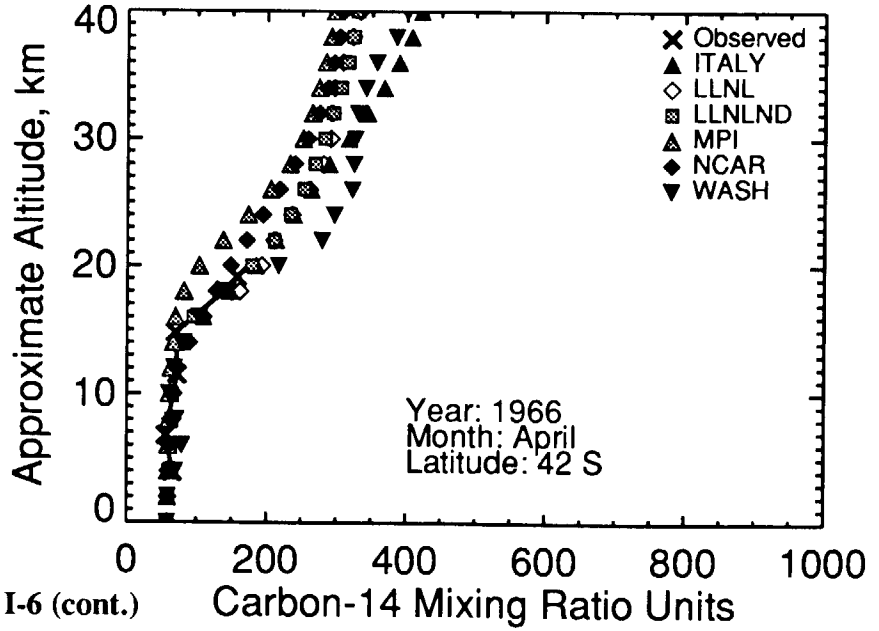

Figure I-6 (cont.)

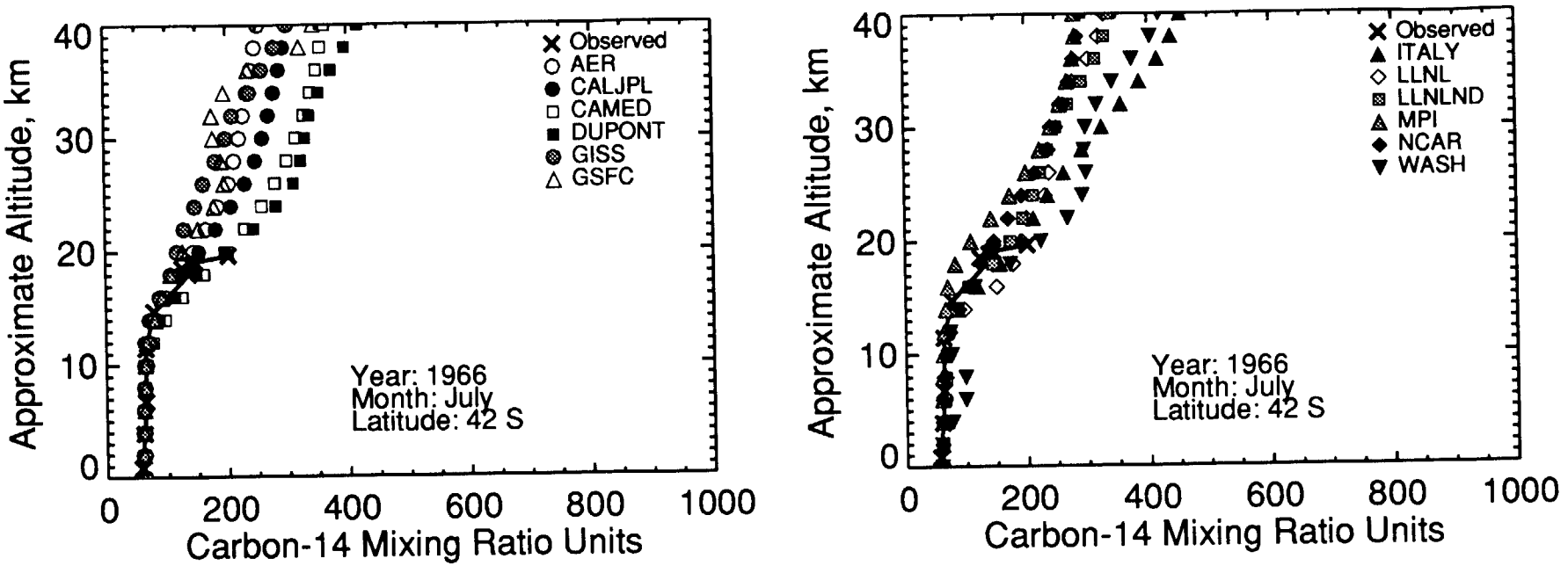

Figure I-6 (cont.)

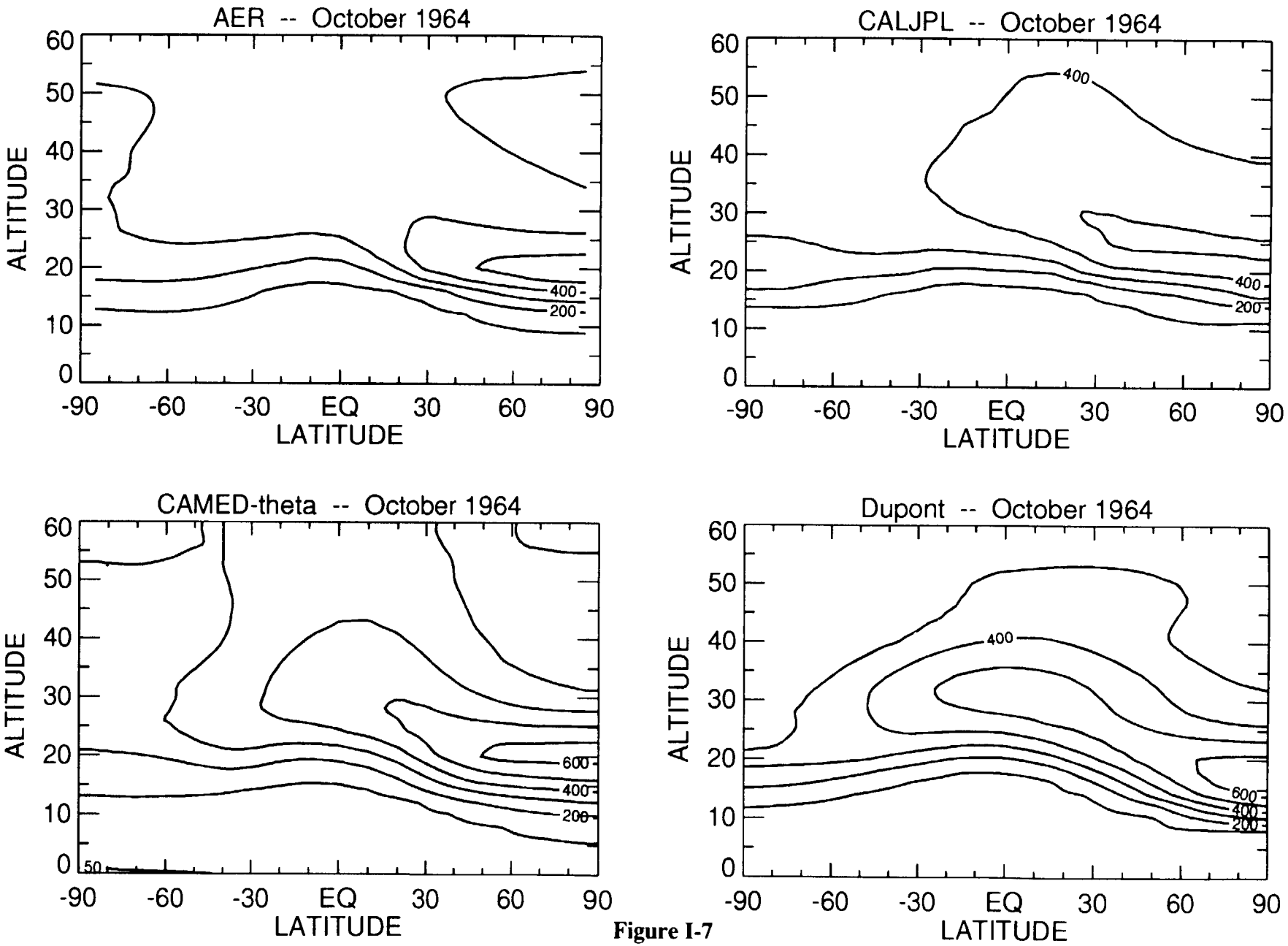
AER -- October 1964
CALJPL -- October 1964
CAMED-theta -- October 1964
Dupont -- October 1964
ALTITUDE
LATITUDE
60
50
40
30
20
10
0
-90
-60
-30
EQ
30
60
90
400
200
600
50

Figure I-7

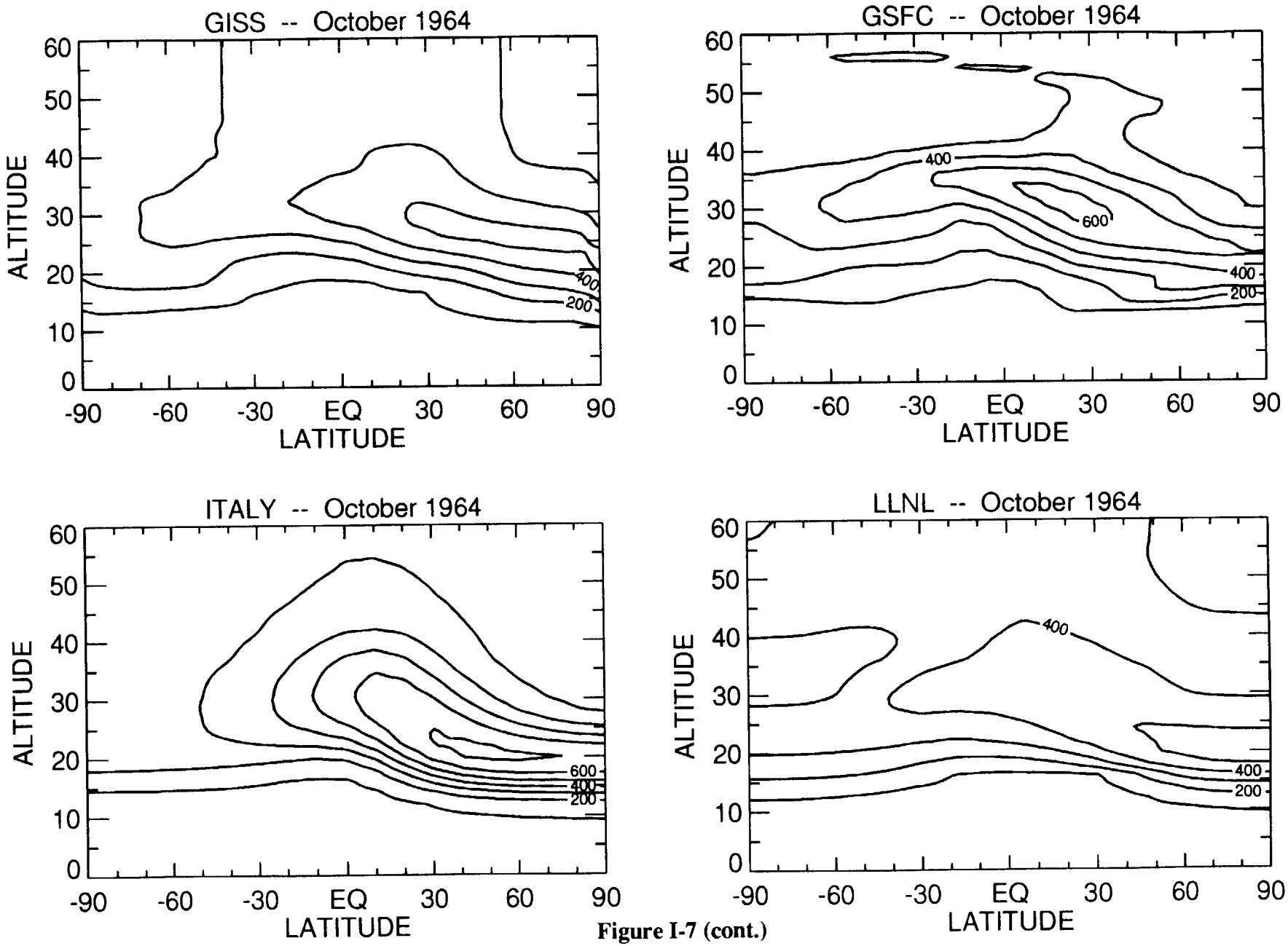

Figure I-7 (cont.)

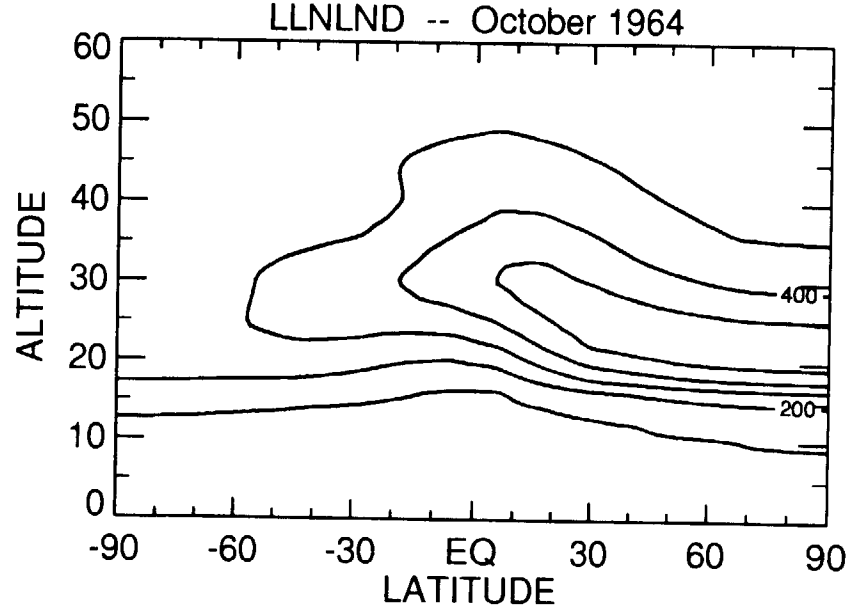

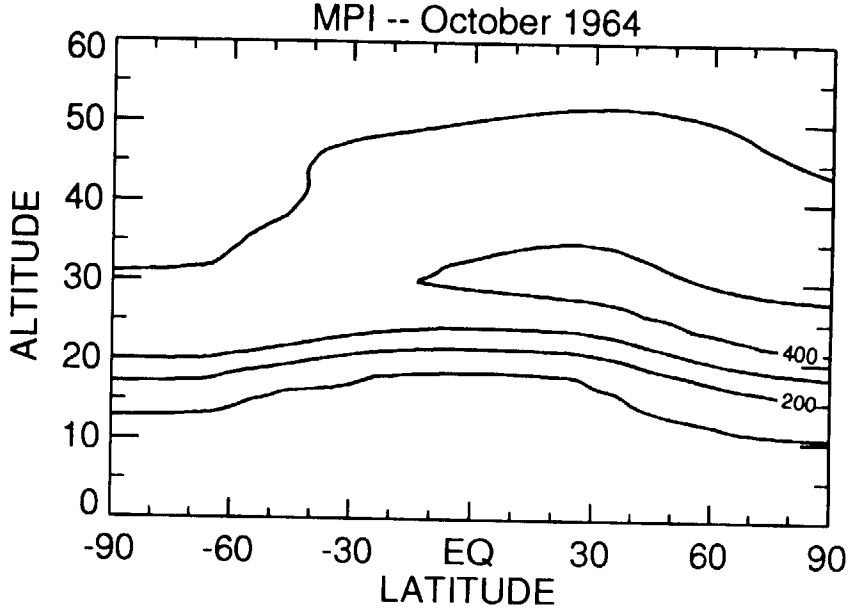

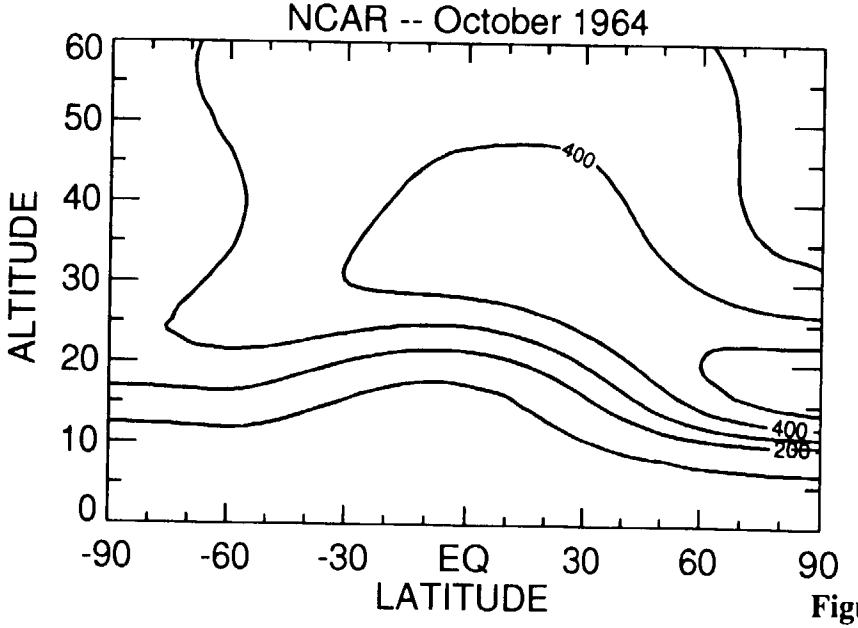

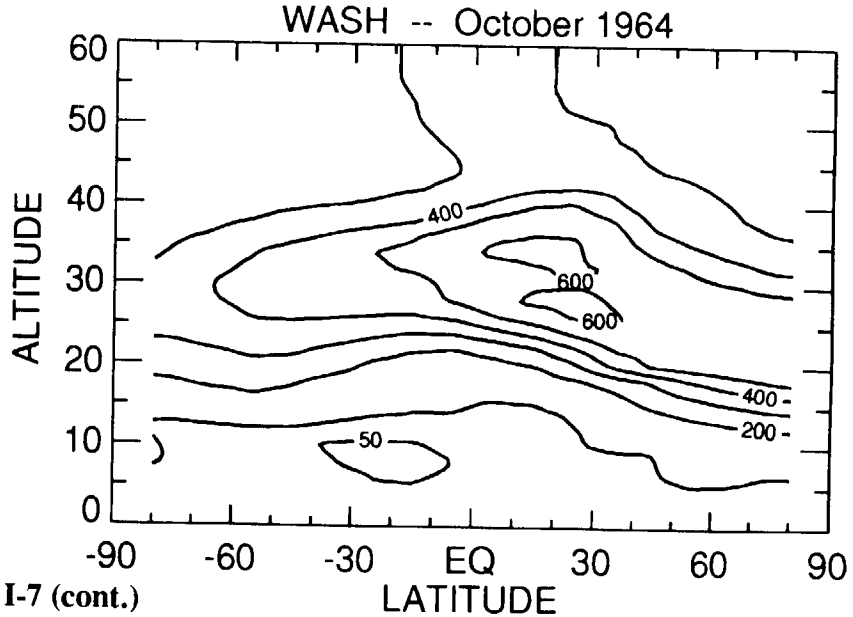

Figure I-7 (cont.)

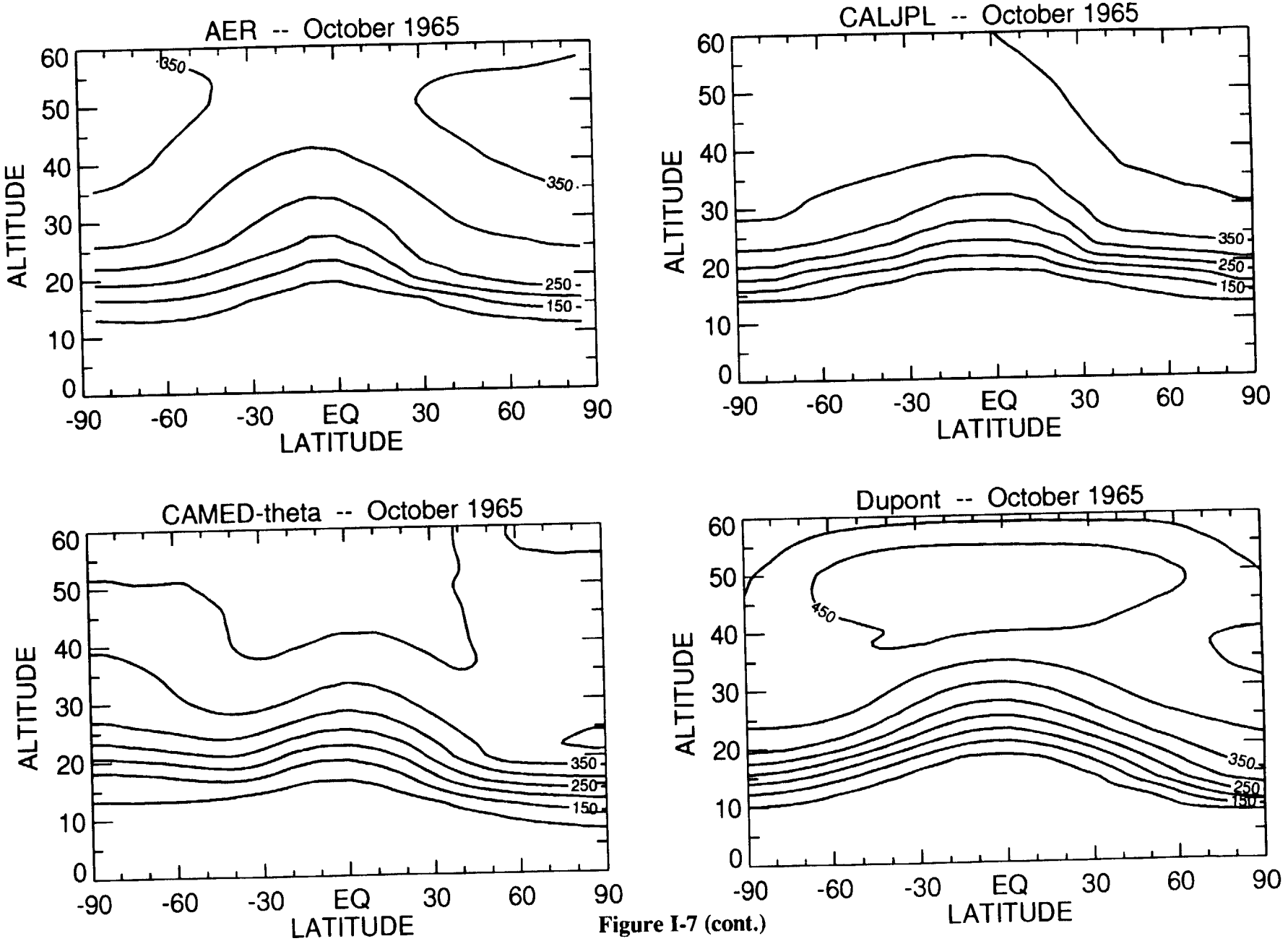

Figure I-7 (cont.)

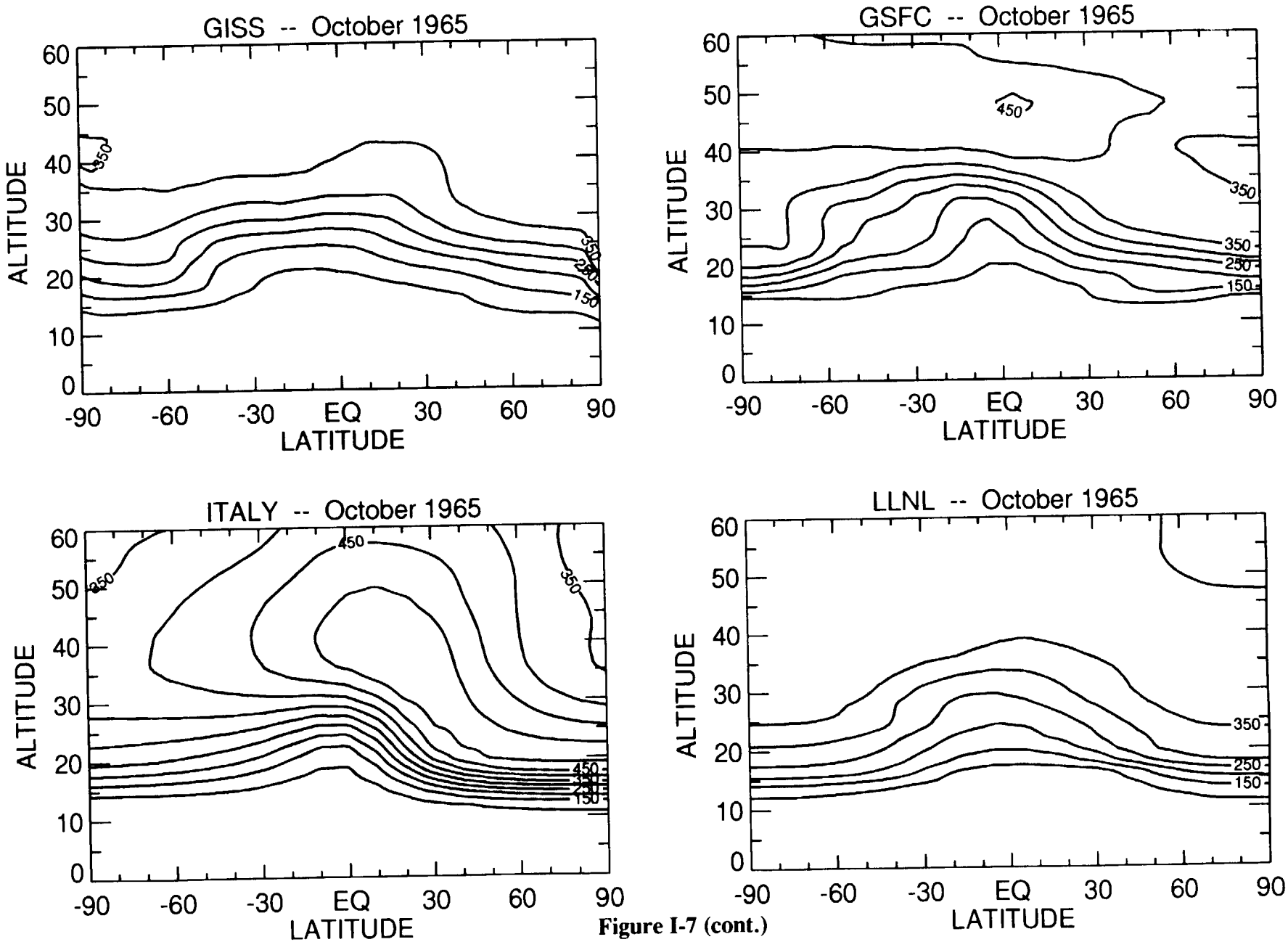

Figure I-7 (cont.)

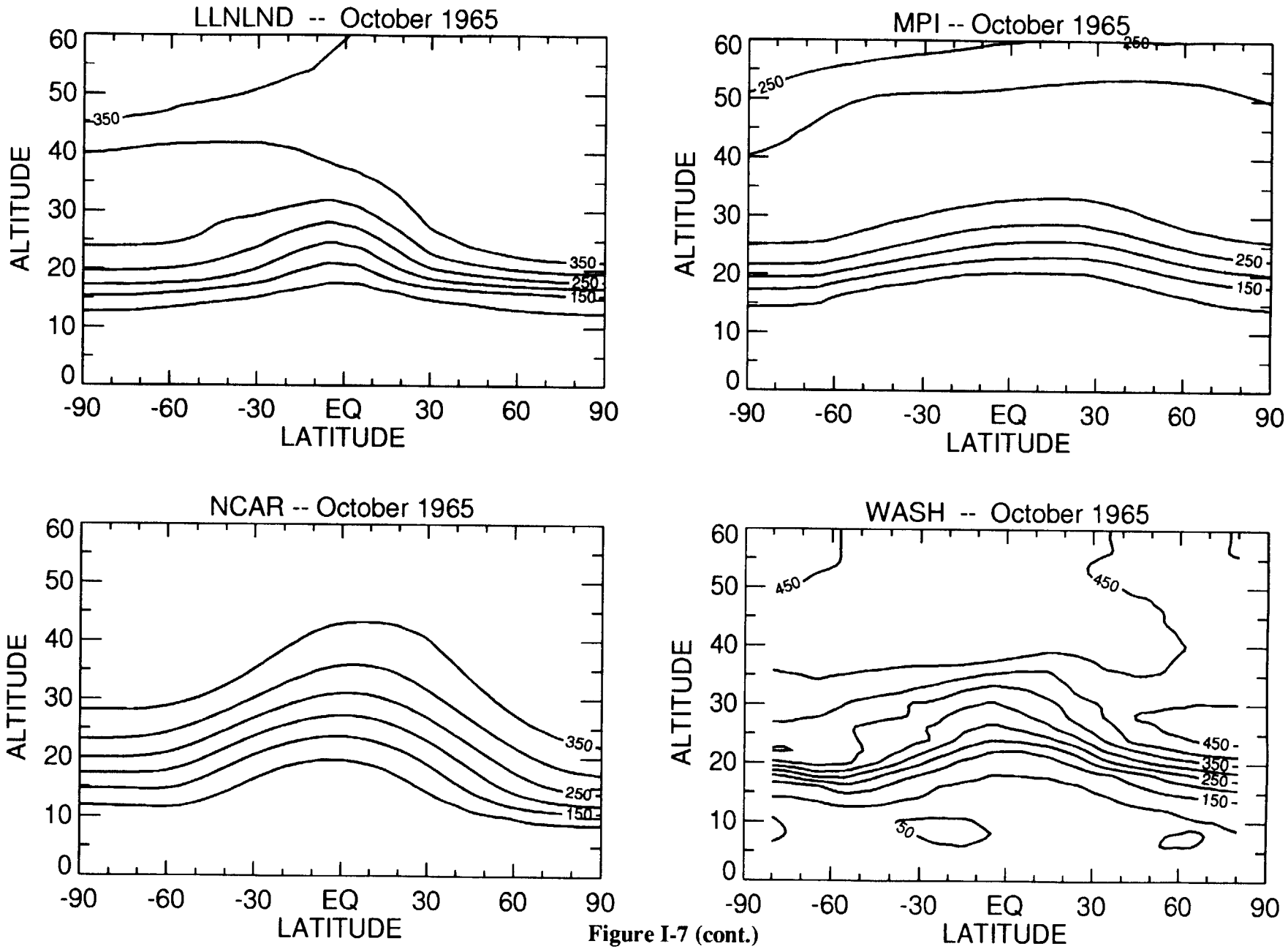

Figure I-7 (cont.)

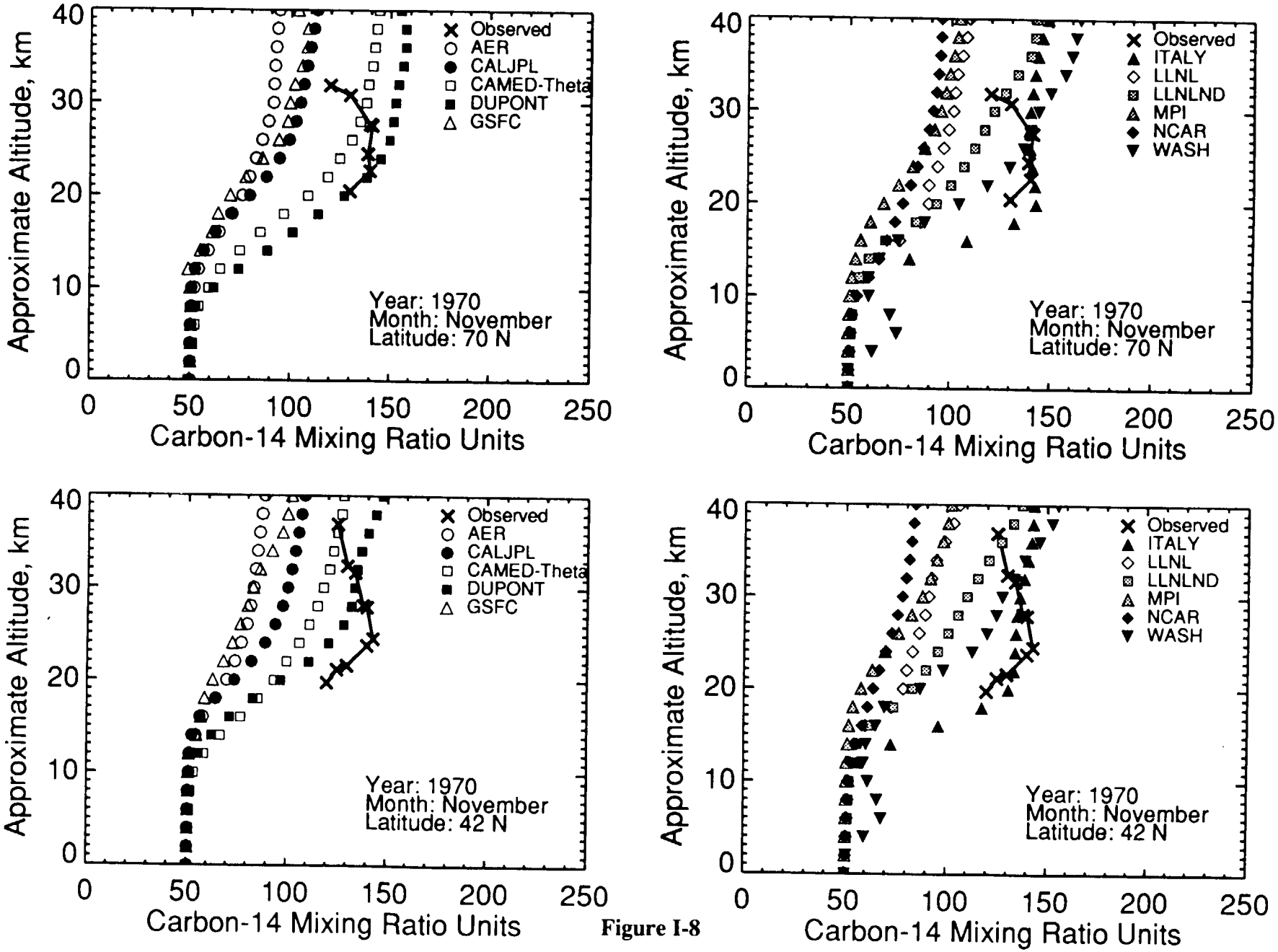
Approximate Altitude, km
Carbon-14 Mixing Ratio Units
Observed
AER
CALJPL
CAMED-Theta
DUPONT
GSFC
Year: 1970
Month: November
Latitude: 70 N
Observed
ITALY
LLNL
LLNLND
MPI
NCAR
WASH
Year: 1970
Month: November
Latitude: 70 N
Year: 1970
Month: November
Latitude: 42 N
Year: 1970
Month: November
Latitude: 42 N

Figure I-8

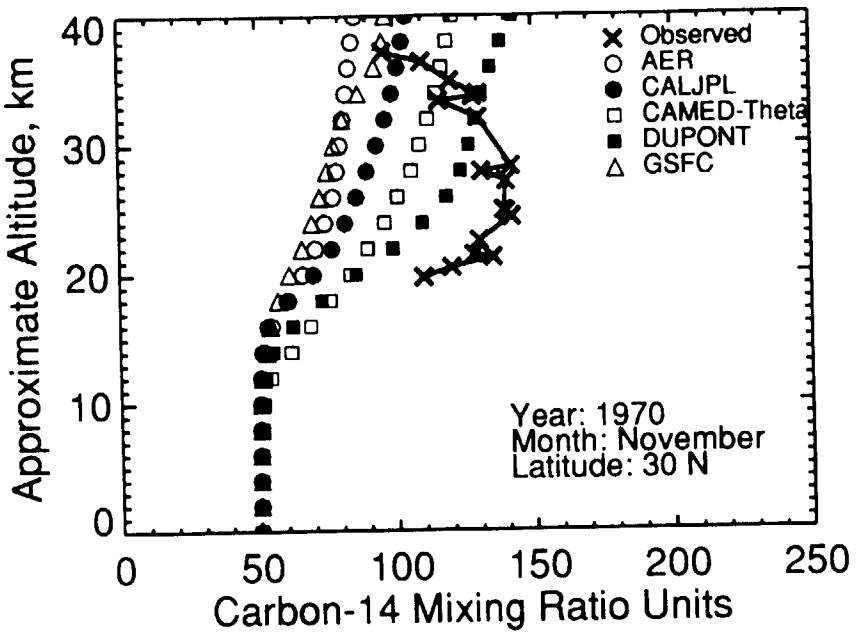

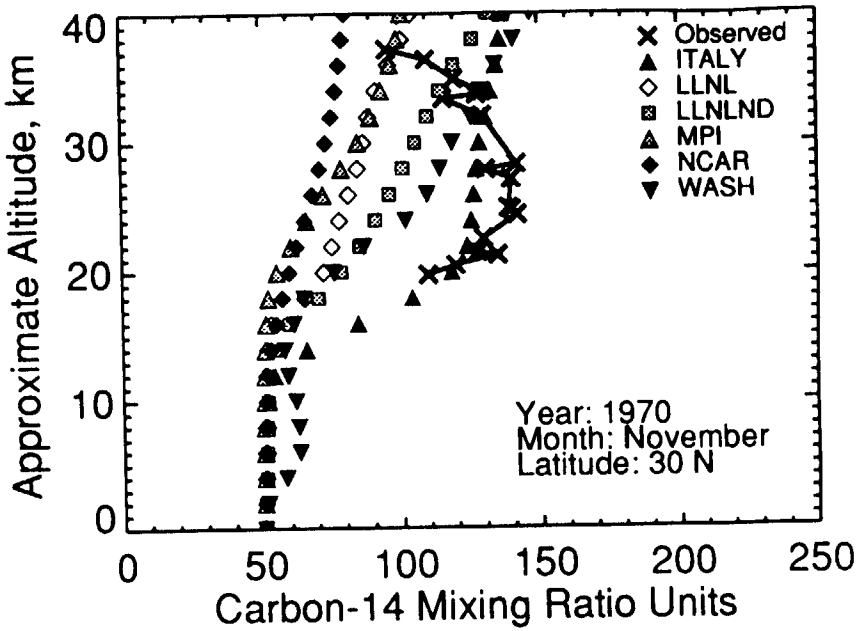

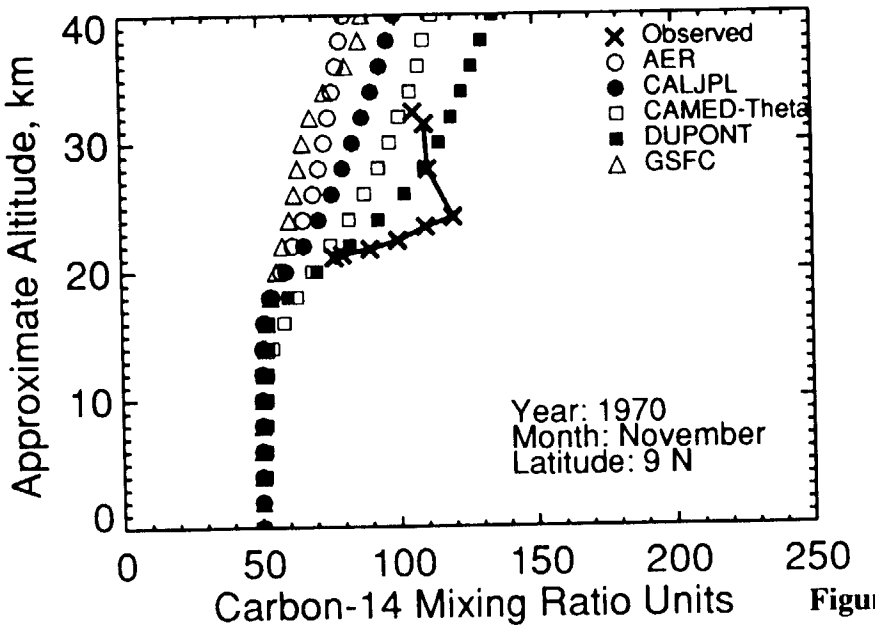

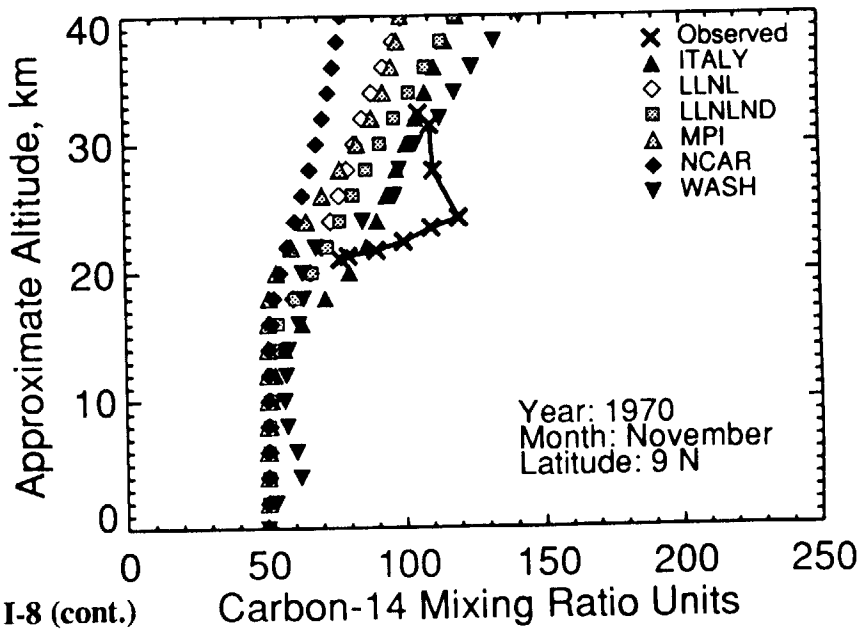

Figure I-8 (cont.)

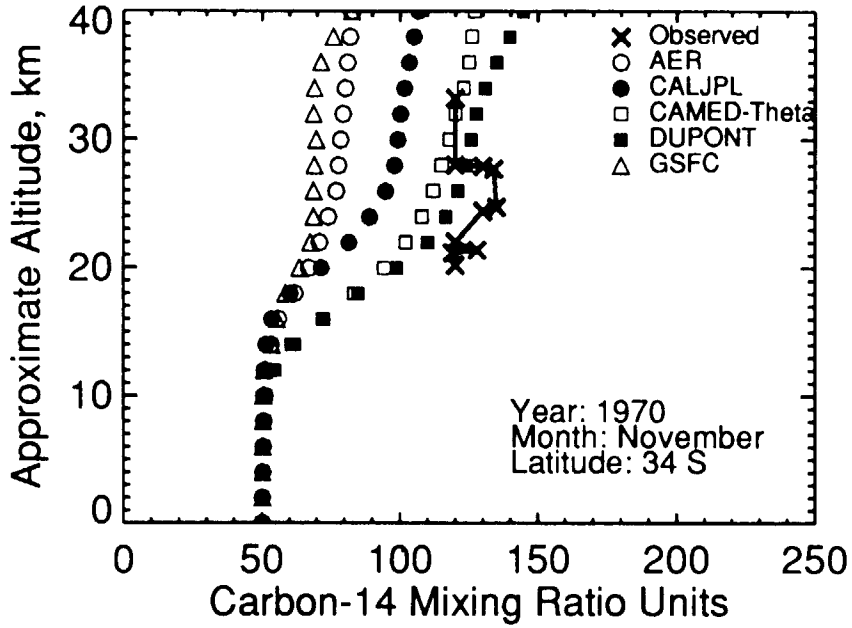

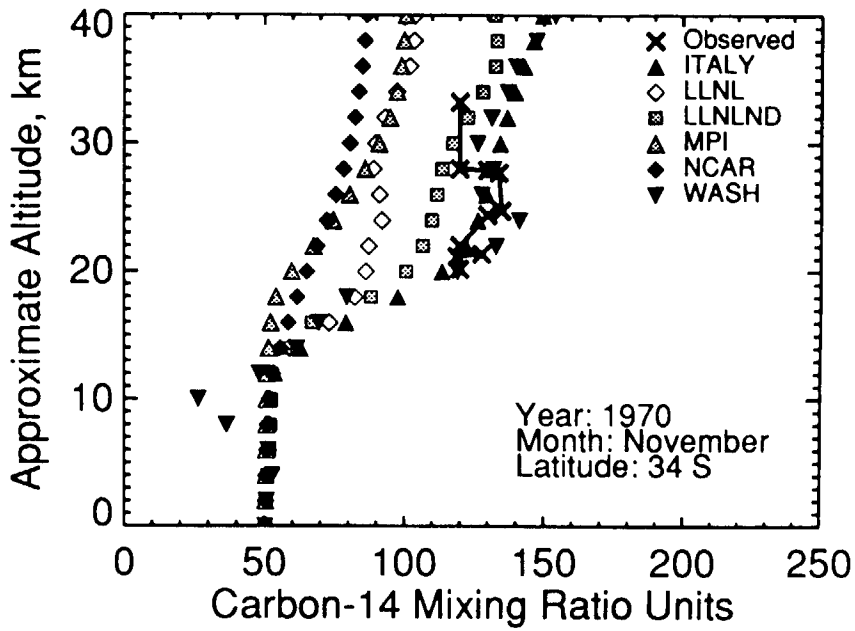

Figure I-8 (cont.)

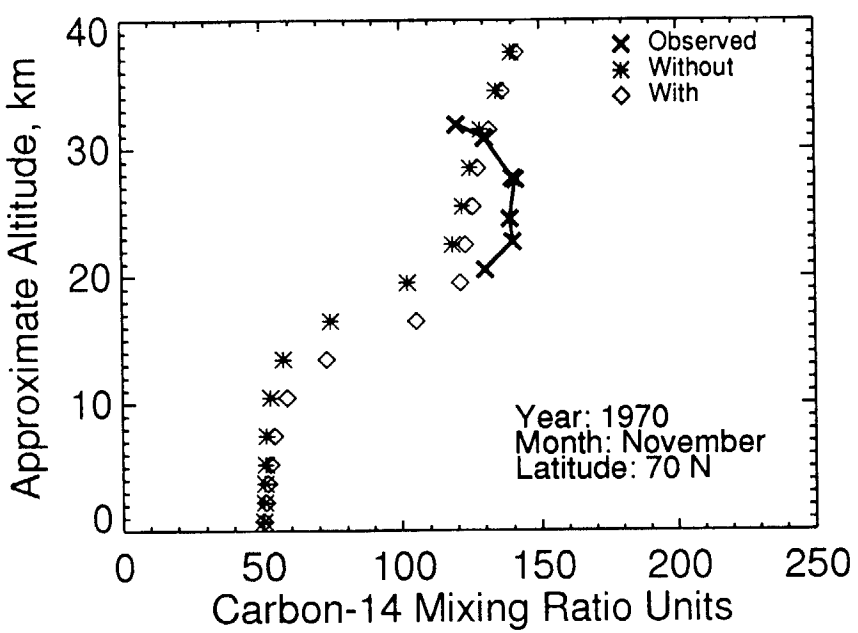
Approximate Altitude, km
Carbon-14 Mixing Ratio Units
Observed
Without
With
Year: 1970
Month: November
Latitude: 70 N

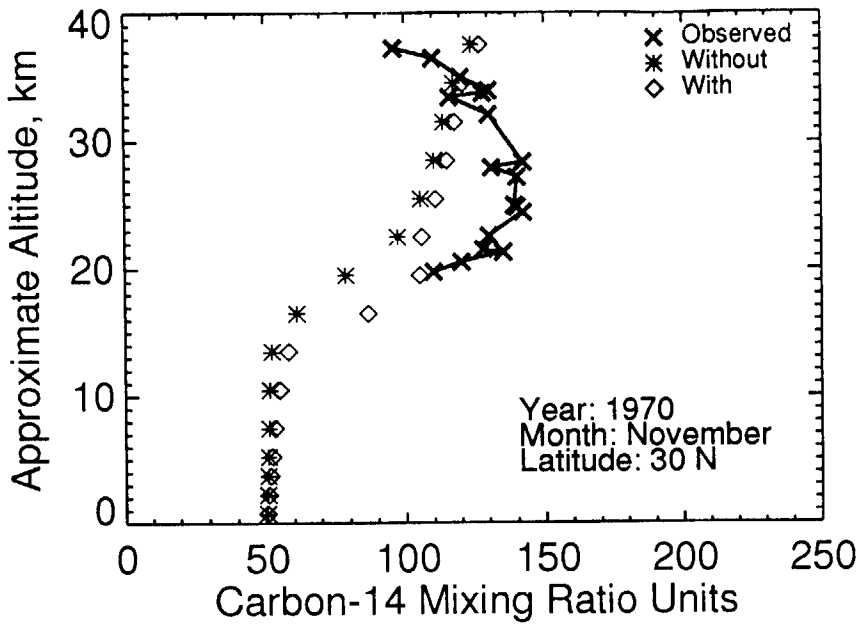
Approximate Altitude, km
Carbon-14 Mixing Ratio Units
Observed
Without
With
Year: 1970
Month: November
Latitude: 30 N

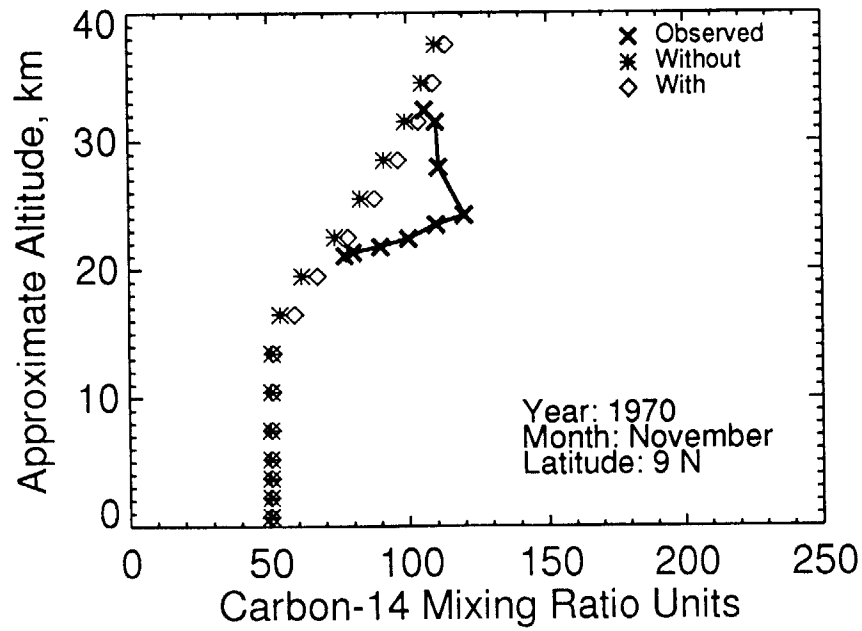
Approximate Altitude, km
Carbon-14 Mixing Ratio Units
Observed
Without
With
Year: 1970
Month: November
Latitude: 9 N

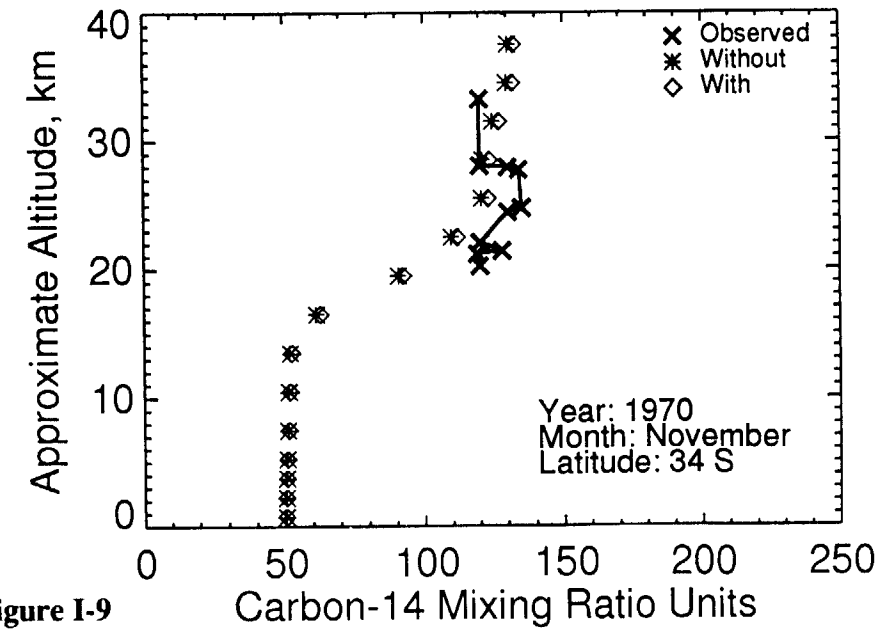
Approximate Altitude, km
Carbon-14 Mixing Ratio Units
Observed
Without
With
Year: 1970
Month: November
Latitude: 34 S

Figure I-9

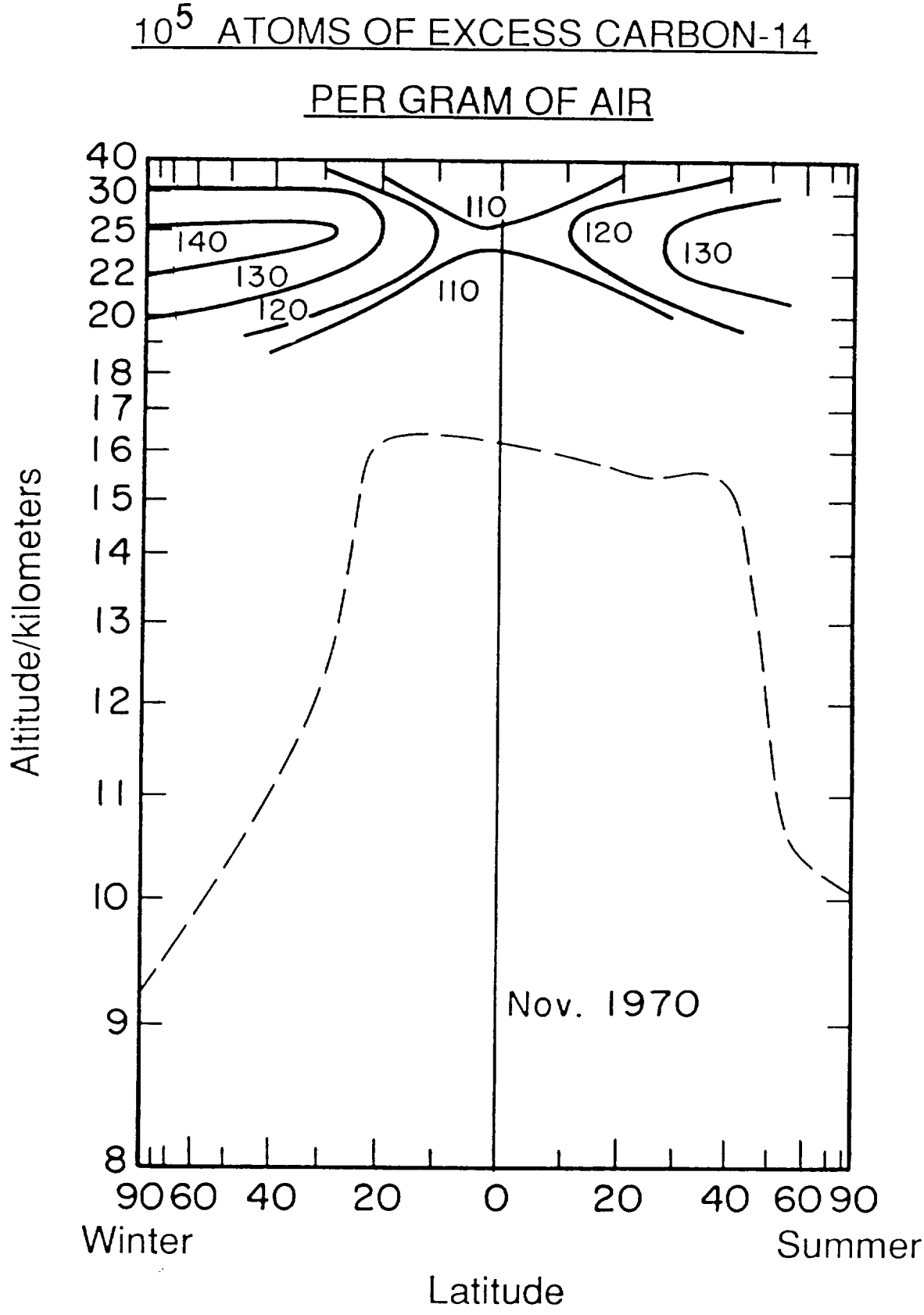
10^5 ATOMS OF EXCESS CARBON-14
PER GRAM OF AIR
Altitude/kilometers
40
30
25
22
20
18
17
16
15
14
13
12
11
10
9
8
140
130
120
110
110
120
130
Nov. 1970
90 60 40 20 0 20 40 60 90
Winter
Summer
Latitude

Figure I-10

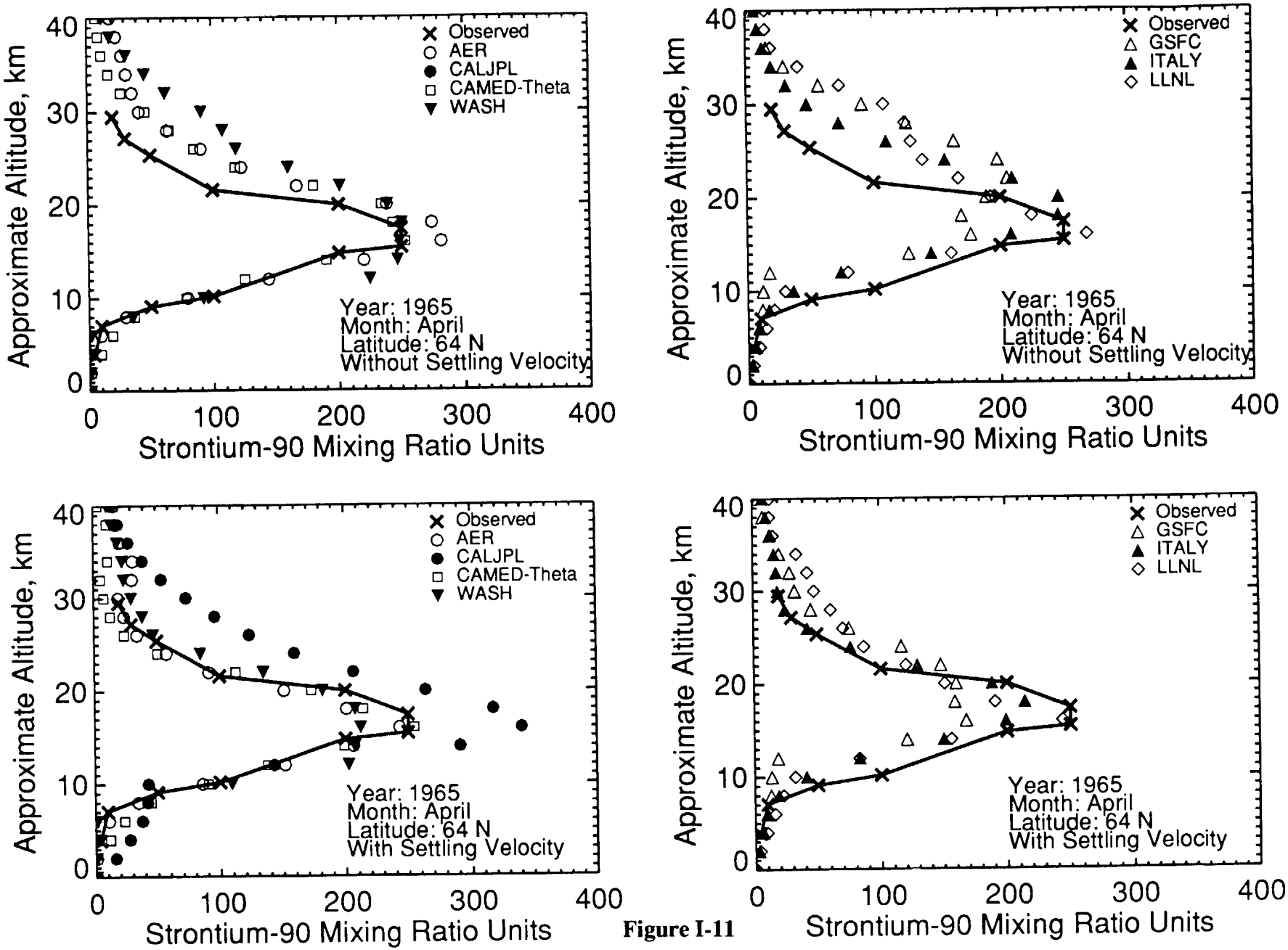
Approximate Altitude, km
Strontium-90 Mixing Ratio Units
Observed
AER
CALJPL
CAMED-Theta
WASH
Year: 1965
Month: April
Latitude: 64 N
Without Settling Velocity
Observed
GSFC
ITALY
LLNL
Year: 1965
Month: April
Latitude: 64 N
Without Settling Velocity
Observed
AER
CALJPL
CAMED-Theta
WASH
Year: 1965
Month: April
Latitude: 64 N
With Settling Velocity
Observed
GSFC
ITALY
LLNL
Year: 1965
Month: April
Latitude: 64 N
With Settling Velocity

Figure I-11

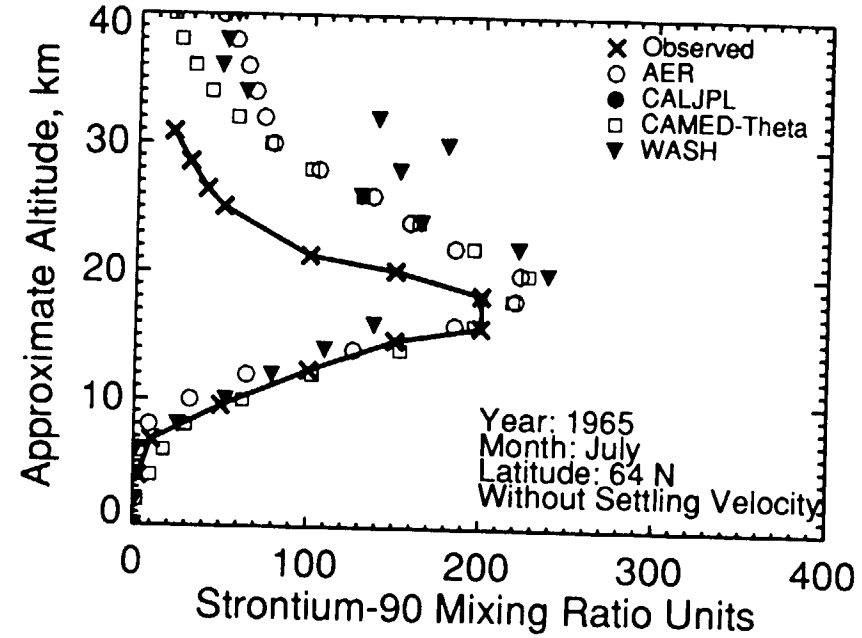

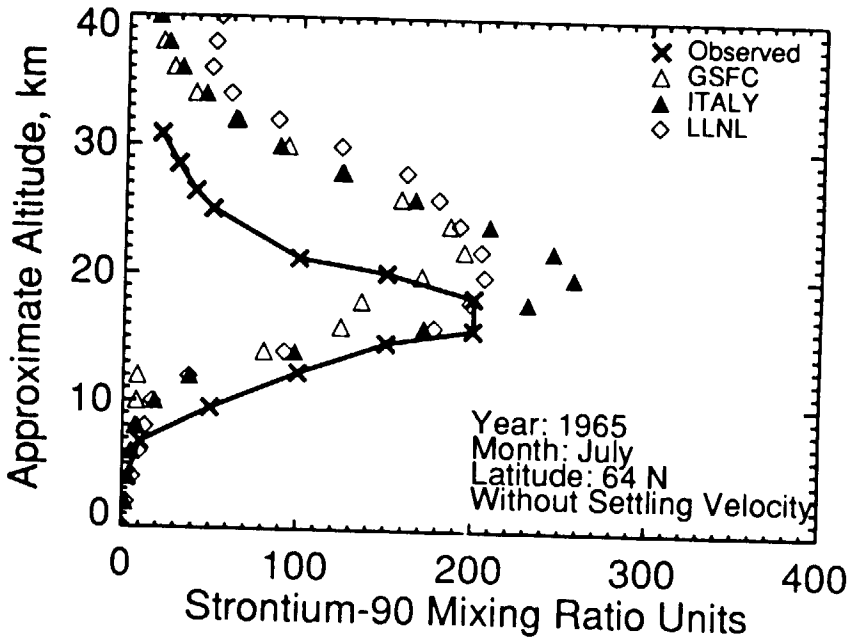

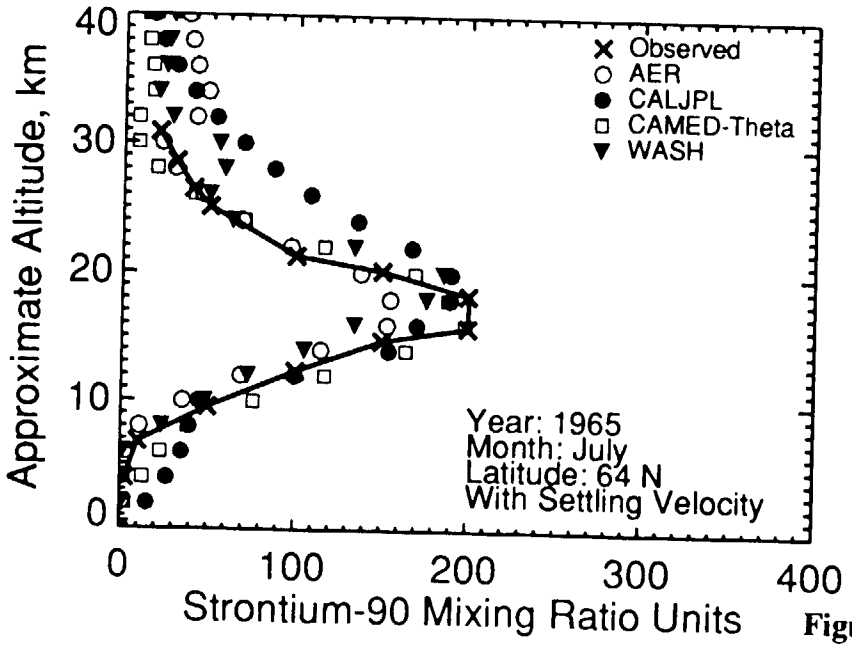

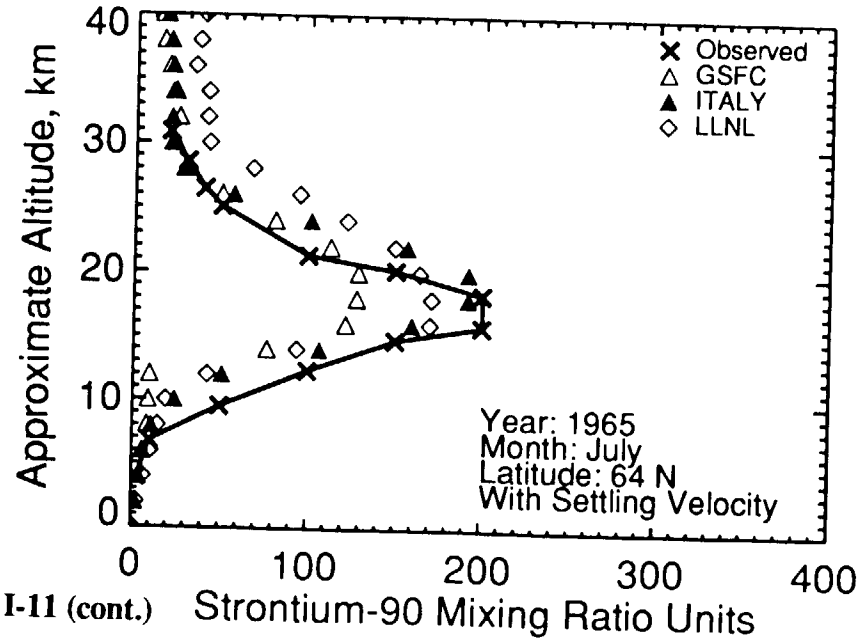

Figure I-11 (cont.)

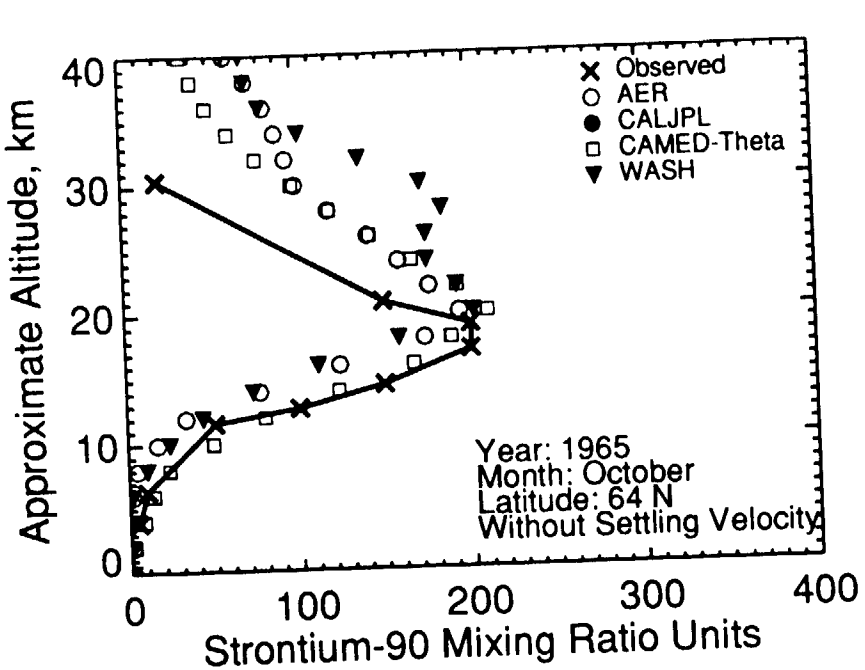

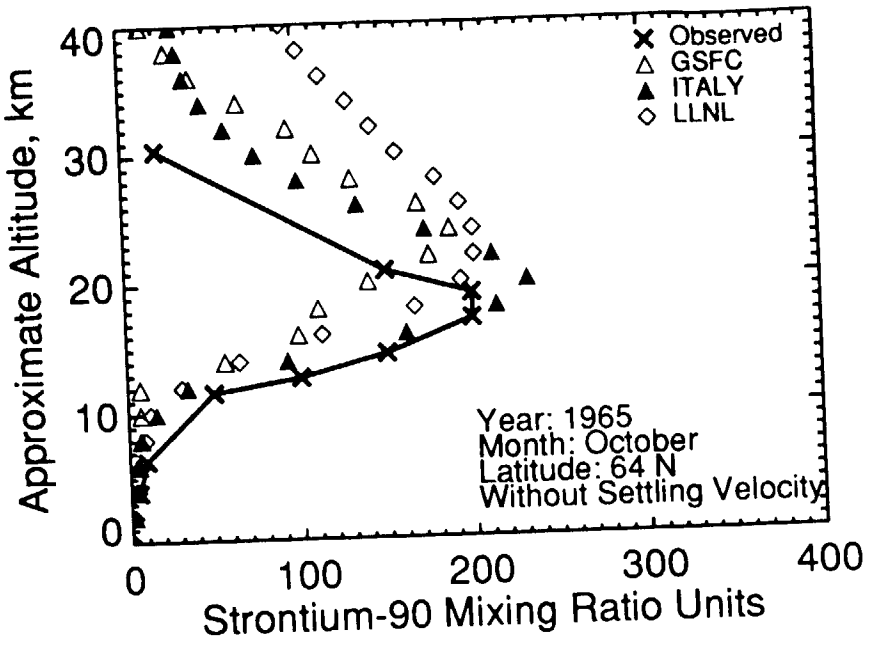

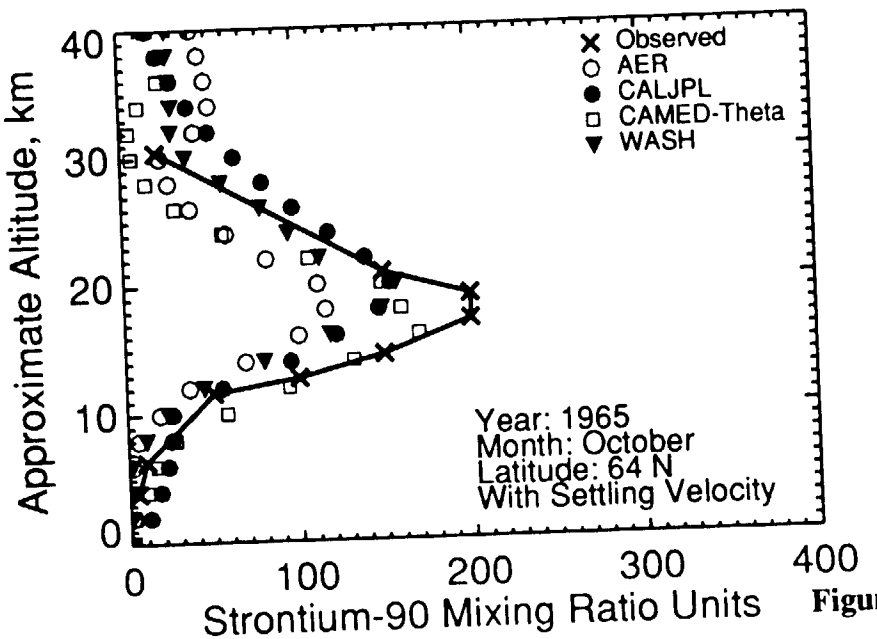

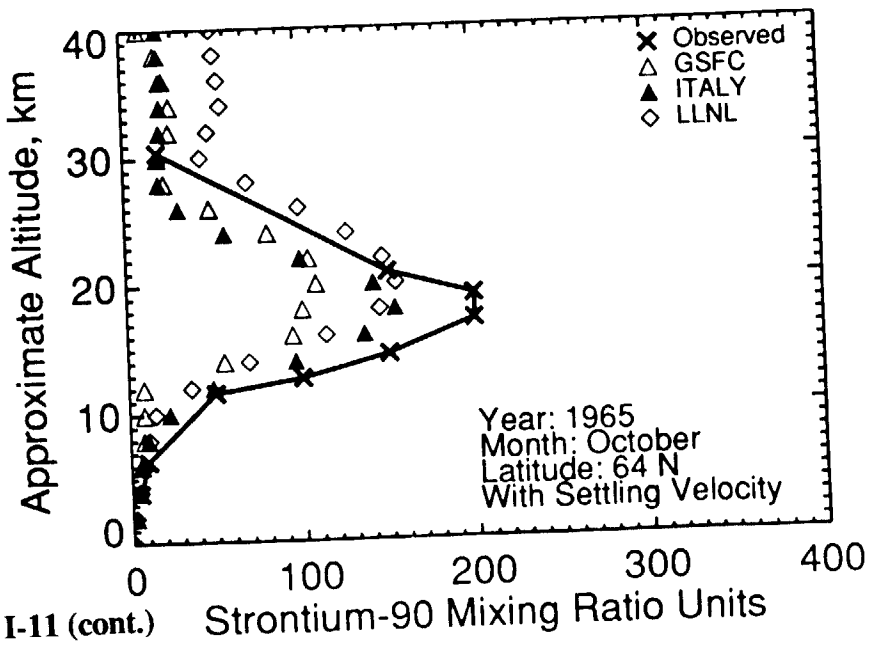

Figure I-11 (cont.)

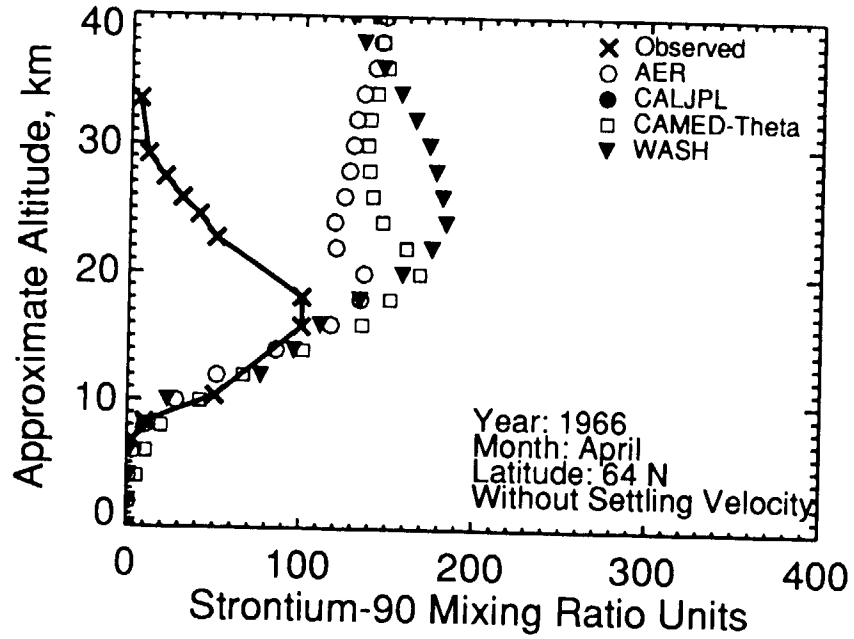

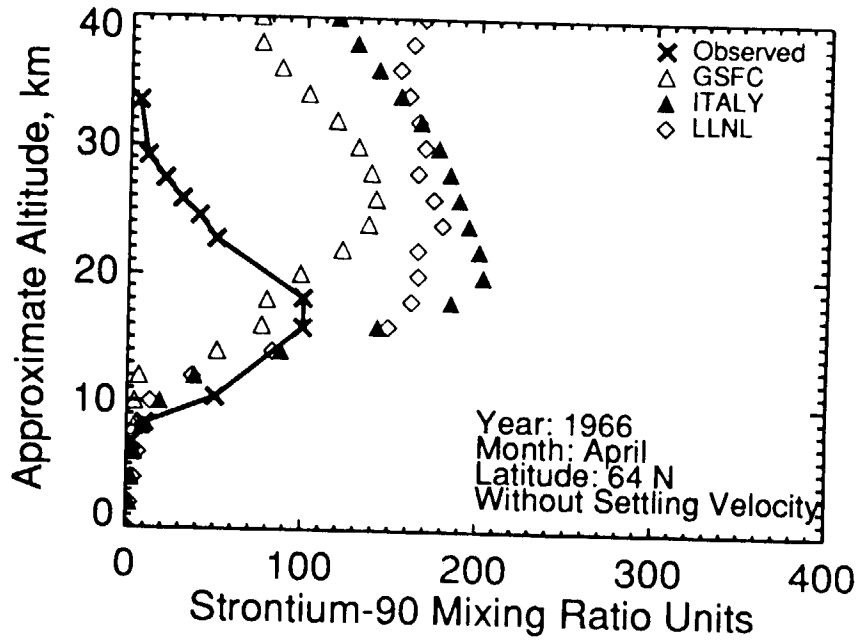

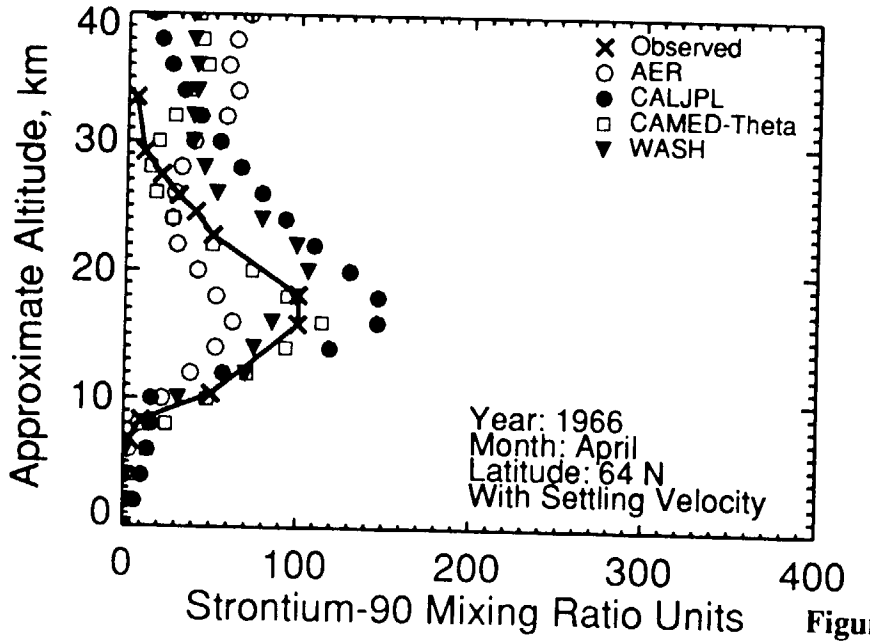

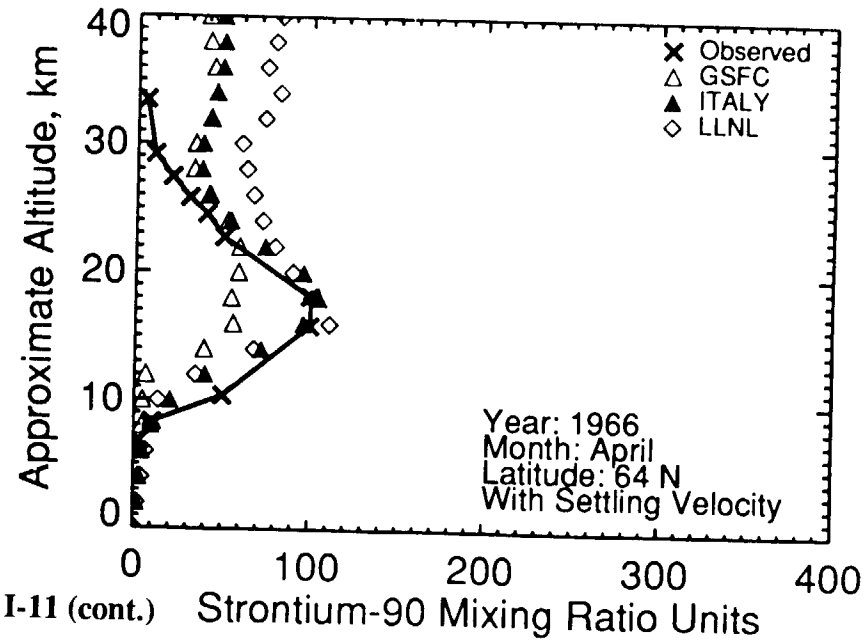

Figure I-11 (cont.)

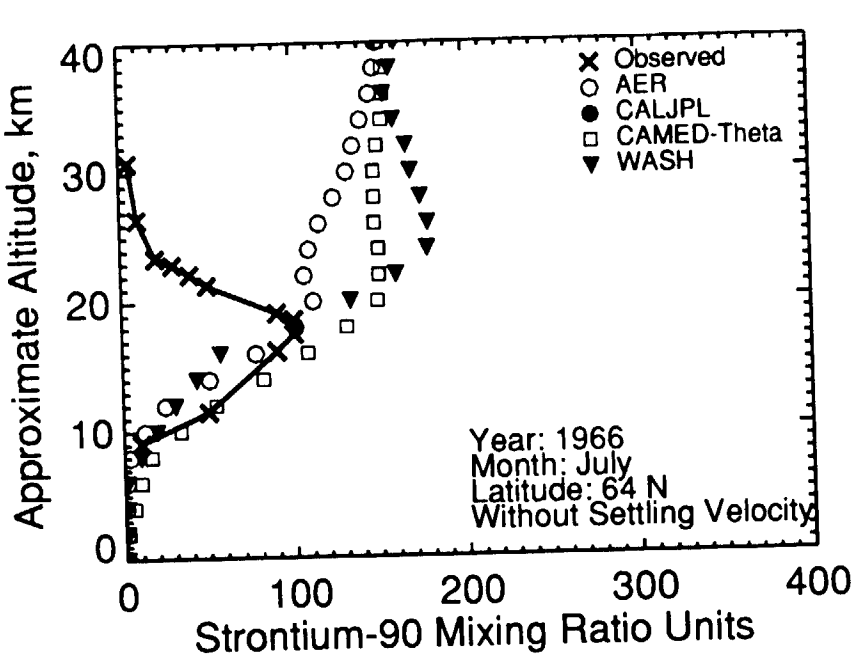

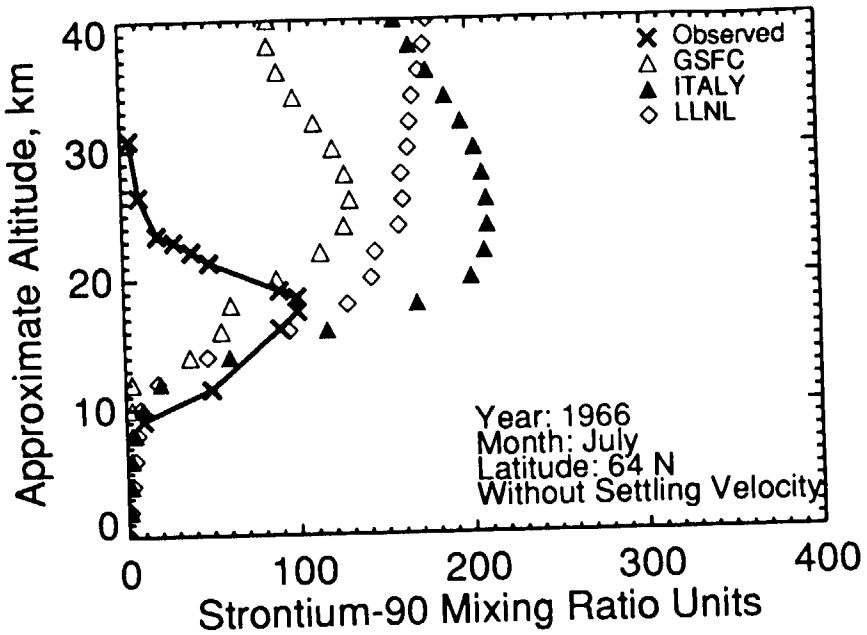

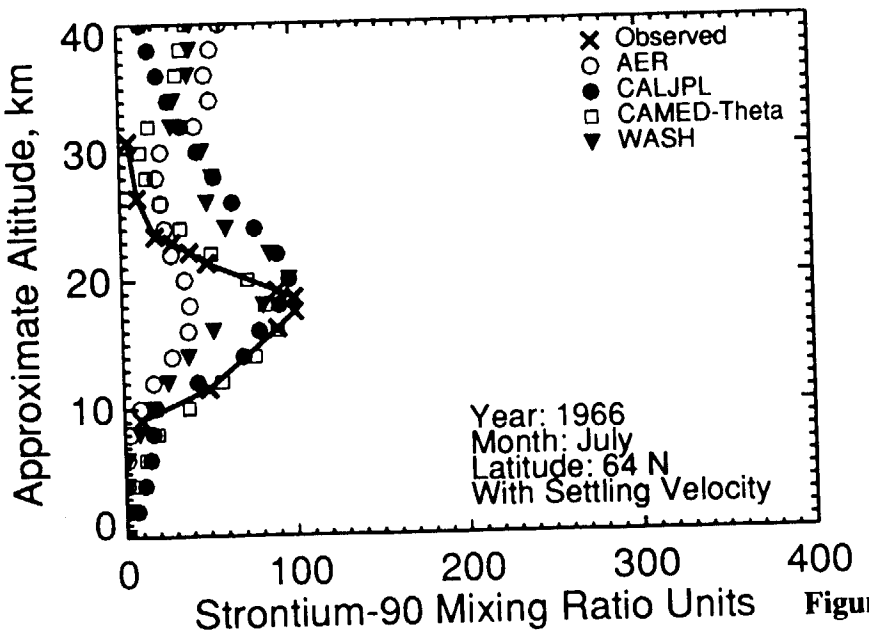

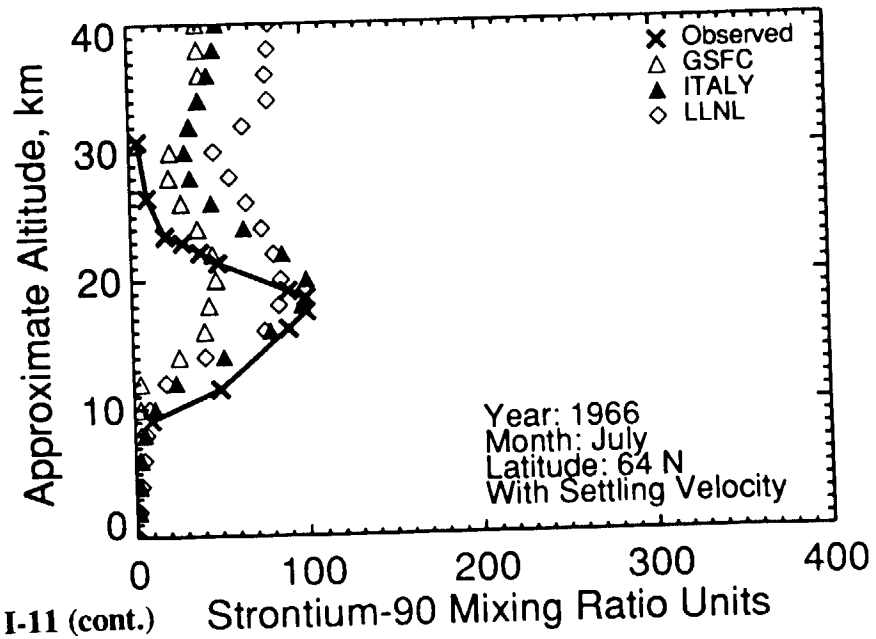

Figure I-11 (cont.)

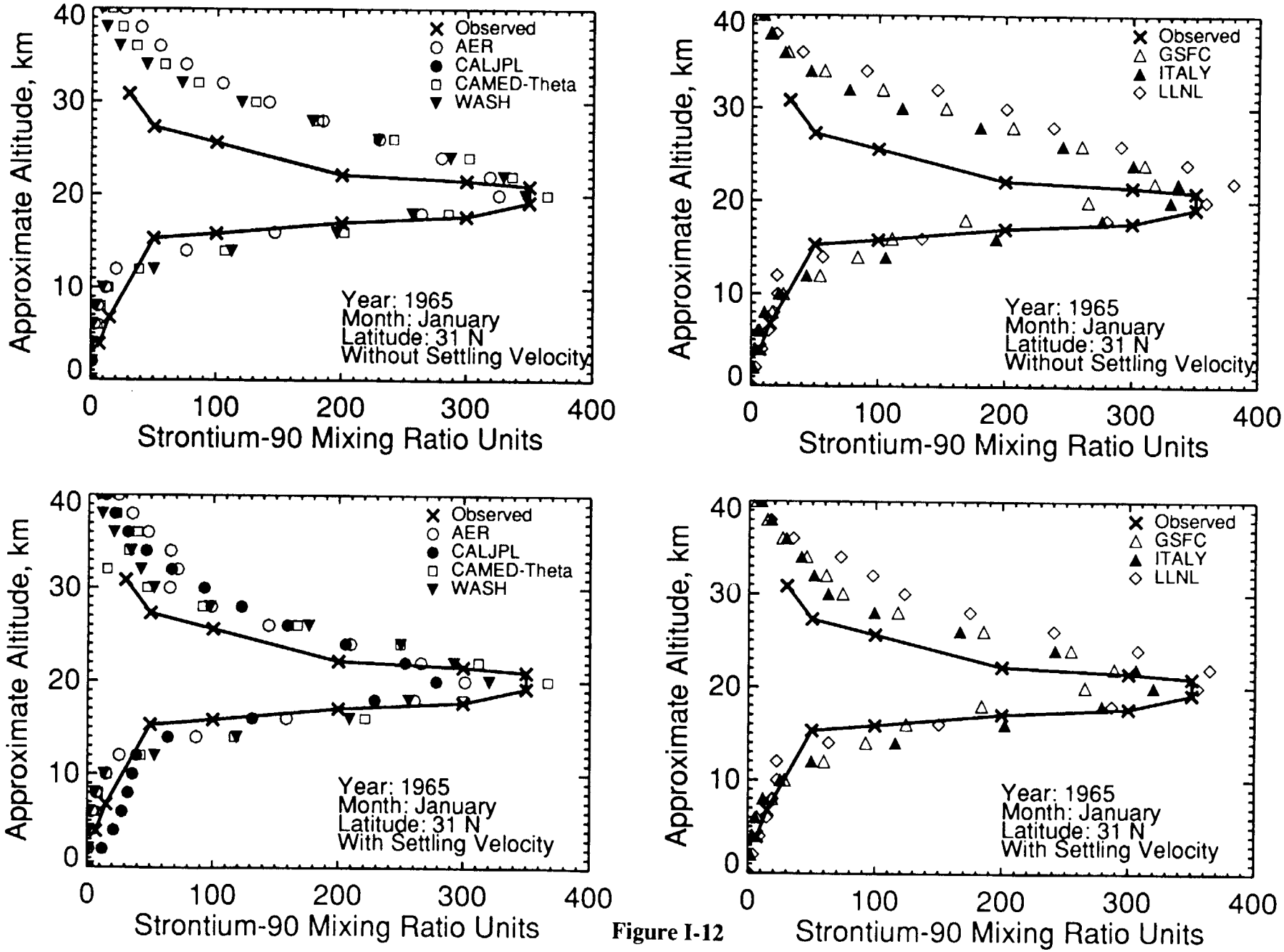
Approximate Altitude, km
Strontium-90 Mixing Ratio Units
Observed
AER
CALJPL
CAMED-Theta
WASH
Year: 1965
Month: January
Latitude: 31 N
Without Settling Velocity
Observed
GSFC
ITALY
LLNL
Year: 1965
Month: January
Latitude: 31 N
Without Settling Velocity
Observed
AER
CALJPL
CAMED-Theta
WASH
Year: 1965
Month: January
Latitude: 31 N
With Settling Velocity
Observed
GSFC
ITALY
LLNL
Year: 1965
Month: January
Latitude: 31 N
With Settling Velocity

Figure I-12

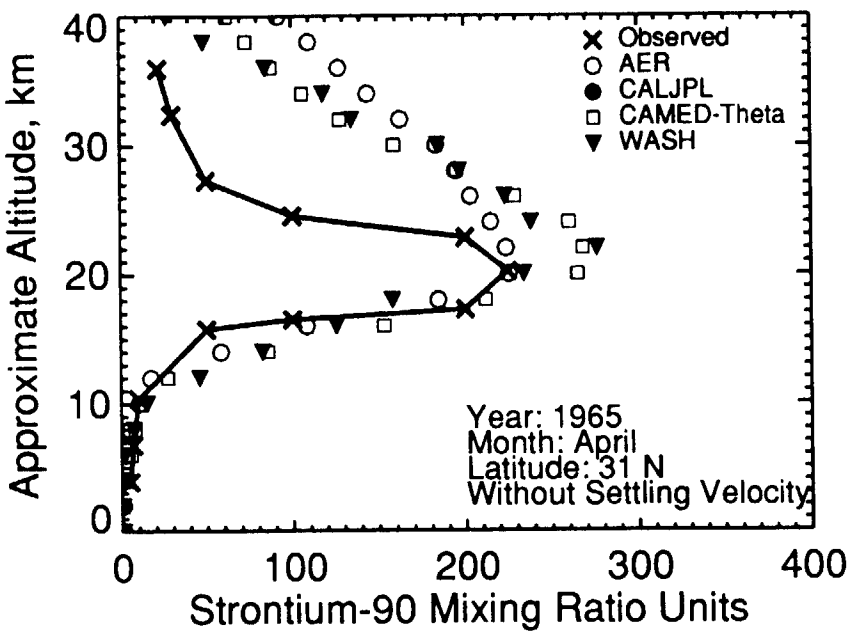

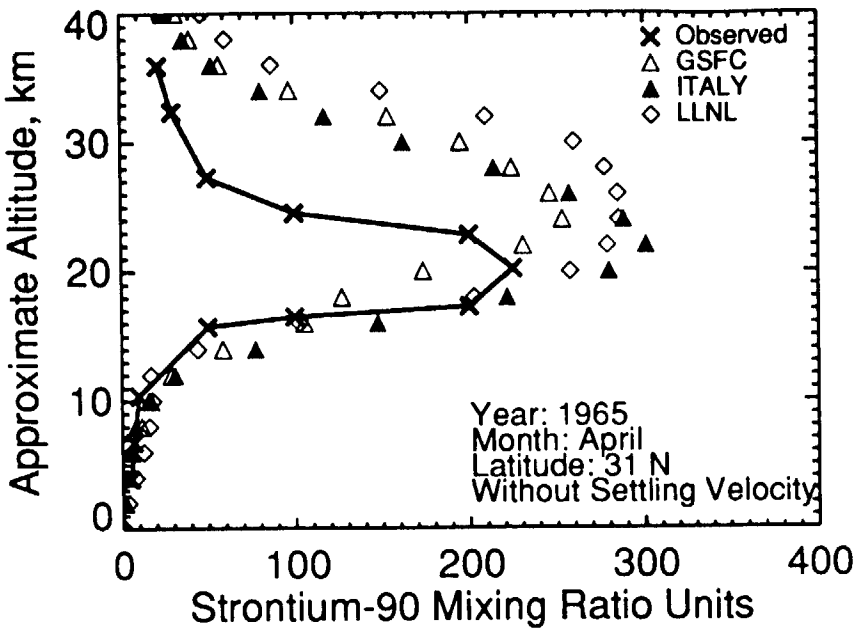

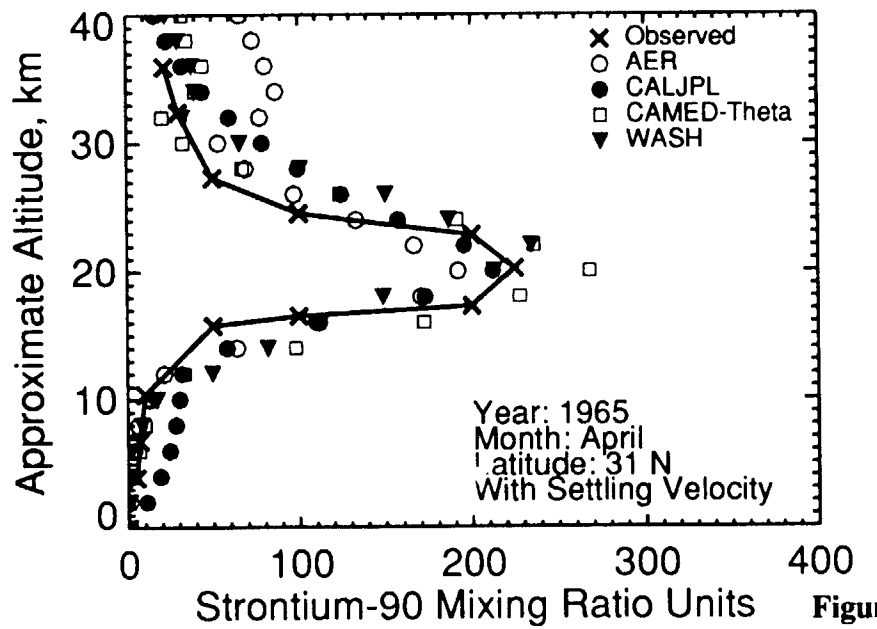

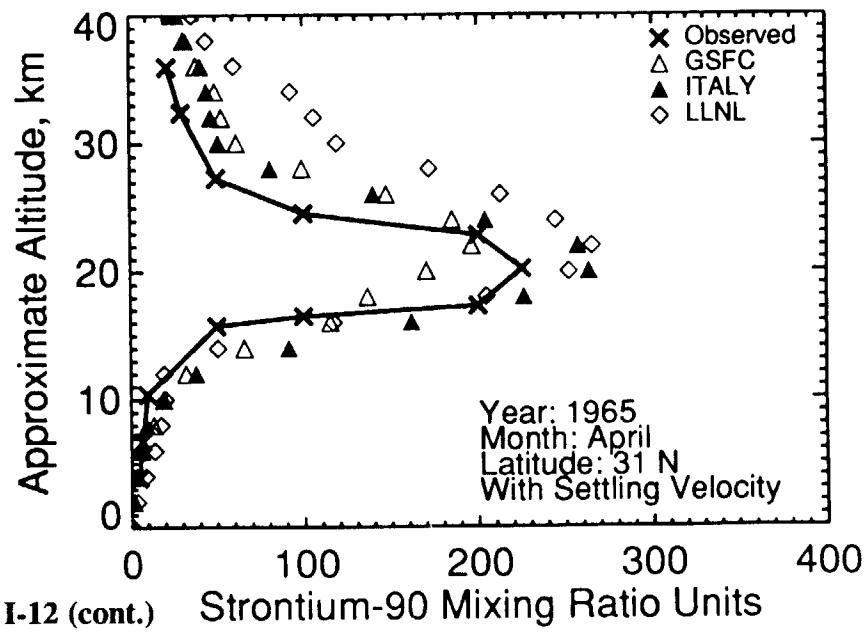

Figure I-12 (cont.)

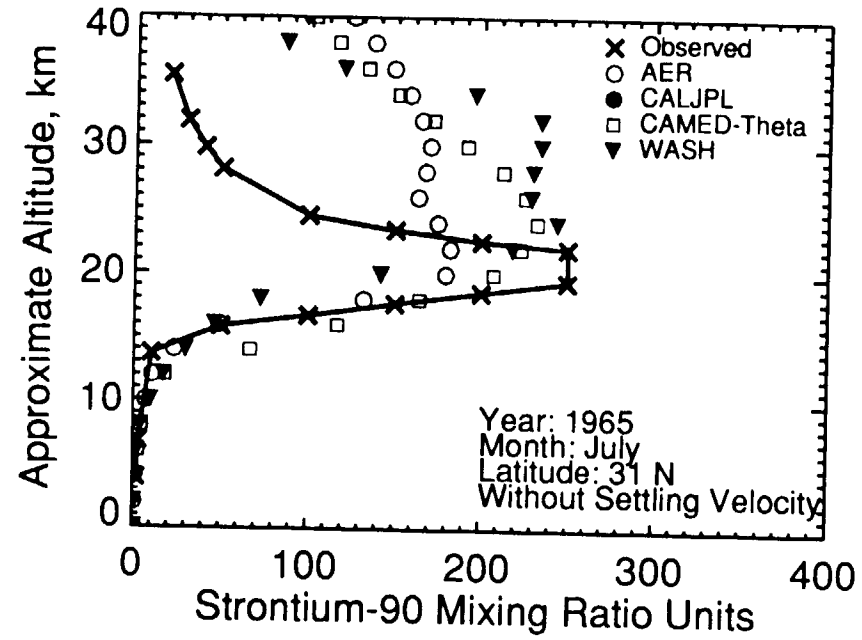

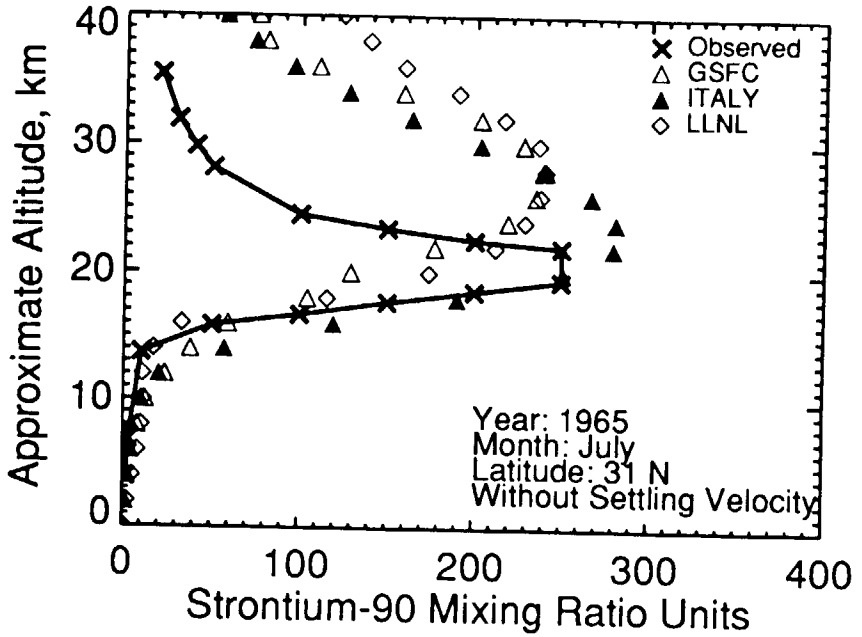

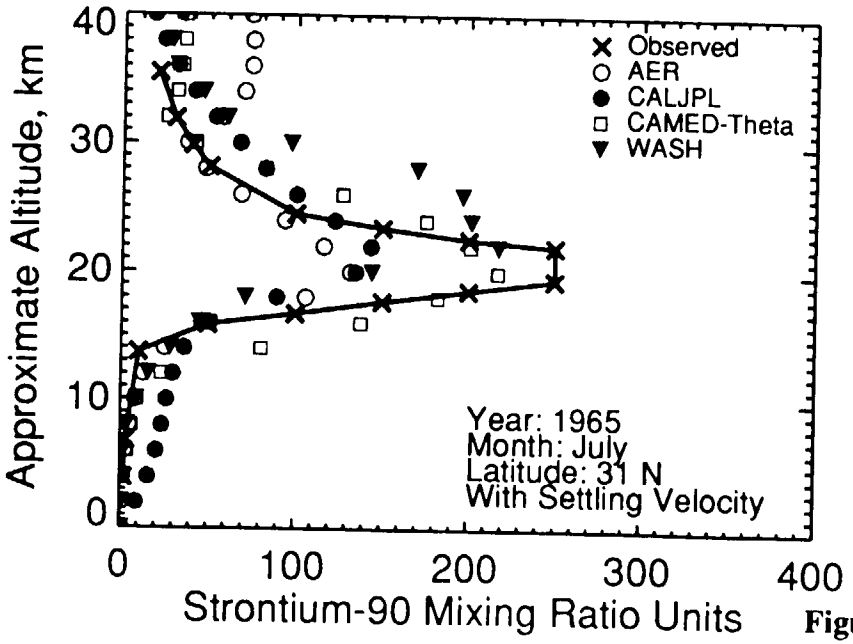

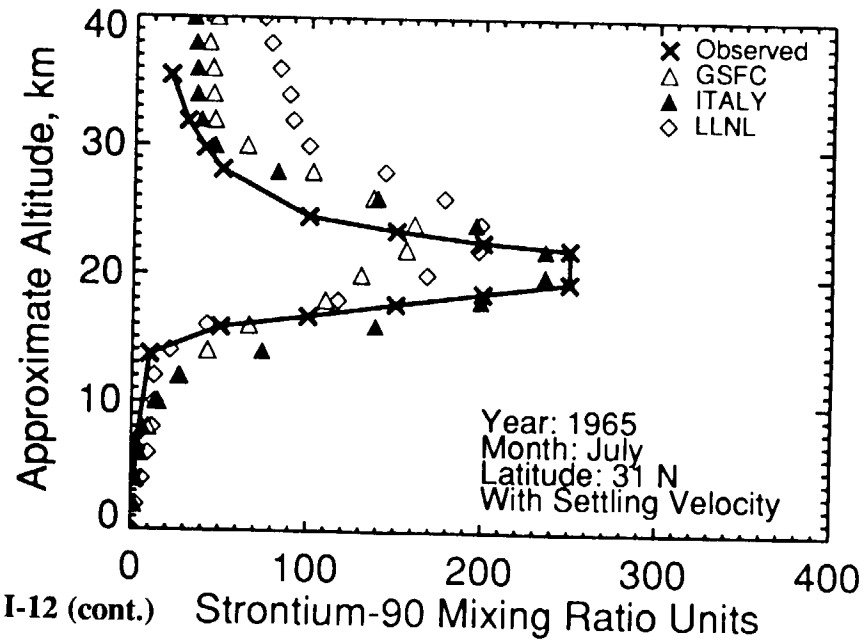

Figure I-12 (cont.)

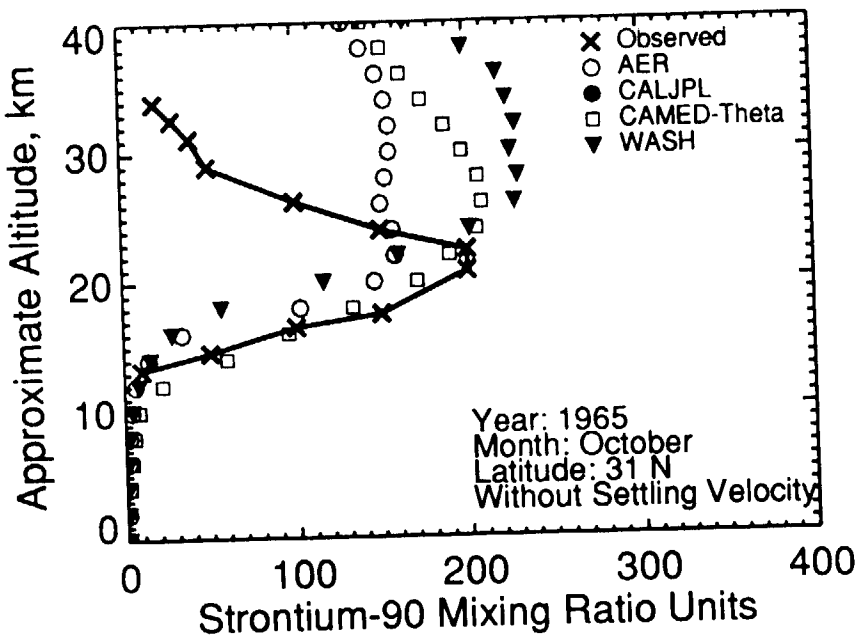

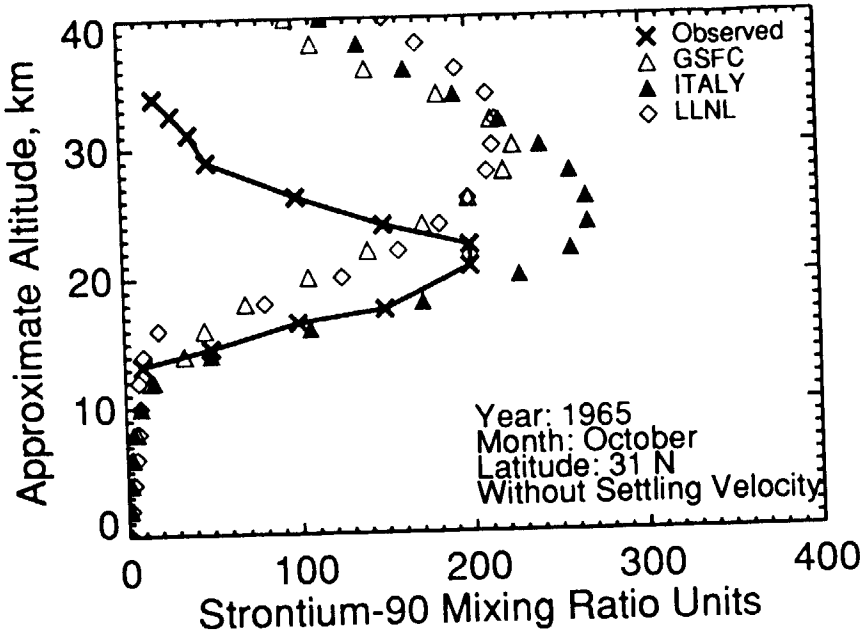

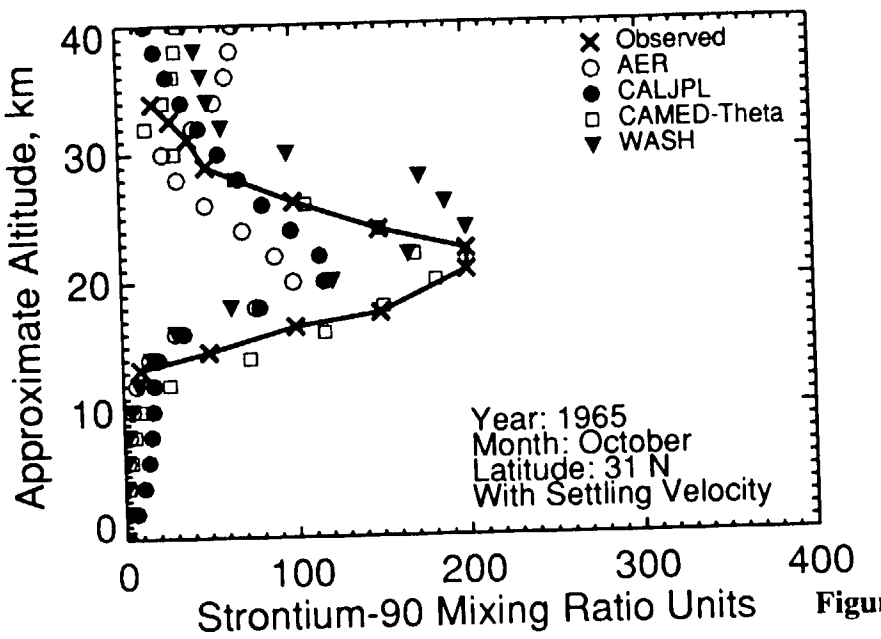

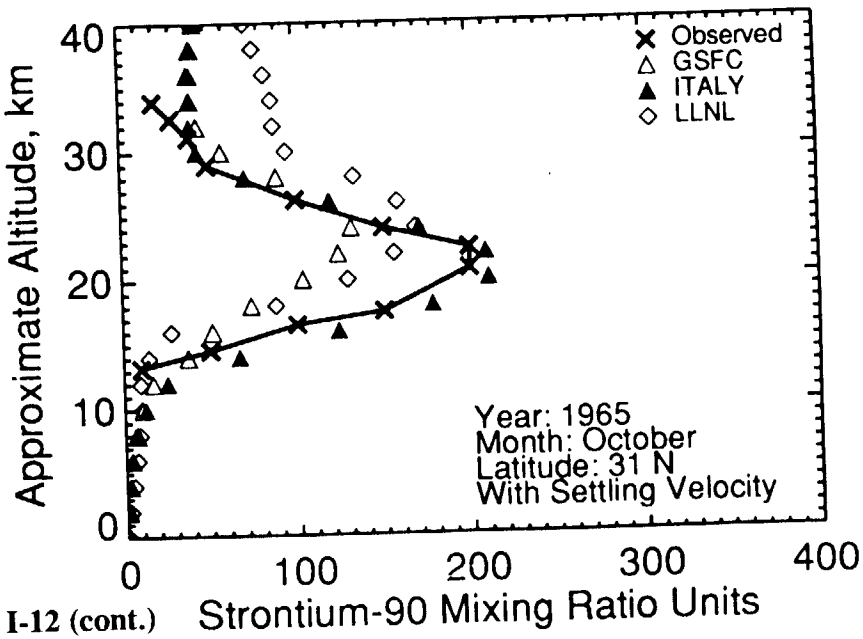

Figure I-12 (cont.)

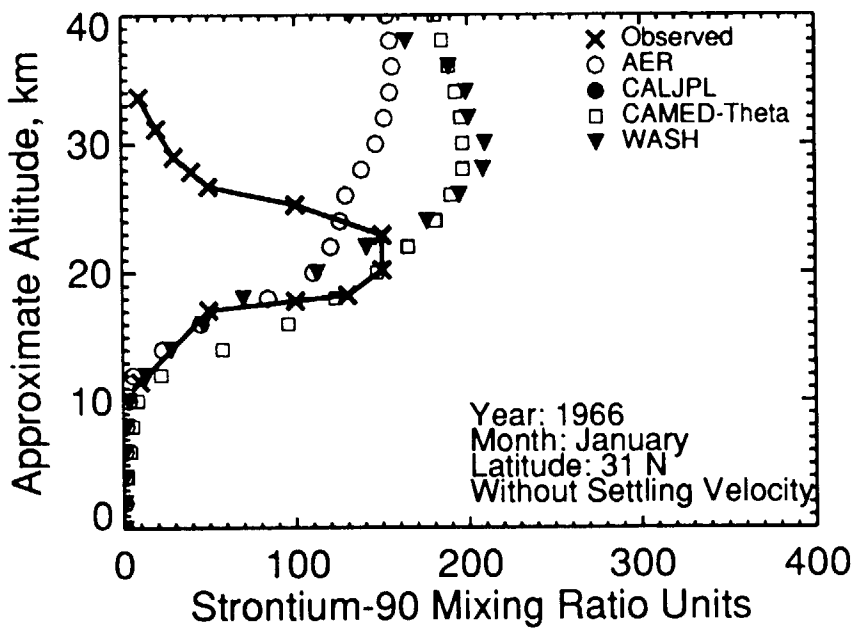

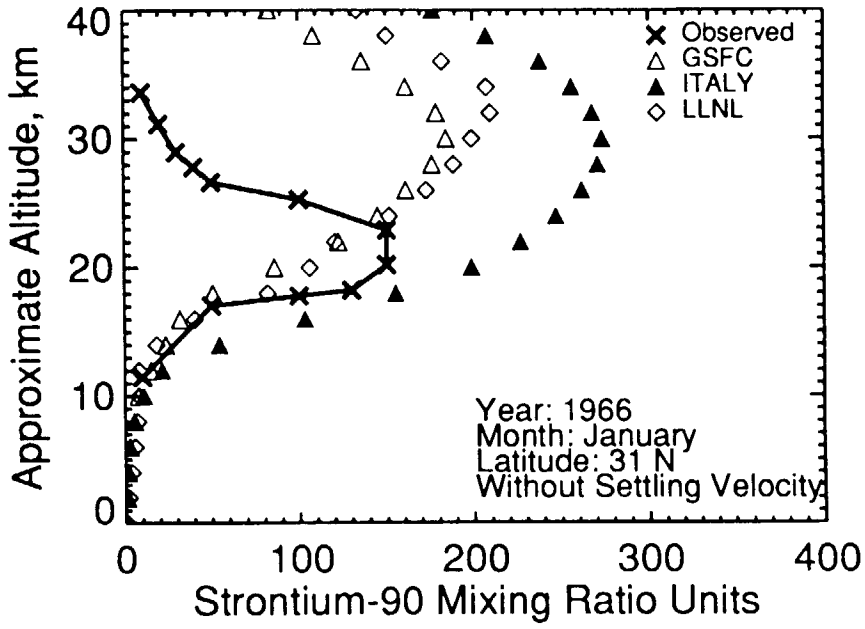

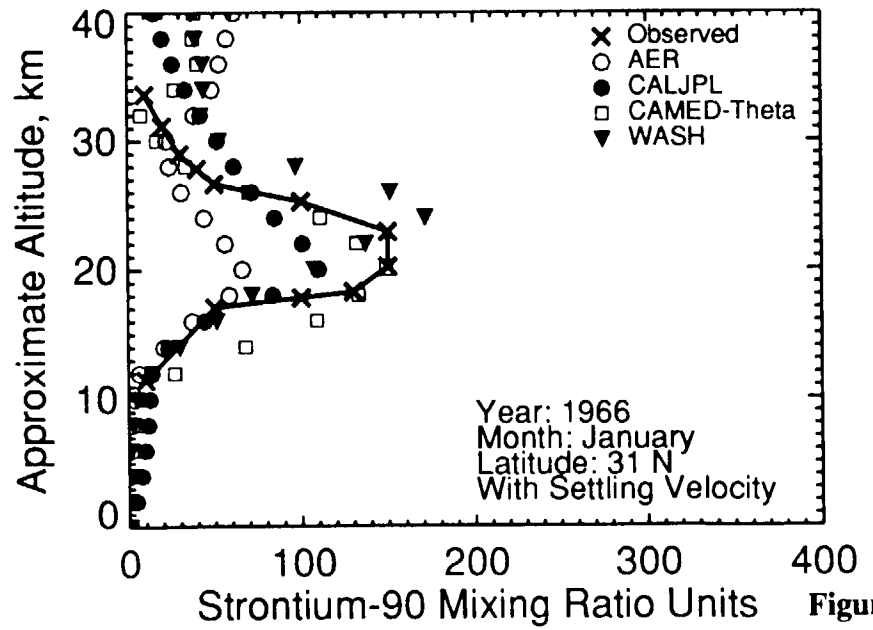

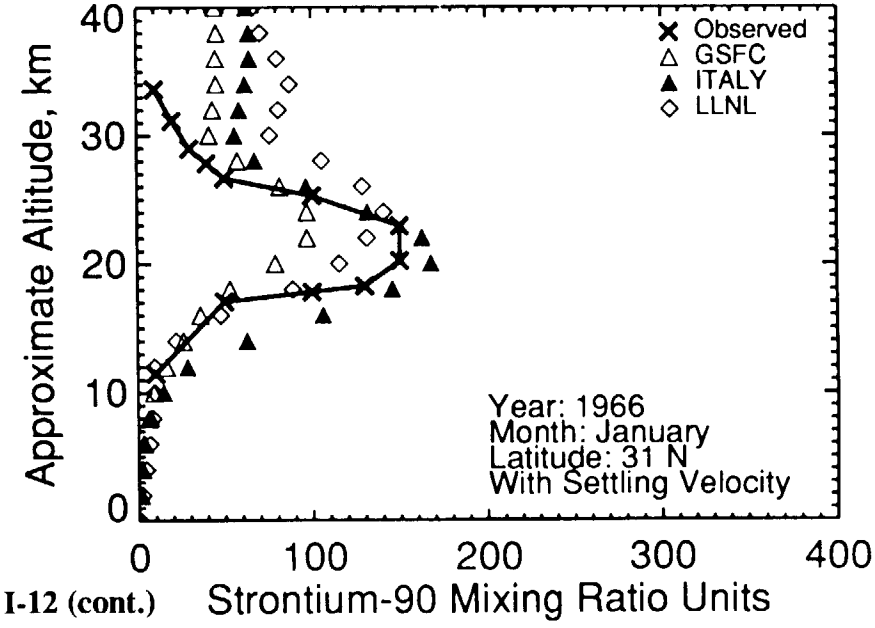

Figure I-12 (cont.)

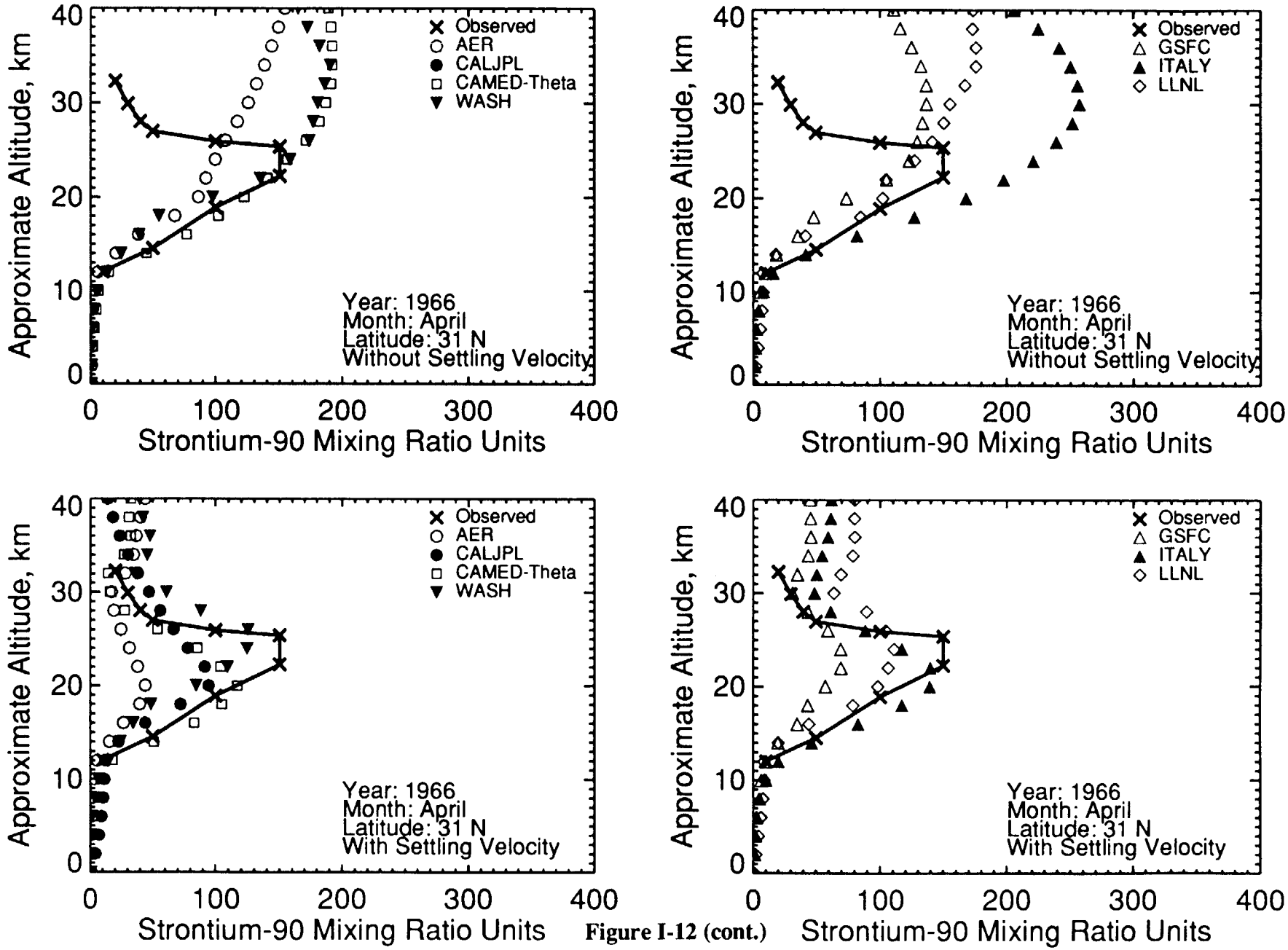

Figure I-12 (cont.)

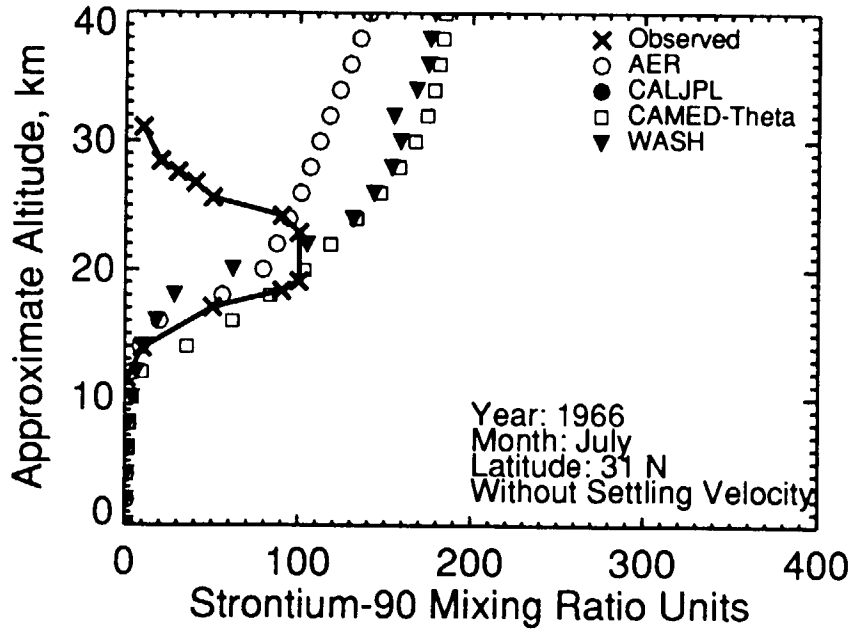

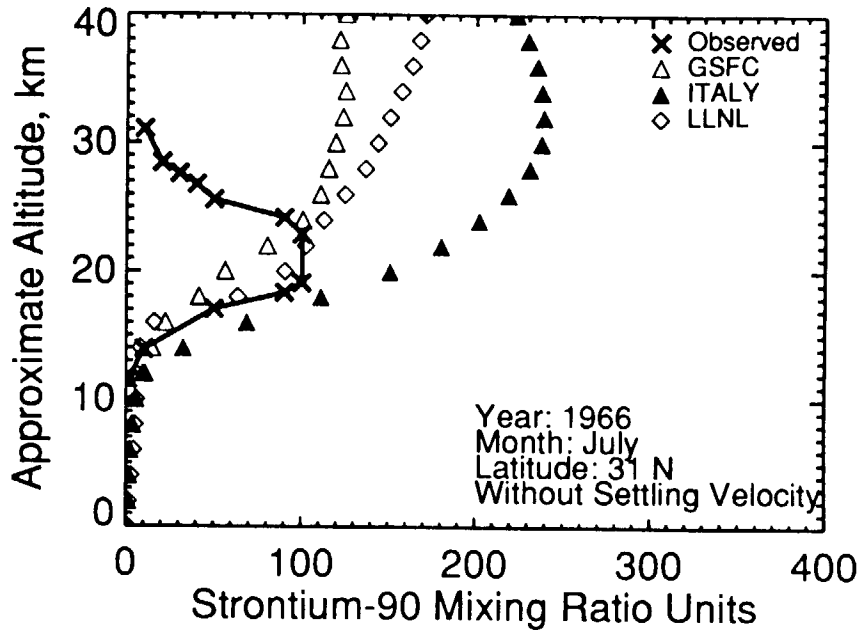

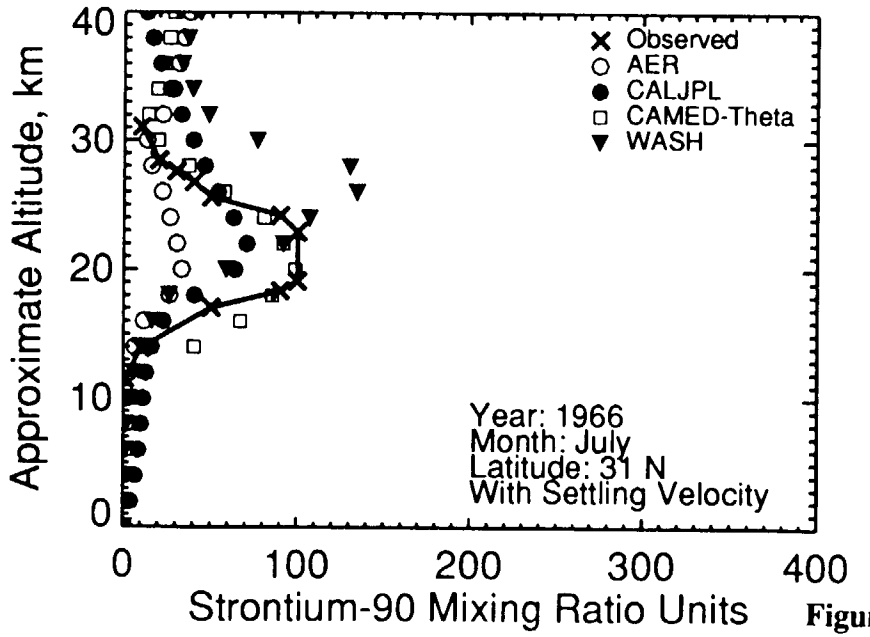

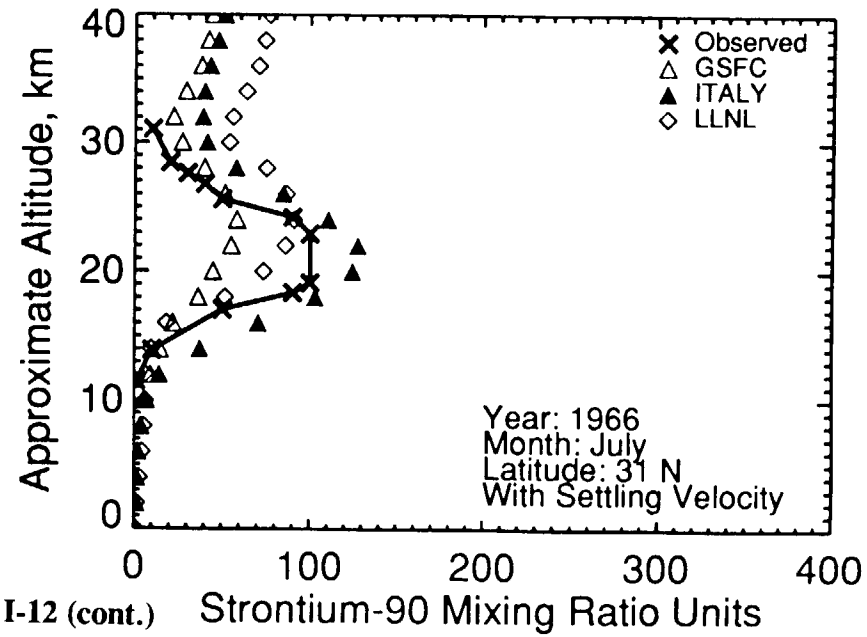

Figure I-12 (cont.)

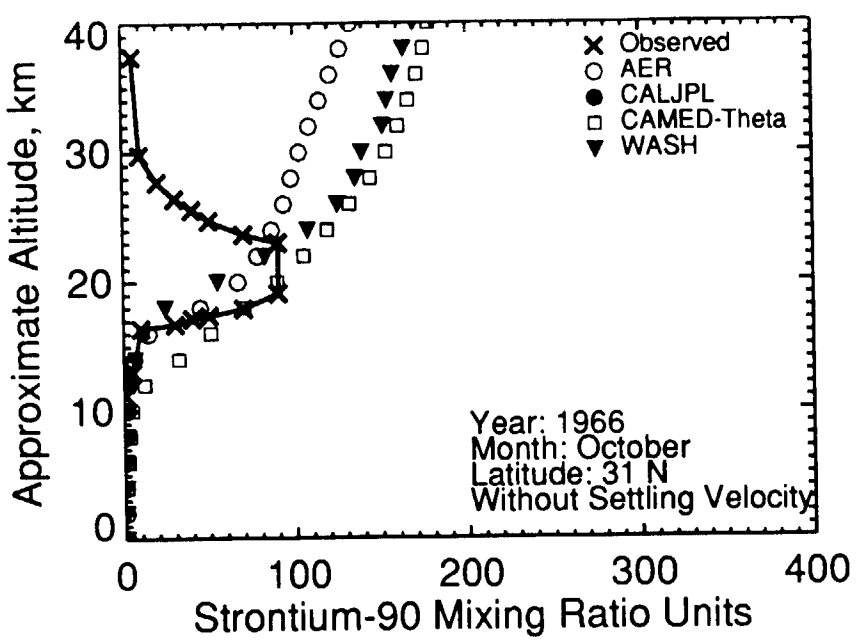

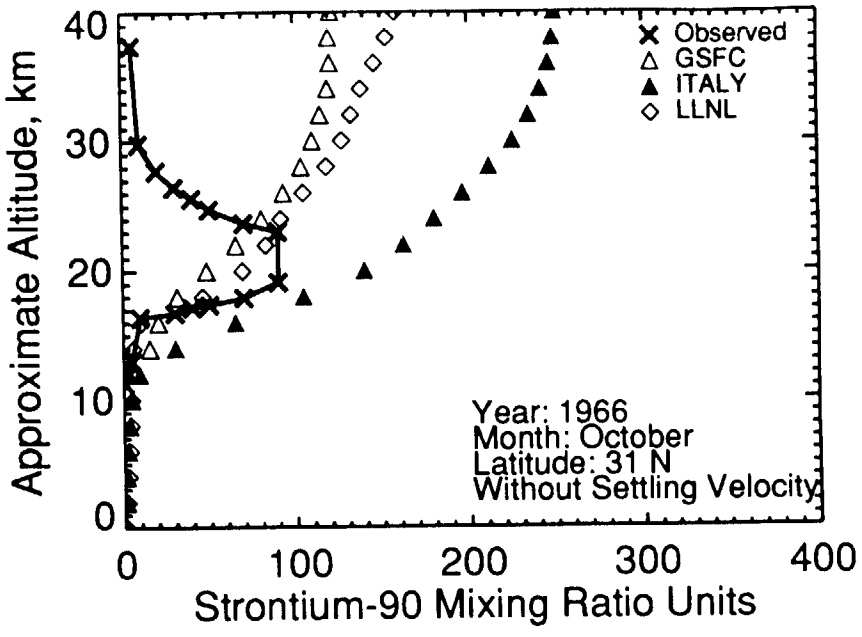

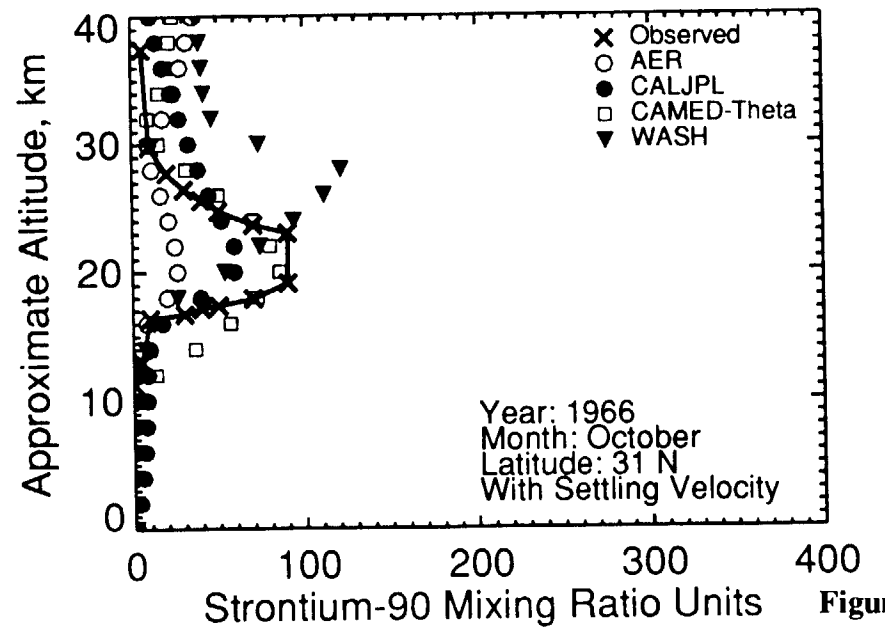

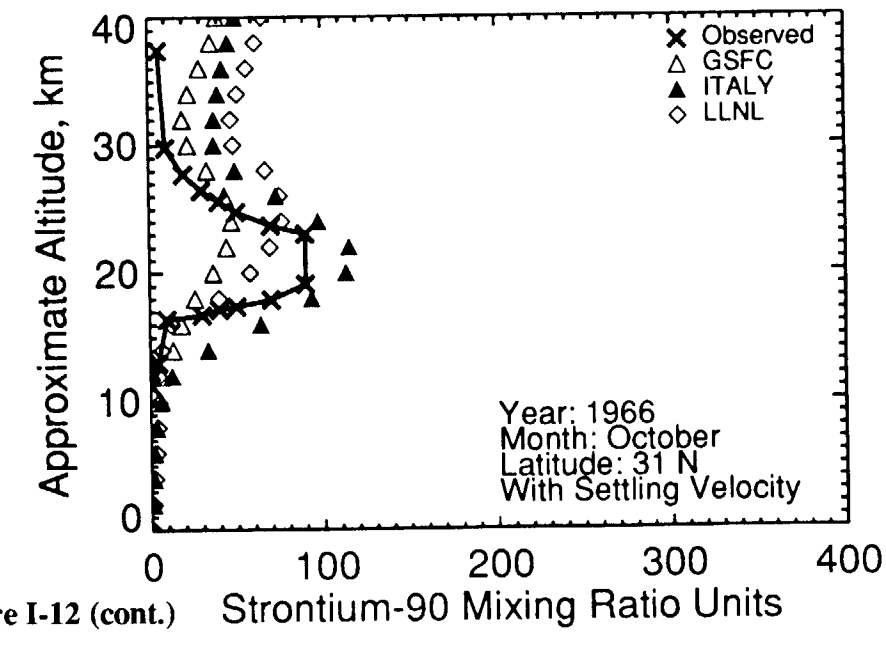

Figure I-12 (cont.)

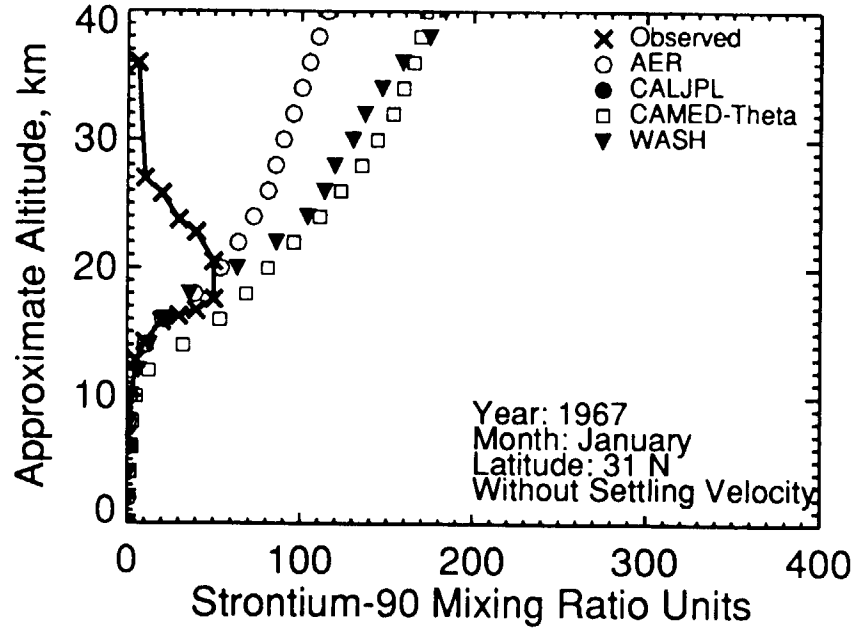

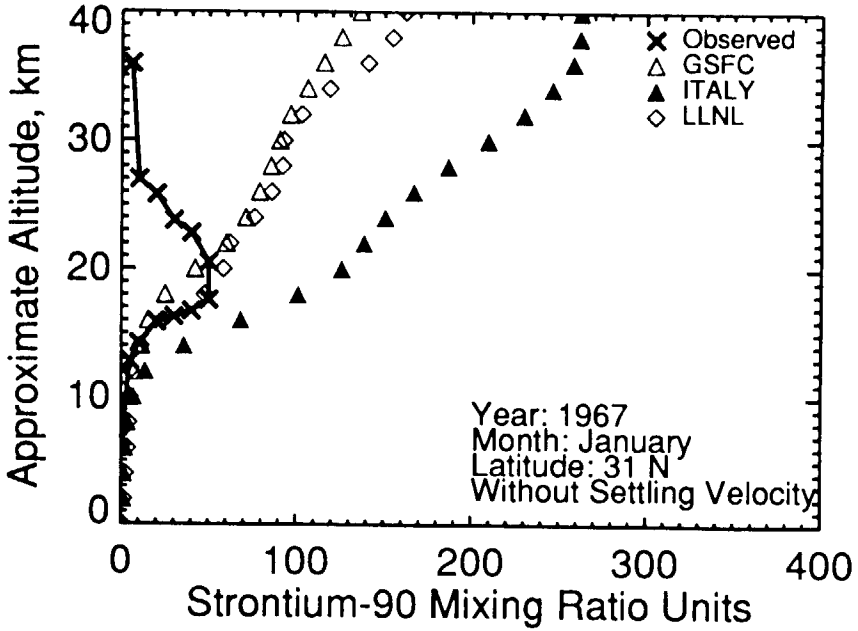

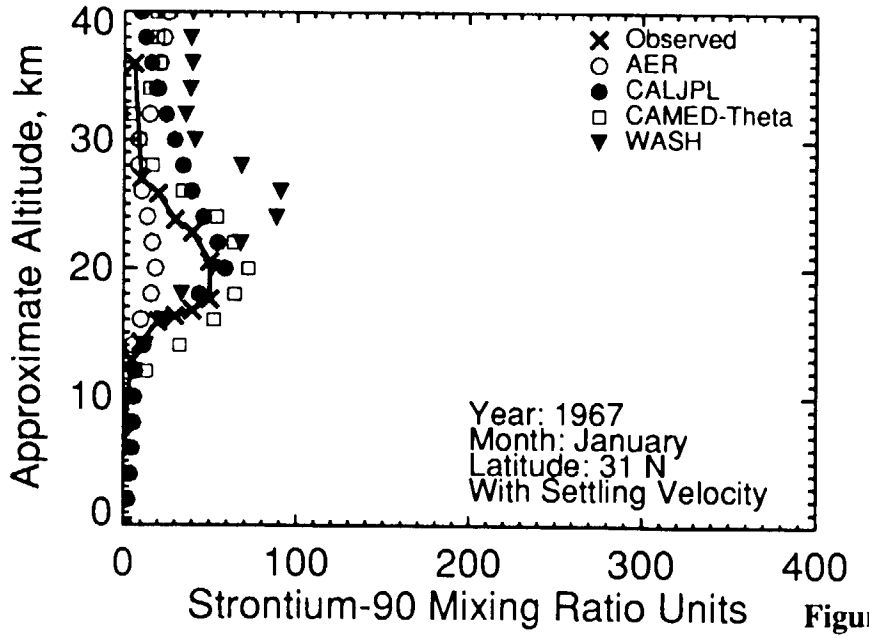

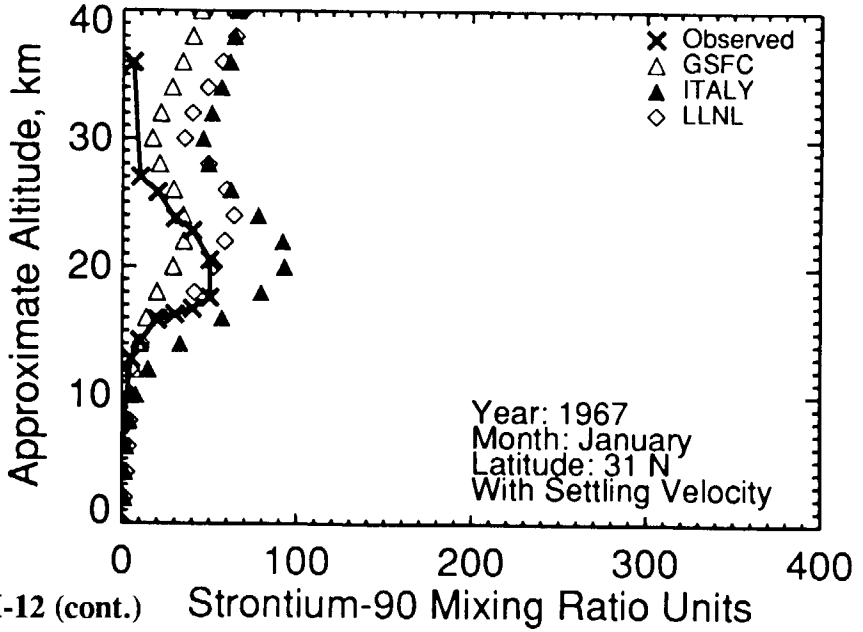

Figure I-12 (cont.)

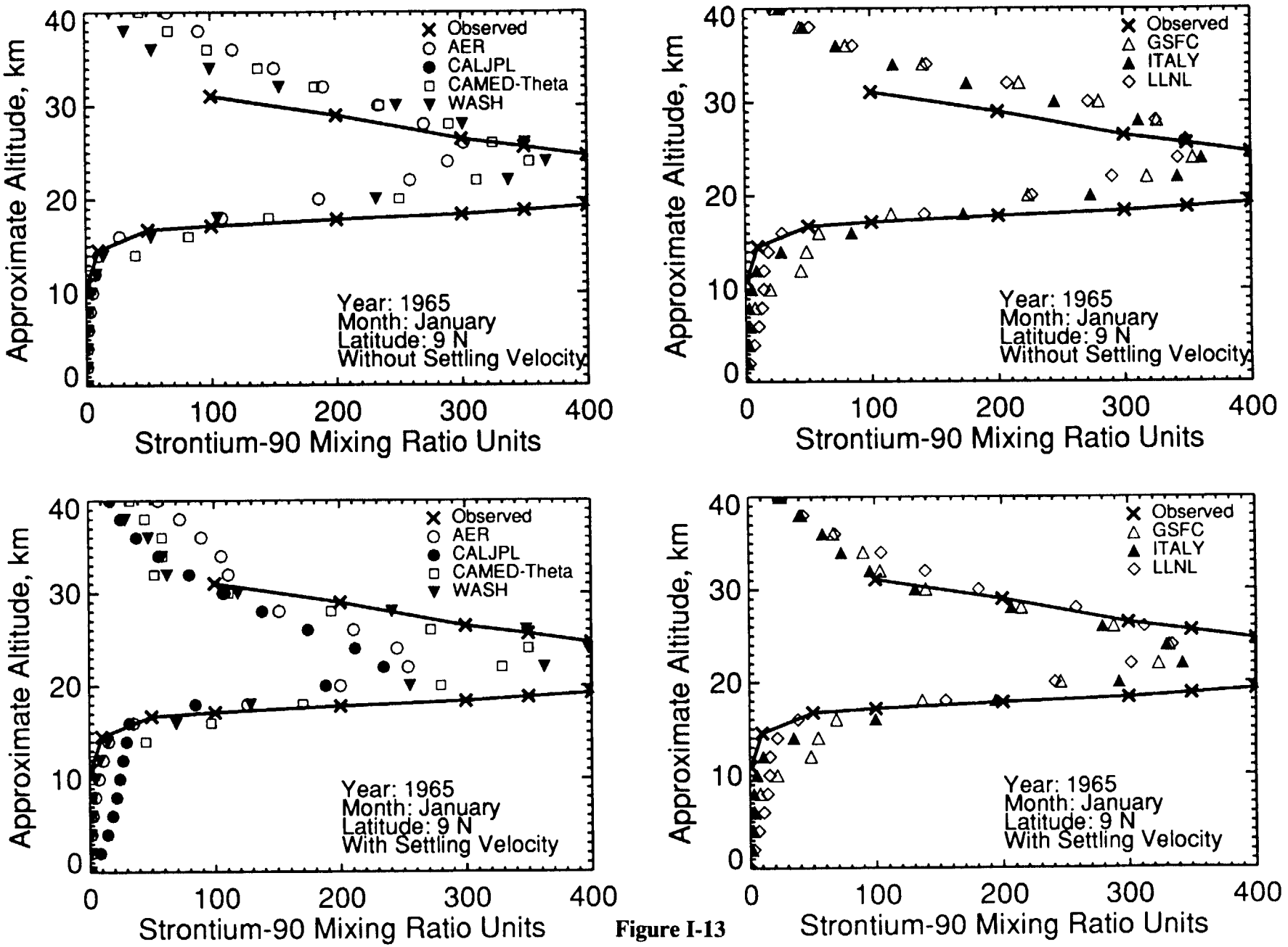
Approximate Altitude, km
Strontium-90 Mixing Ratio Units
Observed
AER
CALJPL
CAMED-Theta
WASH
GSFC
ITALY
LLNL
Year: 1965
Month: January
Latitude: 9 N
Without Settling Velocity
With Settling Velocity

Figure I-13

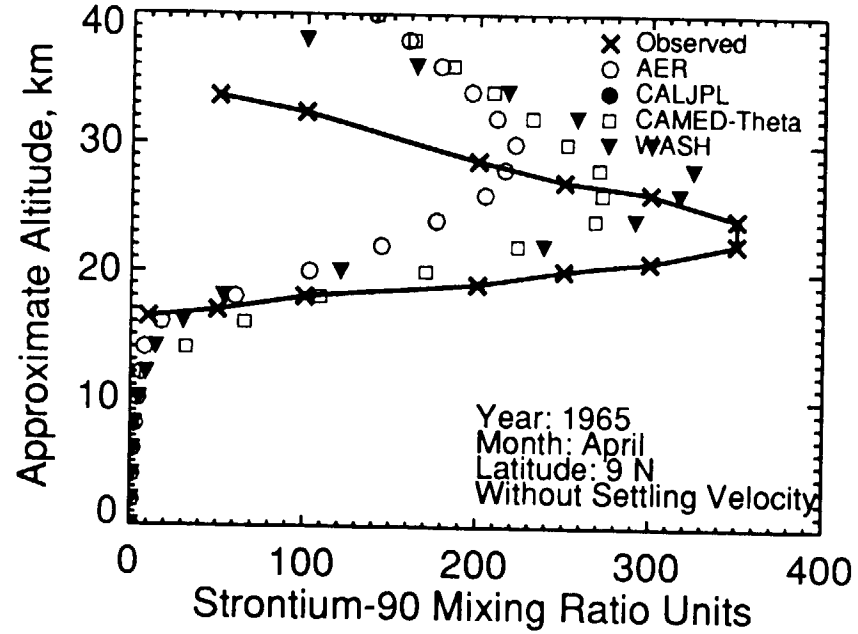

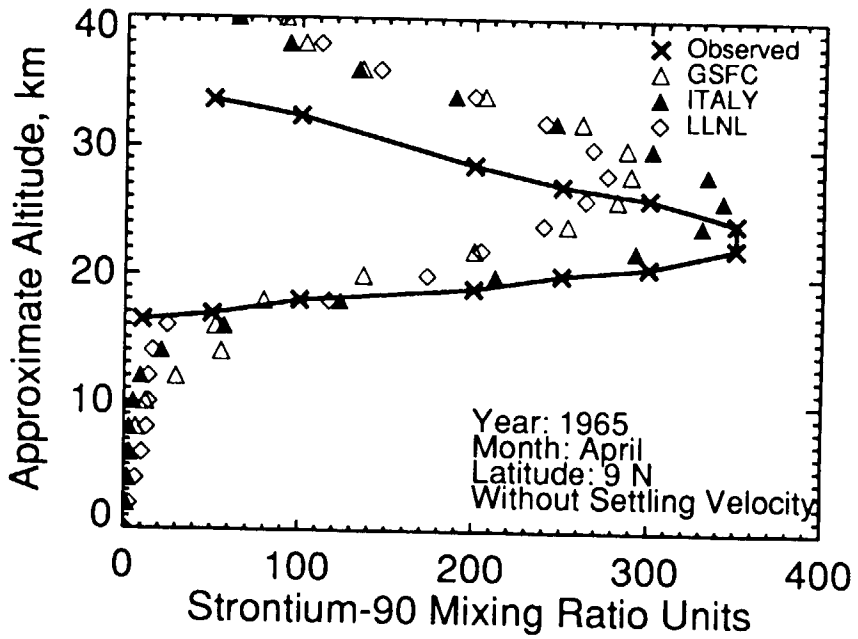

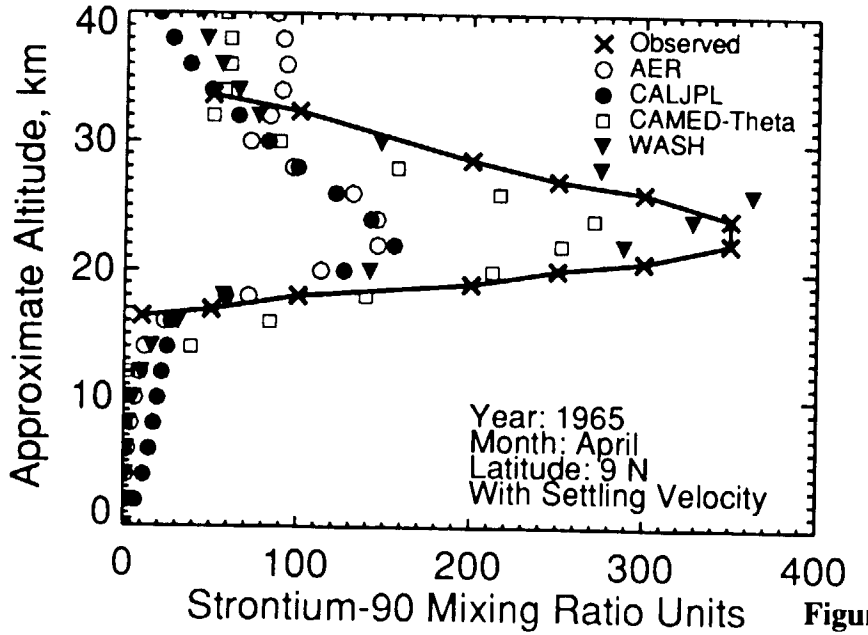

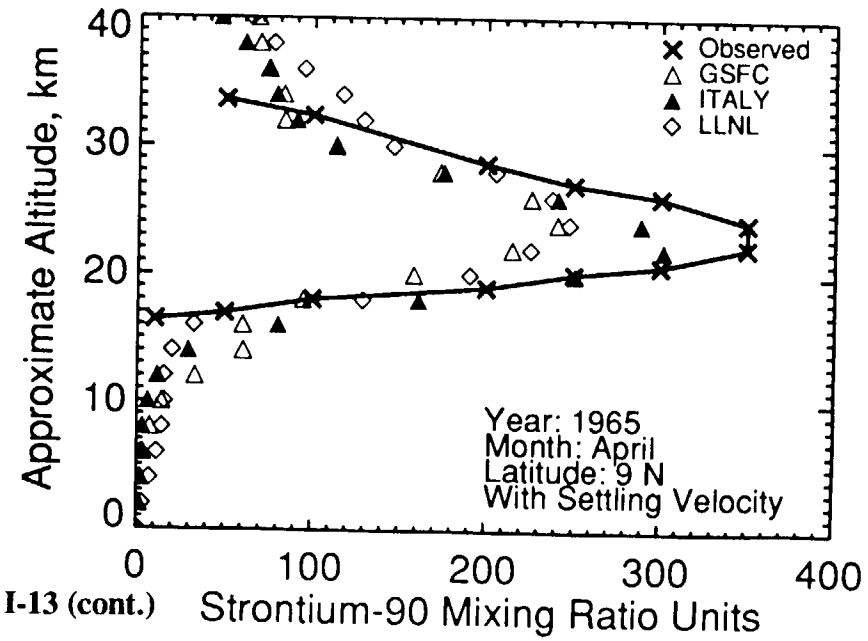

Figure I-13 (cont.)

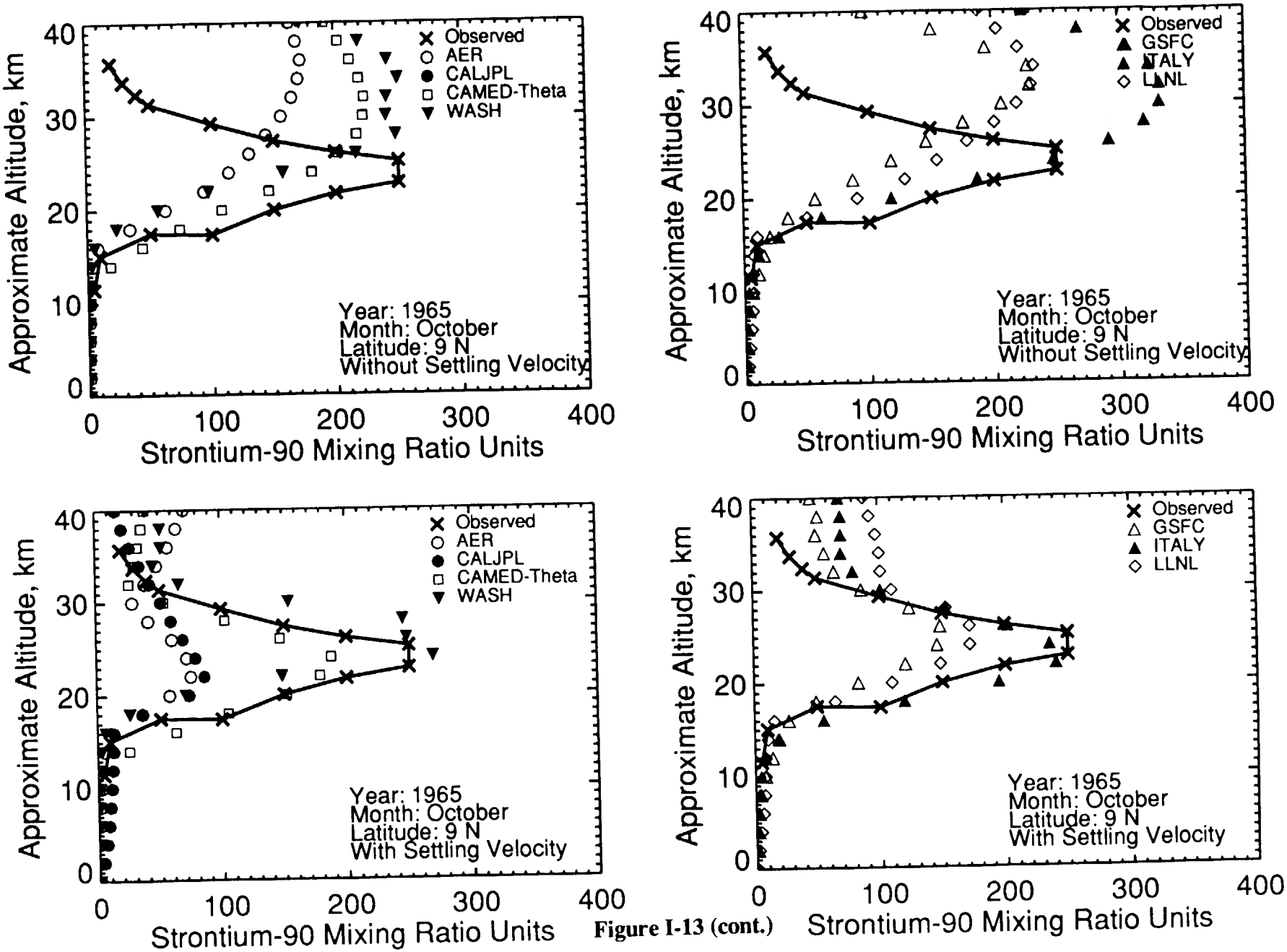

Figure I-13 (cont.)

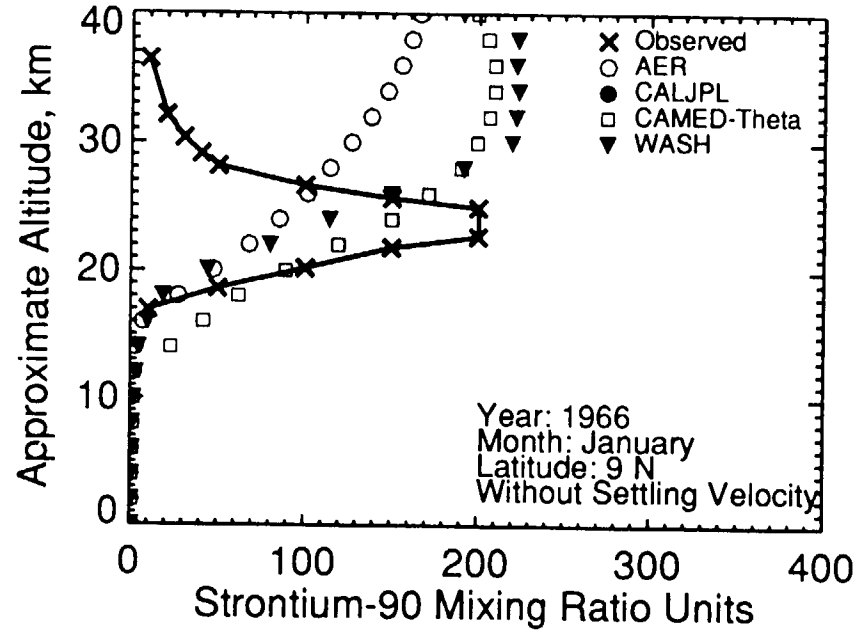

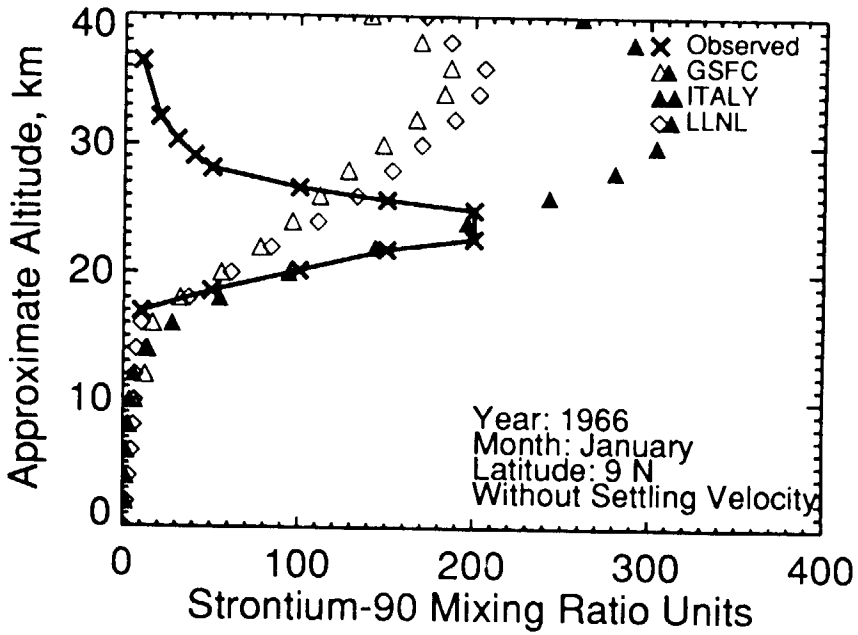

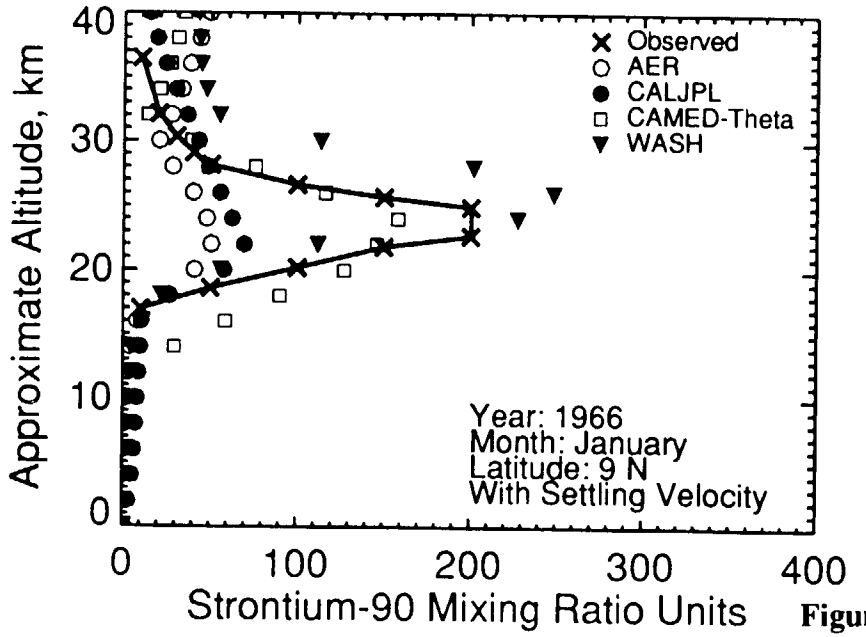

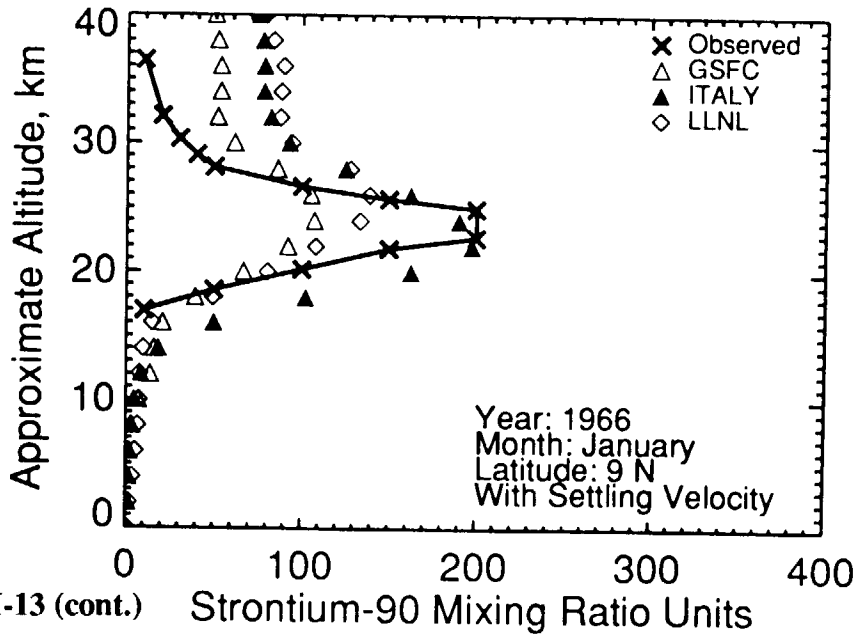

Figure I-13 (cont.)

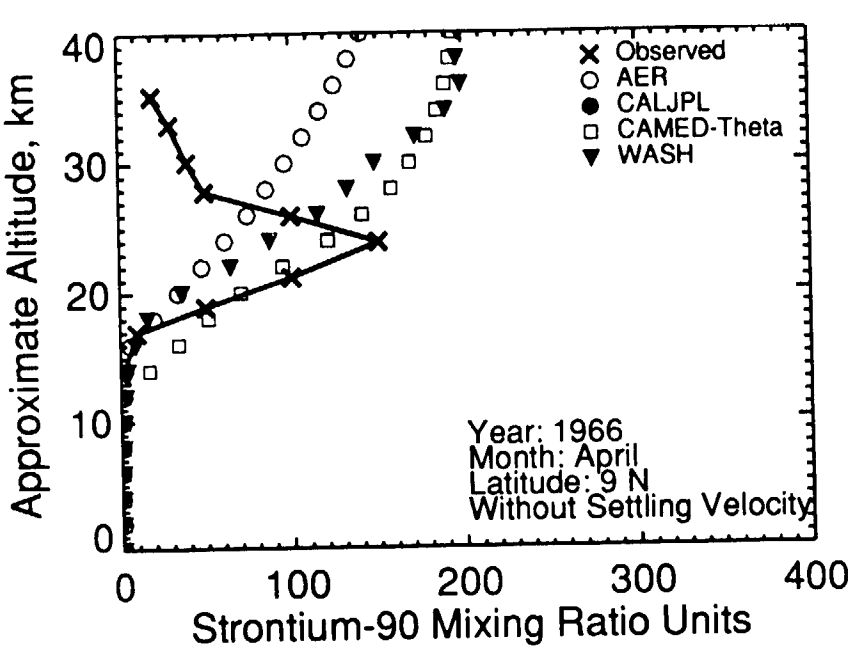

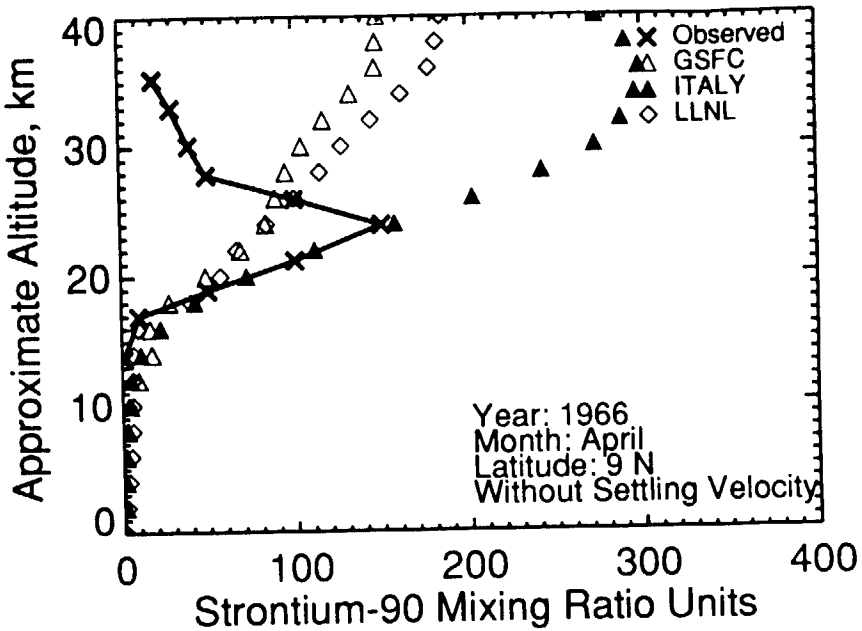

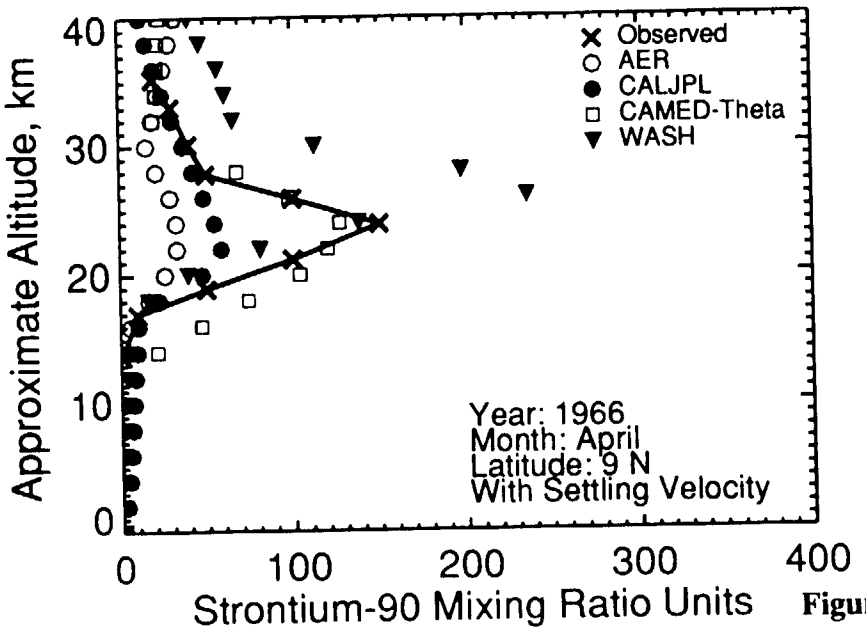

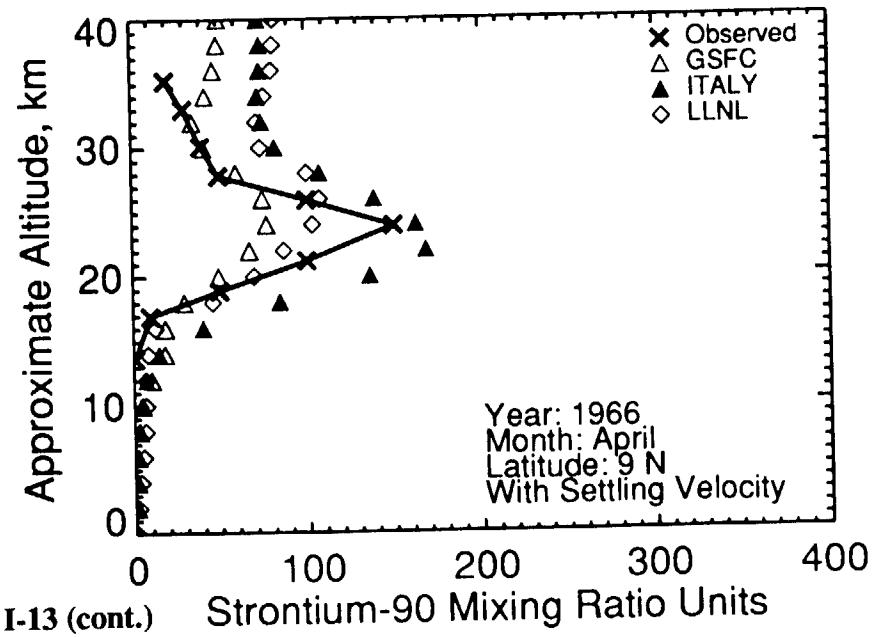

Figure I-13 (cont.)

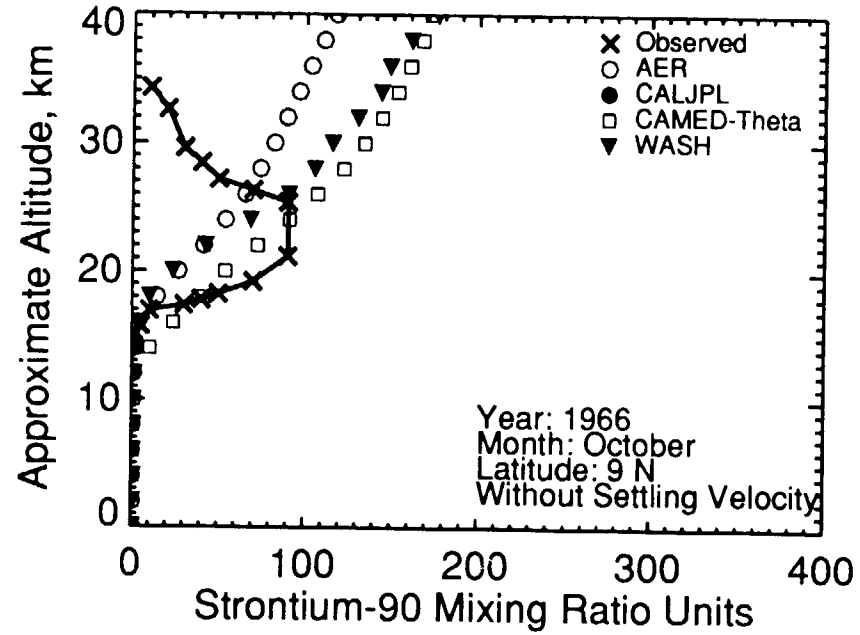

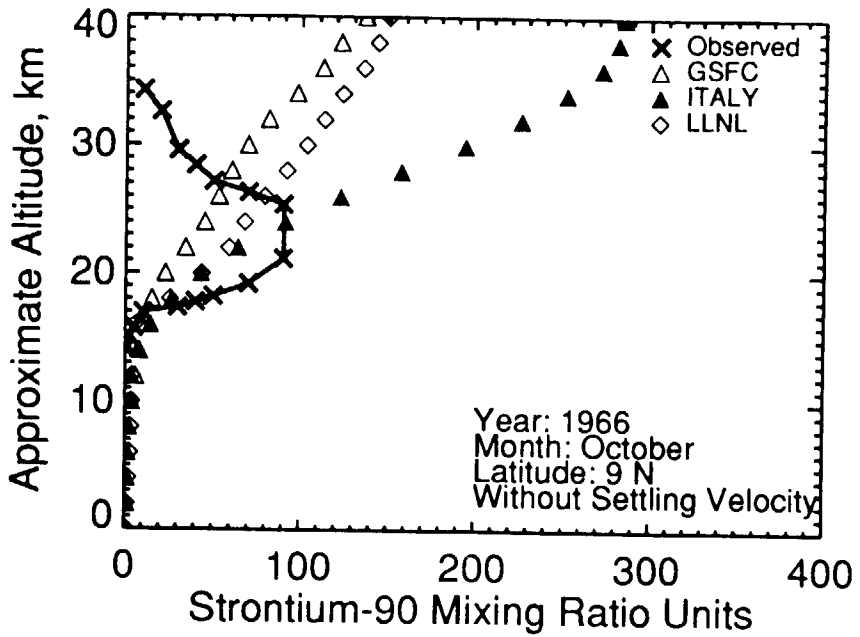

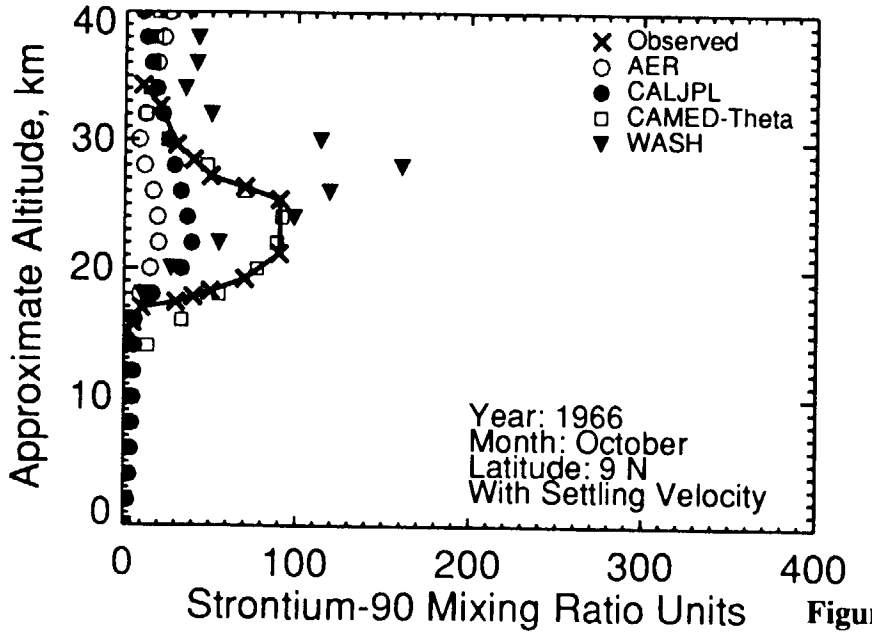

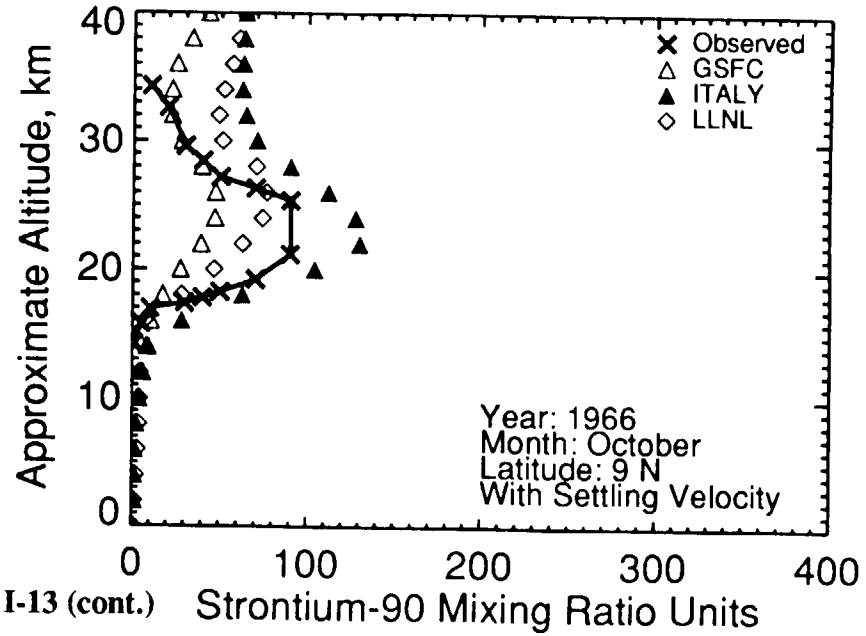

Figure I-13 (cont.)

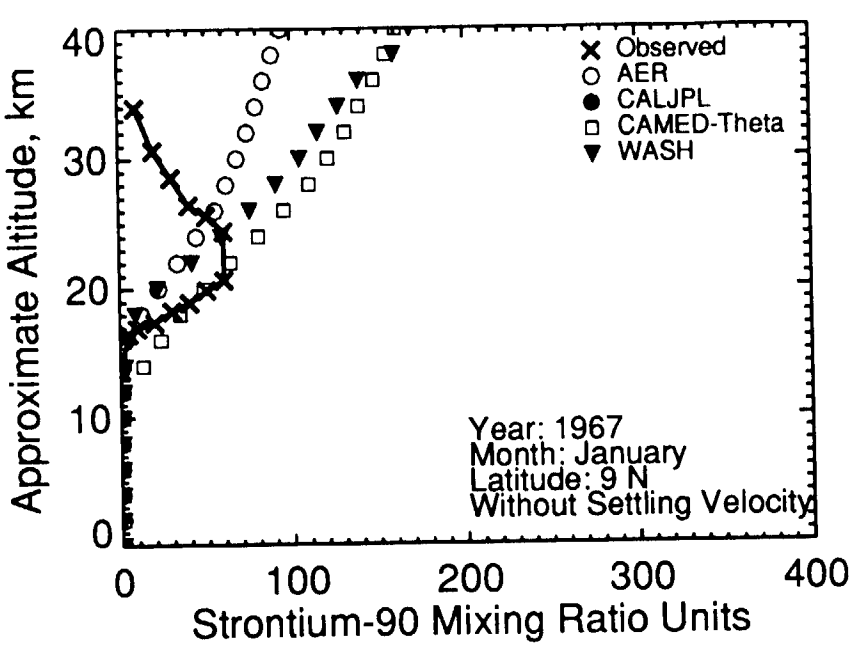

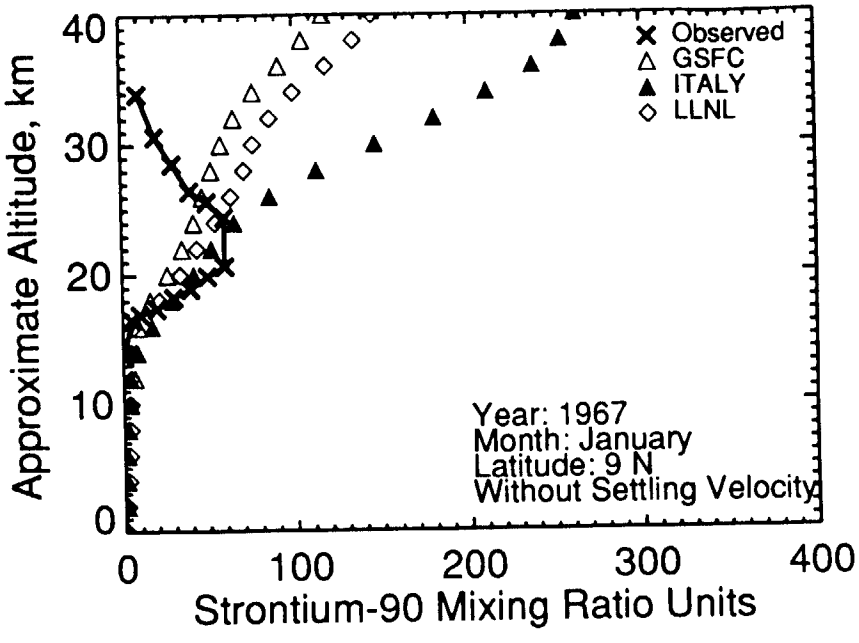

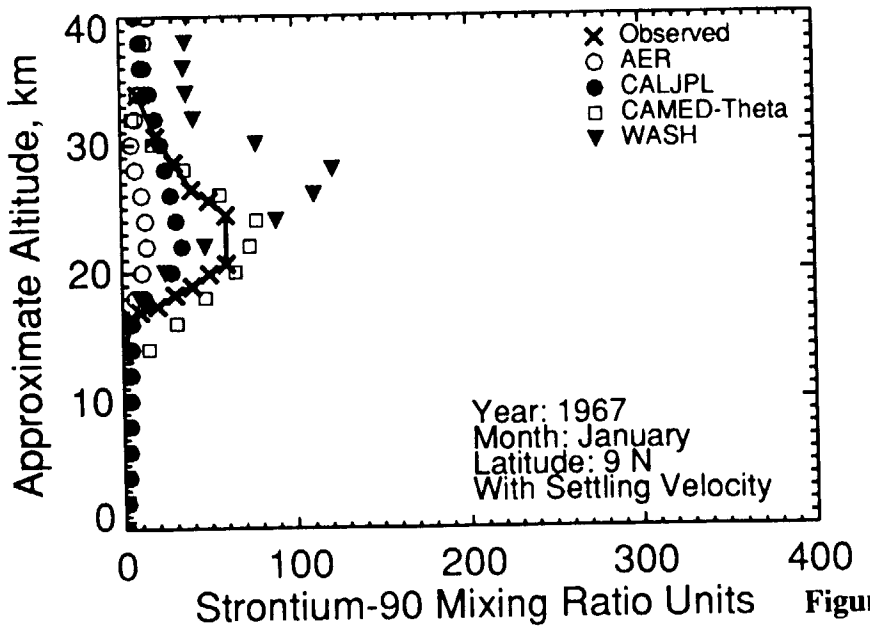

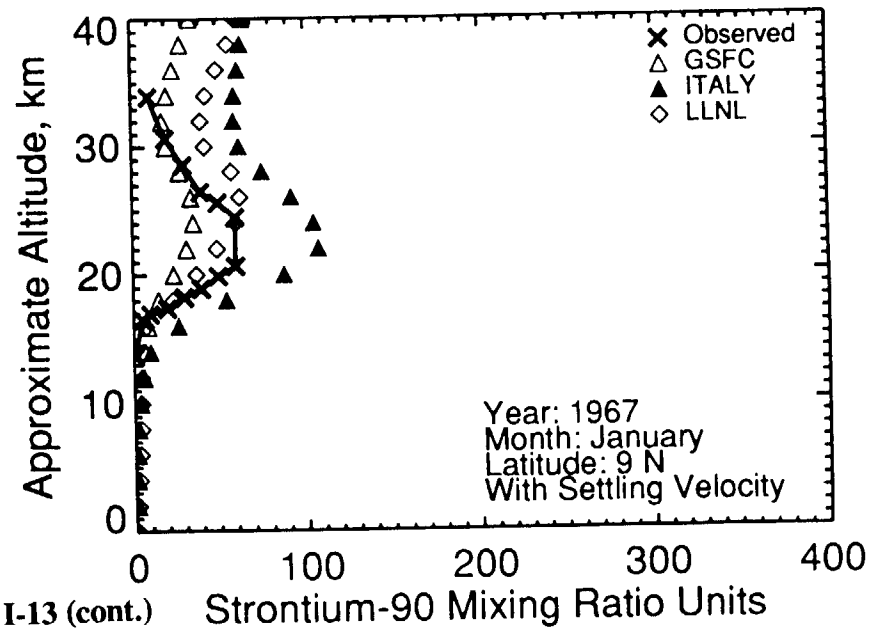

Figure I-13 (cont.)

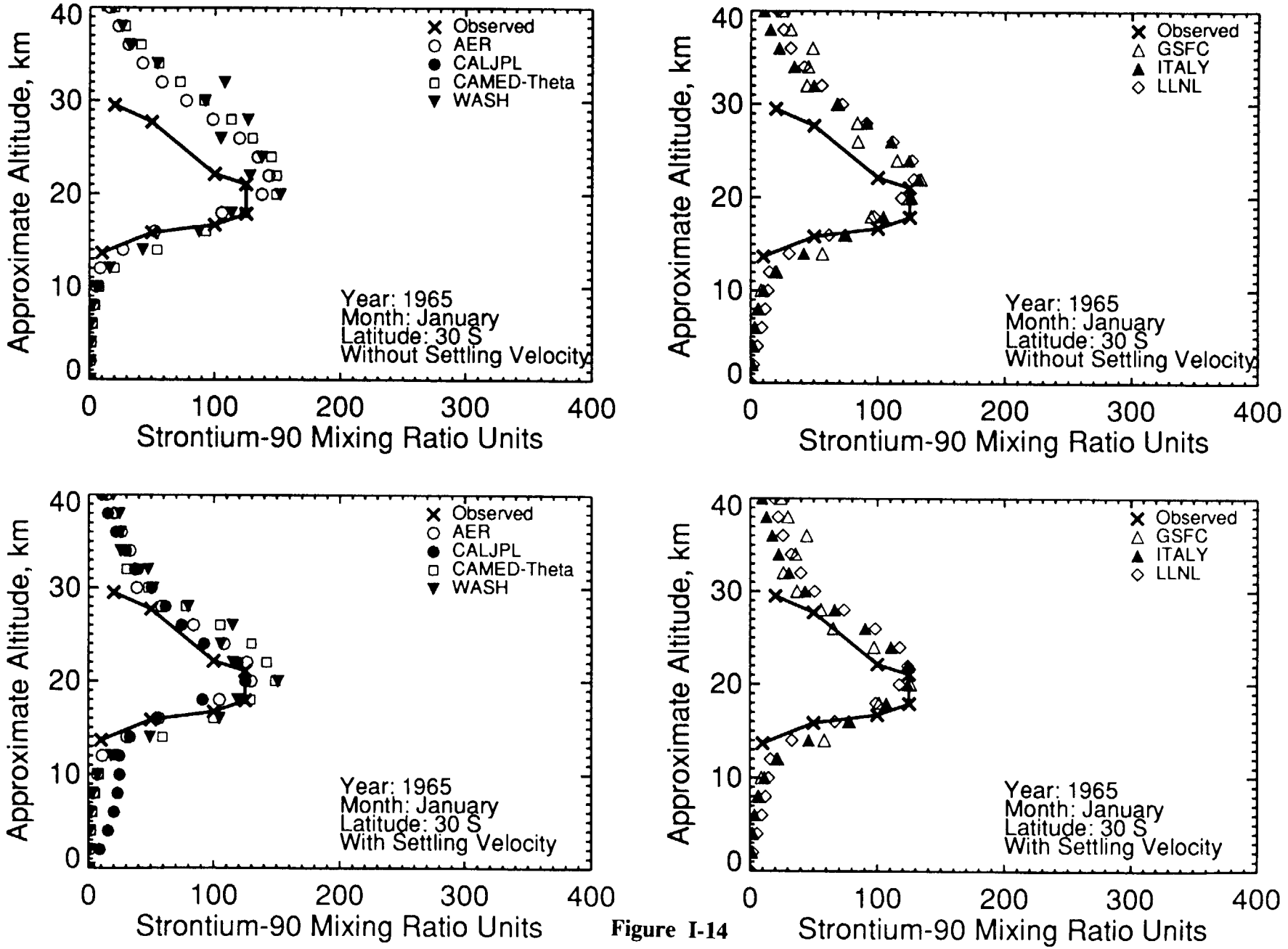
Approximate Altitude, km
Strontium-90 Mixing Ratio Units
Observed
AER
CALJPL
CAMED-Theta
WASH
Year: 1965
Month: January
Latitude: 30 S
Without Settling Velocity
Observed
GSFC
ITALY
LLNL
Year: 1965
Month: January
Latitude: 30 S
Without Settling Velocity
Observed
AER
CALJPL
CAMED-Theta
WASH
Year: 1965
Month: January
Latitude: 30 S
With Settling Velocity
Observed
GSFC
ITALY
LLNL
Year: 1965
Month: January
Latitude: 30 S
With Settling Velocity

Figure I-14

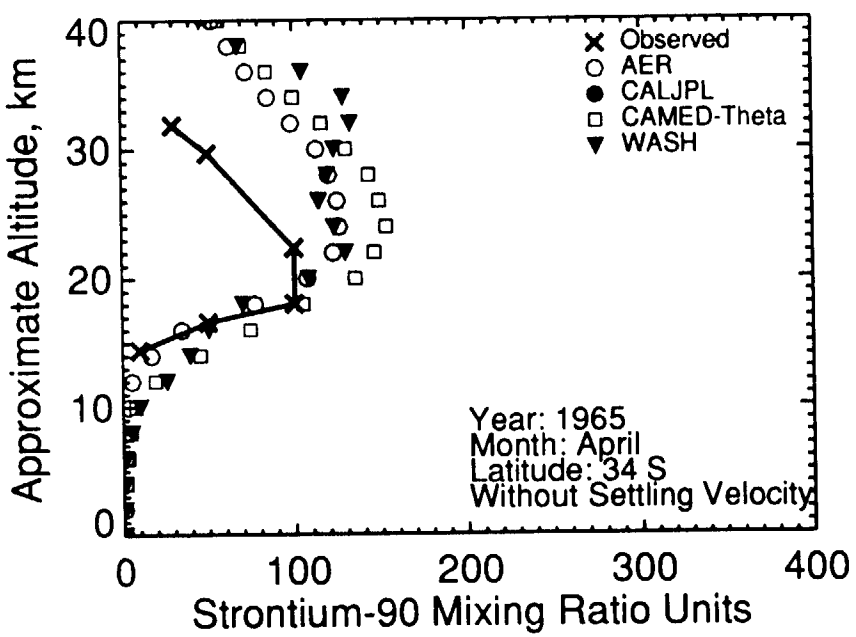

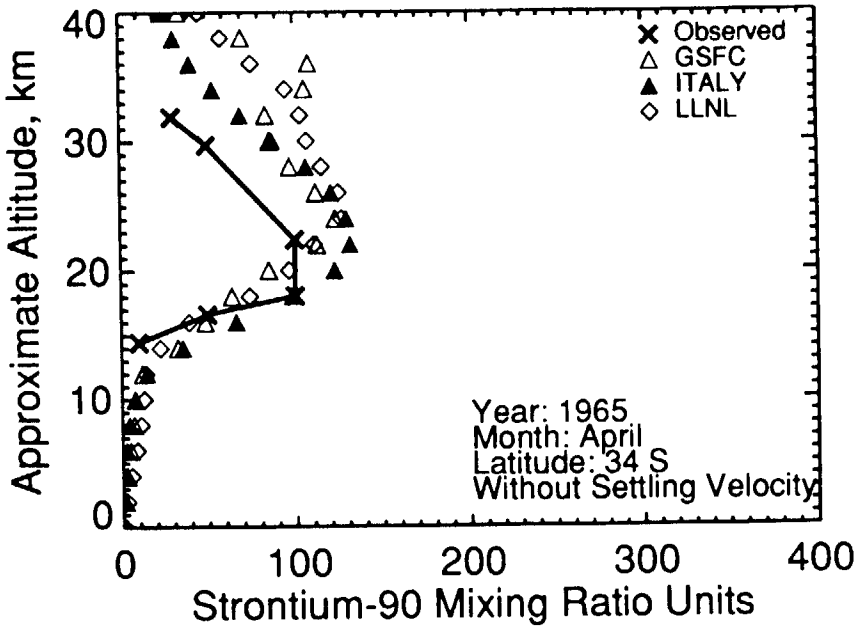

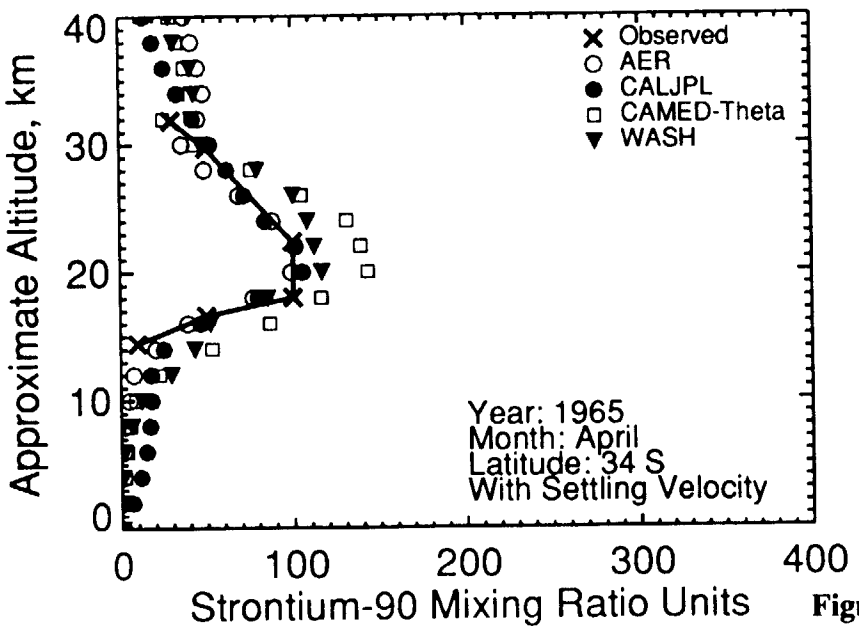

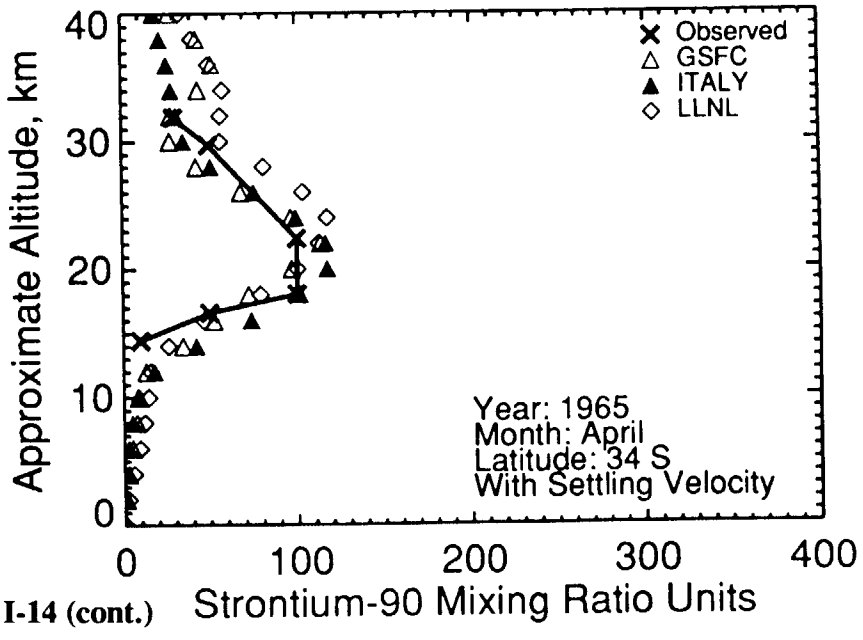

Figure I-14 (cont.)

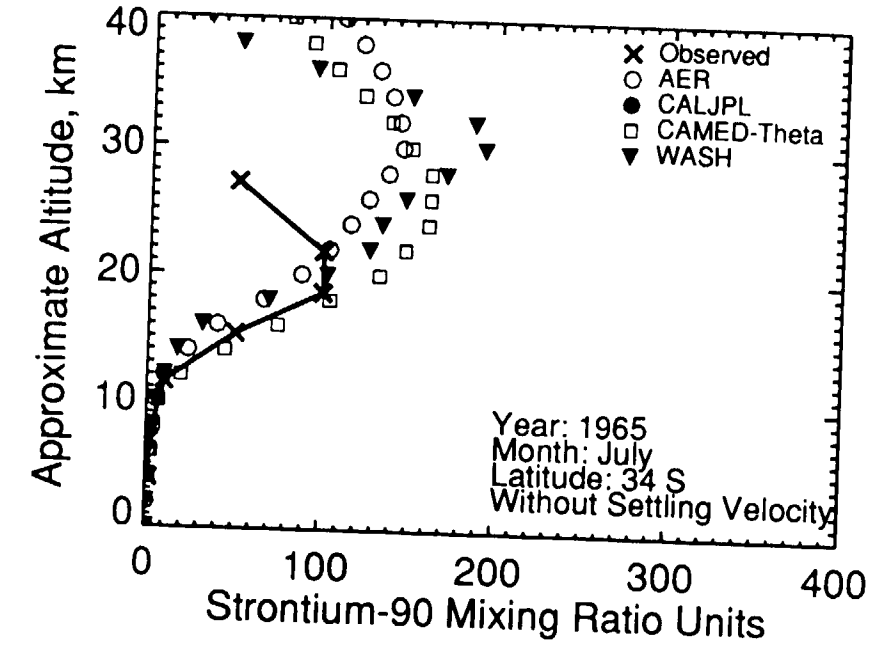

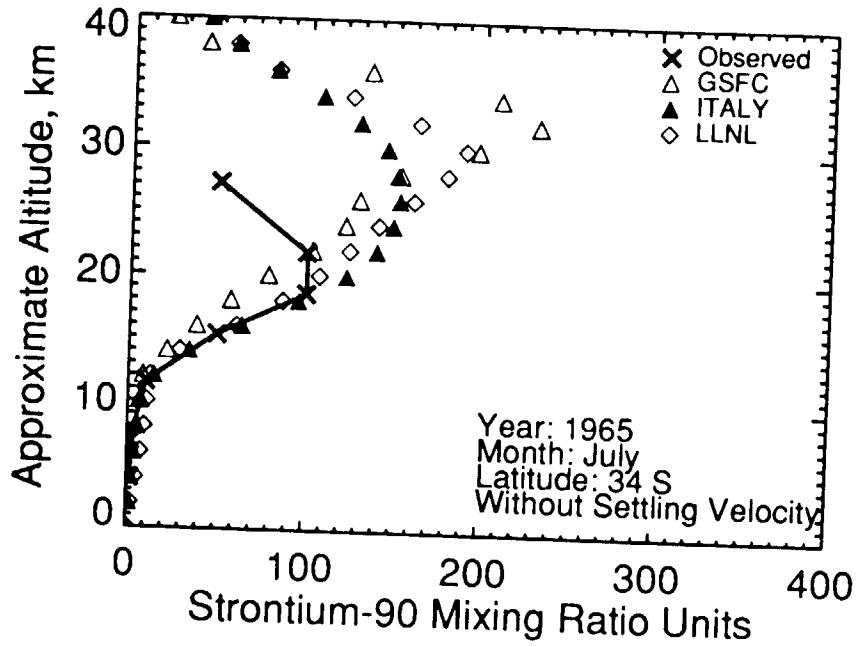

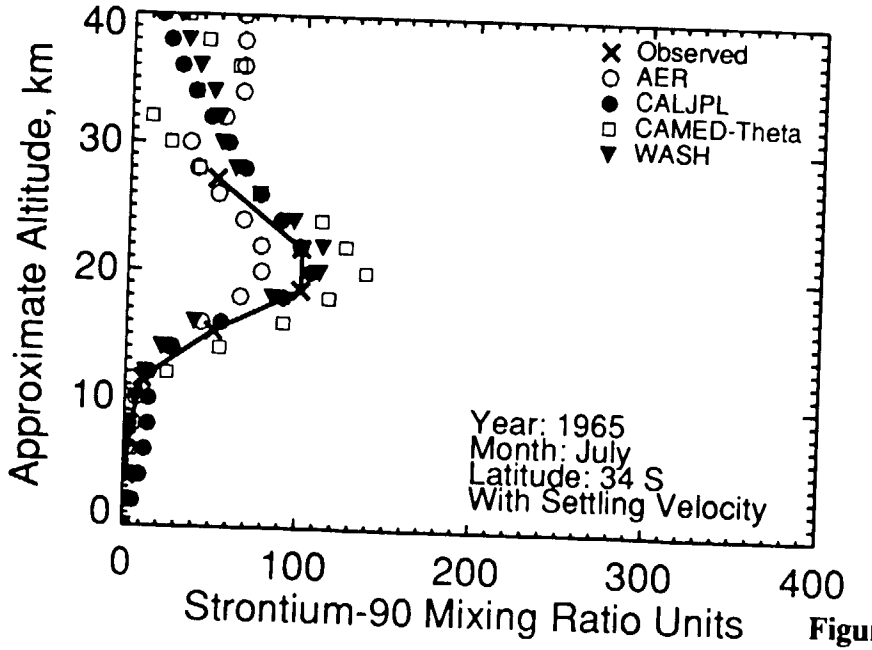

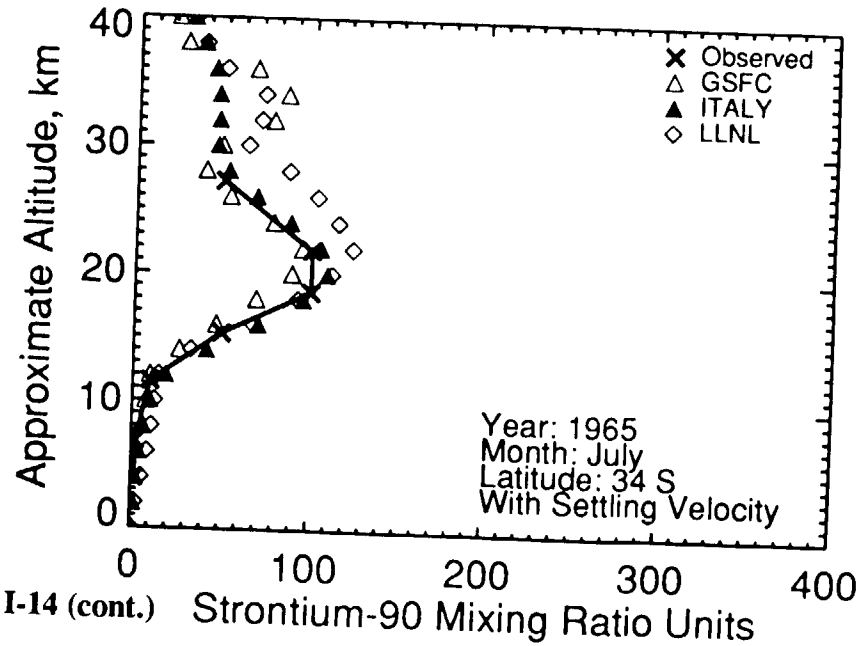

Figure I-14 (cont.)

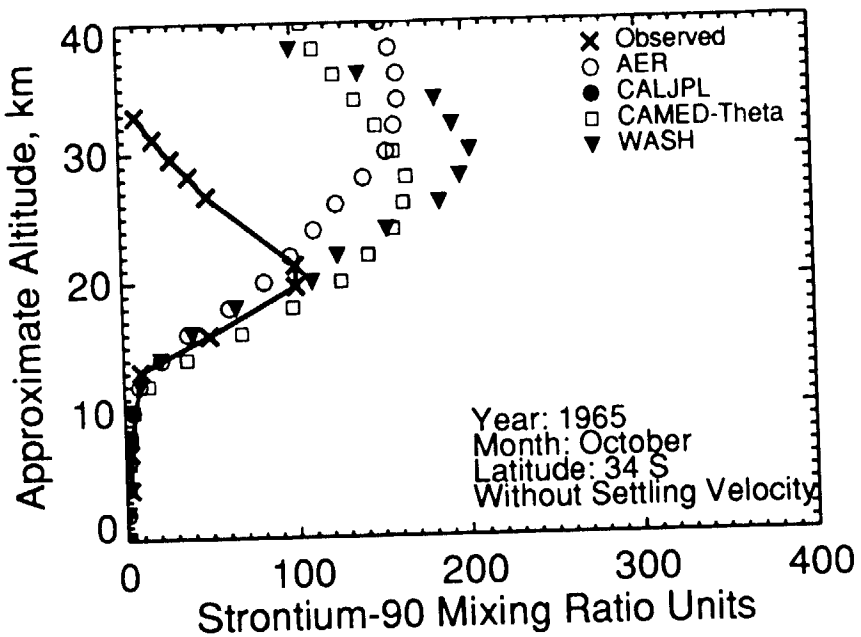

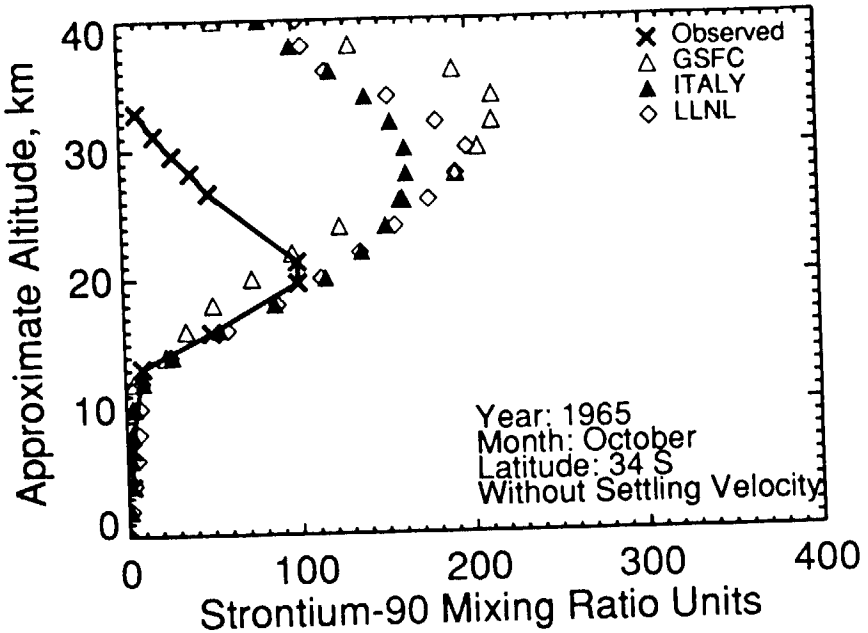

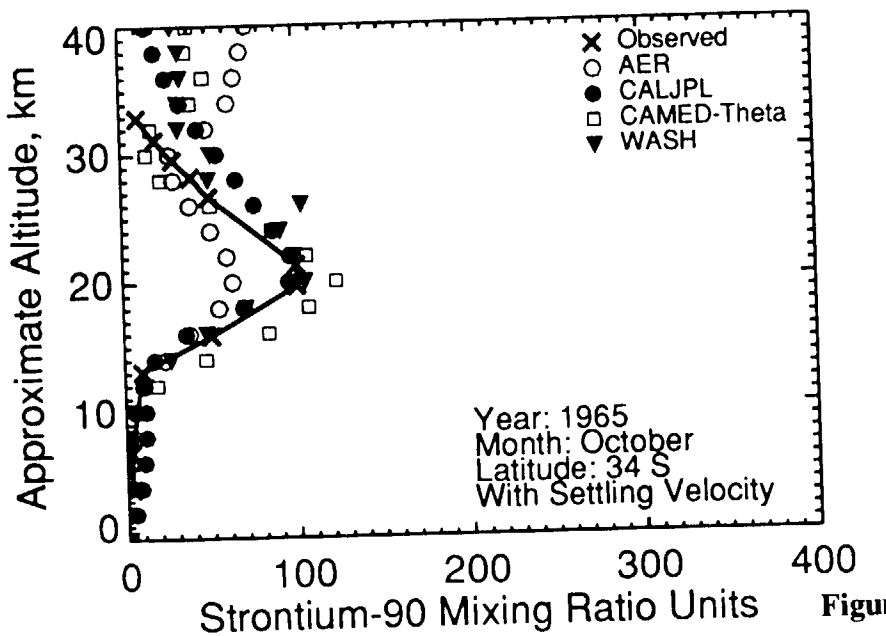

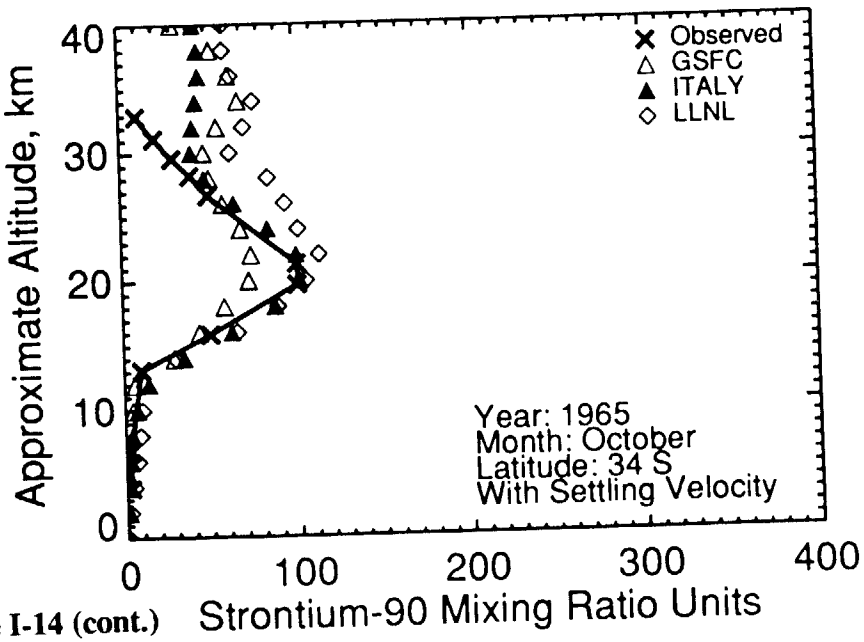

Figure I-14 (cont.)

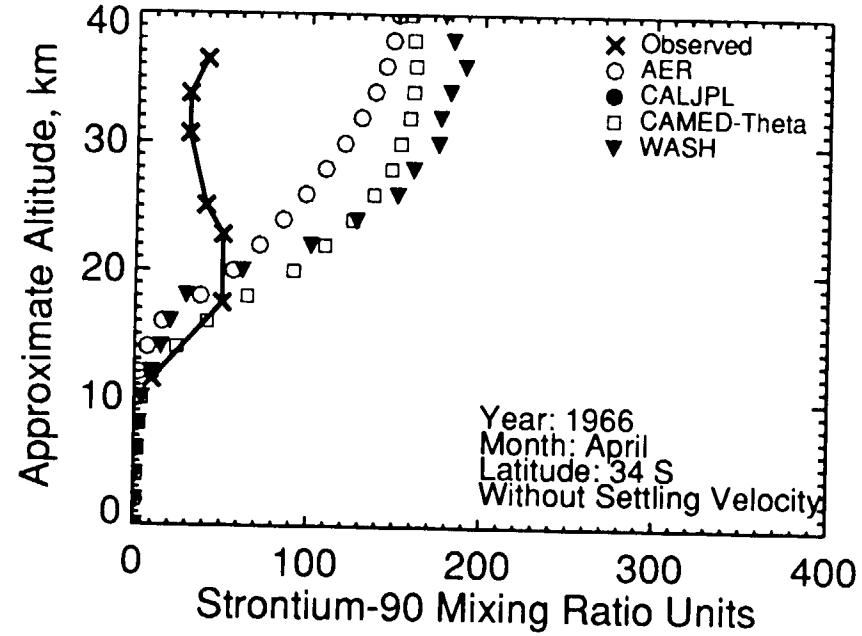

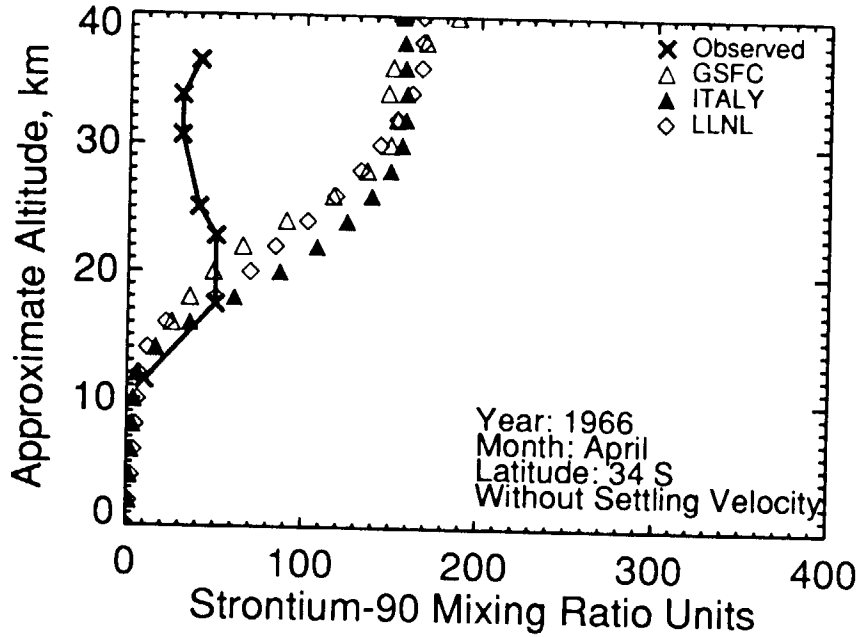

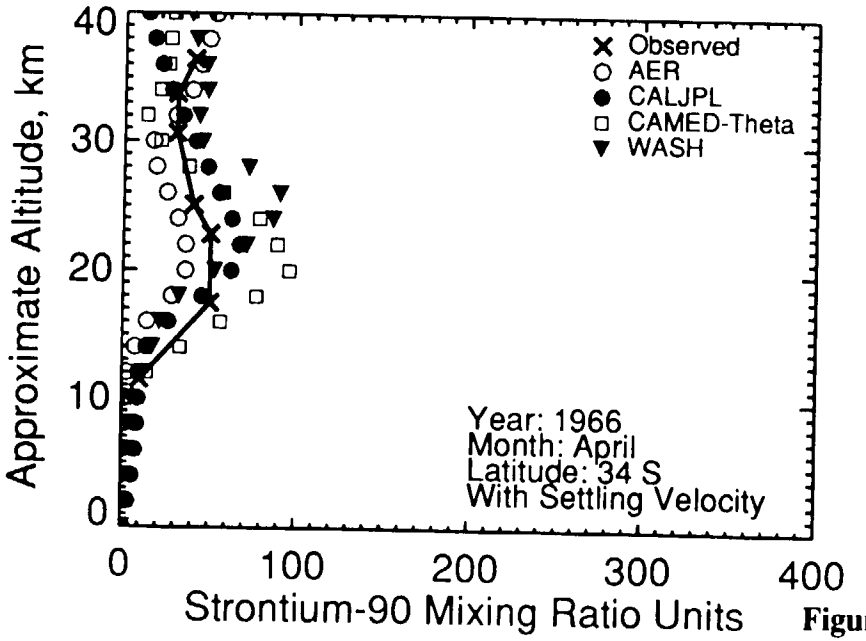

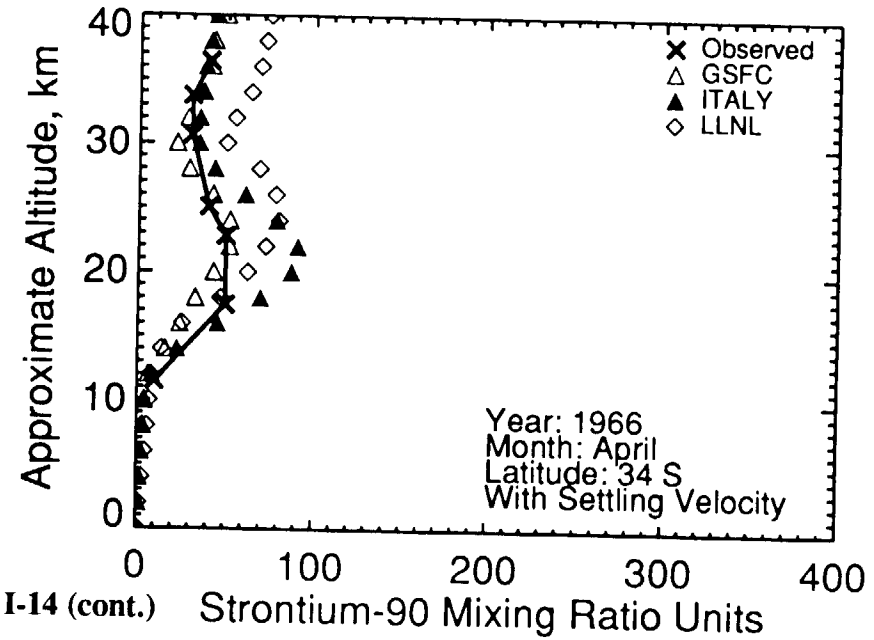

Figure I-14 (cont.)

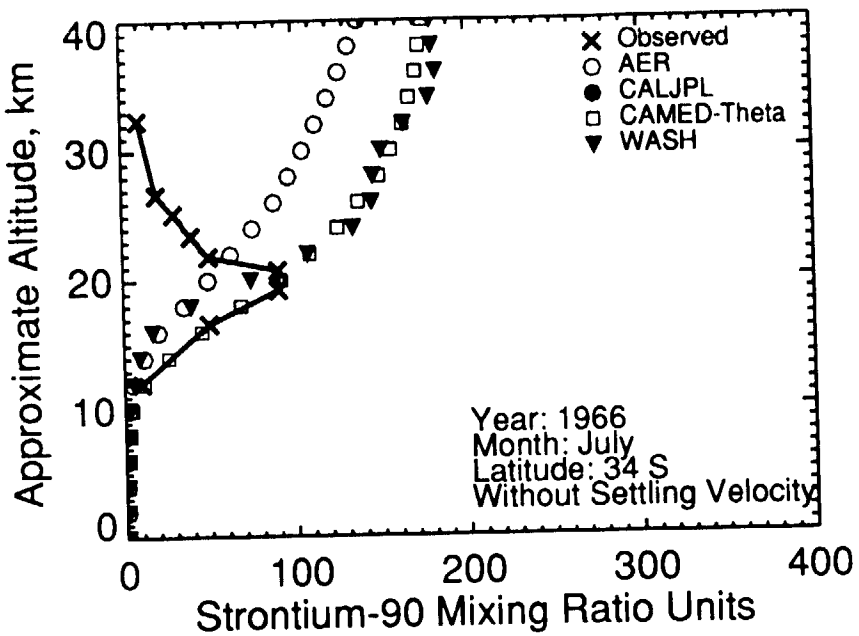

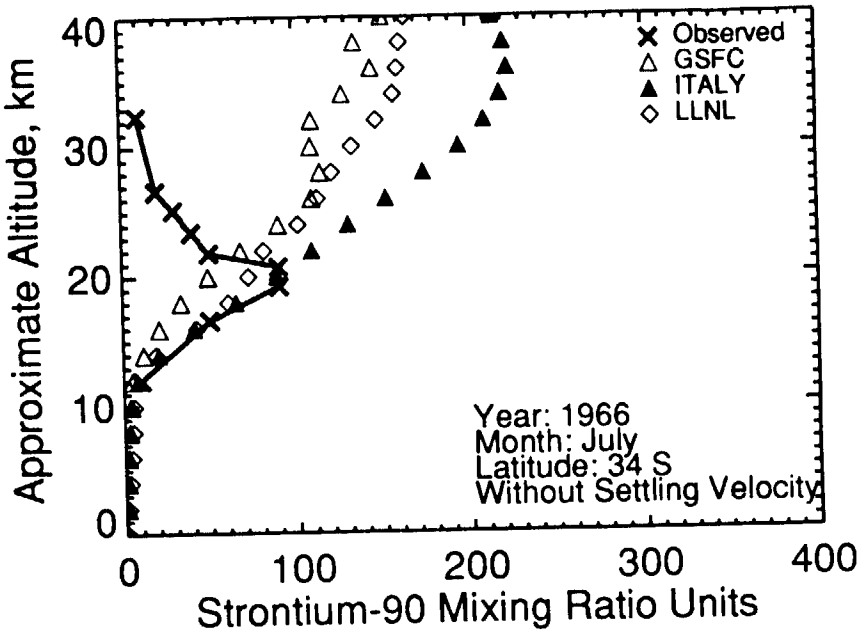

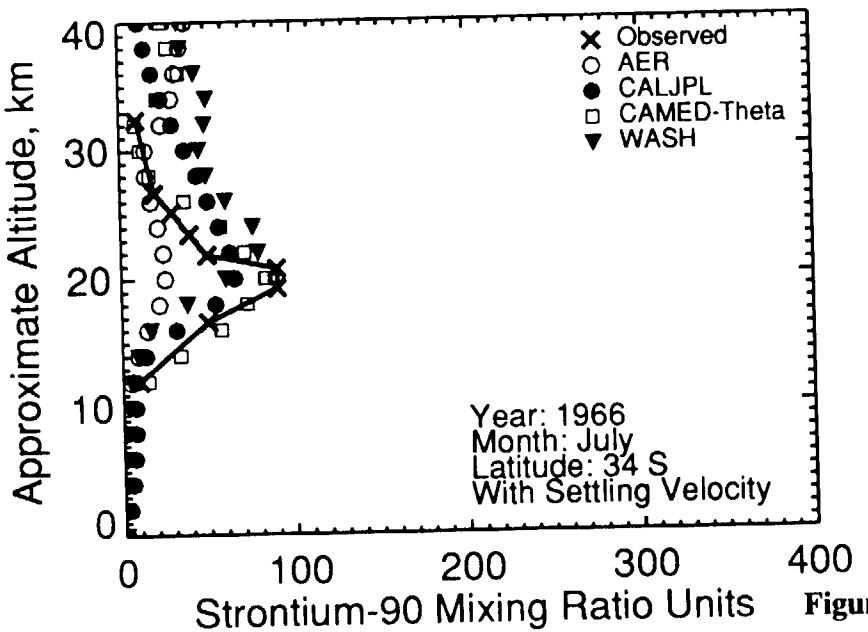

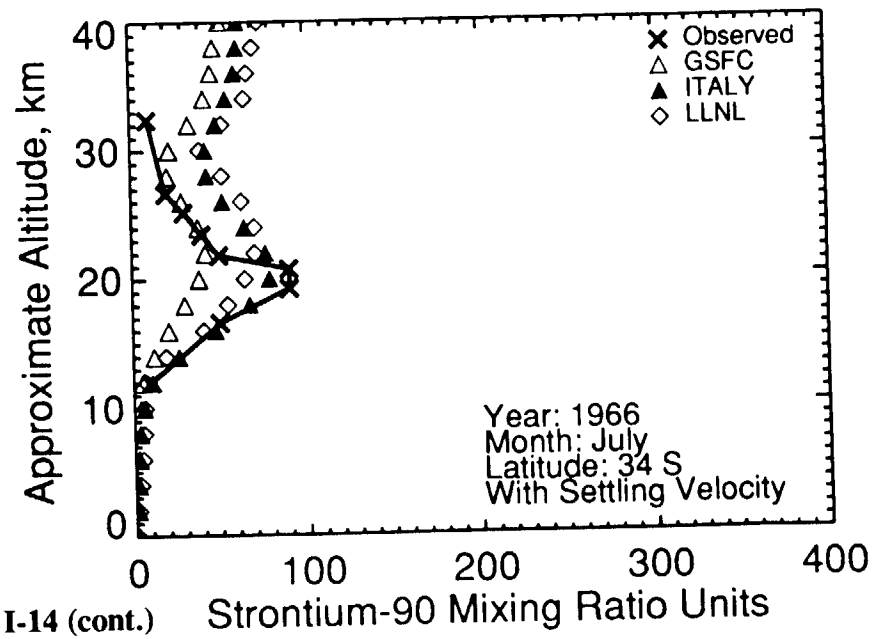

Figure I-14 (cont.)

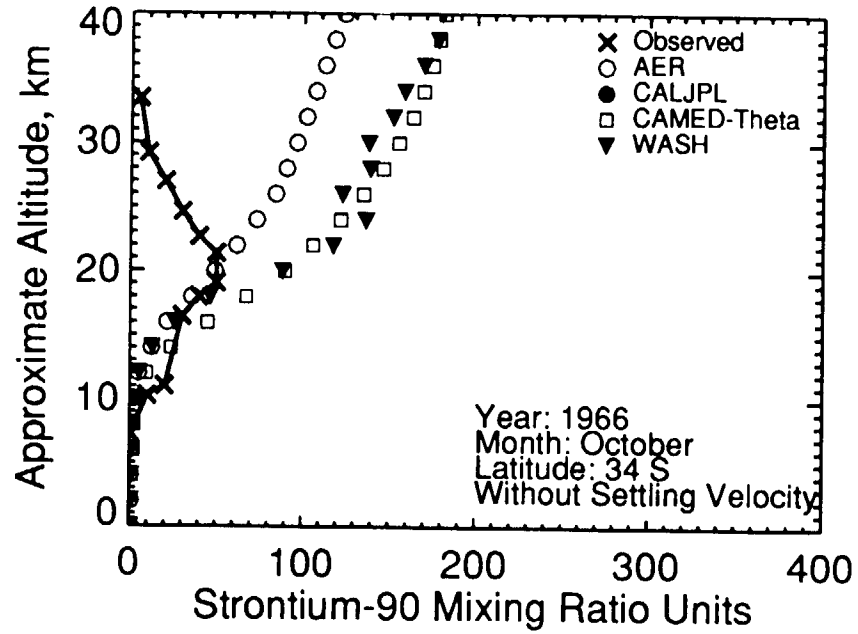

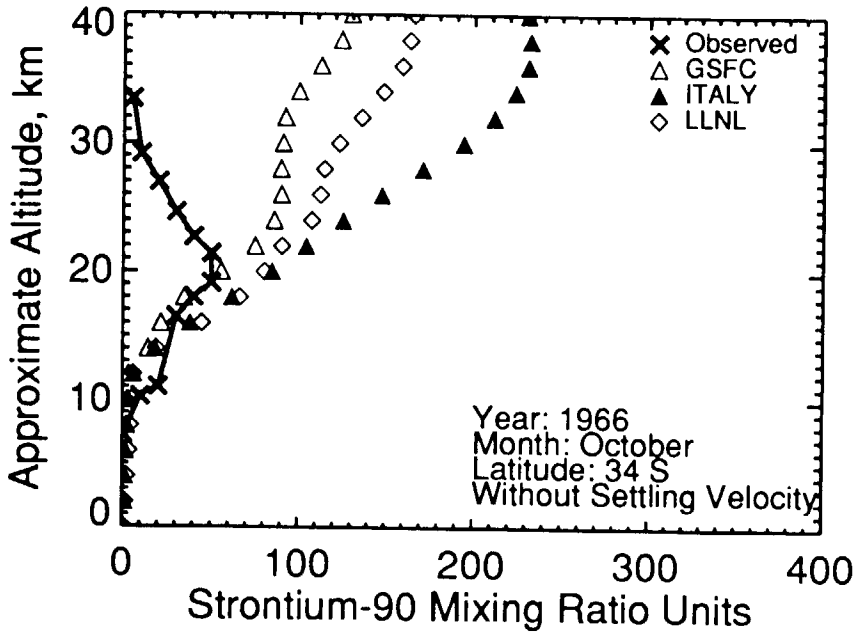

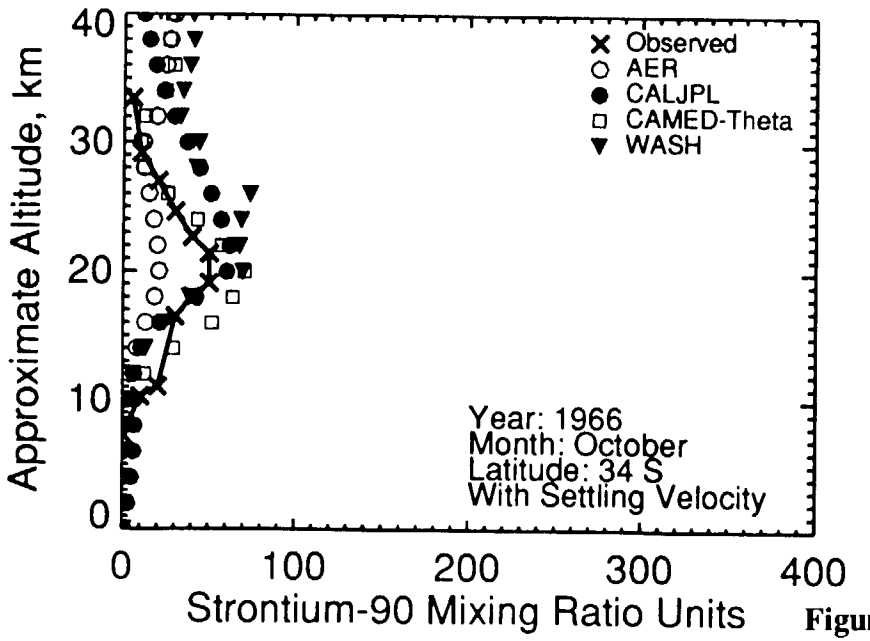

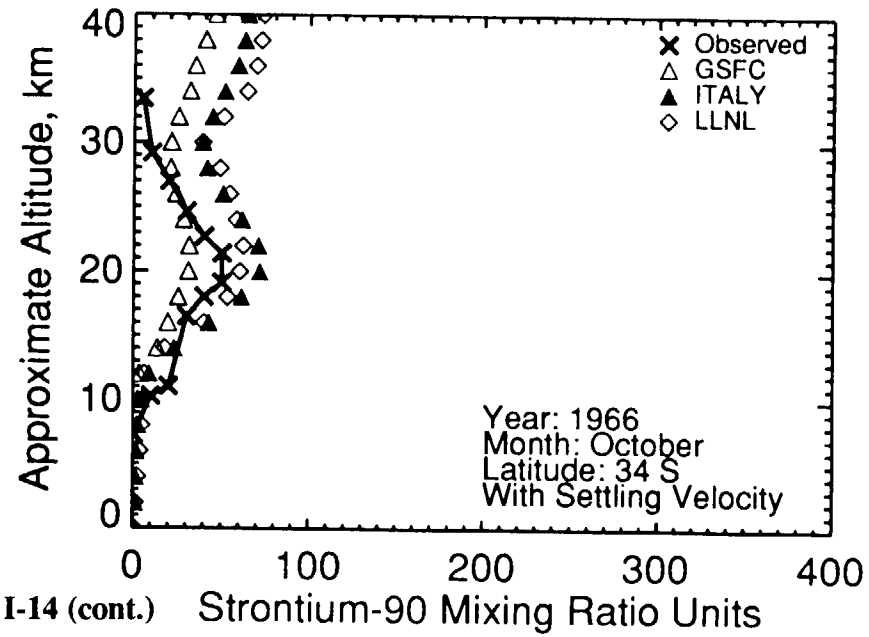

Figure I-14 (cont.)

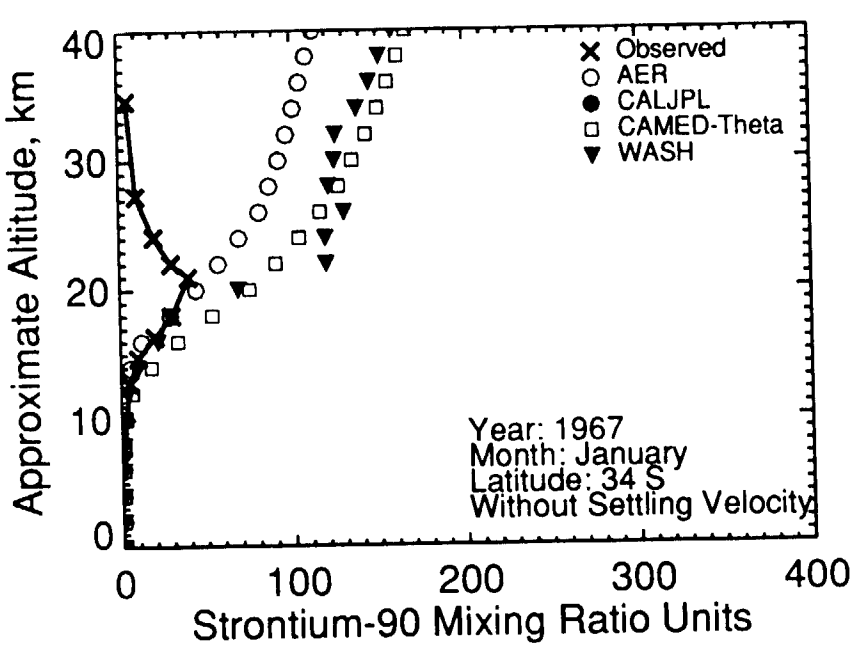

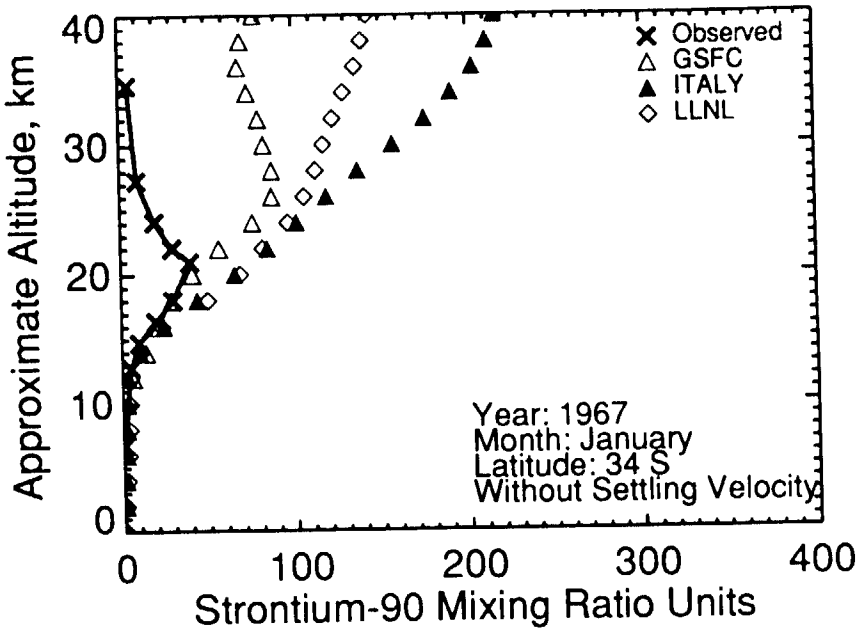

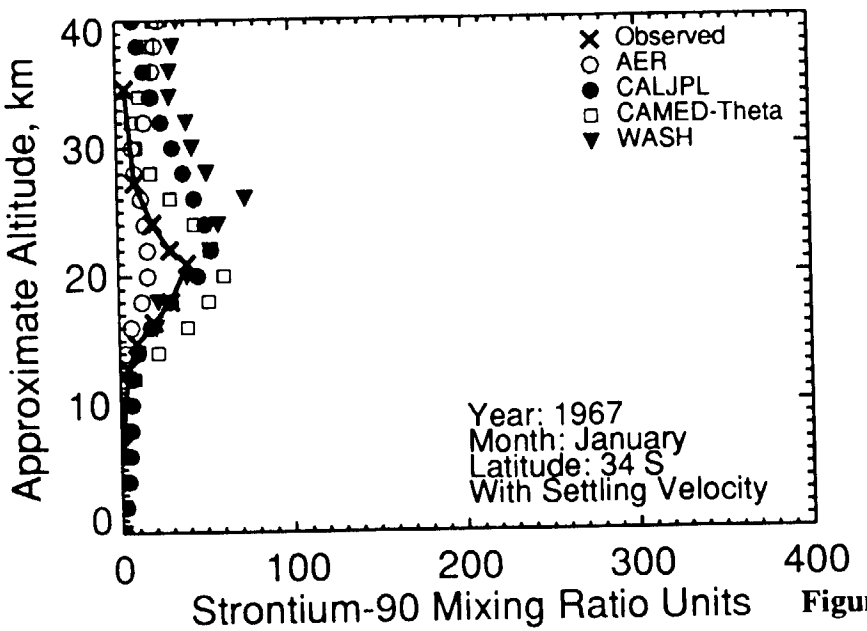

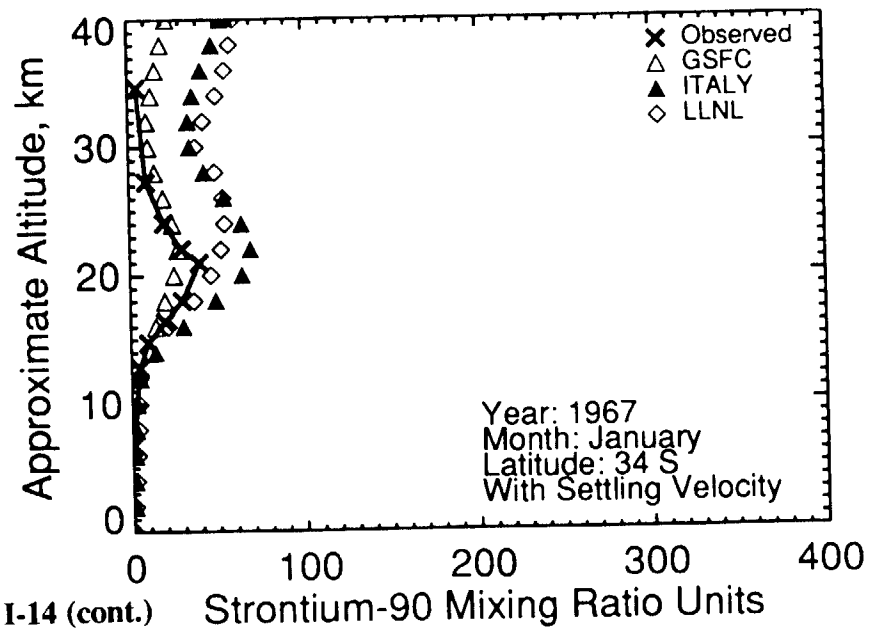

Figure I-14 (cont.)

J: Mt. Ruiz Volcanic Cloud

J: Ruiz Cloud Experiment

G. K. Yue
NASA-Langley Research Center

M. H. Hitchman
Universityof Wisconsin-Madison

G. Pitari
Universita' degli Studi L'Aquila

INTRODUCTION

Stratospheric aerosols from the eruption of a volcano are a unique indicator of stratospheric transport. These particles may evolve from the SO_2 injected by the volcano. They are transported globally, and eventually are removed by both sedimentation and large-scale transport on time scales ranging from a year to a few years, depending on the magnitude and location of the eruption. Like the exotic radionuclides, they provide a direct measure of the global spread of a species injected in the lower stratosphere.

The eruption on 13 November 1985 of the volcano Nevado del Ruiz (5N, 75W) in Columbia was observed by the Stratospheric Aerosol and Gas Experiment II (SAGE II) satellite experiment. This was the strongest volcanic eruption observed by SAGE II before the eruption of Pinatubo on 15 June 1991. The optical depth of aerosol particles associated with Ruiz reached a maximum in February 1986 and about 2 years later decayed into the background levels of aerosols left by El Chichon (Yue et al., 1991). Initial distributions (z^* by latitude) of particle number concentrations for 1 February 1986 were derived from the SAGE II data set by assuming a lognormal size distribution (Yue et al., 1986). In addition, the settling velocities were also derived by the size distributions inferred from the SAGE II data set (Kasten, 1968). Each model used the same initial conditions and settling velocities in their model simulation and the modeling results of aerosol number concentrations measured on the 15th of each month were intercompared. The capability of simulating the transport of a tracer by two-dimensional models was studied by comparing modeling and measurement results. It should be noted that because of the possible presence of clouds around the tropopause and much larger uncertainties of aerosol extinction at shorter wavelengths in the troposphere, the size distributions of aerosol particles in the troposphere and around the tropopause derived from the SAGE II data set are not reliable. The aerosol extinctions at shorter wavelengths at altitudes higher than 30 km also have large uncertainties. In addition, aerosol particles become small enough to act like a gas ($v_{set} = 0$) at altitudes above 30 km. The comparison among modeling results discussed in this paper is limited to altitudes between 10 and 30 km, and the comparison between modeling and experimental results is limited to altitudes between the tropopause and 30 km.

To avoid the complex level of model development required on most two-dimensional models for accurate aerosol microphysical simulations aerosol particles are treated as one constituent with a single size. Such treatment is understandably oversimplified: stratospheric aerosols have a relatively large range of sizes that continually change due to microphysical processes, including coagulation, condensation, evaporation, and sedimentation. However, the change of aerosol size distribution should not be very dramatic since this was a moderate eruption and the simulation was begun a few months after the eruption when most of the excess SO_2 already had been converted to sulfate.

INTER-MODEL AND MODEL-EXPERIMENT COMPARISONS

Figure J-1 shows altitude-latitude contour plots of aerosol number concentration, based on SAGE II observations, used by all models as initial conditions. Model simulation started on 1 February 1986. The initial concentrations of aerosol particles at altitudes below 8 km are all set to 2 per cm^3. The peak of Ruiz aerosols is at 20 km and over the equator. The injection occurred during the easterly phase of the quasi-biennial oscillation (QBO) when lofting and equatorial confinement are expected (Trepte and Hitchman, 1992).

The initial aerosol number concentrations and settling velocities are listed in Tables J-1 and J-2, respectively. The settling velocities were derived from the mass mean radii that conserve the total mass of aerosols in a size distribution.

Seven groups have submitted model results for this experiment. The contour plots of aerosol number concentration for the months of April and August 1986 are shown in Figures J-2 and J-3, respectively. The intervals between contours in these plots are 1. It can be seen that among seven two-dimensional models, AER and CALJPL have the most rapid transport out of the tropics. In April, while most models show a maximum of about 5 at 20 km over the equator, the maximum is only about 3 in the CALJPL and AER models. The maximum value derived from the SAGE II data set is about 8, which is higher than the values obtained by all model simulations. In addition, the location of peak concentration has moved up to 22 km and remains there for the rest of the year. By August, most of the Ruiz debris has been transported to higher latitudes in the AER and CALJPL models. For the other five models, the maximum concentration of Ruiz aerosols is still at about 20 or 22 km, and is less than observed but still in reasonably good agreement with the experimental result. It is of interest to note that the maximum aerosol concentrations for the GSFC and LLNL models are no longer over the equator - they have shifted to higher latitudes in the southern hemisphere.

Profile comparisons over the equator are shown in Figures J-4a, b, c, and d, for the months of March, June, September, and December 1986, respectively. For the month of March 1986, the differences of aerosol concentrations among models and experimental results are very small for altitudes above 25 km. The small coefficients k_{zz} above 25 km used in the models are in good agreement with the weak lofting observed by the experiment. However, in regions around the maximum concentration there are large differences between model and observational results. Among model results, the CALJPL and AER have the lowest peak concentration values as shown in the contour plots. The CALJPL model normally runs with the dynamics specified as a streamfunction. These runs were made in a nonstandard mode with dynamics specified as velocity fields, and the results may contain a small error. Three months later better agreement is seen between SAGE values and the model results of CAMED, GSFC, ITALY, LLNL, and WASH, even though below 19 km the CAMED results are higher than observed and the WASH results are lower. Since in the previous months the peaks of profiles of AER and CALJPL are lower than the peaks of profiles of other model results, it is not surprising that they remain lower for subsequent months. By September WASH results are in good agreement with the observations, but the CAMED results below 19 km are much higher. By December 1986 the broadening of the peak is shown in all results. The comparison is excellent insofar as the settling velocity is needed to explain the first-order effects on the aerosol. After June the GSFC, ITALY, LLNL, and WASH models do reasonably well, indicating possibly a good averaged circulation. The CAMED model looks good but is centered too low; perhaps there is a problem with the effective tropopause. The AER and CALJPL models diverge significantly over the long term. All of the models have difficulty preserving the peak concentrations; they seem to wash out the detailed structure.

Profile comparisons at 35S and 35N for June 1986 are shown in Figures J-4e and J-4f, respectively. Although there are discrepancies about the location and value of the peak among different model profiles, they all demonstrate the influence of Ruiz aerosols on the number concentrations at altitudes below 22 km. It is of interest to note that the influence of Ruiz aerosols does not appear in SAGE II profiles above 20 km at 35N, since the main Ruiz layer was confined in tropical regions between 30S and 30N.

The temporal variations of aerosol number concentration at different locations are shown in Figures J-5a, b, c, and d. Figure J-5a shows that near the injection point, in the first few months of simulation, the decay rates of all models are faster than the measurement results. However, after July the decay rates are all in rather good agreement. The differences in concentrations for different models in the later months of the year are mainly due to the differences resulting from transport in the early months of the simulation. It is of interest to note that already by mid-February, the concentration of aerosol particles in the CALJPL model is much lower than that in other models. This may be a result of stronger diffusivity used in the model. However, it is more likely a basic problem with the initialization to the grid points of each model. In general, there are large differences in decay rates among model and observational results in the first few months of simulation. However, the decay rates after July 1986 at different altitudes at the equator shown by different models and the SAGE II data set are in reasonably good agreement. At low latitudes, the agreement between experimental and modeling results is still quite good; however, transport to higher latitudes in the models is much faster than observed (Figure J-5d).

A quantitative assessment of the transport in each model can be conducted by examining the model-derived maximum concentrations at several latitudes in the tropical region listed in Table J-3. The AER and CALJPL models have more rapid mixing out of the tropics. By May 1986, AER results show that the peak concentration of Ruiz aerosols has disappeared from the equator and has been transported to higher latitudes in both hemispheres. The same is true for the CALJPL model in June1986. In both models the peak number concentrations have been reduced to about 2 by June. On the other hand CAMED, ITALY, and WASH have weak transport in comparison with other models. They preserved the peak aerosol concentration in the tropical region almost until the end of the year. The transport in the GSFC and LLNL models is in-between, since by June the aerosol concentrations over the equator were relatively high, but the peak gradually shifted to higher latitudes in the southern hemisphere in subsequent months.

In Table J-4, the SAGE II and model-derived aerosol concentrations at 0 degree are shown for altitudes from 16 to 24 km. Since aerosol particles over the equator are rapidly transported to higher latitudes in the AER and CALJPL models, the effect of upwelling on aerosol particles is weak. On the other hand the effects of upwelling can be seen in GSFC and ITALY models, since the peaks of aerosol concentration have been gradually shifted to 22 km. For the WASH model, the concentrations in the altitude range 22 and 24 km are high in comparison with the very low concentrations below 20 km. Additionally, the peak of aerosol concentration has shifted to 24 km by the end of 1986. It is of interest to see that the CAMED model not only has weak transport but also weak upwelling. By the later months of the year, relatively high concentrations of aerosol particles have remained at all altitudes below 22 km in the CAMED results, while all other models show very low concentrations due to either rapid advection or diffusion.

It should be noted that all model results have been obtained with parameterized washout included. We have tried to compare model results with relatively large initial concentrations of aerosol particles in the troposphere and no washout processes. It has been found that some of the aerosol number concentrations in the lower stratosphere are unrealistically high. Clearly we need more accurate microphysical models for removal of aerosols near the tropopause if we are to include tropospheric aerosols in these simulations.

CONCLUSIONS

Comparison between models and observations has shown that all models do poorly in the first few months of simulation when there are large aerosol gradients. When gradients have become smoother a few months later, the models perform better. Intercomparison of the models shows that the AER and CALJPL models have the strongest transport out of the tropics, losing the peak concentrations in just a few months. The peaks of aerosol concentrations remained over the equator in the CAMED, ITALY, and WASH models, whereas the GSFC and LLNL models have stronger transport in the southern hemisphere that developed high-latitude maximum concentration through transport. The GSFC, ITALY, and WASH models seem to have strong upwelling, whereas the CAMED model has less upwelling. Alternatively, there may be problems with the interpolation of the initial conditions in some of the models.

A given eruption occurs during a specific phase of the QBO. During easterly shear, aerosols will be lofted and confined in the tropics, whereas during westerly shear, aerosols may spread out more easily, being more rapidly transported poleward and downward a few kilometers above the tropopause. SAGE II results show that Ruiz aerosols are confined in the tropics, but this behavior is not being taken into account in current models. The comparison between models and the observed evolution of volcanic debris suggests that the influence of the QBO on the mean tropical circulation may need to be included in future model development. This circulation may be specified readily from previous theoretical and modeling studies of the QBO.

The good agreement of decay rates obtained by modeling and measurement results in the later months of simulation suggests that modeling can be a useful tool to estimate the global decay of volcanic debris or engine exhaust from supersonic aircraft in the stratosphere. On the other hand, the accuracy of simulating the advective and diffusive processes in the models can be improved by comparing modeling and experimental results when the opportunity occurs. Better agreement is expected if we can have a better dynamical model for the exchange and transport near the tropopause, if it can be modified to have better vertical and latitudinal resolutions, and if it can include some microphysical processes that are taking place in the volcanic aerosols.

REFERENCES

Kasten, F., Falling speed of aerosol particles, *J. Appl. Meteorol, 7*, 944-947, 1968.

Trepte, C. R. and M. H. Hitchman, Tropical stratospheric circulation deduced from satellite aerosol data, *Nature, 355*, 626-628, 1992.

Yue, G. K., M. P. McCormick, and E. W. Chiou, Stratospheric aerosol optical depth observed by the Stratospheric Aerosol and Gas Experiment II: decay of the El Chichon and Ruiz volcanic perturbations, *J. Geophys. Res., 96*, 5209-5219, 1991.

Yue, G. K., M. P. McCormick, and W. P. Chu, Retrieval of composition and size distribution of stratospheric aerosols with the SAGE II satellite experiment, *J. Atmos. Oceanic Technol., 3*, 371-380, 1986.

Table J-1: Initial Concentrations (number/cm^3) at Seven Latitudes

Z* (km)	30°S	20°S	10°S	0°	10°N	20°N	30°N
28	1.5	1.3	0.9	1.1	0.8	0.9	1.2
26	1.4	1.4	1.2	2.5	1.1	0.9	1.0
24	1.0	1.3	1.5	4.2	2.4	1.1	1.2
22	1.5	2.2	4.1	8.6	4.1	1.5	1.6
20	2.6	4.6	7.1	10.8	6.8	4.1	2.4
18	4.7	4.9	6.3	5.9	7.4	9.1	4.9
16	5.1	4.6	3.8	3.3	3.0	6.3	6.2
14	3.2	3.0	4.3	4.0	4.0	2.6	4.3

Table J-2: Initial setting velocities (cm/sec) at Seven Latitudes

Z* (km)	30°S	20°S	10°S	0°	10°N	20°N	30°N
28	2.2e-2	2.5e-2	3.4e-2	3.6e-2	3.4e-2	2.7e-2	2.3e-2
26	1.9e-2	2.1e-2	2.7e-2	2.8e-2	2.7e-2	2.2e-2	2.1e-2
24	1.8e-2	1.8e-2	2.1e-2	2.1e-2	2.1e-2	1.8e-2	1.7e-2
22	1.5e-2	1.5e-2	1.6e-2	1.6e-2	1.6e-2	1.5e-2	1.4e-2
20	1.1e-2	1.0e-2	1.2e-2	1.2e-2	1.1e-2	1.1e-2	1.1e-2
18	7.2e-3	7.3e-3	7.3e-3	8.3e-3	7.4e-3	6.1e-3	8.0e-3
16	5.0e-3	5.2e-3	5.4e-3	6.6e-3	5.8e-3	4.6e-3	5.7e-3
14	4.5e-3	4.3e-3	4.2e-3	5.4e-3	4.6e-3	4.5e-3	5.0e-3

Table J-3: Model-Derived Maximum Concentrations (number / cm^3) at Seven Latitudes

AER							
Month	30°S	20°S	10°S	0°	10°N	20°N	30°N
February	3.1	3.7	5.4	6.9	5.8	4.0	4.2
March	2.4	3.1	3.9	4.5	4.5	3.9	3.7
April	2.3	2.5	2.8	3.1	3.3	3.5	3.6
May	2.3	2.2	2.3	2.4	2.6	3.0	3.2
June	2.2	2.1	2.0	2.0	2.1	2.5	2.9
July	2.2	2.0	1.8	1.8	1.8	2.1	2.5
August	2.1	1.9	1.6	1.6	1.6	1.9	2.3
September	1.9	1.7	1.4	1.4	1.4	1.7	2.1
October	1.8	1.6	1.2	1.2	1.3	1.6	2.0
November	1.6	1.3	1.0	1.0	1.2	1.6	1.8
December	1.5	1.1	0.9	0.9	1.1	1.5	1.7

CALJPL							
Month	30°S	20°S	10°S	0°	10°N	20°N	30°N
February	3.2	3.7	4.1	4.4	4.2	4.1	3.4
March	2.8	3.0	3.6	3.7	3.5	3.0	3.0
April	2.5	2.6	3.1	3.2	3.0	2.6	2.7
May	2.4	2.4	2.6	2.6	2.5	2.3	2.4
June	2.2	2.1	2.2	2.2	2.1	2.0	2.1
July	2.1	1.9	1.9	1.9	1.8	1.8	1.8
August	1.9	1.7	1.7	1.7	1.6	1.6	1.7
September	1.7	1.6	1.6	1.5	1.5	1.5	1.5
October	1.5	1.4	1.4	1.4	1.2	1.4	1.5
November	1.4	1.3	1.3	1.2	1.2	1.3	1.4
December	1.2	1.2	1.1	1.1	1.1	1.2	1.3

Table J-3 (cont.)

CAMED							
Month	30°S	20°S	10°S	0°	10°N	20°N	30°N
February	4.3	4.3	5.6	7.9	7.0	5.3	5.0
March	3.9	4.2	5.4	6.6	6.1	5.0	4.7
April	3.7	4.1	5.1	5.7	5.5	4.7	4.4
May	3.6	4.0	4.8	5.2	5.0	4.4	4.1
June	3.7	3.9	4.5	4.7	4.6	4.1	3.9
July	3.7	3.9	4.2	4.4	4.3	3.9	3.7
August	3.6	3.8	4.0	4.1	4.0	3.7	3.6
September	3.5	3.6	3.6	3.8	3.8	3.6	3.5
October	3.3	3.4	3.5	3.6	3.6	3.5	3.5
November	3.1	3.2	3.3	3.4	3.4	3.3	3.5
December	2.9	3.0	3.1	3.2	3.3	3.3	3.5

GSFC							
Month	30°S	20°S	10°S	0°	10°N	20°N	30°N
February	4.1	4.6	6.7	8.7	6.6	5.5	4.6
March	3.6	4.1	5.7	6.5	5.1	4.3	4.0
April	3.3	3.9	5.0	5.2	4.3	3.6	3.6
May	3.1	3.7	4.3	4.3	3.7	3.3	3.3
June	3.1	3.4	3.8	3.8	3.3	3.0	2.4
July	3.0	3.2	3.5	3.4	2.9	2.6	2.7
August	3.0	3.1	3.2	3.0	2.6	2.3	2.4
September	2.8	2.8	2.9	2.6	2.3	2.1	2.2
October	2.5	2.5	2.6	2.4	2.1	2.0	2.1
November	2.3	2.3	2.3	2.1	1.9	1.9	2.0
December	2.0	2.1	2.0	1.9	1.8	1.9	1.9

Table J-3 (cont.)

ITALY							
Month	30°S	20°S	10°S	0°	10°N	20°N	30°N
February	4.1	4.2	5.3	6.8	6.4	5.2	4.8
March	2.9	3.4	4.7	5.7	5.4	4.1	3.4
April	2.6	3.3	4.4	5.0	4.7	3.7	3.0
May	2.6	3.3	4.2	4.6	4.3	3.4	2.8
June	2.7	3.3	4.0	4.3	4.0	3.2	2.7
July	2.8	3.3	3.9	4.1	3.8	3.0	2.6
August	2.7	3.2	3.7	4.0	3.6	2.9	2.5
September	2.6	3.1	3.6	3.8	3.5	2.9	2.5
October	2.5	2.9	3.4	3.6	3.4	2.9	2.6
November	2.3	2.7	3.0	3.3	3.2	2.9	2.7
December	2.2	2.5	2.9	3.1	3.0	2.8	2.7

LLNL							
Month	30°S	20°S	10°S	0°	10°N	20°N	30°N
March	4.1	4.2	5.0	6.0	5.7	4.6	4.8
April	3.5	3.9	4.6	5.0	4.7	4.0	4.1
May	3.4	3.8	4.3	4.3	4.0	3.5	3.4
June	3.5	3.8	4.0	3.8	3.5	3.1	2.9
July	3.5	3.7	3.6	3.5	3.1	2.8	2.6
August	3.5	3.5	3.5	3.3	3.6	2.5	2.4
September	3.4	3.3	3.2	3.0	2.7	2.4	2.3
October	3.1	3.0	2.9	2.7	2.5	2.4	2.3
November	2.7	2.6	2.5	2.4	2.3	2.3	2.3
December	2.3	2.2	2.2	2.2	2.2	2.2	2.3

Table J-3 (cont.)

WASH							
Month	30°S	20°S	10°S	0°	10°N	20°N	30°N
February	4.2	4.0	4.6	7.2	5.8	4.6	4.8
March	3.8	3.6	4.7	6.3	4.6	3.4	4.4
April	3.4	3.3	4.6	5.6	4.7	3.0	3.5
May	3.2	3.0	4.4	5.0	4.0	2.8	2.9
June	3.2	3.1	4.2	4.3	3.5	2.8	2.7
July	3.3	3.1	3.9	4.0	3.4	3.0	2.9
August	3.2	3.1	3.7	3.8	3.4	3.0	3.0
September	3.1	2.9	3.5	3.6	3.2	2.9	2.9
October	2.7	2.8	3.3	3.3	3.1	2.8	2.7
November	2.4	2.6	2.9	3.0	2.9	2.6	2.6
December	2.1	2.1	2.5	2.6	2.8	2.5	2.1

Table J-4: SAGE II and Model-Derived Concentrations (number/cm^3) at 0°

SAGE II					
Month	16 km	18 km	20 km	22 km	24 km
March	2.8	5.7	7.9	9.4	4.6
April	2.4	4.6	6.5	7.9	4.1
May	2.3	3.5	5.4	6.4	3.5
June	2.2	2.3	4.2	4.8	3.3
July	2.0	2.1	3.8	4.5	3.2
August	2.0	2.0	3.7	4.4	3.1
September	1.9	1.7	3.0	3.7	3.0
October	1.9	1.8	2.7	3.0	2.0
November	1.8	1.8	2.5	2.5	2.0
December	1.7	1.9	2.3	2.3	2.1

AER					
Month	16 km	18 km	20 km	22 km	24 km
February	3.0	5.9	6.9	5.7	4.0
March	1.9	3.7	4.5	4.0	3.0
April	1.3	2.4	3.1	3.0	2.4
May	0.9	1.8	2.3	2.4	2.0
June	0.7	1.5	1.9	2.0	1.7
July	0.6	1.3	1.7	1.8	1.5
August	0.5	1.1	1.4	1.6	1.3
September	0.4	0.9	1.2	1.4	1.1
October	0.4	0.8	1.1	1.2	1.0
November	0.3	0.7	1.0	1.0	0.8
December	0.3	0.7	0.9	0.9	0.7

Table J-4 (cont.)

CALJPL					
Month	16 km	18 km	20 km	22 km	24 km
February	1.6	2.8	4.4	4.4	3.3
March	1.1	1.9	3.4	3.7	2.9
April	0.7	1.3	2.7	3.2	2.5
May	0.5	1.0	2.2	2.6	2.2
June	0.4	0.9	1.9	2.2	1.9
July	0.3	0.8	1.7	1.9	1.7
August	0.3	0.7	1.5	1.7	1.5
September	0.2	0.6	1.3	1.5	1.3
October	0.2	0.6	1.2	1.4	1.2
November	0.2	0.5	1.1	1.2	1.1
December	0.2	0.4	0.9	1.1	1.0

CAMED					
Month	16 km	18 km	20 km	22 km	24 km
February	4.6	6.0	7.9	6.2	3.5
March	4.2	5.5	6.6	5.0	3.0
April	3.6	5.0	5.7	4.4	2.7
May	3.3	4.6	5.2	3.9	2.5
June	3.1	4.2	4.7	3.6	2.3
July	3.0	4.0	4.4	3.3	2.2
August	2.9	3.8	4.1	3.1	2.0
September	2.7	3.5	3.8	2.9	1.9
October	2.5	3.3	3.6	2.7	1.8
November	2.4	3.1	3.4	2.5	1.7
December	2.3	3.0	3.2	2.4	1.6

Table J-4 (cont.)

GSFC					
Month	16 km	18 km	20 km	22 km	24 km
February	4.8	7.0	8.7	7.3	4.4
March	3.8	5.2	6.5	6.0	4.2
April	2.9	4.9	5.1	5.2	3.9
May	2.3	3.3	4.3	4.3	3.5
June	2.0	2.9	3.7	3.8	3.2
July	1.9	2.6	3.3	3.4	2.9
August	1.6	2.3	2.9	3.0	2.6
September	1.4	2.1	2.6	2.6	2.3
October	1.3	1.8	2.3	2.4	2.1
November	1.1	1.6	2.1	2.1	1.9
December	0.9	1.3	1.8	1.9	1.7

ITALY					
Month	16 km	18 km	20 km	22 km	24 km
February	5.1	6.1	6.8	5.8	3.9
March	2.6	4.5	5.7	5.1	3.6
April	1.7	3.5	5.0	4.7	3.4
May	1.3	3.1	4.6	4.5	3.3
June	1.2	2.8	4.3	4.3	3.1
July	1.0	2.6	4.1	4.1	3.0
August	0.9	2.4	3.9	4.0	2.8
September	0.8	2.3	3.7	3.8	2.7
October	0.7	2.1	3.5	3.6	2.6
November	0.7	1.9	3.2	3.3	2.4
December	0.6	1.8	2.9	3.1	2.2

Table J-4 (cont.)

LLNL					
Month	16 km	18 km	20 km	22 km	24 km
March	2.9	5.3	6.0	5.3	3.3
April	2.1	4.3	5.0	4.5	3.0
May	1.6	3.6	4.3	4.0	2.8
June	1.4	3.2	3.8	3.5	2.6
July	1.3	3.0	3.5	3.2	2.4
August	1.3	2.8	3.3	2.9	2.2
September	1.1	2.6	3.0	2.7	2.1
October	0.9	2.3	2.7	2.5	2.0
November	0.7	1.9	2.4	2.3	1.8
December	0.6	1.7	2.2	2.1	1.7

WASH					
Month	16 km	18 km	20 km	22 km	24 km
February	4.2	5.2	7.2	6.9	4.3
March	2.5	2.7	5.3	6.3	4.1
April	1.4	1.2	3.6	5.6	4.1
May	1.0	0.7	2.7	5.0	4.1
June	0.8	0.8	2.4	4.3	3.9
July	0.8	0.9	2.4	4.0	3.7
August	0.8	0.9	2.4	3.8	3.5
September	0.5	0.8	2.3	3.6	3.4
October	0.4	0.6	1.9	3.3	3.1
November	0.4	0.6	1.6	3.0	2.8
December	0.4	0.5	1.2	2.6	2.6

FIGURE CAPTIONS

Figure J-1. Initial concentrations (number/cm^3) for model simulation.

Figure J-2. SAGE II and model-derived concentration (number/cm^3) contour plots for April 1986.

Figure J-3. SAGE II and model-derived concentration (number/cm^3) contour plots for August 1986.

Figure J-4. Comparison of profiles of aerosol number concentration.

- **(a)** 0°, March 1986;
- **(b)** 0°, June 1986;
- **(c)** 0°, September 1986;
- **(d)** 0°, December 1986;
- **(e)** 35S, June 1986;
- **(f)** 35N, June 1986.

Figure J-5. Comparison of temporal variations of aerosol number concentration.

- **(a)** 20 km, 0°;
- **(b)** 26 km, 0°;
- **(c)** 20 km, 15S;
- **(d)** 20 km, 25N.

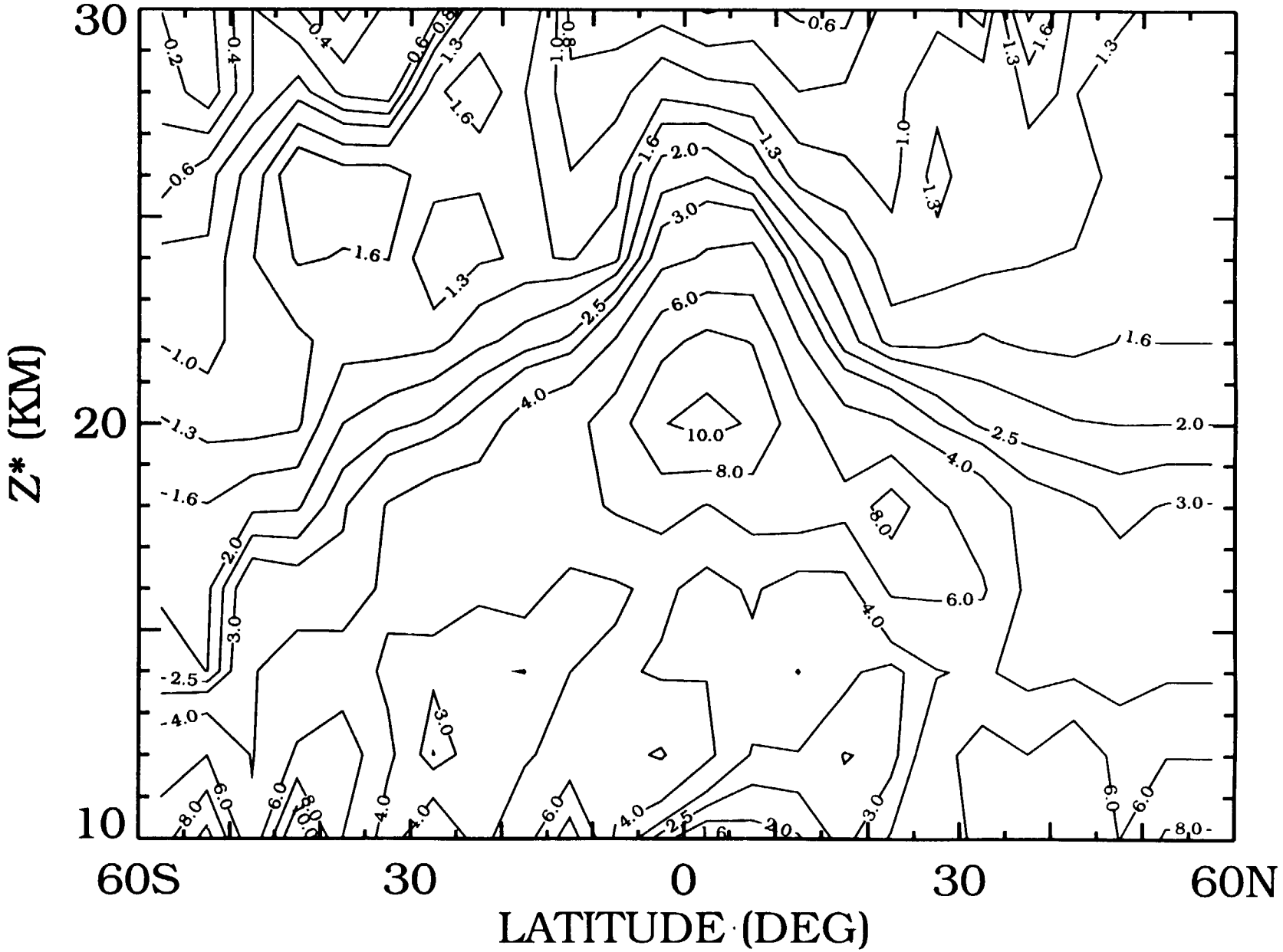

Figure J-1

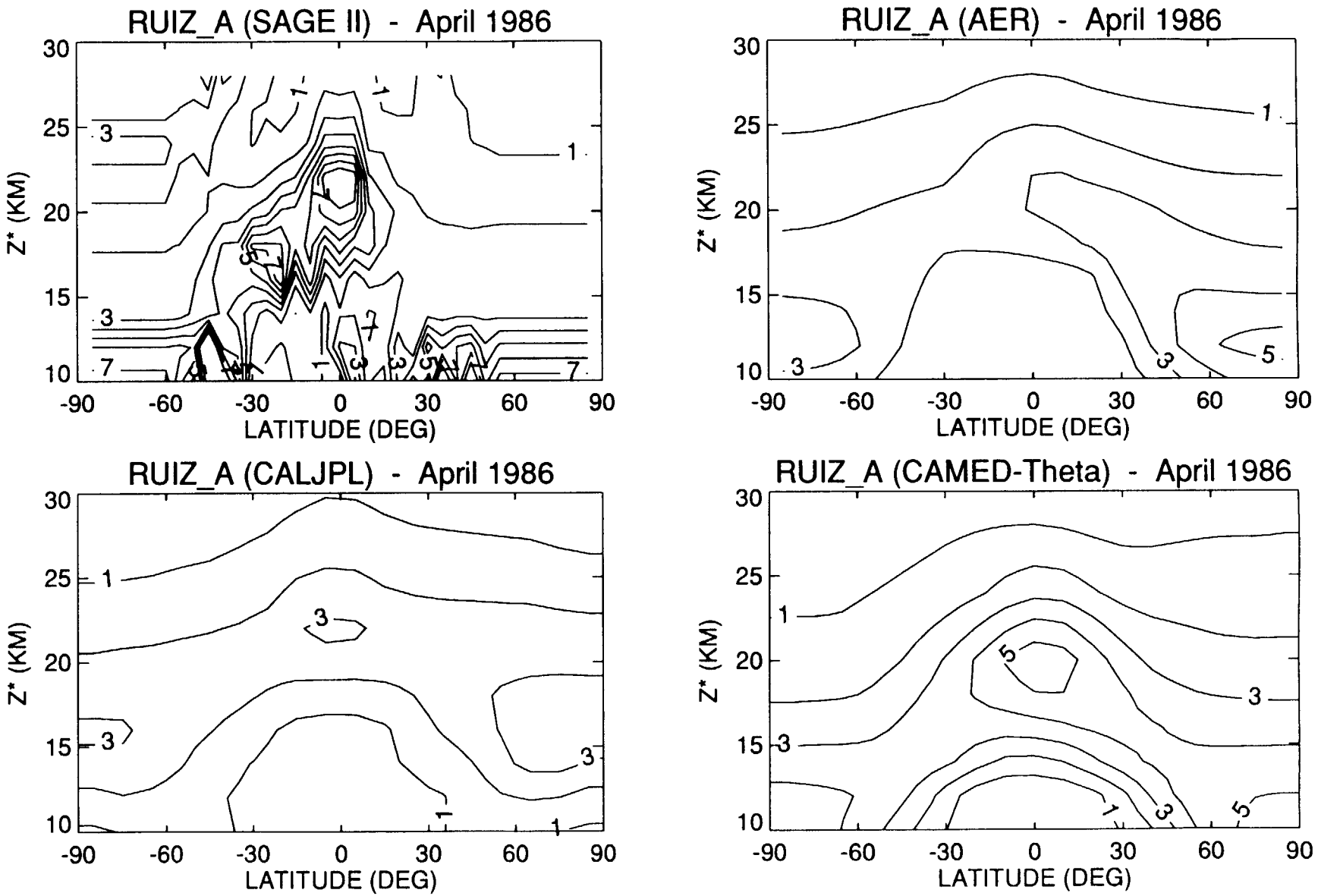
RUIZ_A (SAGE II) - April 1986
RUIZ_A (AER) - April 1986
RUIZ_A (CALJPL) - April 1986
RUIZ_A (CAMED-Theta) - April 1986
Z* (KM)
LATITUDE (DEG)
30
25
20
15
10
-90
-60
-30
0
30
60
90

Figure J-2

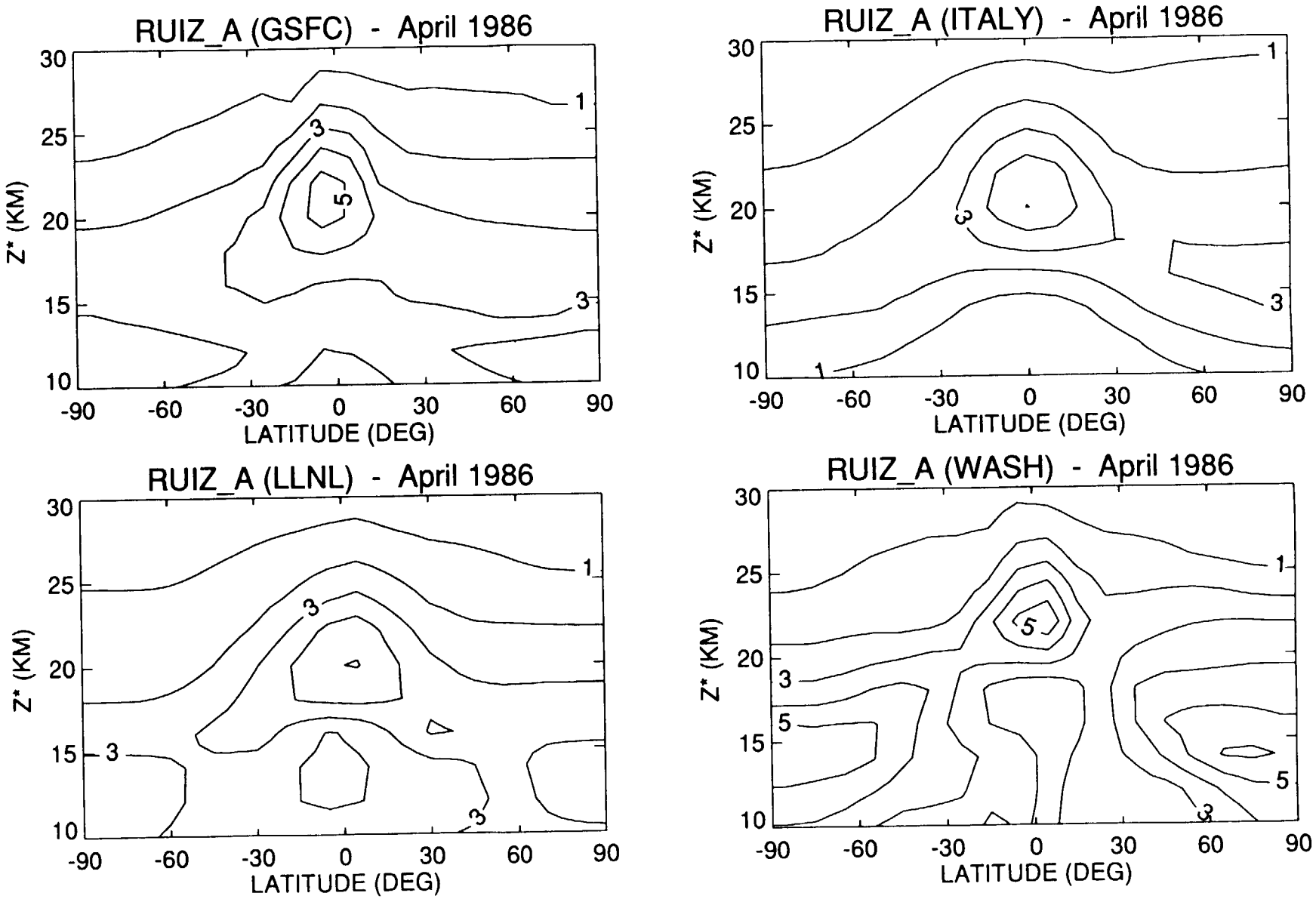

Figure J-2 (cont.)

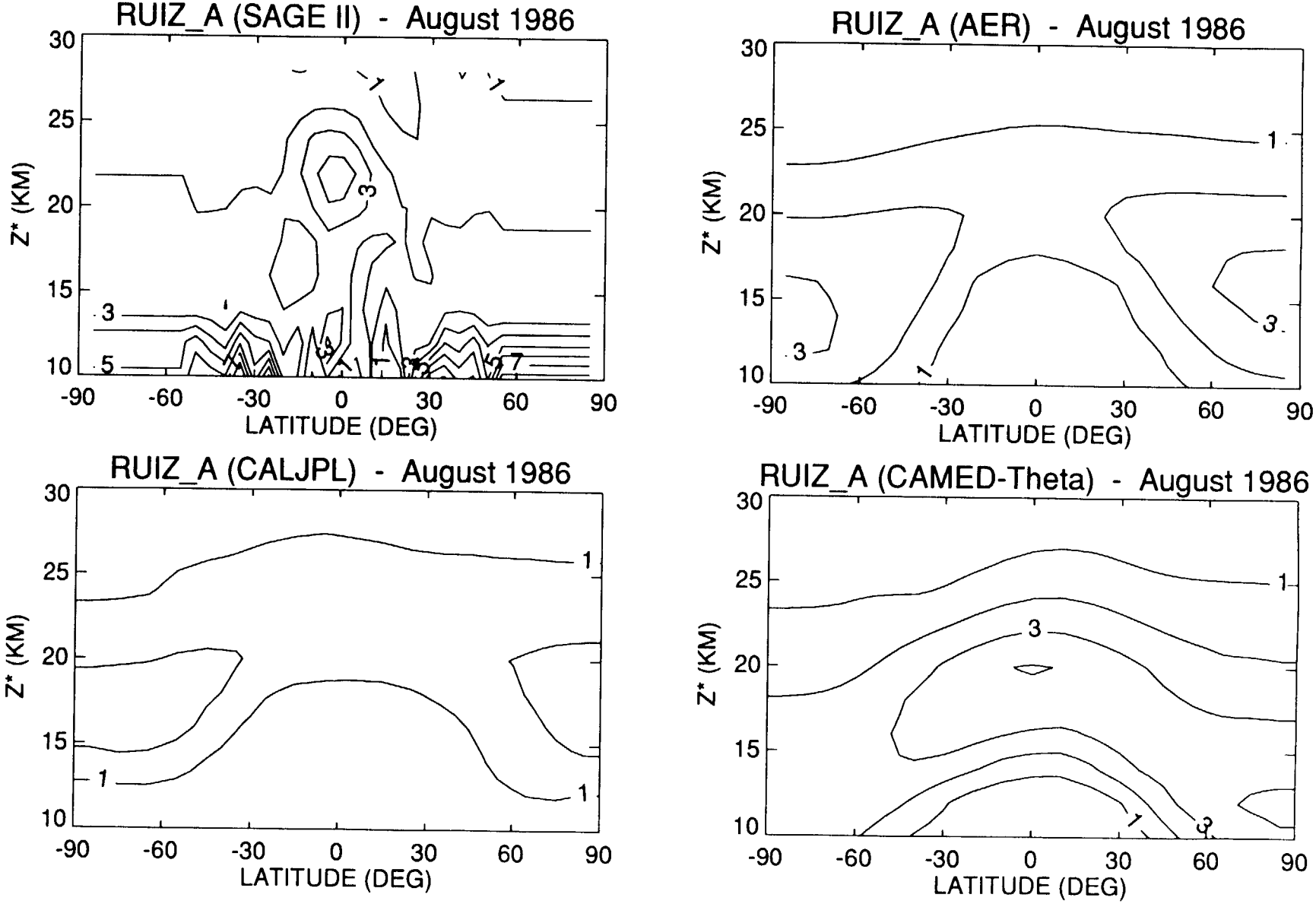
RUIZ_A (SAGE II) - August 1986
RUIZ_A (AER) - August 1986
RUIZ_A (CALJPL) - August 1986
RUIZ_A (CAMED-Theta) - August 1986
Z* (KM)
LATITUDE (DEG)
30
25
20
15
10
-90
-60
-30
0
30
60
90

Figure J-3

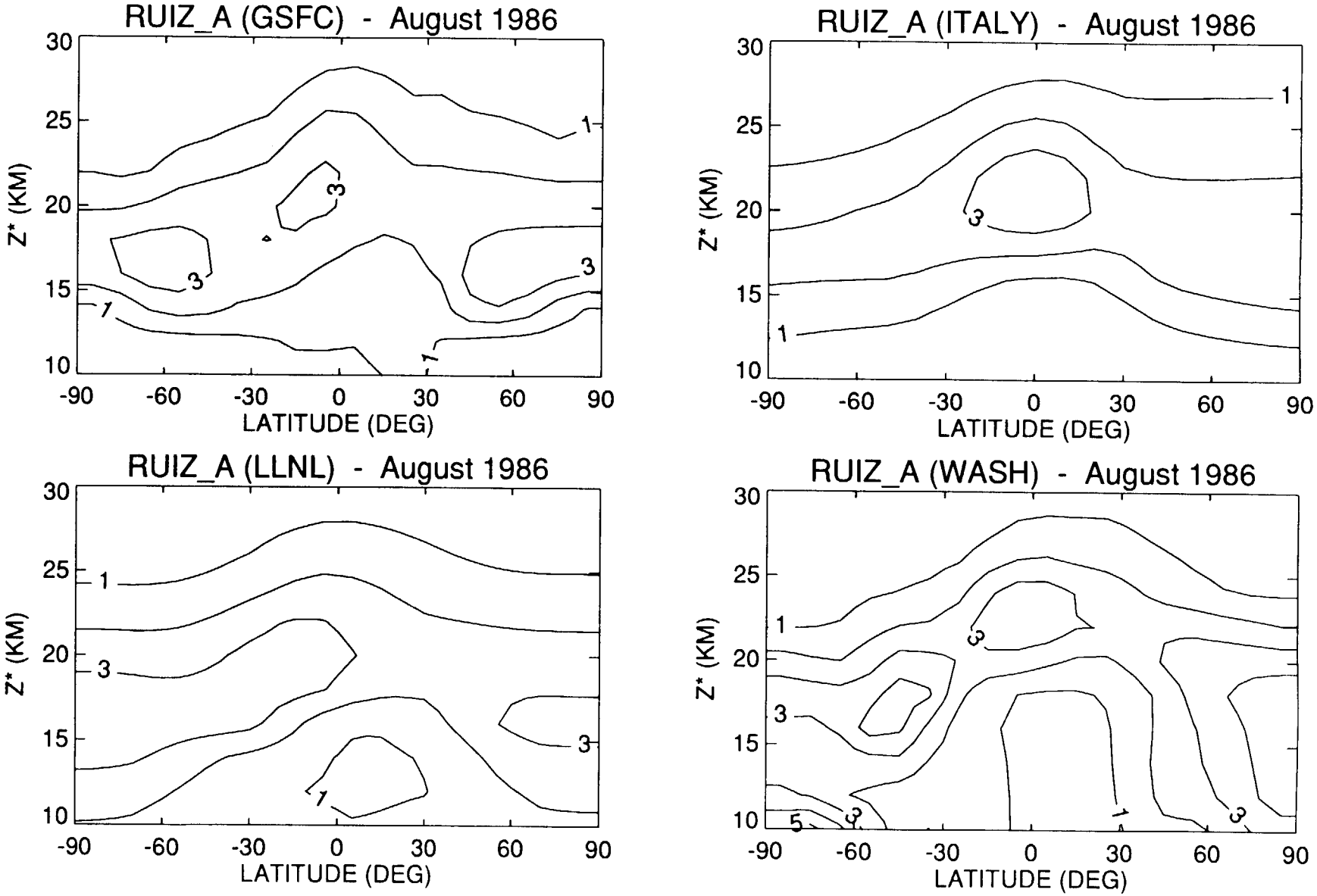

Figure J-3 (cont.)

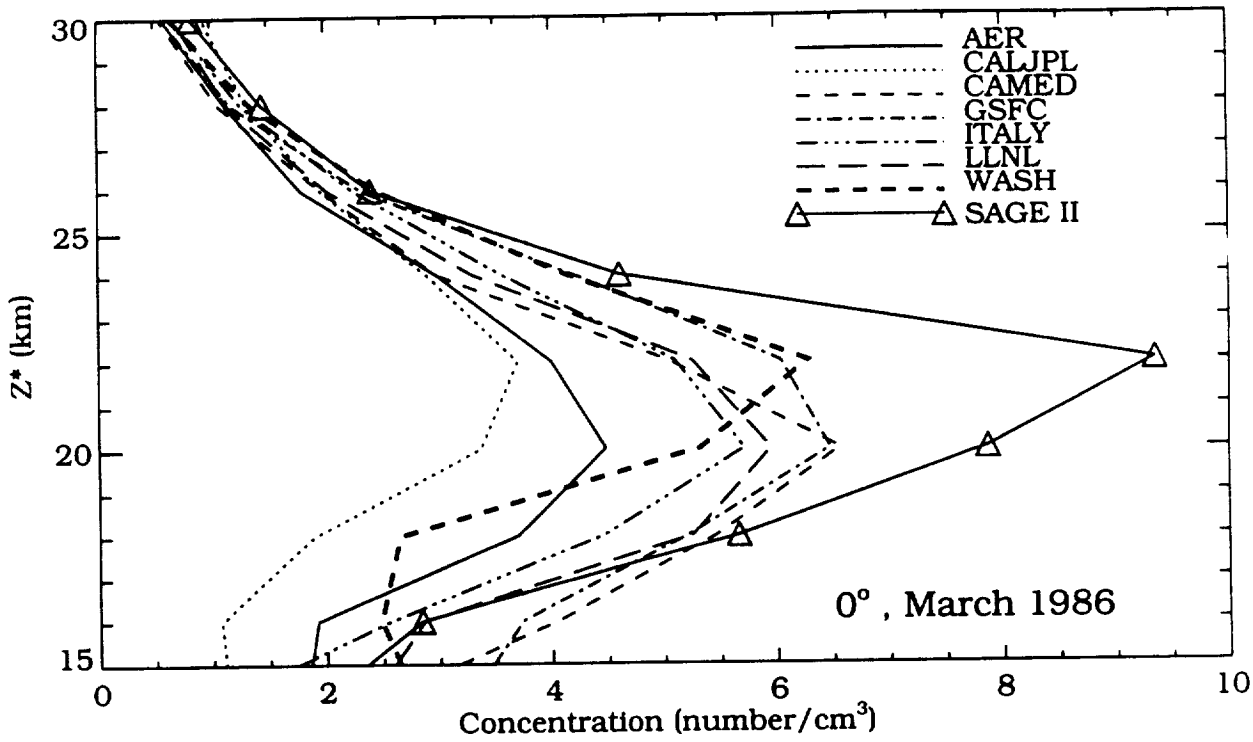
AER
CALJPL
CAMED
GSFC
ITALY
LLNL
WASH
SAGE II
0° , March 1986
Z* (km)
Concentration (number/cm3)
30
25
20
15
0
2
4
6
8
10

Figure J-4 a

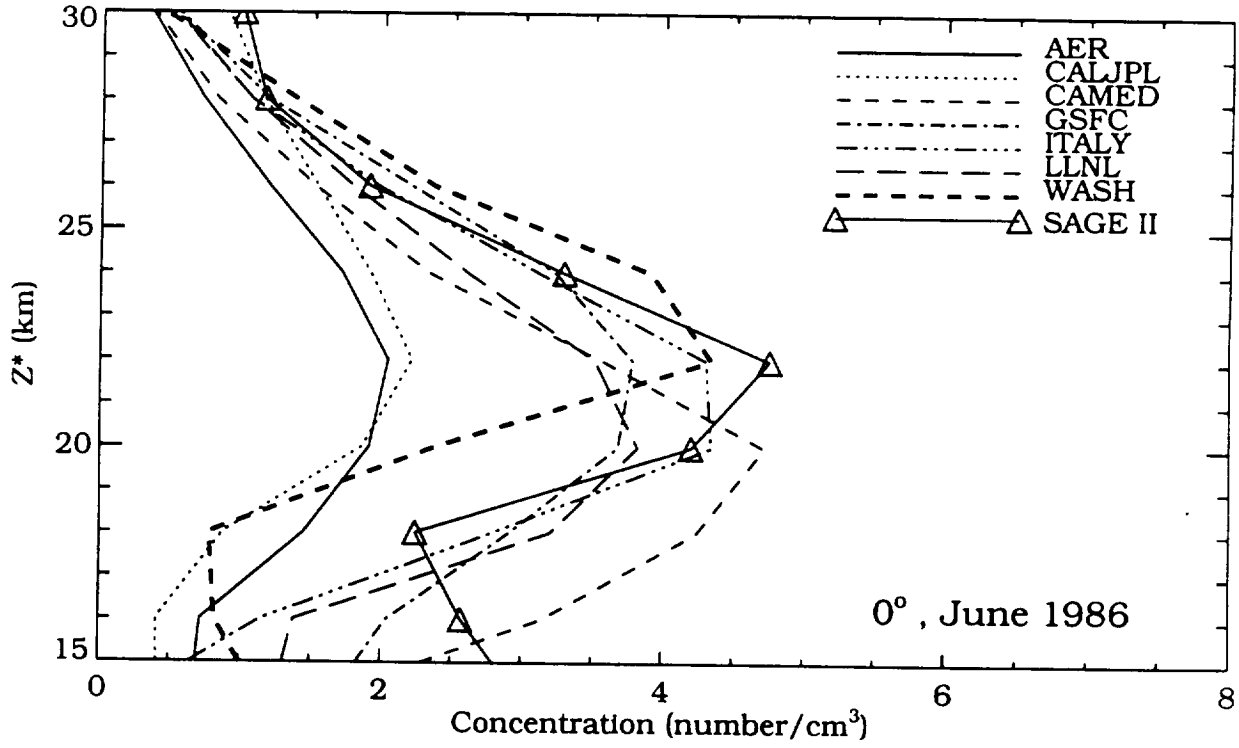
AER
CALJPL
CAMED
GSFC
ITALY
LLNL
WASH
SAGE II
0° , June 1986
Z* (km)
Concentration (number/cm³)
30
25
20
15
0
2
4
6
8

Figure J-4 b

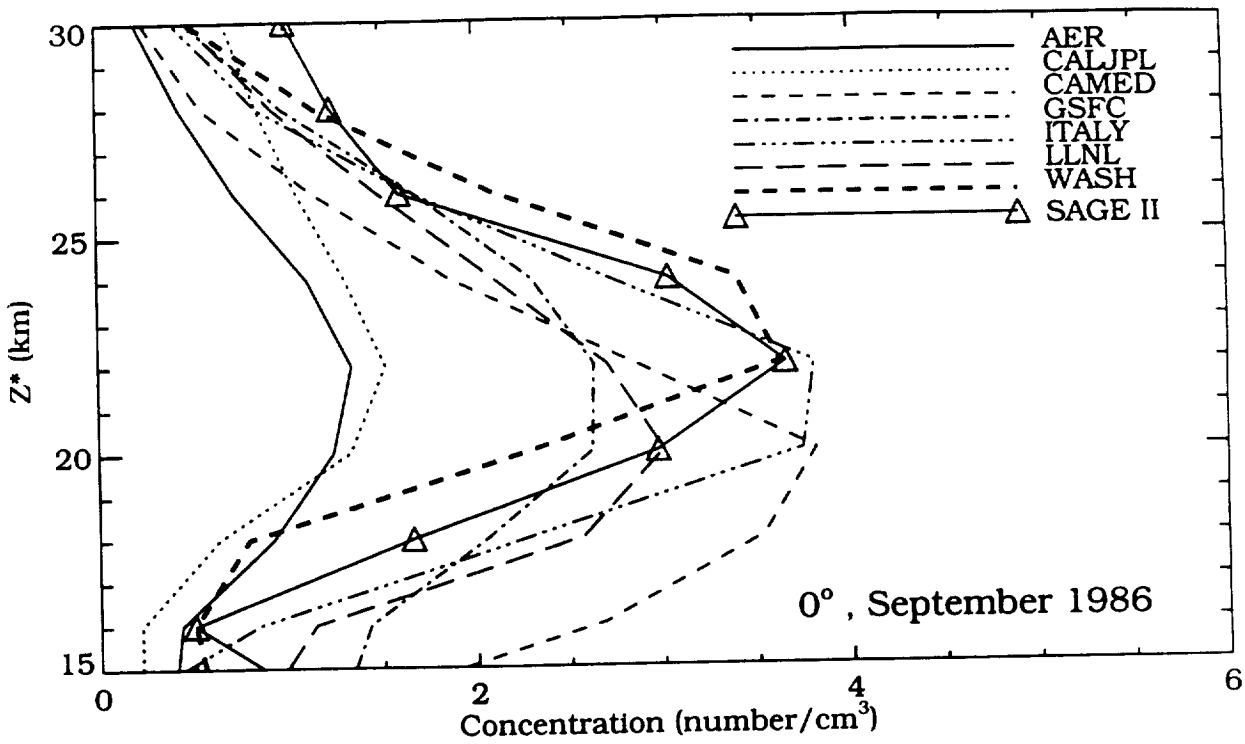
AER
CALJPL
CAMED
GSFC
ITALY
LLNL
WASH
SAGE II
0° , September 1986
Z* (km)
30
25
20
15
0
2
4
6
Concentration (number/cm3)

Figure J-4 c

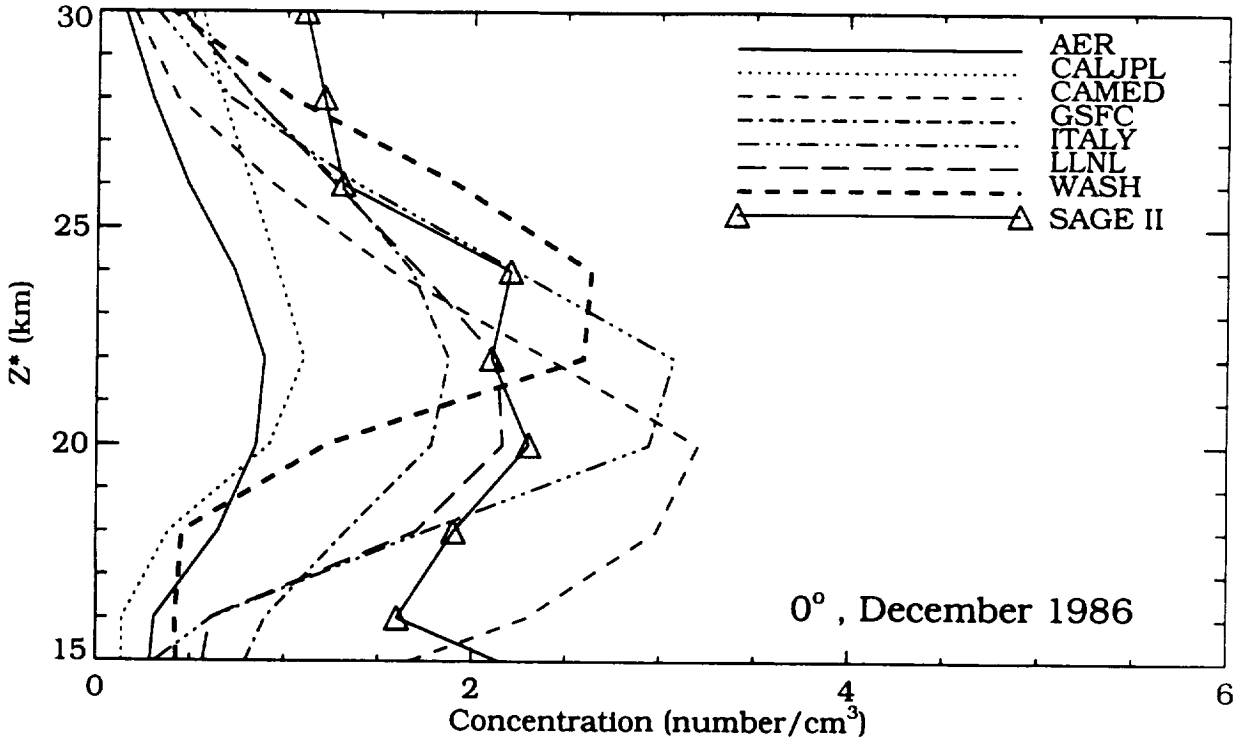
30
25
20
15
Z* (km)
0
2
4
6
Concentration (number/cm3)
AER
CALJPL
CAMED
GSFC
ITALY
LLNL
WASH
SAGE II
0° , December 1986

Figure J-4 d

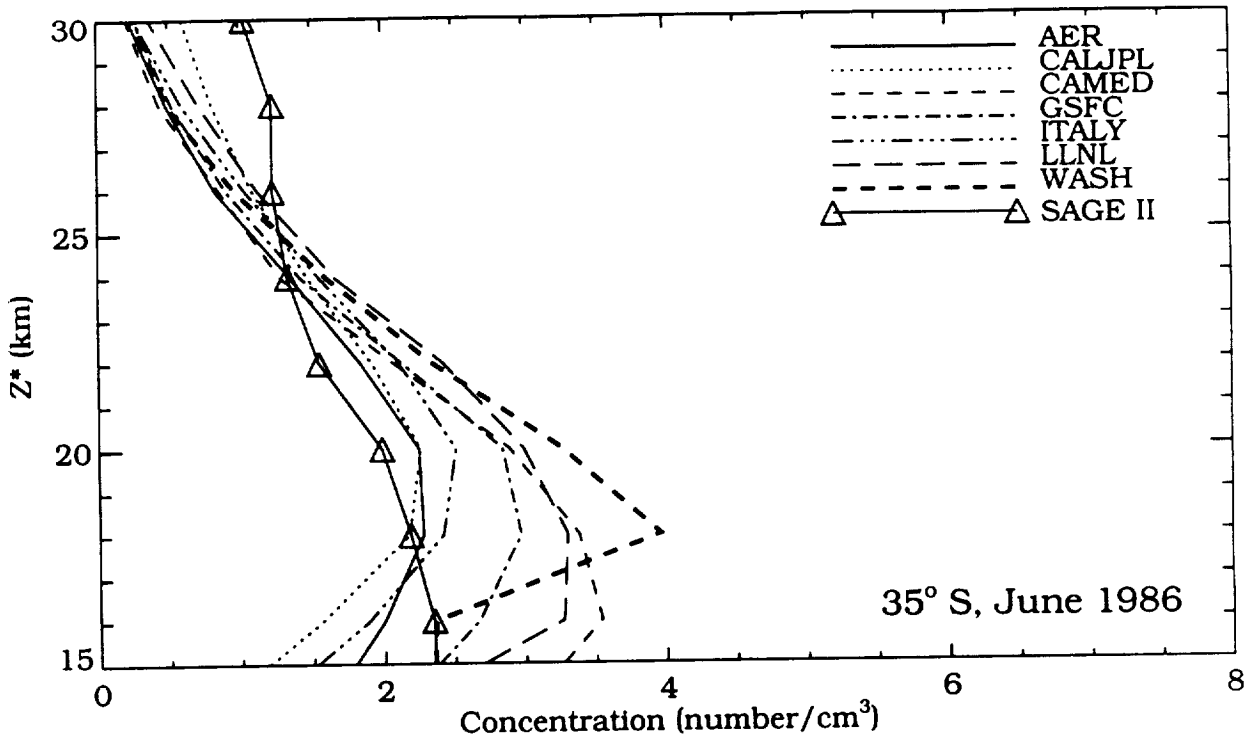
AER
CALJPL
CAMED
GSFC
ITALY
LLNL
WASH
SAGE II
35° S, June 1986
Z* (km)
Concentration (number/cm3)
30
25
20
15
0
2
4
6
8

Figure J-4 e

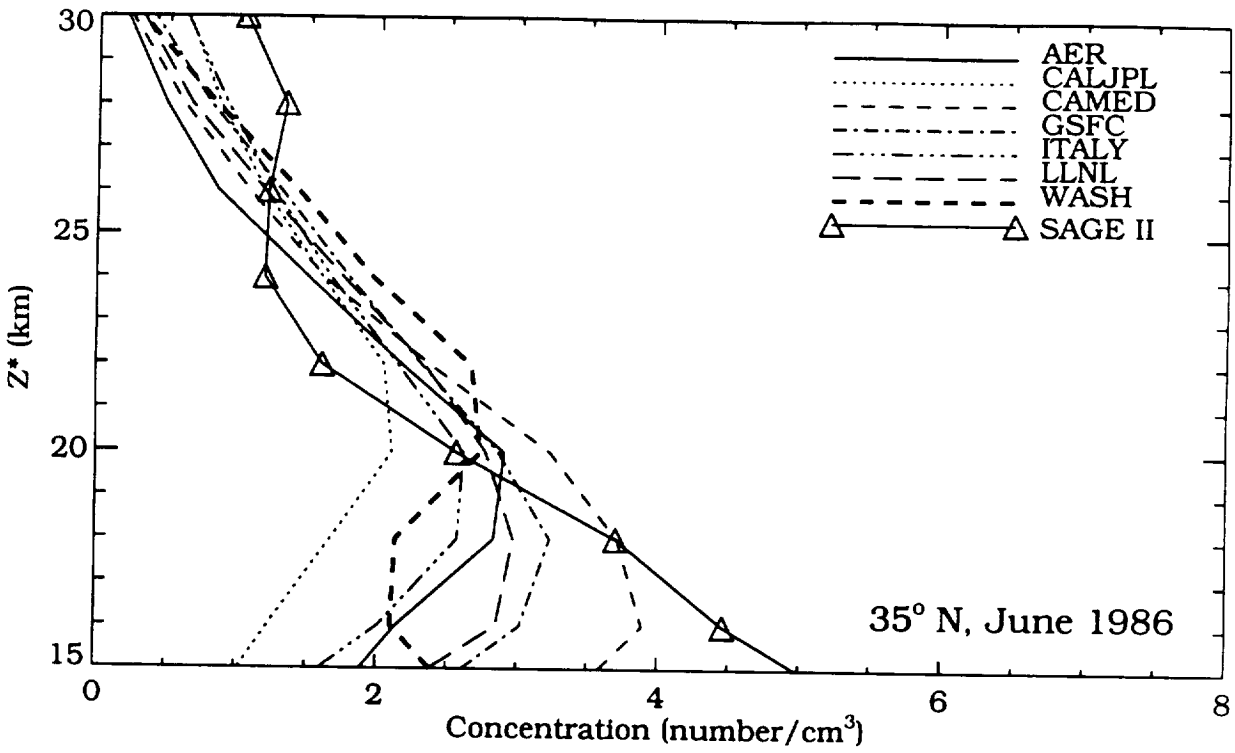
AER
CALJPL
CAMED
GSFC
ITALY
LLNL
WASH
SAGE II
35° N, June 1986
Z* (km)
Concentration (number/cm³)
30
25
20
15
0
2
4
6
8

Figure J-4 f

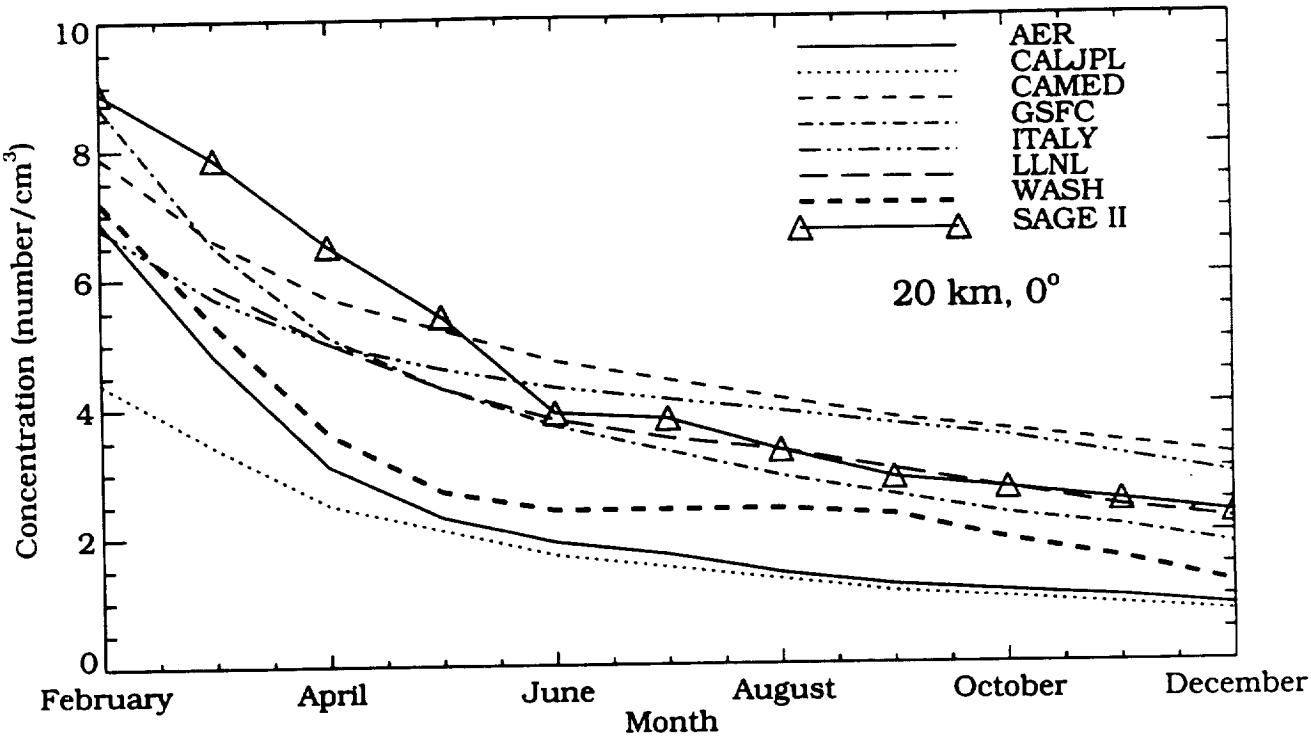
AER
CALJPL
CAMED
GSFC
ITALY
LLNL
WASH
SAGE II
20 km, 0°
Concentration (number/cm3)
10
8
6
4
2
0
February
April
June
August
October
December
Month

Figure J-5 a

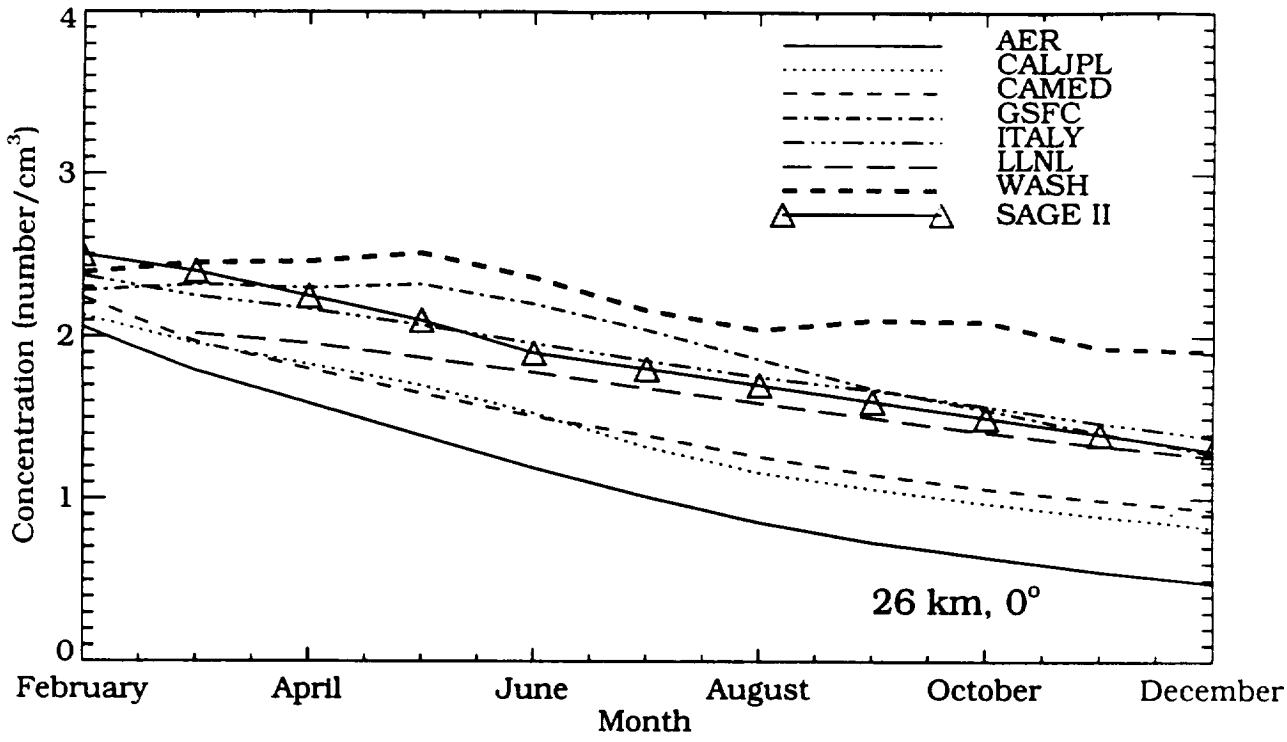
AER
CALJPL
CAMED
GSFC
ITALY
LLNL
WASH
SAGE II
26 km, 0°
Concentration (number/cm3)
0
1
2
3
4
February
April
June
August
October
December
Month

Figure J-5 b

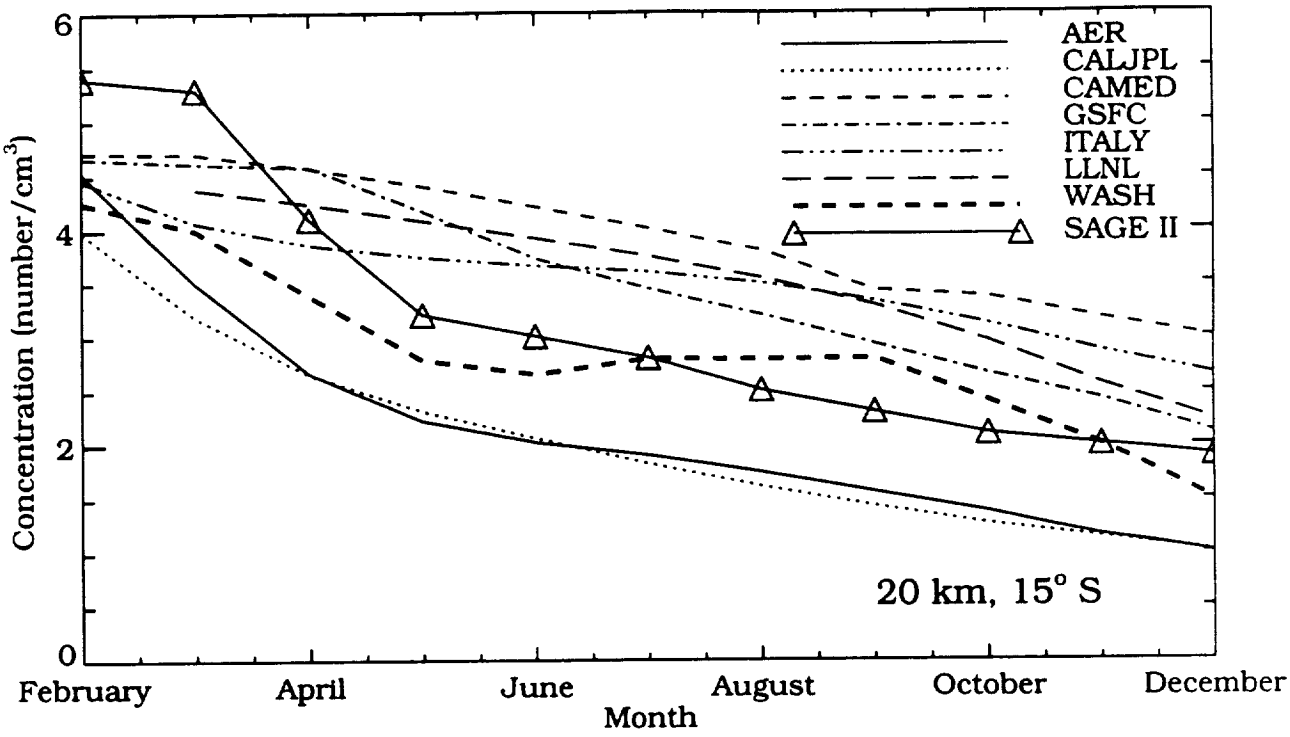
AER
CALJPL
CAMED
GSFC
ITALY
LLNL
WASH
SAGE II
20 km, 15° S
Concentration (number/cm3)
0
2
4
6
February
April
June
August
October
December
Month

Figure J-5 c

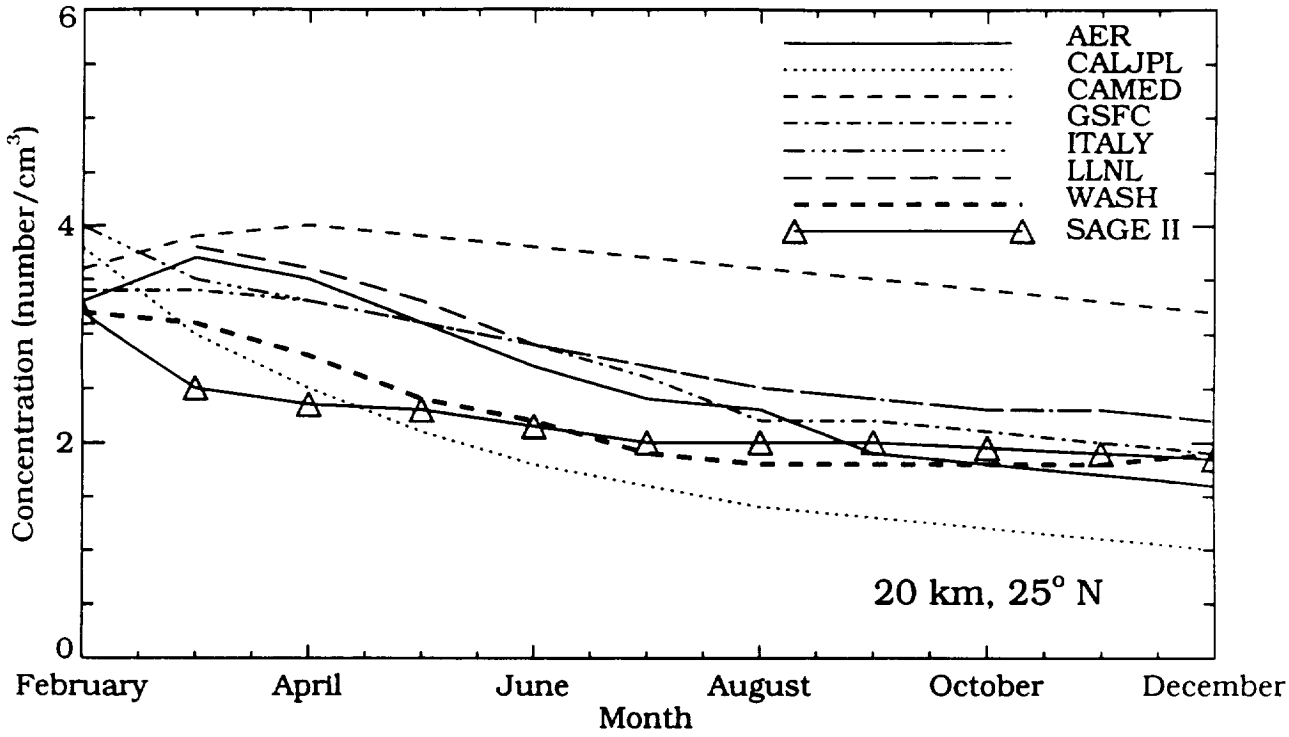
AER
CALJPL
CAMED
GSFC
ITALY
LLNL
WASH
SAGE II
20 km, 25° N
Concentration (number/cm3)
0
2
4
6
February
April
June
August
October
December
Month

Figure J-5 d

K: Photodissociation Rates

Overview
Sections K, L, and M: The ATMOS Profiles

Sections K, L, and M have a common theme in that we have adopted a mean atmospheric profile based on the ATMOS solar occultation measurements made during a Space Shuttle flight in May 1985. Section K examines photolysis rates (i.e., J-values), and section L compares the model chemistry of rates and radicals. These sections are basically model intercomparisons; they address critical issues that remain unresolved since the last model-model intercomparison. Section M is a true model and measurement comparison: the models were meant to simulate the sunset measurements made at latitudes near 30N. The ATMOS 30N atmosphere defined in the table below is a mixture of ATMOS observations, some model interpolation, some climatologies and tracer correlations (see section H), and a bit of guess work. It should provide a common framework with which to compare the basic photochemistry of the models independent of transport.

TABLE KLM-1. The ATMOS 30N Atmospheric Profile

z* (km)	p (mbar)	T (K)	O_3 (ppm)	NO_y (ppb)	CH_4 (ppm)	H_2O (ppm)	Cl_y# (ppb)	Aerosol Area‡ (10^{-8}/cm)
0	1000	294	0.05					
2	750	284	0.05		Use latitude = +30°			
4	562	272	0.05		Use solar declination = +15°			
6	422	259	0.05					
8	316	245	0.05		Use Br_y = 15 ppt everywhere			
10	237	231	0.10					
12	178	220	0.20					
14	133	204.1	0.34	0.80	1.61	6.01	0.20	1.0
16	100	205.6	0.72	1.09	1.57	4.14	0.30	1.0
18	75	207.9	1.38	2.16	1.50	3.39	0.60	1.0
20	56.2	210.8	2.34	4.24	1.39	3.84	1.20	0.8
22	42.2	214.1	3.53	6.48	1.26	4.62	1.70	0.6
24	31.6	217.8	4.88	8.59	1.12	4.90	2.15	0.4
26	23.7	221.9	6.18	10.83	0.98	4.88	2.45	0.3
28	17.8	226.3	7.15	12.89	0.86	5.07	2.60	0.2
30	13.3	230.7	7.76	15.15	0.77	5.41	2.75	0.1
32	10.0	234.3	8.07	15.93	0.74	5.57	2.80	0.05
34	7.50	237.8	8.08	15.40	0.76	5.53	2.75	0
36	5.62	243.1	7.71	16.06	0.80	5.47	2.80	.
38	4.22	249.6	6.95	16.20	0.82	5.48	2.80	.
40	3.16	255.6	5.87	16.71	0.78	5.60	2.80	.
42	2.37	261.3	4.77	16.76	0.70	5.78	2.80	.
44	1.78	267.5	4.04	16.91	0.60	5.99	2.80	.
46	1.33	272.1	3.53	15.35	0.52	6.24	2.80	
48	1.00	273.1	3.06	13.14	0.45	6.50	2.80	
50	0.750	270.7	2.60	11.11	0.39	6.63	2.80	
52	0.562	265.7	2.13	8.87	0.33	6.60	2.80	
54	0.422	259.6	1.65					
56	0.316	253.3	1.22					
58	0.237	247.2	0.95		# Uses empirical NO_y-Cl_y from ER-2 data			
60	0.178	241.0	0.77					
62	0.133	234.7	0.63		‡ Use $k = 5200 \times AA \times G$ (sec^{-1})			
64	0.100	228.7	0.50		$G = 0.1$ for N_2O_5 + aerosol			
66	0.075	223.4	0.37		$G = 0.006 \exp[-0.15(T-200)]$			
68	0.056	218.8	0.24		for $ClONO_2$ + aerosol			

K: Model-Model Intercomparison: Photodissociation Rates

Richard S. Eckman
NASA-Langley Research Center

Gail P. Anderson
Air Force Geophysical Laboratory

Yuk L. Yung
California Institute of Technology

INTRODUCTION AND EXPERIMENT DESCRIPTION

A disturbing conclusion from the 1988 intercomparison of two-dimensional models (Jackman et al., 1989) was that substantial unresolved differences existed, of the order of a factor of two, among the photodissociation rates calculated for a specified atmosphere. Not all modelers use the same calculation methods or parameterizations, particularly for absorption in the O_2 Schumann-Runge band region. Nonetheless, a degree of consistency is essential for an intercomparison of other model-calculated chemical quantities to be meaningful.

For the 1992 Models and Measurements Workshop, further constraints were placed on the specification of the model atmosphere. A standard atmosphere based on Atmospheric Trace Molecule Spectroscopy (ATMOS) occultation profiles at 30N was used to specify the temperature and ozone vertical profiles. The solar zenith angle was fixed at 15 degrees, which is the value at local noon for this latitude on May 1. Four cases were considered:

Case 1. A full calculation including Rayleigh-phase scattering and surface albedo of 0.3, and J-values reported at all solar wavelengths.

Case 2. Scattering and albedo included, but J-values reported only below 200 nm in an effort to isolate the contribution of the O_2 Schumann-Runge band absorption .

Case 3. No scattering and no surface albedo; J-values reported at all wavelengths.

Case 4. As above, but J-values reported at wavelengths less than 200 nm only .

Noontime values were reported in all four cases with a 24-hour average also calculated for case (1). Many models use diurnal averages of the photodissociation rates, and it is only the average that is important in stratospheric photolysis of O_2 and CFCs. Thus, it was felt that this final case would be illustrative of how models perform this average. For a comparison of diurnal averaging of species and rates see section L.

The photodissociation rate (or J-value) is defined as:

$$J(z,\chi) = \text{integral } \sigma(\lambda)\, F(\lambda,z,\chi)\, d\lambda$$

where σ is the cross section of the molecule, and $F(\lambda,z,\chi)$ is the sum of the attenuated direct solar irradiance and the mean intensity of the diffuse (scattered) light at the altitude, z, at solar zenith angle χ. The attenuated solar irradiance at this height depends on the absorption by O_2 and O_3 above this altitude, multiple scattering, and albedo. For this experiment, the extraterrestrial solar irradiance was not specified. However, most modelers used the spectrum recommended in the 1985 WMO Ozone Assessment Report, which is reported in 500 cm^{-1}

spectral intervals, the resolution used in many, but not all, of the models under consideration. Cross sections were in most instances taken from the most recent recommendations (JPL, 1990) with the exception of the O_2 Schumann-Runge band region where a number of techniques were employed to parameterize these values. Table K-1 shows the inputs used by each of the participating models.

Table K-1. Solar Irradiances and O_2 Cross Sections

Model	Solar UV	O_2 SRB Cross Sections	O_2 Herzberg C.S.
AER	WMO (82)	WMO (86)	JPL (90)
AFGL	SUSIM	Harvard-AFGL line-by-line	Yoshino (88)
CALJPL	+	Allen & Frederick (82)	Yoshino (88)
CAMED	WMO (86)	Frederick (84)	WMO (86)
DUPONT	WMO (86)	Nicolet & Peetermans (80)	WMO (86)
GISS	WMO (86)	Fang et al. (74)*	JPL (90)
GSFC	WMO (86)	Allen & Frederick (82)	WMO (86)
ITALY	WMO (86)	Park (74)	JPL (90)
LLNL	WMO (86)	Allen & Frederick (82)	WMO (86)
MPI	WMO (82)	Allen & Frederick (82)	WMO (86)
NCAR	Brasseur & Simon (81)	Nicolet & Kennes (89)	JPL (90)
WASH	WMO (86)	Allen & Frederick (82)	WMO (86)

+ CALJPL solar irradiance:

$\lambda > 3300$ A: WMO (1982)
$2800 < \lambda <= 3300$ A: Mentall et al. (1981)
$1172 < \lambda <= 2800$ A: Mount and Rottman (1983)

* Includes updates for $J(O_2)$

The only current source of comparison to measurements is the Harvard-Air Force Geophysical Laboratory (AFGL) line-by-line model results, provided by Gail Anderson, which are based on the high-resolution spectra measured by Yoshino et al. (1983), and calibrated against balloon-borne high-resolution spectra (Anderson and Hall, 1986).

Absorption by O_2 in this wavelength range (175-205 nm) is critically important to the photochemistry of the middle atmosphere. Because of the complex nature of this spectral region, atmospheric modelers have typically used analytic expressions or simplified parameterizations (e.g., Fang et al., 1974; Nicolet and Peetermans, 1980; Allen and Frederick, 1982).

The following quantities were calculated as a function of z* (0-60 km) for the intercomparison:

(a) column of O_2 overhead
(b) column of O_3 overhead
(c) $J(O_2)$
(d) J(NO)
(e) $J(N_2O)$
(f) J(CFC-11)
(g) J(CFC-12)
(h) $J(O_3 \rightarrow O(^1D))$
(i) $J(O_3 \rightarrow O(^3P))$
(j) $J(HNO_3)$
(k) $J(ClONO_2)$
(l) $J(N_2O_5)$
(m) $J(NO_2)$
(n) $J(NO_3 \rightarrow NO+O_2)$

RESULTS AND DISCUSSION

(a,b) Column Densities of O_2 and O_3

In principle, given that the vertical temperature structure has been specified, the O_2 column density may be calculated in a straightforward manner. Figure K-1 shows a comparison of the results of nine models that participated in this experiment. The AFGL results are represented by a solid line. With the exception of the ITALY and the NCAR models, all of the results are within 3% of the AFGL reference profile. Both ITALY and NCAR exhibit small variations about the reference with maximum differences of about 10%.

The ozone column density is shown in Figure K-2. Somewhat larger differences are seen among the models, particularly near 60 km. Since the overhead abundance is dependent on the ozone distribution above this altitude, it is not surprising that models with differing upper boundary levels and specifications of the ozone abundance above the top level would exhibit such differences in calculated column ozone. A majority of the models are within a few percent of the group average. Exceptions are the ITALY and NCAR models which exhibit values which are systematically higher than others, by 20%-30% at 60 km decreasing towards the surface. Errors resulting in the interpolation of the values to the standard vertical grid may account for at least some of the discrepancy.

Overall, the results of this comparison show good agreement and eliminate the column density calculation as a significant source of disagreement in the ensuing photodissociation rate intercomparison.

(c) $J(O_2)$

The photolysis of molecular oxygen plays a key role in atmospheric processes. It is the dominant source of odd oxygen (O, $O(^1D)$, and O_3) production in the middle atmosphere. However, the Schumann-Runge band region from 175 to 205 nm, which contributes much of the mesospheric component, is difficult to represent accurately in low resolution (e.g., 500 cm^{-1} spectral interval) calculations as the absorption cross section varies by 5 orders of magnitude.

The O_2 photolysis at wavelengths less than 200 nm is depicted in Figure K-3a. A spread of values is seen throughout the vertical profile. In this instance, we use the high-resolution calculations provided by Gail Anderson at AFGL as the baseline for comparison which is represented as a solid line. Figure K-3b shows the ratio of the model results to the AFGL calculation. Those models using the family of parameterizations based on the work of Frederick and Hudson (1979, 1980) and Fang et al. (1974) are within 20%-30% of the AFGL results, particularly above 40 km. At lower altitudes, discrepancies are greater; however, the SRB region is of reduced importance at these levels and the accuracy of the Frederick parameterizations (i.e., Allen and Frederick, 1982; Frederick, 1984; WMO, 1986) is reduced at higher optical depths. The AER model is from 50% below to 30% above the AFGL baseline from 40-60 km. While this model uses the O_2 cross sections recommended by Frederick in the WMO Report (1986), the resolution is lower than models employing 500 cm^{-1} bins in the SRB region (approximately 1.5-2 nm) as it uses 48 bins of 5 nm resolution.

Those models using other parameterizations generally show greater differences. The DUPONT model is systematically lower than the AFGL results by approximately 25% from 40-60 km. This is likely due to their use of the Nicolet and Peetermans (1980) parameterization. The ITALY model, using the parameterization of Park (1974), is about 30% lower than the AFGL results at 60 km, but is 20% higher than AFGL at 40 km, which is consistent with its

relatively low column O_3 abundance (*see* Figure K-2). The NCAR model is also systematically lower than the AFGL calculation throughout the atmosphere.

If the AFGL $J(O_2)$ calculations in the SRB are taken as the most "correct" currently available, then the intercomparison suggests that those models using the Frederick "family" of parameterizations and the GISS model, which utilizes the Fang et al. (1974) SRB opacity parameterization, yield the closest answers to this standard.

Recently, a polynomial coefficient representation of the Harvard-AFGL line-by-line model was developed by Minschwaner et al. (1992). In the future, it will be useful to employ this parameterization as a standard to examine the quality of more time-efficient methods for the calculation of O_2 absorption in this region.

When all wavelengths are included in the calculation of $J(O_2)$, agreement between models is improved, as seen in Figure K-4a. Agreement with respect to the AFGL calculation is typically better than 15% above 30 km as seen in Figure K-4b. This improved agreement is not surprising as the Herzberg continuum is the dominant source of O_2 absorption below 60 km and all of the models use recent values of these cross sections reported by the Harvard group (Yoshino et al., 1983, 1988). Below 30 km the agreement is less satisfactory, with differences approaching 50% for the DUPONT, NCAR, and ITALY models.

Calculations made with the inclusion of scattering and albedo effects show negligible impact above 20 km, not unexpected given that O_2 absorbs UV radiation only below 242 nm.

(d) J(NO)

Photolysis of NO initiates the only loss of NO_y in the stratosphere and therefore controls the roll-off of NO_y mixing ratios in the middle stratosphere.

Only the δ(0-0) at 190.9 nm and δ(0-1) bands at 182.7 nm need to be considered in the calculation of the photolysis of nitric oxide in the middle atmosphere. The attenuation of the solar irradiance in this region is due to SRB O_2 absorption. Thus, results will again depend on the parameterization used for the SRB O_2 cross sections as well as those used for the two NO bands.

Figure K-5a shows the results for J(NO) for no scattering and wavelengths below 200 nm. This case is also representative of the other three cases owing to the location of the delta bands at short wavelengths. Agreement between the models is less good than that of $J(O_2)$, typically within 30%-40% above 40 km. Both the CAMED and LLNL models are consistently lower than the average throughout the vertical domain, while GISS and ITALY (which do not employ the Allen and Frederick NO cross-section parameterization) are on the high side of the comparison. The ITALY model results are again well correlated with their lower than average stratospheric column O_3 abundance. We have not yet established a reference calculation for J(NO) as we have for O_2.

The 30-50 km altitude range is enlarged in Figure K-5b. In this region, NO photolysis accounts for almost all atomic nitrogen production, which reacts with NO to destroy midstratospheric odd nitrogen. The spread in values is a factor of six at 30 km, decreasing at higher levels.

(e,f,g) $J(N_2O)$, J(CFC-11), J(CFC-12)

The photodissociation rates of these constituents are treated as a group because of the similarity of the spectral distribution of their absorption cross sections. All three constituents have cross sections that peak around 190 nm and fall off rapidly towards 230 nm. Because of this, all three should show similar behavior with respect to the SRB and Herzberg O_2 cross sections employed. As with $J(O_2)$ and J(NO), scattering has a negligible impact above 20 km on the calculated photodissociation rate.

The photolysis of N_2O is presented in Figure K-6. Above 30 km, agreement is good with all models within 30% of the group average. At 20 km, differences of a factor of 1.5 are evident.

Figures K-7a and K-7b show the CFC-11 photolysis rates and their ratio to the group average, respectively. Better than 20% agreement is seen above 30 km, but considerably worse agreement in the critical lower stratosphere region. The spread at 20 km is over a factor of two with the AER, CAMED, GSFC, and NCAR models showing the largest deviations from the average.

The CFC-12 photolysis rate and its ratio to the group average are presented in Figures K-8a and K-8b. The behavior is similar to that of CFC-11, with good agreement above 30 km and deteriorating rapidly below this level. The CAMED and NCAR models again show large deviations from the group average.

(h) $J(O_3 \rightarrow O(^1D))$

As the quantum yield for the photolysis of O_3 to $O(^1D)$ is significant only below 320 nm, scattering has less of a role in this rate in the stratosphere, but is still very important in the troposphere (i.e., Rayleigh scattering optical depth at 310 nm is about 1). Figure K-9 shows the photolysis rate with no scattering included. Agreement is good, particularly above 20 km with differences less than 10% for most models compared with the group average. The NCAR model shows discrepancies of up to 50% above 30 km. At 20 km factor of two differences are seen among all of the models.

(i) $J(O_3 \rightarrow O(^3P))$

Scattering plays an important role in the photolysis of O_3 yielding $O(^3P)$. Figures K-10 and K-11 show the photolysis rate with and without the effects of scattering included reported at all wavelengths. With the exceptions of CAMED, NCAR, and Washington, agreement throughout the entire altitude range of the no-scattering case is very good with values within about 5% of the group average. JPL - Publication 90-1 (1990) recommends a change in the maximum quantum yield for the $O(^1D)$ channel from 0.90 to 0.95. The value of 0.95 was used by CAMED, WASH, and NCAR, thus accounting for their results lying on the low side of the group average.

With scattering included, agreement is still very good, excepting the three models mentioned above, with some increased divergence in the troposphere, particularly by the GSFC model.

(j) $J(HNO_3)$

This molecule has an absorption spectrum below 320 nm. Once again, scattering is of negligible importance above 25 km. As shown in Figure K-12, agreement between the models is very good, particularly above 25 km. The NCAR model is consistently lower than others in the midstratosphere, but this discrepancy is reduced when scattering is included (not shown). This

may be a fortuitous result. Otherwise, agreement among the models to within 30% is seen in the middle and upper stratosphere.

(k) $J(ClONO_2)$

Figure K-13 shows the photolysis of $ClONO_2$ with no scattering included. Agreement is at the 20% level above 30 km with larger differences below, excepting the NCAR and CAMED models, which exhibit larger differences. The CAMED model is higher than the group average throughout the entire vertical domain. With scattering included (not shown), enhanced rates are calculated below 30 km. The comparison between the models remains consistent with the no scattering case.

(l) $J(N_2O_5)$

The N_2O_5 photolysis rate without scattering is shown in Figure K-14. The spread of the results is within 30% of the average above 40 km. The AER, GSFC, and NCAR models are on the low side of the other seven models presented. At 30 km, discrepancies of 60% are evident, increasing to a factor of two at 20 km. The comparison with scattering included is very similar to that of the no-scattering case. It looks as though temperature dependence is not included in the DUPONT, NCAR, GISS, and ITALY models, but is in the other models.

(m) $J(NO_2)$

With no scattering included, the agreement between models for NO_2 photolysis is very good, to within 5% as illustrated by Figure K-15. Figure K-16 shows the result with scattering included. Agreement among models is within 30%. The CAMED model includes a surface albedo of 0.30, but does not include scattering, accounting for its low value with respect to the group average.

Apparently, the inclusion of scattering leads to greater discrepancies among the models. Figure K-17 shows the ratio of the scattering to no scattering cases. CAMED shows a uniform enhancement of about 30%, which is consistent with a daytime average for a nonscattering atmosphere with a surface albedo (i.e., J-values increase by a factor of 1 + 2 x albedo x $\cos(\chi)$, which at noon in this example is 1.58). Other models vary from 45%-70% enhancements above 20 km, with some models calculating nearly factor of two enhancements in the troposphere, while others show falloffs in this region.

(n) $J(NO_3 \rightarrow NO+O_2)$

Figure K-18a shows the photolysis rate of NO_3 without scattering included. The models exhibit a considerable spread in results with differences of up to a factor of 2. Both DUPONT and GISS lie on the high side, while MPI lies on the low side of the other four models. These four models are close to the overhead sun value of 0.022 sec^{-1} of Magnotta and Johnston (1980), which remains at the value recommended by JPL Publication 90-1 (1990). The AER model results are much higher than the other seven models and are not shown on the plot.

With scattering included (Figure K-18b) the comparison among the models is substantially worsened. This is surprising since the wavelengths that NO_3 photolyzes (around 600 nm) are almost insensitive to Rayleigh scattering. Only ground albedo should have a substantial impact.

DIURNAL AVERAGES

A good degree of consistency is evident in the methods by which the photolysis rates are diurnally averaged. Figures K-19—K-21 show three examples of the ratio of the diurnally averaged rate to the noontime calculation. In each instance both Rayleigh-phase scattering and surface albedo are included. Figure K-19 shows the ratio for $J(O_2)$. Only the ITALY model shows a significant difference from the group average, being about a factor of 1.8 below the other models. This is a consistent feature of the ITALY model for all of the diurnal to noontime ratios. The ratio for J(NO) is presented in Figure K-20. In this instance, the LLNL model shows a different vertical structure compared with the other models, being consistently higher at all altitudes. Figure K-21 shows the ratio for $J(NO_2)$. The curvature of the NO_2 ratio in the troposphere is due to the Rayleigh scattering; the two models with just surface albedo and nonscattering atmospheres (AER and CAMED) do not show this. The increase in this ratio for CALJPL above 40 km is not easily explained, possibly due to twilight photolysis in a spherical atmosphere (although this is supposedly included in some other models). See section L on diurnal averaging of the rates. Once again, LLNL is at variance with the group average, being on the low side of the other models. The tendency of the LLNL model to diverge from the group average is also evident in the ratios for $J(ClONO_2)$, $J(HNO_3)$, and $J(N_2O_5)$ (not shown). For all other constituents, the LLNL results are very close to the group average.

CONCLUSIONS

It is evident that a substantial improvement has been made in the consistency with which photodissociation rates are calculated compared with the previous model intercomparison (Jackman et al., 1989). The O_2 Schumann-Runge band region remains a potential problem, though those models using the family of Frederick-derived parameterizations and the Fang et al. parameterization agreed best with the Harvard-AFGL line-by-line calculations. At lower altitudes, the total $J(O_2)$ results are less satisfactory. Differences of 50% are seen in the 20-30 km region.

Other photolysis rates that depend strongly on Schumann-Runge band O_2 absorption exhibit mixed results. J(NO) model agreement is poor below 40 km. The photodissociation of CFC-11 and CFC-12 also show large differences in the lower stratosphere.

Generally good agreement was seen in the photolysis rates of constituents where both the O_2 SRB region and scattering were relatively unimportant as in the case of $J(O_3 \rightarrow O(^1D))$ and $J(HNO_3)$.

Where scattering is important, the results are, once again, more disparate. $J(O_3 \rightarrow O(^3P))$ discrepancies are small, though the results emphasize the importance of the $O(^1D)$ quantum yield parameterization. However, this difference is not important for the calculated $O(^3P)$ since it is the total production of O, including the quenched $O(^1D)$, which defines its abundance (*see* section L). The agreement for $J(NO_2)$ is only fair and emphasizes that the diverse approaches of including scattering in models lead to increased differences, as shown in Figure K-17. N_2O_5 photolysis results exhibit large differences, as do those for NO_3. The latter is clearly more distressing in view of the recommended rate for clear sky photolysis.

REFERENCES

Allen, M. and J. E. Frederick, Effective photodissociation cross sections for molecular oxygen and nitric oxide in the Schumann-Runge bands, *J. Atmos. Sci., 39*, 2066-2075, 1982.

Anderson, G. P., and L. A. Hall, Stratospheric determination of O_2 cross sections and photodissociation rate coefficients: 191-215 nm, J. *Geophys. Res., 91*, 14509-14514, 1986.

Brasseur, G. and P. Simon, Stratospheric chemical and thermal response to long-term variability in solar UV irradiance, *J. Geophys. Res., 86*, 7343-7362, 1981.

Cheung, A. S.-C., K. Yoshino, W. H. Parkinson, and D. E. Freeman, Herzberg continuum cross section of oxygen in the wavelength region 193.5-204.0 nm: New laboratory measurements and stratospheric implications, *Geophys. Res. Lett., 11*, 580-582, 1984.

Fang, T.-M., S. C. Wofsy, and A. Dalgarno, Opacity distribution functions and absorption in Schumann-Runge bands of molecular oxygen, *Planet. Space Sci., 22*, 413-425, 1974.

Frederick, J. E., The incident solar spectral irradiance and cross sections of molecular oxygen and ozone for use in the 1985 NASA Assessment Report, unpublished manuscript, 1984.

Frederick, J. E. and R. D. Hudson, Predissociation linewidths and oscillator strengths for the (2-0) to (13-0) Schumann-Runge bands of O_2, *J. Molec. Spectrosc. 74*, 247-258, 1979.

Frederick, J. E. and R. D. Hudson, Dissociation of molecular oxygen in the Schumann-Runge bands, *J. Atmos. Sci., 37*, 1099-1106, 1980.

Jackman, C. H., R. K. Seals, Jr., and M. J . Prather, eds., *Two-dimensional Intercomparison of Stratospheric Models, NASA Conference Publication 3042*, NASA, Washington, D.C., 1989, 595pp.

Jet Propulsion Laboratory, *Chemical Kinetics and Photochemical Data for Use in Stratospheric Modeling, JPL Publication 90-1*, Pasadena, CA, 1990, 217pp.

Magnotta, F. and H. S. Johnston, Photodissociation quantum yields for the NO_3 free radical, *Geophys. Res. Lett., 7*, 769-772, 1980.

Mentall, J. E., J. E. Frederick, and J. R. Herman, The solar irradiance from 200-300 nm, *J. Geophys. Res., 86*, 9881-9884, 1981.

Minschwaner, K., G. P. Anderson, L. A. Hall, and K. Yoshino, Polynomial coefficients for calculating O_2 Schumann-Runge cross sections at 0.5 cm^{-1} resolution, *J. Geophys. Res., 97*, 10103-10108, 1992.

Mount G. H and G. J. Rottman, The solar absolute spectral irradiance 1150-3173 A: May 17, 1982, *J. Geophys. Res., 88*, 6807-6811, 1983.

Nicolet, M. and W. Peetermans, Atmospheric absorption in the O_2 Schumann-Runge bands spectral range and photodissociation rates in the stratosphere and mesosphere, *Planet. Space Sci., 28*, 85-103, 1980.

Nicolet, M. and R. Kennes, Aeronomic problems of molecular oxygen photodissociation-VI. Photodissociation frequency and transmittance in the spectral range of the Schumann-Runge bands, *Planet. Space Sci., 37*, 459-491, 1989.

Park, J. H., The equivalent mean absorption cross sections for the O_2 Schumann-Runge bands: Application to the H_2O and NO photodissociation rates, J. *Atmos. Sci., 31*, 1893-1897, 1974.

World Meteorological Organization (WMO), *The Stratosphere 1981: Theory and Measurements, Research Project Report No. 11*, WMO, Geneva, 1982.

World Meteorological Organization (WMO), *Atmospheric Ozone 1985: Assessment of Our Understanding of the Processes Controlling its Present Distribution and Change, Research Project Report No. 16*, WMO, Geneva, 1986.

Yoshino, K., D. E. Freeman, J. R. Esmond, and W. H. Parkinson, High resolution absorption cross section measurements and band oscillator strengths of the (1,0)-(12,0) Schumann-Runge bands of O_2, *Planet. Space Sci., 31*, 339-353, 1983.

Yoshino, K. et al., Improved absorption cross sections of oxygen in the wavelength region 205-240 nm of the Herzberg continuum, *Planet. Space Sci., 36*, 1469-1475, 1988.

FIGURE CAPTIONS

Figure K-1. O_2 column abundance (molecules/cm^2) as a function of altitude. Solid line represents the AFGL reference profile.

Figure K-2. O_3 column abundance (molecules/cm^2) as a function of altitude.

Figure K-3a. O_2 photolysis rate (sec^{-1}) as a function of altitude for wavelengths less than 200 nm and no scattering or surface albedo. Solid line represents the AFGL reference profile.

Figure K-3b. Ratio of model O_2 photolysis rates to AFGL reference profile for wavelengths less than 200 nm and no scattering or surface albedo.

Figure K-4a. As in Figure K-3a except for all wavelengths.

Figure K-4b. As in Figure K-3b except for all wavelengths.

Figure K-5a. NO photolysis rate as a function of altitude for wavelengths less than 200 nm and no scattering or surface albedo.

Figure K-5b. As in Figure K-5a except for the altitude range of 30-50 km only.

Figure K-6. N_2O photolysis rate as a function of altitude for all wavelengths with no scattering or surface albedo.

Figure K-7a. CFC-11 photolysis rate as a function of altitude for all wavelengths and no scattering or surface albedo.

Figure K-7b. Ratio of model CFC-11 photolysis rates to the group average for all wavelengths and no scattering or surface albedo.

Figure K-8a. CFC-12 photolysis rate as a function of altitude for all wavelengths and no scattering or surface albedo.

Figure K-8b. Ratio of model CFC-12 photolysis rates to the group average for all wavelengths and no scattering or surface albedo.

Figure K-9. O_3-->$O(^1D)$ photolysis rate as a function of altitude for all wavelengths and no scattering or surface albedo.

Figure K-10. O_3-->$O(^3P)$ photolysis rate as a function of altitude for all wavelengths and no scattering or surface albedo.

Figure K-11. As in Figure K-10 except with scattering and surface albedo included.

Figure K-12. HNO_3 photolysis rate as a function of altitude for all wavelengths and with no scattering or surface albedo.

Figure K-13. $ClONO_2$ photolysis rate as a function of altitude for all wavelengths and with no scattering or surface albedo.

Figure K-14. N_2O_5 photolysis rate as a function of altitude for all wavelengths and with no scattering or surface albedo.

Figure K-15. NO_2 photolysis rate as a function of altitude for all wavelengths and with no scattering or surface albedo.

Figure K-16. As in Figure K-15 except with scattering and surface albedo included.

Figure K-17. Ratio of photolysis of NO_2 for scattering to that with no scattering included.

Figure K-18a. NO_3 photolysis rate as a function of altitude for all wavelengths and with no scattering or surface albedo.

Figure K-18b. As in Figure K-18a except with scattering and surface albedo included.

Figure K-19. Diurnal average of O_2 photolysis rate for all wavelengths with scattering and surface albedo included.

Figure K-20. Diurnal average of NO photolysis rate for all wavelengths with scattering and surface albedo included.

Figure K-21. Diurnal average of NO_2 photolysis rate for all wavelengths with scattering and surface albedo included.

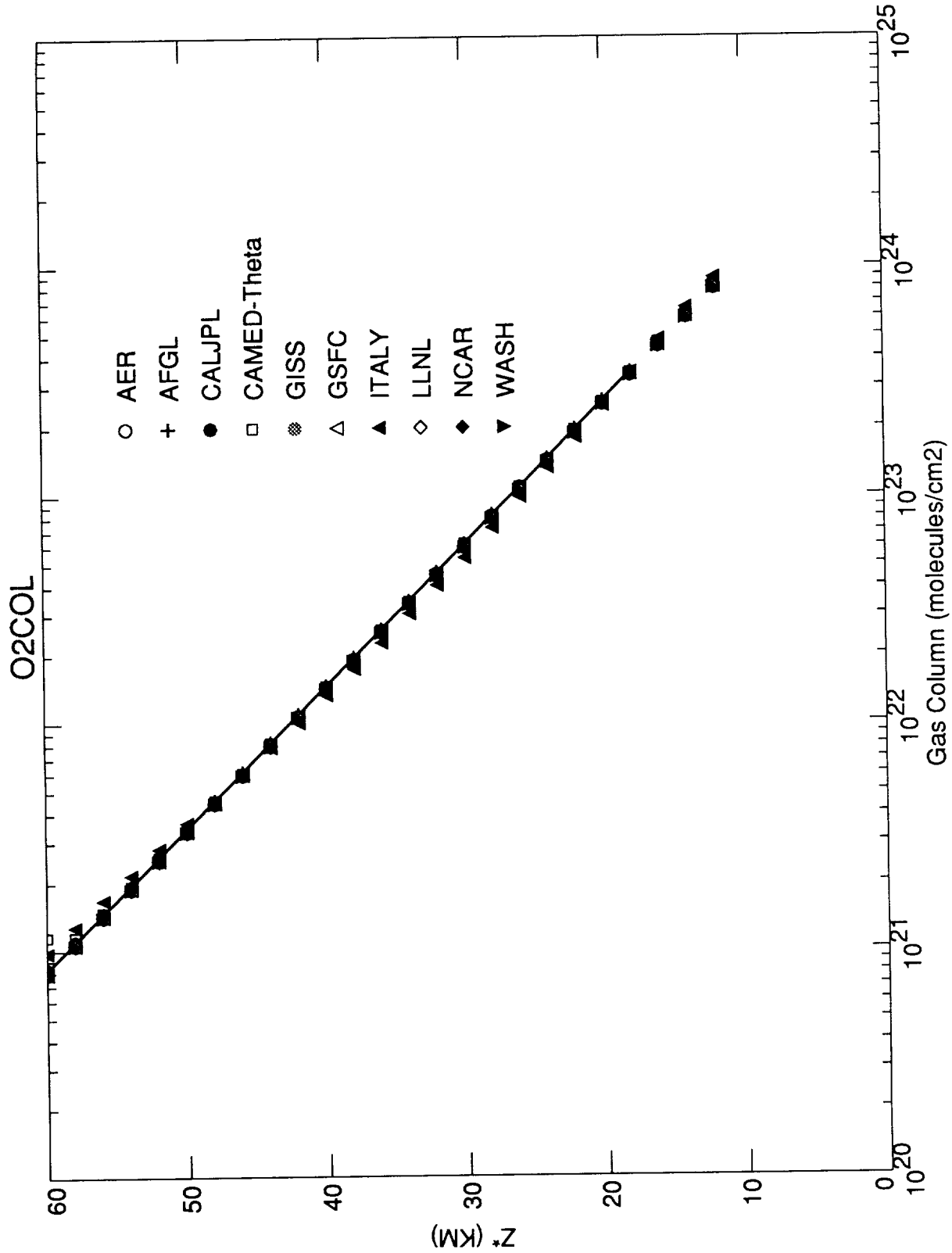
O2COL
AER
AFGL
CALJPL
CAMED-Theta
GISS
GSFC
ITALY
LLNL
NCAR
WASH
Z* (KM)
0
10
20
30
40
50
60
Gas Column (molecules/cm2)
10^{20}
10^{21}
10^{22}
10^{23}
10^{24}
10^{25}

Figure K-1

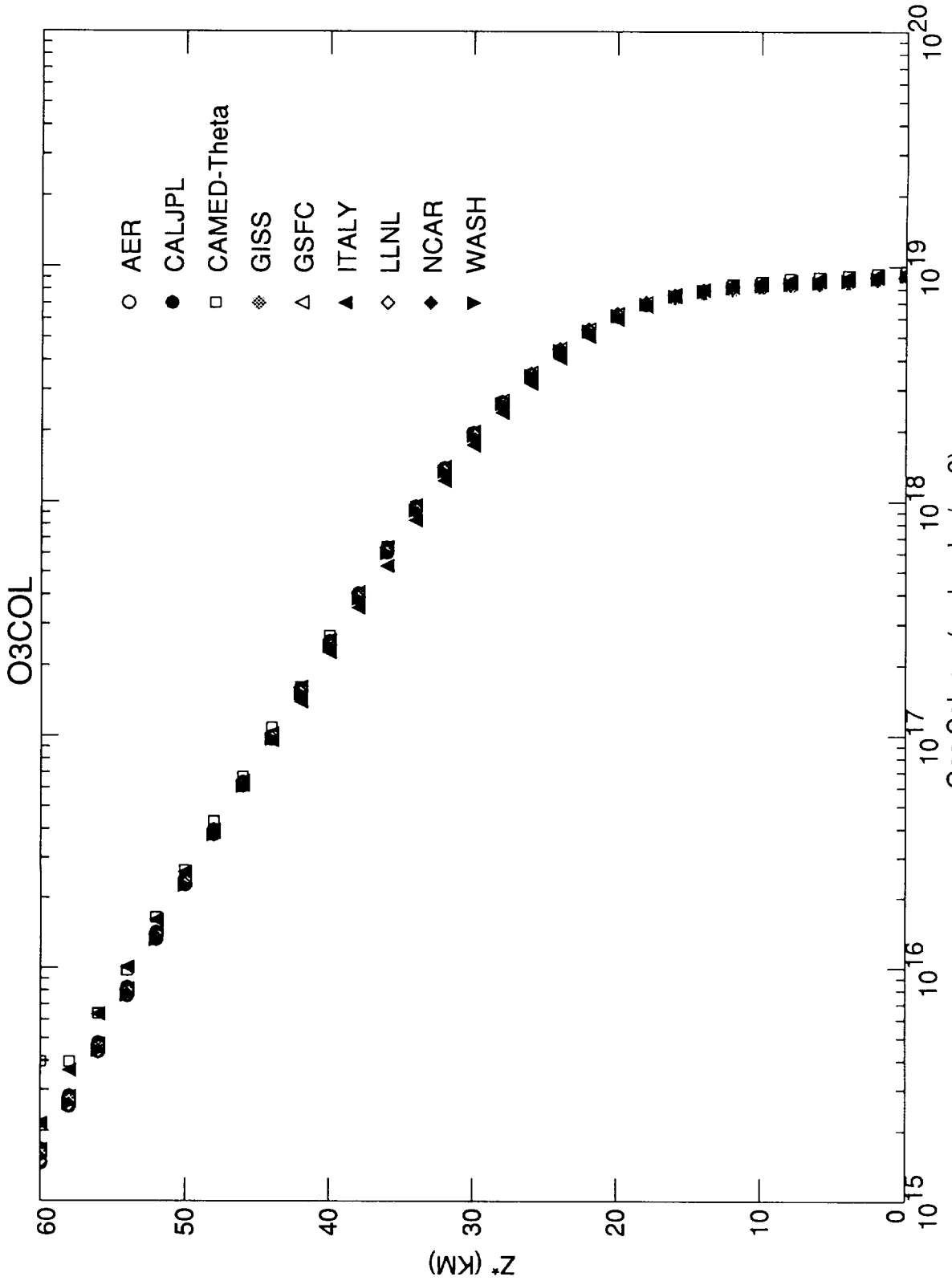
O3COL
AER
CALJPL
CAMED-Theta
GISS
GSFC
ITALY
LLNL
NCAR
WASH
Z* (KM)
Gas Column (molecules/cm2)
0
10
20
30
40
50
60
10^15
10^16
10^17
10^18
10^19
10^20

Figure K-2

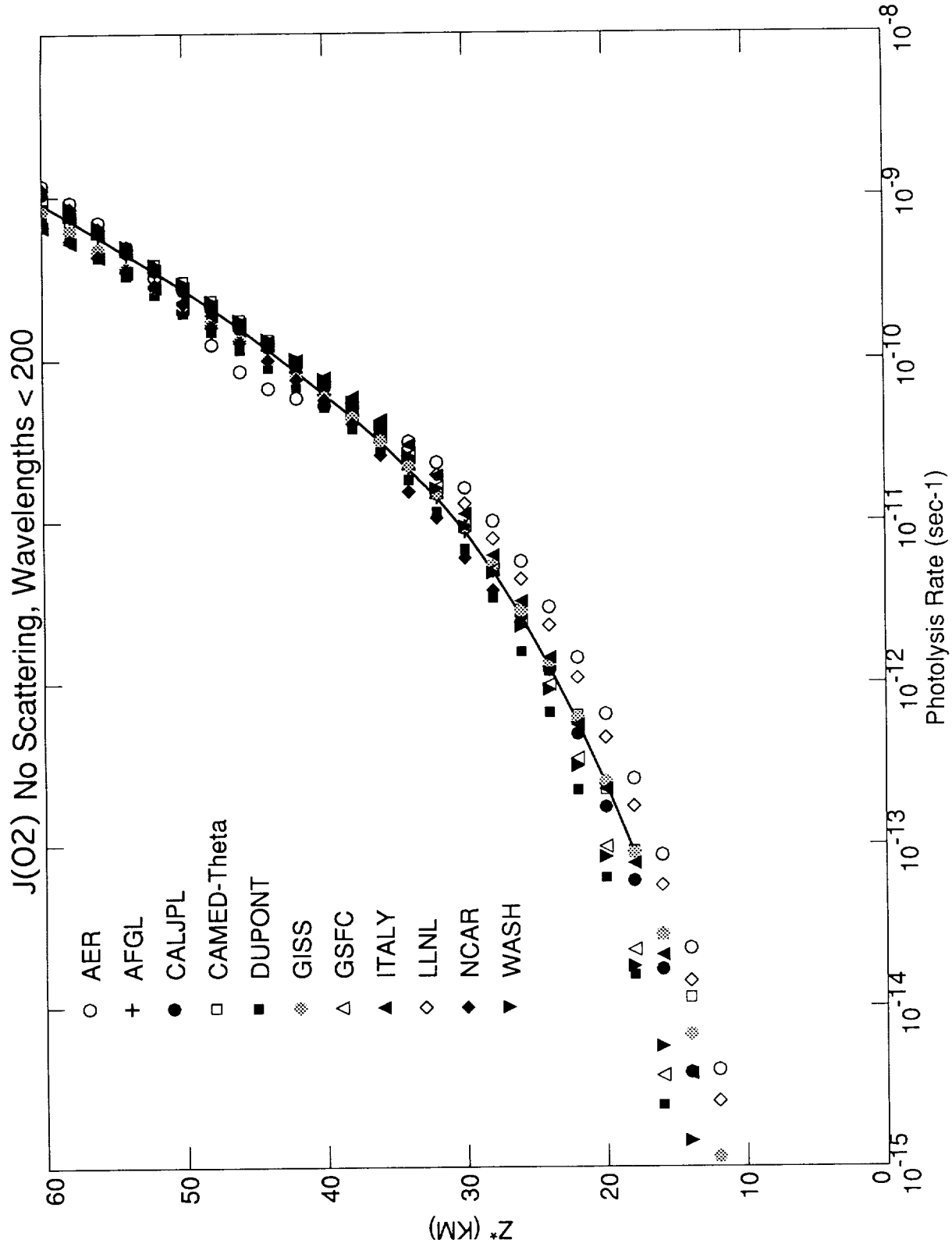
J(O2) No Scattering, Wavelengths < 200
AER
AFGL
CALJPL
CAMED-Theta
DUPONT
GISS
GSFC
ITALY
LLNL
NCAR
WASH
Z* (KM)
Photolysis Rate (sec-1)
60
50
40
30
20
10
0
10-15
10-14
10-13
10-12
10-11
10-10
10-9
10-8

Figure K-3 a

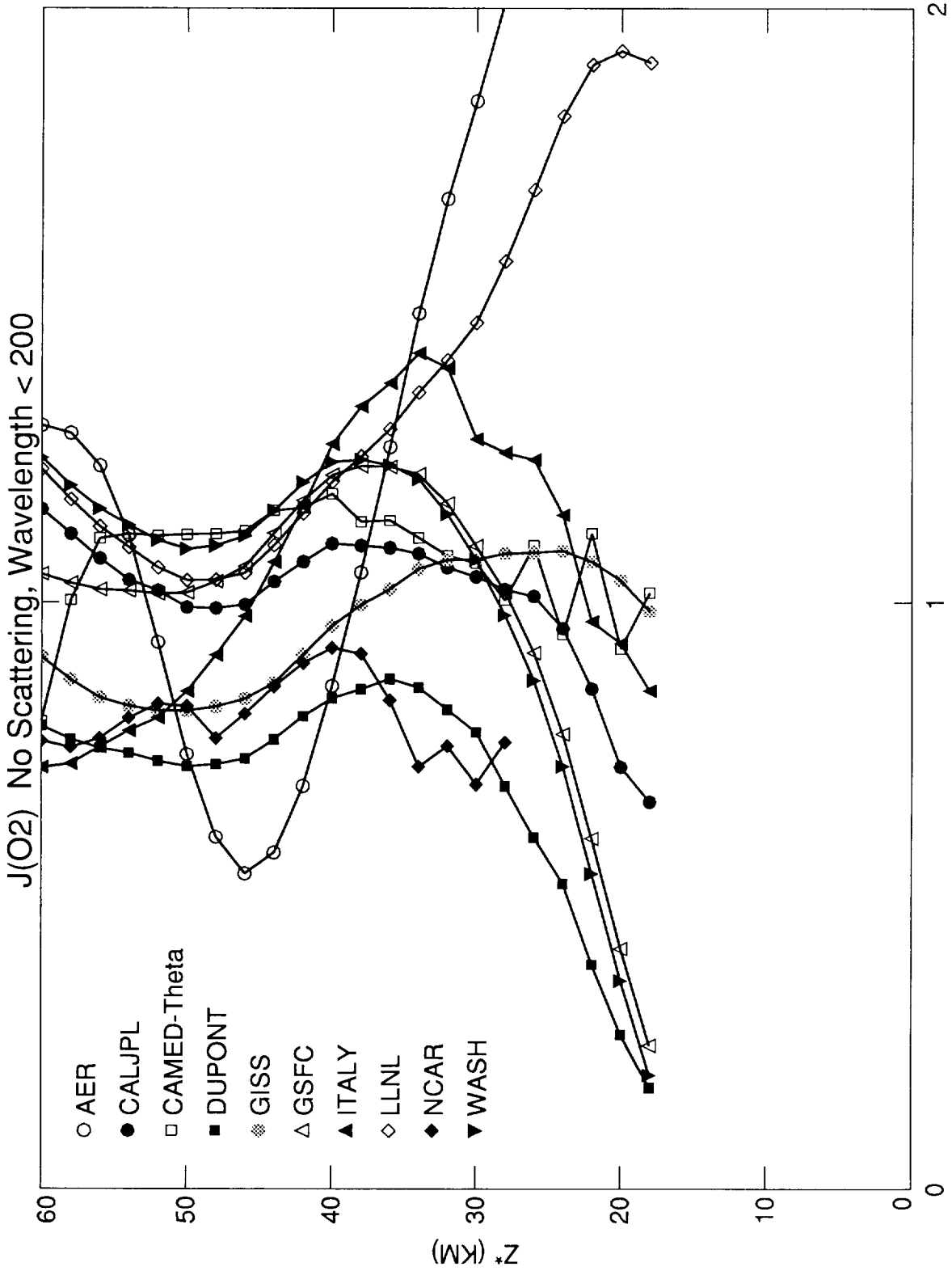

Figure K-3 b

C-3

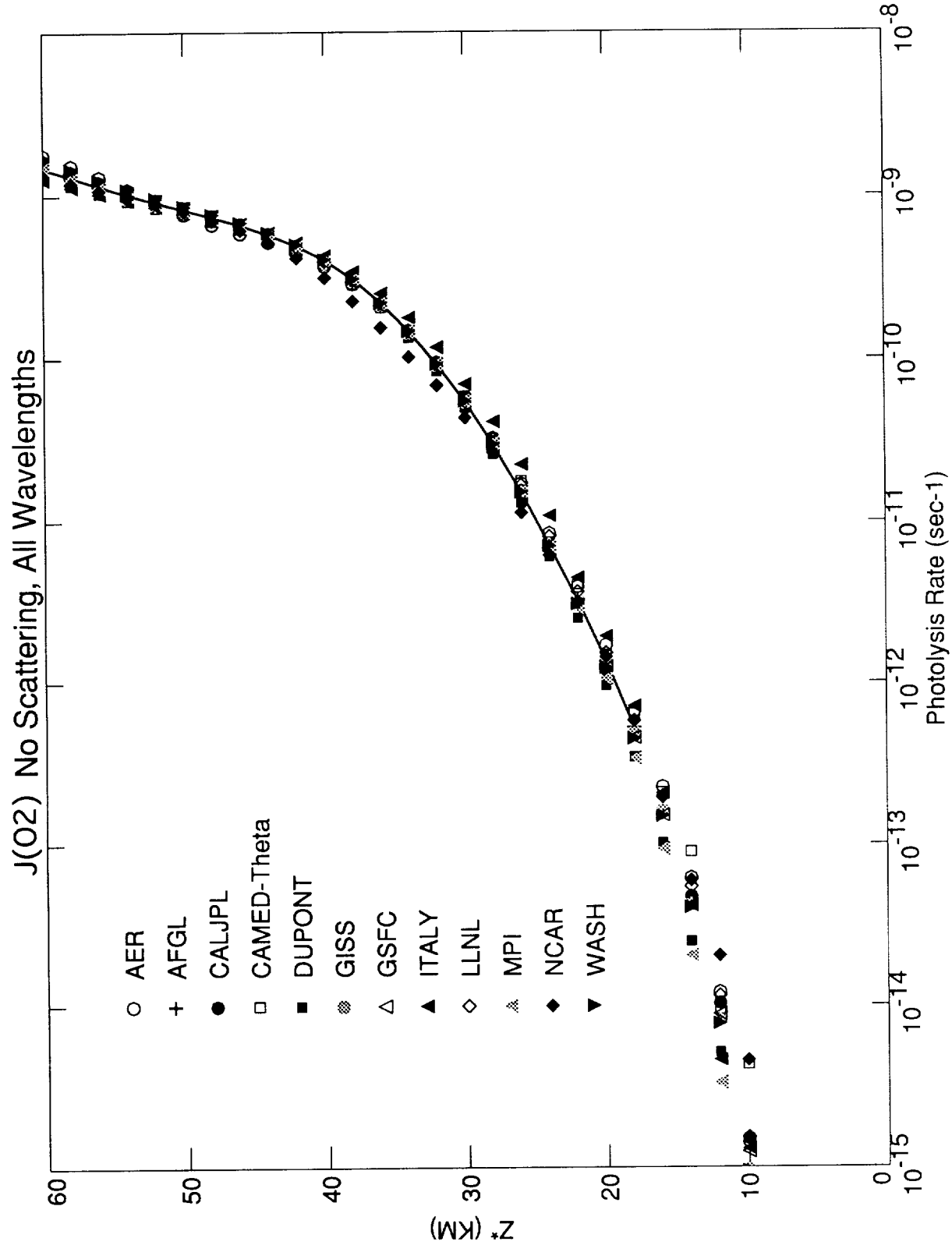
J(O2) No Scattering, All Wavelengths
AER
AFGL
CALJPL
CAMED-Theta
DUPONT
GISS
GSFC
ITALY
LLNL
MPI
NCAR
WASH
Z* (KM)
Photolysis Rate (sec-1)
0
10
20
30
40
50
60
10-15
10-14
10-13
10-12
10-11
10-10
10-9
10-8

Figure K-4 a

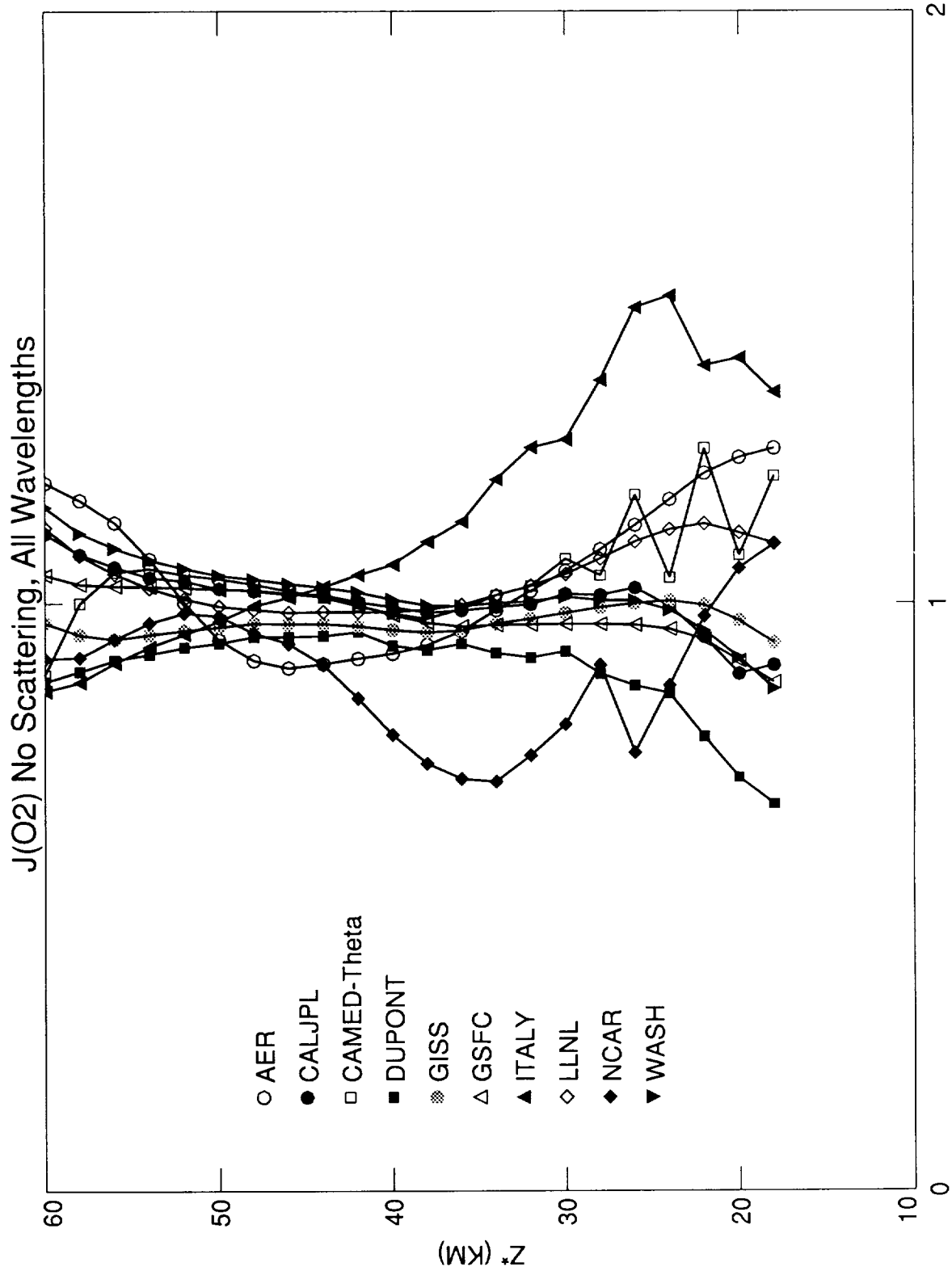
J(O2) No Scattering, All Wavelengths
Z* (KM)
Model/AFGL Ratio
60
50
40
30
20
10
0
1
2
AER
CALJPL
CAMED-Theta
DUPONT
GISS
GSFC
ITALY
LLNL
NCAR
WASH

Figure K-4 b

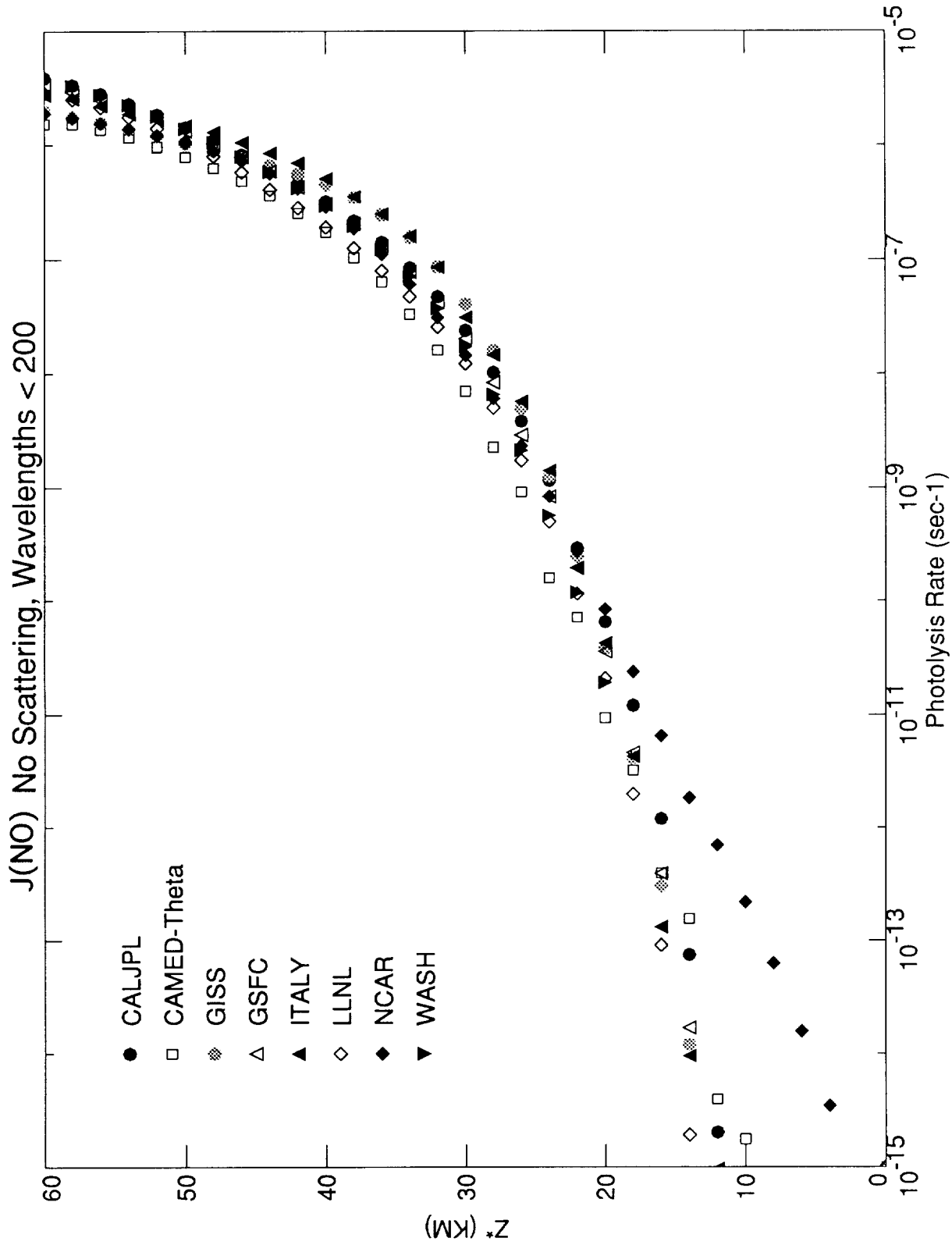
J(NO) No Scattering, Wavelengths < 200
CALJPL
CAMED-Theta
GISS
GSFC
ITALY
LLNL
NCAR
WASH
Z* (KM)
Photolysis Rate (sec-1)
0
10
20
30
40
50
60
10-15
10-13
10-11
10-9
10-7
10-5

Figure K-5 a

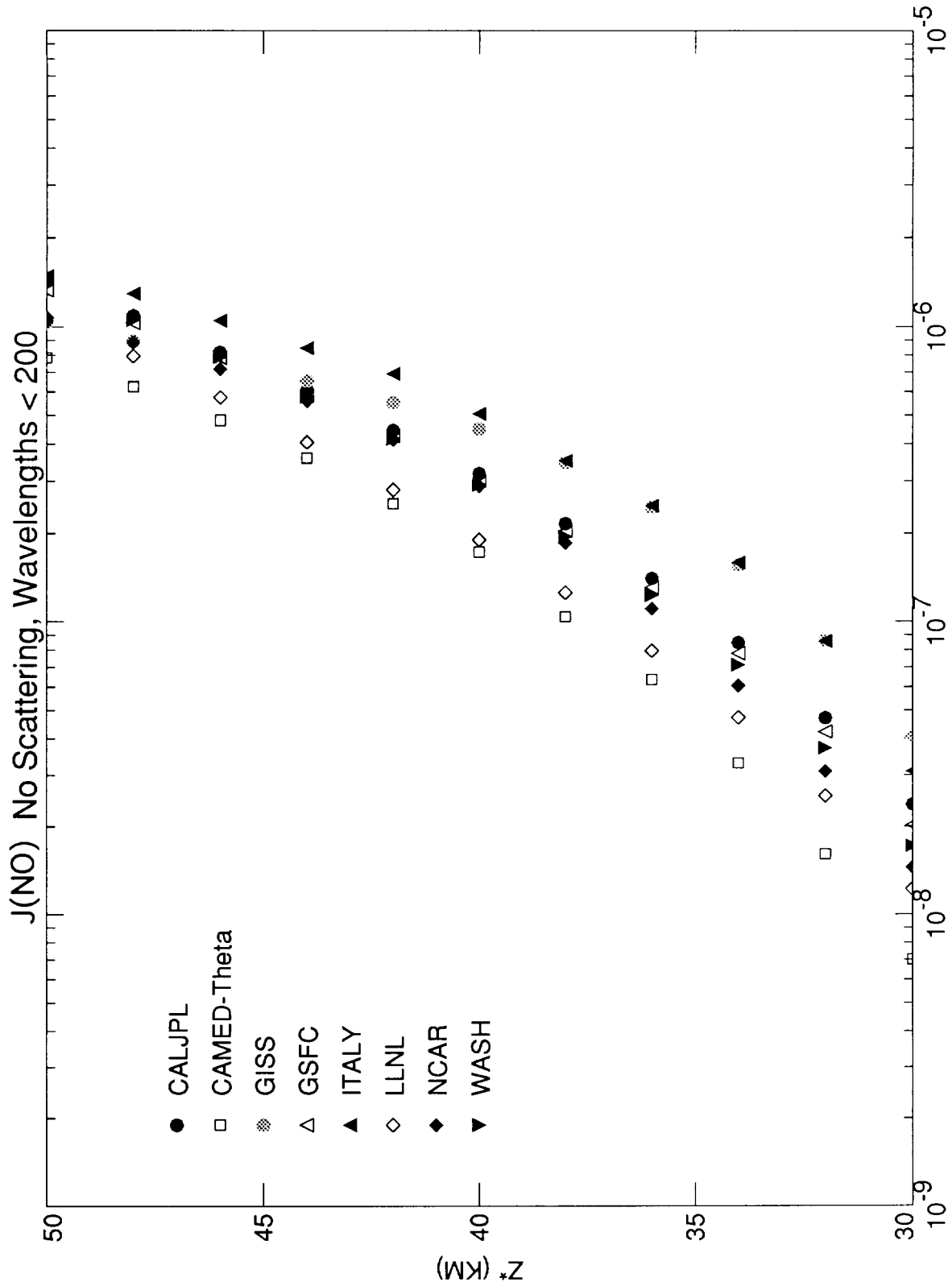
J(NO) No Scattering, Wavelengths < 200
CALJPL
CAMED-Theta
GISS
GSFC
ITALY
LLNL
NCAR
WASH
Z* (KM)
Photolysis Rate (sec-1)
50
45
40
35
30
10-9
10-8
10-7
10-6
10-5

Figure K-5 b

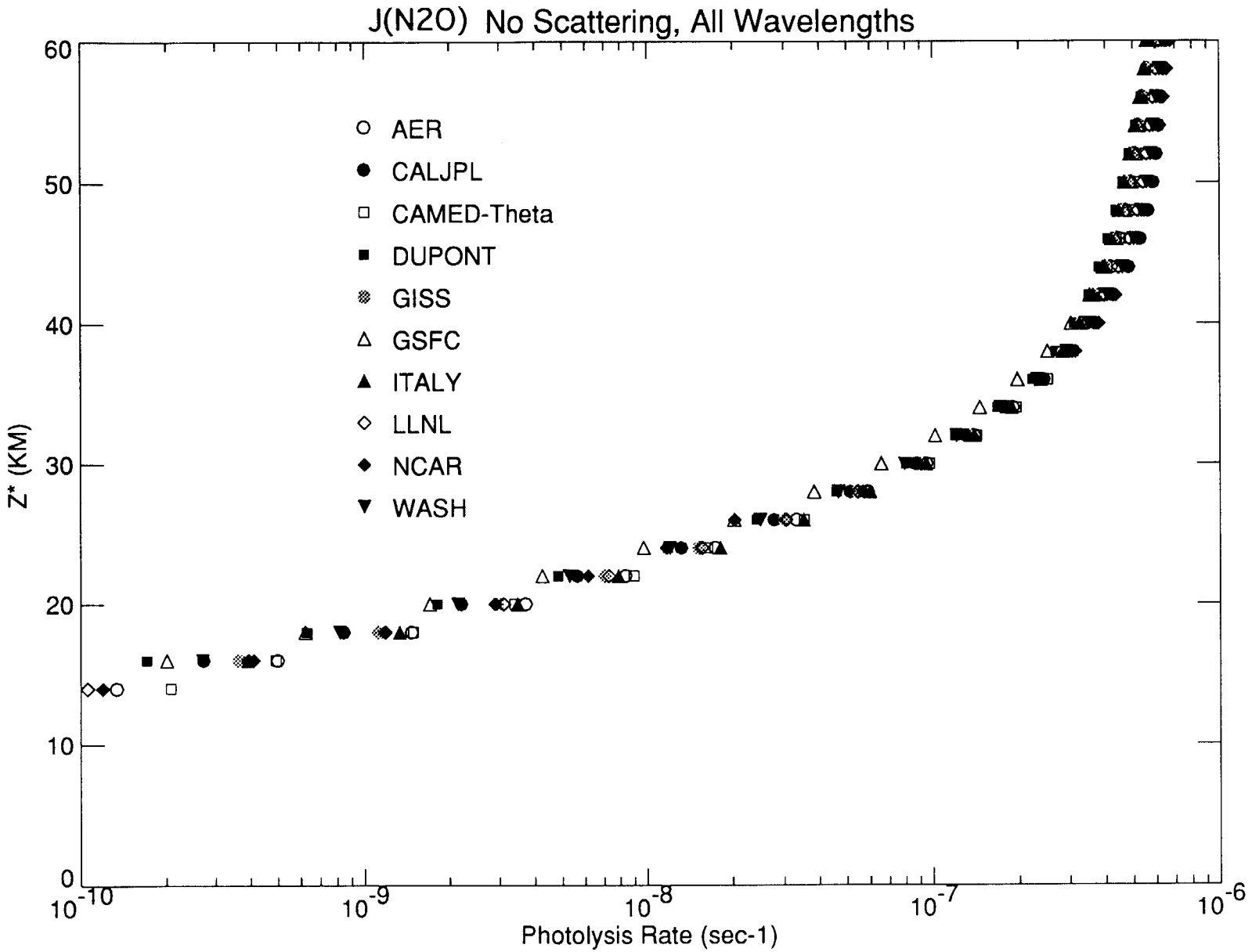
J(N2O) No Scattering, All Wavelengths
AER
CALJPL
CAMED-Theta
DUPONT
GISS
GSFC
ITALY
LLNL
NCAR
WASH
Z* (KM)
Photolysis Rate (sec-1)
0
10
20
30
40
50
60
10-10
10-9
10-8
10-7
10-6

Figure K-6

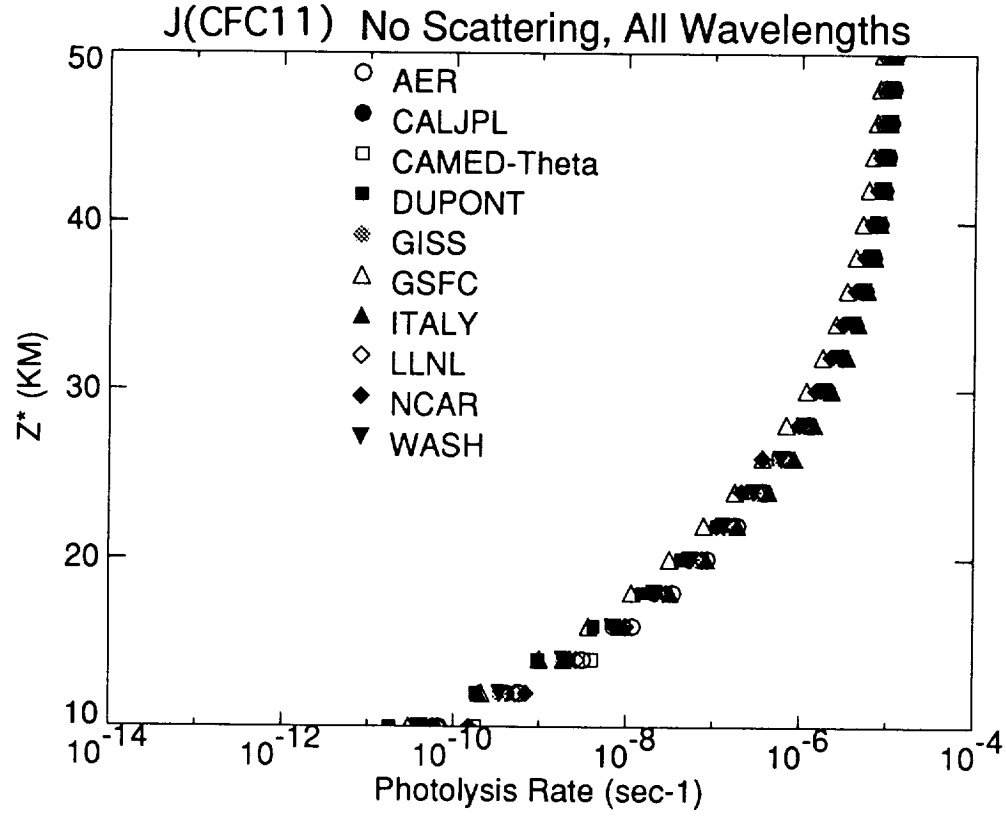

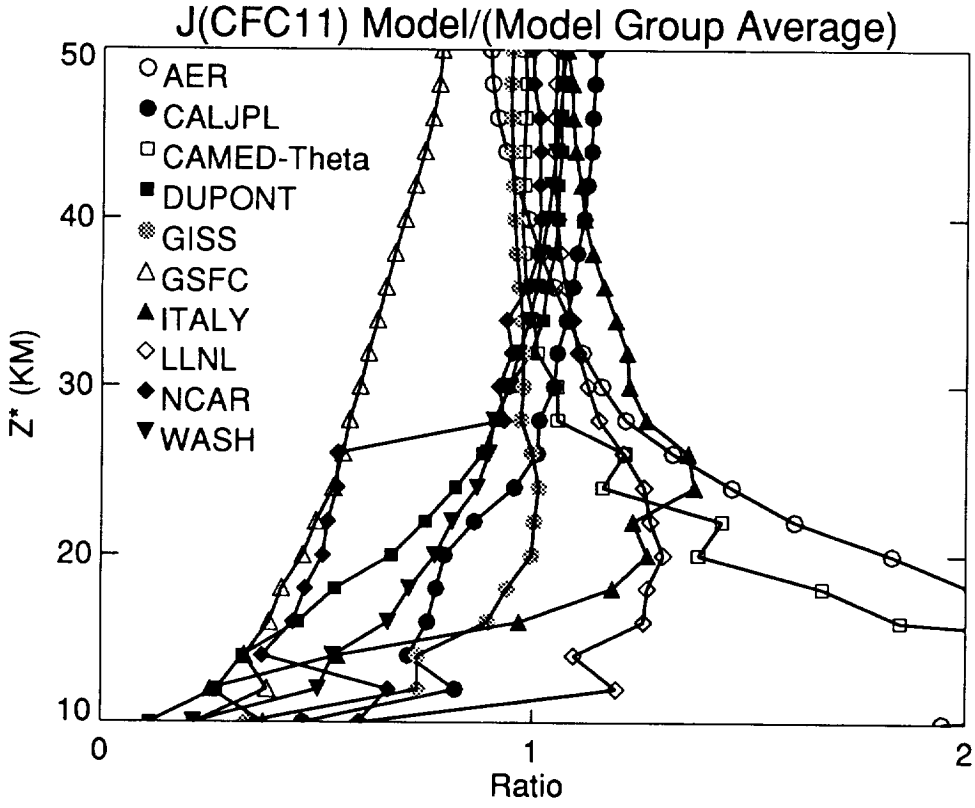

Figure K-7a (top) **Figure K-7b (bottom)**

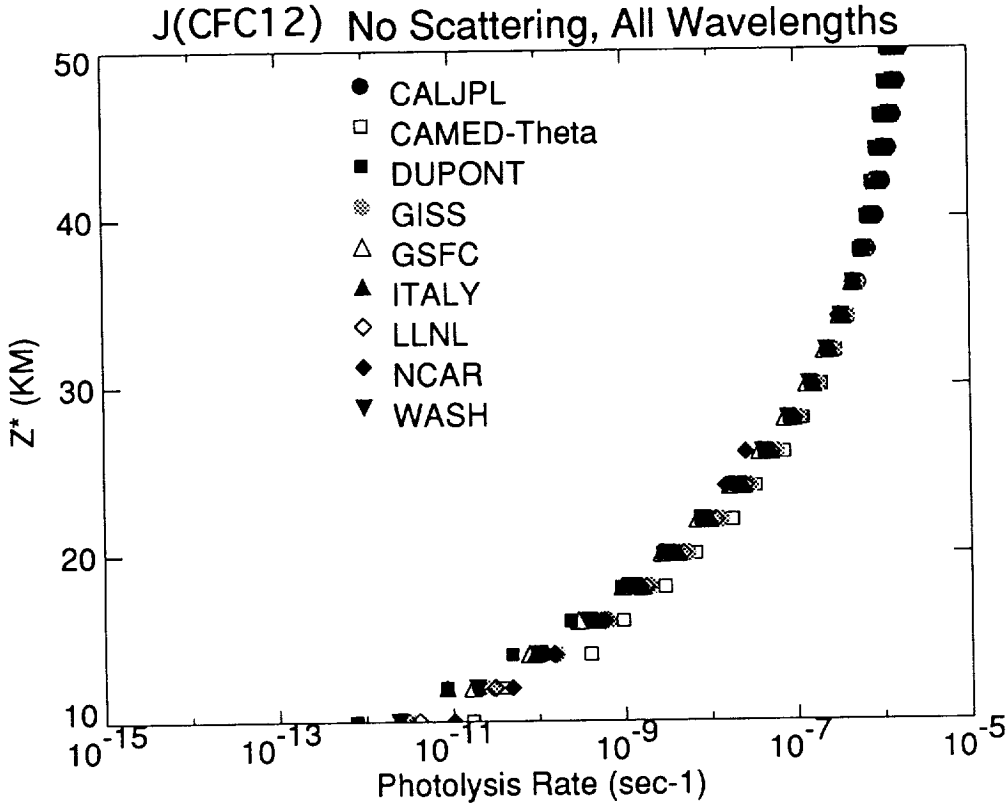

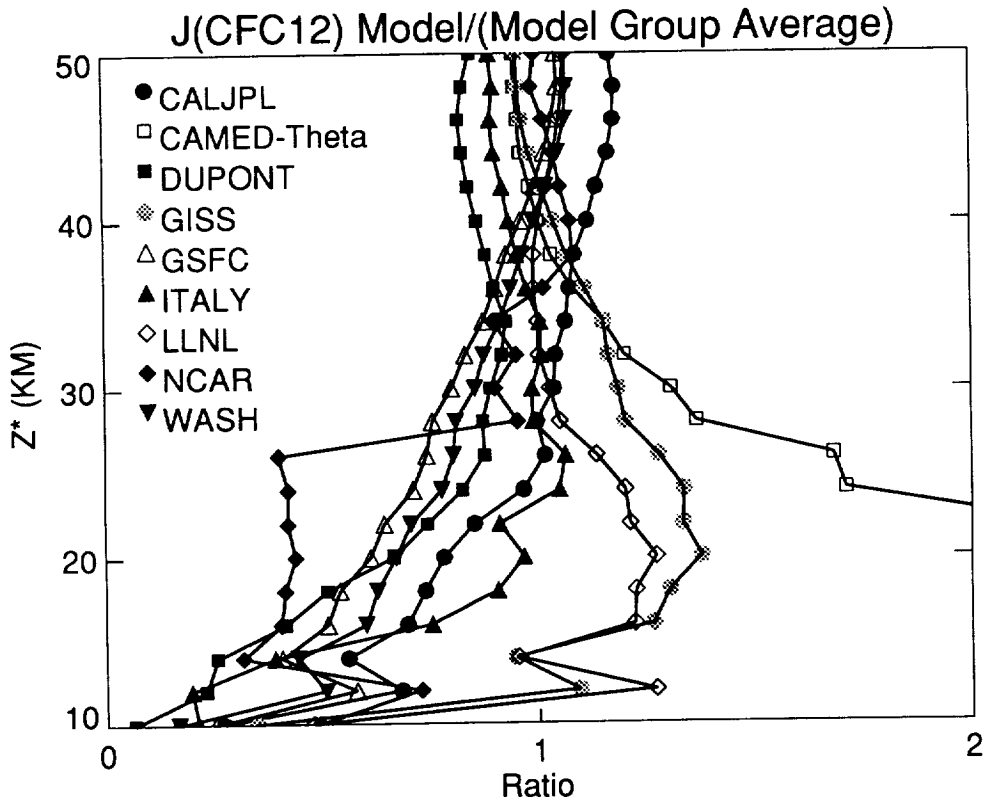

Figure K-8a (top) **Figure K-8b (bottom)**

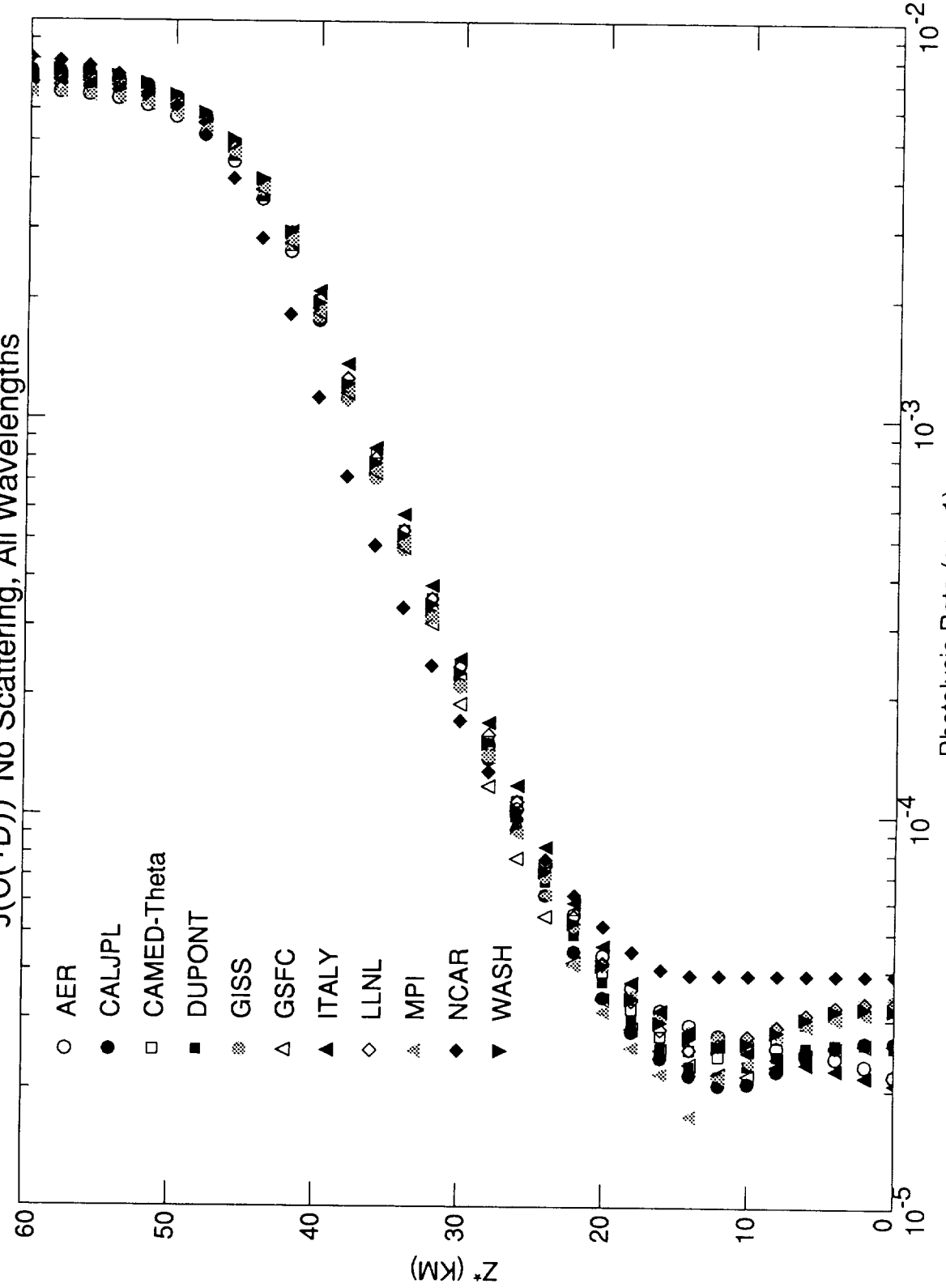
J(O(1D)) No Scattering, All Wavelengths
AER
CALJPL
CAMED-Theta
DUPONT
GISS
GSFC
ITALY
LLNL
MPI
NCAR
WASH
Z* (KM)
Photolysis Rate (sec-1)
0
10
20
30
40
50
60
10-5
10-4
10-3
10-2

Figure K-9

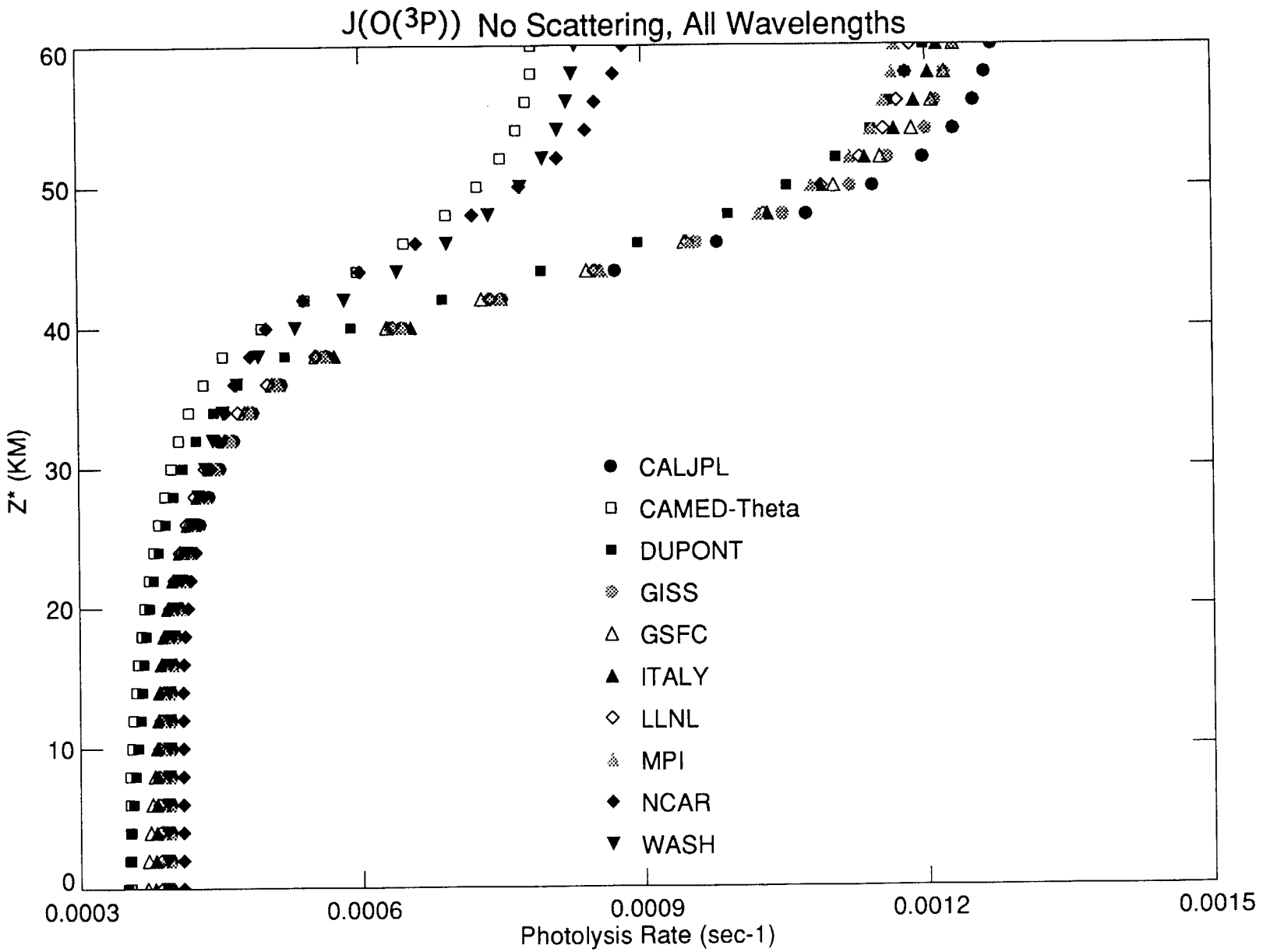
J(O(3P)) No Scattering, All Wavelengths
Z* (KM)
Photolysis Rate (sec-1)
0
10
20
30
40
50
60
0.0003
0.0006
0.0009
0.0012
0.0015
CALJPL
CAMED-Theta
DUPONT
GISS
GSFC
ITALY
LLNL
MPI
NCAR
WASH

Figure K-10

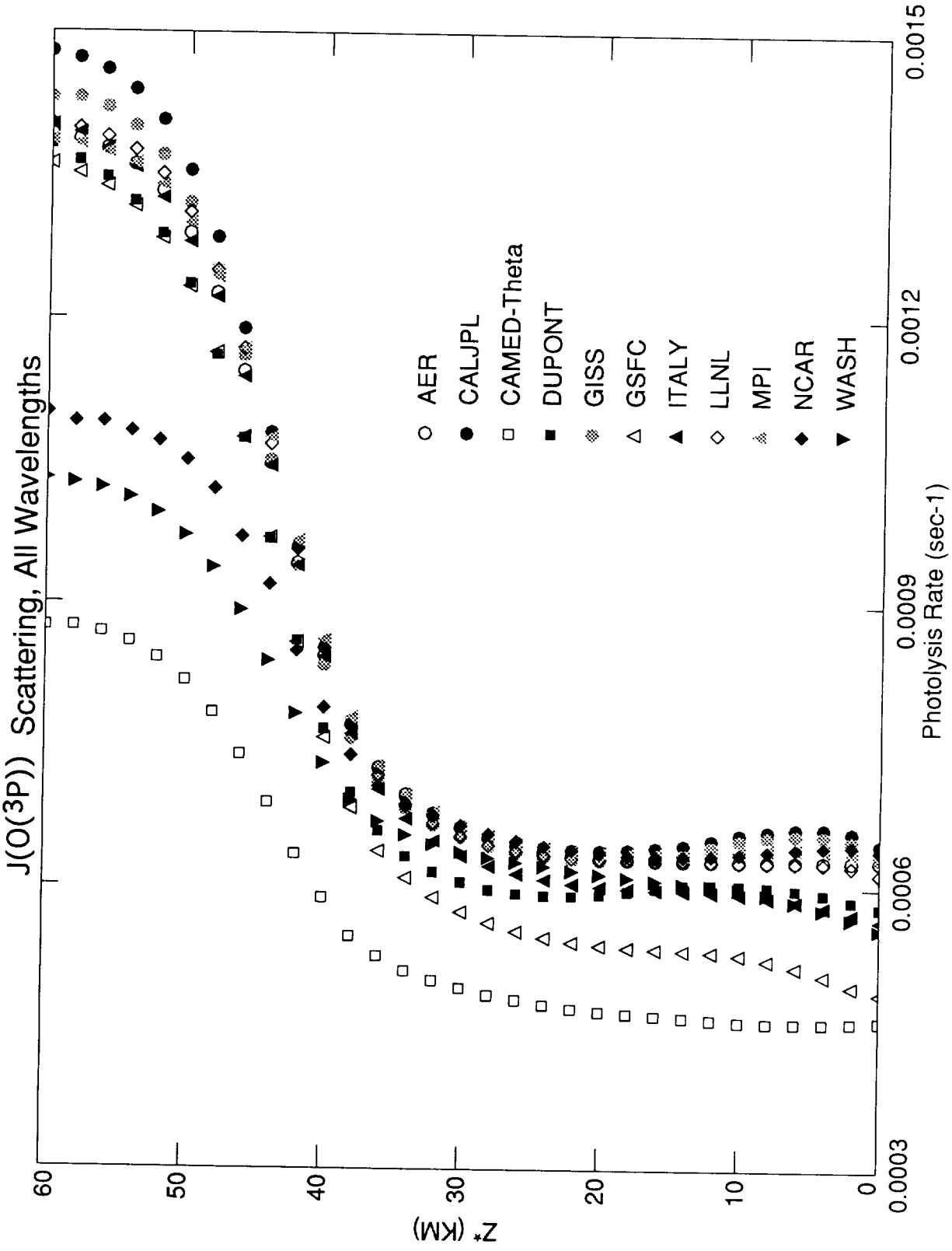
J(O(3P)) Scattering, All Wavelengths
Z* (KM)
Photolysis Rate (sec-1)
0.0003
0.0006
0.0009
0.0012
0.0015
0
10
20
30
40
50
60
AER
CALJPL
CAMED-Theta
DUPONT
GISS
GSFC
ITALY
LLNL
MPI
NCAR
WASH

Figure K-11

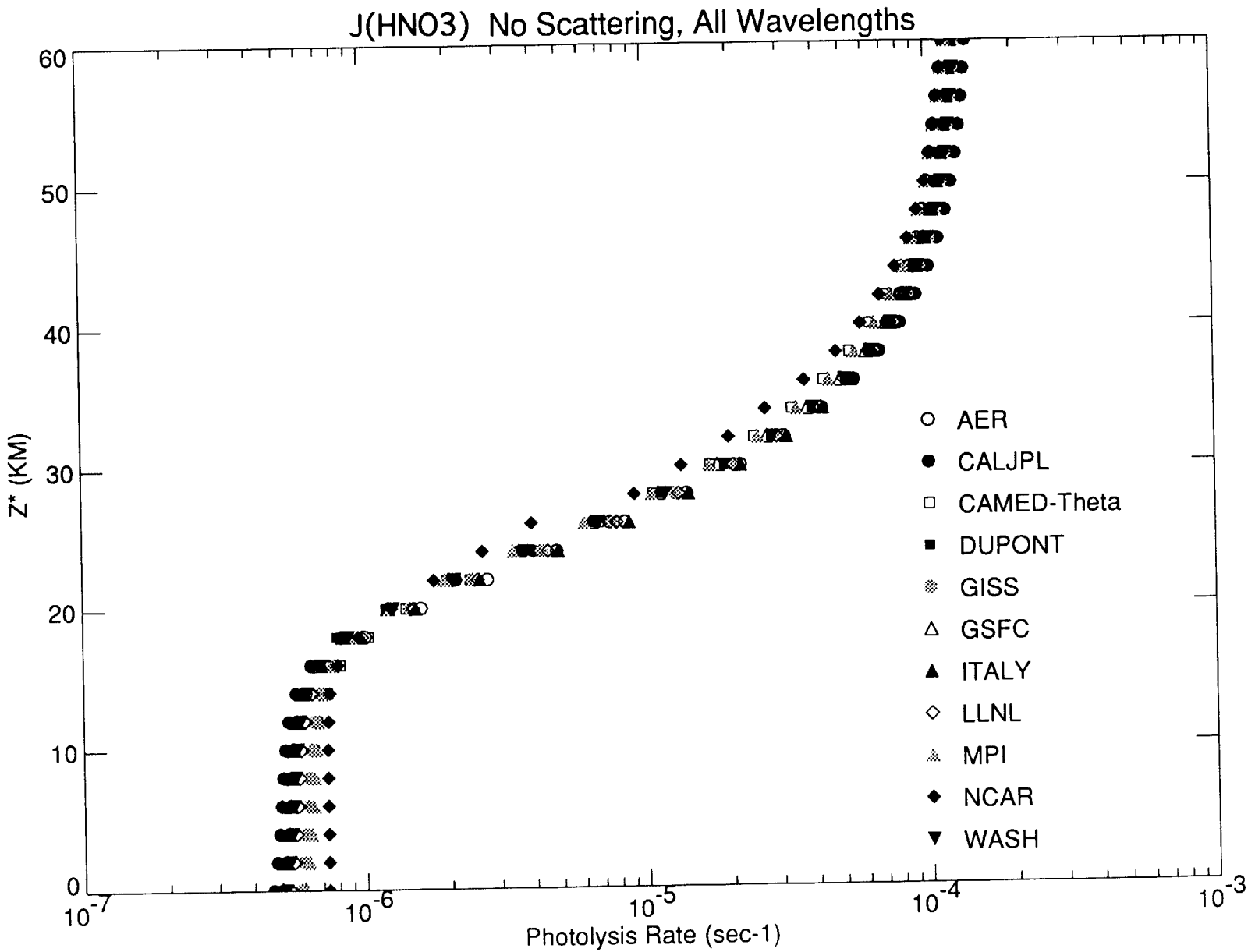
J(HNO3) No Scattering, All Wavelengths
Z* (KM)
60
50
40
30
20
10
0
10^{-7}
10^{-6}
10^{-5}
10^{-4}
10^{-3}
Photolysis Rate (sec-1)
AER
CALJPL
CAMED-Theta
DUPONT
GISS
GSFC
ITALY
LLNL
MPI
NCAR
WASH

Figure K-12

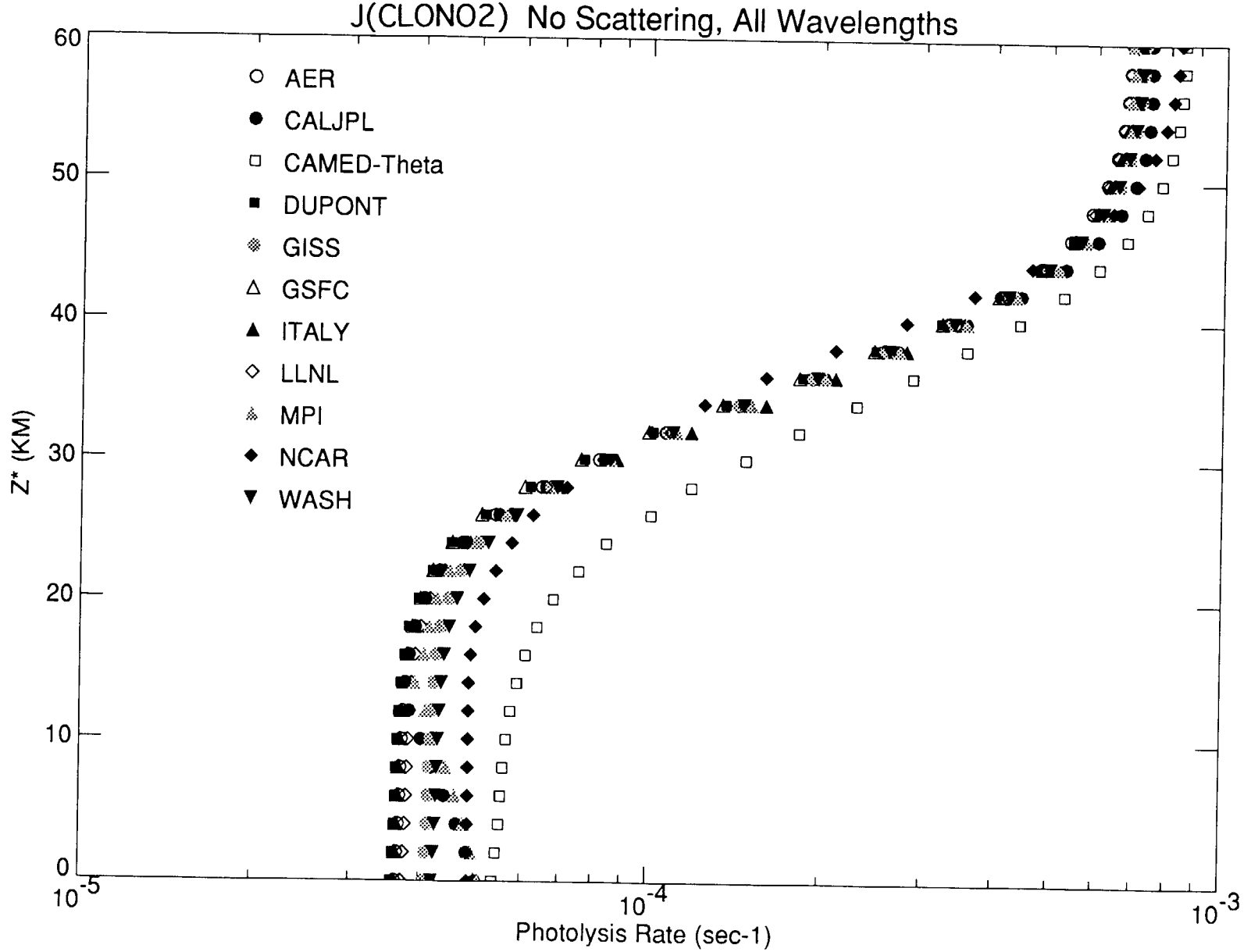
J(CLONO2) No Scattering, All Wavelengths
AER
CALJPL
CAMED-Theta
DUPONT
GISS
GSFC
ITALY
LLNL
MPI
NCAR
WASH
Z* (KM)
60
50
40
30
20
10
0
10^-5
10^-4
10^-3
Photolysis Rate (sec-1)

Figure K-13

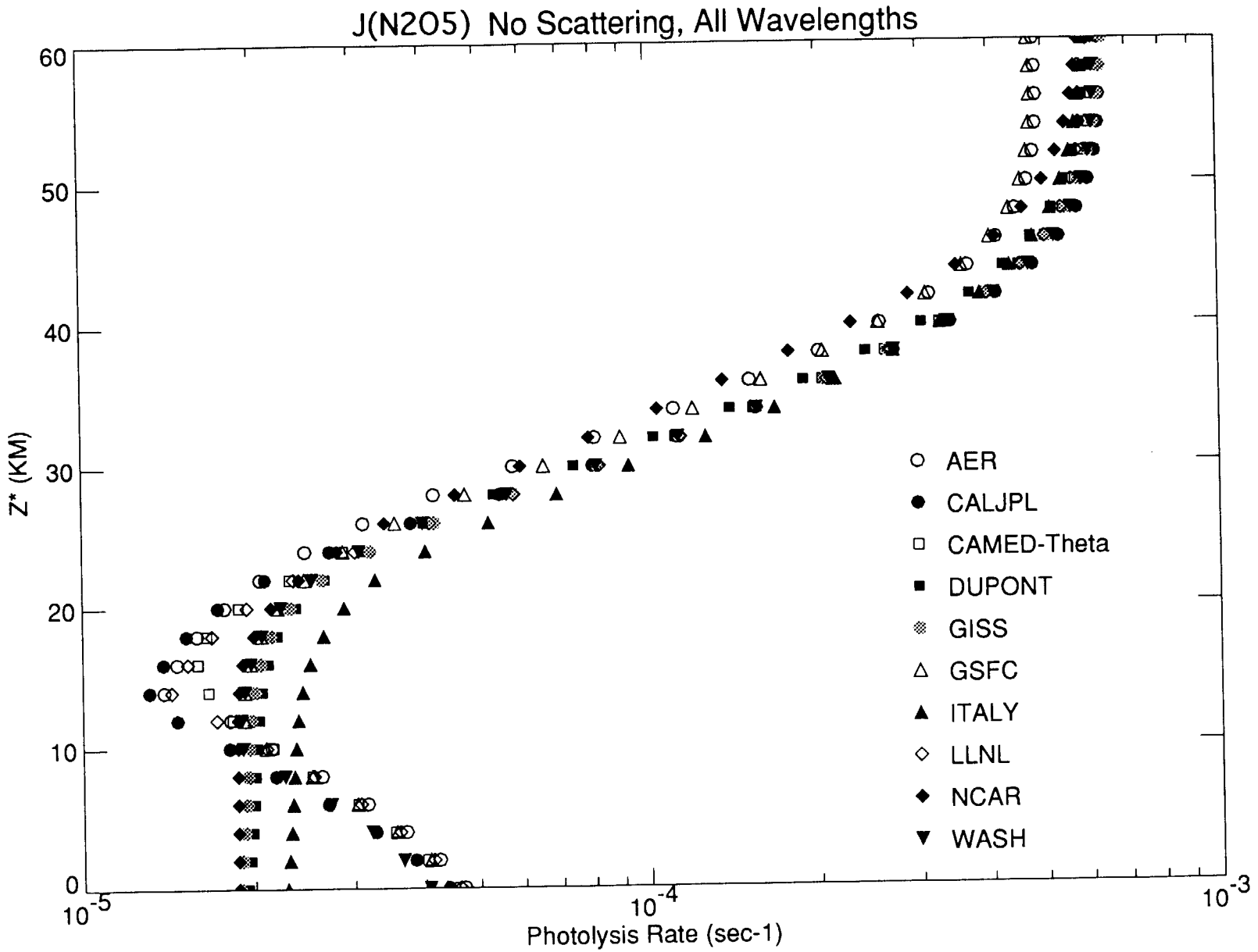
J(N2O5) No Scattering, All Wavelengths
Z* (KM)
60
50
40
30
20
10
0
10-5
10-4
10-3
Photolysis Rate (sec-1)
AER
CALJPL
CAMED-Theta
DUPONT
GISS
GSFC
ITALY
LLNL
NCAR
WASH

Figure K-14

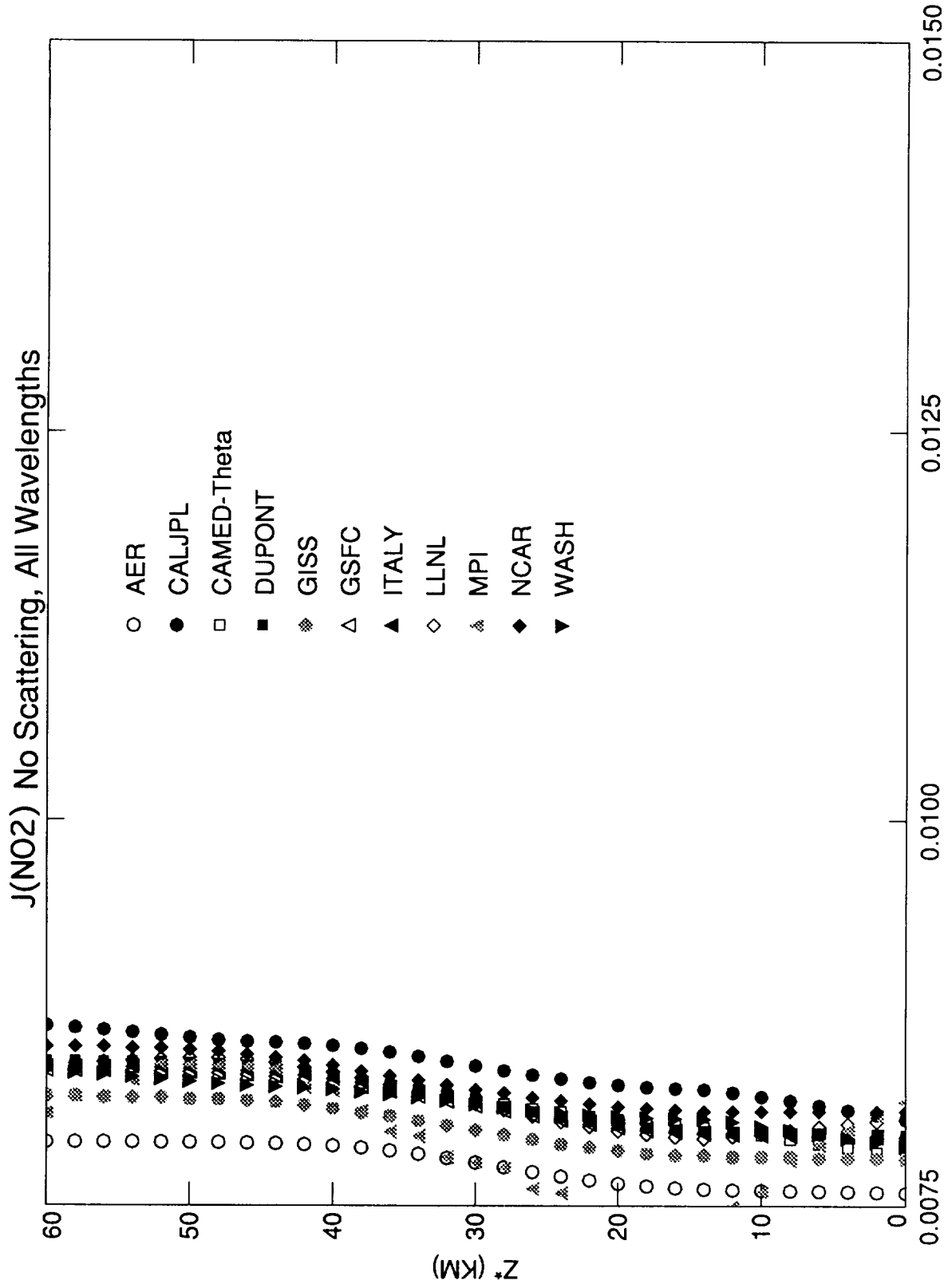
J(NO2) No Scattering, All Wavelengths
AER
CALJPL
CAMED-Theta
DUPONT
GISS
GSFC
ITALY
LLNL
MPI
NCAR
WASH
Z* (KM)
0
10
20
30
40
50
60
0.0075
0.0100
0.0125
0.0150
Photolysis Rate (sec-1)

Figure K-15

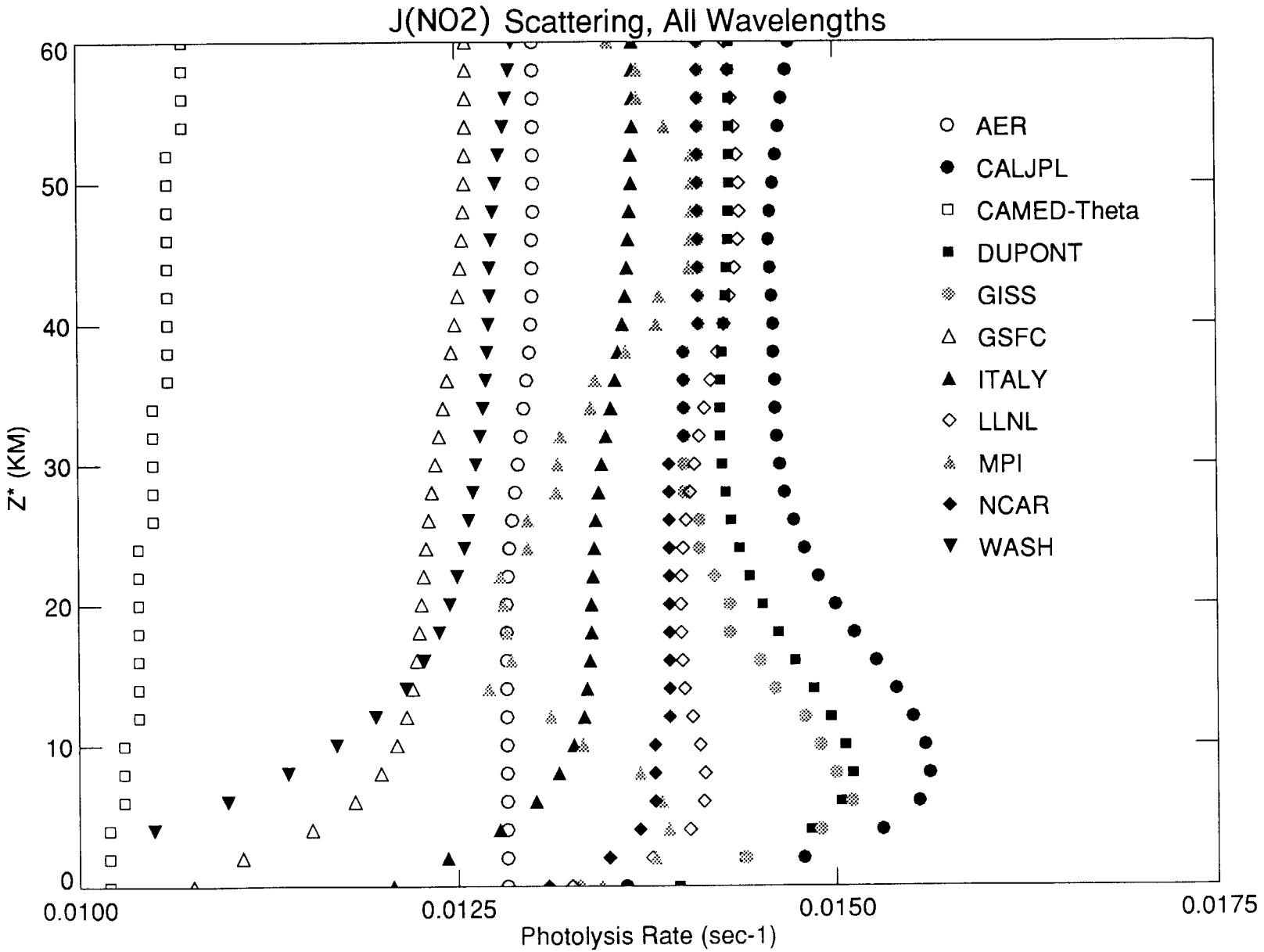
J(NO2) Scattering, All Wavelengths
Z* (KM)
Photolysis Rate (sec-1)
0
10
20
30
40
50
60
0.0100
0.0125
0.0150
0.0175
AER
CALJPL
CAMED-Theta
DUPONT
GISS
GSFC
ITALY
LLNL
MPI
NCAR
WASH

Figure K-16

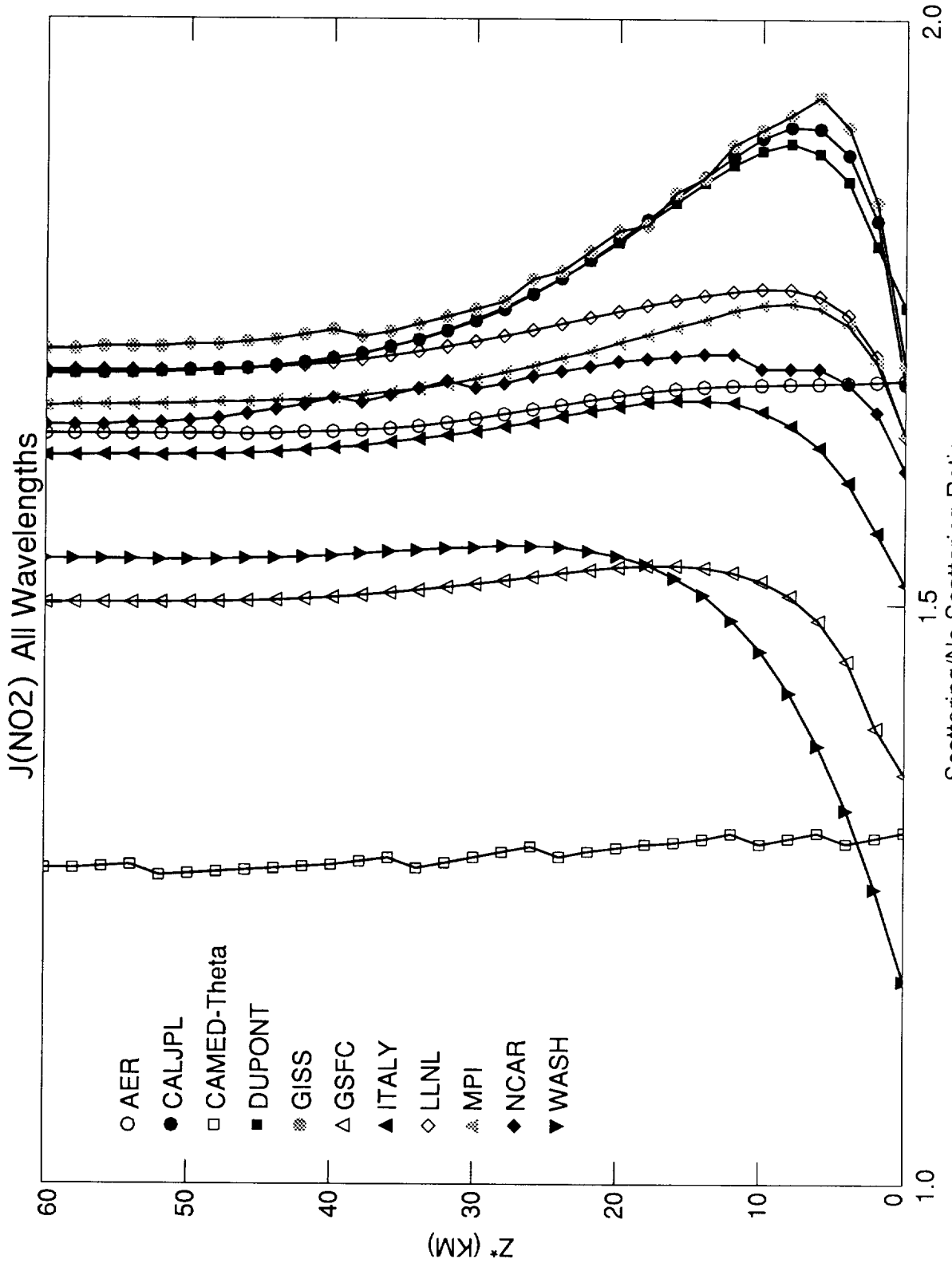
J(NO2) All Wavelengths
Z* (KM)
Scattering/No Scattering Ratio
0
10
20
30
40
50
60
1.0
1.5
2.0
AER
CALJPL
CAMED-Theta
DUPONT
GISS
GSFC
ITALY
LLNL
MPI
NCAR
WASH

Figure K-17

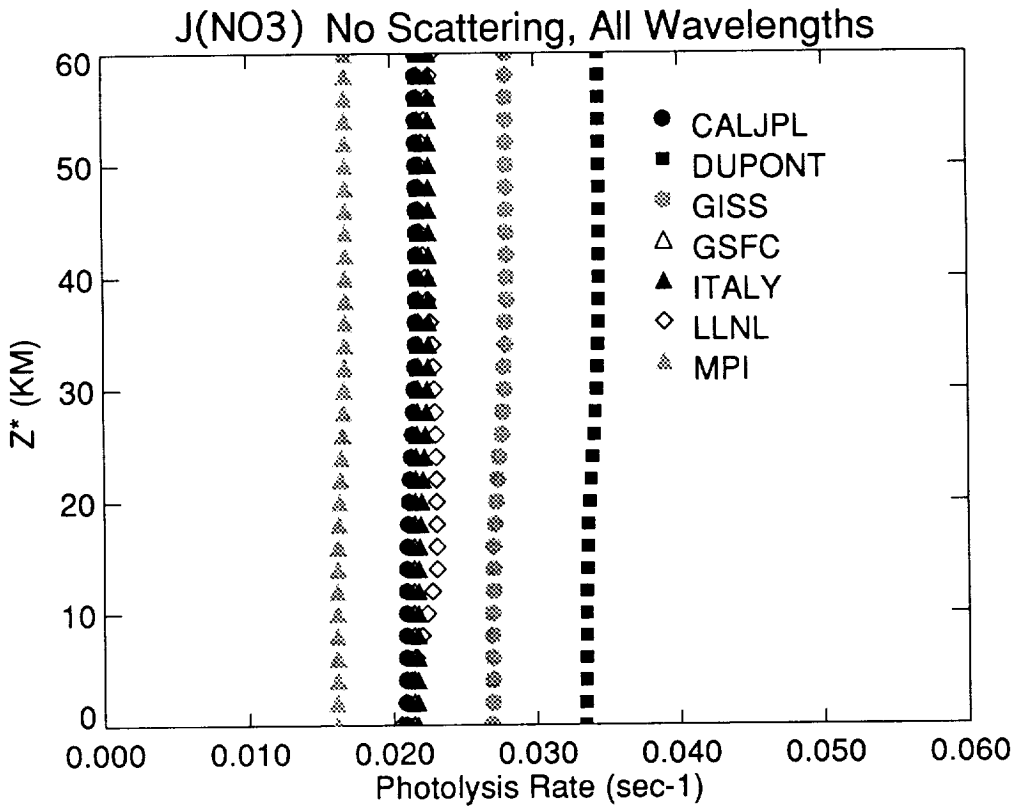

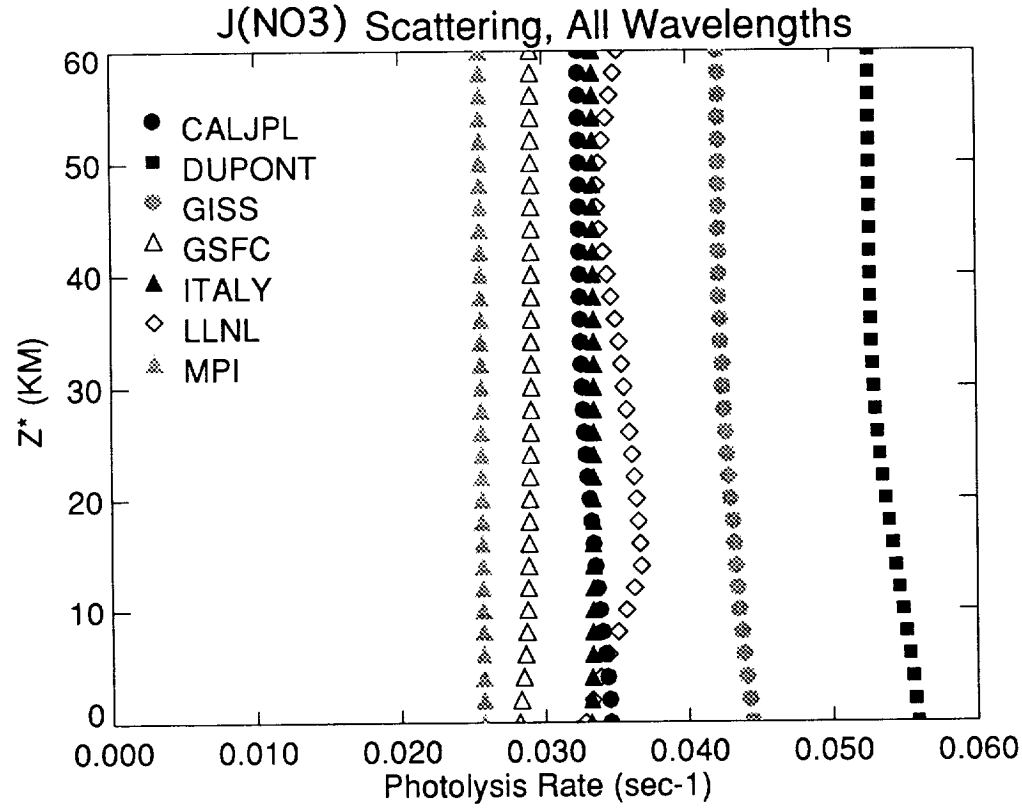

Figure K-18 a (top) **Figure K-18b (bottom)**

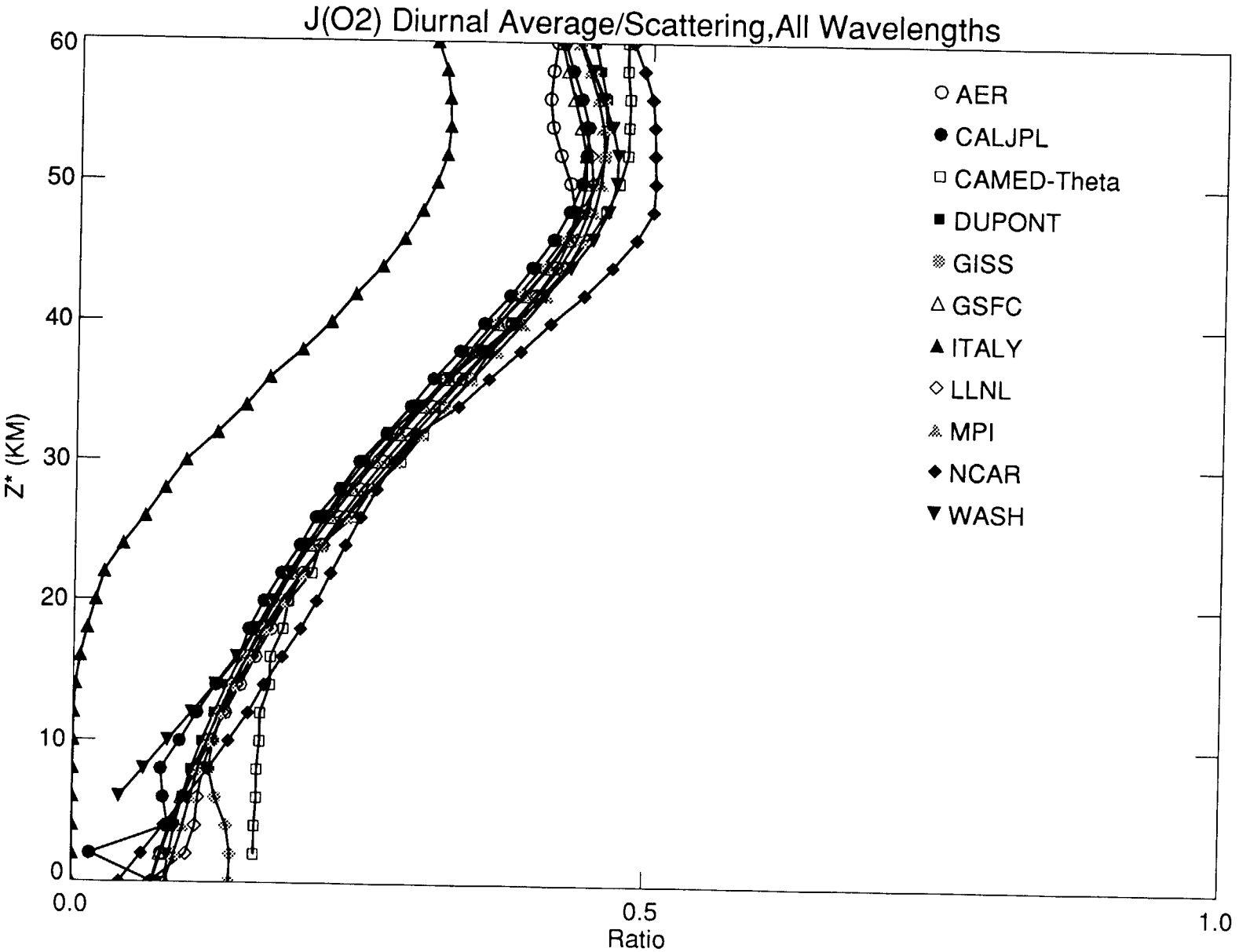
J(O2) Diurnal Average/Scattering,All Wavelengths
Z* (KM)
60
50
40
30
20
10
0
0.0
0.5
1.0
Ratio
AER
CALJPL
CAMED-Theta
DUPONT
GISS
GSFC
ITALY
LLNL
MPI
NCAR
WASH

Figure K-19

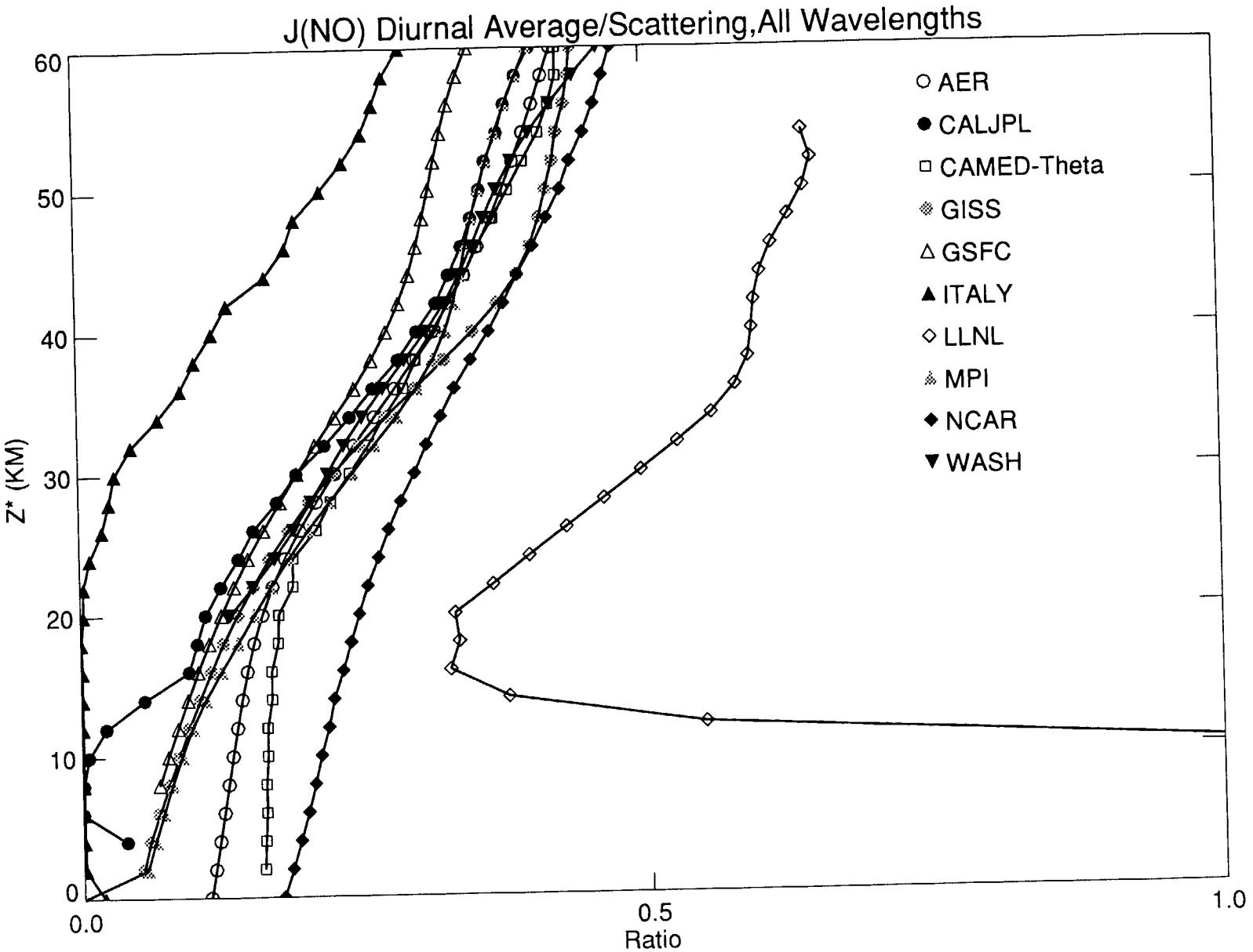
J(NO) Diurnal Average/Scattering,All Wavelengths
Z* (KM)
60
50
40
30
20
10
0
0.0
0.5
1.0
Ratio
AER
CALJPL
CAMED-Theta
GISS
GSFC
ITALY
LLNL
MPI
NCAR
WASH

Figure K-20

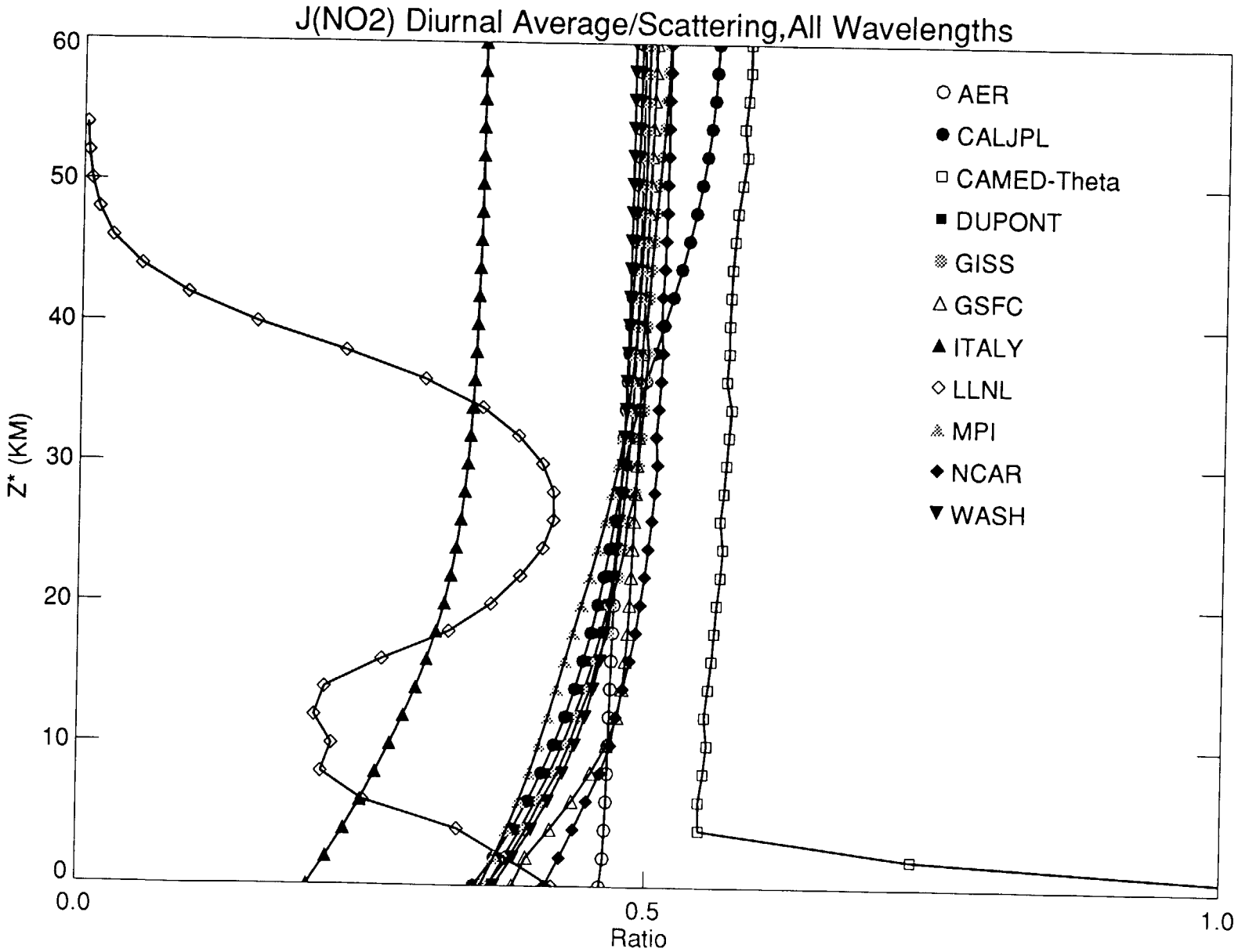
J(NO2) Diurnal Average/Scattering,All Wavelengths
Z* (KM)
60
50
40
30
20
10
0
0.0
0.5
1.0
Ratio
AER
CALJPL
CAMED-Theta
DUPONT
GISS
GSFC
ITALY
LLNL
MPI
NCAR
WASH

Figure K-21

L: Photochemistry of Radicals and Rates

L. Photochemistry of Radicals and Rates

Michael J. Prather
University of California-Irvine

INTRODUCTION

We examine the detailed photochemistry of the stratospheric models using the ATMOS 30N "atmosphere" to define a restricted calculation (*see* Table in KLM Overview section). No measurements are available for such diagnostics (e.g., the 24-hour average rate of reaction of O with NO_2), and thus we are limited to a model-model intercomparison. Nevertheless, this section is a very important check on the models: do we all calculate the same photochemical budgets for ozone given a prescribed atmosphere? The models simulated both gas-phase and heterogeneous sulfate-layer chemistry. We show first the gas-phase-only results and then the relative changes induced by the prescribed heterogeneous chemistry (*see* Table KLM-1).

Noontime Profiles of Radicals: O, O(^{1}D), OH, HO_2, NO, NO_2, ClO.

The density of atomic oxygen in daylight is determined primarily by a balance between photolysis of O_3, quenching, and recombination with O_2:

$$O_3 + \text{photon} \rightarrow O(^3P) + O_2$$
$$\rightarrow O(^1D) + O_2$$

$$O(^1D) + (N_2, O_2) \rightarrow O(^3P) + (N_2, O_2)$$
$$O(^3P) + O_2 + (N_2, O_2) \rightarrow O_3 + (N_2, O_2)$$

The lifetime of O [= O(^{3}P)] is much less than a minute throughout the stratosphere and troposphere. Profiles of O and O(^{1}D) are shown in Figures L-1 and L-2. Noontime densities of O and O(^{1}D) agree to within 50% with the exception of the CAMED-theta model. The CAMED model uses diurnal "factors" and calculates an effective daytime average for most of the radicals which cannot be directly compared with the noontime densities from other models. Near 40 km, LLNL and NCAR do show some deviations from the pack, especially for O(^{1}D). The sudden shift in AER values above 50 km is inexplicable. More distressing is the large spread, more than a factor of 1.5, in O(^{1}D) in the lower stratosphere, whose cause can be directly attributed to the disagreement in corresponding photolysis rates (see Section K).

The odd-hydrogen (HO_x) radicals, OH and HO_2, are critical to the balance of odd-nitrogen (NO_y) family of species and to the inorganic chlorine (Cl_y) family. The system of reactions controlling the OH and HO_2 densities is complex and changes dramatically from the lower to upper stratosphere. A primary source of OH is generated by O(^{1}D),

$$O(^1D) + H_2O \rightarrow OH + OH,$$

which is augmented in the lower stratosphere by oxidation of CH_4, generating 1 to 3 HO_2 radicals per methane molecule. The individual lifetimes of OH and HO_2 are typically less than 100 sec, but this time scale is dominated by reactions that interchange OH for HO_2. Loss of odd-hydrogen requires recombination of OH and HO_2,

$$OH + HO_2 \rightarrow H_2O + O_2$$

or in the lower stratosphere proceeds through the NO_y family,

$$OH + NO_2 + (N_2, O_2) \rightarrow HNO_3 + (N_2, O_2)$$
$$OH + HNO_3 \rightarrow H_2O + NO_3$$

When heterogeneous reactions on the sulfate aerosols become important in the lower stratosphere, NO_2 concentrations are suppressed, and the production of HNO_3 and HOCl from water in the sulfate particles,

$$N_2O_5 + (H_2O, \text{sulfate}) \rightarrow 2\,HNO_3 + (\text{sulfate})$$
$$ClONO_2 + (H_2O, \text{sulfate}) \rightarrow HNO_3 + HOCl + (\text{sulfate}),$$

leads to generation of additional OH by photolysis,

$$HNO_3 + \text{photon} \rightarrow OH + NO_2$$
$$HOCl + \text{photon} \rightarrow OH + Cl$$

The modeled noontime OH and HO_2 densities (Figures L-3 and L-4) agree very well above 30 km, but diverge substantially below and are not always in proportion to the primary source, $O(^1D)$. This is particularly noticeable for the GSFC (low) and the GISS+LLNL (high). The differences in the lower stratosphere apply to both OH and HO_2, and thus reflect the budget for total HO_x rather than cycling between OH and HO_2.

The NO_x ($NO + NO_2$) forms of odd nitrogen (NO_y) are involved in most of the important chemical reactions of the NO_y family. In daylight NO and NO_2 interchange rapidly on times scales of 100 seconds or less,

$$NO_2 + \text{photon} \rightarrow NO + O$$
$$NO + O_3 \rightarrow NO_2 + O_2;$$

however, in the lower stratosphere reactions with the Cl_y family are also important in determining the ratio NO/NO_2,

$$NO + ClO \rightarrow NO_2 + Cl$$

In daytime NO_x is predicted to be typically less than 25% of the NO_y below 25 km altitude. Including heterogeneous chemistry reduces this to about 16% at the minimum (about 20 km) under background conditions, but much less than 10% following volcanic enhancements of the sulfate layer. The combined NO_x exceeds 50% of total NO_y above 30 km and 95% above 40 km.

The modeled noontime NO and NO_2 densities, Figures L-5 and L-6, are in reasonable agreement. The CAMED model stands out again because it calculates only "daytime" averages rather than noontime densities. Agreement is excellent above 40 km (where all of the specified NO_y is in the form of NO_x), but the range at 30 km and below is about a factor of 1.4 (readily visible in the linear scale for the NO figure). Much of this dispersion must be related to the relative abundance of HNO_3; the predicted ratio NO/NO_2 agrees to within a factor of 1.2 (see later discussion of Figure L-27).

Atomic chlorine (Cl) and ClO interchange rapidly through the reaction

$$Cl + O_3 \rightarrow ClO + O_2$$

followed by

$$ClO + NO \rightarrow Cl + NO_2$$
$$ClO + O \rightarrow Cl + O_2.$$

Additionally, in the lower stratosphere and under volcanically perturbed conditions, models predict that a large fraction of ClO proceeds to Cl through the formation of intermediates such as $ClONO_2$, HOCl, OClO and BrCl. Atomic chlorine with a lifetime of less than 0.1 second is predicted to be a small fraction of the Cl+ClO group, and the abundance of ClO is determined primarily by a balance between HCl and Cl through the following reactions:

$$Cl + CH_4 \rightarrow HCl + CH_3$$
$$Cl + CH_2O \rightarrow HCl + CHO$$

and

$$HCl + OH \rightarrow Cl + H_2O.$$

The noontime ClO density (Figure L-7) has nearly a factor of 2 spread across the models throughout much of the stratosphere, but the basic shape of the profile is similar for all models. The CALJPL model appears to have used Cl_y concentrations different from those specified in Table KLM-1(*see also* Section M). There is some consistency in that the models with the larger OH (L-3) tend to have larger ClO densities.

PHOTOCHEMICAL LOSS OF NO_Y

The fall-off in NO_x observed above 40 km reflects the photochemical loss of NO_y. Photodissociation of NO in the delta bands (*see* section K),

$$NO + photon \rightarrow N + O$$

can be followed by regeneration

$$N + O_2 \rightarrow NO + O$$

or loss of NO_y

$$N + NO \rightarrow N_2 + O$$

Figure L-8 shows that this loss rate for NO_y ([N + NO] averaged over 24 hours, times 2) spans a factor of 4 across the models and is greatest near 40 km where the peak destruction occurs. This discrepancy points to long-standing problems on predicting the NO_y peak mixing ratio near 35 km: the Harvard model (propagated here as the GISS model) always predicted very low maximum NO_y, about 16 ppb; whereas the LLNL (not shown here) and NCAR models predicted more than 23 ppb. The present CAMED model predicts the least NO_y loss and thus should have the largest NO_y mixing ratios in the upper stratosphere. The GISS model has the largest rate of NO_y destruction, but among the model results shown here it has one of the few independent approaches for calculating radiation in the Schumann-Runge bands (*see* chapter 4, Model Descriptions). At these altitudes, photolysis of NO occurs only in the delta-(0,0) band about 191 nm, and further analysis of the O_2 photolysis in the S-R bands (*see* section K) should resolve these discrepancies.

Ozone Budget in the Upper Stratosphere: $O+O_3$, $O+NO_2$, $O+ClO$, $O+OH$

In the upper stratosphere the photochemical loss of O_3 is driven by reactions involving atomic oxygen, and we examine in Figures L-9 through L-12 the average rates for $O+O_3$, $O+OH$, $O+NO_2$, and $O+ClO$, respectively. Focusing on 40 km altitude, we note that the spread in rates is much larger than the corresponding range in noontime O densities (Figure L-1). (The average rates from the CAMED model in the upper stratosphere fall within the range of the other models; such comparison provides a critical test of the CAMED diurnal averaging factors.) The model spread in the $O+O_3$ rate must be due to differences in averaging over the diurnal cycle since O_3 is fixed. For $O+OH$, the LLNL model is higher than expected from the noontime O and OH densities, and the CAMED model has the lowest average. The spread in the $O+ClO$ rate is comparable to but larger than the range in noontime ClO densities (Figure L-7), probably due to diurnal averaging. The NCAR model stands out here with some unusually large average rates above 36 km as compared with the noontime densities.

Ozone Budget in the Lower Stratosphere: HO_2+O_3, HO_2+NO, $HOCl+hv$, NO_3+hv, $ClO+BrO$, Cl_2O_2+hv

The ozone photochemical budget in the lower stratosphere is more complex and involves much coupling of reactions across the HO_x, NO_y, Br_y, and Cl_y families. Thus, the divergence of the model budgets is to be expected. In the lower stratosphere, the source of HO_2 radicals involves O_3.

$$OH + O_3 \rightarrow HO_2 + O_2$$

The loss of odd oxygen by this reaction (not plotted here) can be negated if followed by

$$HO_2 + NO \rightarrow OH + NO_2,$$

(shown in Figure L-14) since the NO_2 photolyzes to give atomic O back again. Otherwise, the reaction (Figure L-13)

$$HO_2 + O_3 \rightarrow OH + O_2 + O_2$$

or the sequence (Figure L-15)

$$Cl + O_3 \rightarrow ClO + O_2$$
$$HO_2 + ClO \rightarrow HOCl + O_2$$
$$HOCl + \text{photon} \rightarrow OH + Cl$$

results in the loss of two O_3. The model calculations of these three rates agrees well with regard to profile shape, but still exhibits a factor of two in range. For the HO_2+O_3 rate, the GSFC model is low as expected from its HO_x levels noted above, but the NCAR model calculates unusually high rates which are not consistent with its typical HO_2 values. The HOCl photolysis is in excellent agreement above 25 km (except for CALJPL with different Cl_y) but diverges rapidly below.

Photolysis of NO_3 occurs rapidly in daylight (0.2 s^{-1}) and about 10% of the yield goes to O_2 (Figure L-16)

$$NO + O_3 \rightarrow NO_2 + O_2.$$

Since most of the NO_3 is formed by processes involving two O_3,

$$NO + O_3 \rightarrow NO_2 + O_2$$
$$NO_2 + O_3 \rightarrow NO_3 + O_2$$

or

$$Cl + O_3 \rightarrow ClO$$
$$ClO + NO_2 + (N_2, O_2) \rightarrow ClONO_2 + (N_2, O_2)$$
$$ClONO_2 + \text{photon} \rightarrow Cl + NO_3$$

this pathway for photolysis leads to loss of two O_3.

The large range in values reported for this path of NO_3 photolysis, more than a factor of 10 at 20 km, is inexplicable in view of the previous level of agreement among the models. The basic shape of the profiles agree, however, the divergence cannot be readily explained. In the GISS model most of the NO_3 is formed by photolysis of $ClONO_2$, but the $ClONO_2$ in the GISS, GSFC, and LLNL models agree (*see* Figure L- 21, and section M). Possibly, this pathway through NO_3 is not being diagnosed in the same manner across the models.

Halogen-driven losses of O_3 occur through a coupled chlorine-bromine reaction,

$$ClO + BrO \rightarrow Br + ClOO$$
$$\rightarrow BrCl + O_2$$
$$\rightarrow Br + OClO$$

and the ClO dimer,

$$ClO + ClO + (N_2, O_2) \rightarrow Cl_2O_2 + (N_2, O_2)$$
$$Cl_2O_2 + \text{photon} \rightarrow ClOO + Cl$$

The sum of the first two paths of the BrO+ClO reaction (Figure L-17) represents about 45% of the total reaction in the lower stratosphere and results in the loss of two O_3. The dimer loss mechanism (Figure L-18), predominant in the Antarctic ozone hole, is not so important at these lower values of ClO. The models show a large range for these rates, much more than a factor of 2 for BrO+ClO. For ClO+BrO the profiles have distinctly different shapes as evidenced by the different model groupings at 26 km (AER/CAMED/GISS vs. GSFC/LLNL/NCAR) and at 18 km (AER/CAMED/GSFC vs. GISS/LLNL/NCAR). The basic chemistry as well as the diurnal cycles of radicals in the lower stratosphere are more complex than in the upper stratosphere. It is likely that model approximations of the diurnal variations in photolysis and kinetic rates is responsible for the growing disagreement in the lower stratosphere (see the following discussion on diurnal averaging). The diurnal averaging factors used by the CAMED model do not appear to work as well in the lower stratosphere where their $O+NO_2$ and Cl_2O_2+hv rates are much larger than those of other models.

The NO_x-NO_y cycling is driven by formation of HNO_3 via gas-phase reaction

$$OH + NO_2 + (N_2, O_2) \rightarrow HNO_3 + (N_2, O_2),$$

by heterogeneous reactions on the sulfate aerosols

$$N_2O_5 + (H_2O, \text{sulfate}) \rightarrow 2\,HNO_3 + (\text{sulfate})$$
$$ClONO_2 + (H_2O, \text{sulfate}) \rightarrow HNO_3 + HOCl + (\text{sulfate})$$

or by polar stratospheric clouds (not part of this simulation).

Under the conditions imposed here–background aerosol levels at midlatitudes–formation of HNO_3 is dominated by the gas phase reaction (Figure L-19). Hydrolysis of N_2O_5 (Figure L-20)

contributes about 20% in the lower stratosphere. Most models predict similar values with the exception of CAMED (lowest N_2O_5 from 20 to 30 km) and NCAR (unusually high N_2O_5 at 20 km and below). For $ClONO_2$ hydrolysis, the NCAR values are unusually low, and the other reporting models are in basic agreement (Figure L-21). These hydrolysis rates are a measure of the effective 24-hour average densities of N_2O_5 and $ClONO_2$.

DIURNAL AVERAGING AND NOONTIME RATIOS

The correct integration of radical and rates over the diurnal cycle is an essential component of modeling stratospheric chemistry. One part is the evaluation of photolysis rates throughout the daylight and twilight hours; another is the integration of the kinetic equations. Section K discusses photolysis rates and their integration over 24 hours. Here we examine a simple diagnostic of the model performance: the ratio of 24-hour-average to noontime densities of the key radicals $O(^1D)$, O, OH, HO_2, and ClO.

The density of $O(^1D)$ responds instantly to the ultraviolet radiation field and is created predominantly by the direct solar beam. Most of the models agree exceptionally well on $O(^1D)$: In Figure L-22 the ratio increases from 0.25 in the lower stratosphere to almost 0.5 above 50 km. In the lower stratosphere $O(^1D)$ is formed predominantly when the sun is close to noon because of the large optical depths for wavelengths less than 310 nm. Above 50 km the atmosphere is optically thin, and $O(^1D)$ is formed at nearly a constant rate as long as the sun is up. The NCAR ratio is in disagreement with all the other models in this and all of these diurnal diagnostics. The CAMED model is a special case since they use diurnal averaging "factors." We have used their daytime average densities as noontime in these ratios, and thus the CAMED ratios all appear greater than 0.5. The interesting structure in these ratios calculated with the diurnal models points to the difficulties in deriving constant factors.

The $O(^3P)$ ratios in Figure L-23 again show similar agreement among the models except for NCAR. In the lower stratosphere $O(^3P)$ is formed primarily by longer wavelength, visible light and hence is maintained throughout the daylight hours (i.e., ratio of about 0.5). In the upper stratosphere, a large fraction of $O(^3P)$ is derived from quenching of $O(^1D)$, which is formed primarily about noon (i.e., ratio drops to 0.4). A probable explanation for the spread in the lower stratosphere is that scattered light, whose intensity varies with solar angle, is important in production of $O(^3P)$.

Figures L-24 and L-25 show that OH and HO_2 densities peak sharply about local noon in the lower stratosphere (ratios of 0.3) and become more uniform during the day at higher altitudes (remember, $O(^1D)$ is a primary source of HO_x). The WASH model shows some anomalies, but the most notable differences occur for HO_2 above 45 km where CALJPL/GISS ratios diverge from GSFC/WASH. It is possible that the increase in high-altitude HO_2 ratios reflects the treatment of the recombination of HO_x after the sun sets.

The comparison of the diurnal averaging for ClO, shown in Figure L-26, is disappointing. Above 45 km, ClO densities increase at twilight and at night; thus, the ratio becomes greater than 1. The CALJPL/GISS/GSFC models agree very well, and if we accept these ratios as correct then the WASH model has a problem with the ClO cycle above 35 km and the NCAR values are systematically in error.

The noontime ratio of NO/NO_2 shown in Figure L-27 has been a classic diagnostic of the chemical models. To first order it represents the ratio of the photolysis rate of NO_2 to the rate coefficient for the $NO+O_3$ rate times the O_3 density. The CAMED diagnostic refers to a ratio of the daytime averages and thus is expected to be less than the noontime ratios from the other models. Although a large portion of the disagreement can be traced to the difference in NO_2

photolysis rates (e.g., GISS/CALJPL have the highest rates, GSFC/WASH have the lowest; *see* section K), the remaining spread in NO/NO_2 ratios demonstrates the importance of ClO, HO_2, etc. in determining this ratio.

Heterogeneous vs. Gas-Phase Chemistry: O, O(^{1}D), NO, NO_2, ClO, OH, HO_2

The inclusion of heterogeneous chemistry in the form of reactions of N_2O_5 and $ClONO_2$ on the sulfate-layer aerosols (*see* Table KLM-1) directly shifts the NO_x-HNO_3 balance, and secondarily affects HO_x densities and the ClO-HCl balance. For the fixed ozone and temperature profiles assumed here, the densities of O and O(^{1}D) should not be affected substantially, as illustrated in Figures L-28 and L- 29.

The noontime densities for both NO and NO_2 (Figures L-30 and L-31) are lowered by heterogeneous processing about 25% at the altitude of peak effectiveness near 18 km. The noontime densities for ClO (Figure L- 32), OH (L-33), and HO_2 (L-34) are all enhanced by heterogeneous reactions: ClO by about 40%-80% at 18-20 km under these background aerosol levels; OH by only about 10%, but HO_2 by about 40%. The overall increase in HO_x is due to the reduced NO_x as discussed above; the larger relative increase in HO_2 is caused by the lower NO concentrations and the corresponding reduction in the recycling of HO_2 to OH by

$$HO_2 + NO \rightarrow OH + NO_2$$

The increases in noontime HO_2 are paralleled by the increases in 24-hour averaged HO_2 (Figure L-35). All models except for NCAR show a similar vertical pattern in these changes. The NCAR model is quite different and indicates very little change in noontime NO_x, HO_x, and ClO for heterogeneous chemistry; however, the diurnal average HO_2 agrees with the other results. (Perhaps this discrepancy is an error in diagnostics.)

Heterogeneous vs. Gas-Phase Chemistry: Ozone Budget Rates

The inclusion of N_2O_5 and $ClONO_2$ heterogeneous processing also causes a substantial shift in the reactions controlling the O_3 photochemical budget in the lower stratosphere (see the discussion in the UNEP/WMO 1991 Ozone Assessment). A summary of the relative changes in the 24-hour averaged rates (*see* Figures L-9 through L-19 above for the gas-phase chemistry alone) is given in Figure L-36 through L-45.

The average $O+O_3$ rate remains unchanged. As expected from the changes in the NO_x, HO_x, and ClO densities, the Cl_y- and HO_x-catalyzed losses increase while the NO_x-catalyzed losses become less important. The HO_2+O_3 and NO_2+O rates parallel the changes in HO_2 and NO_2 respectively. The rate of $O+NO_2$ is reduced by 20%-40%; but HO_2+O_3 increases by a factor of about 1.5, making it the dominant ozone loss mechanism in the lower stratosphere. The rate of HO_2+NO is almost unchanged because of canceling effects on the HO_2 and NO densities. Formation of HNO_3 by gas-phase reaction ($OH+NO_2$) is suppressed slightly, but more than offset by heterogeneous production.

All of the halogen catalytic cycles are enhanced by factors of 1.5 to 2 or more near 20 km. The NO_3 photolysis channel leading to ozone loss becomes less important in most models, but in the GISS model (with its enhanced $ClONO_2$ source of NO_3) it remains unchanged. Overall, the impact of heterogeneous chemistry on the ozone-destroying catalytic cycles in the lower stratosphere is consistent among the models. However, relative changes in the ClO-related cycles have the largest range among the models.

SUMMARY

This effort in model-model comparison has shown that the stratospheric models generally agree on radicals and rates to within a factor of 1.5 or better. Considering the large changes in photochemical environment from the tropopause to the upper stratosphere, the agreement among models is very good. We have already identified some essential differences in model formulation and pointed to possible numerical errors among the suite of participating models. There remain many differences that cannot be ascribed a cause. Most of these discrepancies cannot be resolved until differences in photolysis rates are understood.

The spread in noontime radical concentrations is worrisome, but we must resolve the discrepancies in J-values first.

OH is the key radical coupling all of the chemical families that has the largest predicted range in the lower stratosphere; this difference should be resolved!

The NO_y loss in the upper stratosphere varies considerably from model to model; both photolysis and kinetic rates need to be evaluated separately.

The diurnal cycle does not appear to be equally well represented in all models; for example the range in average $O+O_3$ rate may be due to diurnal resolution as well as photolysis rates.

The importance of NO_3 photolysis in the ozone budget of the lower stratosphere is highly uncertain given the range in modelresults; this uncertainty carries through to the impact with theterogeneous chemistry included.

Chlorine reactions leading to ozone loss show the largest spread among the models; these discrepancies need to be understood if we are to rely on model predictions of O_3 change with enhanced sulfate-layer aerosols or with changing Cly levels.

Heterogeneous chemistry has a consistent impact on the models, but is still not uniformly effective.

The largest changes due to heterogeneous processing by the sulfate-layer aerosols appears in the 16-20 km range for which we have been and are able to make measurements of radicals and their cycles with the ER-2. Hopefully such data will resolve some of these disagreements among the models, and allow us to calibrate the impact of heterogeneous chemistry which is likely to be more complex than the simple parameterization used in this comparison.

A review of sections K and L in a year or so might show progress and aid further model development, but additional ATMOS profiles (section M) are probably needed to resolve some differences in the lower stratosphere.

FIGURE CAPTIONS

Figure L-1. O density (noon, 30N)

Figure L-2. O[^{1}D] density (noon, 30N)

Figure L-3. OH density (noon, 30N)

Figure L-4. HO_2 density (noon, 30N)

Figure L-5. NO density (noon, 30N)

Figure L-6. NO_2 density (noon, 30N)

Figure L-7. ClO density (noon, 30N)

Figure L-8. 2x[N+NO] rate (24-hr avg, 30N)

Figure L-9. [$O+O_3$] rate (24-hr avg, 30N)

Figure L-10. [O+OH] rate (24-hr avg, 30N)

Figure L-11. [$O+NO_2$] rate (24-hr avg, 30N)

Figure L-12. [O+ClO] rate (24-hr avg, 30N)

Figure L-13. [HO_2+O_3] rate (24-hr avg, 30N)

Figure L-14. [HO_2+NO] rate (24-hr avg, 30N)

Figure L-15. [HOCl+hv] rate (24-hr avg, 30N)

Figure L-16. [$NO_3+hv \rightarrow NO+O_2$] rate (24-hr avg, 30N)

Figure L-17. [ClO+BrO] rate (24-hr avg, 30N)

Figure L-18. [Cl_2O_2+hv] rate (24-hr avg, 30N)

Figure L-19. [NO_2+OH] rate (24-hr avg, 30N)

Figure L-20. [$N_2O_5+H_2O$] rate (24-hr avg, 30N)

Figure L-21. [$ClONO_2+H_2O$] rate (24-hr avg, 30N)

Figure L-22. O[^{1}D] ratio (24-hr/noon, 30N)

Figure L-23. O ratio (24-hr/noon, 30N)

Figure L-24. OH ratio (24-hr/noon, 30N)

Figure L-25. HO_2 ratio (24-hr/noon, 30N)

Figure L-26. ClO ratio (24-hr/noon, 30N)

Figure L-27. NO/NO_2 ratio (at noon, 30N)

Figure L-28. O (noon) ratio (het/gas, 30N)

Figure L-29. $O[^1D]$ (noon) ratio (het/gas, 30N)

Figure L-30. NO (noon) ratio (het/gas, 30N)

Figure L-31. NO_2 (noon) ratio (het/gas, 30N)

Figure L-32. ClO (noon) ratio (het/gas, 30N)

Figure L-33. OH (noon) ratio (het/gas, 30N)

Figure L-34. HO_2 (noon) ratio (het/gas, 30N)

Figure L-35. HO_2 (24-hr) ratio (het/gas, 30N)

Figure L-36. $[O+O_3]$ (24-hr) ratio (het/gas, 30N)

Figure L-37. $[O+NO_2]$ (24-hr) ratio (het/gas, 30N)

Figure L-38. $[HO_2+O_3]$ (24-hr) ratio (het/gas, 30N)

Figure L-39. $[HO_2+NO]$ (24-hr) ratio (het/gas, 30N)

Figure L-40. [O+ClO] (24-hr) ratio (het/gas, 30N)

Figure L-41. [HOCl+hv] (24-hr) ratio (het/gas, 30N)

Figure L-42. [ClO+BrO] (24-hr) ratio (het/gas, 30N)

Figure L-43. $[Cl_2O_2+hv]$ (24-hr) ratio (het/gas, 30N)

Figure L-44. $[NO_3+hv \rightarrow NO+O_2]$ (24-hr) ratio (het/gas, 30N)

Figure L-45. $[OH+NO_2]$ (24-hr) ratio (het/gas, 30N)

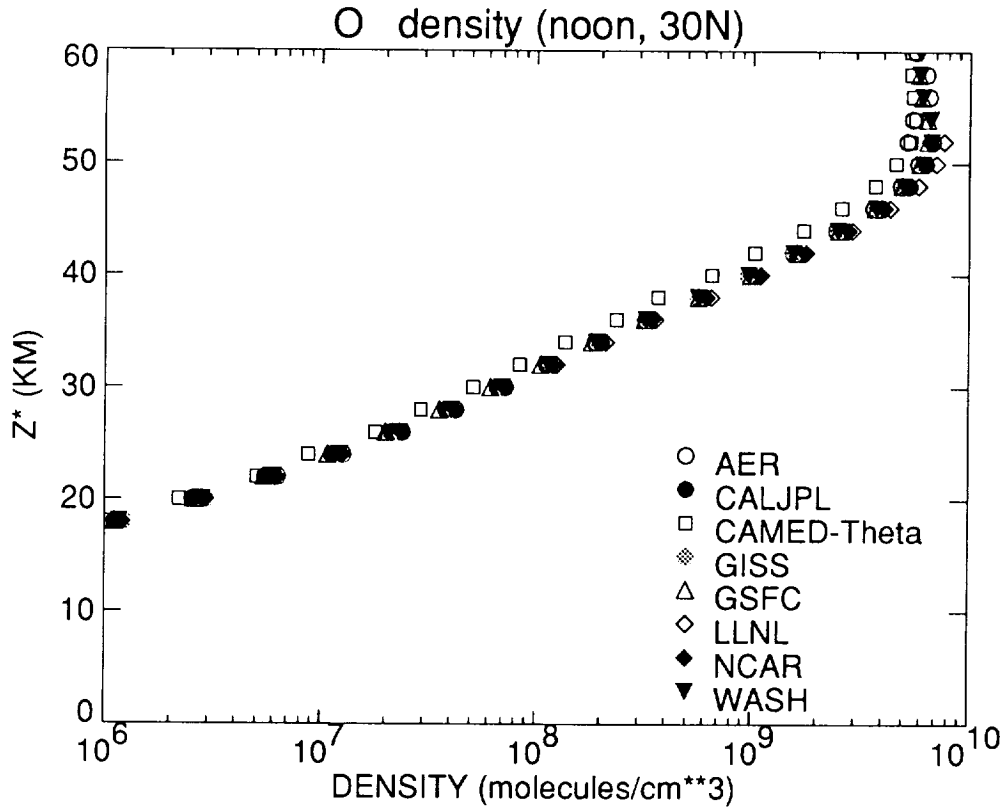

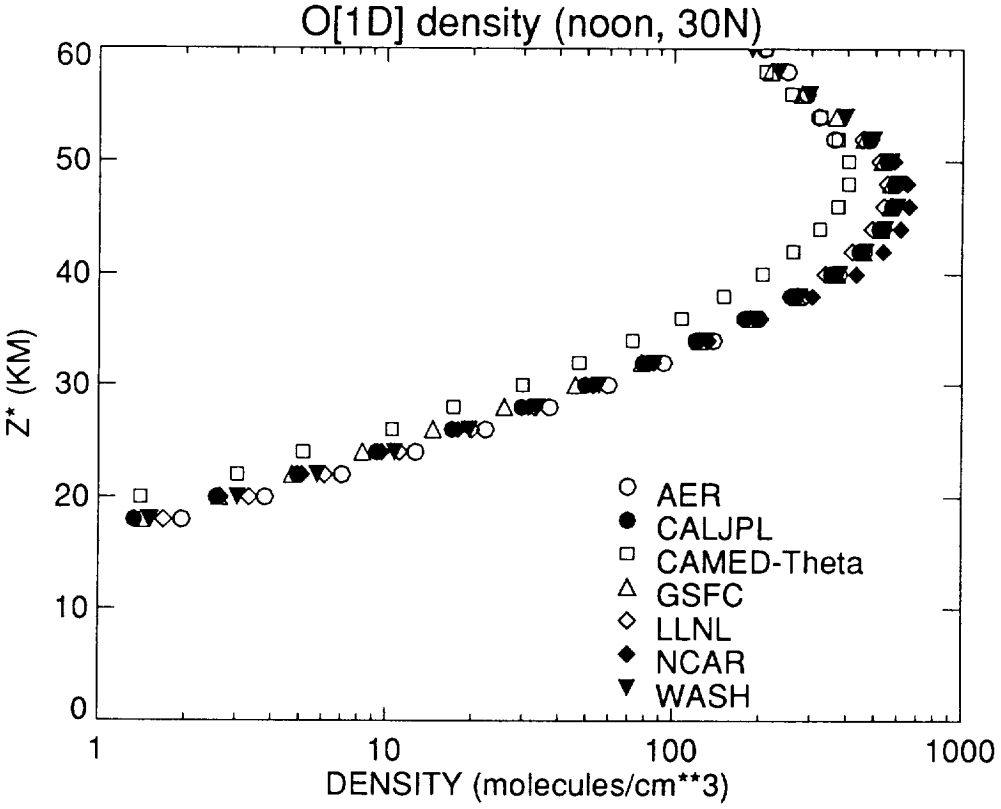

Figure L-1 (top) **Figure L-2 (bottom)**

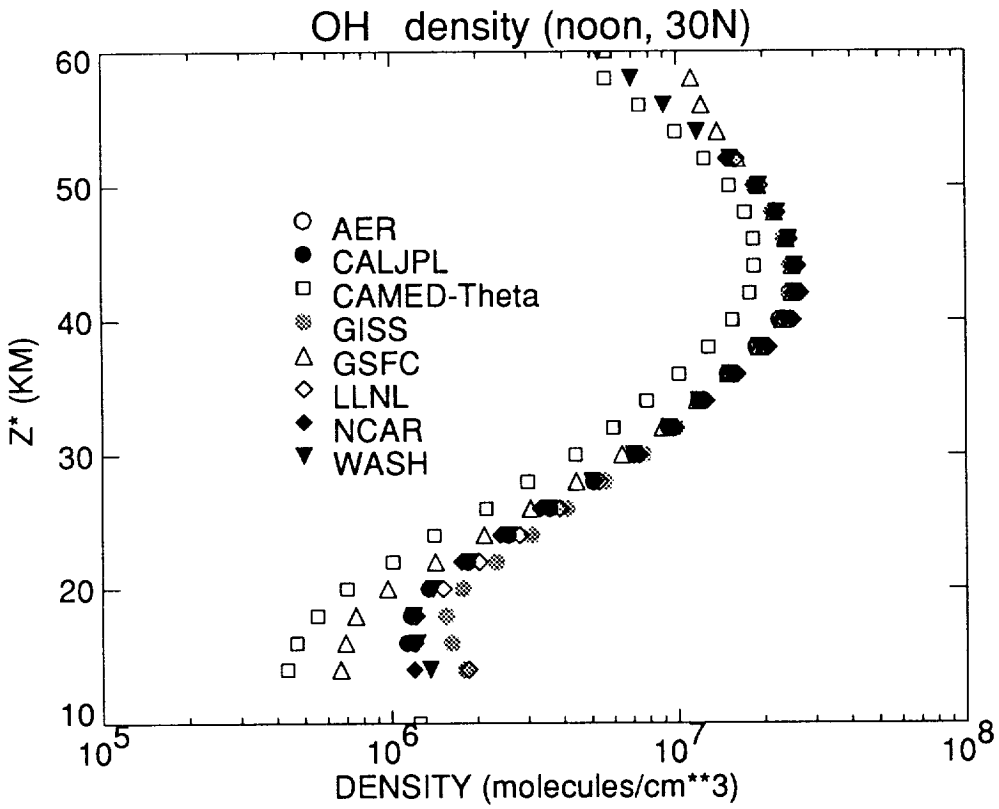

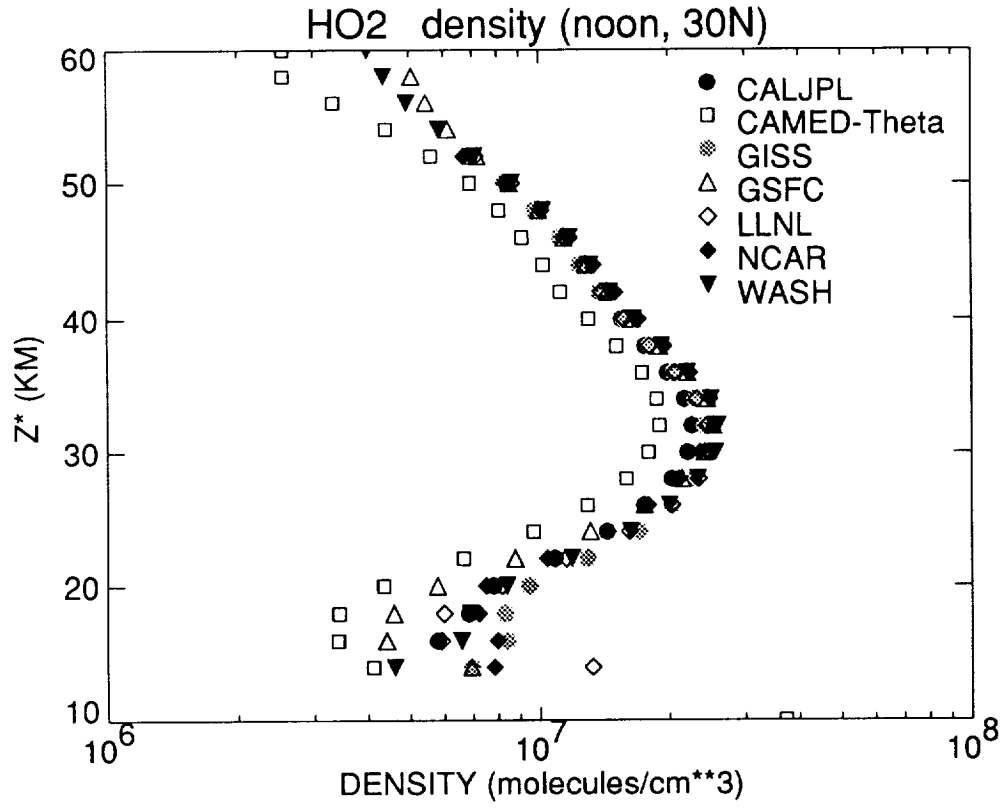

Figure L-3 (top) **Figure L-4 (bottom)**

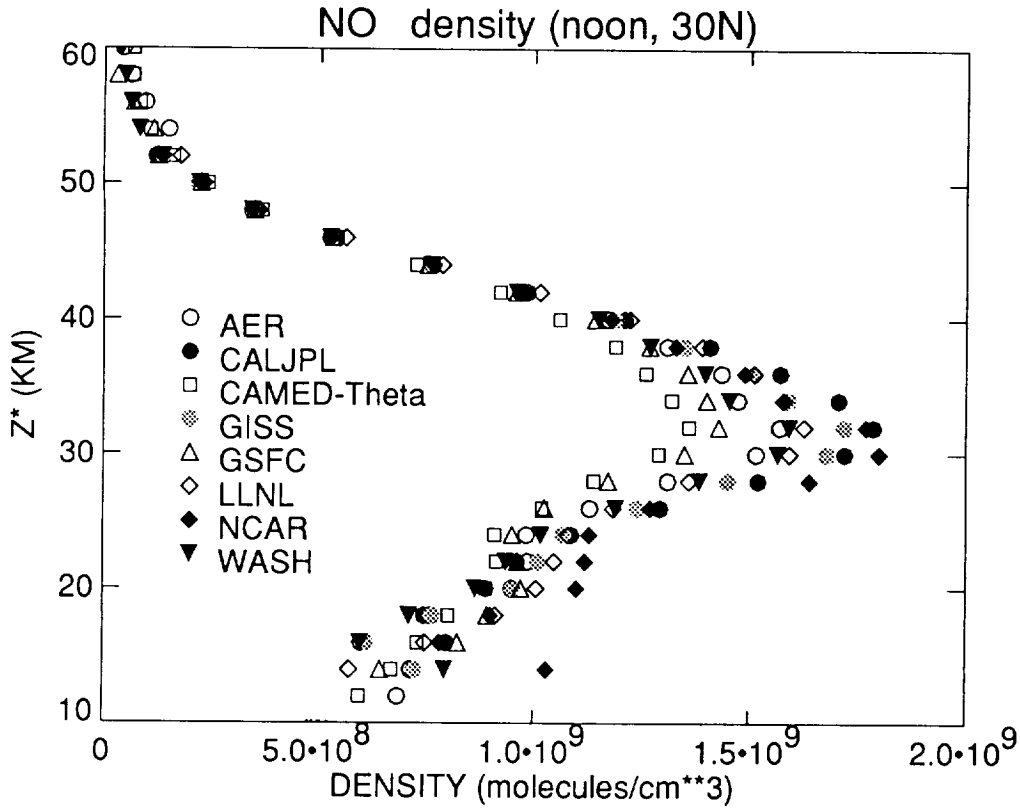

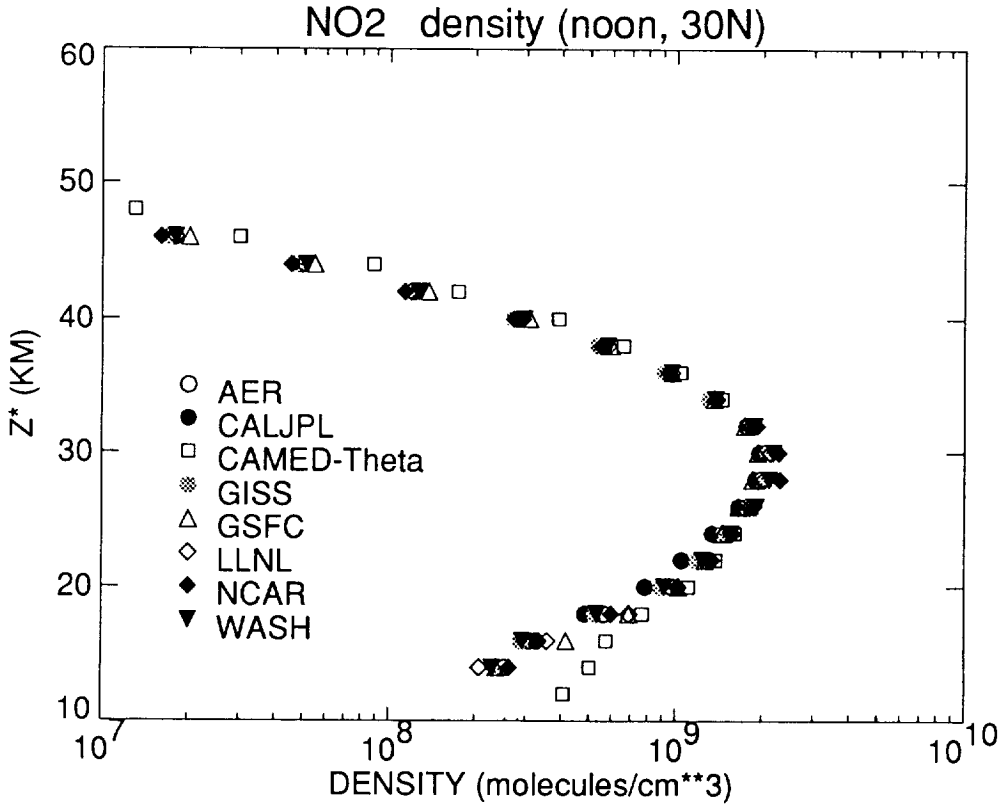

Figure L-5 (top) **Figure L-6 (bottom)**

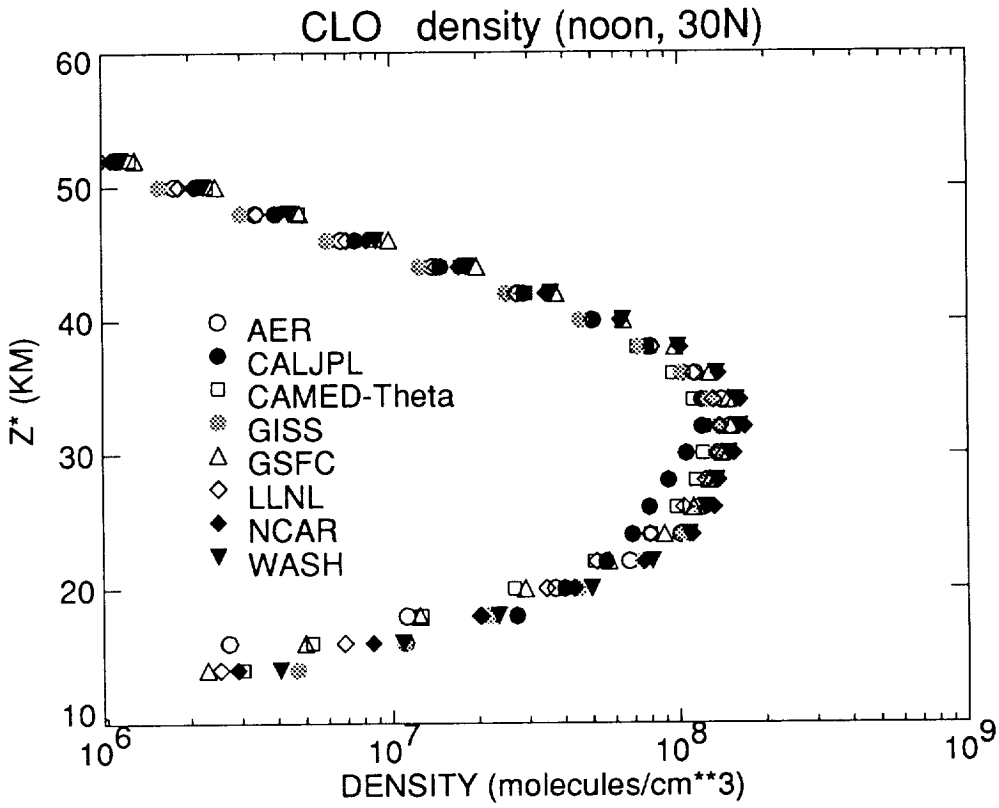

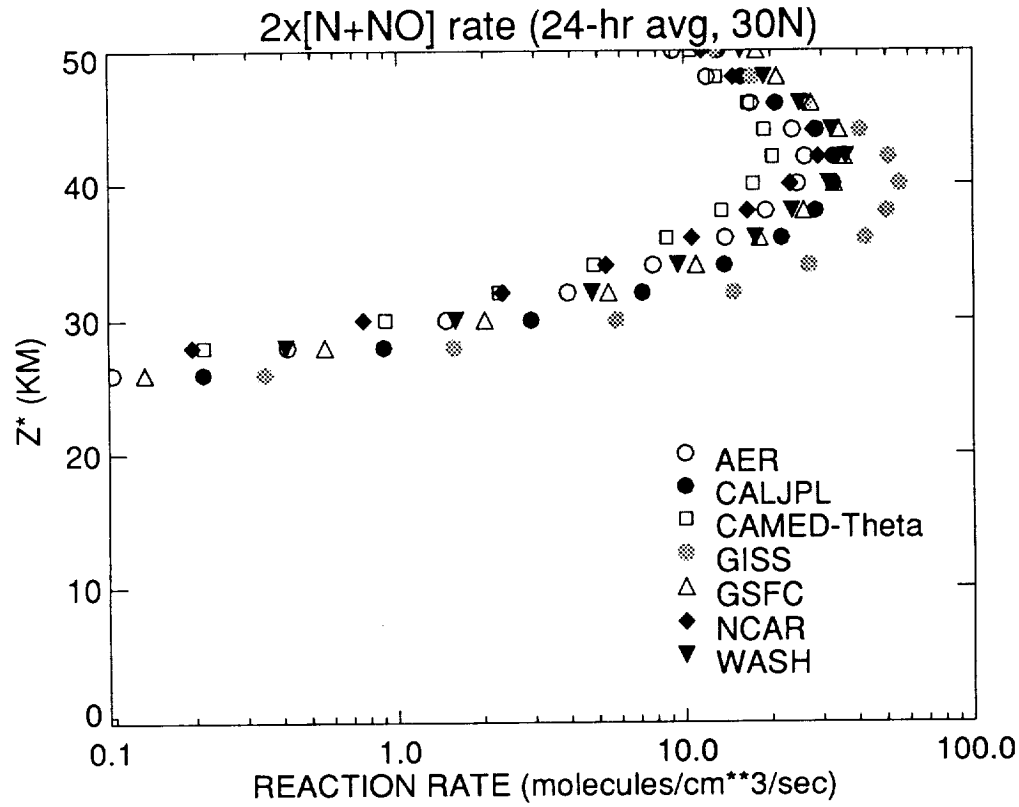

Figure L-7 (top) **Figure L-8 (bottom)**

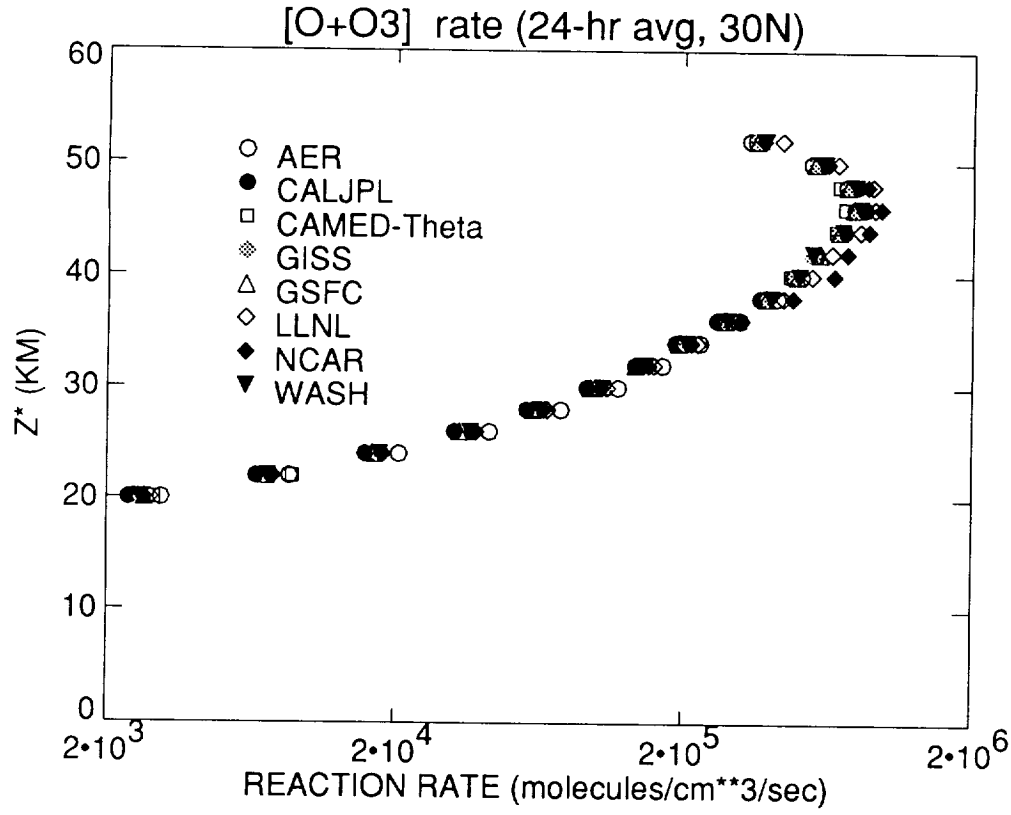

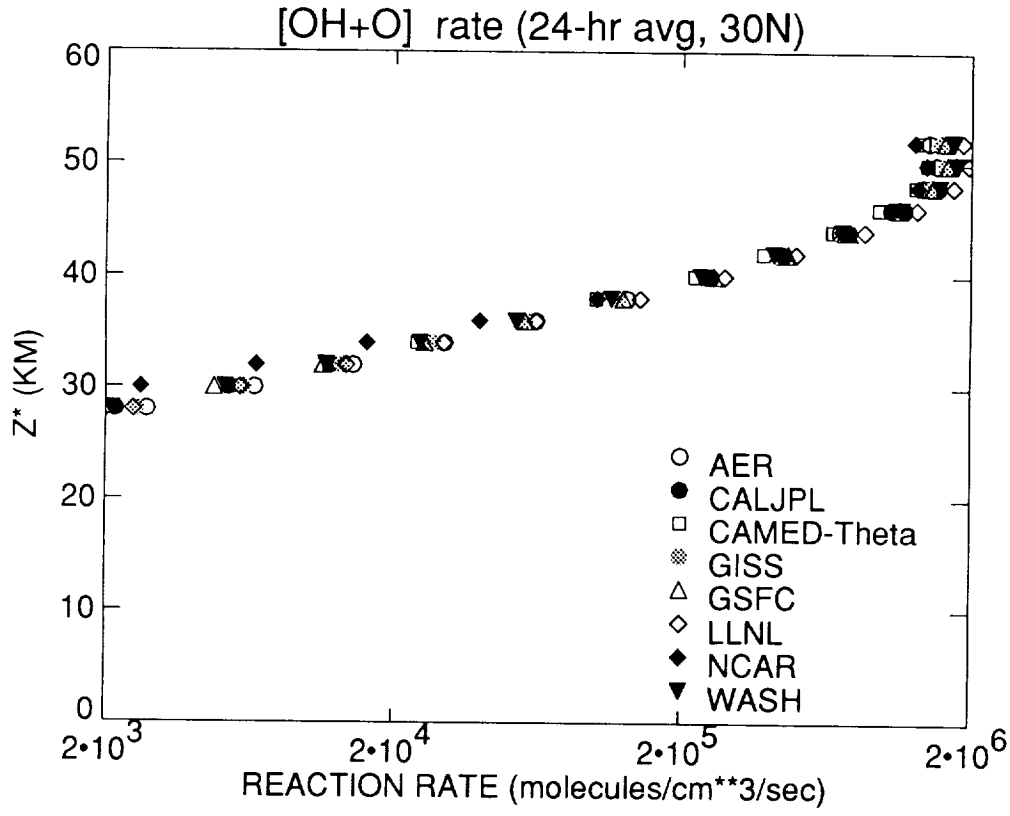

Figure L-9 (top) **Figure L-10 (bottom)**

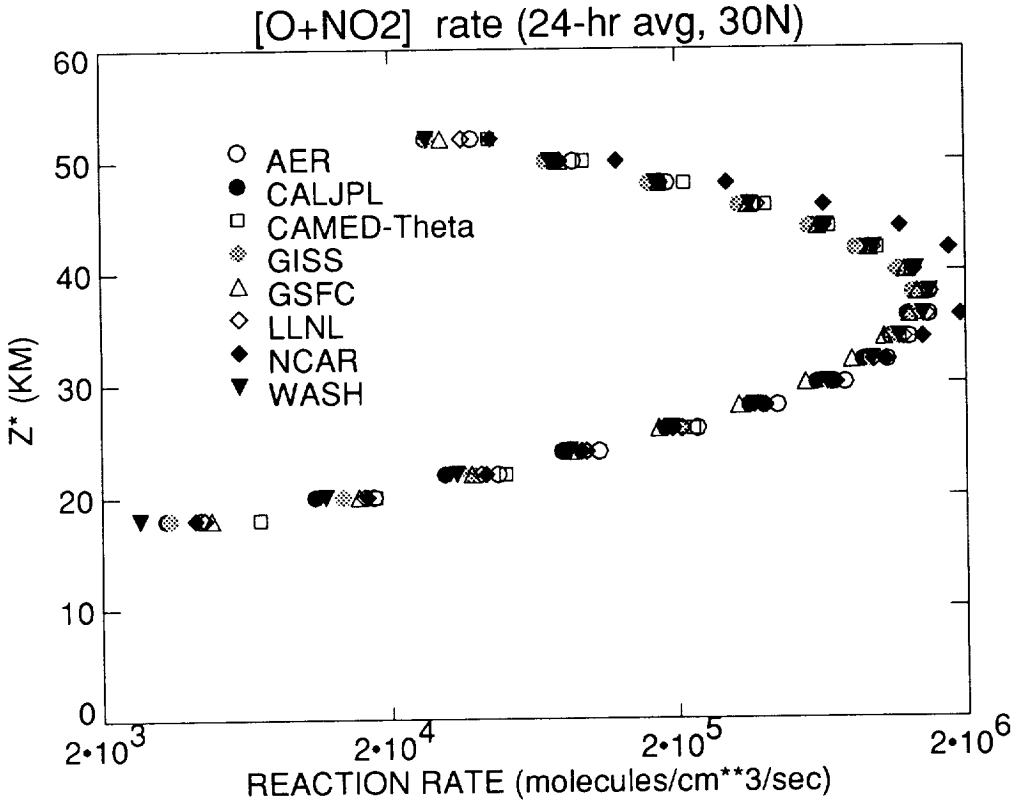

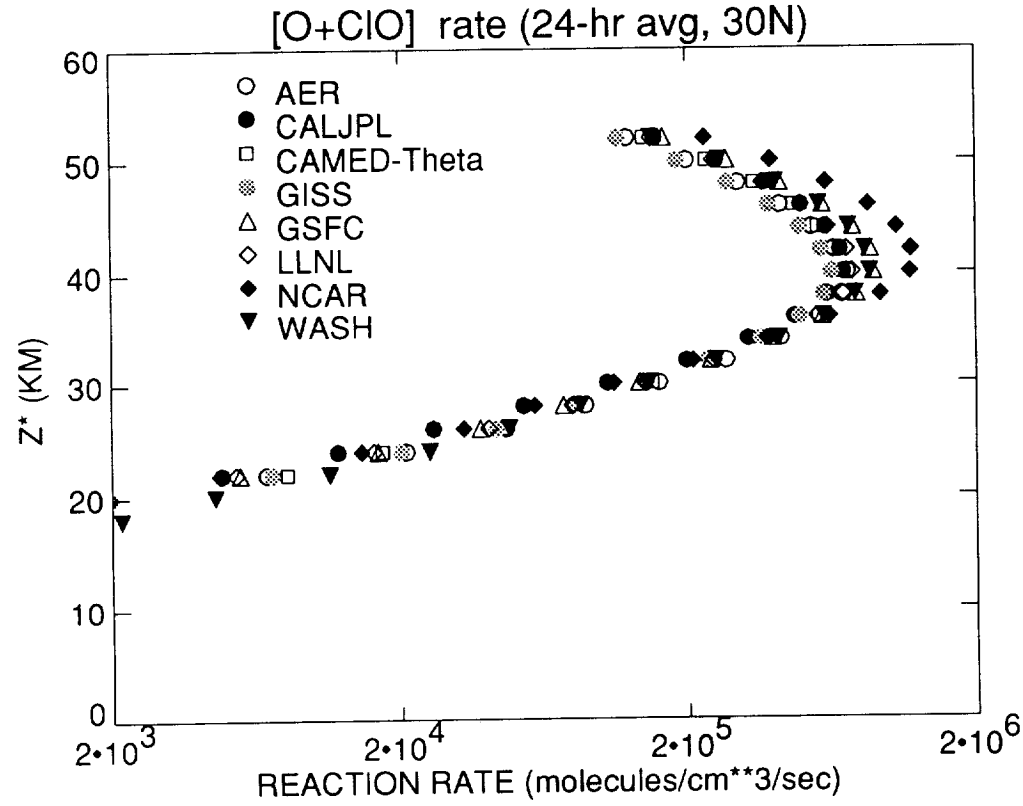

Figure L-11 (top) **Figure L-12 (bottom)**

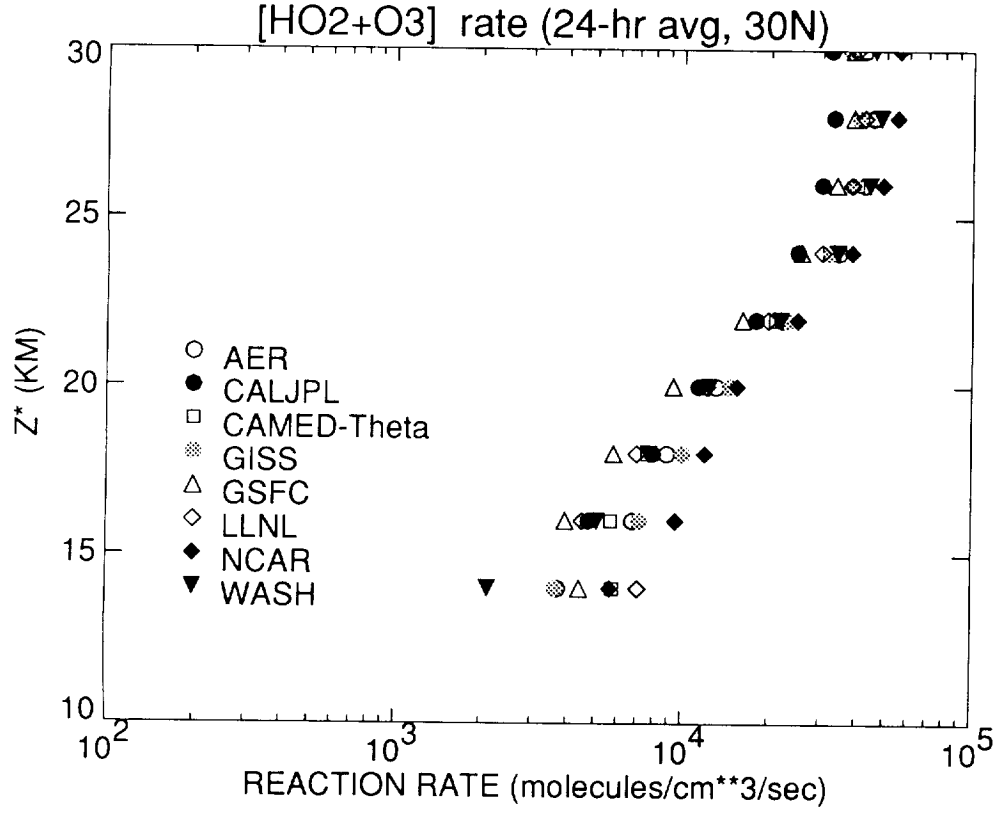

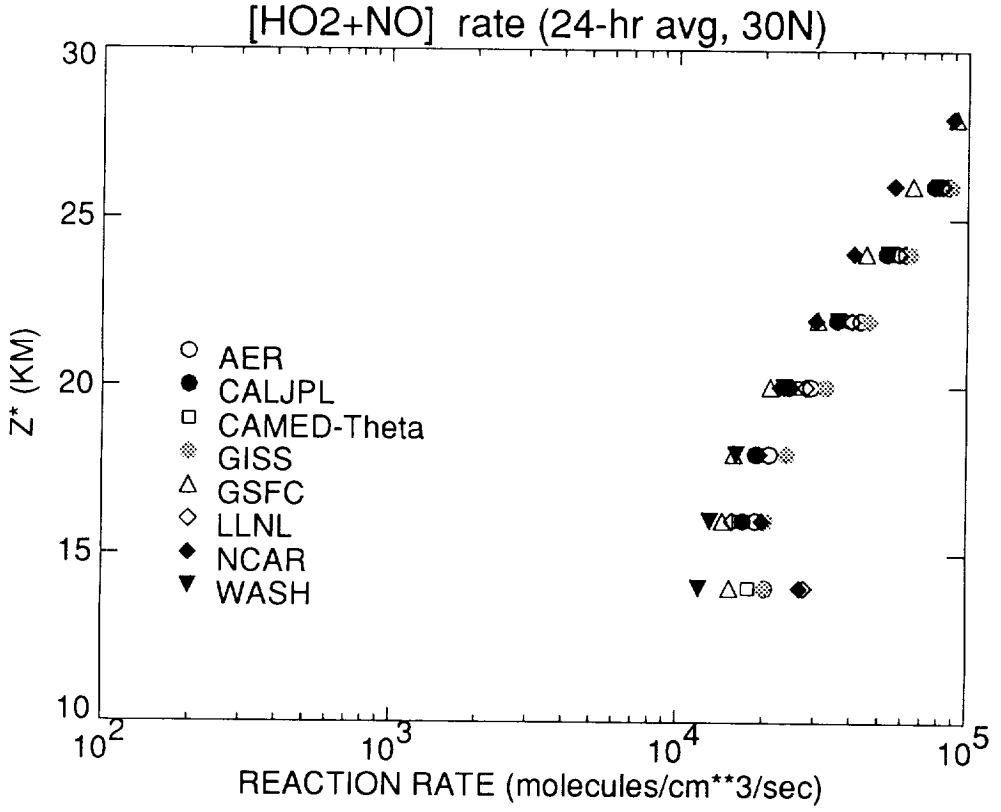

Figure L-13 (top) **Figure L-14 (bottom)**

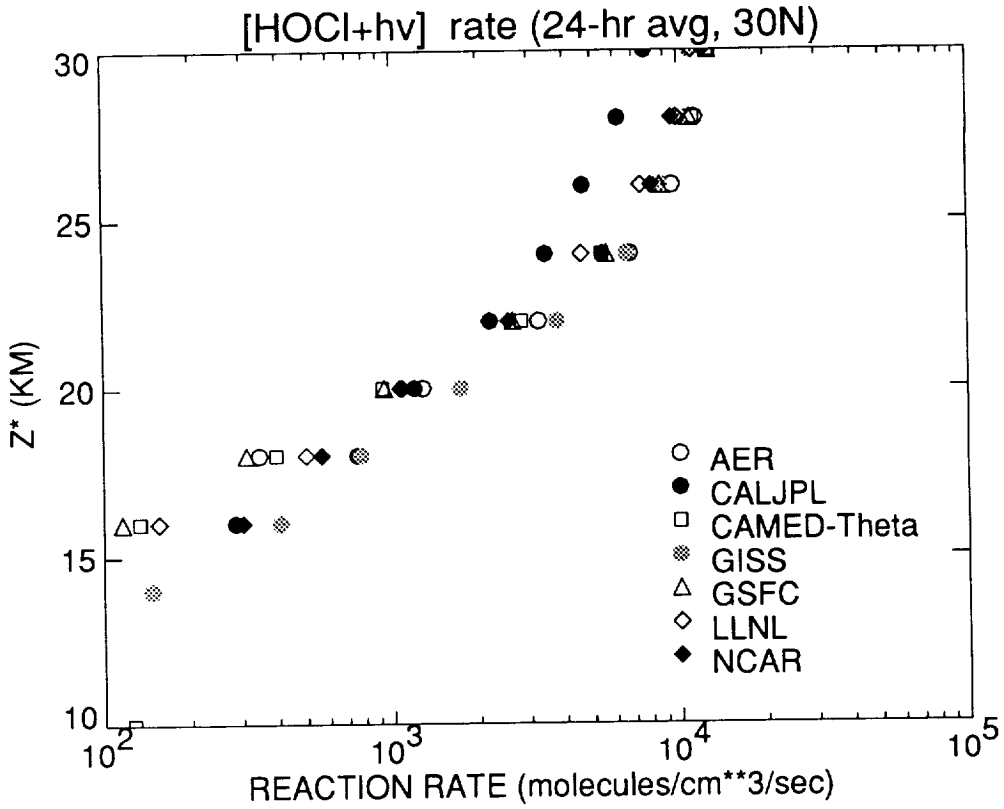

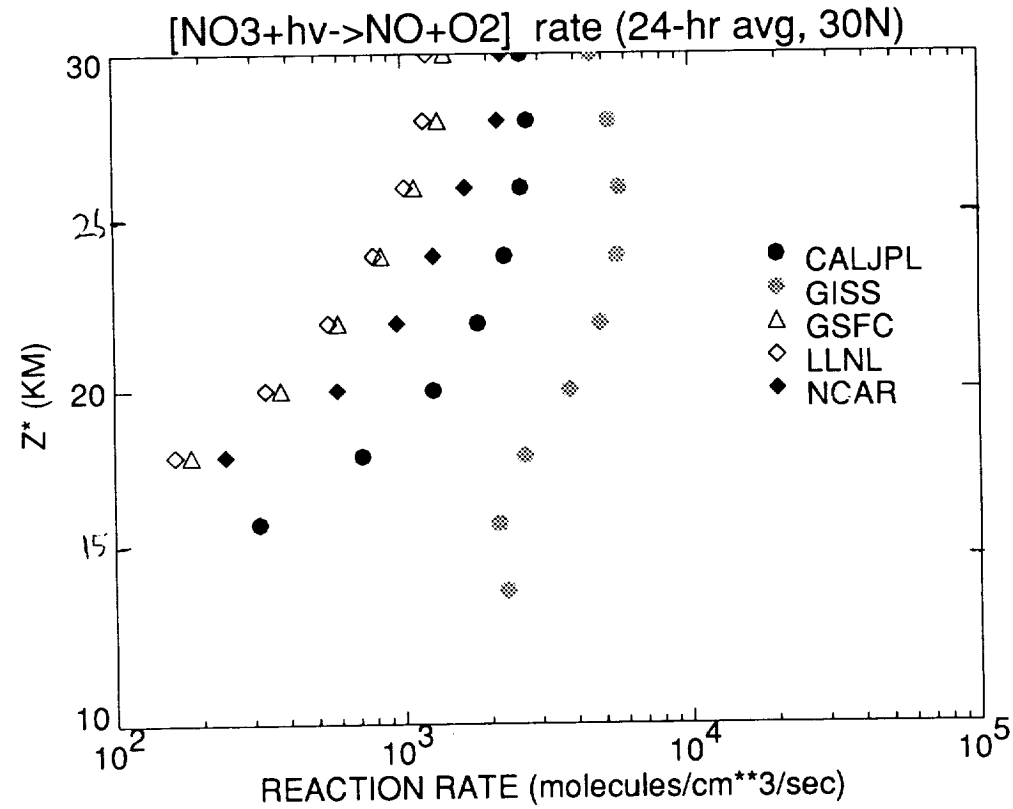

Figure L-15 (top) **Figure L-16 (bottom)**

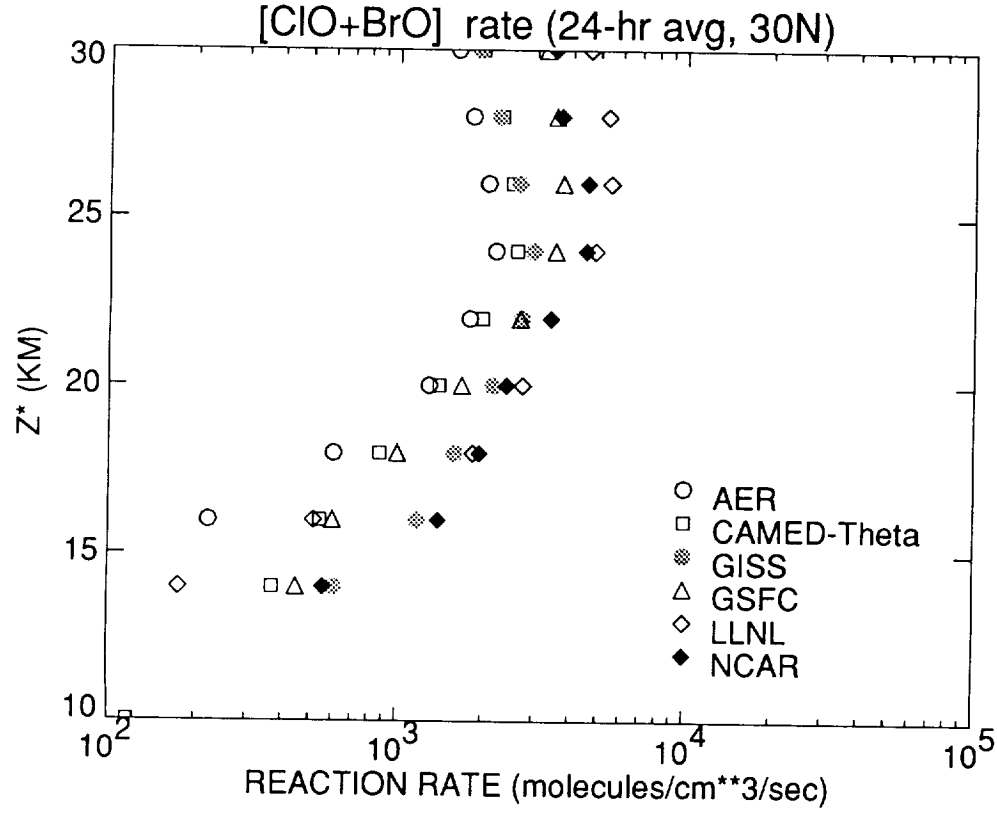

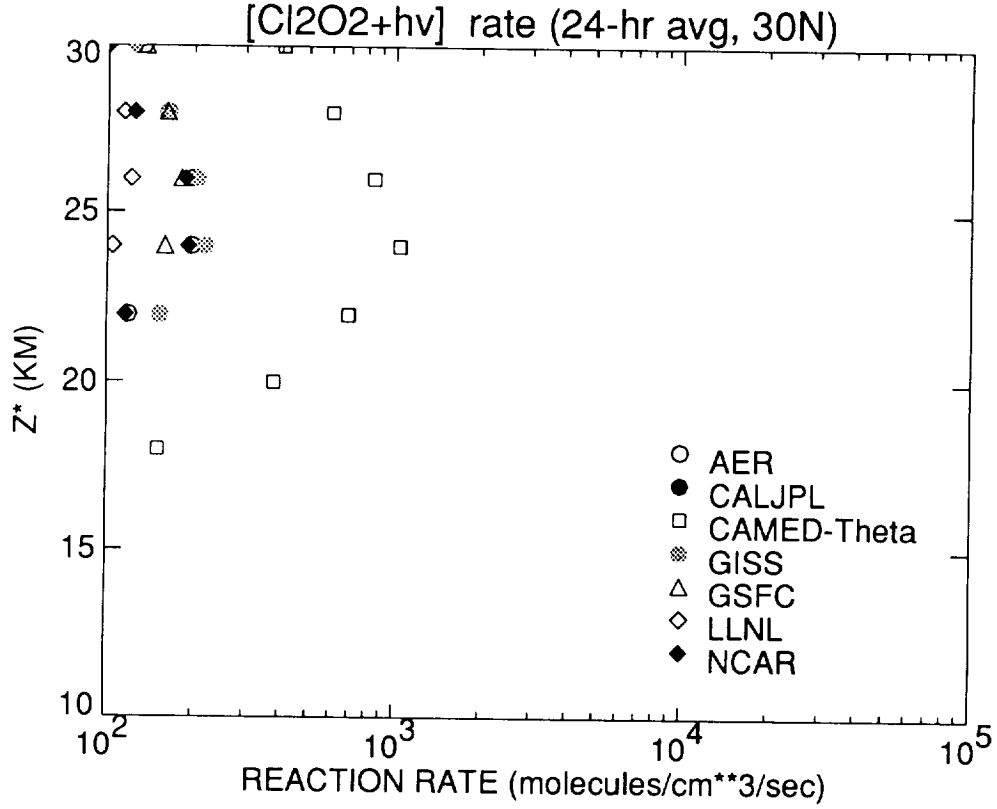

Figure L-17 (top) **Figure L-18 (bottom)**

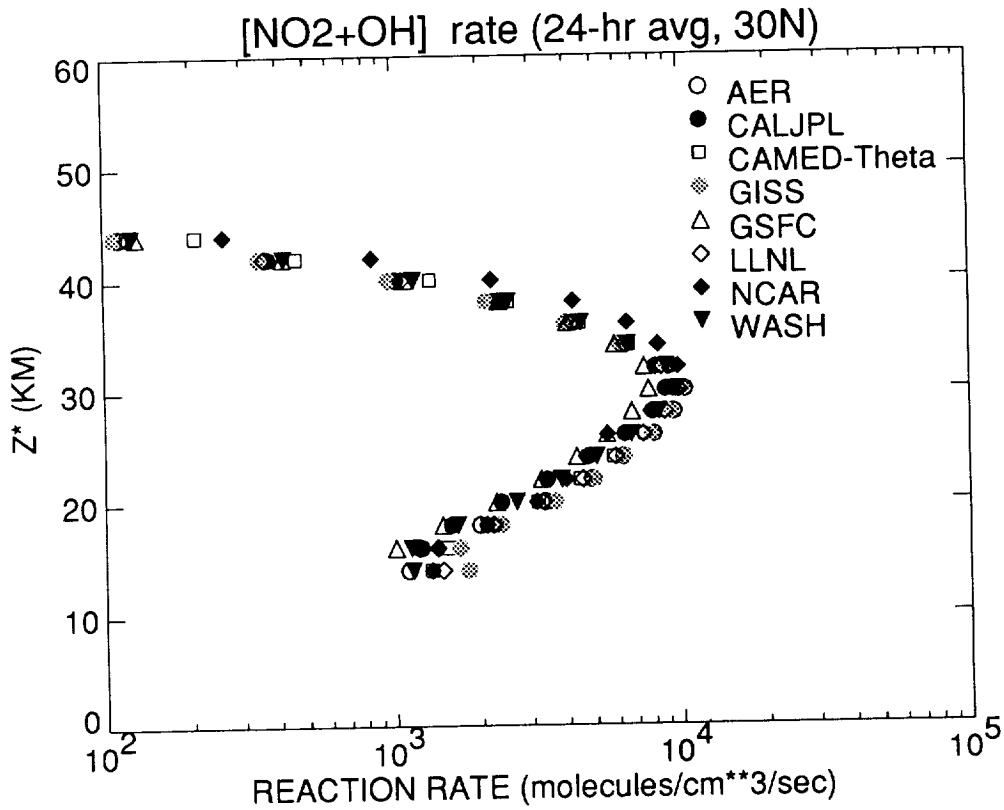

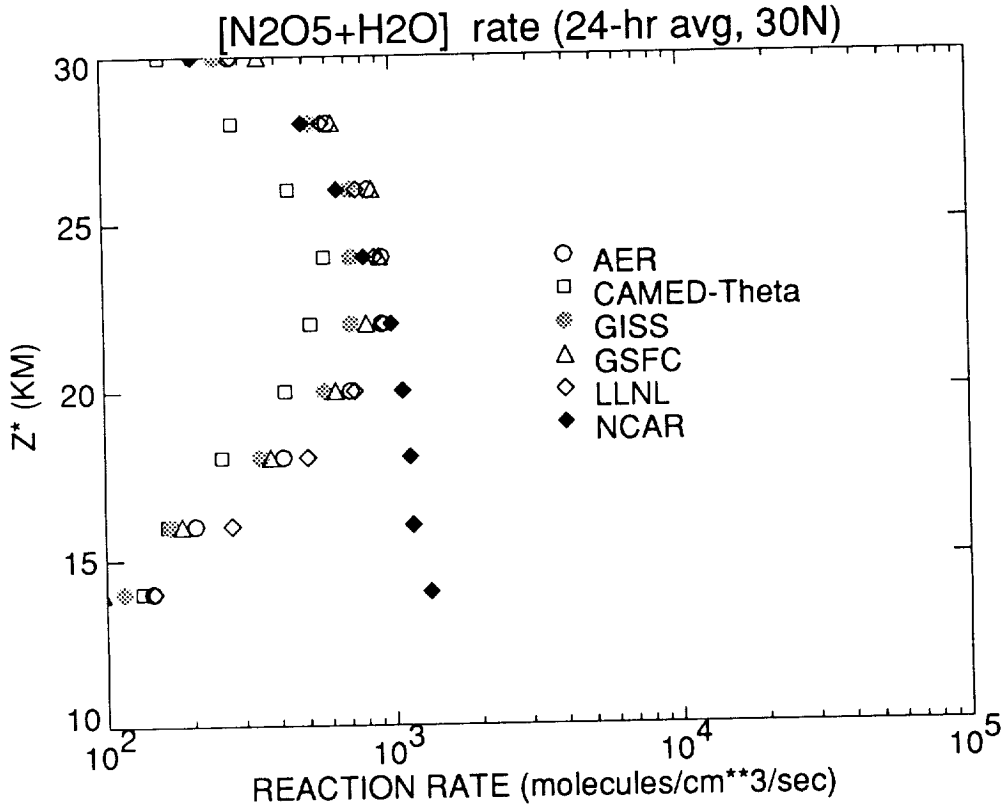

Figure L-19 (top) **Figure L-20 (bottom)**

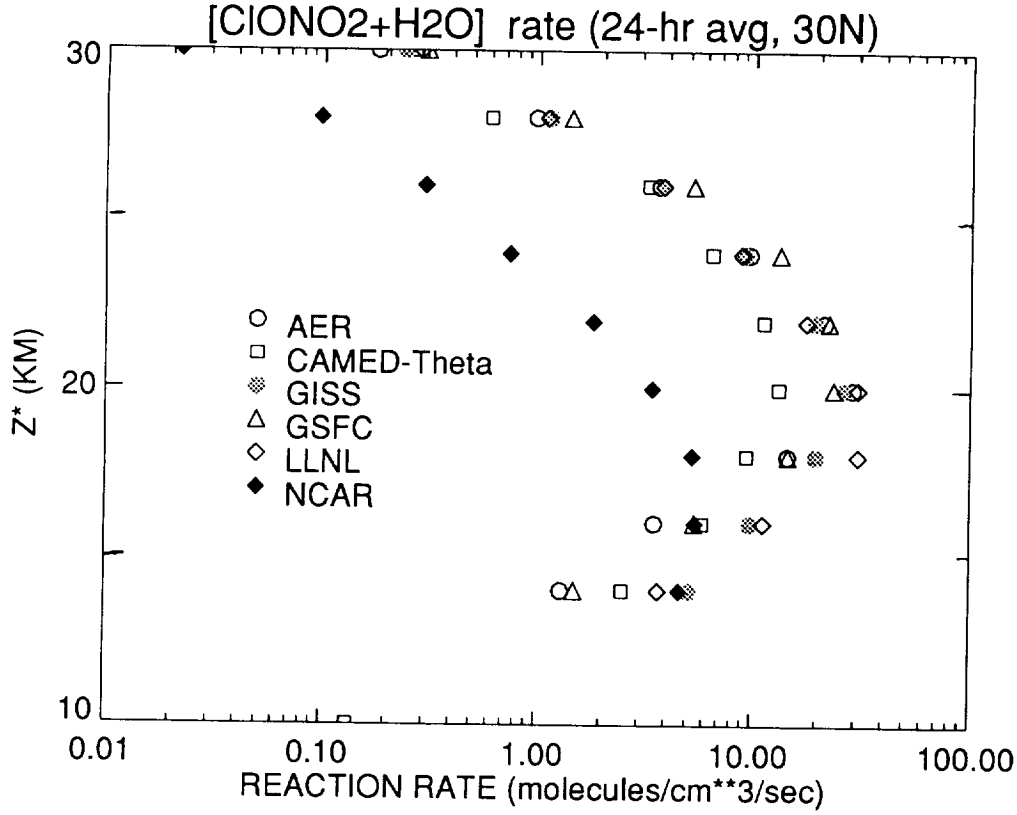
[ClONO2+H2O] rate (24-hr avg, 30N)
30
20
10
Z* (KM)
AER
CAMED-Theta
GISS
GSFC
LLNL
NCAR
0.01
0.10
1.00
10.00
100.00
REACTION RATE (molecules/cm**3/sec)

Figure L-21

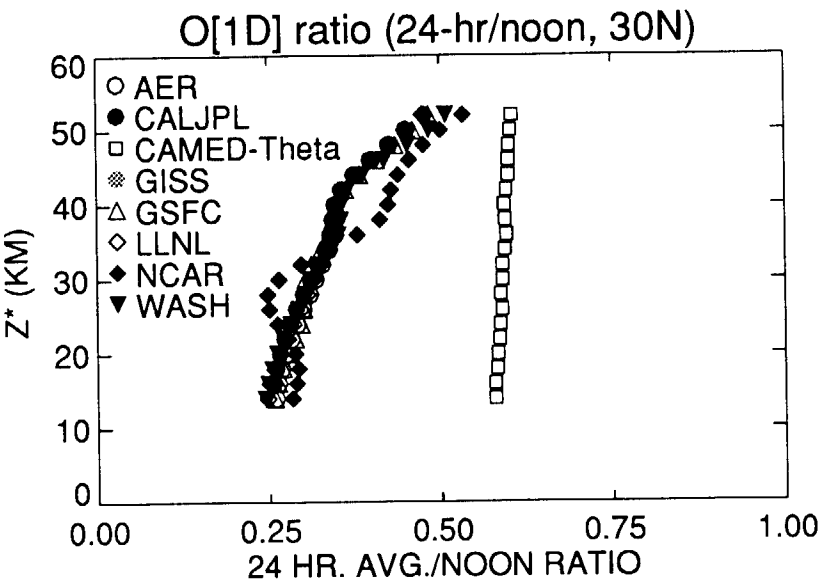

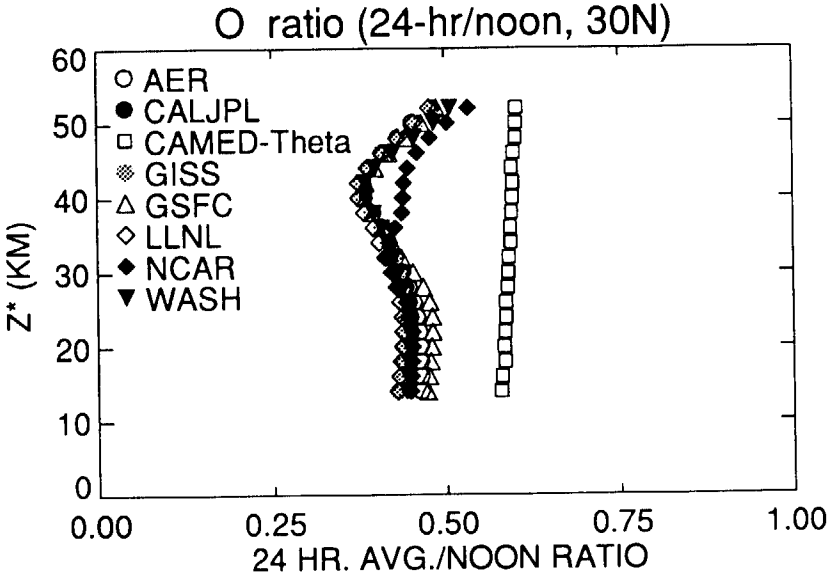

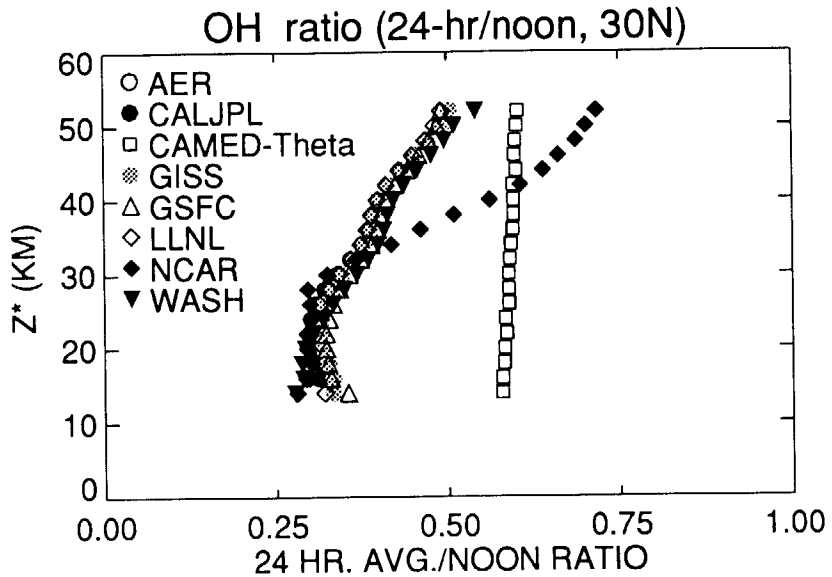

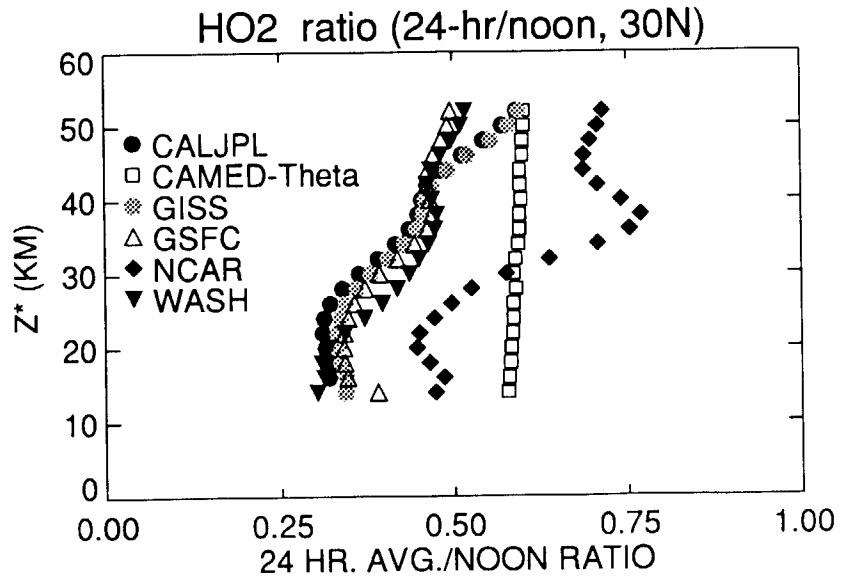

Figure L-22 (top, left) **Figure L-23 (top, right)**

Figure L-24 (bottom, left) **Figure L-25 (bottom, right)**

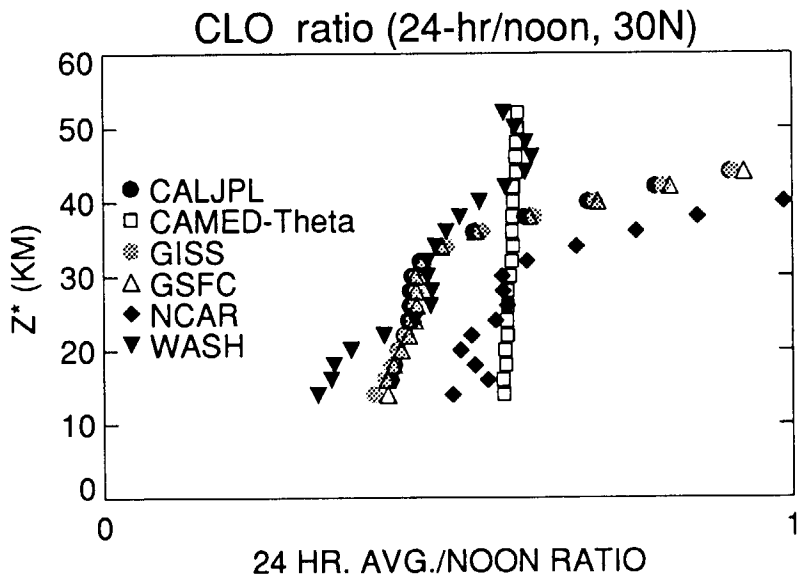

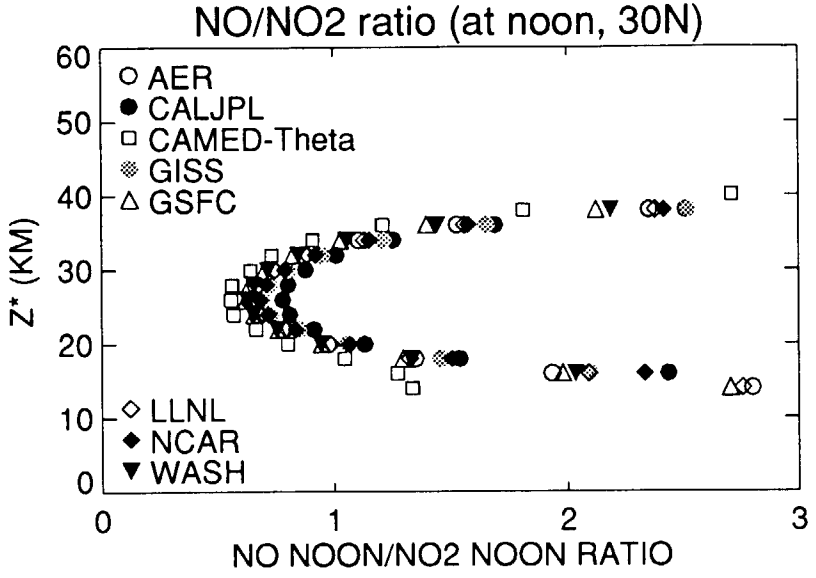

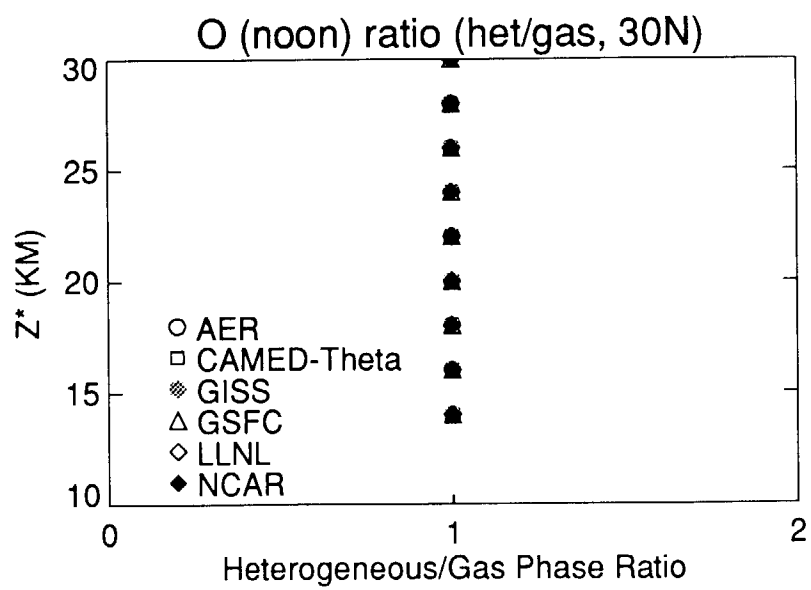

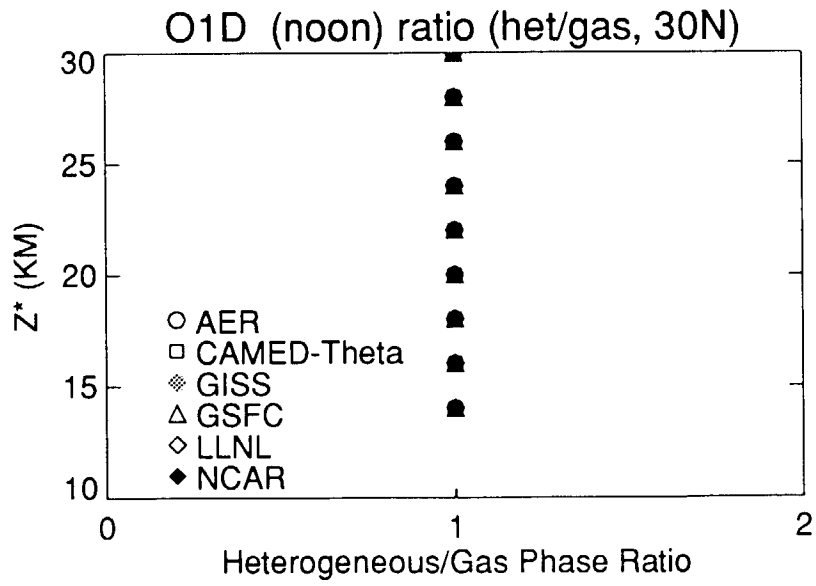

Figure L-26 (top, left) **Figure L-27 (top, right)**

Figure L-28 (bottom, left) **Figure L-29 (bottom, right)**

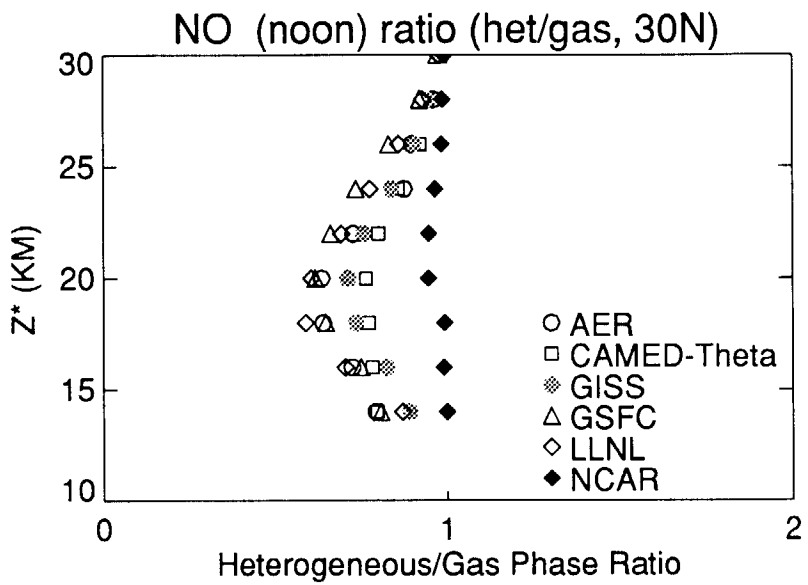

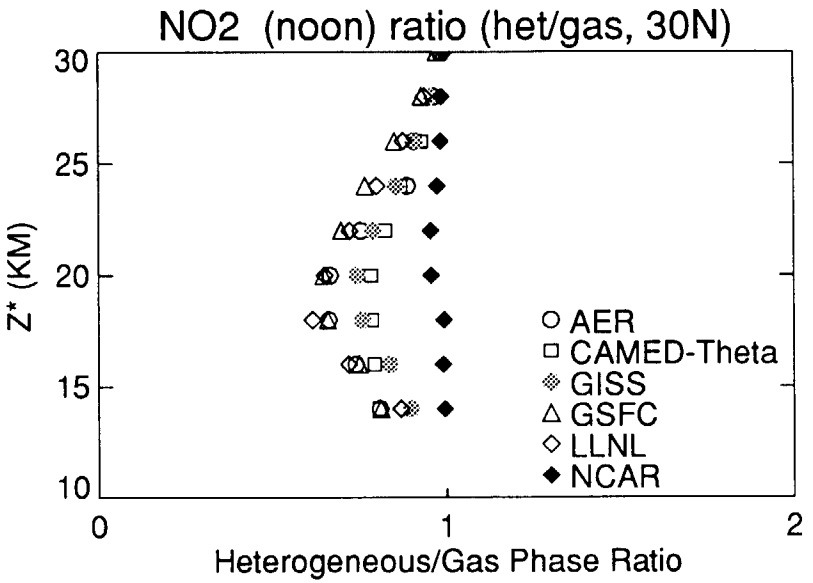

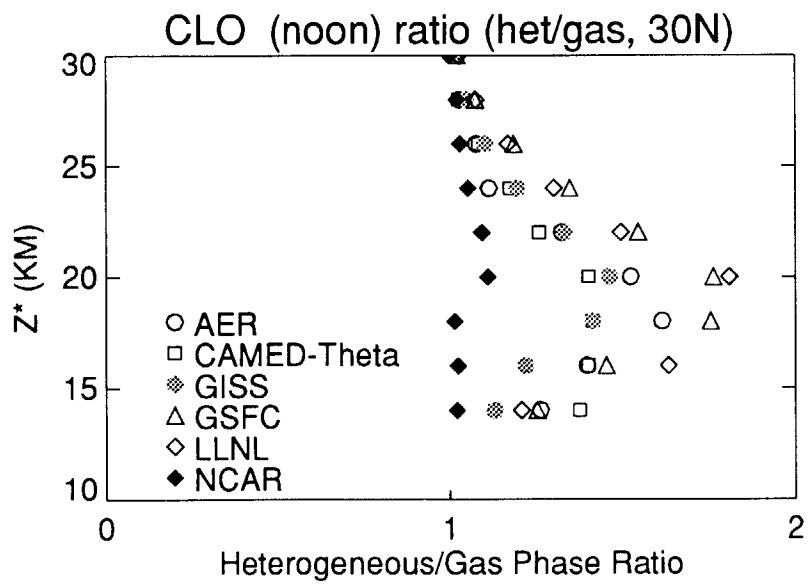

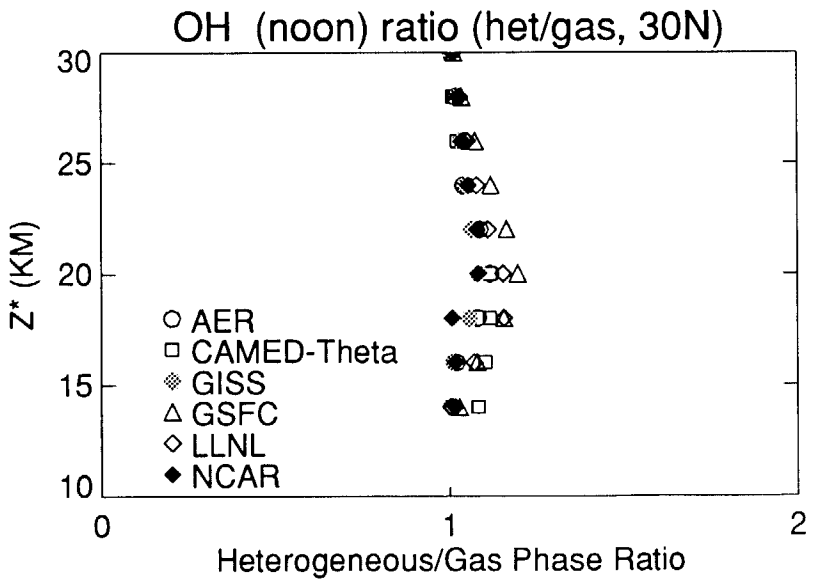

Figure L-30 (top, left) **Figure L-31 (top, right)**

Figure L-32 (bottom, left) **Figure L-33 (bottom, right)**

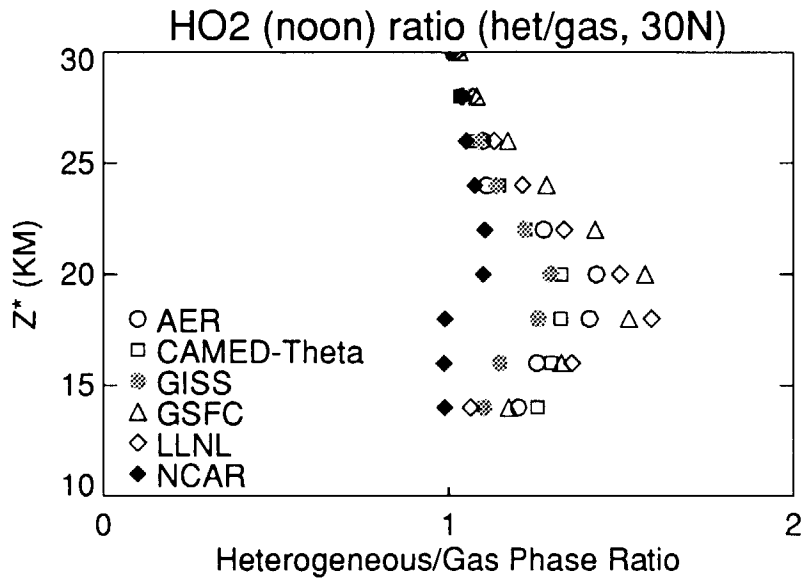

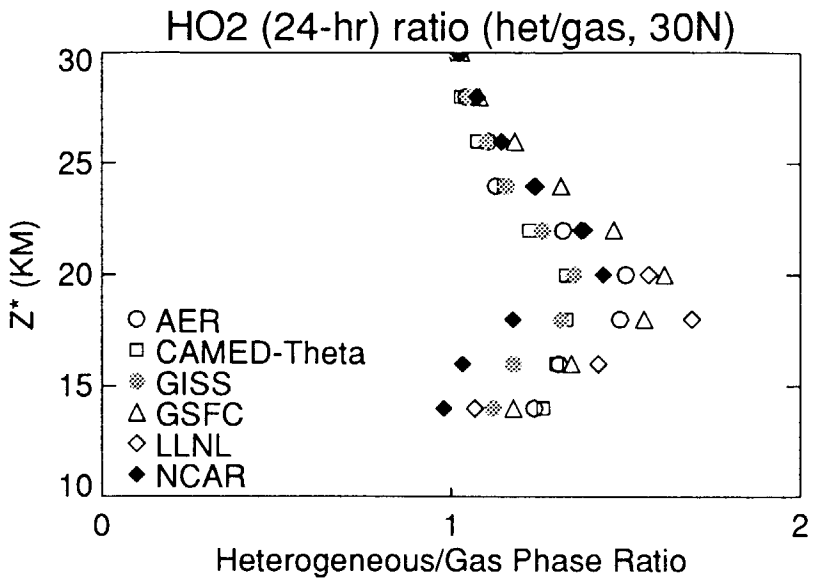

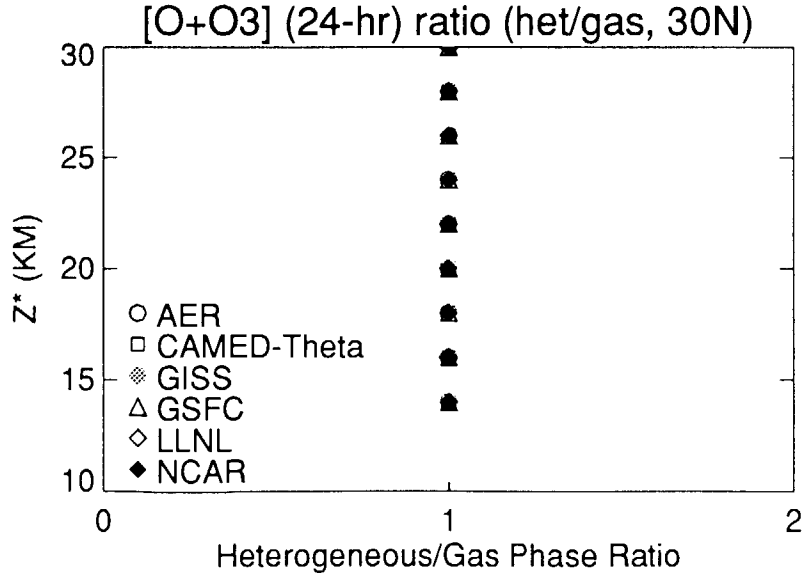

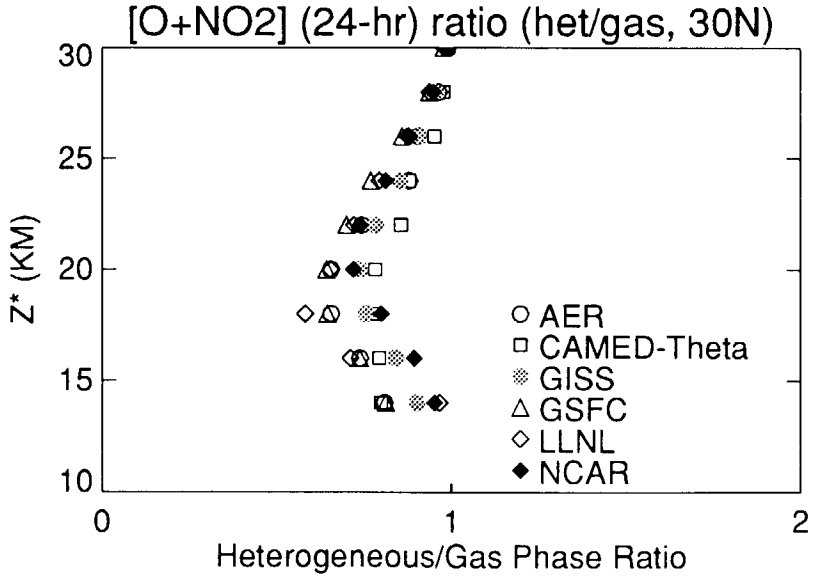

Figure L-34 (top, left) **Figure L-35 (top, right)**

Figure L-36 (bottom, left) **Figure L-37 (bottom, right)**

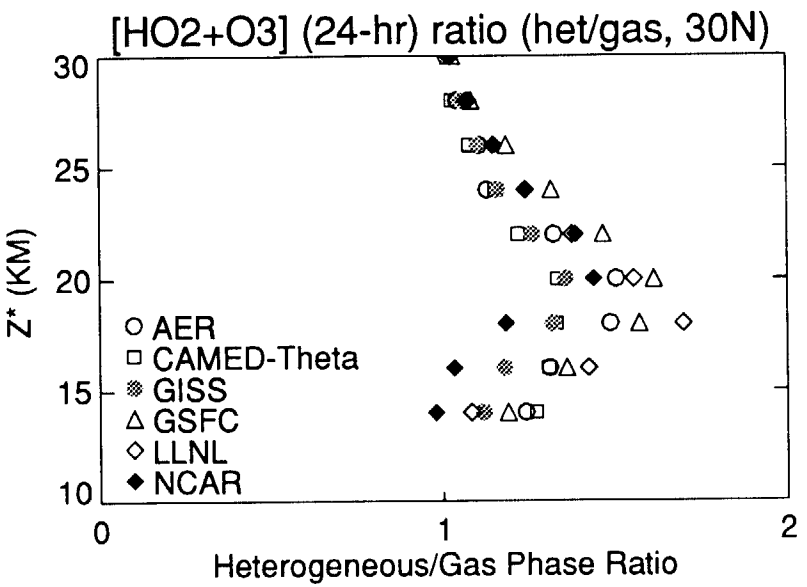

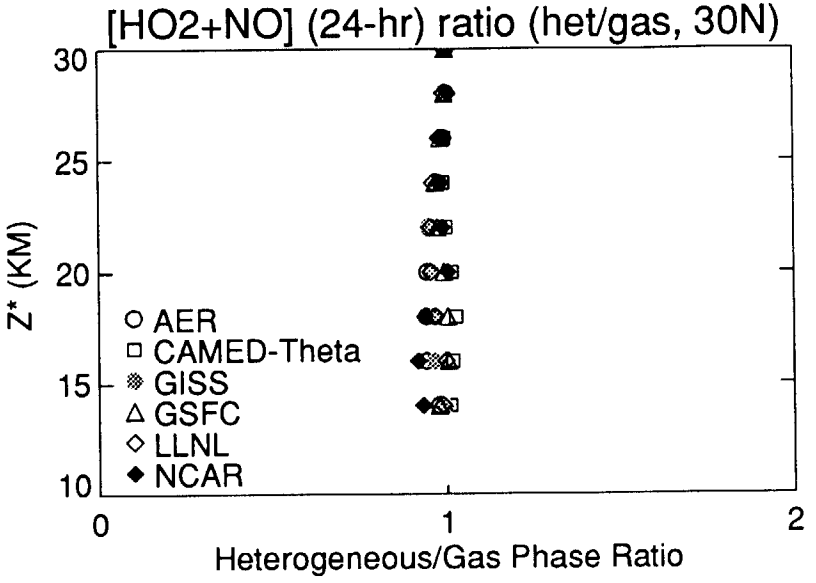

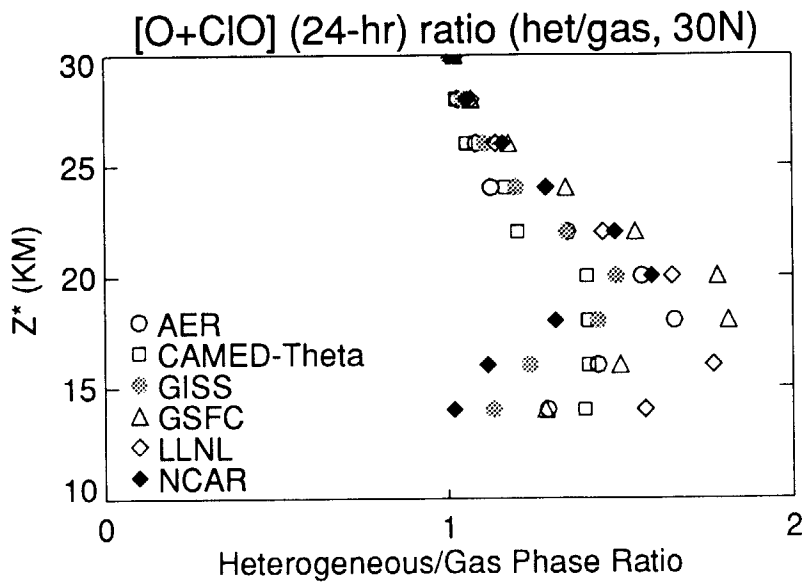

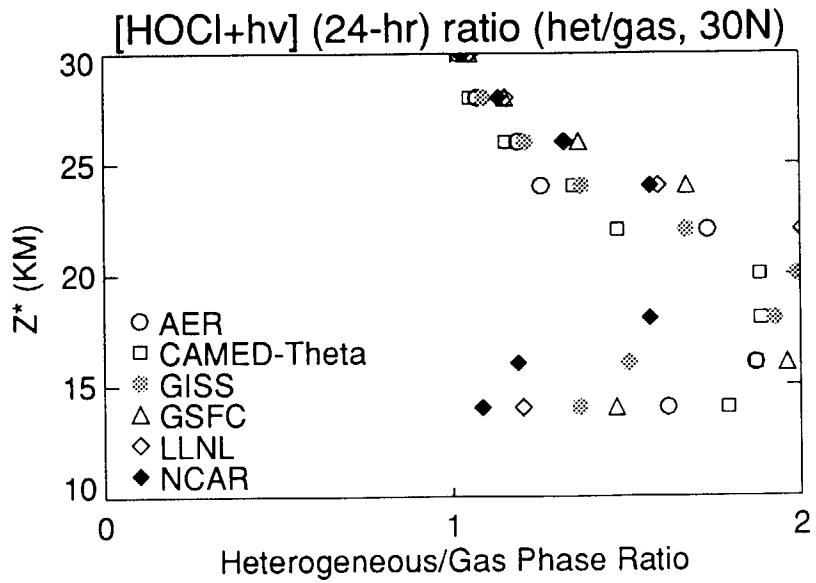

Figure L-38 (top, left) **Figure L-39 (top, right)**

Figure L-40 (bottom, left) **Figure L-41 (bottom, right)**

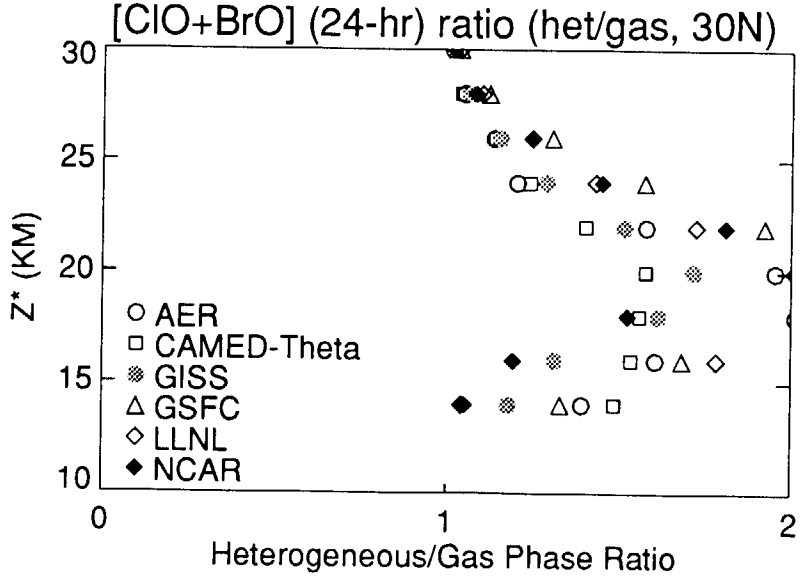

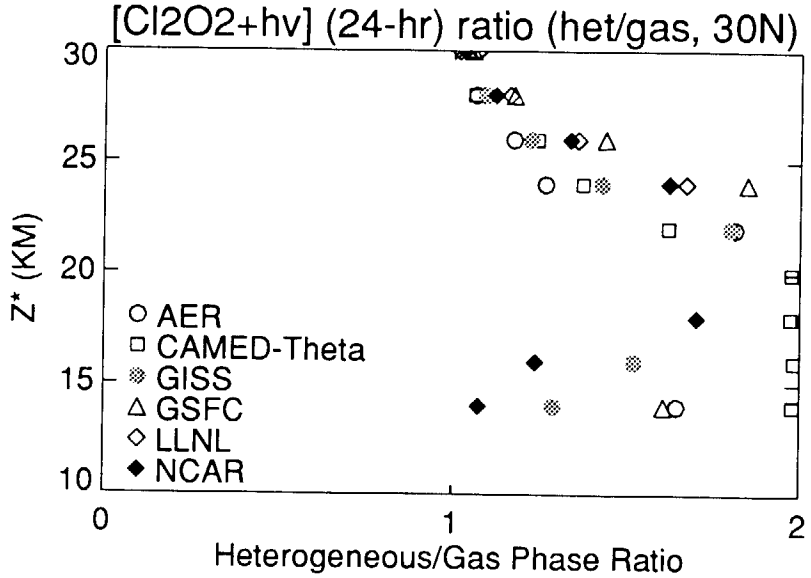

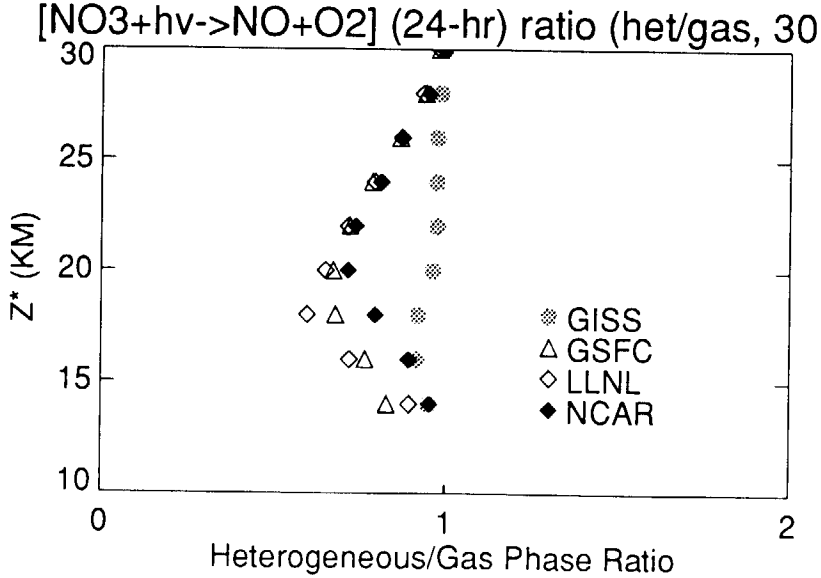

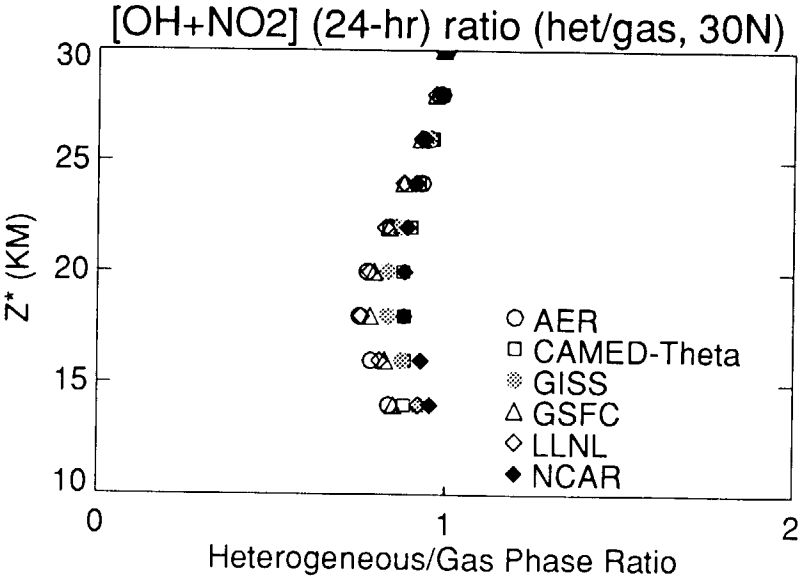

Figure L-42 (top, left) **Figure L-43 (top, right)**

Figure L-44 (bottom, left) **Figure L-45 (bottom, right)**

M: Species Comparisons with ATMOS at Sunset

M: The ATMOS Comparison

Michael J. Prather
University of California, Irvine

Curtis P. Rinsland
NASA-Langley Research Center

INTRODUCTION

The simultaneous measurement of many chemical species by the Atmospheric Trace Molecules Spectroscopy (ATMOS) instrument on the Space Shuttle provides a fundamental test of the photochemical model's partitioning of the chemical families under highly restricted conditions. Because the ATMOS observations define many quantities in the atmospheric profile (e.g., O_3, H_2O, CH_4, NO_y), this comparison tests only the photochemical components of the stratospheric models and is independent of many other components, such as the large-scale transport of tracers and predictions of ozone.

ATMOS is a solar occultation instrument that makes nearly simultaneous measurements of NO, NO_2, HNO_3, HO_2NO_2, N_2O_5, $ClONO_2$, and HCl. These measurements define the partitioning of the odd-nitrogen family (NO_y) over a large range of the middle latitude stratosphere and, additionally, put constraints on the chlorine chemistry. We are using the ATMOS measurements of 12 sunsets between 26N and 33N made on Spacelab 3 from 29 April to 1 May 1985. Sunset observations were chosen over the sunrise measurements (near 48S) because of the larger number and better quality of available profiles. The inclusion of sunrise data from this or subsequent ATMOS flights is necessary in future models and measurements comparison because the partitioning of radicals at sunrise provides a separate and distinct test of the photochemical models.

The family abundances of NO_y (from ATMOS), Cl_y (from empirical correlations with NO_y), and Br_y (fixed at 15 ppt) are summarized in Table KLM-1 along with temperature, ozone, methane, and water vapor. The geometry for the solar zenith angles is based on a latitude of +30 degrees with a solar declination of +15 degrees. We have chosen sulfate aerosol areas based on the WMO (1992) definitions for clean, non-volcanic background conditions (G. Yue, L. Poole, and L. Thomason, private communication). Results for both gas phase and heterogeneous sulfate chemistries were reported. We show only the heterogeneous results here; look at section L for direct comparisons of these two chemistries.

GEOMETRY AND MODELING OF SUNSET PROFILES

The models were asked to calculate a photochemical steady-state (i.e., repeating 24-hour cycles) and then to sample the species' densities at "sunset" for the altitude range 14 to 52 km. We have been very careful here in defining sunset as the time of day for the tangent point along the occultation path from satellite to sun. This corresponds to a solar zenith angle of exactly 90 degrees. The middle stratosphere remains illuminated by direct sunlight until the sun is more than 4 degrees below the horizon at the surface, i.e., solar zenith angles greater than 94 degrees.

There were many initial "bugs" in the reporting of these ATMOS profiles, primarily because most global models were never designed to calculate densities at a solar zenith angle of exactly 90 degrees. The calculation requires use of a quasi-spherical atmosphere for the radiative transfer. The details of the rapid chemical change near sunset are of interest as a check on the chemical models (the reason for their inclusion in this Models and Measurements Workshop Report), but such details have very little impact on the overall budgets and balances, which are dominated by

what happens within several hours of noon. Therefore, many of the chemical parameterizations used in the global models were unable to compute a sunset value (e.g., the CAMED model uses diurnal "factors," and the NCAR model calculates 24-hour photolysis rates in deriving radicals and rates); others had to revise significantly their photochemical modules. In general, it was agreed that such comparisons are needed to test the ozone assessment models and that the photochemical modules in the global models should be capable of diagnosing sunset and sunrise values.

UNCERTAINTIES OF THE ATMOS OBSERVATIONS

Estimated uncertainties for the ATMOS/Spacelab profiles are summarized in Table M-1 (*see* Rinsland, 1989; Russell, 1988; Zander, 1990, 1992). We recognize that the 12 occultation profiles made at sunset, ranging in latitude from 25.6N to 32.7N over the period 29 April to 1 May 1985, are not necessarily representative of the entire middle-latitude stratosphere. Some of the chemical partitioning may take days to establish, and we do not know the trajectories (i.e., photolytic history) of the sampled air. Only HO_2NO_2 and N_2O_5 have uncertainties large enough to affect the interpretation of the simulations below, although the 27% uncertainty in HNO_3 introduces a significant range to the assumed NO_y profile in the lower stratosphere. Future models and measurements comparisons should consider that the potential systematic errors included in Table M-1 would not affect the shape of the profile, and thus the relative profiles may be more tightly constrained than Table M-1 implies.

Table M-1. Uncertainties of 30N ATMOS/Spacelab 3 Volume Mixing Ratio Profiles

Altitude	p	Percent Relative Uncertainty (1-sigma)						
(km)	(mb)	NO	NO_2	HNO_3	HO_2NO_2	N_2O_5	$ClONO_2$	HCl
51.5	0.7	20	25	--	--	--	--	11
47.5	1.2	20	25	--	--	--	--	11
43.5	1.9	20	15	--	--	--	--	10
39.5	3.2	20	15	27	--	--	--	10
35.5	5.5	20	15	27	--	--	15	10
31.5	9.7	20	15	27	70	--	12	10
27.5	17	20	15	27	40	32	12	10
23.5	32	20	15	27	40	--	15	10
19.5	60	20	15	27	50	--	20	10

NO_2 and NO [Figures M-1 and M-2]

The agreement of ATMOS measurements and the models for NO and NO_2 is surprisingly good. In the upper stratosphere, these species comprise the majority of the NO_y, and thus the specification of NO_y forces some of this agreement. However, the fall-off of NO_2 above 35 km is a true test of the models, and it is excellently reproduced. In the lower-middle stratosphere, given the number of factors affecting NO_x/NO_y partitioning (e.g., OH, heterogeneous chemistry, three-body rates), the model agreement with ATMOS for both NO and NO_2 is a very successful test. Differences over the critical region 16-26 km are less than 30%. There is a systematic tendency for the models to underpredict the NO_2/NO ratio by about 20% throughout the profile, but one must consider the difficult geometries in calculating NO_2 photolysis through sunset.

Grade: A-

HNO_3 [Figure M-3]

The models agree with the ATMOS profile for HNO_3 to better than 20% over most of the stratosphere. A most important region is the fall-off above 30 km where the HNO_3 abundance reflects a balance between the OH + NO_2 reaction and photolysis. The comparison here, where HNO_3 is a small fraction of the NO_y family, is excellent.

Grade: A

HO_2NO_2 [Figure M-4]

The majority of the models (CALJPL, GISS, LLNL) agree with the ATMOS profile over the limited range (20-34 km) to better than 30%. The GSFC model is generally larger by as much as a factor of about 2. The shape of the profile with a peak mixing ratio near 28 km is accurately predicted by all models.

Average Grade: B+

N_2O_5 [Figure M-5]

The difference among models, a factor of 2, is larger than for the previous NO_y species. The ATMOS measurements are systematically smaller than all of the model predictions by at least a factor of 3. At sunset, N_2O_5 has been photolyzed all day and is predicted (and observed) to be a small fraction of the total NO_y species; near sunrise, however, there is an accumulation of N_2O_5 resulting from its formation throughout the night. (In the GISS model the ratio of sunrise to sunset is about a factor of 6 at 30 km and smaller below 30 km.) An earlier model analysis of the ATMOS N_2O_5 measurements (Rinsland et al., 1989) showed that the sunrise data (taken at 48S, not part of the current comparison) are in reasonable agreement with model predictions. One possible cause of the discrepancy shown here might be that photolytic loss of N_2O_5 during the day is underestimated by the models (see discussion in Rinsland et al., 1989); however, the 48S profiles represent quite different atmospheric conditions in terms of temperature and photolysis rates, and the combination of 48S at sunrise followed by 30N at sunset cannot be viewed simply as a measure of the diurnal cycle of N_2O_5.

Nevertheless, the overestimate of N_2O_5 is worrisome, because our heterogeneous chemical removal of NO_x to HNO_3, proportional to N_2O_5, would also be in error. (However, the NO_x/HNO_3, ratios noted above look good.) It is important to re-evaluate this problem, focusing on altitudes below 25 km in light of the importance of the N_2O_5-sulfate reaction. We recommend extending this comparison to the 48S sunrise data and to the recent 1992 ATMOS measurements.

Grade: C

$ClONO_2$ [Figure M-6]

The model predictions are in good agreement with each other where the peak levels of $ClONO_2$ occur between 26 and 34 km. However, they are uniformly greater than the ATMOS profiles by about a factor of 1.5. An exception is the CALJPL model, which shows excellent agreement between 20 and 30 km; however, the CALJPL model chose a Cl_y profile, different from that recommended in Table KLM-1, based on their previous analysis of the ATMOS profiles. (The CALJPL choice appears optimized to $ClONO_2$ rather than HCl; see next section.) Possibly, some of the problems with overpredicting N_2O_5 at sunset apply to $ClONO_2$, which is also photolyzed at long ultraviolet wavelengths. Overall, the shape of the profile is excellent.

Grade: B+

HCl [Figure M-7]

The predicted HCl profile shows a lot of structure in the lower stratosphere, with a minimum mixing ratio in some cases near 28 km at the $ClONO_2$ maximum. The range in model results for HCl between 20 and 40 km can in general be attributed to the different predictions for $ClONO_2$ below 30 km and that for ClO above. The ATMOS profile does indeed show an inflection point near 24 km, but its shape is different from the models. One source of this discrepancy may be the prescribed Cl_y profile (based loosely on aircraft and balloon data correlations of halocarbons with N_2O and thence NO_y), which may be too large in the lower stratosphere. (The CALJPL profile has less Cl_y in the lower stratosphere.) There still remain some obvious problems with the Cl_y partitioning, because if we look at the ratio $ClONO_2$/HCl all of the models (including CALJPL) would be systematically higher than ATMOS.

Grade: B-

ClO and HOCl [Figures M-8 and M-9]

We include the modeled sunset profiles of ClO and HOCl for completeness, although ATMOS did not measure them. Although all of the reporting models produce a similar profile for both ClO and HOCl, there are some large differences. CALJPL has, of course, lower ClO mixing ratios between 20 and 30 km because of their lower Cl_y profile; however, that does not explain the much larger range of results for HOCl. The GSFC model diverges above 40 km, predicting substantially more ClO and HOCl than the other models. However, the models (AER, CALJPL, GISS, GSFC, LLNL) agree reasonably for HOCl and ClO (and hence Cl_y partitioning) in the lower stratosphere near 20 km. In future models and measurements comparisons it may be possible to use the simultaneous measurements of ClO and HCl from the ER-2 to augment the ATMOS test in the lower stratosphere.

BrO, $BrONO_2$, and HBr [Figures M-10, M-11, and M-12]

The predicted partitioning of key species of the bromine family are also included here for completeness of documenting the models. The sunset values of BrO range from 2 to 4 ppt near 20 km where the bromine catalyzed ozone loss is important. Throughout the lower stratosphere $BrONO_2$ is expected to be about 10 ppt and is the dominant form of bromine. (The LLNL model has an unusual $BrONO_2$ profile below 25 km and must have the Br_y in some other form.) HBr is expected to be small, less than 1 ppt, in all reporting models; but the GSFC model here is aberrant. It is not clear whether we will ever have any pair of Br_y species measured that would test this partitioning.

SUMMARY

In summary, the ATMOS comparison was surprisingly good once the "sunset" reporting difficulties were overcome. The N_2O_5 discrepancy is worrisome, but the NO_x/HNO_3 partitioning in the lower stratosphere looks good. More effort needs to be put in the Cl_y analysis, perhaps resetting the profile, before we can examine the HCl profiles in detail.

Despite the large range (factor of 1.5 to 2) in model profiles relative to the ATMOS measurements, this comparison is quite encouraging. For example, most of the differences correspond to less than a 2-km shift in the profiles. If we are incorrectly modeling any key reactions that control such partitioning then it must have a profile similar to the currently modeled reactions. Therefore, matching the observed ATMOS profiles over two orders of magnitude

throughout the stratosphere demonstrates that the basic mechanisms partitioning the chemical families are probably well represented in the models.

REFERENCES

Rinsland, C. P., G. C. Toon, C. B. Farmer, R. H. Norton, and J. S. Namkung, Stratospheric N_2O_5 profiles at sunrise and sunset from further analysis of the ATMOS/Spacelab 3 solar spectra, *J. Geophys. Res., 94*, 18341-18349, 1989.

Russell, J. M. III, C. B. Farmer, C. P. Rinsland, R. Zander, L. Froidevaux, G. C. Toon, B. Gao, J. Shaw, and M. Gunson, Measurements of odd nitrogen compounds in the stratosphere by the ATMOS experiment on Spacelab 3, *J. Geophys. Res., 93*, 1718-1736, 1988.

World Meteorological Organization (WMO), *Scientific Assessment of Ozone Depletion, 1991*, Global Ozone Research and Monitoring Project Report No. 25, WMO, Geneva, 1992.

Zander, R., M. R. Gunson, J. C. Foster, C. P. Rinsland, and J. Namkung, Stratospheric $ClONO_2$, HCl, and HF concentration profiles derived from ATMOS Spacelab 3 observations: An update, *J. Geophys. Res., 95*, 20519-20525, 1990.

Zander, R., M. R. Gunson, C. B. Farmer, C. P. Rinsland, F. W. Irion, and E. Majieu, The 1985 chlorine and fluorine inventories in the stratosphere based on ATMOS observation at 30 north latitude, *J. Atmos. Chem., 15*, 171-186, 1992.

FIGURE CAPTIONS

Figure M-1. NO_2 (het, sunset, May 30N).

Figure M-2. NO (het, sunset, May 30N).

Figure M-3. HNO_3 (het, sunset, May 30N).

Figure M-4. HO_2NO_2 (het, sunset, May 30N).

Figure M-5. N_2O_5 (het, sunset, May 30N).

Figure M-6. $ClONO_2$ (het, sunset, May 30N).

Figure M-7. HCl (het, sunset, May 30N).

Figure M-8. ClO (het, sunset, May 30N).

Figure M-9. HOCl (het, sunset, May 30N).

Figure M-10. BrO (het, sunset, May 30N).

Figure M-11. $BrONO_2$ (het, sunset, May 30N).

Figure M-12. HBr (het, sunset, May 30N).

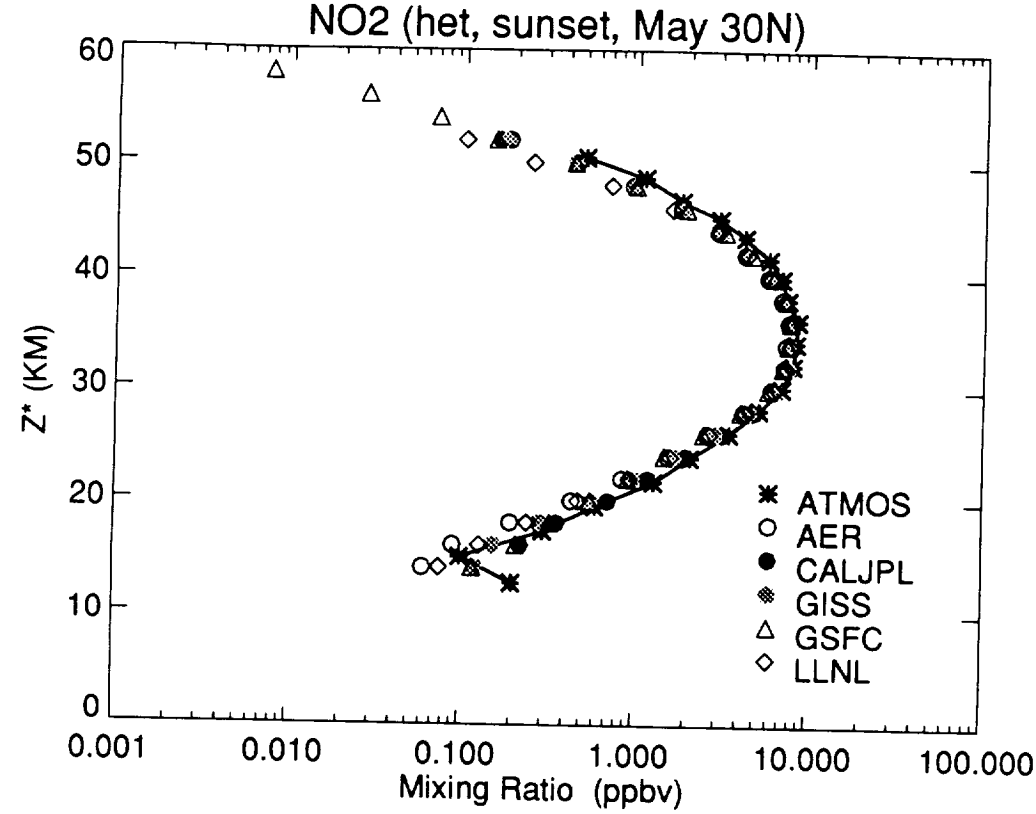

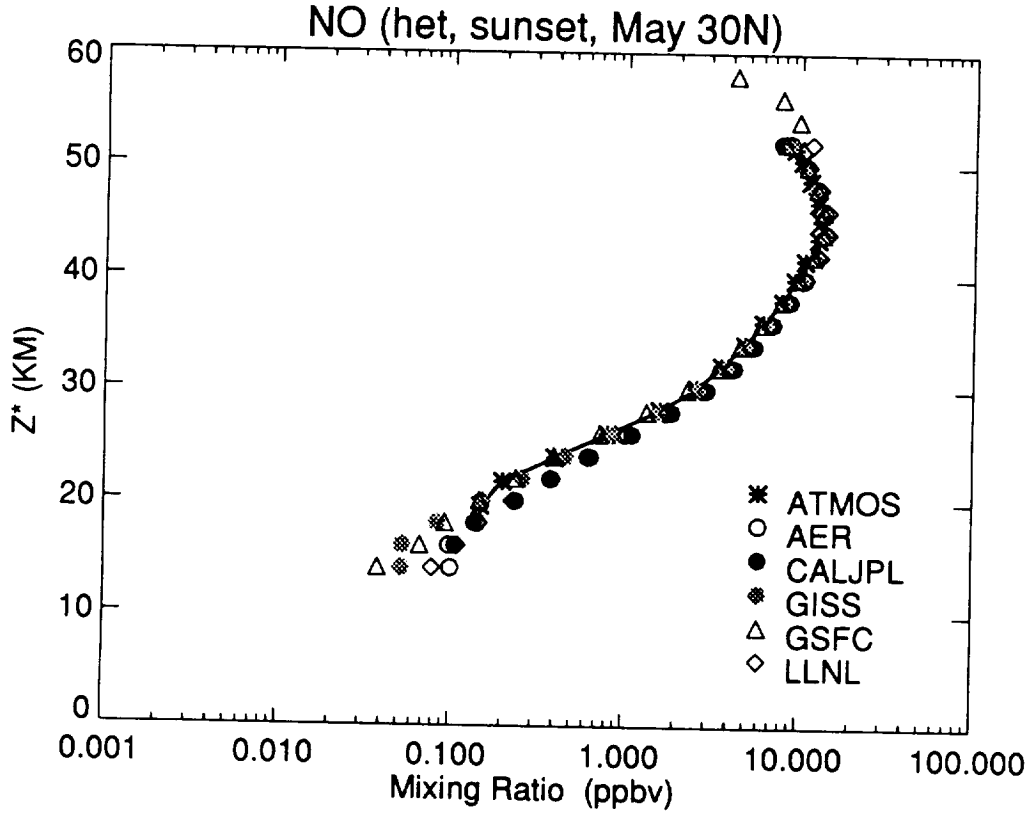

Figure M-1 (top) Figure M-2 (bottom)

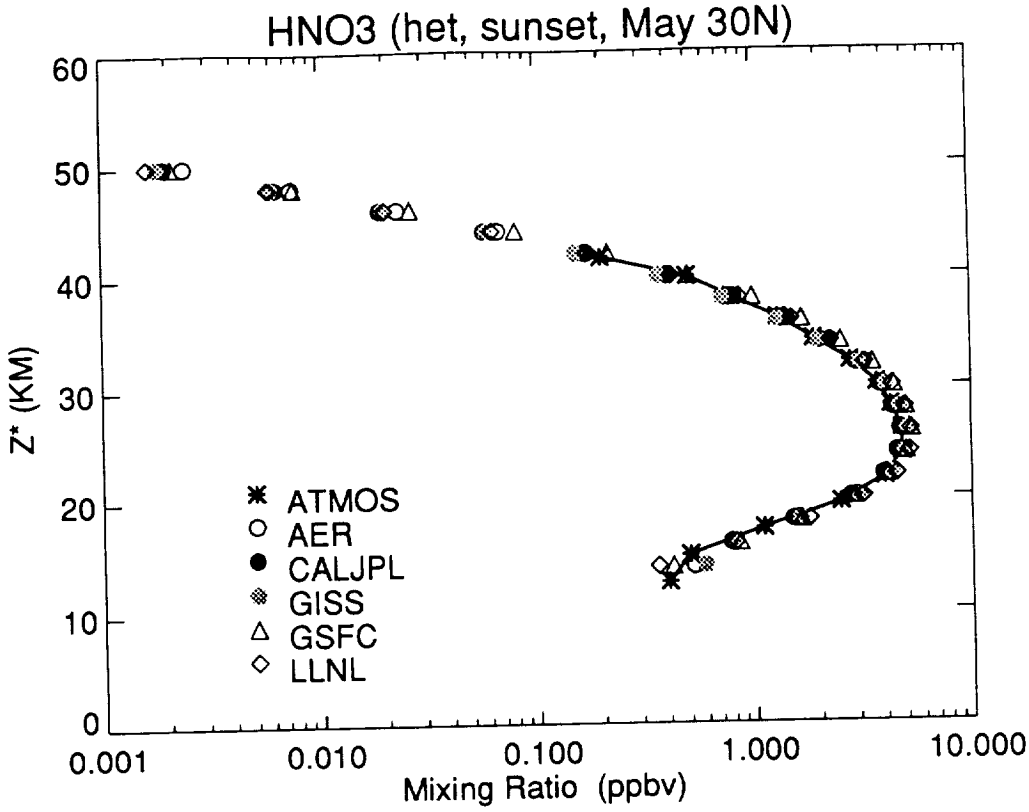

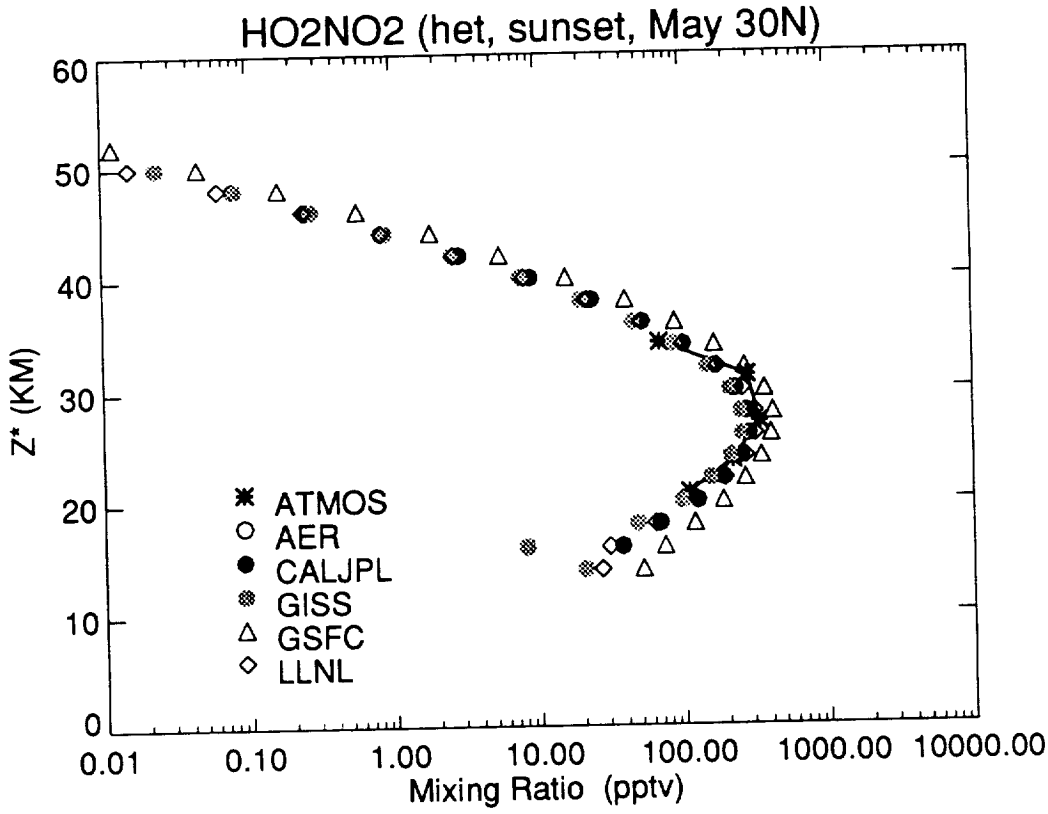

Figure M-3 (top) Figure M-4 (bottom)

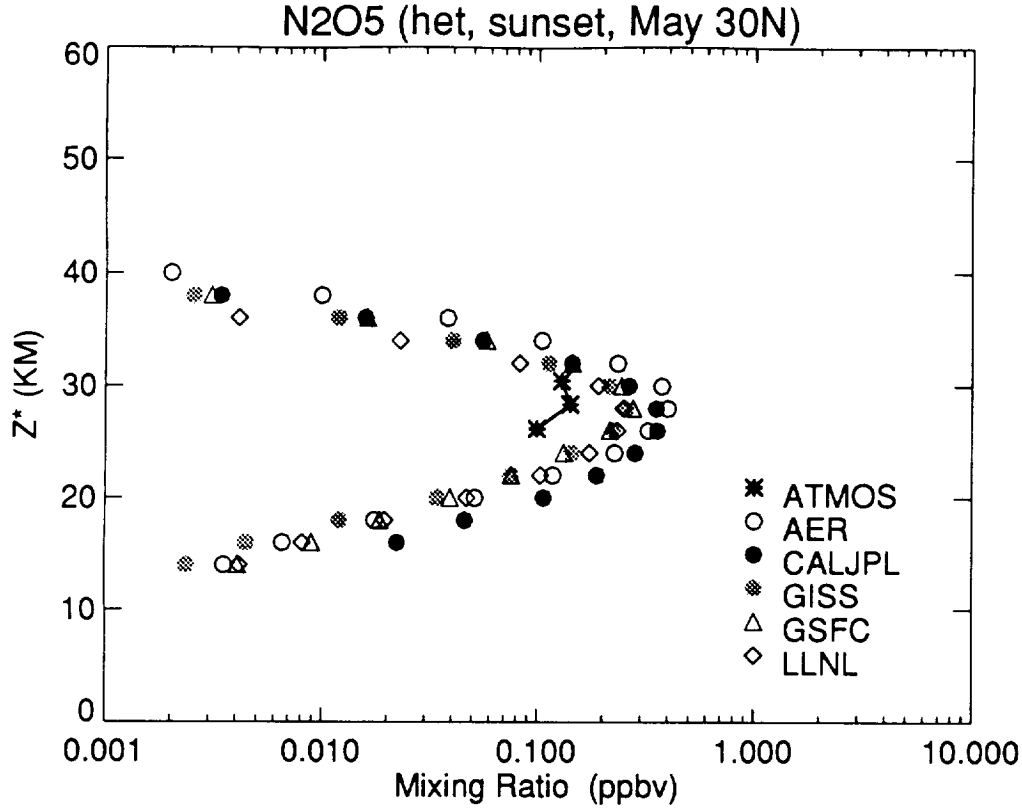

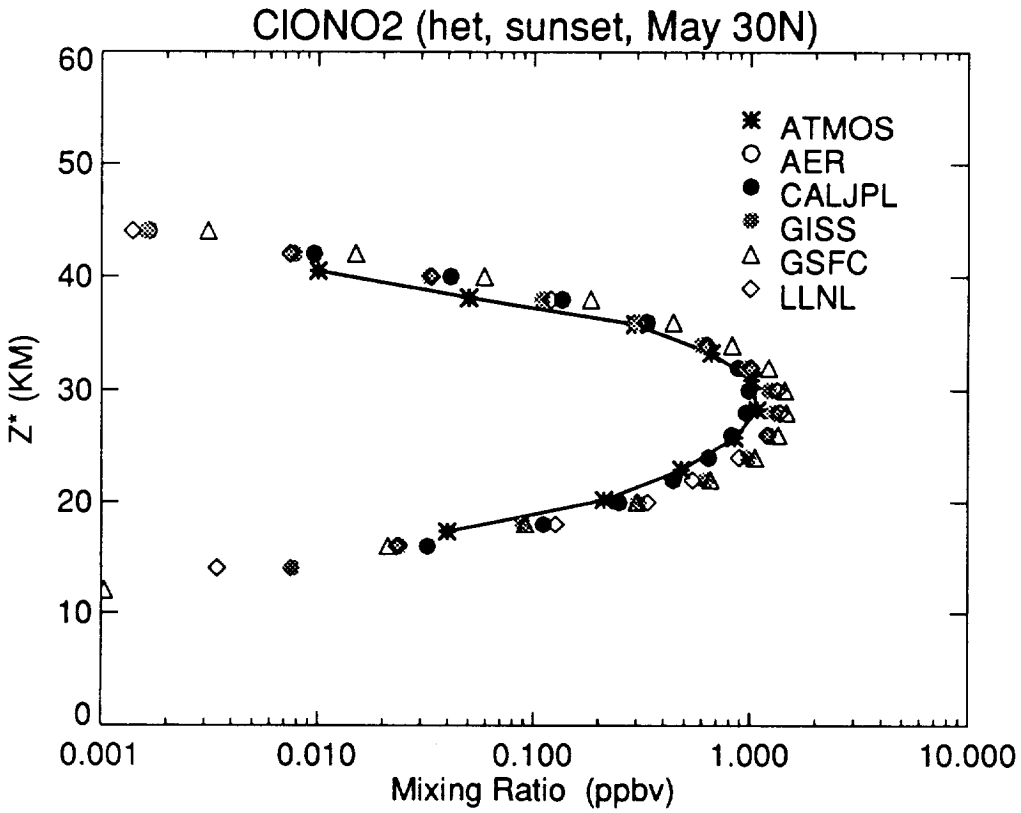

Figure M-5 (top) Figure M-6 (bottom)

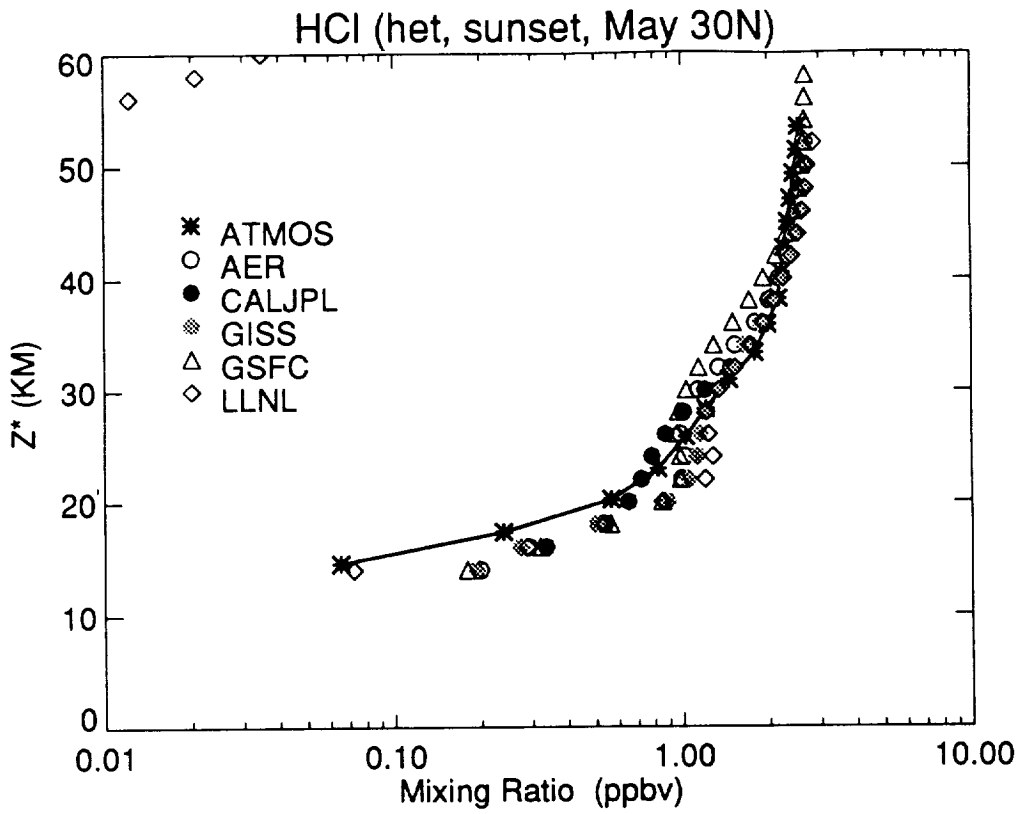

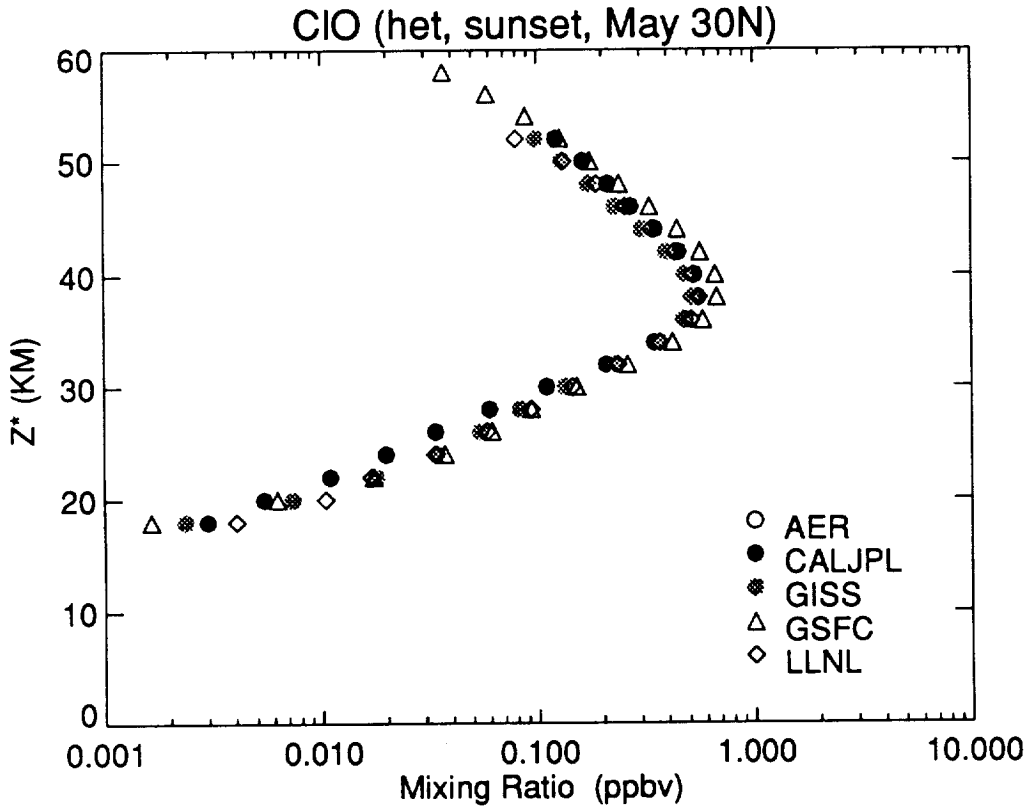

Figure M-7 (top) Figure M-8 (bottom)

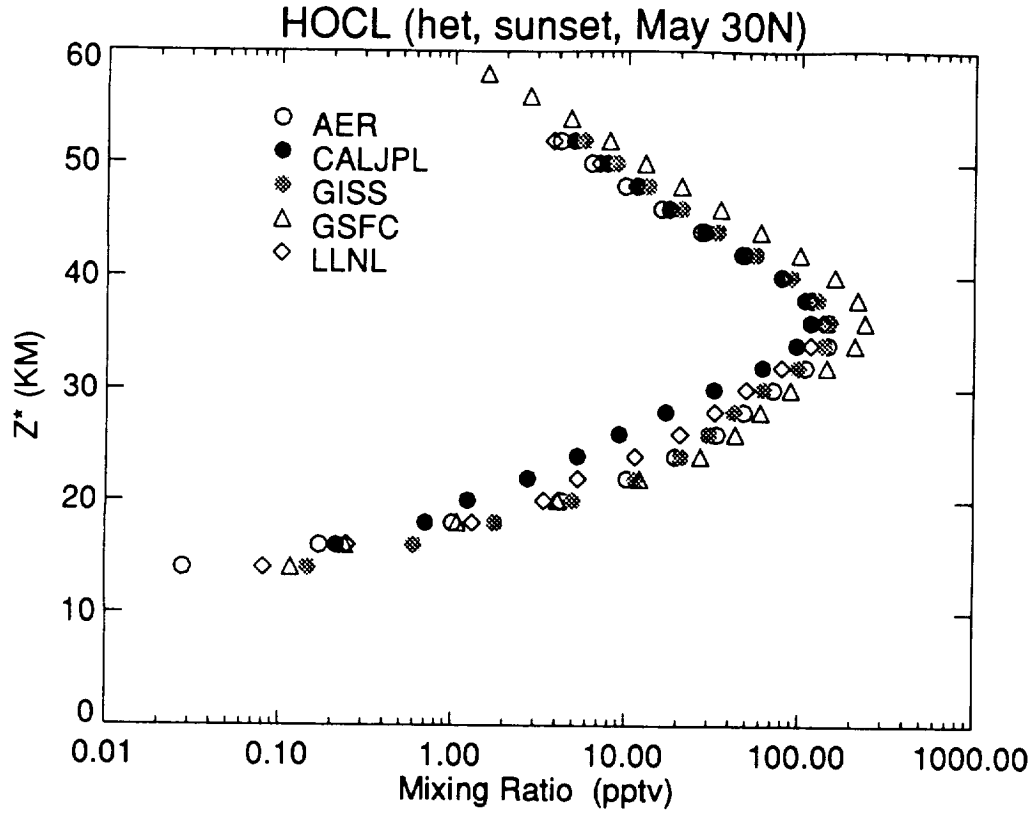

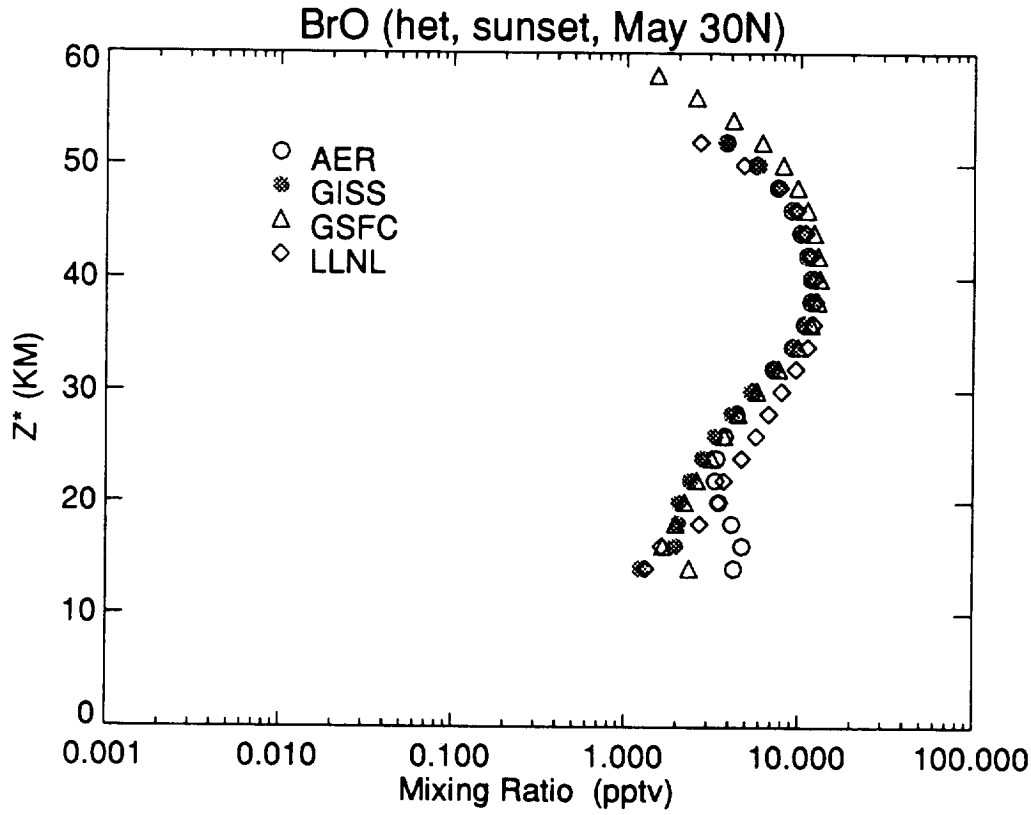

Figure M-9 (top) Figure M-10 (bottom)

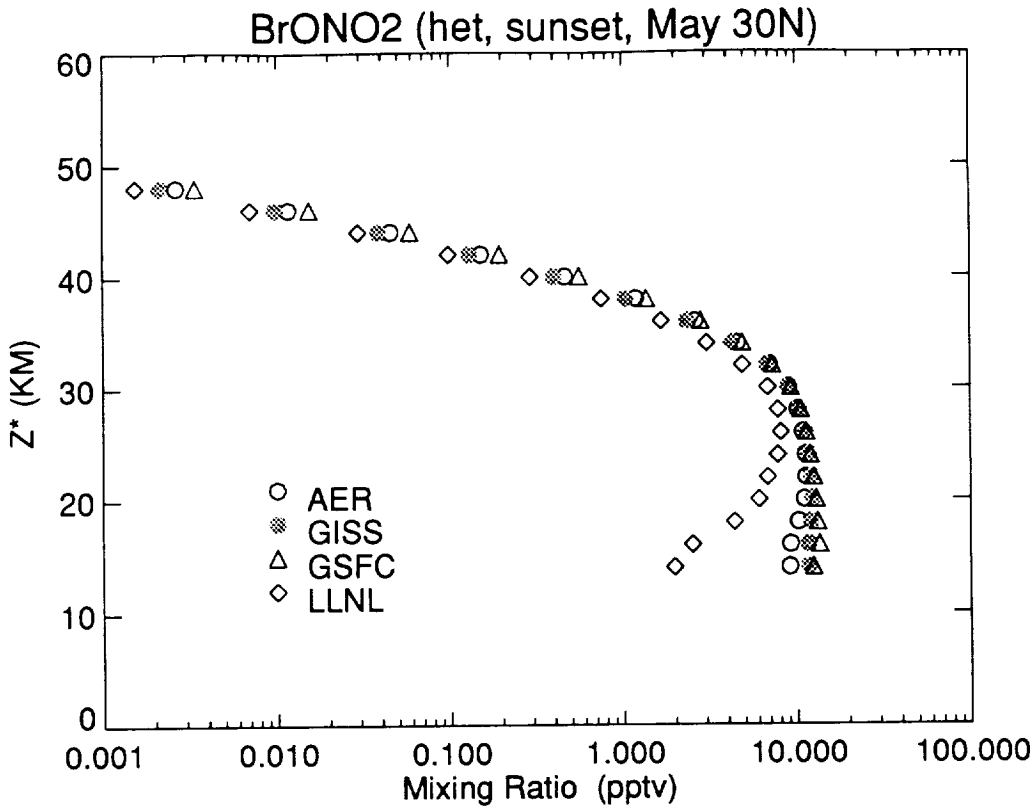

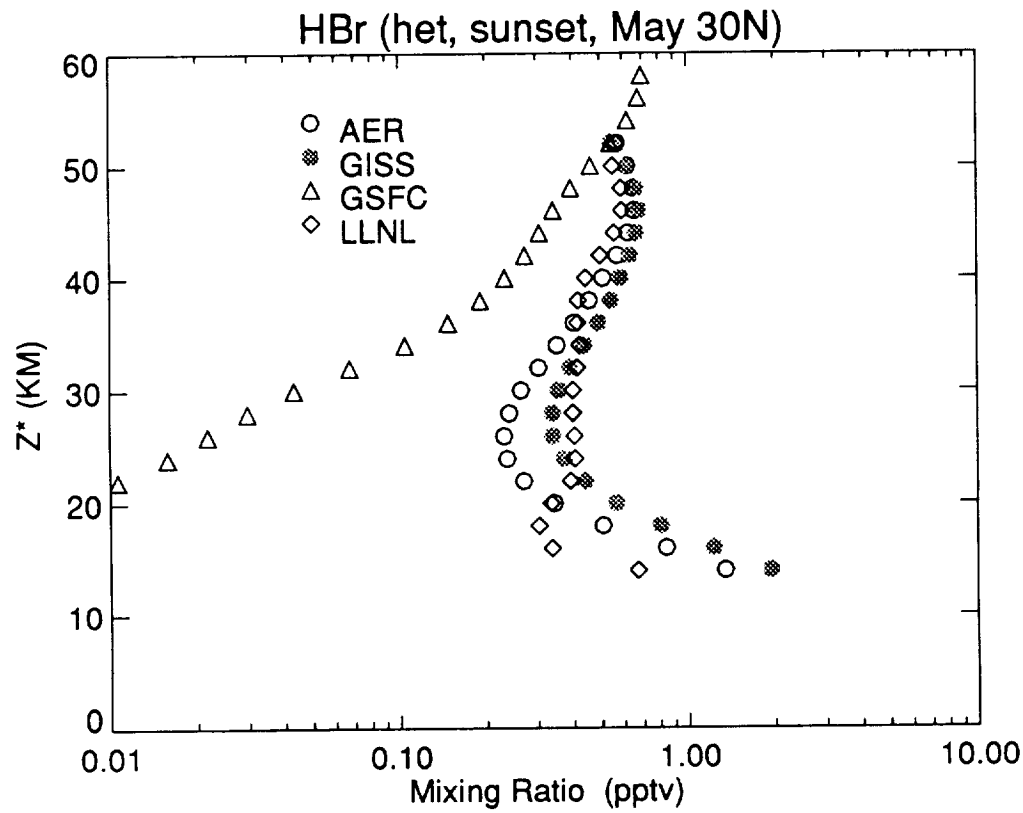

Figure M-11 (top) Figure M-12 (bottom)

N: Transport Fluxes

N: Transport Fluxes

Malcolm Ko
Atmospheric and Environmental Research, Inc.

INTRODUCTION

The local tendency of the continuity equation can be separated into terms representing transport processes and photochemical production/loss. In order to understand the modeled response of the trace gases to changes in the photochemical environment, it is desirable to compare the magnitudes of these terms. This experiment represents a first effort at examining the balance on a seasonal time scale.

It is clear that the balance depends on the distribution of the trace gas being considered. For instance, the steady-state mixing ratio for an inert tracer is constant in space and time, and the transport fluxes due to advection and eddy diffusion vanish at every time-step. In this experiment we have examined O_3 and N_2O. Nitrous oxide has also been chosen to illustrate a typical upward-diffusing trace gas. The aim is to derive a methodology to illustrate which terms determine the seasonal tendency of the trace gas. A next step would be to perform appropriate spatial and temporal averages to understand the year-to-year and steady-state balance among the terms.

THE EQUATION

The continuity equation can be written in the form

$$\frac{\partial f}{\partial t} = +S_{adv} + S_{diff} + P - L,$$

where $\frac{\partial f}{\partial t}$ is the net tendency term for the mixing ratio f; S_{adv} is the tendency due to transport by the zonal mean circulation; S_{diff} is the tendency due to eddy transport parameterized by the eddy diffusion coefficient; P is the local photochemical production rate; and L is the local photochemical removal rate.

The terms S_{adv} and S_{diff} can be separated into the horizontal and vertical components. The exact forms for S_{adv} and S_{diff} depend on the formulation and coordinates being used. For example, in pressure coordinates, the term S_{adv} can be written as

$$S_{adv} = -\frac{\partial(vf)}{\partial y} - \frac{\partial(wf)}{\partial z} \qquad \text{or} \qquad -v\frac{\partial f}{\partial y} - w\frac{\partial f}{\partial z} .$$

Although the terms add up to the same sum in each case, the separation into the horizontal and vertical components is different depending on whether the differentials are calculated as finite differences between adjacent grid points or directly as fluxes across boundaries of the grid boxes.

For S_{diff},

$$S_{diff} = -\frac{\partial}{\partial y}\left(Kyy\frac{\partial f}{\partial y}\right) - \frac{\partial}{\partial y}\left(Kyz\frac{\partial f}{\partial z}\right) - \frac{\partial}{\partial z}\left(Kzy\frac{\partial f}{\partial y}\right) - \frac{\partial}{\partial z}\left(Kzz\frac{\partial f}{\partial z}\right) .$$

In displaying the results, we have used the following labels :

$$H_{adv} = -\frac{\partial(vf)}{\partial y} \text{ [flux form]} \quad \text{or} \quad -v\frac{\partial f}{\partial y} \text{ [gradient form]}$$

$$V_{adv} = -\frac{\partial(wf)}{\partial z} \text{ [flux form]} \quad \text{or} \quad -w\frac{\partial f}{\partial z} \text{ [gradient form]}$$

$$S_{adv} = H_{adv} + V_{adv}$$

$$H_{diff} = -\frac{\partial}{\partial y}(Kyy\frac{\partial f}{\partial y}) - \frac{\partial}{\partial y}(Kyz\frac{\partial f}{\partial z})$$

$$V_{diff} = -\frac{\partial}{\partial z}(Kzy\frac{\partial f}{\partial y}) - \frac{\partial}{\partial z}(Kzz\frac{\partial f}{\partial z})$$

$$S_{diff} = H_{diff} + V_{diff}$$

$$TRAN = S_{adv} + S_{diff}$$

$$TEND = \frac{\partial f}{\partial t} = TRAN + P - L \ .$$

BRIEF DESCRIPTIONS OF THE MODELS

Five models contributed results for this experiment. Table N-1 summarizes some of the key differences among the models. For more detailed descriptions of the model formulation, see chapter 4.

Table N-1. Model Descriptions

Model	Coordinate and Numerical Scheme	Circulation	Eddy Diffusion in the Stratosphere
AER	log-pressure; Smolarkiewicz	diabatic circulation; prescribed	Kyy = $3x10^9$ -$1x10^{10}$ cm^2 sec^{-1}, Kzz = $1x10^3$ cm^2 sec^{-1}, Kyz by projection of isentropic surfaces on to pressure surface
CAMED-θ	isentropic; Adam-Bashforth	interactive	Kyy, calculated, different for N_2O and O_3 Kzz = $3x10^3$ cm^2 sec^{-1}, no Kyz
GSFC	log-pressure; Prather scheme	residual mean from prescribed diabatic heating	Kyy, calculated, Kzz = $2x10^3$ cm^2 sec^{-1}, Kyz by projection of isentropic surfaces on to pressure surface

ITALY	log-pressure; centered-differencing with Lorentz N-cycle time integration	diabatic; from 3-D spectral model	Kyy calculated from 3-D spectral model, typical values 1-5x10^8 cm^2 sec^{-1}, in the tropics, 3-8x10^9 cm^2 sec^{-1} extra-tropics Kzz < 5x10^2 cm^2 sec^{-1} tropics, 10^3 cm^2 sec^{-1} in the extra-tropics Kyz by projection of isentropic surfaces on to pressure surface
LLNL	log-pressure; Smolarkiewicz	residual mean from prescribed diabatic heating	Kyy, 2x10^9 cm^2 sec^{-1}, Kzz = 1x10^3 cm^2 sec^{-1}, Kyz by projection of isentropic surfaces on to pressure surface

The diagnostic quantities discussed in the Equation section are given in flux form in all the models except for the CAMED-θ model, which uses the gradient form for H_{adv} and V_{adv}.

DATA COLLECTION

The quantities requested are H_{adv}, V_{adv}, H_{diff}, V_{diff}, P, and L. These were entered in the data base in standard UADP format for March 15, June 15, September 15 and December 15. The quantities TRAN, TEND, and P-L were calculated by the data base. The following two points should be noted in the interpretation of the results :

(1) Because of the different formulations in the models, some of the quantities requested may not be the form used in the actual time integration of the model equations. In those cases, the quantities are calculated off-line as diagnostic variables. Thus, differences in these quantities do not necessarily explain differences in model results.

(2) The data requested represent a snapshot on a particular day. While it has been verified in some of the models that the snapshot is representative of the monthly mean, this has not been done for all the models. Despite this, the discussion in this section will assume that the values are representative of the monthly mean.

RESULTS FOR N_2O

The results for N_2O are shown in Figures N-1 through N-5 for each of the five models. Results for March 15 are used throughout. There are four panels in Figure N-1a. The upper left panel is the calculated mixing ratio of N_2O (in ppbv). The remaining panels and all six panels in Figure N-1b are time rates of change of f in units of 10^{-15} volume mixing ratio sec^{-1}.

Since we are interested in the seasonal time scale, it is useful to define a measure for the rates to determine whether they may affect the mixing ratio on a seasonal time scale. Listed in the table below is the local rate which, if sustained, will change the local mixing ratio by 20% over a 90-day period.

Table N-2. The Rate of Change That Would Affect the Given Mixing Ratio by 20% Over a 90-day Period

Local Mixing Ratio of N_2O (ppbv)	Rate (in 10^{-15} sec^{-1}) That Will Begin to Affect Seasonal Behavior
300	8
280	7
240	6
200	5
100	3
50	1
20	0.5
10	0.3
5	0.1
2	0.05
1	0.03

The following points are noted :

(1) There is no in situ production of N_2O in the atmosphere. It is transported from the troposphere to the stratosphere where it is removed by photochemical reactions. N_2O is a vertically stratified tracer, i.e., the mixing ratio decreases with height. All models show a downward sloping of the surface of constant mixing ratio from the tropics towards the pole.

(2) Above 30 km in the tropics, L is balanced by the TRAN term to the first order. The cancellation is less complete in the tropics for the GSFC and LLNL models. The difference between L and TRAN is shown in TEND which is the time rate of change. There are significant differences among the models in TEND at high latitudes in the lower stratosphere. This would imply significant differences in the seasonal behavior of N_2O in those regions if the values given are interpreted as seasonal changes.

(3) The S_{adv} term and the S_{diff} term are opposite in sign. S_{adv} is positive in the tropics and negative at high latitudes, consistent with the upward motions and downward motions in the respective regions. The behavior of S_{diff} (negative in the tropics and positive at high latitudes) is consistent with the down-gradient transport expected from the eddy-diffusion formulation. The magnitude of S_{adv} is larger than that of S_{diff} in the tropics, resulting in a positive TRAN term.

(4) In all the models that use the flux form, the V_{adv} term carries the N_2O from the lower tropical stratosphere to the mid stratosphere to maintain the concentration against photochemical removal. Both H_{adv} and H_{diff} help carry material from the tropics to the extra-tropics. The downward motion in the extra tropics also shows up as a negative contribution to V_{adv}. The behavior of H_{adv} in the CAMED-θ model is different because the gradient form is used. As v and $\partial f/\partial y$ are in the same direction, H_{adv} is everywhere positive.

(5) A general comment is that the fields in the GSFC and LLNL results show more vertically layered structure, while the AER, CAMED-θ, and ITALY model results are smoother.

The SAMS monthly mean data have limited utility in providing values for the observed tendency. Jones and Pyle (1984) estimated uncertainties of ~15% or 30 ppbv for the derived monthly mean N_2O mixing ratio in the lower stratosphere. This corresponds to an uncertainty in the tendency of about 10^{-14} volume mixing ratio sec^{-1}. Both the 1979 and 1980 data show tendencies between $\pm 5 \times 10^{-15}$ volume mixing ratio sec^{-1} and $\pm 10 \times 10^{-15}$ volume mixing ratio sec^{-1} at 40 km and 30 km, respectively. However, the spatial behaviors of the tendencies from each of the 2 years are quite different . More data are needed to obtain climatological mean values with smaller uncertainty for comparison with model results.

RESULTS FOR OZONE

The results for O_3 are shown in Figures N-6 to N-10. The (a) panels of Figure N-6 to N-10 show the calculated mixing ratio, TEND, TRAN, and P-L. The mixing ratio is given in ppmv. All the time rates of change are in 10^{-15} volume mixing ratio sec^{-1}. The following table relates the rate that will give rise to significant seasonal changes for a given mixing ratio.

Table N-3. The Rate of Change That Would Affect the Given Mixing Ratio by 20% Over a 90-Day Period

Local Mixing Ratio for O_3 (ppmv)	Rate (in 10^{-15} sec^{-1}) That Will Begin to Affect Seasonal Behavior
10	260
8	210
6	150
4	100
2	50
1	26
0.5	13
0.2	5
0.1	2.5

In the case of O_3 where there are both in situ photochemical production and removal, it is important that one compare the transport terms with the P term and the L term separately instead of just looking at the net term (P-L) (*see* Ko et al., 1989). We added a set of figures for the ozone results in the (c) panels of Figures N-6 through N-10, which show the individual terms P and L, and the quantity EQ defined as

$$EQ = \frac{abs(P) - abs(L)}{abs(P) + abs(L)}$$

where abs(.) is the absolute value. Noting that when P is equal to L in the photochemical equilibrium region, $EQ \approx 0$ in that region. The condition $EQ > 0$ marks the region where production is balanced by transport away from the region, while $EQ < 0$ marks the region where local removal is balanced by transport into the region.

The following comments can be made concerning the O_3 results:

- Above 30 km in the tropics, both the P and L terms are at least two orders of magnitude larger than any of the transport terms. Thus ozone is photochemically controlled in that region as is evident from the top panel of (c) in each model.

- In the lower stratosphere, production in the tropics is balanced by transport away from the region. For results presented in flux form, both V_{adv} and H_{adv} play a role in exporting the ozone from the lower tropical stratosphere. In most of the models, the magnitude of S_{adv} is larger than that of S_{diff}. It is an order of magnitude larger in the tropics and a factor of 2 larger in the extra tropics.

To further examine the seasonal behavior of ozone, we present a number of figures representing the local lifetimes defined by each process. We define the lifetimes corresponding to each tendency term as follows :

$$\tau_{PROD} = \frac{f}{abs(PROD)} \qquad \tau_{LOSS} = \frac{f}{abs(LOSS)}$$

$$\tau_{TEND} = \frac{f}{abs(TEND)} \qquad \tau_{TRAN} = \frac{f}{abs(TRAN)}$$

$$\tau_{Sadv} = \frac{f}{abs(S_{adv})} \qquad \tau_{Sdiff} = \frac{f}{abs(S_{diff})} .$$

The lifetimes are calculated for two latitude bands (20S to 20N; 45N to 90N) and plotted as functions of altitudes. The convention used is that if the tendency is positive, τ is plotted with a solid line. If the tendency is negative, τ is plotted with a dashed line. The figures for the models are shown in Figures N-11to N-15.

We note that :

- The τ_{TEND} in the tropics around 20 km is of the order of 1000 days for all seasons, consistent with the lack of observed seasonal variation in that region. The differences among the models are probably insignificant.

- In the tropics, between 16 to 24 km, photochemical production is balanced by TRAN. Above the model tropopause, S_{adv} is larger than S_{diff}. However, the behavior of S_{adv} and S_{diff} around the tropopause is very different among the models.

- In the tropics, between 16 to 24 km, all model results show that the lifetime due to photochemical removal (L) is about 1000 days, much longer than the lifetime due to P or TRAN. This would suggest that ozone in the tropics would not be very sensitive to chemical perturbations. There are some differences in the P and TRAN. The model results separate into two groups. The AER, GSFC, and ITALY results indicate that the lifetimes due to P and TRAN are longer than 100 days. In the cases of LLNL and CAMED-θ, the lifetimes are shorter than 100 days.

- The seasonal signal is much stronger in the mid- and high-latitudes. For March, the net tendency lifetime at $z^* = 20$ km is 1000 days and longer, with advection balancing eddy diffusion and local loss. In June most models show that all the terms contributing to the TRAN are negative, leaving a negative tendency with a lifetime of about 200 to 500 days. The exception is GSFC, which shows a positive tendency due to advection, resulting in a positive TRAN term. In December there is a positive net tendency for all models with lifetimes of 200 to 500 days where both the advection and diffusion terms are positive. Again, the exception is in the GSFC case in which the diffusion term is negative.

A τ_{TEND} of 200 days implies a change of 15% in one month. A more typical value of 400 days would imply a change of 8% in one month. Although the uncertainty for the monthly mean SBUV data is ~20% in the lower stratosphere (McPeters et al., 1984), the precision of the SBUV

version 6 data is estimated to be a few percent. It would be worthwhile to examine the data to see if useful estimates of τ_{TEND} can be derived.

DISCUSSION

In this section we examined the model results from several models and discussed how the individual terms in the mass-continuity equation contribute to the control of the spatial and temporal behavior of N_2O and O_3. Clearly, the results are model dependent. The models that contributed to this section all use the diabatic/residual-mean formulation. The results support the idea that advection plays a more dominant role than eddy diffusion. Unfortunately, there is no simple way to make use of observations to determine if the models are providing an accurate representation of what is occurring.

The analysis of the O_3 lifetime is useful for understanding how model-calculated O_3 responds to changes in circulation and photochemical parameters (*see* Ko et al., 1989). According to the analysis, O_3 in the lower stratosphere would respond to changes in circulation at all latitudes. For example, a stronger upwelling at the tropics accompanied by stronger downward motion at high latitudes would lead to a decrease in the O_3 content at the tropics and an increase at high latitudes. The O_3 response to perturbations to the photochemical terms are distinctly different at different latitudes. While O_3 in the tropical lower stratosphere will respond to changes in the local photochemical production term, it will not begin to respond to changes in the photochemical removal term unless the removal rate increases by more than an order of magnitude. At high latitude, O_3 in the lower stratosphere is sensitive to changes in the photochemical removal rate and insensitive to the local photochemical production.

The point was raised earlier in the section of whether the tendency term obtained from a snapshot is really representative of the seasonal behavior. Given that the lifetime for ozone at $z^* =$ 20 km is around 200 days, it is clear that the response of ozone to perturbations in that region represents a cumulative response over at least one year. To get at the interannual time scale, one must perform seasonal averaging over appropriate regions of the atmosphere. This should be a focus of future studies.

REFERENCES

Jones, R. L. and J. A. Pyle, Observations of CH_4 and N_2O by Nimbus 7 SAMS: A comparison with in situ data and two-dimensional numerical model calculations, *J. Geophys. Res., 89*, 5263-5279, 1984.

Ko, M. K. W., N. D. Sze, and D. K. Weisenstein, The roles of dynamical and chemical processes in determining the stratospheric concentration of ozone in one-dimensional and two-dimensional models, *J. Geophys. Res., 94*, 9889-9896, 1989.

McPeters, R. D., D. F. Heath, and P. K. Bhartia, Average ozone profiles for 1979 from Nimbus 7 SBUV instrument, *J. Geophys. Res., 89*, 5199-5214, 1984.

FIGURE CAPTIONS

Figure N-1. Model calculated results for N2O for March 15 from AER model. (a) Four panels -- the upper left is the mixing ratio shown in ppbv. Contour intervals are 300 ppbv, 280 ppbv, 250 ppbv, 200 ppbv, 100 ppbv, 50 ppbv, 20 ppbv, 10 ppbv, 5 ppbv, 2 ppbv, 1 ppbv, 0.5 ppbv, 0.2 ppbv and 0.1 ppbv. The remaining three panels give the time rate of change in 10^{-15} sec^{-1}. The contour intervals are: ±10, ±5, ±2, ±1, ±0.5, ±0.1, ±0.05, and ±0.01. See text for definition of the labels. (b) Six panels -- individual tendency terms for N_2O.

Figure N-2. Same as Figure N-1 except the results are from the CAMED-θ model.

Figure N-3. Same as Figure N-1 except the results are from the GSFC model.

Figure N-4. Same as Figure N-1 except the results are from the Italy model.

Figure N-5. Same as Figure N-1 except the results are from the LLNL model.

Figure N-6. As in Figure N-1, but for O3 for March 15 from AER model. The mixing ratio in the upper left panel of (a) is in ppmv. The contour intervals are 10 ppmv, 8 ppmv, 6 ppmv, 4 ppmv, 2 ppmv, 1 ppmv, 0.5 ppmv, 0.2, and 0.1 ppmv. The time rate of change is in 10^{-15} sec^{-1}. See text for definition of the labels. The contour intervals in the remaining panels of (a) and in (b) are ±1000, ±500, ±200, ±100, ±50, ±10, ±5, and ±1. (c) Three panels -- the terms P and L and the quantity EQ (see text). The quantity EQ is dimensionless.

Figure N-7. Same as Figure N-6 except the results are from the CAMED-θ model.

Figure N-8. Same as Figure N-6 except the results are from the GSFC model.

Figure N-9. Same as Figure N-6 except the results are from the ITALY model.

Figure N-10. Same as Figure N-6 except the results are from the LLNL model.

Figure N-11. Model calculated lifetimes for specific mechanism from the AER model for March, June and December. The lifetimes are calculated for two latitude bands -- (a) 20S to 20N, three panels and (b) 45N to 90N, three panels -- and are plotted as functions of altitudes. The convention used is that if the tendency is positive, t is plotted with a solid line. If the tendency is negative, t is plotted with a dashed line.

Figure N-12. Same as Figure N-11 except the results are from the CAMED-θ model.

Figure N-13. Same as Figure N-11 except the results are from the GSFC model.

Figure N-14. Same as Figure N-11 except the results are from the ITALY model.

Figure N-15. Same as Figure N-11 except the results are from the LLNL model.

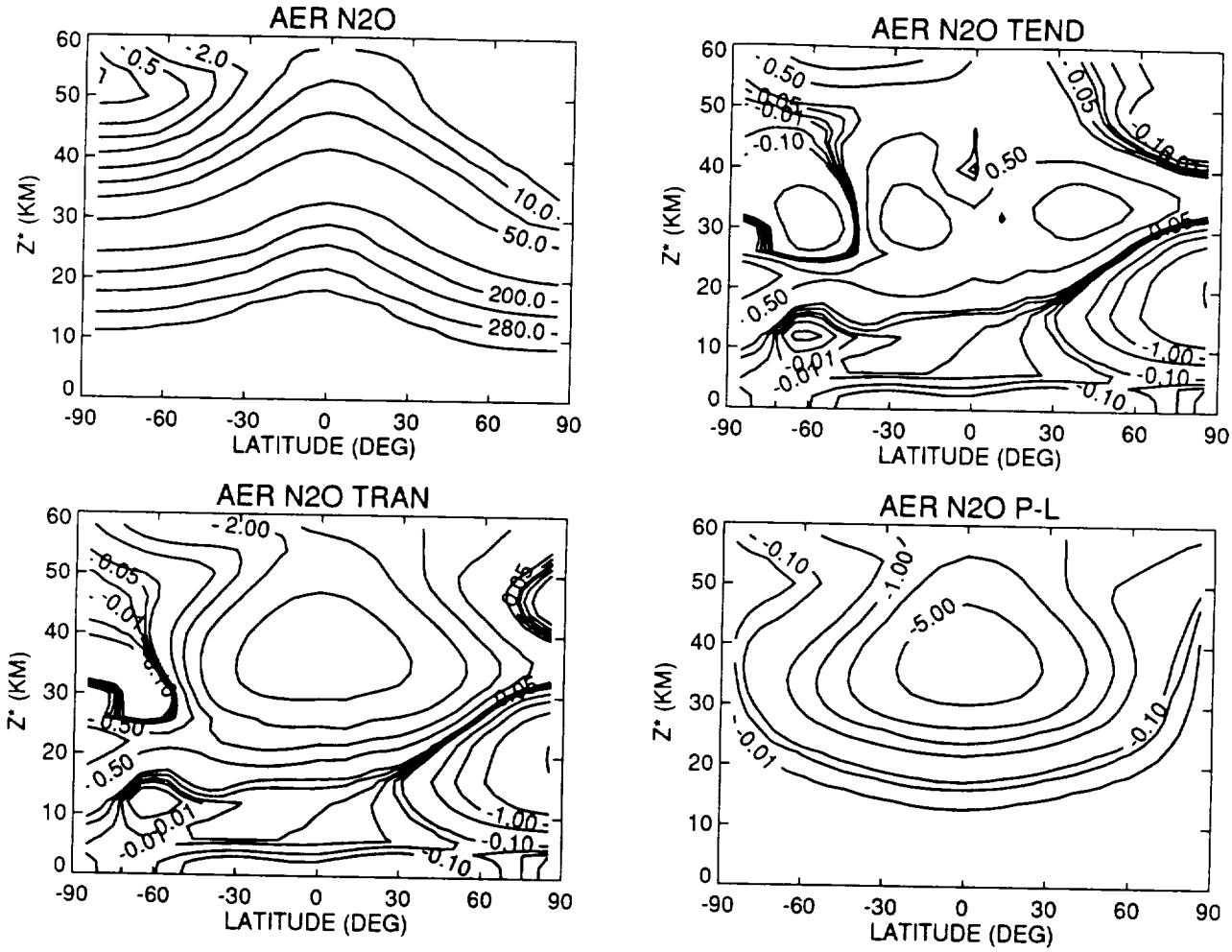
AER N2O
AER N2O TEND
AER N2O TRAN
AER N2O P-L
Z* (KM)
LATITUDE (DEG)
-90 -60 -30 0 30 60 90
0 10 20 30 40 50 60
1
-0.5
-2.0
10.0
50.0
200.0
280.0
0.50
0.05
0.01
0.10
0.50
1.00
5.00
0.01

Figure N-1 a

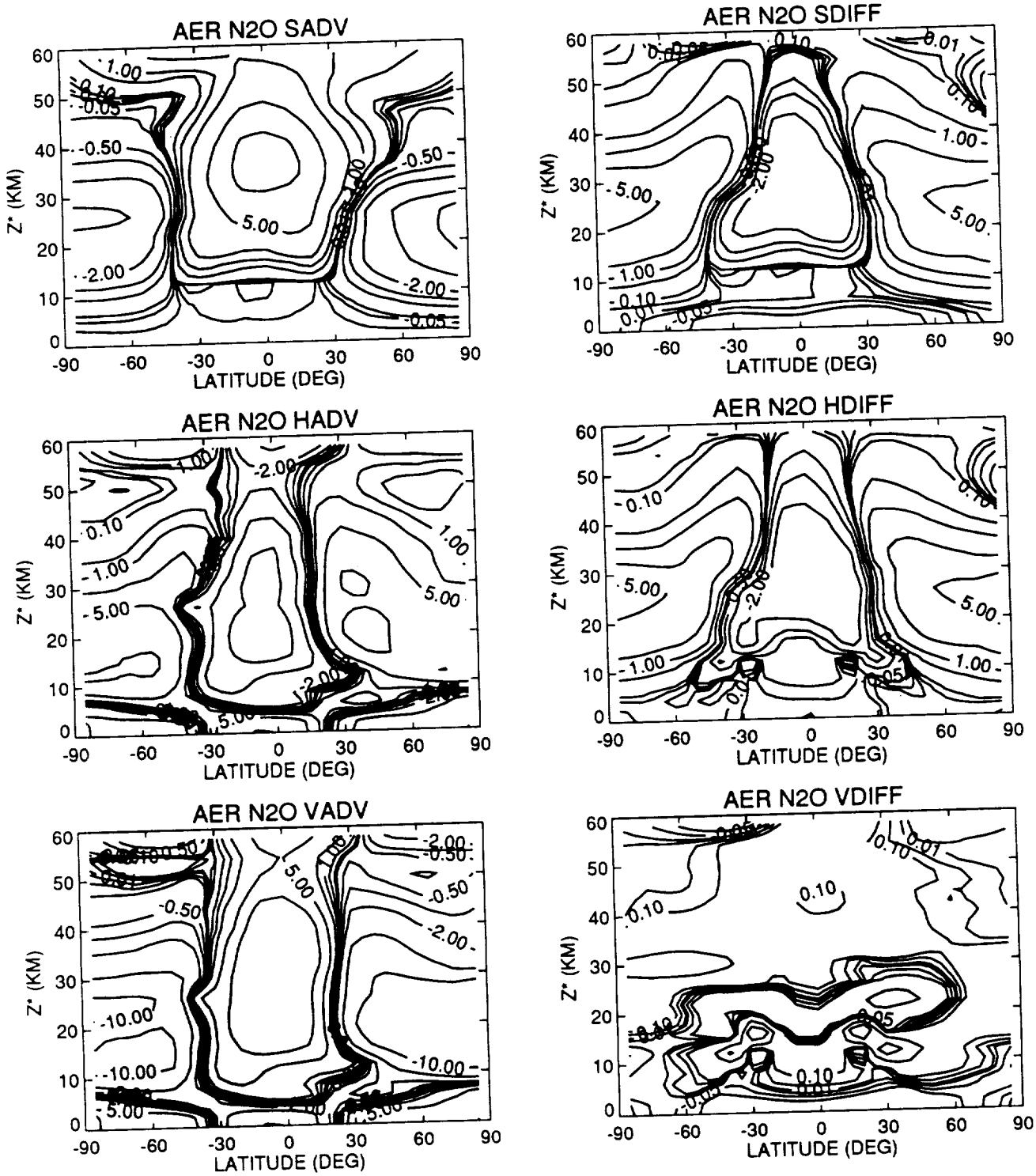
AER N2O SADV
AER N2O SDIFF
AER N2O HADV
AER N2O HDIFF
AER N2O VADV
AER N2O VDIFF
Z* (KM)
LATITUDE (DEG)

Figure N-1 b

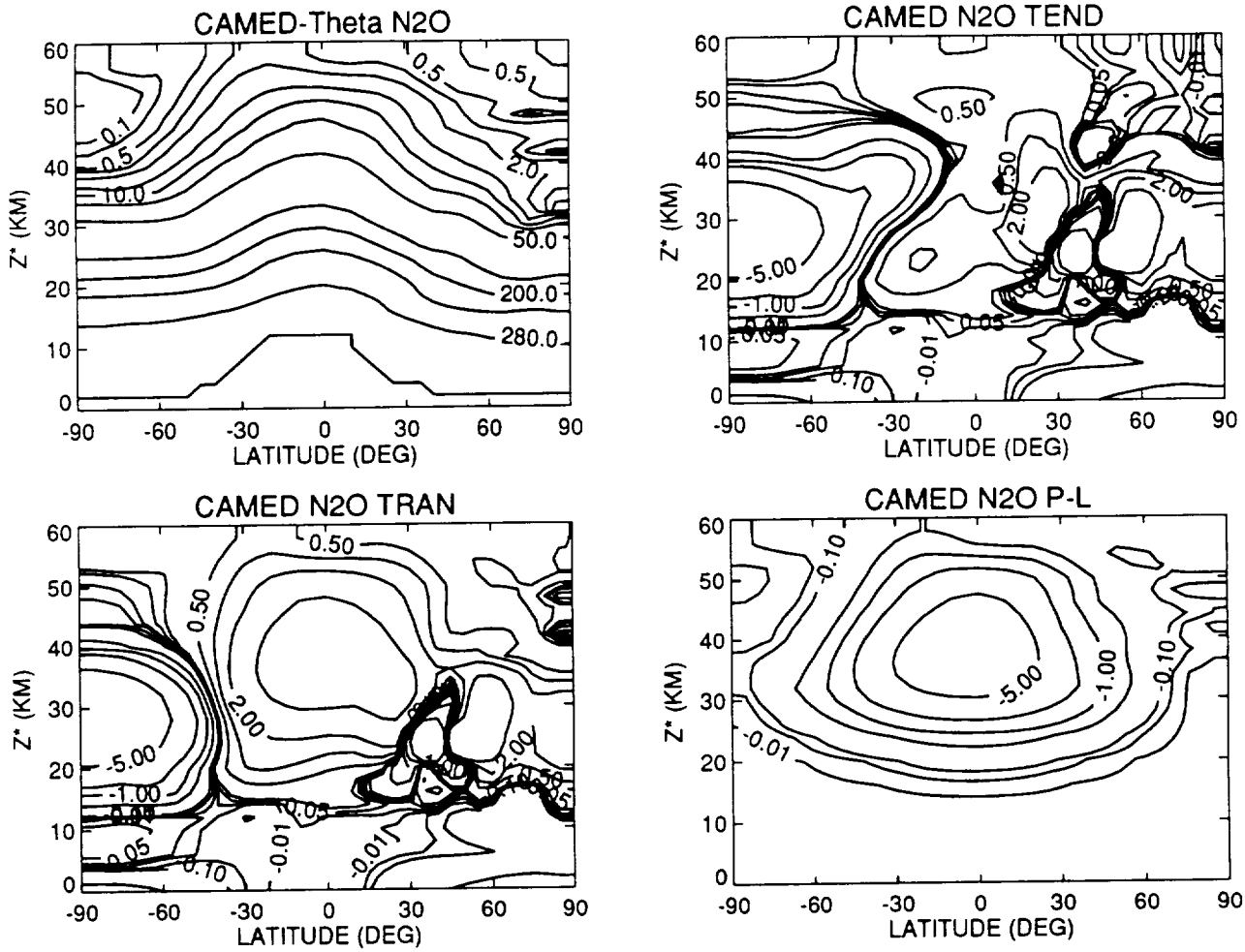
CAMED-Theta N2O
CAMED N2O TEND
CAMED N2O TRAN
CAMED N2O P-L
Z* (KM)
LATITUDE (DEG)

Figure N-2 a

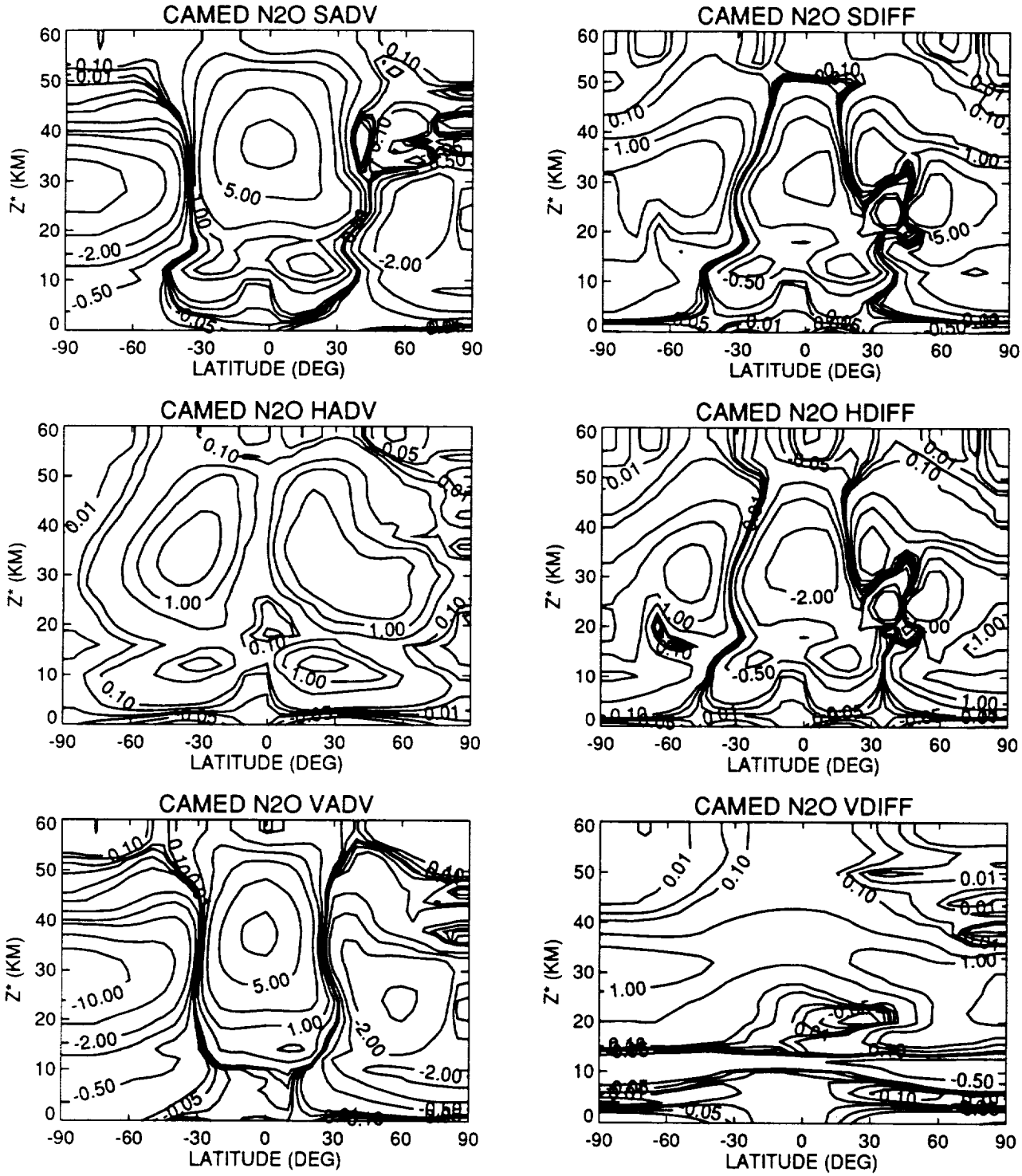
CAMED N2O SADV
CAMED N2O SDIFF
CAMED N2O HADV
CAMED N2O HDIFF
CAMED N2O VADV
CAMED N2O VDIFF
Z* (KM)
LATITUDE (DEG)

Figure N-2 b

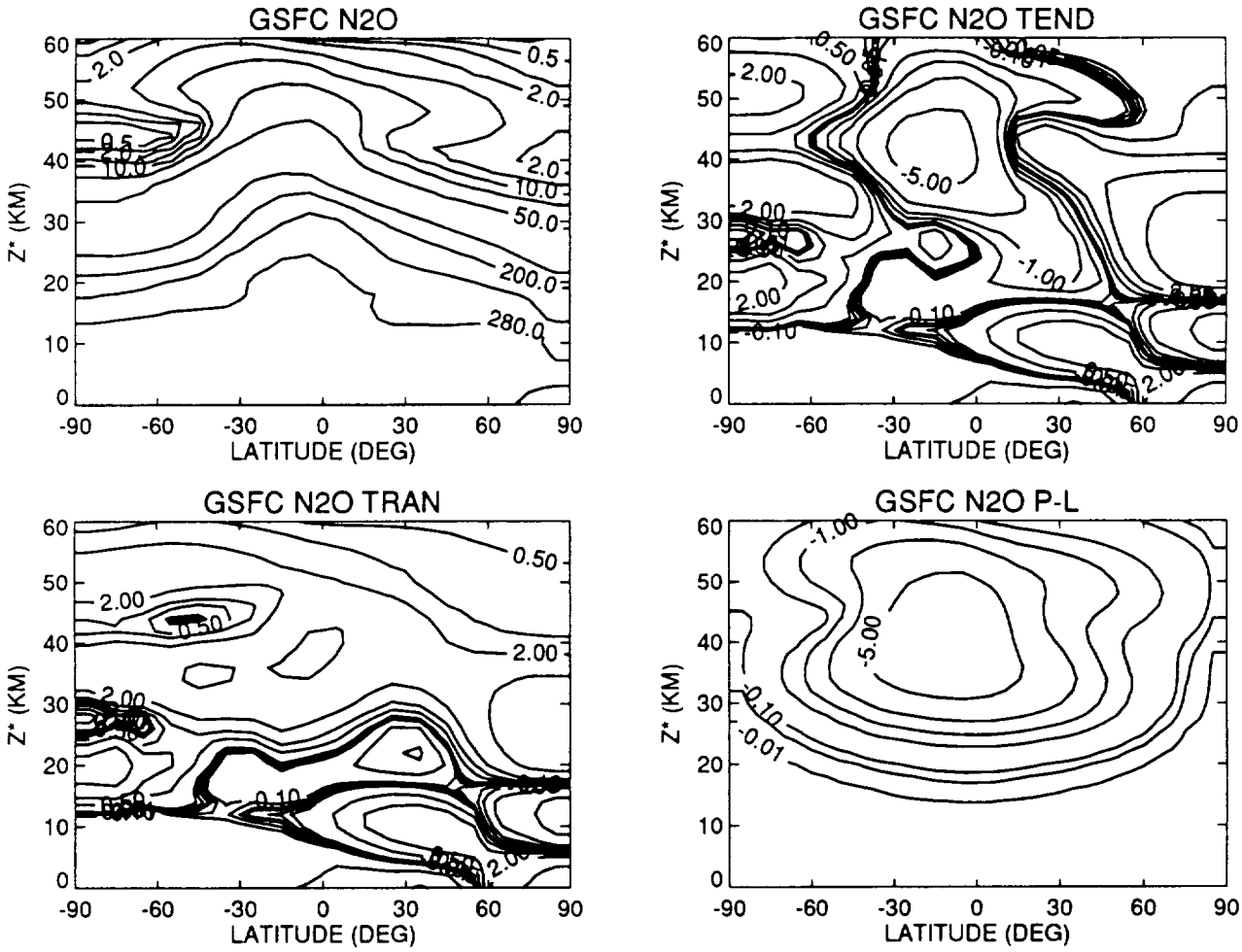
GSFC N2O
GSFC N2O TEND
GSFC N2O TRAN
GSFC N2O P-L
Z* (KM)
LATITUDE (DEG)
-90 -60 -30 0 30 60 90
0 10 20 30 40 50 60
0.5
2.0
10.0
50.0
200.0
280.0
-0.50
2.00
-5.00
-1.00
-0.10
0.10
-0.01

Figure N-3a

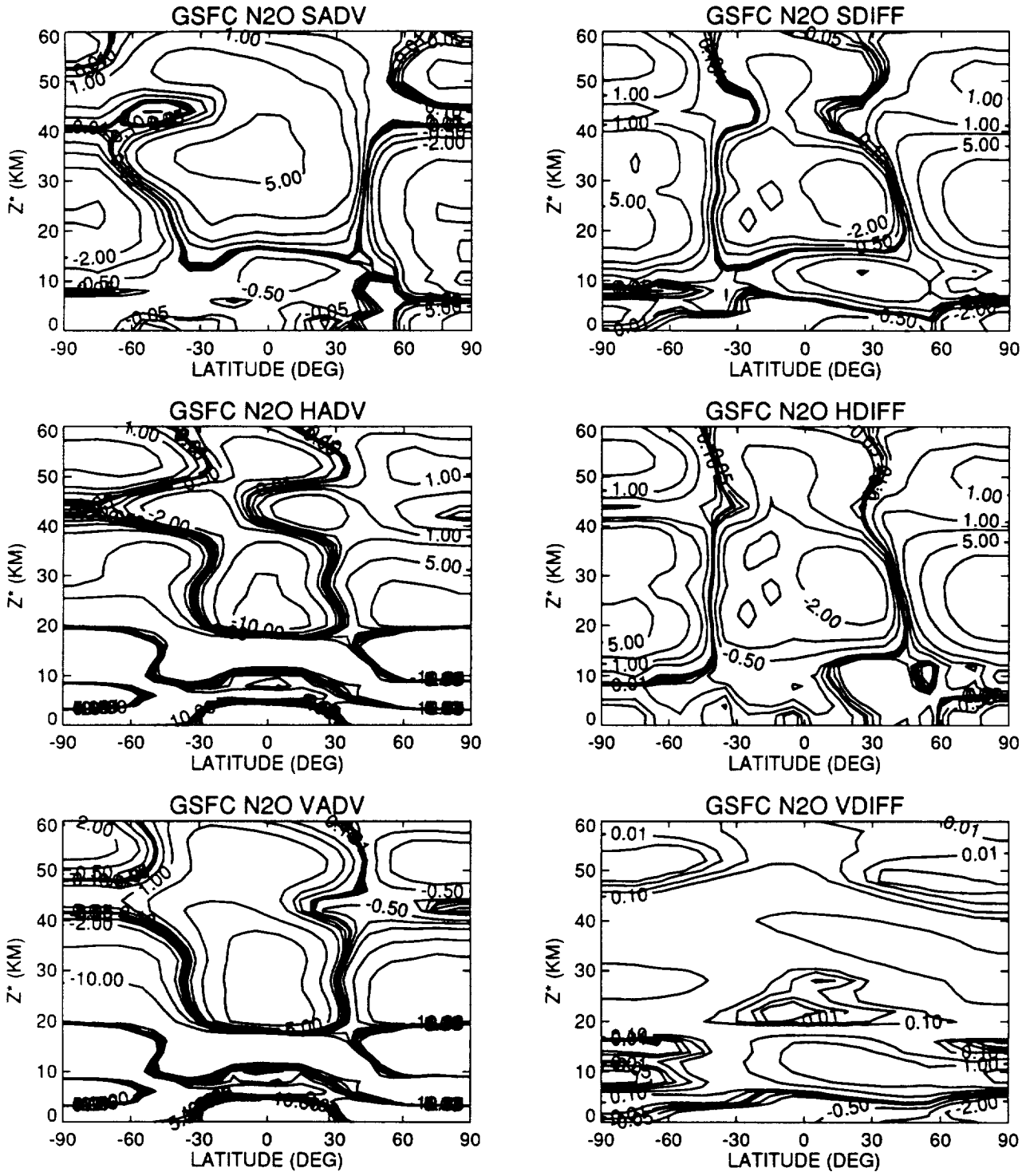
GSFC N2O SADV
GSFC N2O SDIFF
GSFC N2O HADV
GSFC N2O HDIFF
GSFC N2O VADV
GSFC N2O VDIFF
Z* (KM)
LATITUDE (DEG)
-90 -60 -30 0 30 60 90
0 10 20 30 40 50 60

Figure N-3b

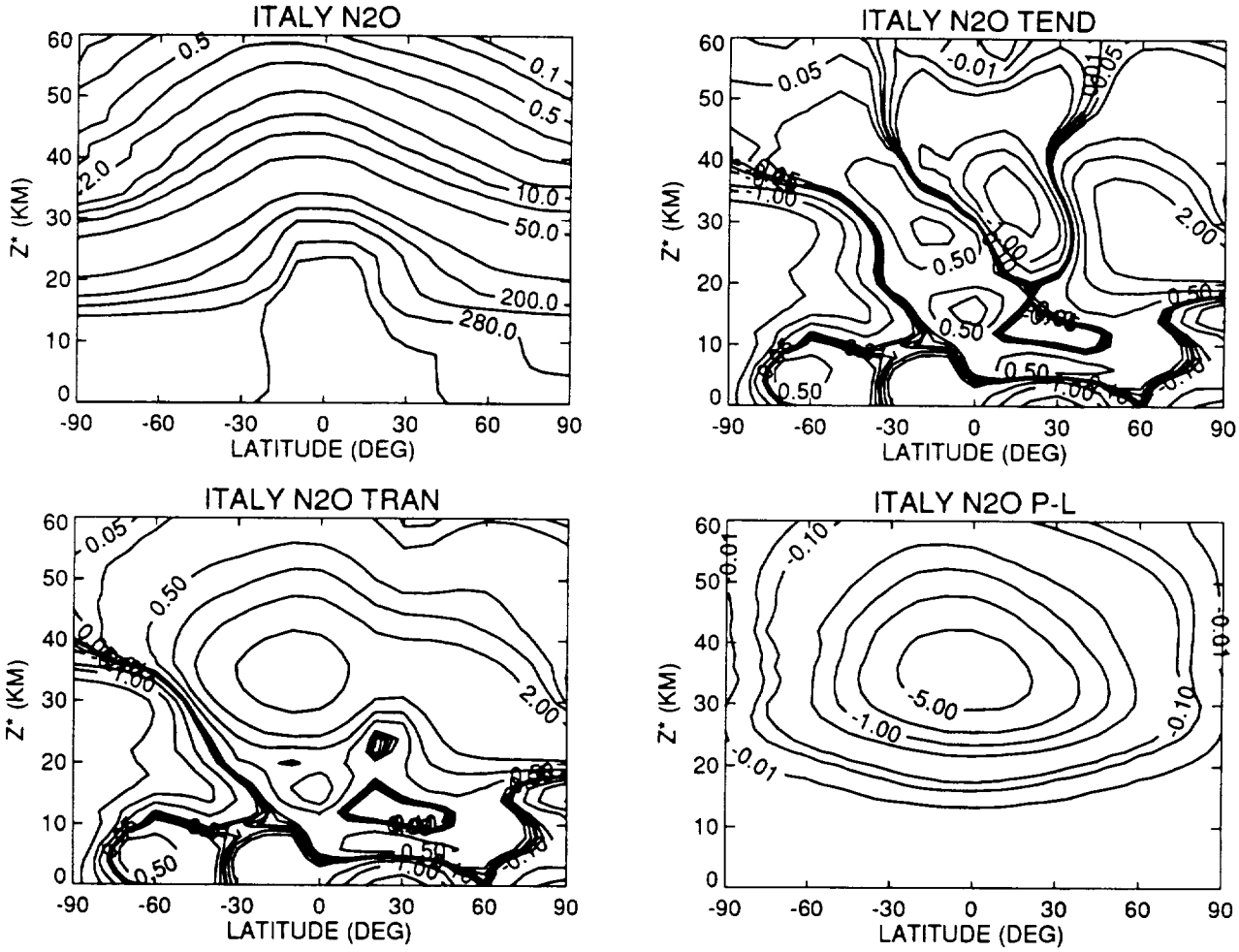
ITALY N2O
ITALY N2O TEND
ITALY N2O TRAN
ITALY N2O P-L
Z* (KM)
LATITUDE (DEG)

Figure N-4a

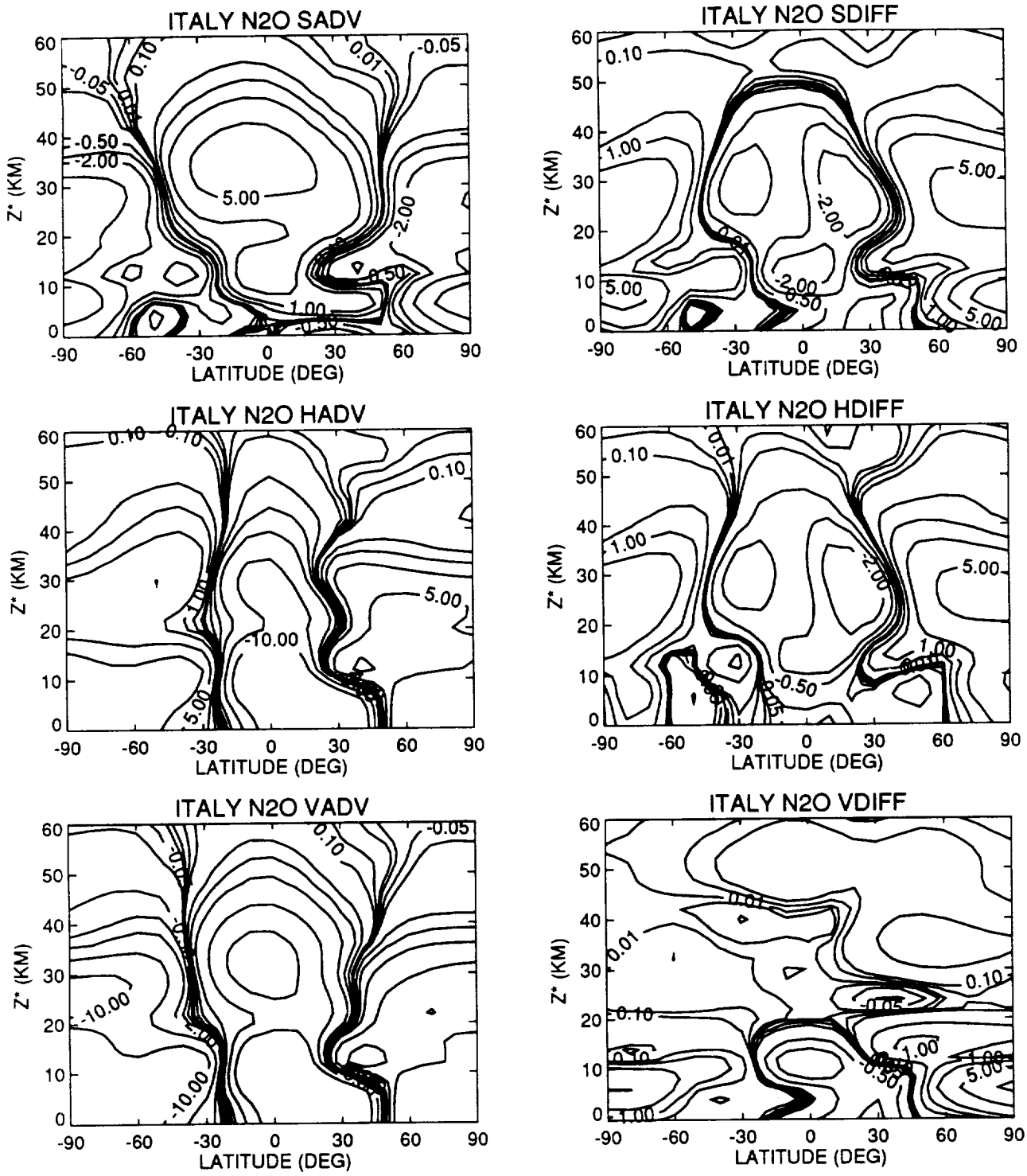
ITALY N2O SADV
ITALY N2O SDIFF
ITALY N2O HADV
ITALY N2O HDIFF
ITALY N2O VADV
ITALY N2O VDIFF
Z* (KM)
LATITUDE (DEG)

Figure N-4b

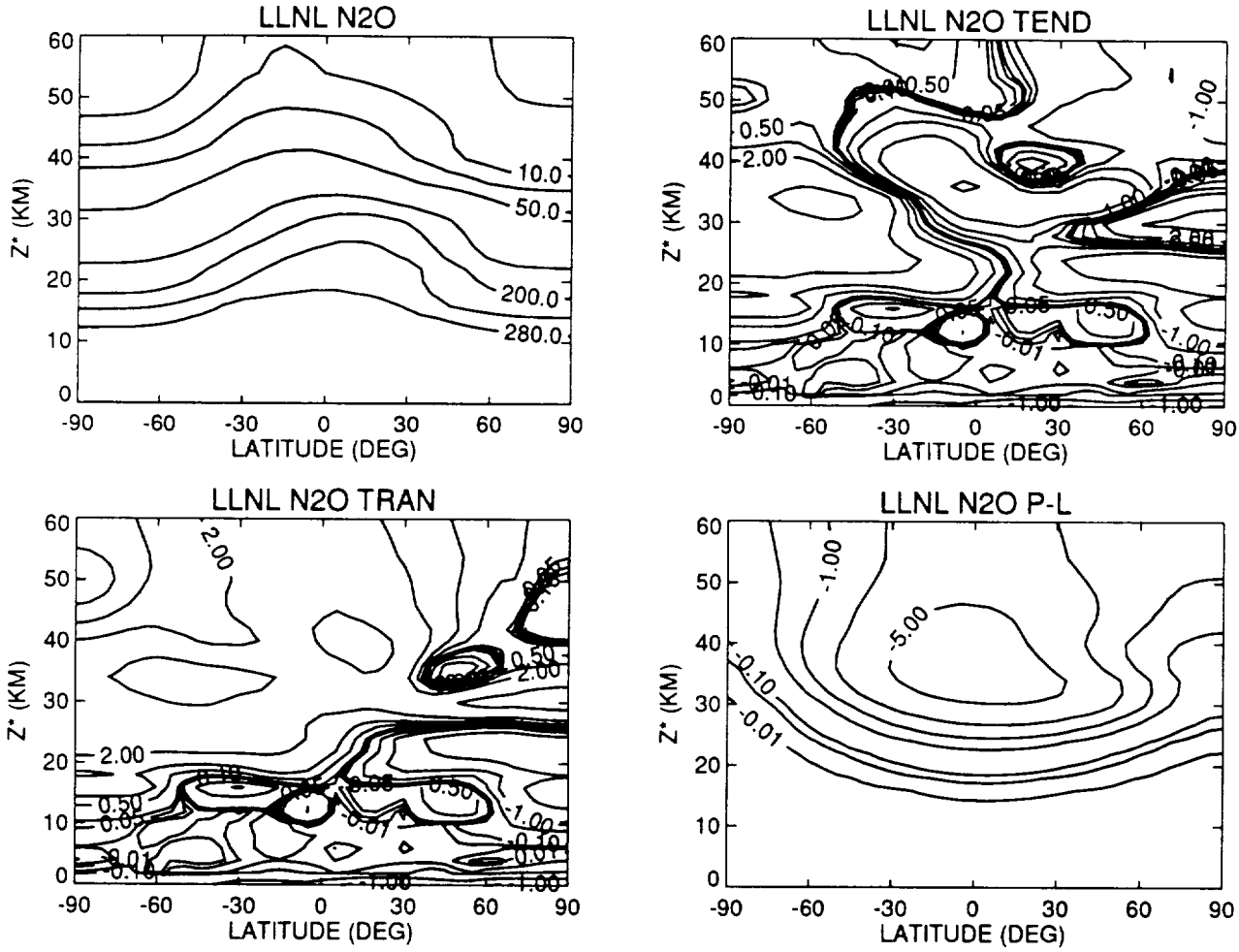
LLNL N2O
LLNL N2O TEND
LLNL N2O TRAN
LLNL N2O P-L
Z* (KM)
LATITUDE (DEG)
10.0
50.0
200.0
280.0
0.50
2.00
-1.00
-5.00
-0.10
-0.01

Figure N-5 a

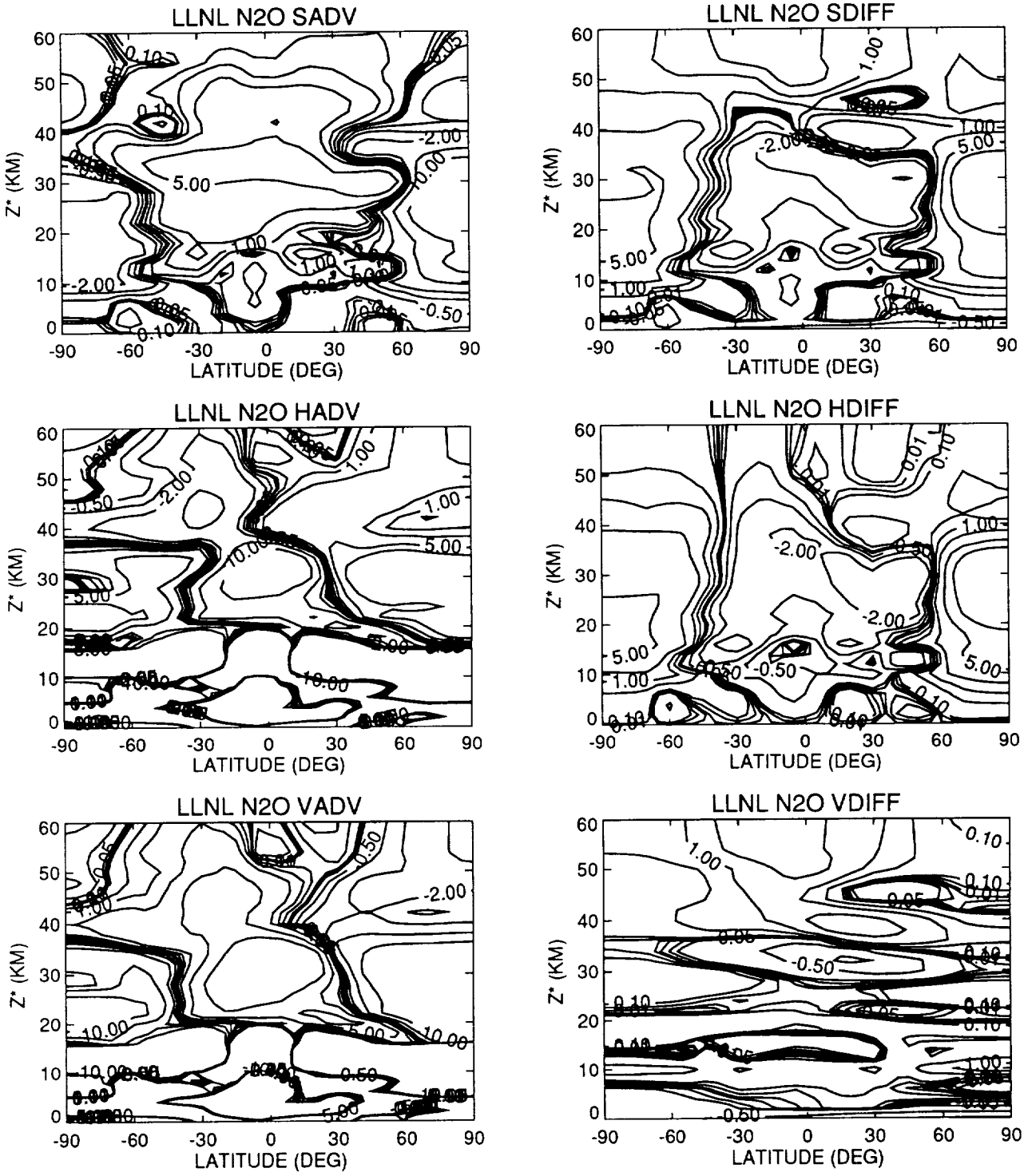
LLNL N2O SADV
LLNL N2O SDIFF
LLNL N2O HADV
LLNL N2O HDIFF
LLNL N2O VADV
LLNL N2O VDIFF
Z* (KM)
LATITUDE (DEG)
-90 -60 -30 0 30 60 90
0 10 20 30 40 50 60

Figure N-5b

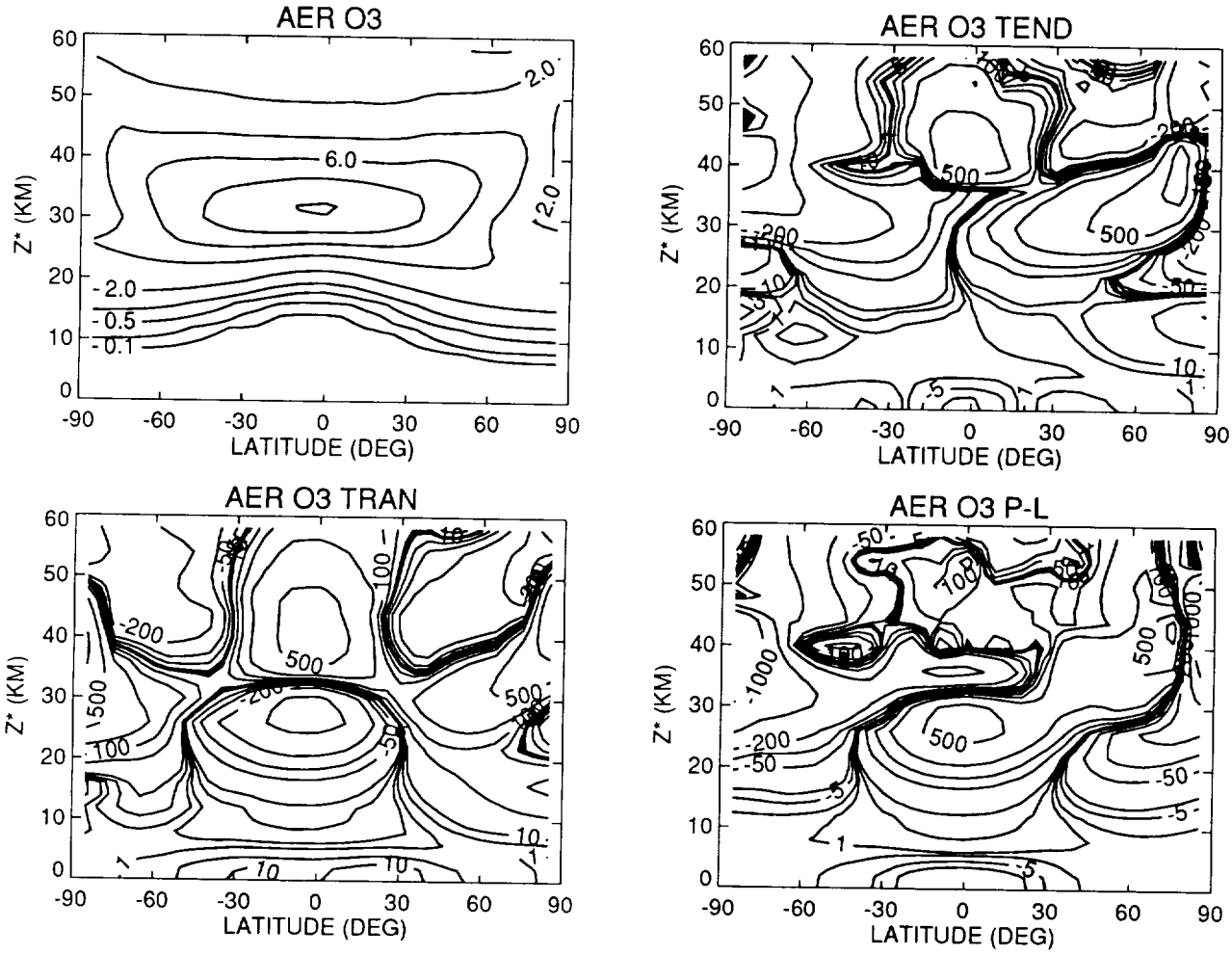
AER O3
AER O3 TEND
AER O3 TRAN
AER O3 P-L
Z* (KM)
LATITUDE (DEG)
-90 -60 -30 0 30 60 90
0 10 20 30 40 50 60
6.0
2.0
-2.0
-0.5
-0.1
500
-200
100
-100
10
1
-5
-50
-1000

Figure N-6a

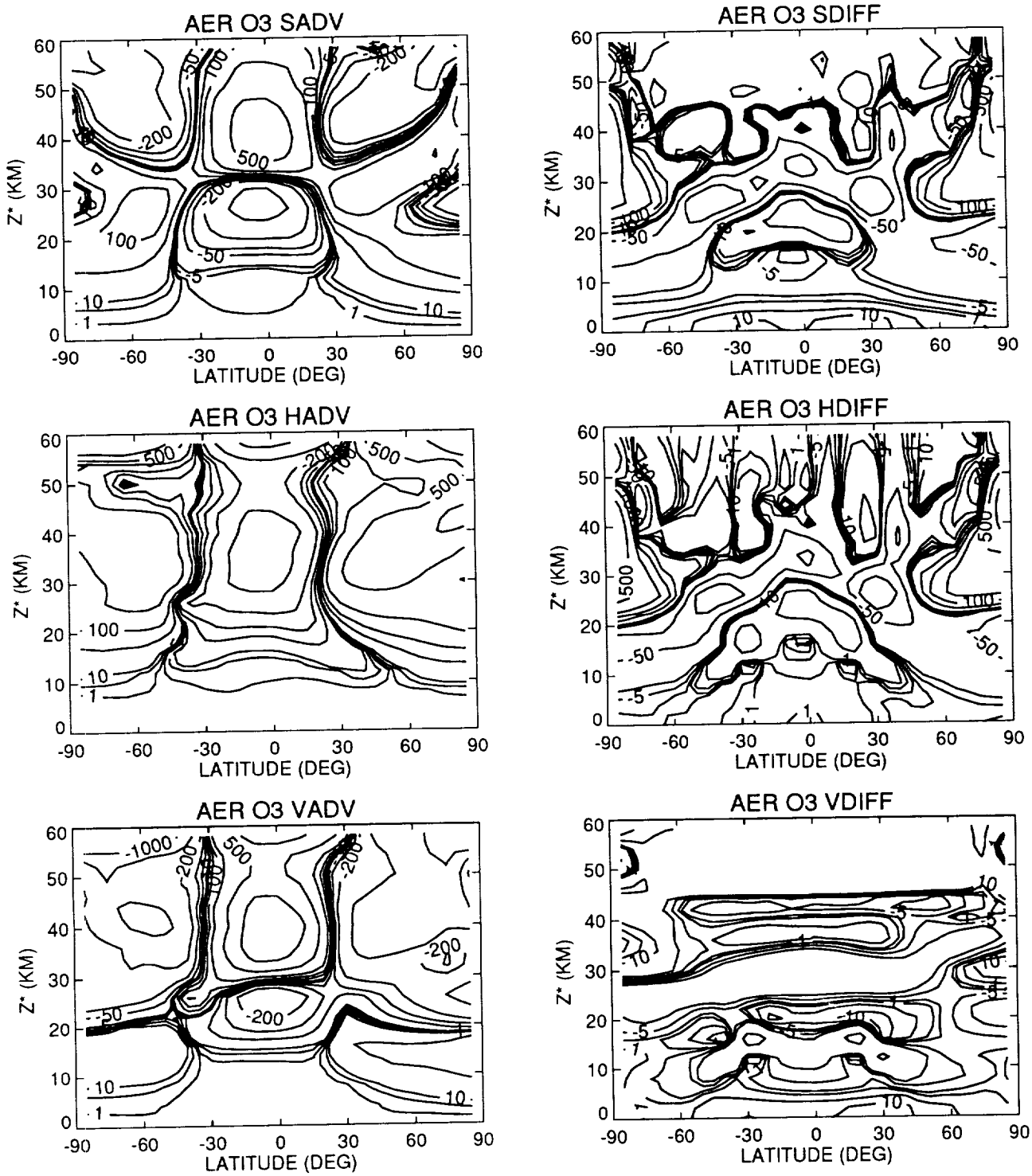
AER O3 SADV
AER O3 SDIFF
AER O3 HADV
AER O3 HDIFF
AER O3 VADV
AER O3 VDIFF
Z* (KM)
LATITUDE (DEG)
-90 -60 -30 0 30 60 90
0 10 20 30 40 50 60

Figure N-6b

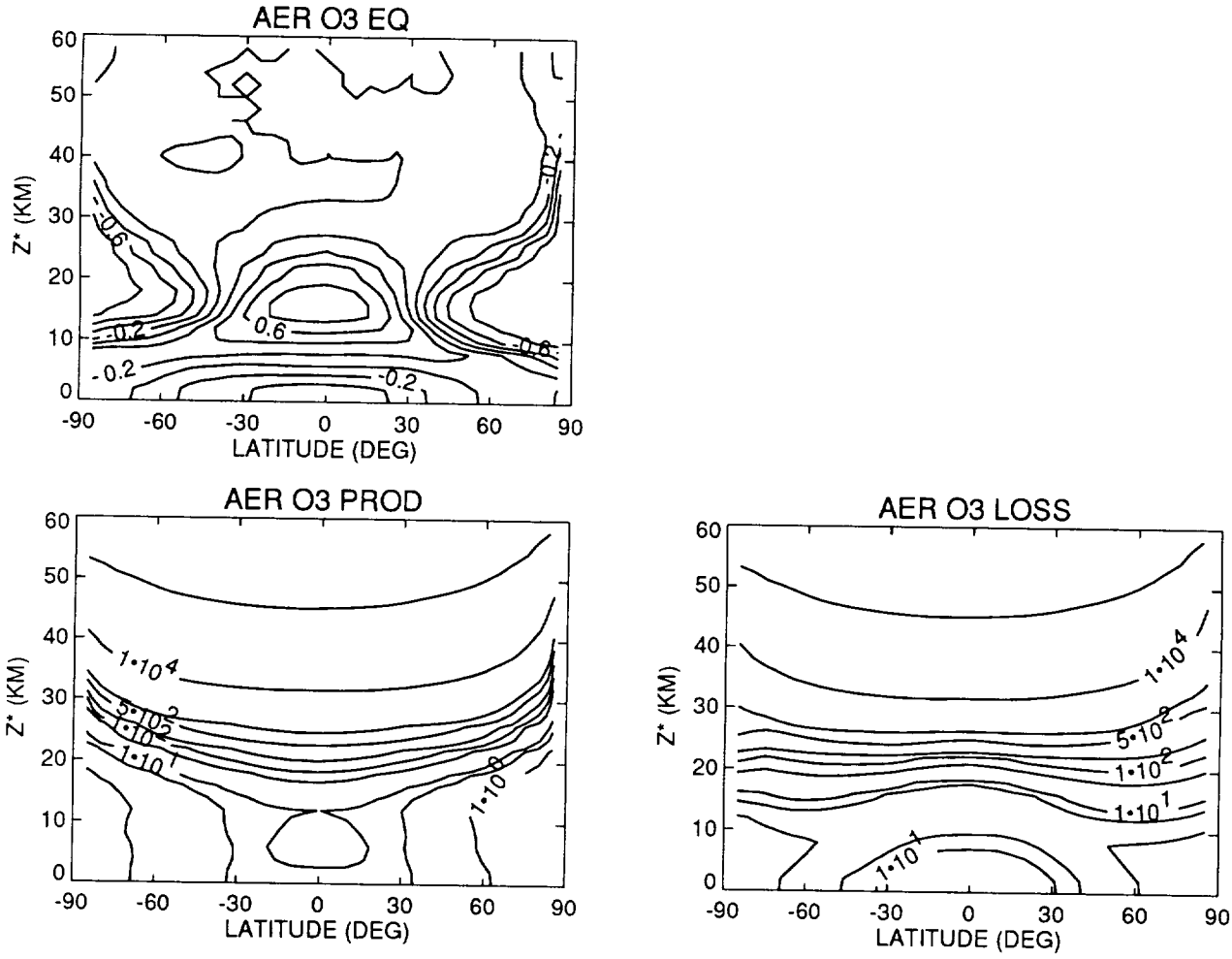
AER O3 EQ
Z* (KM)
LATITUDE (DEG)
-0.6
-0.2
0.6
AER O3 PROD
1•10^4
5•10^2
1•10^2
1•10^1
1•10^-8
AER O3 LOSS
1•10^4
5•10^2
1•10^2
1•10^1
1•10^1

Figure N-6c

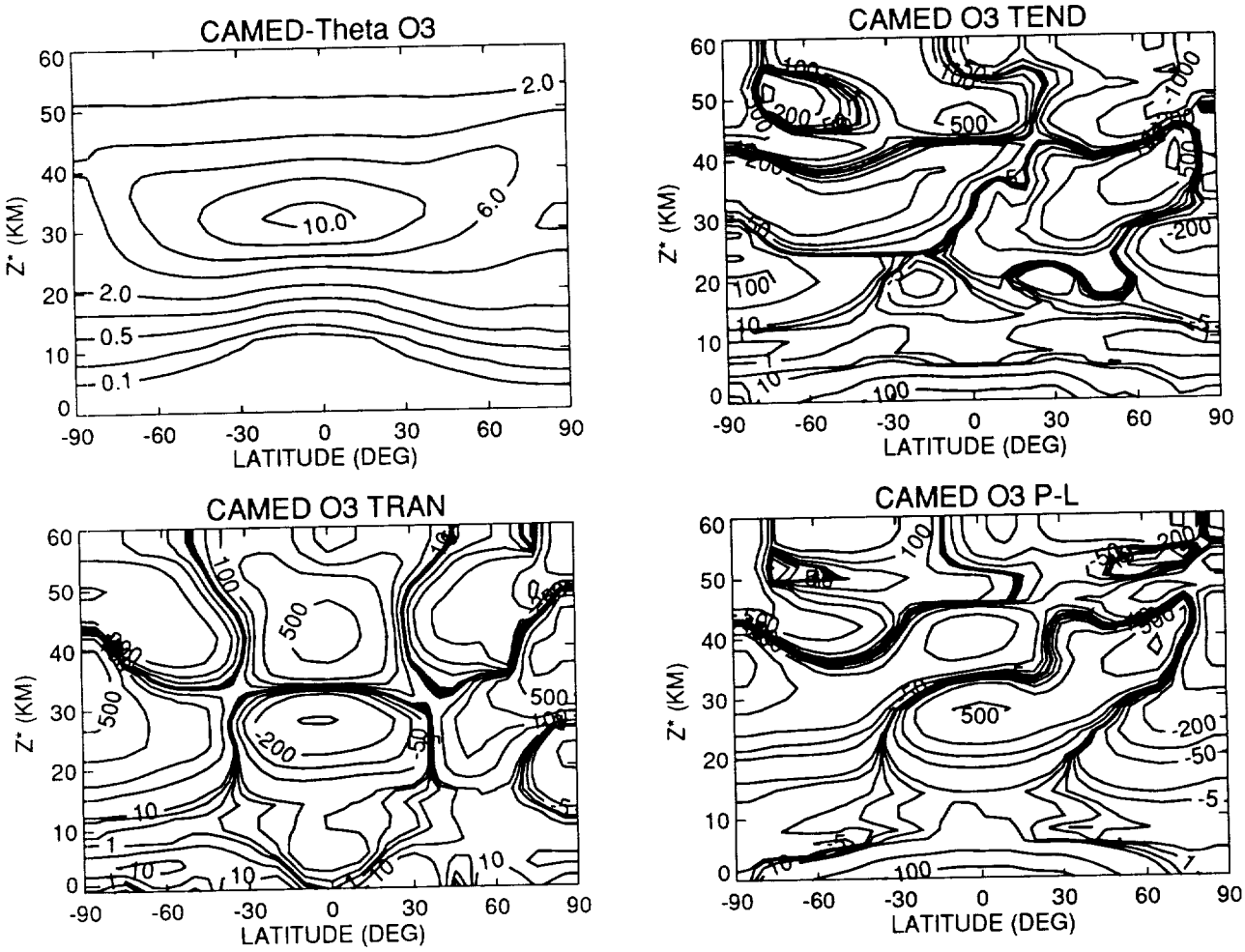
CAMED-Theta O3
CAMED O3 TEND
CAMED O3 TRAN
CAMED O3 P-L
Z* (KM)
LATITUDE (DEG)

Figure N-7a

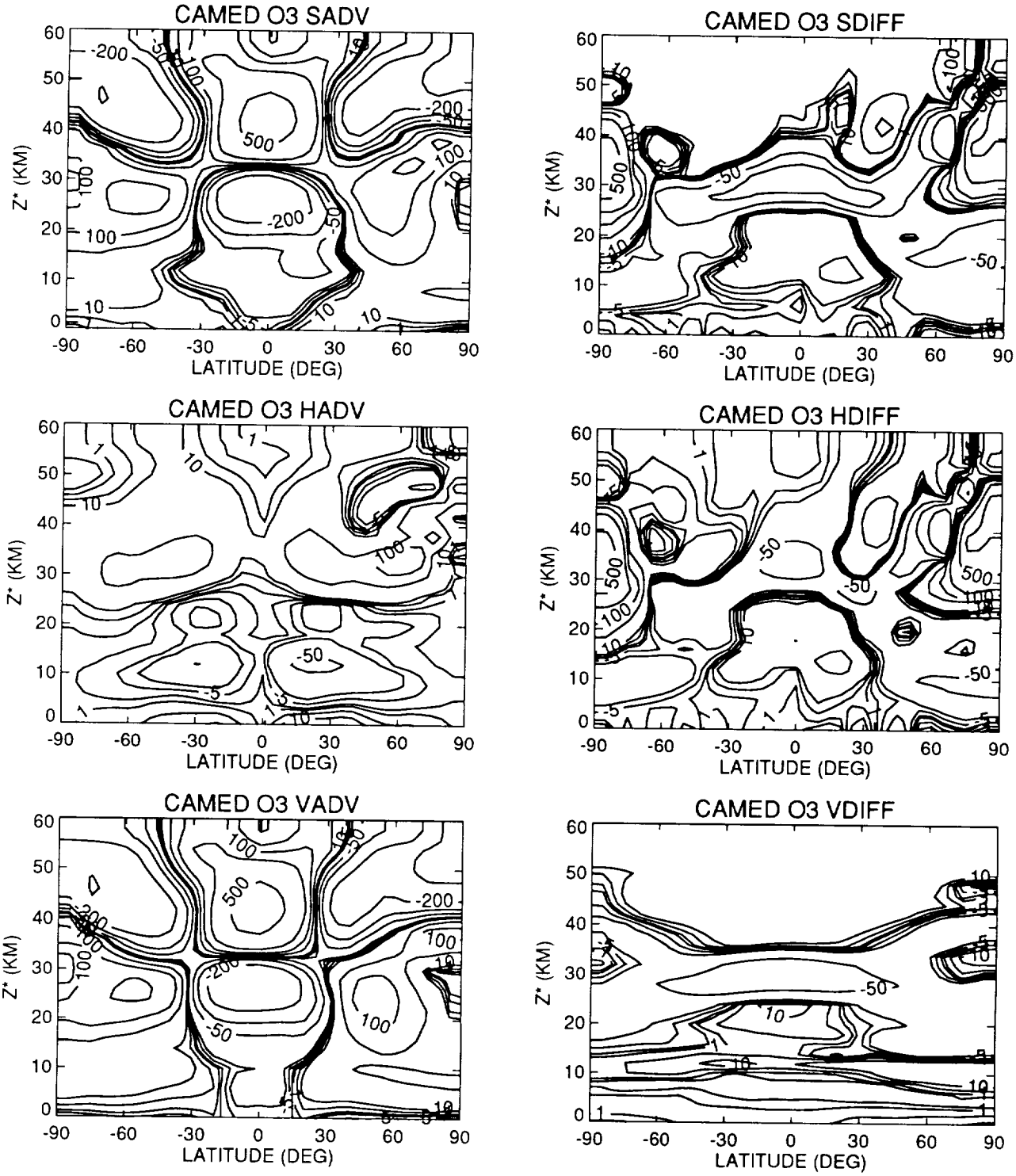
CAMED O3 SADV
CAMED O3 SDIFF
CAMED O3 HADV
CAMED O3 HDIFF
CAMED O3 VADV
CAMED O3 VDIFF
Z* (KM)
LATITUDE (DEG)

Figure N-7b

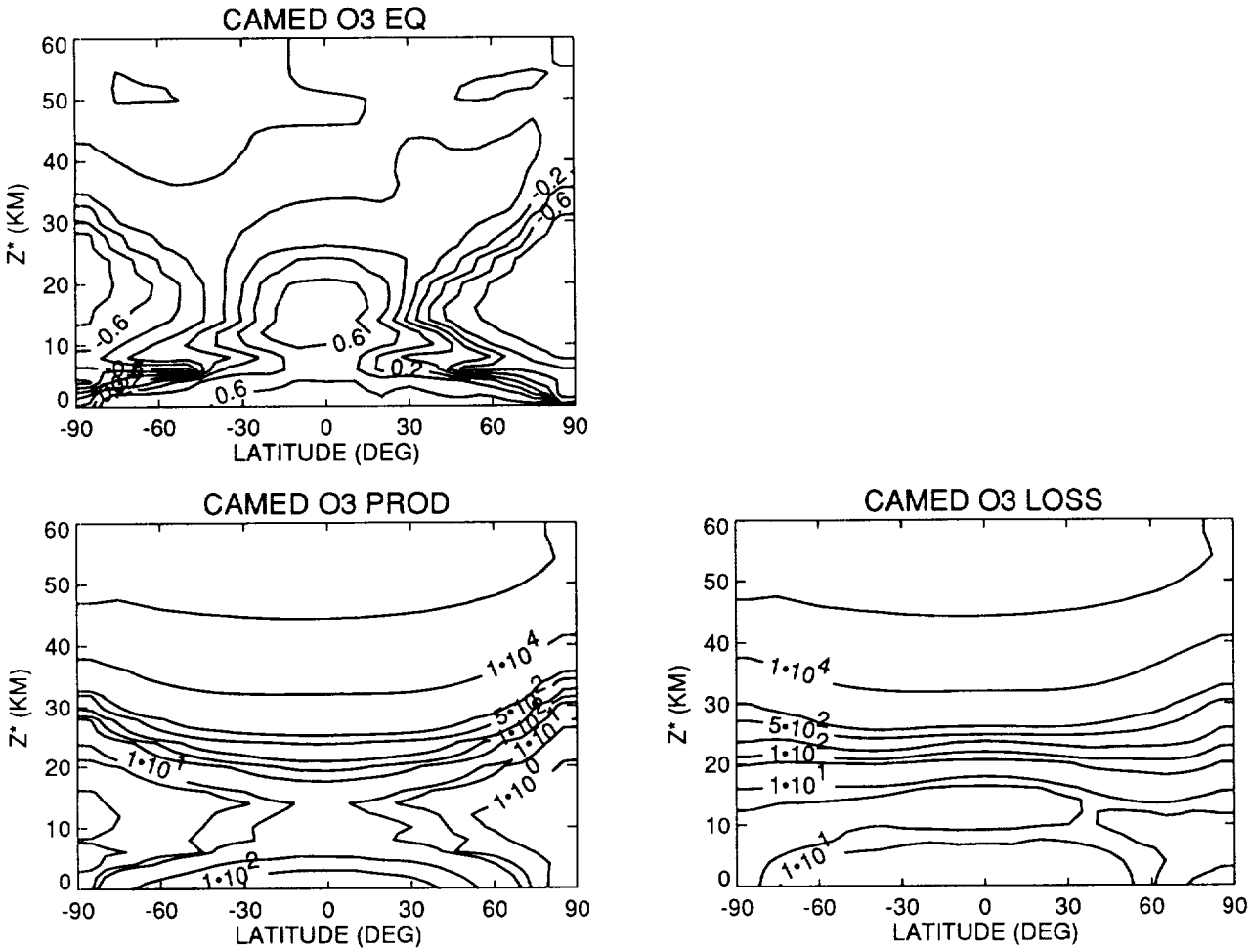
CAMED O3 EQ
Z* (KM)
LATITUDE (DEG)
-0.6
-0.2
0.6
0.2
CAMED O3 PROD
1•10^4
5•10^2
1•10^2
1•10^1
1•10^0
1•10^-1
1•10^2
CAMED O3 LOSS
1•10^4
5•10^2
1•10^2
1•10^1
1•10^1

Figure N-7c

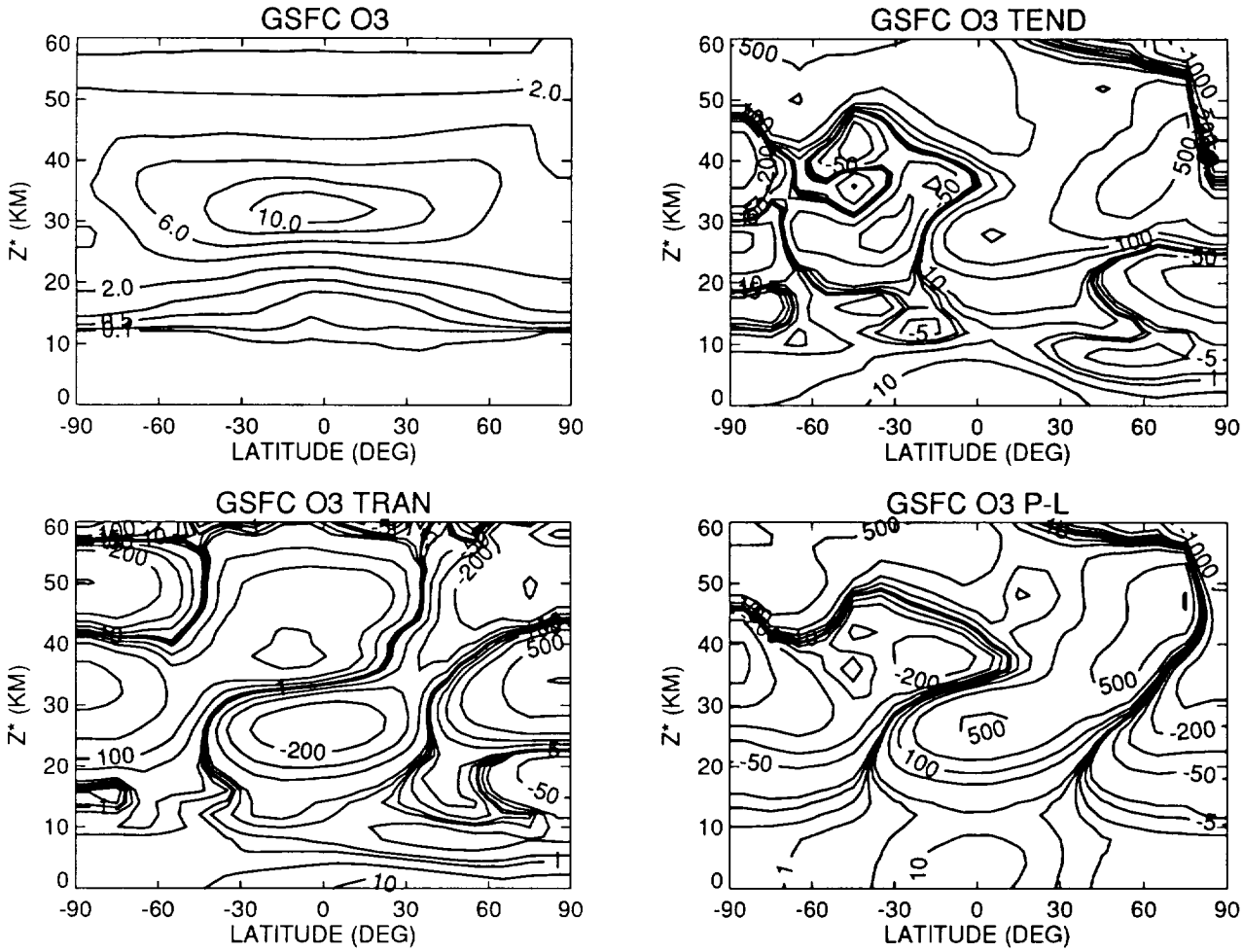
GSFC O3
GSFC O3 TEND
GSFC O3 TRAN
GSFC O3 P-L
Z* (KM)
LATITUDE (DEG)
-90 -60 -30 0 30 60 90
0 10 20 30 40 50 60
2.0
6.0
10.0
0.5
0.1
500
1000
200
100
50
10
5
1
-200
-50
-1000
-500
-100
-10

Figure N-8a

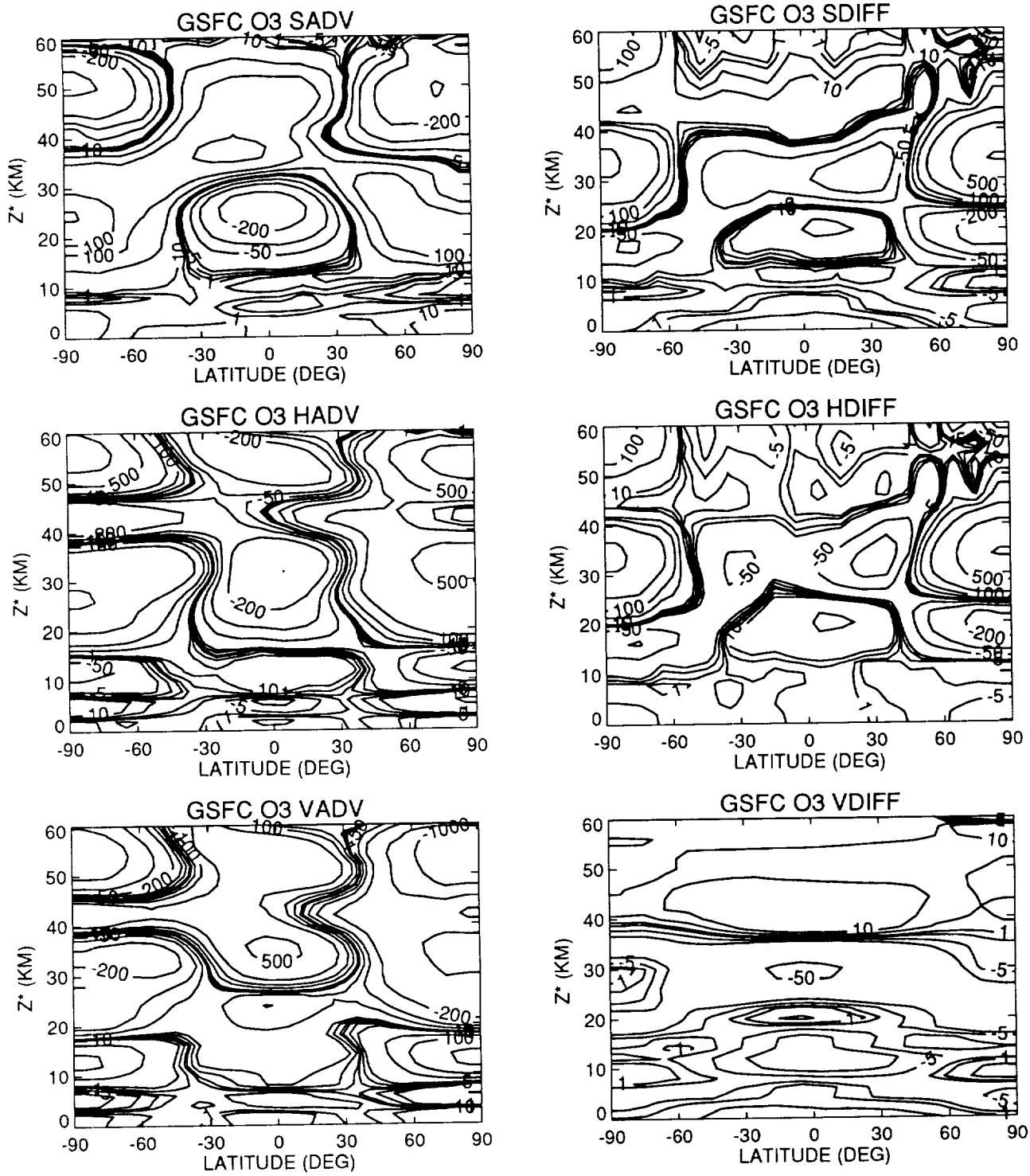
GSFC O3 SADV
GSFC O3 SDIFF
GSFC O3 HADV
GSFC O3 HDIFF
GSFC O3 VADV
GSFC O3 VDIFF
Z* (KM)
LATITUDE (DEG)
-90 -60 -30 0 30 60 90
0 10 20 30 40 50 60

Figure N-8b

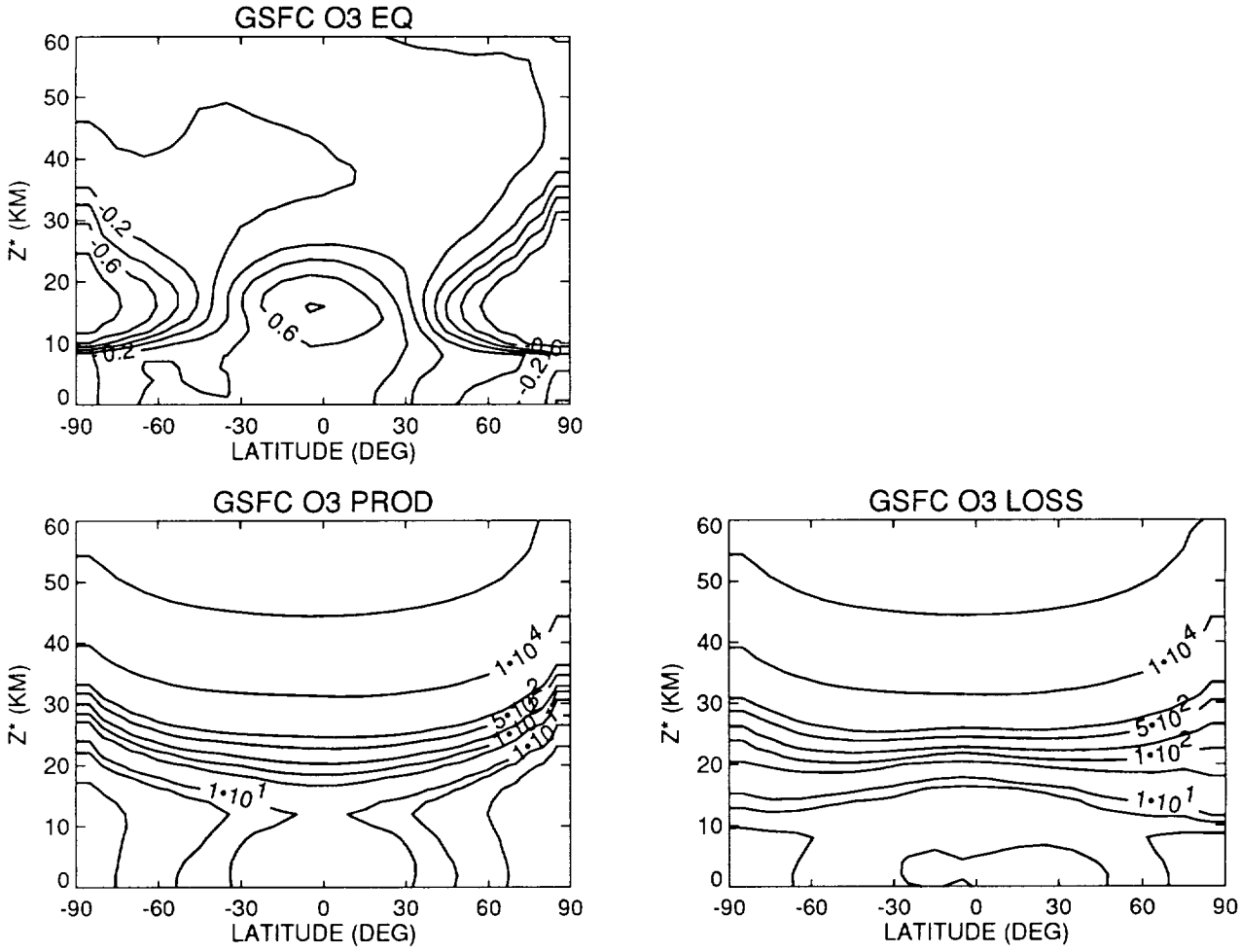
GSFC O3 EQ
Z* (KM)
LATITUDE (DEG)
-0.2
-0.6
0.6
GSFC O3 PROD
1•10^4
5•10^2
1•10^2
1•10^1
GSFC O3 LOSS

Figure N-8c

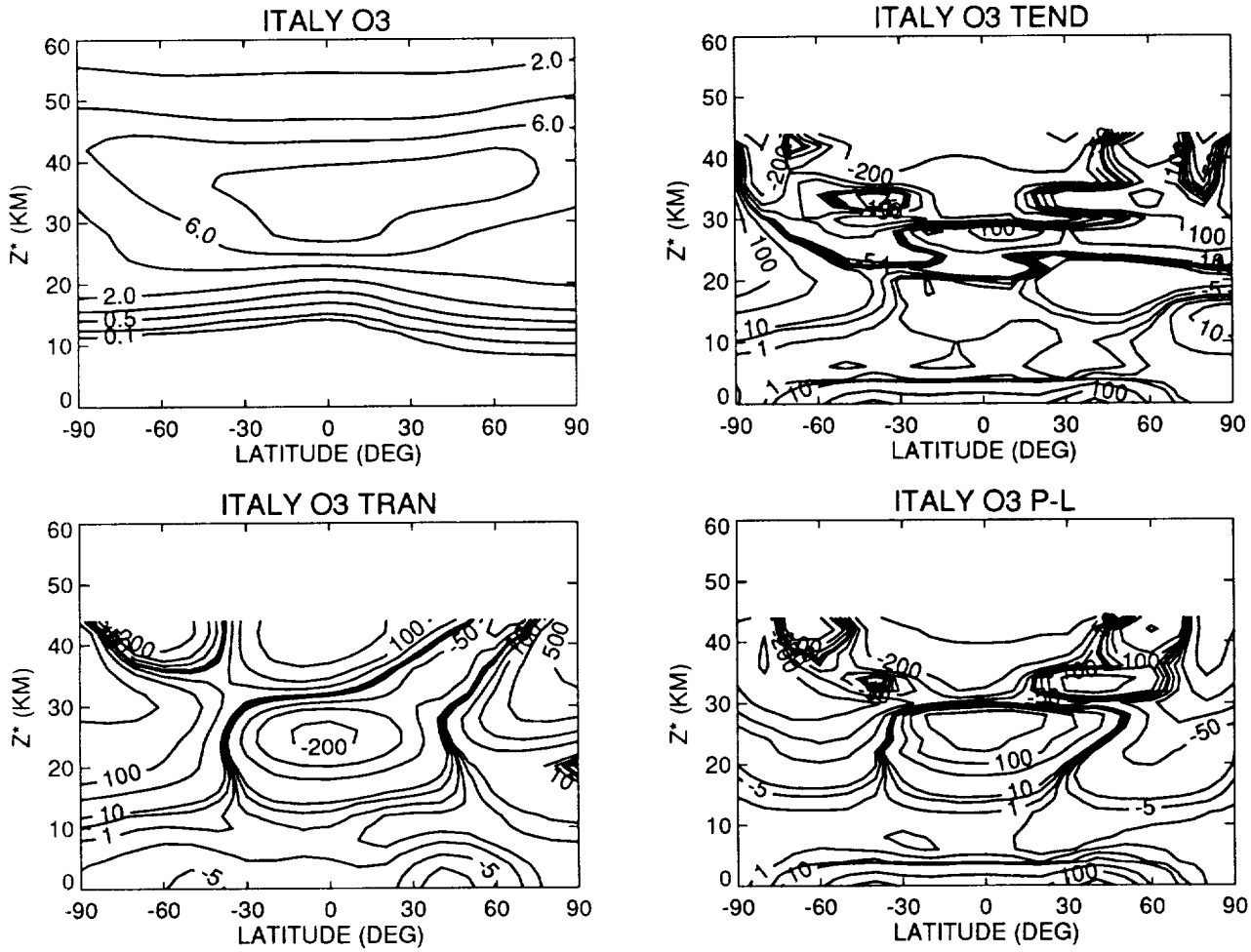
ITALY O3
ITALY O3 TEND
ITALY O3 TRAN
ITALY O3 P-L
Z* (KM)
LATITUDE (DEG)

Figure N-9a

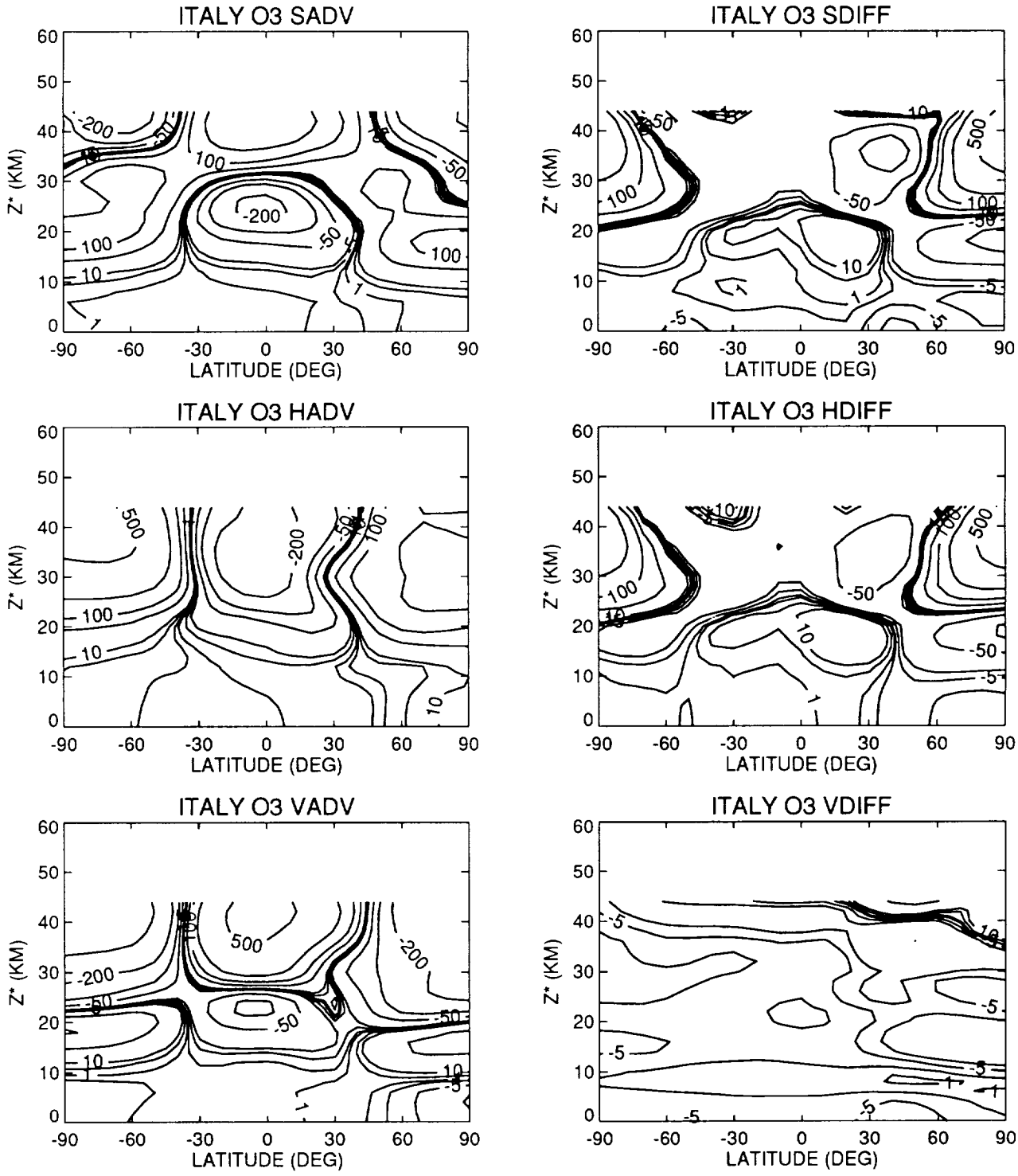
ITALY O3 SADV
ITALY O3 SDIFF
ITALY O3 HADV
ITALY O3 HDIFF
ITALY O3 VADV
ITALY O3 VDIFF
Z* (KM)
LATITUDE (DEG)
0
10
20
30
40
50
60
-90
-60
-30
0
30
60
90

Figure N-9b

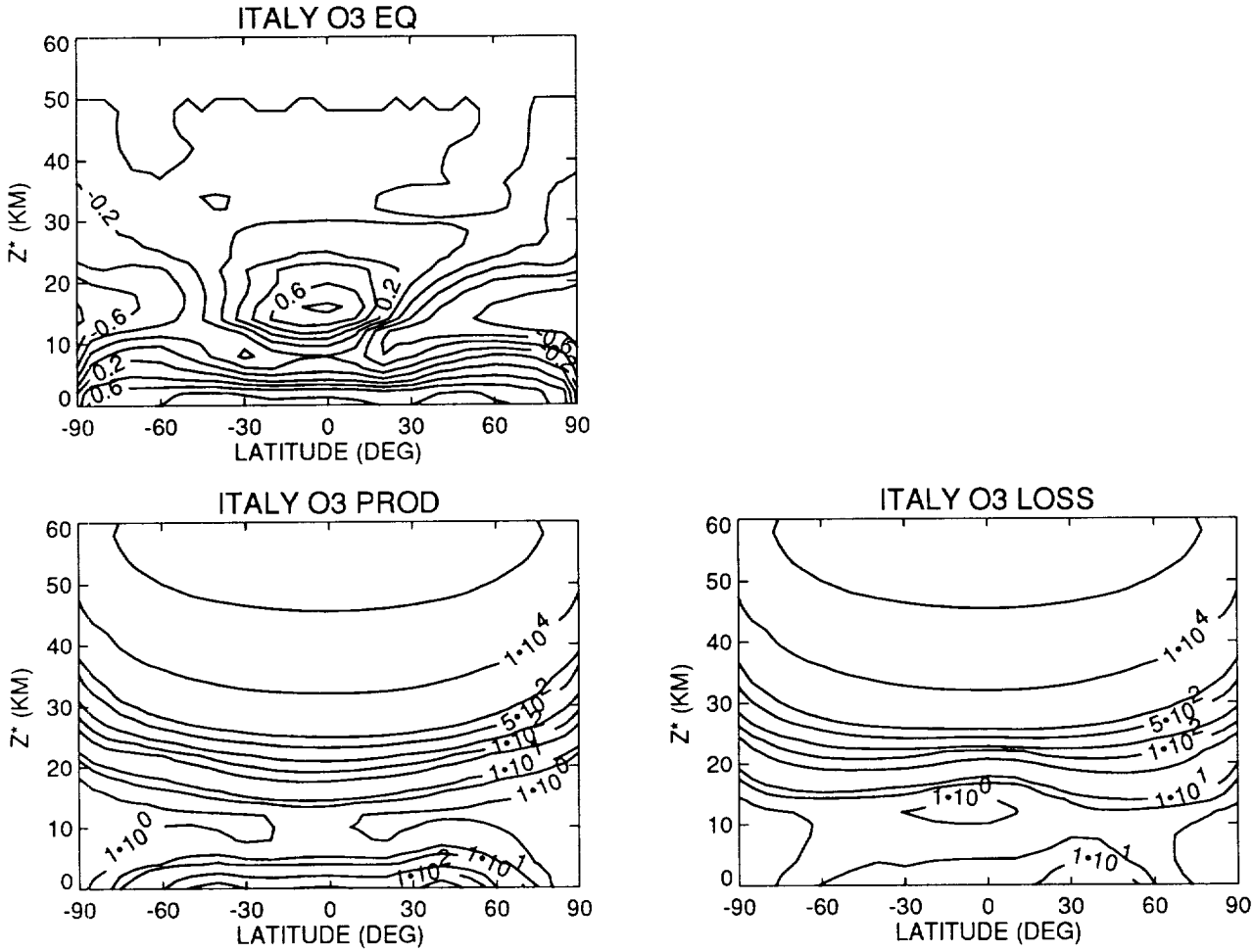
ITALY O3 EQ
Z* (KM)
LATITUDE (DEG)
ITALY O3 PROD
Z* (KM)
LATITUDE (DEG)
ITALY O3 LOSS
Z* (KM)
LATITUDE (DEG)

Figure N-9c

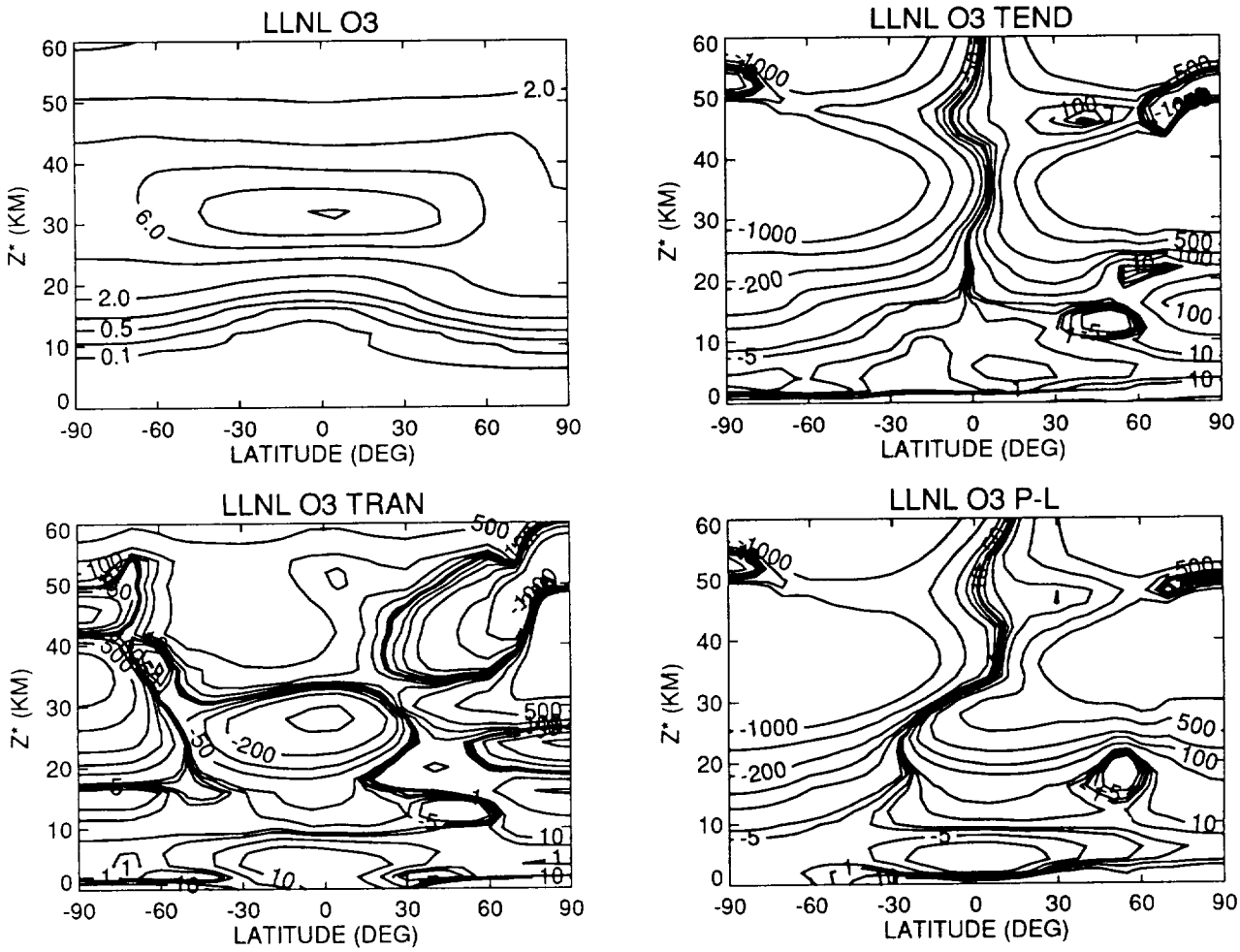
LLNL O3
LLNL O3 TEND
LLNL O3 TRAN
LLNL O3 P-L
Z* (KM)
LATITUDE (DEG)
-90 -60 -30 0 30 60 90
0 10 20 30 40 50 60
2.0
6.0
0.5
0.1
-1000
-200
-5
500
100
10
1

Figure N-10a

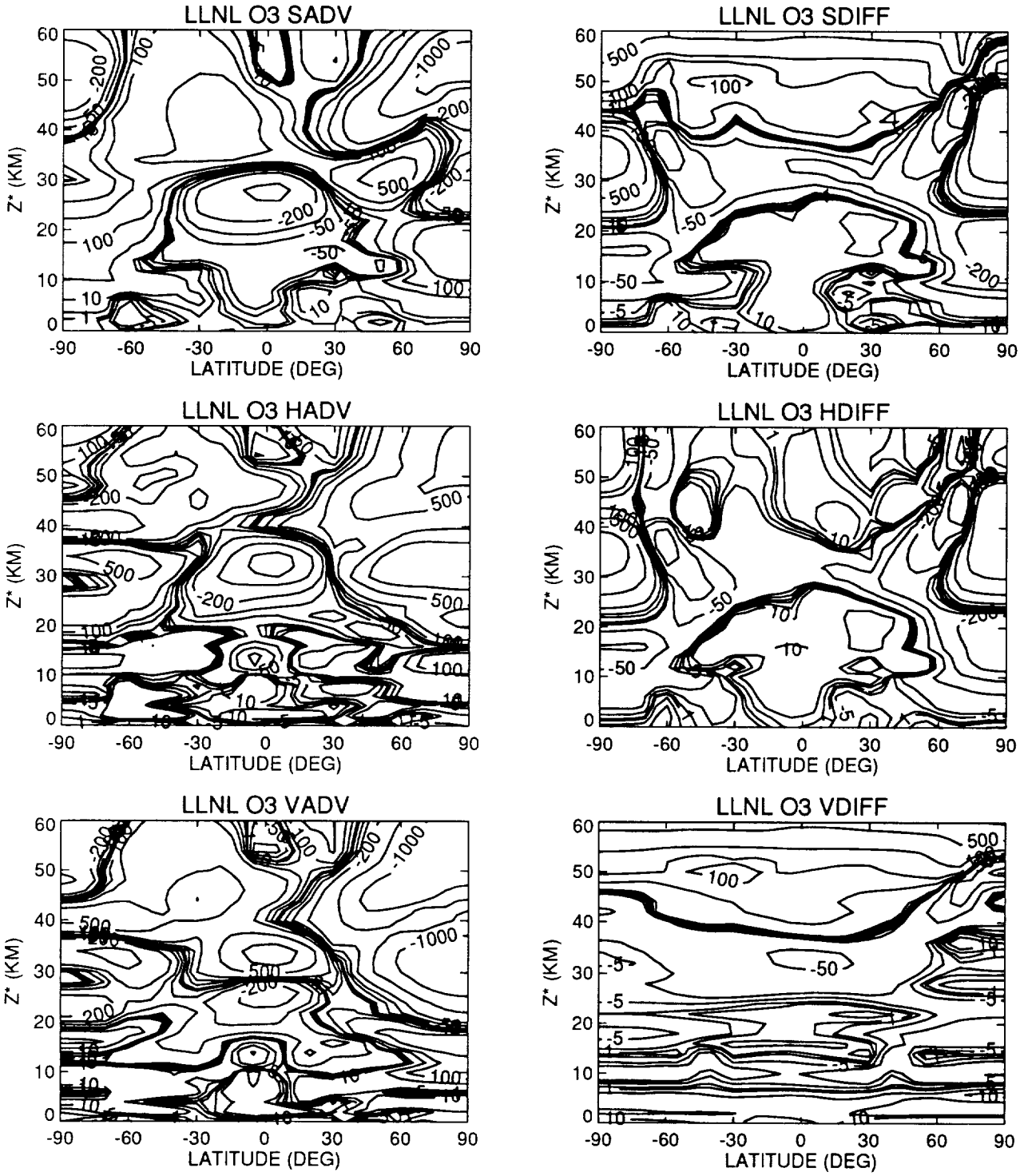
LLNL O3 SADV
LLNL O3 SDIFF
LLNL O3 HADV
LLNL O3 HDIFF
LLNL O3 VADV
LLNL O3 VDIFF
Z* (KM)
LATITUDE (DEG)
-90 -60 -30 0 30 60 90
0 10 20 30 40 50 60

Figure N-10b

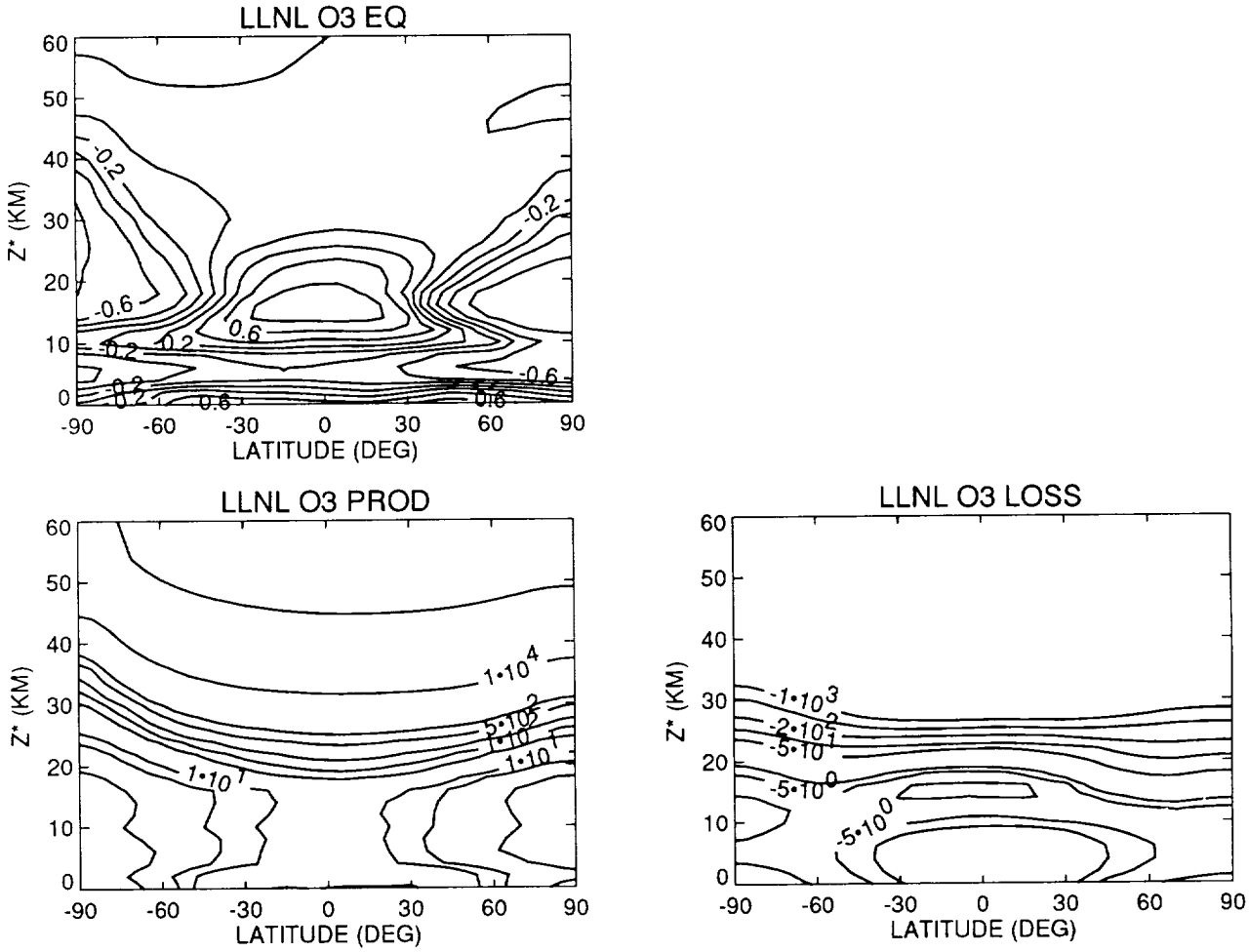
LLNL O3 EQ
Z* (KM)
LATITUDE (DEG)
-0.2
-0.6
0.6
0.2
LLNL O3 PROD
1•10^4
5•10^2
1•10^2
1•10^1
1•10^1
LLNL O3 LOSS
-1•10^3
-2•10^2
-5•10^1
-5•10^0
-5•10^0

Figure N-10c

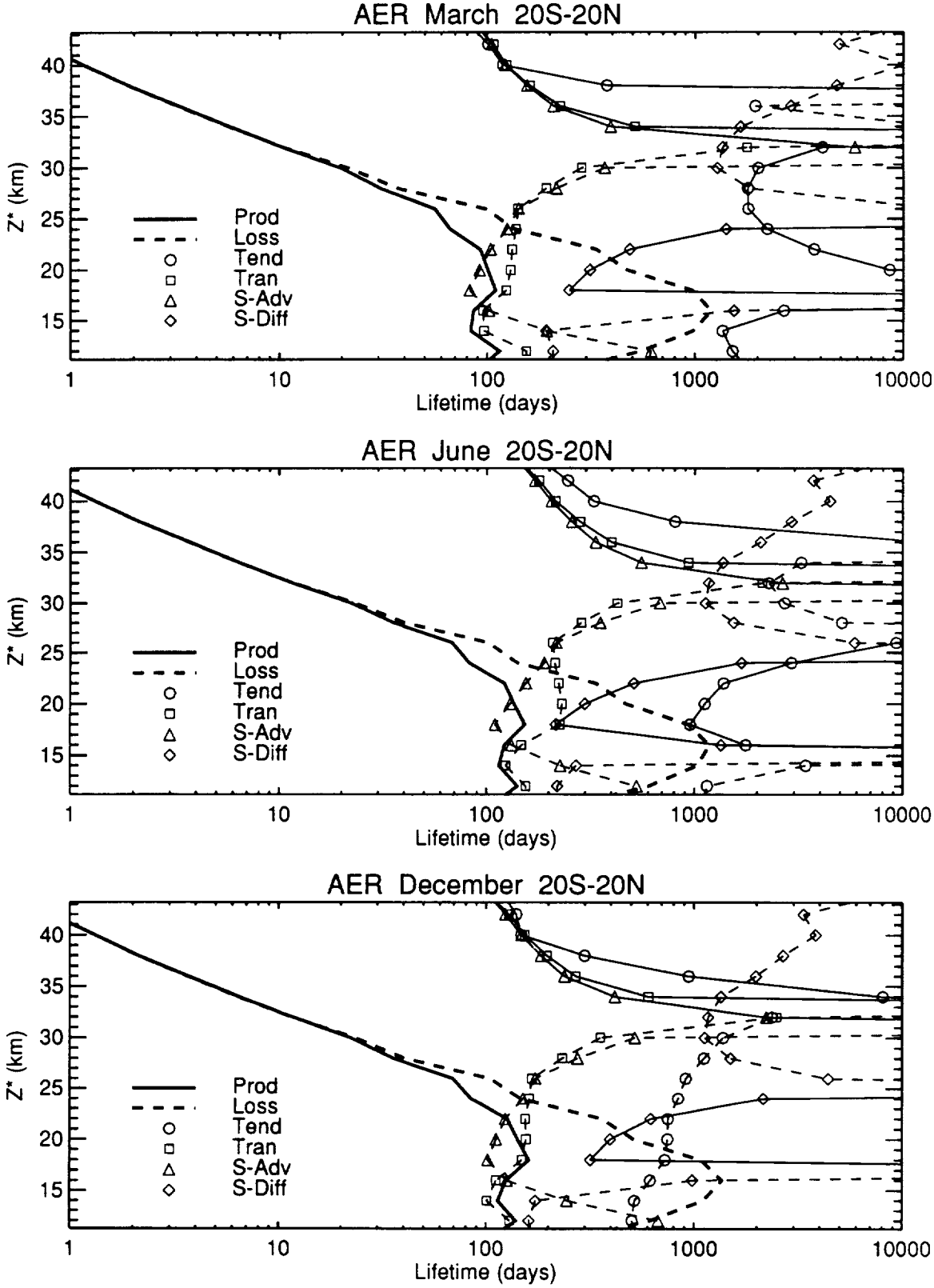
AER March 20S-20N
AER June 20S-20N
AER December 20S-20N
Z* (km)
Lifetime (days)
Prod
Loss
Tend
Tran
S-Adv
S-Diff
40
35
30
25
20
15
1
10
100
1000
10000

Figure N-11a

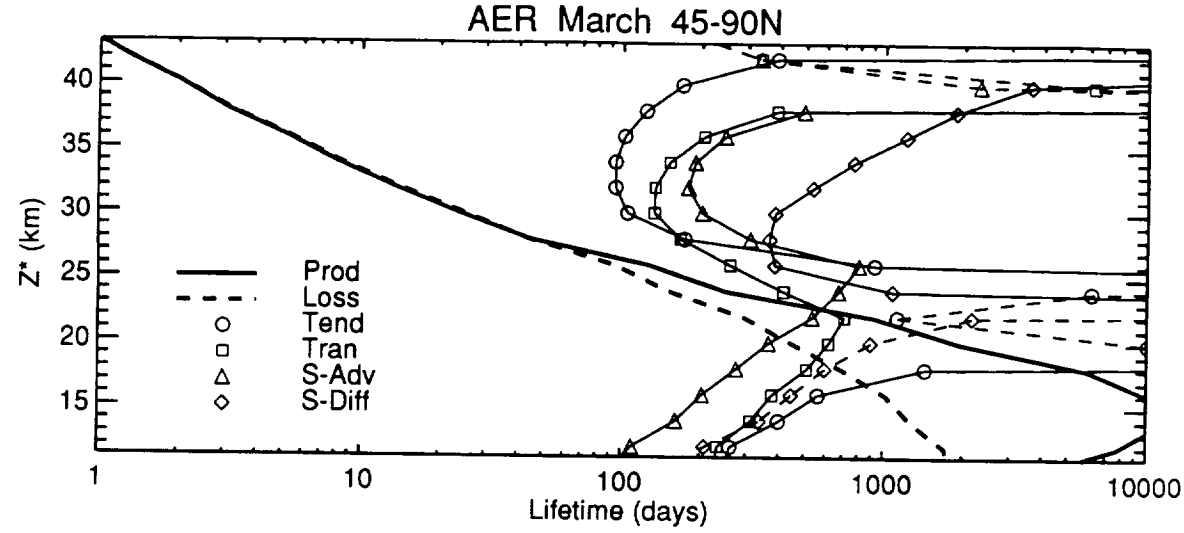
AER March 45-90N
Z* (km)
40
35
30
25
20
15
Prod
Loss
Tend
Tran
S-Adv
S-Diff
1
10
100
1000
10000
Lifetime (days)

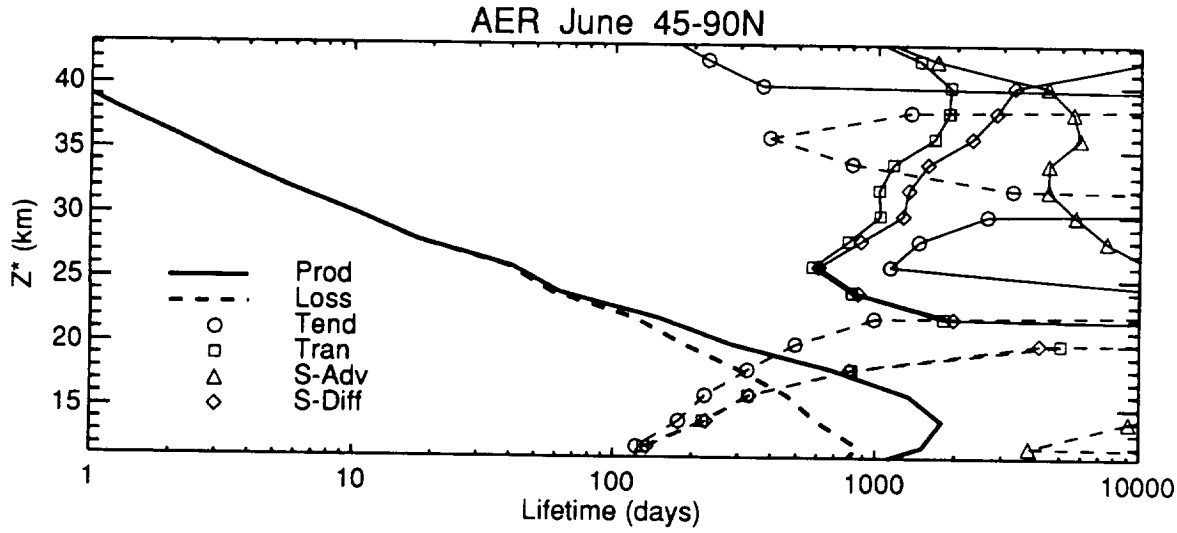
AER June 45-90N
Z* (km)
40
35
30
25
20
15
Prod
Loss
Tend
Tran
S-Adv
S-Diff
1
10
100
1000
10000
Lifetime (days)

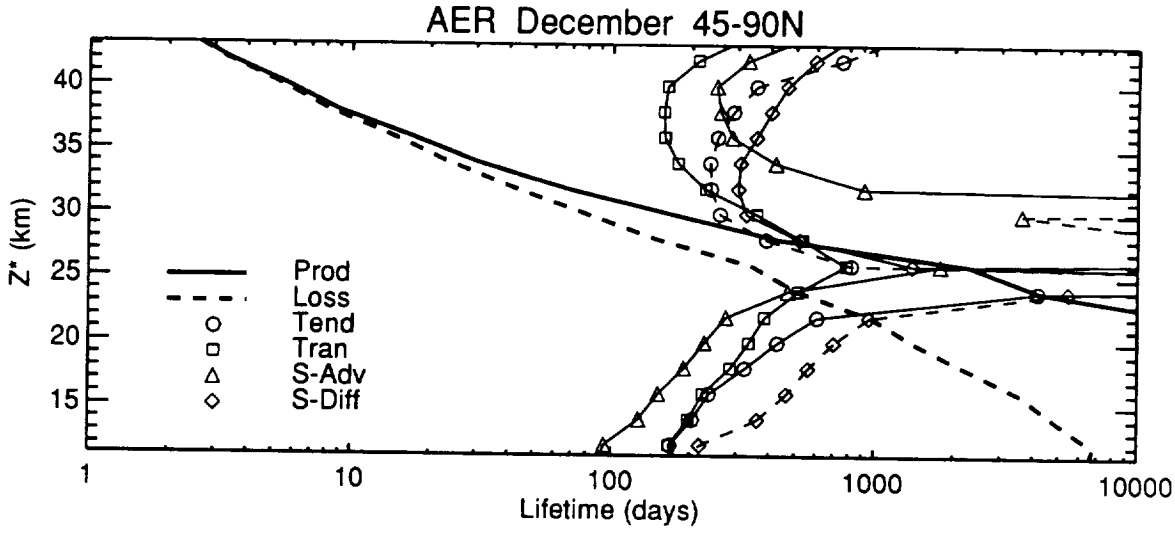
AER December 45-90N
Z* (km)
40
35
30
25
20
15
Prod
Loss
Tend
Tran
S-Adv
S-Diff
1
10
100
1000
10000
Lifetime (days)

Figure N-11b

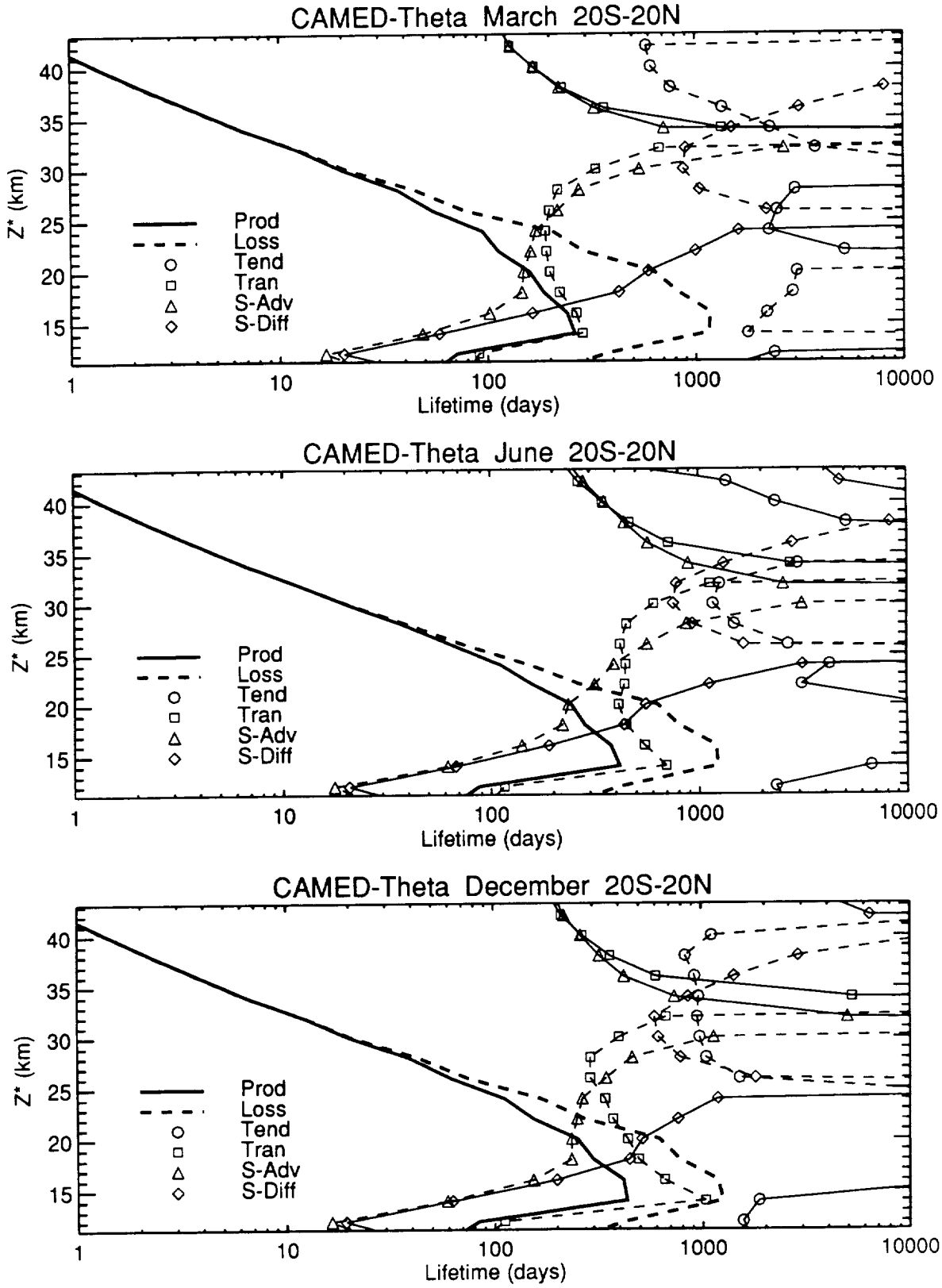
CAMED-Theta March 20S-20N
Z* (km)
Lifetime (days)
Prod
Loss
Tend
Tran
S-Adv
S-Diff
CAMED-Theta June 20S-20N
Z* (km)
Lifetime (days)
Prod
Loss
Tend
Tran
S-Adv
S-Diff
CAMED-Theta December 20S-20N
Z* (km)
Lifetime (days)
Prod
Loss
Tend
Tran
S-Adv
S-Diff

Figure N-12a

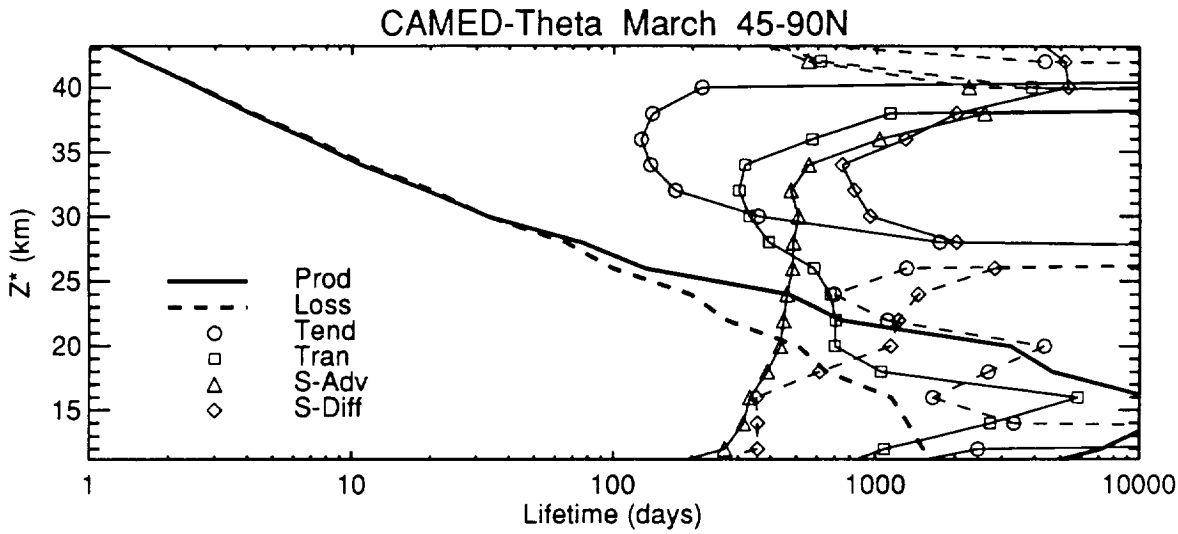
CAMED-Theta March 45-90N
Z* (km)
40
35
30
25
20
15
Prod
Loss
Tend
Tran
S-Adv
S-Diff
1
10
100
1000
10000
Lifetime (days)

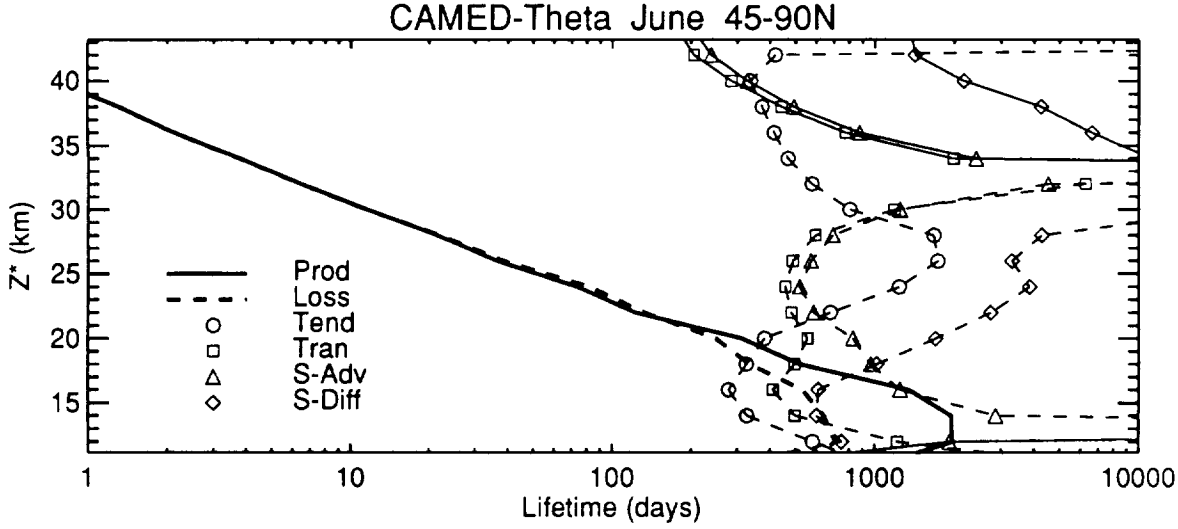
CAMED-Theta June 45-90N
Z* (km)
40
35
30
25
20
15
Prod
Loss
Tend
Tran
S-Adv
S-Diff
1
10
100
1000
10000
Lifetime (days)

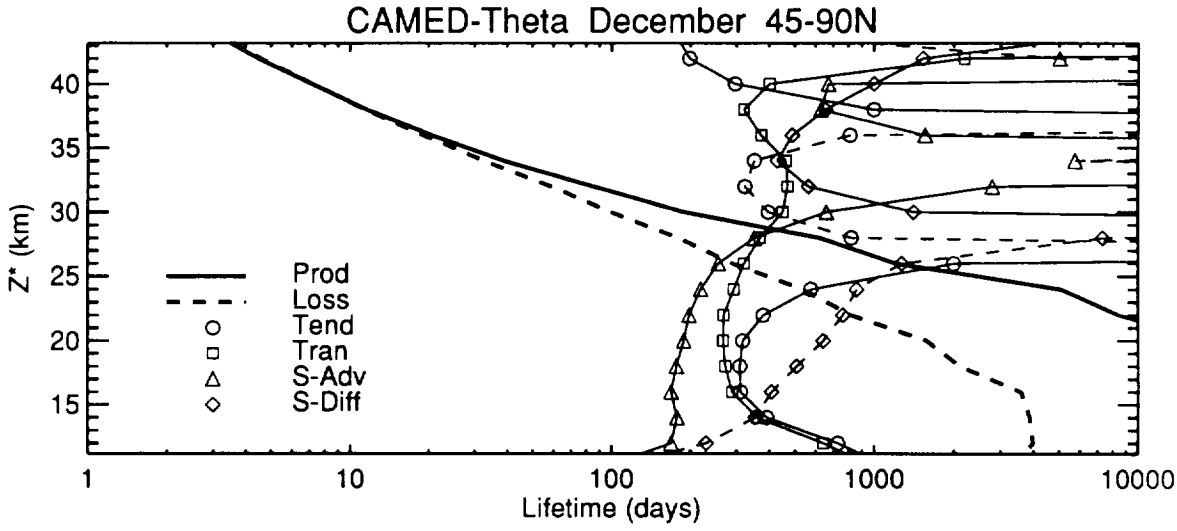
CAMED-Theta December 45-90N
Z* (km)
40
35
30
25
20
15
Prod
Loss
Tend
Tran
S-Adv
S-Diff
1
10
100
1000
10000
Lifetime (days)

Figure N-12b

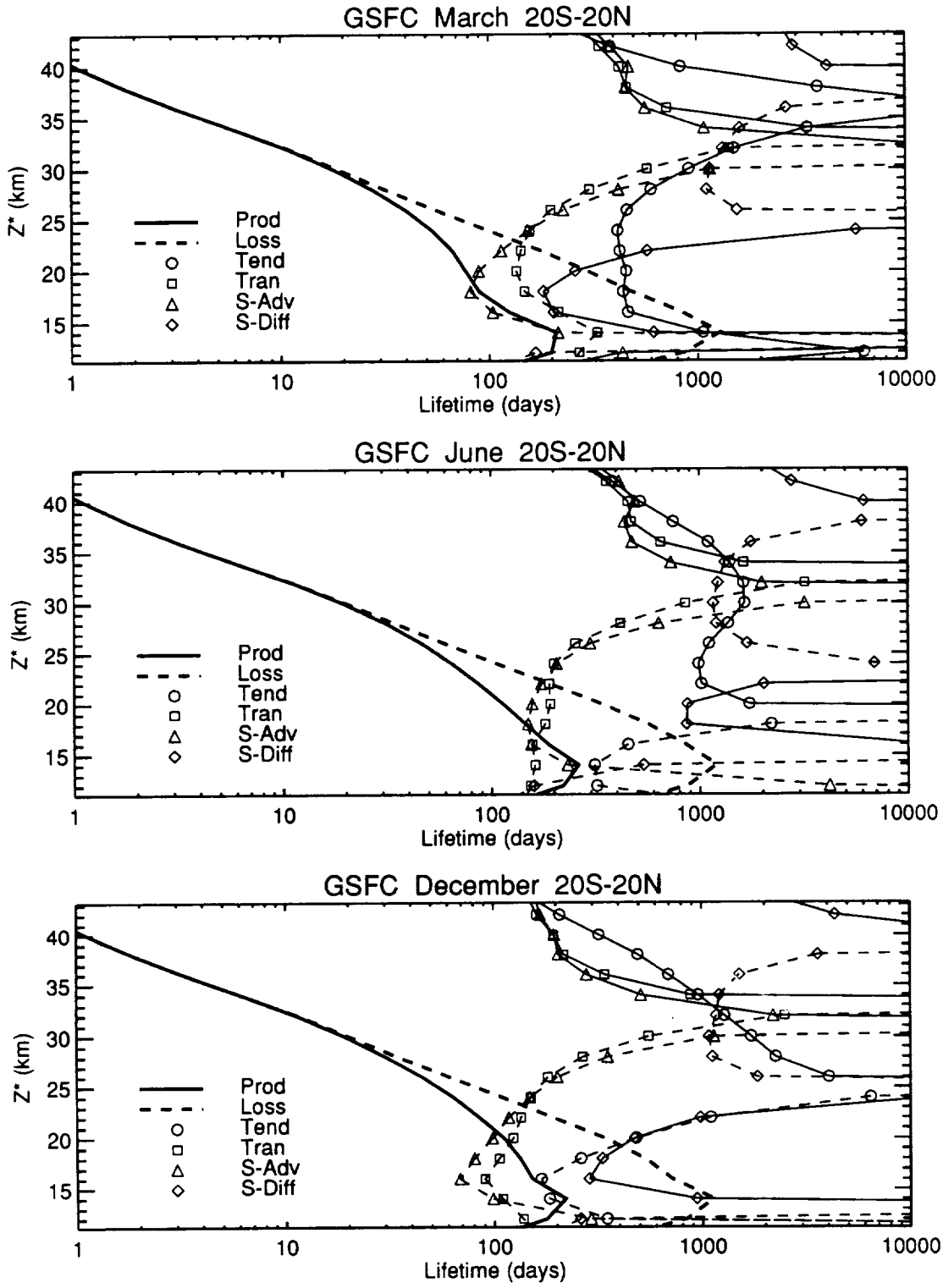
GSFC March 20S-20N
Z* (km)
Lifetime (days)
Prod
Loss
Tend
Tran
S-Adv
S-Diff
GSFC June 20S-20N
Z* (km)
Lifetime (days)
Prod
Loss
Tend
Tran
S-Adv
S-Diff
GSFC December 20S-20N
Z* (km)
Lifetime (days)
Prod
Loss
Tend
Tran
S-Adv
S-Diff

Figure N-13a

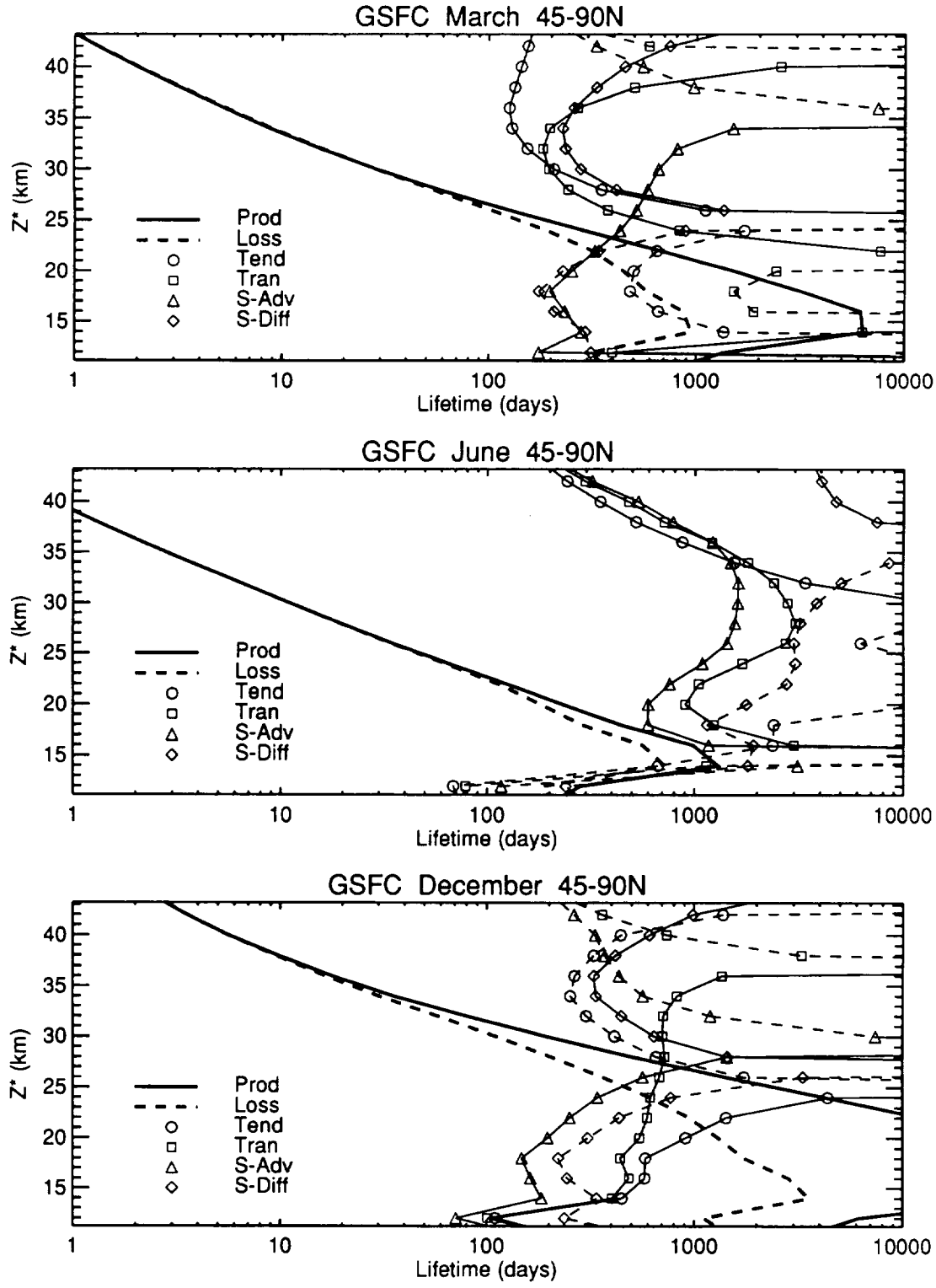
GSFC March 45-90N
GSFC June 45-90N
GSFC December 45-90N
Z* (km)
Lifetime (days)
Prod
Loss
Tend
Tran
S-Adv
S-Diff
40
35
30
25
20
15
1
10
100
1000
10000

Figure N-13b

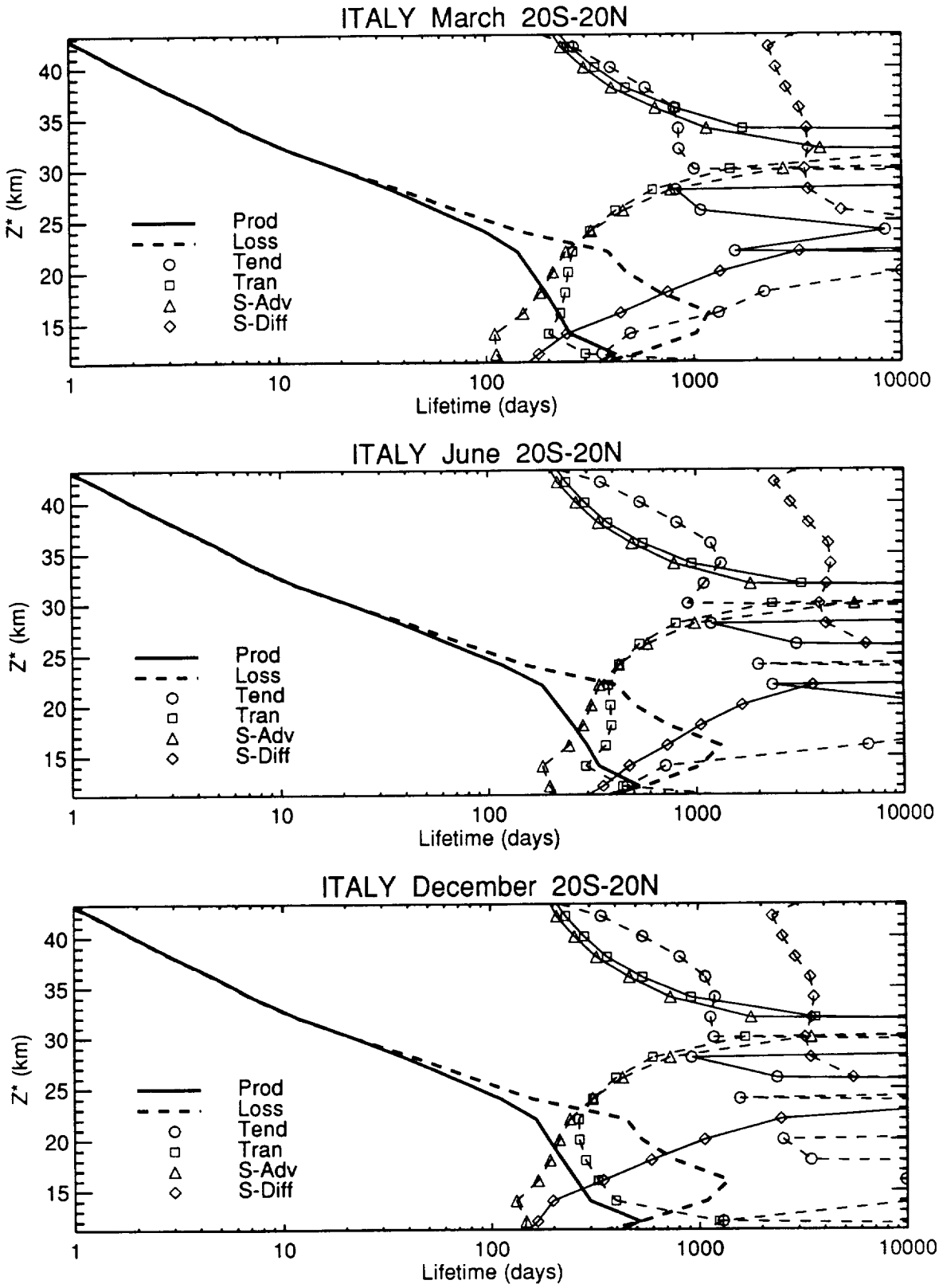
ITALY March 20S-20N
Z* (km)
40
35
30
25
20
15
Prod
Loss
Tend
Tran
S-Adv
S-Diff
1
10
100
1000
10000
Lifetime (days)
ITALY June 20S-20N
Z* (km)
40
35
30
25
20
15
Prod
Loss
Tend
Tran
S-Adv
S-Diff
1
10
100
1000
10000
Lifetime (days)
ITALY December 20S-20N
Z* (km)
40
35
30
25
20
15
Prod
Loss
Tend
Tran
S-Adv
S-Diff
1
10
100
1000
10000
Lifetime (days)

Figure N-14a

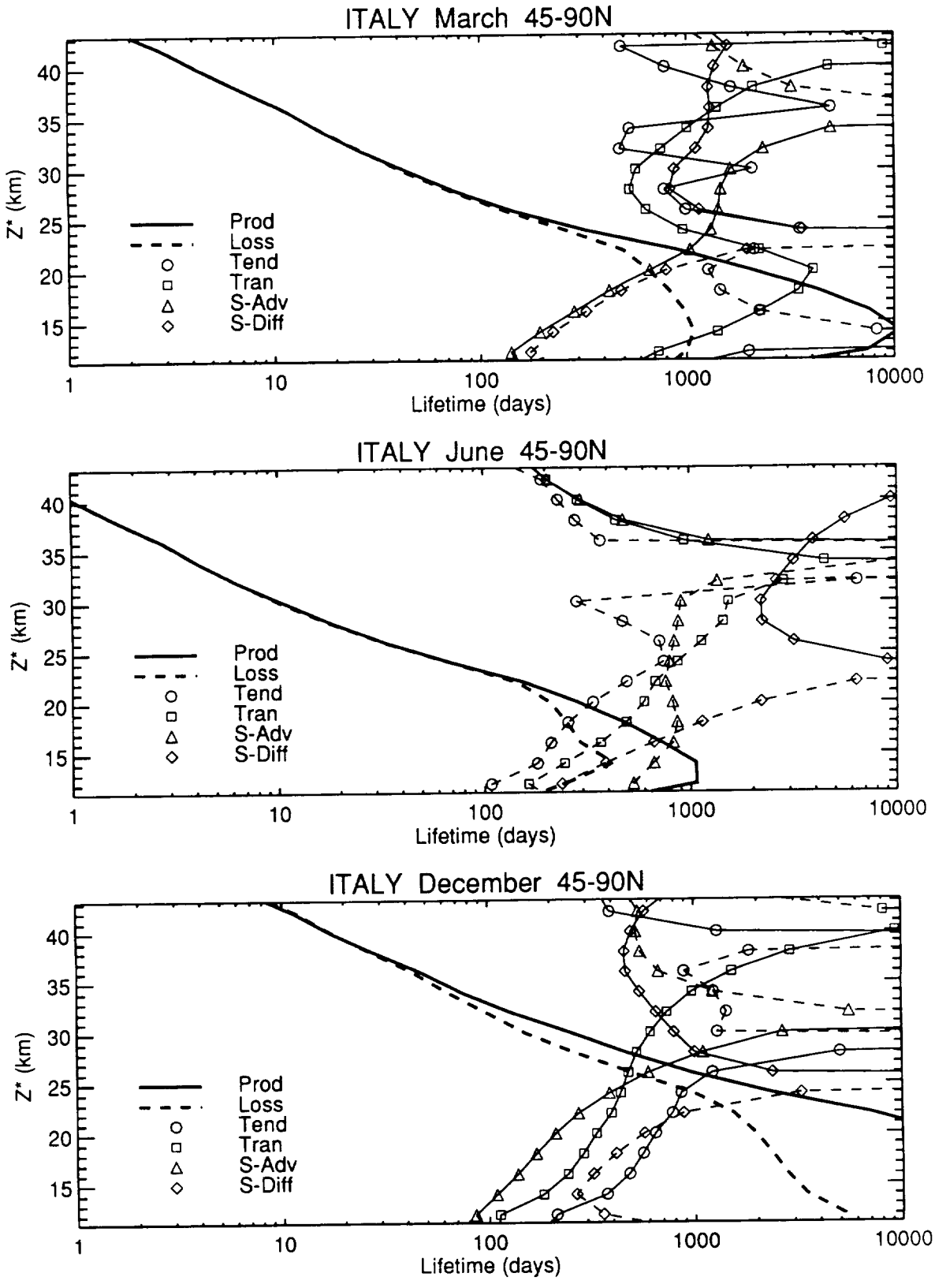
ITALY March 45-90N
Z* (km)
40
35
30
25
20
15
Prod
Loss
Tend
Tran
S-Adv
S-Diff
1
10
100
1000
10000
Lifetime (days)
ITALY June 45-90N
Z* (km)
40
35
30
25
20
15
Prod
Loss
Tend
Tran
S-Adv
S-Diff
1
10
100
1000
10000
Lifetime (days)
ITALY December 45-90N
Z* (km)
40
35
30
25
20
15
Prod
Loss
Tend
Tran
S-Adv
S-Diff
1
10
100
1000
10000
Lifetime (days)

Figure N-14b

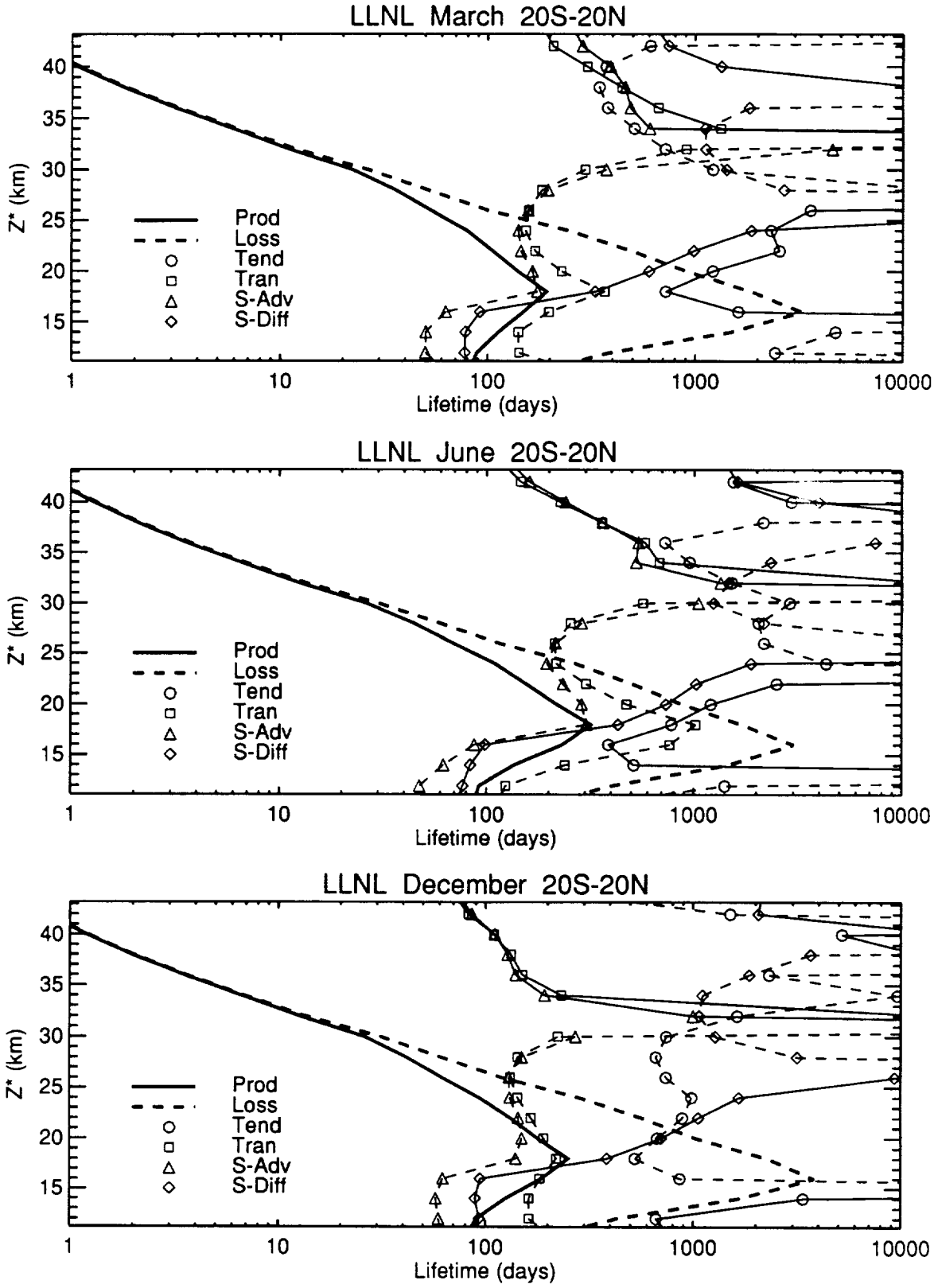
LLNL March 20S-20N
Z* (km)
Lifetime (days)
Prod
Loss
Tend
Tran
S-Adv
S-Diff
LLNL June 20S-20N
Z* (km)
Lifetime (days)
Prod
Loss
Tend
Tran
S-Adv
S-Diff
LLNL December 20S-20N
Z* (km)
Lifetime (days)
Prod
Loss
Tend
Tran
S-Adv
S-Diff

Figure N-15a

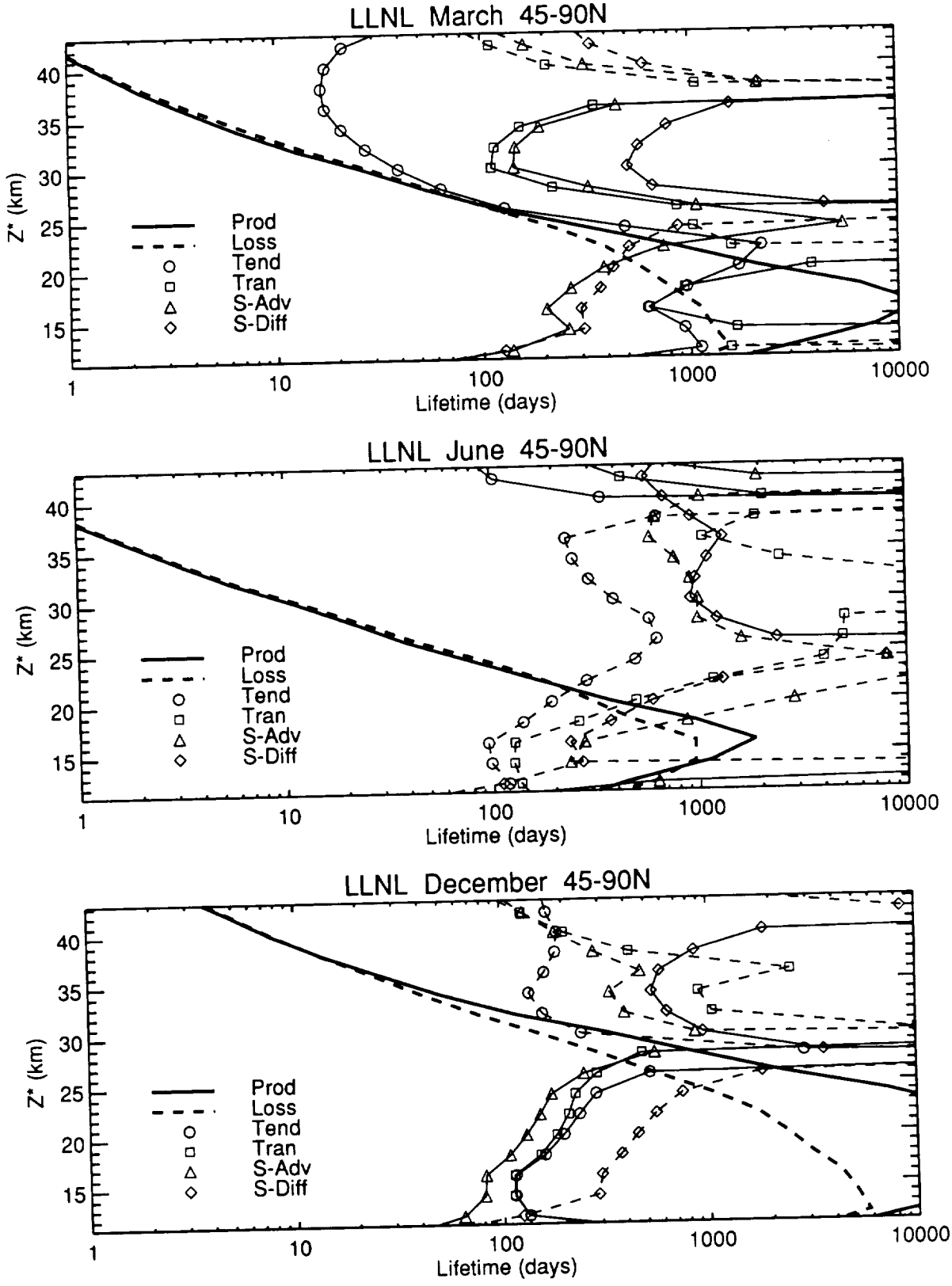
LLNL March 45-90N
Z* (km)
Lifetime (days)
Prod
Loss
Tend
Tran
S-Adv
S-Diff
LLNL June 45-90N
Z* (km)
Lifetime (days)
Prod
Loss
Tend
Tran
S-Adv
S-Diff
LLNL December 45-90N
Z* (km)
Lifetime (days)
Prod
Loss
Tend
Tran
S-Adv
S-Diff

Figure N-15b

O: Model-Model Comparison of Idealized Tracers, X1 and X2

O. Model-Model Comparison of Idealized Tracers X1 & X2

Charles H. Jackman
NASA-Goddard Space Flight Center

Donald J. Wuebbles
Lawrence Livermore National Laboratory

INTRODUCTION

These simple experiments allow us to calibrate the transport of the different models, isolating the effect of transport on lifetimes and tracer distributions. We define two tracers, X1 and X2, which have their mixing ratio set to 1 ppbv everywhere below 500 mbar. The loss frequency, L(p), for X1 and X2 is only a function of pressure p, is independent of latitude and season, and is defined as the following:

L(p) for X1 (sec^{-1})	L(p) for X2 (sec^{-1})	Pressure range
0.0	0.0	$p > 100$ mbar
$3.0E\text{-}6/p^2$	$1.5E\text{-}6/p^2$	$1 < p < 100$ mbar
3.0E-6	1.5E-6	$p < 1$ mbar

Modelers were asked to run the experiment to a steady-state distribution and report the steady-state lifetimes and the latitude-z^* grid of monthly mean mixing ratios for X1 and X2.

The loss frequencies defined for X1 and X2 were picked to give lifetimes for these gases that were around a century or more. These lifetimes are similar to those expected for source gases N_2O and several of the chlorofluorocarbons. The results of these idealized model studies are, therefore, relevant to sections E (Large-scale Structures in N_2O and CH_4) and H (Correlation of Long-lived Species in Simultaneous Observations). Since the distributions of X1 and X2 are dependent on the transport of the individual models, we rely on some information sent for section A (Temperatures and Net Radiative Heating) in the analysis of these results, namely, the vertical velocity.

MODEL RESULTS AND ANALYSIS

Tracer X2, with the smaller loss frequency, is transported to higher altitudes and thus fills more of the 0 to 60 km domain of the UADP grid. We have, therefore, plotted the March, June, September, and December latitude-z^* grids of X2 for each model in Figures O-1 to O-10. The distribution of tracer X2 is affected by the total transport (both advection and diffusion); however, there is a strong correlation with vertical velocity, w, which is also plotted in Figure O-1. The influence of vertical advection on X2 is clearly evident for all models. Strong regions of upward motion apparently control the height and latitude of maximum vertical extent of X2 in all models. The mixing ratio contours are clearly responding to the circulation changes over the course of a year (see all plots in Figures O-1 to O-10). The differences in tracer distribution and vertical wind fields are also apparent among the 10 models shown here.

A lifetime of X1 (or X2), L_{X1} (or L_{X2}), is defined by the ratio of the total burden over the total loss rate, all averaged over a year. If we maintain a steady flux of X1 (or X2) such that the

concentrations exactly repeat an annual cycle, then we derive a steady-state lifetime. If the flux is stopped, then the annual cycle of concentrations will decay from year to year with a 1/e folding time that is very close, but not identical, to the steady-state lifetime. (The 1/e folding time in this transient decay period will be slightly faster than the steady state because the stratosphere, which lags behind the troposphere, will have a slight excess of X1 (or X2) compared with steady state and hence slightly greater loss.) The lifetimes L_{X1} and L_{X2} are given in Table O-1.

Table O-1. Lifetimes of X1 and X2 and Their Ratio for the Individual Models

Model	L_{X1}(years)	L_{X2}(years)	L_{X1}/L_{X2}
AER	117	146	0.801
CALJPL	101	124	0.815
CAMED	114	145	0.786
DUPONT	122	152	0.803
GSFC	98	134	0.731
ITALY	110	142	0.775
LLNL	105	132	0.795
NCAR	101	134	0.754
NOCAR	92	118	0.780
WASH	127	161	0.789

The range of L_{X1} is from 92-127 years and of L_{X2} is from 118-161 years. The ratio of the largest to the smallest lifetime for X1 is 1.38 and for X2 is 1.36. The range of L_{X1}/L_{X2} is from 0.731 to 0.815 and the ratio of the largest to the smallest value of L_{X1}/L_{X2} is 1.11. Generally, a short lifetime for X1 implies a short lifetime for X2 when compared with other models.

The models can be grouped according to X1 lifetimes as follows:

Short lifetimes	- CALJPL, GSFC, NCAR, and NOCAR
Medium lifetimes	- CAMED, ITALY, and LLNL
Long lifetimes	- AER, DUPONT, and WASH.

A comparison of our groupings of models and their respective lifetimes to those for carbon-14 (in Table I-2e of section I) show some similarities and some differences. There exists agreement in groupings of the models between this classification and those in section I for GSFC, NCAR, CAMED, LLNL, DUPONT, and WASH. Models AER, CALJPL, and ITALY are grouped differently in the two sections. Since carbon-14 is input at high latitudes in the lower stratosphere and X1 is input at the ground, a straightforward total consensus in lifetime groupings between this section and section I is not expected. Generally, however, a model that computes a shorter lifetime for X1 will tend to predict a shorter residence time for carbon-14 and vice versa.

The lifetimes are mainly determined by the speed at which the vertical advection deposits the tracer in its primary loss region. For example, a large upward motion in the equatorial region should lead to more tracer X1 in the middle stratosphere, which will lead to more X1 loss and a shorter lifetime. We show plots of tracer X1 as a function of month for several latitudes and altitudes in Figure O-11. Models with short L_{X1}'s show larger abundances of X1 at 20 and 30 km near the equator and 35N (see NOCAR and GSFC values in Figures O-11a-d) than those models with long L_{X1}'s (see WASH and DUPONT values in Figures O-11a-d). At higher latitudes, it is not clear which model should show the larger X1 abundance. A large upward vertical motion in the tropics must be compensated by large downward vertical motions at other latitudes due to the

balance of mass motion required across a pressure level. Thus the X1 abundance at high latitudes for models with short lifetimes may be depressed relative to the other models. The reverse may also be true: the X1 abundance at high latitudes for models with long lifetimes may be enhanced, relative to the other models. Such is the case of WASH at 70N and 30 km (Figure O-11f).

The seasonal change in the transport is also apparent in Figure O-11 for latitudes 35N and 70N. In Figure O-11d most models show a seasonal dependence with maximum mixing ratios of tracer X1 predicted in the late summer and early fall time period; presumably occurring after a few months of upward motion. The only model that shows a different pattern from this behavior is LLNL (with maximum X1 abundances in late winter). Although all models at 70N (Figures O-11e and O-11f) show generally the same pattern with maximum X1 abundances in the summer to fall months, there are model differences in predicting the peak X1 abundance (e.g., ITALY shows a peak in June or July, while LLNL shows a peak in November at 30 km).

Plots of X2 are shown in Figure O-12 for all models. We show the same latitudes and altitudes as shown in Figure O-11, but also extend to 40 km because of the smaller loss frequency of X2. We expect that a large upward motion in the equatorial region should lead to more tracer X2 in the middle stratosphere, which will lead to more X2 loss and a shorter lifetime. This statement is more difficult to prove with X2 because the smaller loss frequency of X2 allows a larger abundance of X2 into more regions of the model regime; therefore, the X2 abundance is controlled by advection over a larger region. NOCAR (with the shortest L_{X2}) shows the largest X2 abundance at 20 km, approximately the third largest X2 abundance at 30 km, and about the second largest X2 abundance at 40 km (Figures O-12.a-c). Clearly the X2 abundance at 35N also makes a difference in the calculation of L_{X2} (notice that NOCAR is at or near the top in X2 abundance for 20, 30, and 40 km in Figures O-12d-f). WASH (with the longest X2 lifetime) fairly consistently shows abundance of X2 at or near the bottom of all the models at both the equator and 35N (*see* Figures O-12a-f).

A model with strong upward motion in one portion of the stratosphere does not necessarily have strong upward motion throughout the entire stratosphere. GSFC, with the second shortest L_{X1}, has the fourth shortest L_{X2}. Both CALJPL and LLNL have longer lifetimes than GSFC for X1, but have shorter lifetimes for X2. GSFC shows the second largest X2 abundance at the equator and 30 km (Figure O-12b), but at the equator and 40 km (Figure O-12c) GSFC has about the smallest X2 abundance. Clearly the upward motion is slowing down significantly (when compared to other models) in GSFC between 30 and 40 km.

Much of the seasonal behavior in the X2 abundance from a particular model is similar to that pointed out for X1. It is interesting to note that at 35N and 40 km (Figure O-12f) the LLNL model shows similar behavior to other models with a peak in the late summertime, while at 35N and 30 km (Figure O-12e) the LLNL model shows a very different behavior compared with the other models. The WASH model shows a very substantial equatorial variation at 20 km in both X1 and X2 that is not predicted in other models (Figures O-11a and O-12a).

The altitude behavior of X1 and X2 is given at five latitudes (70S, 35S, O, 35N, and 70N) for March in Figures O-13 and O-14. This allows for inspection of the very different altitude structure of the tracers from the various model simulations. No one model shows the largest abundance of X1 or X2 throughout the entire altitude range for any of the latitudes. The models (as noted earlier) are each different and unique. The movement of X1 and X2 in each model cannot be adequately described in this brief report, but we do mention some of the more interesting model behavior below.

For example, the ITALY model has nearly the smallest abundance of X1 at 35S (Figure O-13b), but the largest abundance of X1 at the equator (up to about 30 km; Figure O-13c). The WASH model predicts the smallest abundance of X1 up to about 23 km, whereas above 28 km the

WASH model predicts the largest abundance of X1 for a few kilometers (Figure O-13a). Clearly substantial transport of X1 (probably from lower latitudes) is taking place in the WASH model that causes this behavior at 70S. Some models show substantial upward transport in certain regions, such as GSFC between 20 and 40 km at 35S (Figure O-13b) and LLNL between 25 and 35 km at 35N (Figure O-13d).

Long-lived species should exhibit approximately linear interrelationships in regions of the atmosphere where the lifetimes are long compared with mixing (Plumb and Ko, 1992). We demonstrate this statement with plots of X1 versus X2 in Figure O-15. The model results are indicated by circles, squares, and triangles for different latitude ranges. The solid line is the theoretical slope (i.e., the ratio of upward fluxes) and indicates the ratio of L_{X1} to L_{X2} for each model. All the models show a very similar shape with a ramp up to the solid line and approximate agreement with the solid line at values of X1 above 0.3 ppbv and X2 above 0.4 ppbv. Some models have more scatter (GSFC, ITALY, and NOCAR), while one model (CALJPL) has very little scatter in the plotted points.

TRACER W

Another tracer, W, was simulated by the AER, GSFC, and WASH models for a separate study connected with the NASA "Report on Concentrations, Lifetimes, and Trends of Chlorofluorocarbons, Halons, and Related Molecules in the Atmosphere." Tracer W has a loss frequency equal to that of X1 but has a temporally changing input flux. The W flux is increased from zero over a course of 10 years, stays constant for a decade, and then is decreased to zero by year 30 (as shown in Table O-2). All model simulations were for 40 years. Tracer W was chosen to be similar to a chlorofluorocarbon, with fluxes increasing in the 1960s and 1970s, leveling off in the 1980s, and decreasing in the 1990s.

Table O-2. Flux Boundary Conditions for W (in 10^9 kg/yr)

Year	Flux	Year	Flux	Year(s)	Flux
1	5.0	11	11.79	21	10.61
2	5.5	12	11.79	22	9.43
3	6.05	13	11.79	23	8.25
4	6.66	14	11.79	24	7.07
5	7.32	15	11.79	25	5.89
6	8.05	16	11.79	26	4.72
7	8.86	17	11.79	27	3.54
8	9.74	18	11.79	28	2.36
9	10.72	19	11.79	29	1.18
10	11.79	20	11.79	30-40	0.0

We graphed W versus X1 in Figures O-16, O-17, and O-18 as a function of year for AER, GSFC, and WASH, respectively. We wanted to find out how many years were necessary in a model simulation before the distributions of a tracer input as a flux (W) compared well with the distributions of a tracer at steady state (X1). Since the flux of W varied temporally, its values had to be normalized to maximum values of 1.0 ppbv in order to ease the comparison.

The points of W versus X1 did not line up on the straight line until year 30 in all three models. There is a wider extent of points from the WASH model for year 30 (Figure O-18f). This is a result of the use of a repeating 4-year cycle of transport in the WASH W simulation (NMC temperatures taken from 1979, 1980, 1981, and 1982) versus a fixed 1 year used in the WASH X1 simulation (NMC temperatures taken from 1980 only).

These results of W versus X1 indicate that if models represent the transport in the atmosphere in a reasonable way, then chlorofluorocarbons might be expected to take up to 30 years or longer from the time they are first released to correlate well with other long-lived constituents (such as N_2O).

CONCLUSIONS

Idealized tracers X1 and X2 help in isolating the effect of transport on lifetimes and tracer distributions. Models predicting short lifetimes for X1 and X2 (NOCAR, GSFC, CALJPL) transport constituents more vigorously upward, while models predicting long lifetimes for X1 and X2 (WASH, DUPONT, AER) transport constituents much more sluggishly. The range of lifetimes for X1 is from 92 to 127 years and of X2 is from 118 to 161 years. These ranges illustrate the approximate bounds of present-day two-dimensional models for simulating these idealized tracers. The ratio of the largest to the smallest lifetime for X1 is 1.38 and for X2 is 1.36. Generally, a short lifetime for X1 implies a short lifetime for X2 when compared with other models. Each model transports constituents in its own individual way: The latitude-z* distributions and temporal behavior of X1 and X2 are different from each model. These model simulations have indicated the large variability in model predictions from only their transport differences.

ACKNOWLEDGMENTS

We thank Linda A. Hunt of PRC at NASA Langley Research Center who provided much needed help in producing the graphics shown in this report and Joan E. Rosenfield of USRA at NASA Goddard Space Flight Center for useful discussions concerning this report. We also thank Anne R. Douglass of NASA-Goddard Space Flight Center, Ellis E. Remsberg of NASA-Langley Research Center, Rolando R. Garcia of the National Center for Atmospheric Research, and Michael J. Prather of the University of California-Irvine for constructive comments on this report.

REFERENCES

Plumb, R. A. and M. K. W. Ko, Interrelationships between mixing ratios of long-lived stratospheric constituents, *J. Geophys. Res., 97,* 10,145-10,156, 1992.

FIGURE CAPTIONS

Figures O-1 to O-10. X2 (in ppbv, represented by large dashed lines) in a) March, b) June, c) September, and d) December for (O-1) AER, (O-2) CALJPL, (O-3) CAMED, (O-4) DUPONT, (O-5) GSFC, (O-6) ITALY, (O-7) LLNL, (O-8) NCAR, (O-9) NOCAR, and (O-10) WASH models. Contour levels are 1.E-5, 1.E-4, 0.001, 0.01, 0.1, 0.2, 0.3, 0.4, 0.5, 0.6, 0.7, 0.8, and 0.9 ppbv. Vertical velocities (w in mm/sec) are also plotted; solid lines indicate positive velocities and dotted lines indicate negative velocities. For contour values in the w field see Figure A-8.

Figure O-11. Tracer X1 (ppbv) from all 10 models as a function of month for (a) equator and 20 km, (b) equator and 30 km, (c) 35N and 20 km, (d) 35N and 30 km, (e) 70N and 20 km, and (f) 70N and 30 km.

Figure O-12. Tracer X2 (ppbv) from all 10 models as a function of month for (a) equator and 20 km, (b) equator and 30 km, (c) equator and 40 km, (d) 35N and 20 km, (e) 35N and 30 km, (f) 35N and 40 km, (g) 70N and 20 km, (h) 70N and 30 km, and (i) 70N and 40 km.

Figure O-13. Tracer X1 (ppbv) from all 10 models in March as a function of altitude for (a) 70S, (b) 35S, (c) the equator, (d) 35N, and (e) 70N.

Figure O-14. Tracer X2 (ppbv) from all 10 models in March as a function of altitude for (a) 70S, (b) 35S, (c) the equator, (d) 35N, and (e) 70N.

Figure O-15. Tracer X1 versus tracer X2 for March from (a) AER, (b) CALJPL, (c) CAMED, (d) DUPONT, (e) GSFC, (f) ITALY, (g) LLNL, (h) NCAR, (i) NOCAR, and (j) WASH. Model results are represented by circles (90S-40S), squares (30S-30N), and triangles (40N-90N). The straight line indicates the ratio of the lifetime of X1 to X2 for each model.

Figure O-16. Tracer W versus tracer X1 for March from AER for years (a) 5, (b) 10, (c) 15, (d) 20, (e) 25, (f) 30, (g) 35, and (h) 40. Model results are represented by circles (90S-40S), squares (30S-30N), and triangles (40N-90N). The straight line indicates the ratio of 1.0 since W and X1 have the same loss frequency.

Figure O-17. Tracer W versus tracer X1 for March from GSFC for years (a) 5, (b) 10, (c) 15, (d) 20, (e) 25, (f) 30, (g) 35, and (h) 40. Model results are represented by circles (90S-40S), squares (30S-30N), and triangles (40N-90N). The straight line indicates the ratio of 1.0 since W and X1 have the same loss frequency.

Figure O-18. Tracer W versus tracer X1 for March from WASH for years (a) 5,(b) 10, (c) 15, (d) 20, (e) 25, (f) 30, (g) 35, and (h) 40. Model results are represented by circles (90S-40S), squares (30S-30N), and triangles (40N-90N). The straight line indicates the ratio of 1.0 since W and X1 have the same loss frequency.

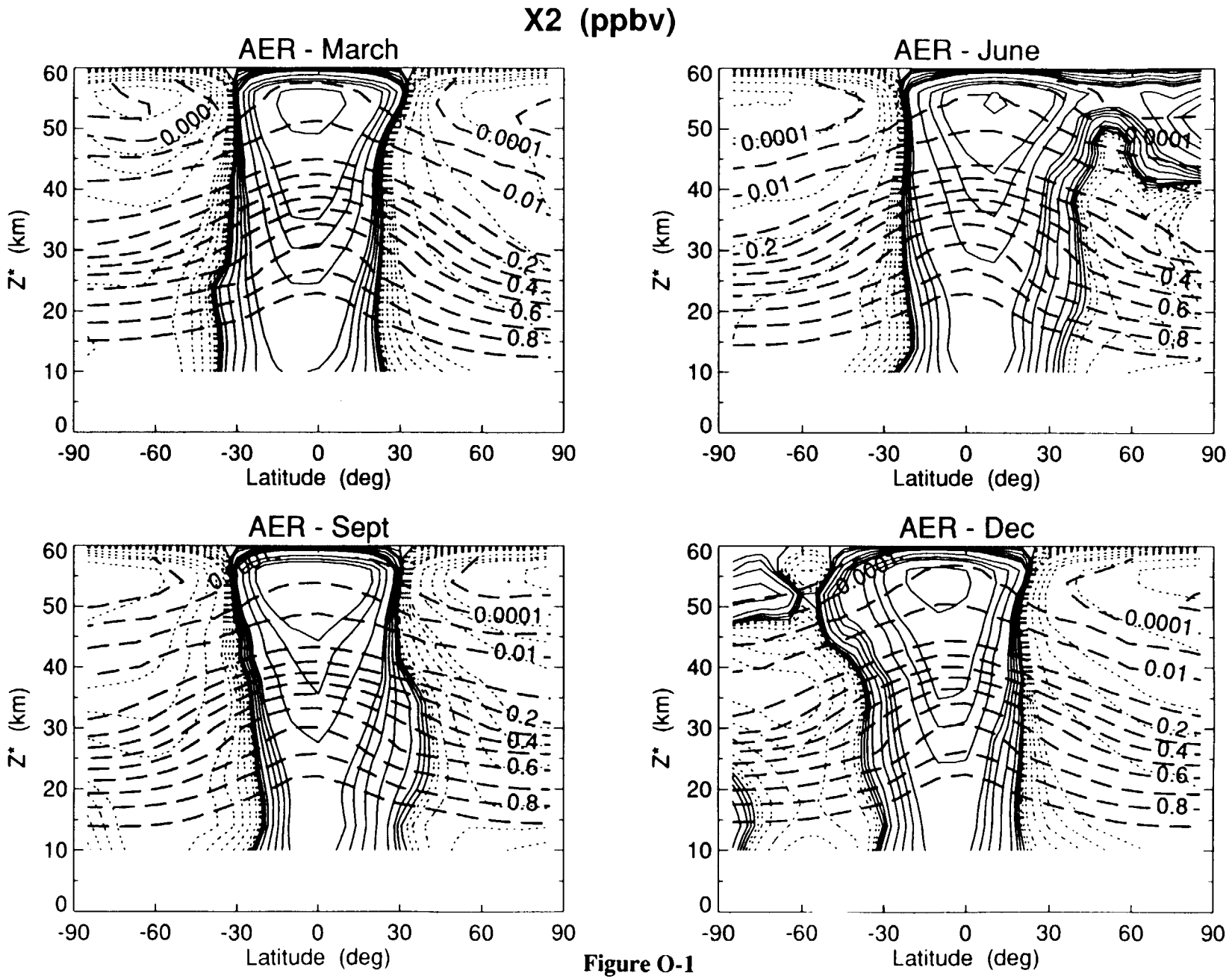
X2 (ppbv)
AER - March
AER - June
AER - Sept
AER - Dec
Z* (km)
Latitude (deg)
0.0001
0.01
0.2
0.4
0.6
0.8
0
10
20
30
40
50
60
-90
-60
-30
0
30
60
90

Figure O-1

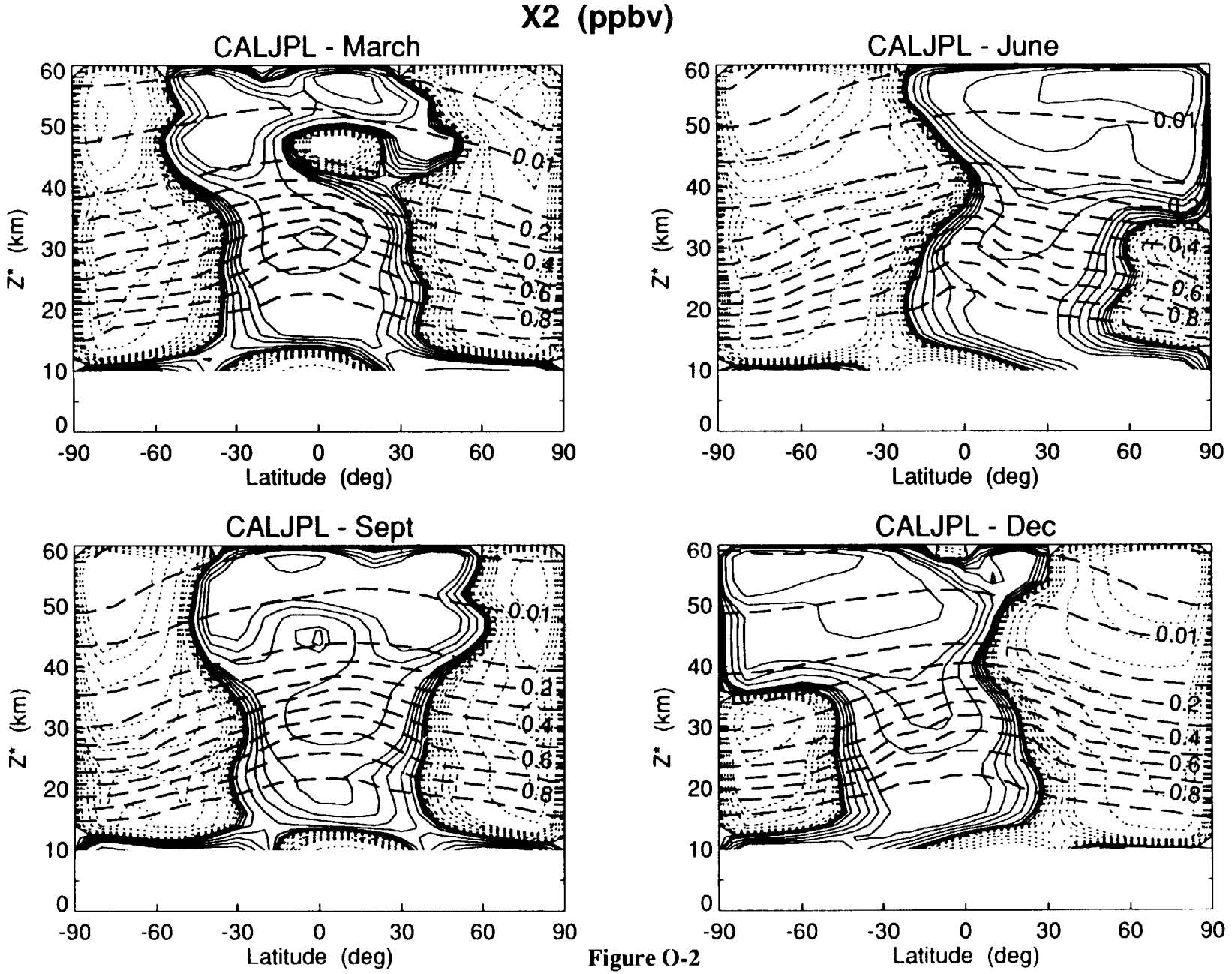
X2 (ppbv)
CALJPL - March
CALJPL - June
CALJPL - Sept
CALJPL - Dec
Z* (km)
Latitude (deg)
0.01
0
0.2
0.4
0.6
0.8

Figure O-2

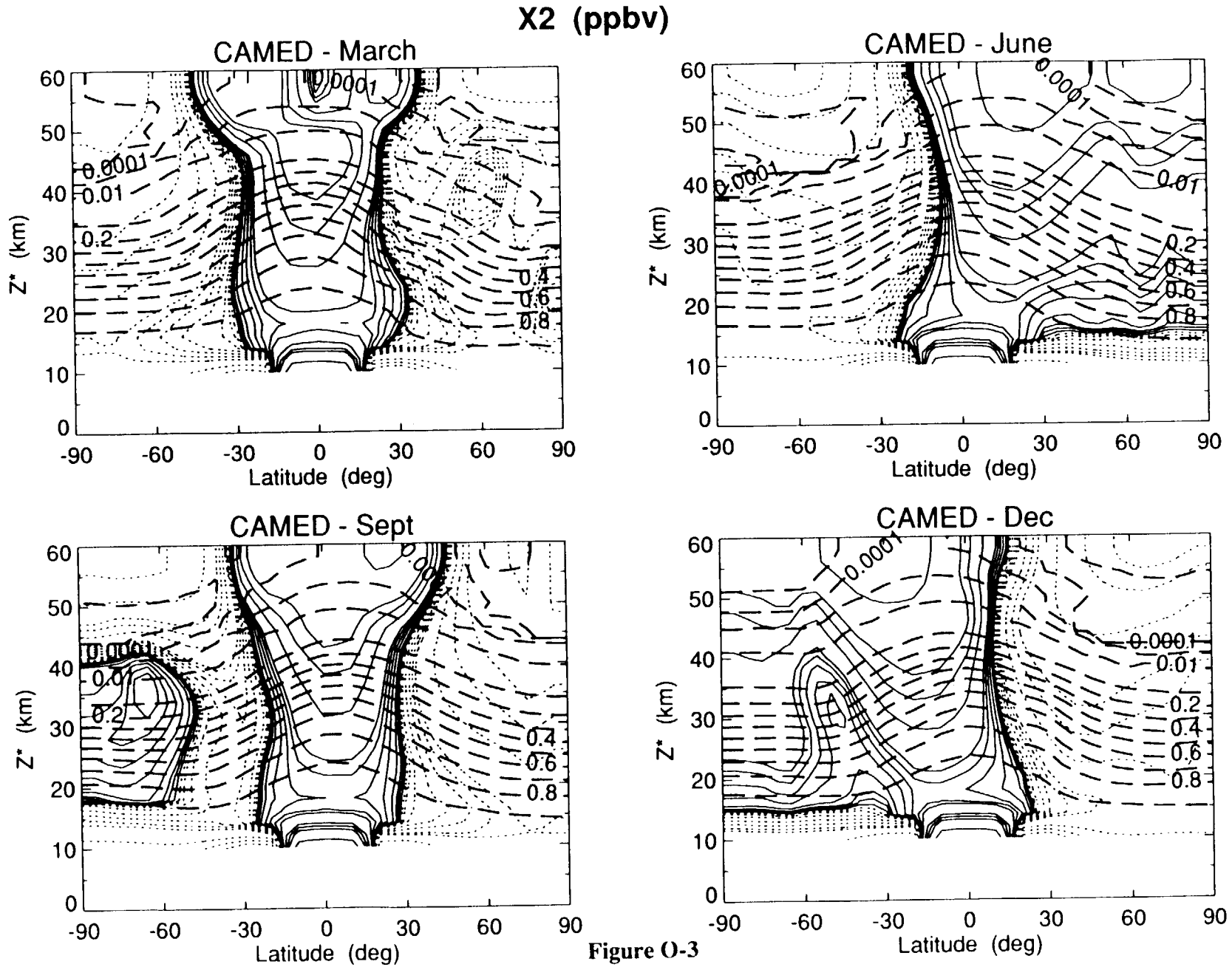
X2 (ppbv)
CAMED - March
CAMED - June
CAMED - Sept
CAMED - Dec
Z* (km)
Latitude (deg)
0.0001
0.01
0.2
0.4
0.6
0.8

Figure O-3

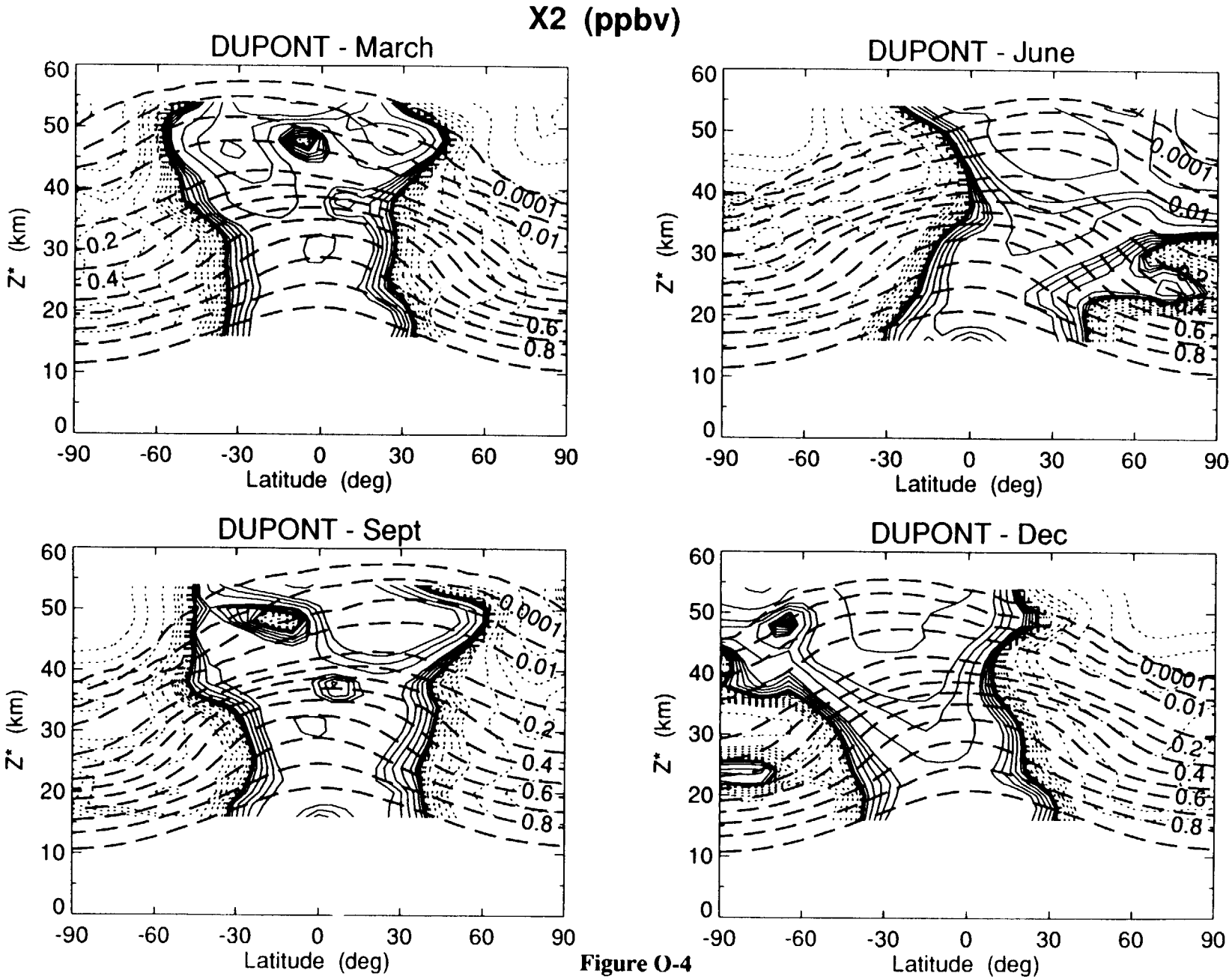
X2 (ppbv)
DUPONT - March
DUPONT - June
DUPONT - Sept
DUPONT - Dec
Z* (km)
Latitude (deg)
0.0001
0.01
0.2
0.4
0.6
0.8

Figure O-4

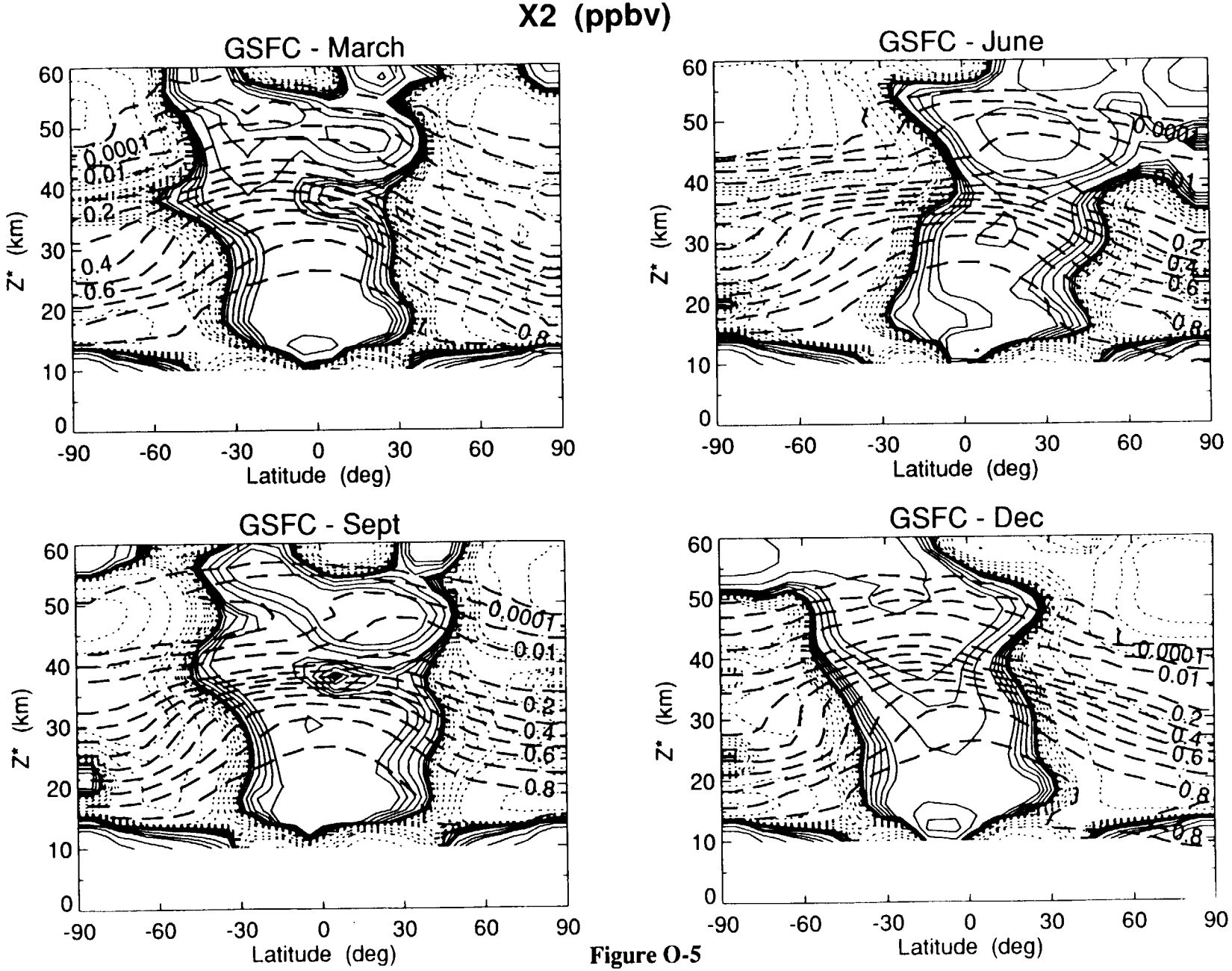
X2 (ppbv)
GSFC - March
GSFC - June
GSFC - Sept
GSFC - Dec
Z* (km)
Latitude (deg)
0.0001
0.01
0.2
0.4
0.6
0.8

Figure O-5

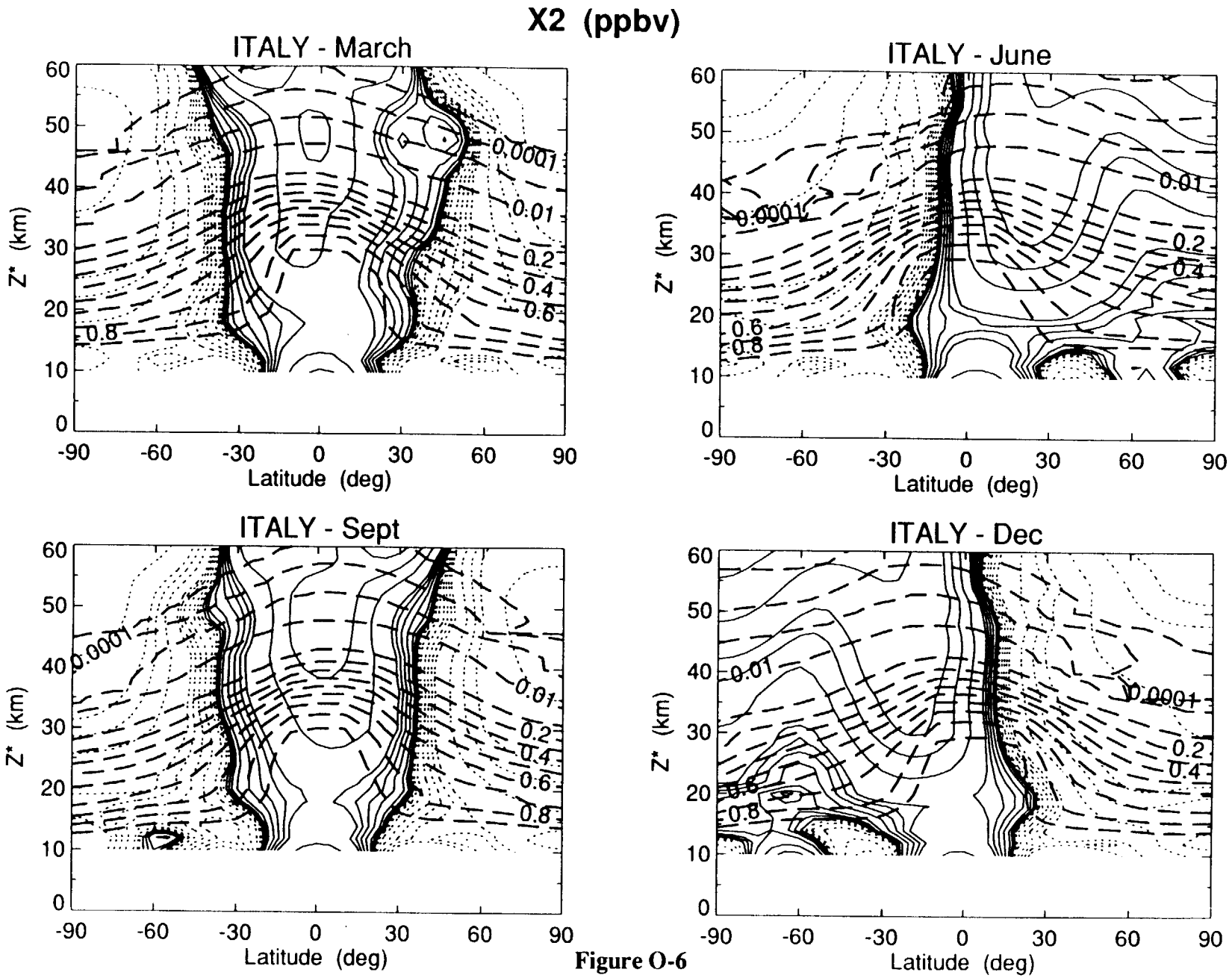
X2 (ppbv)
ITALY - March
ITALY - June
ITALY - Sept
ITALY - Dec
Z* (km)
Latitude (deg)
0.0001
0.01
0.2
0.4
0.6
0.8

Figure O-6

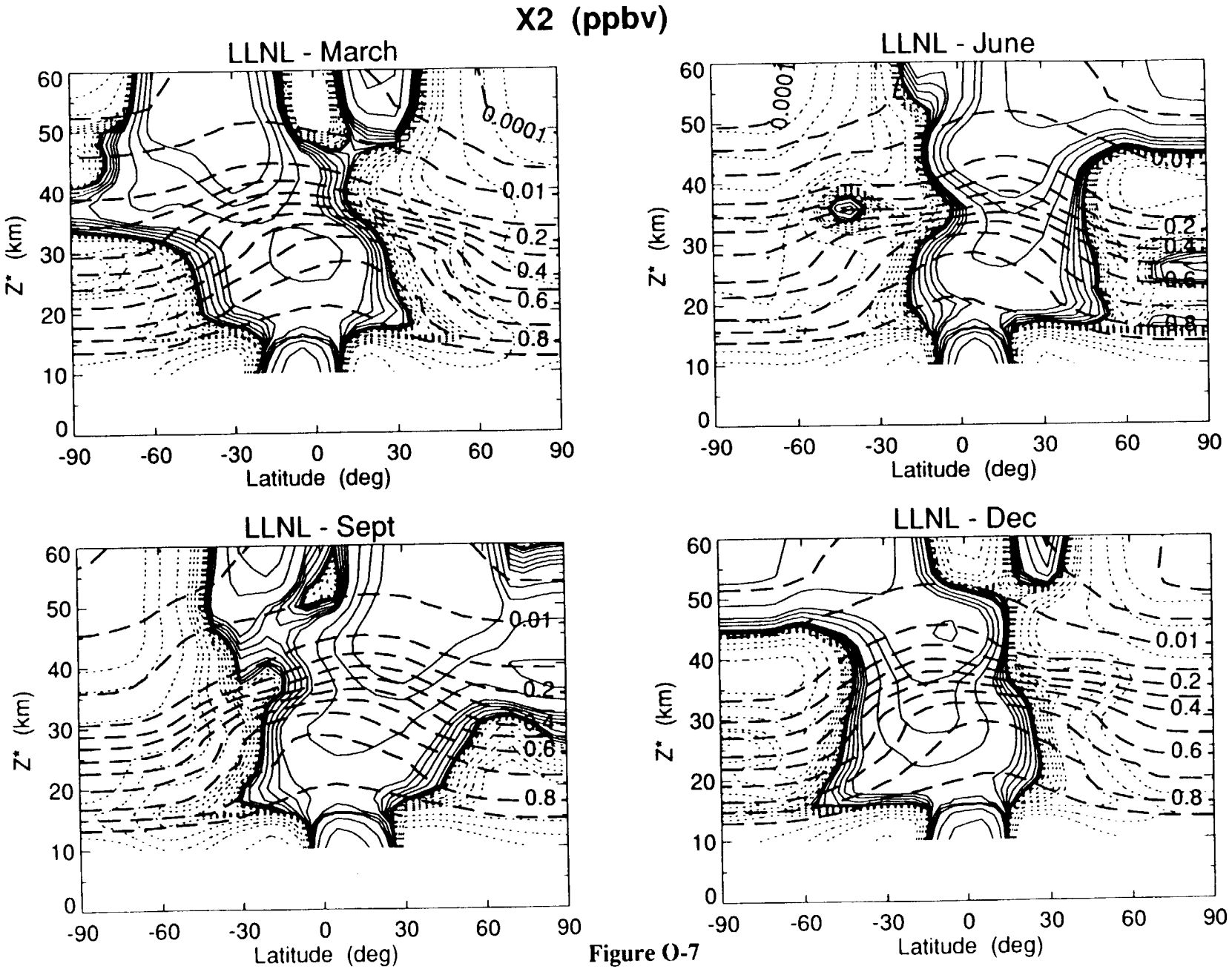
X2 (ppbv)
LLNL - March
LLNL - June
LLNL - Sept
LLNL - Dec
Z* (km)
Latitude (deg)
0.0001
0.01
0.2
0.4
0.6
0.8

Figure O-7

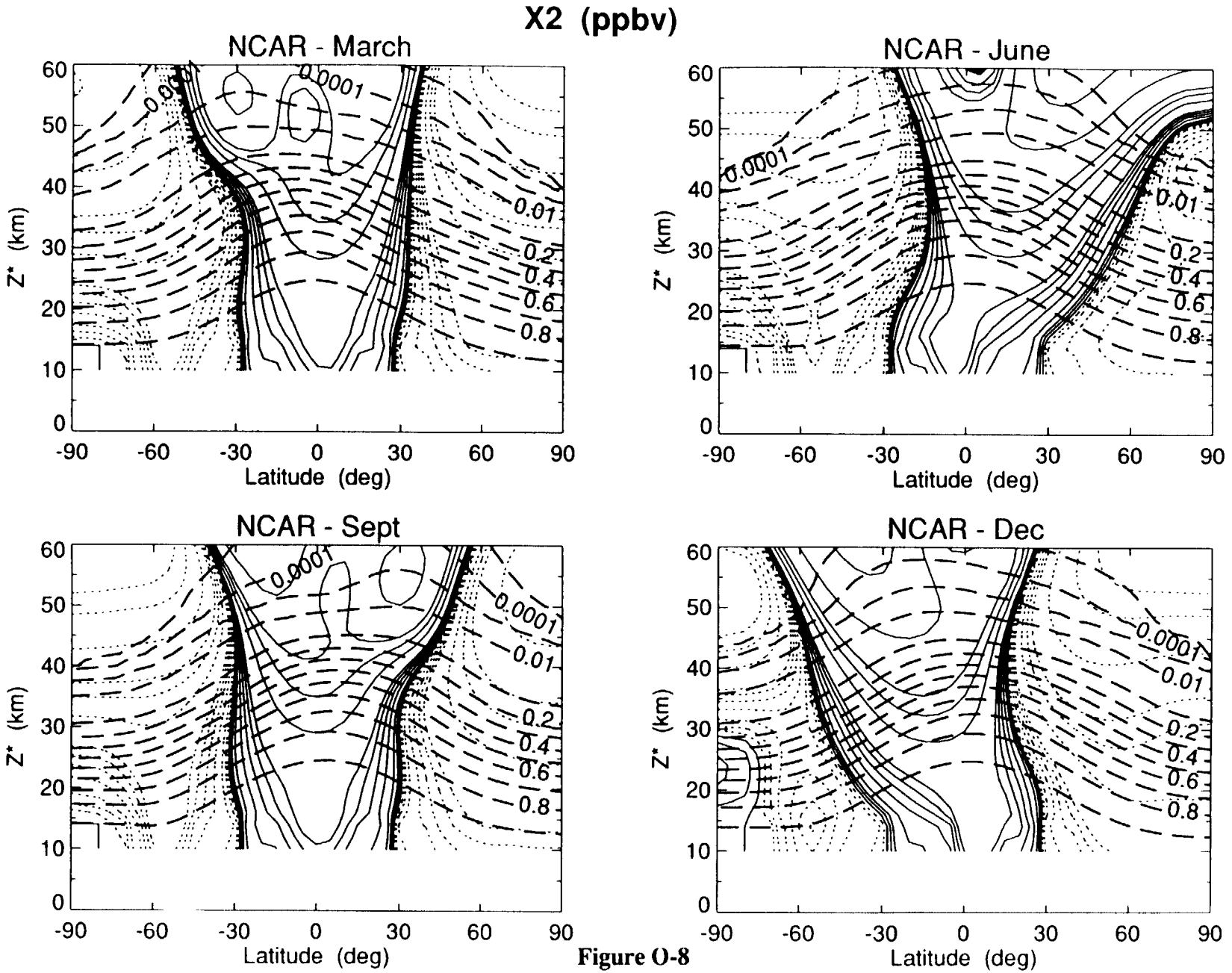
X2 (ppbv)
NCAR - March
NCAR - June
NCAR - Sept
NCAR - Dec
Z* (km)
Latitude (deg)
0.0001
0.01
0.2
0.4
0.6
0.8
60
50
40
30
20
10
0
-90
-60
-30
0
30
60
90

Figure O-8

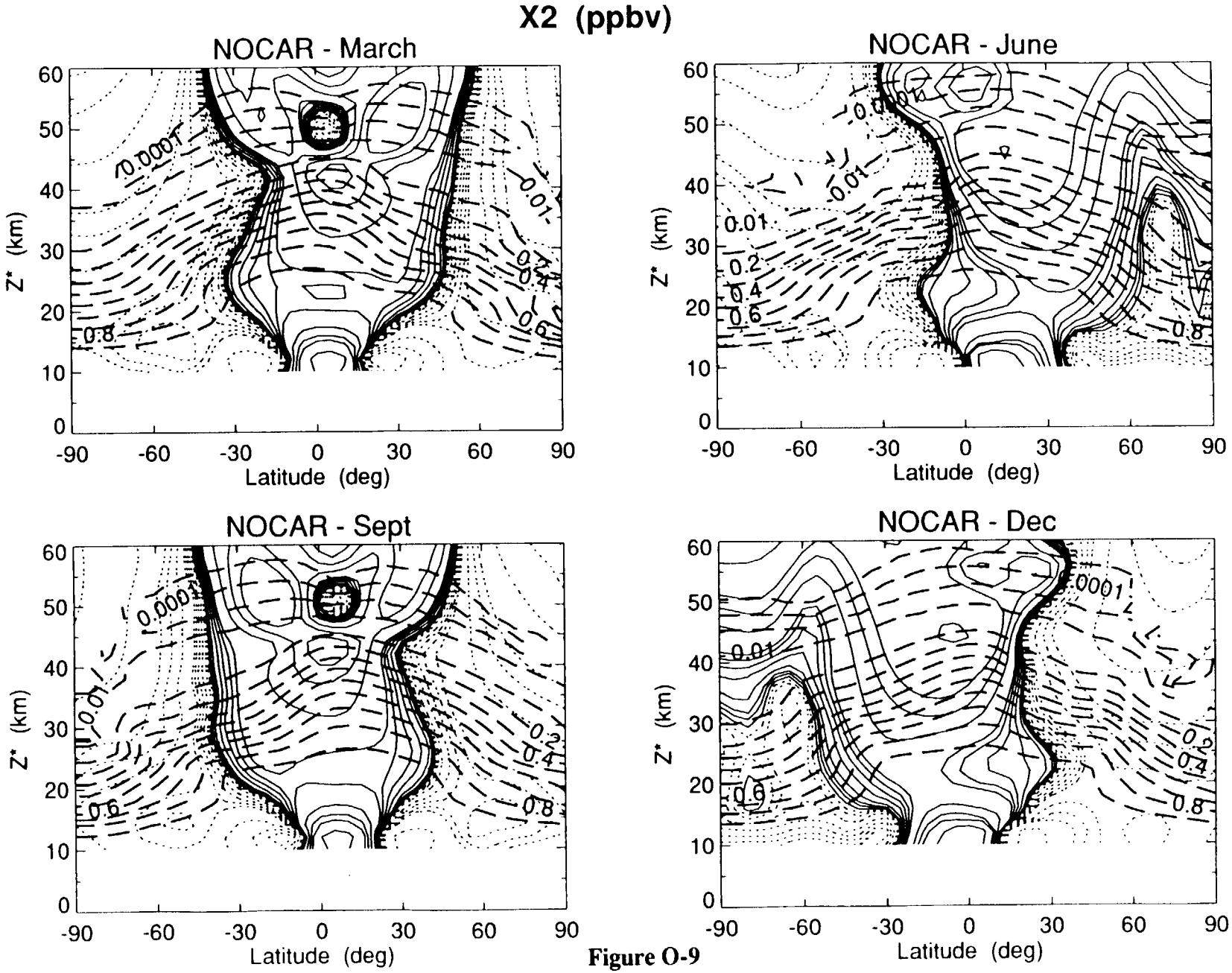
X2 (ppbv)
NOCAR - March
NOCAR - June
NOCAR - Sept
NOCAR - Dec
Z* (km)
Latitude (deg)
0
10
20
30
40
50
60
-90
-60
-30
0
30
60
90
0.0001
0.001
0.01
0.2
0.4
0.6
0.8
0.9

Figure O-9

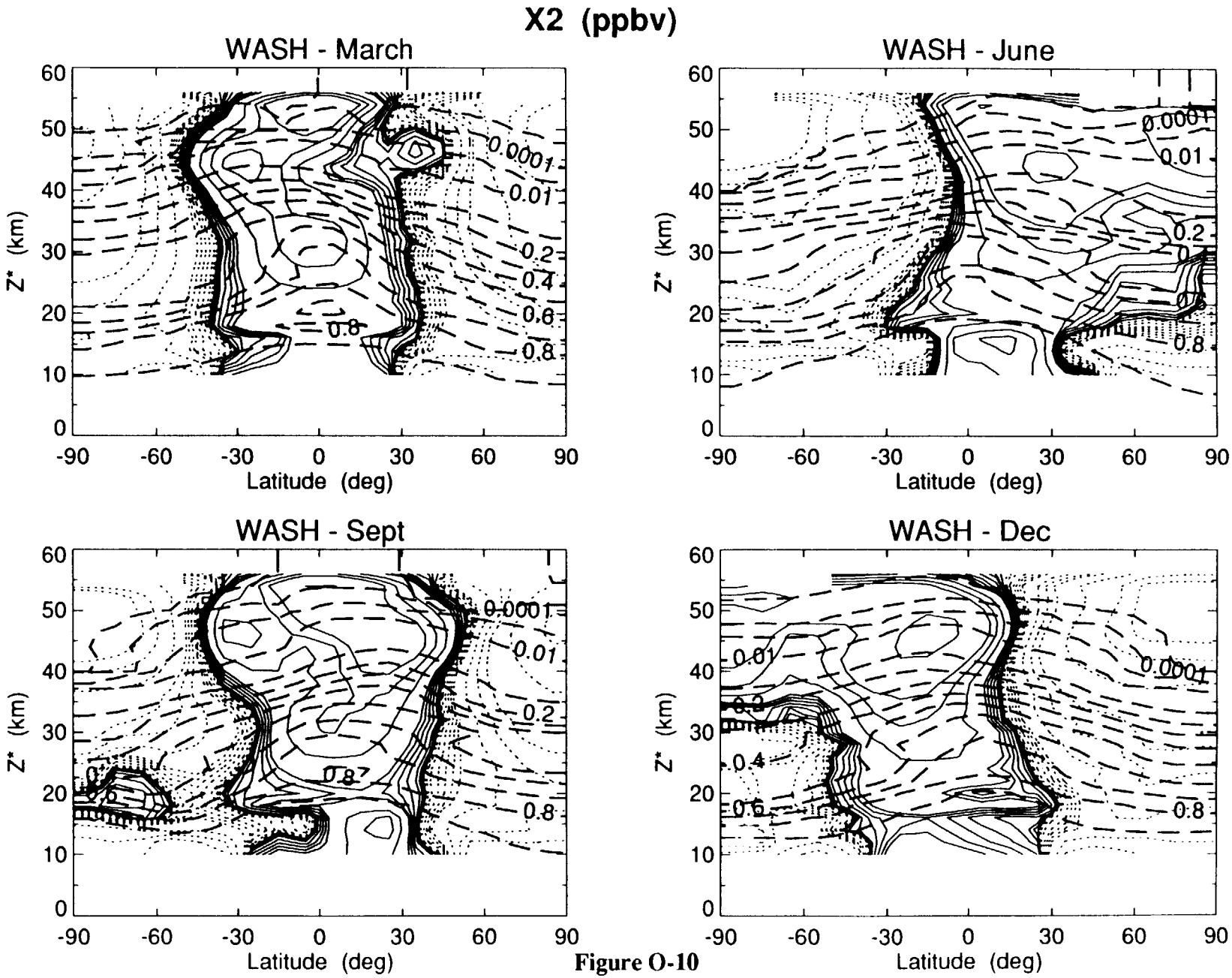
X2 (ppbv)
WASH - March
WASH - June
WASH - Sept
WASH - Dec
Z* (km)
Latitude (deg)
0.0001
0.01
0.2
0.4
0.6
0.8
-90
-60
-30
0
30
60
90
0
10
20
30
40
50
60

Figure O-10

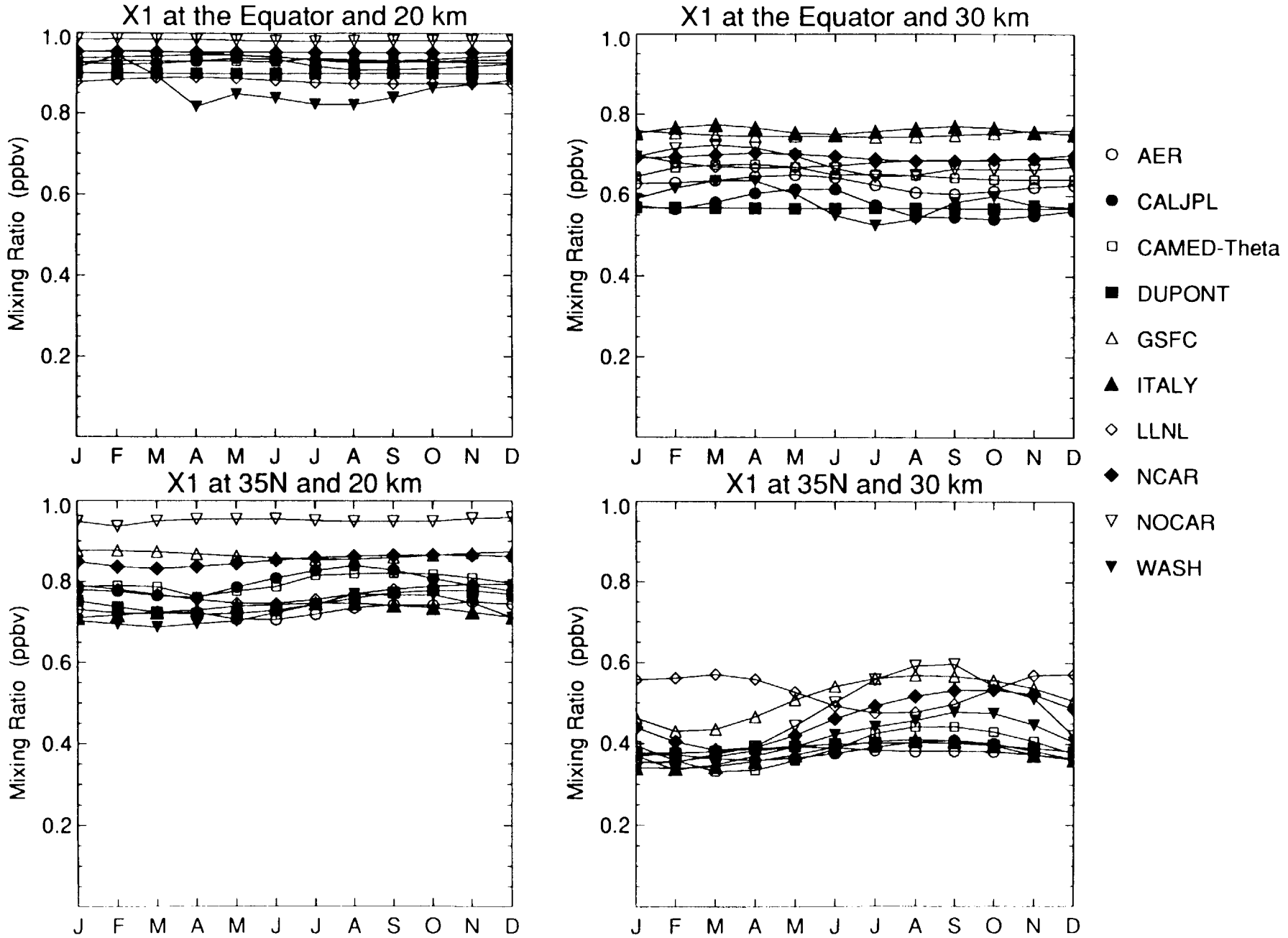
X1 at the Equator and 20 km
X1 at the Equator and 30 km
X1 at 35N and 20 km
X1 at 35N and 30 km
Mixing Ratio (ppbv)
1.0
0.8
0.6
0.4
0.2
J F M A M J J A S O N D
AER
CALJPL
CAMED-Theta
DUPONT
GSFC
ITALY
LLNL
NCAR
NOCAR
WASH

Figure O-11

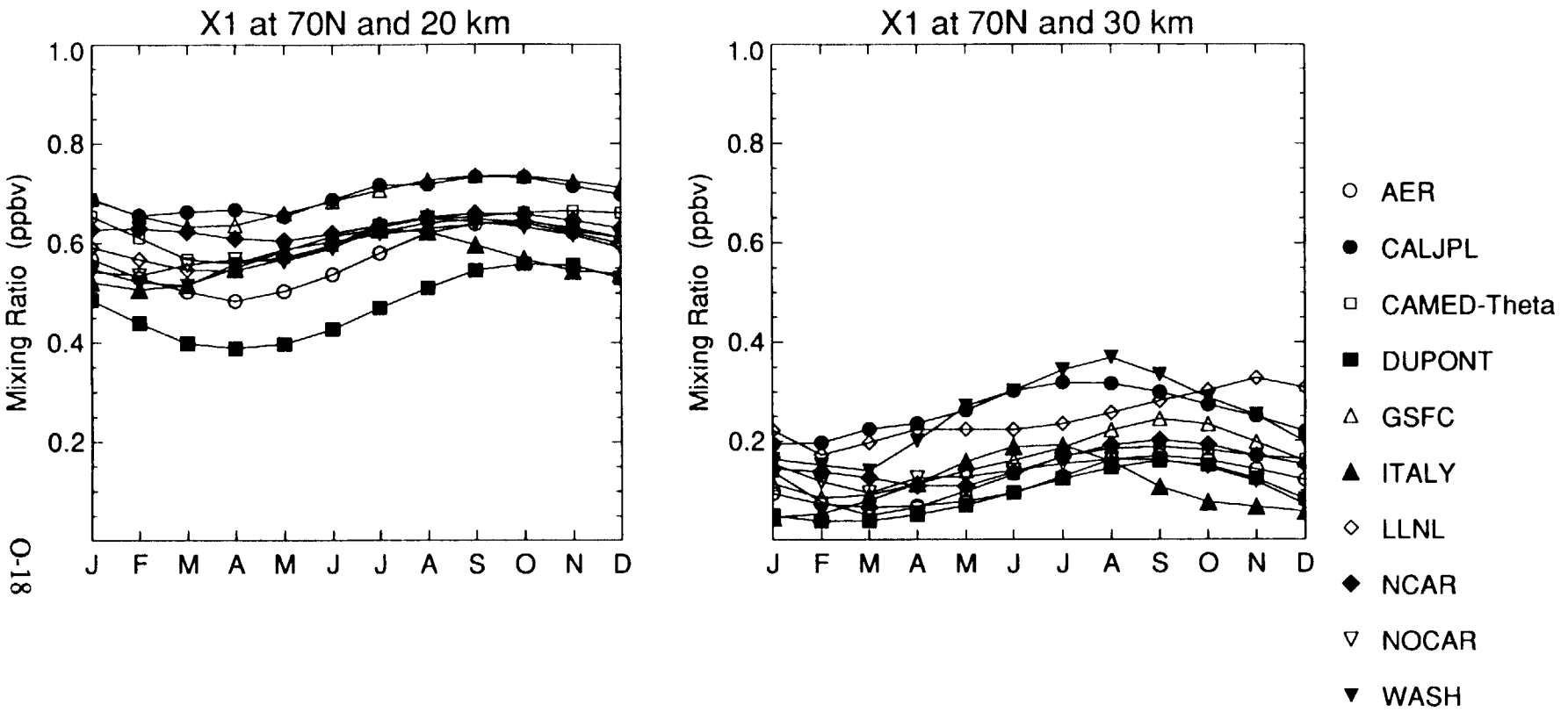

Figure O-11 (cont.)

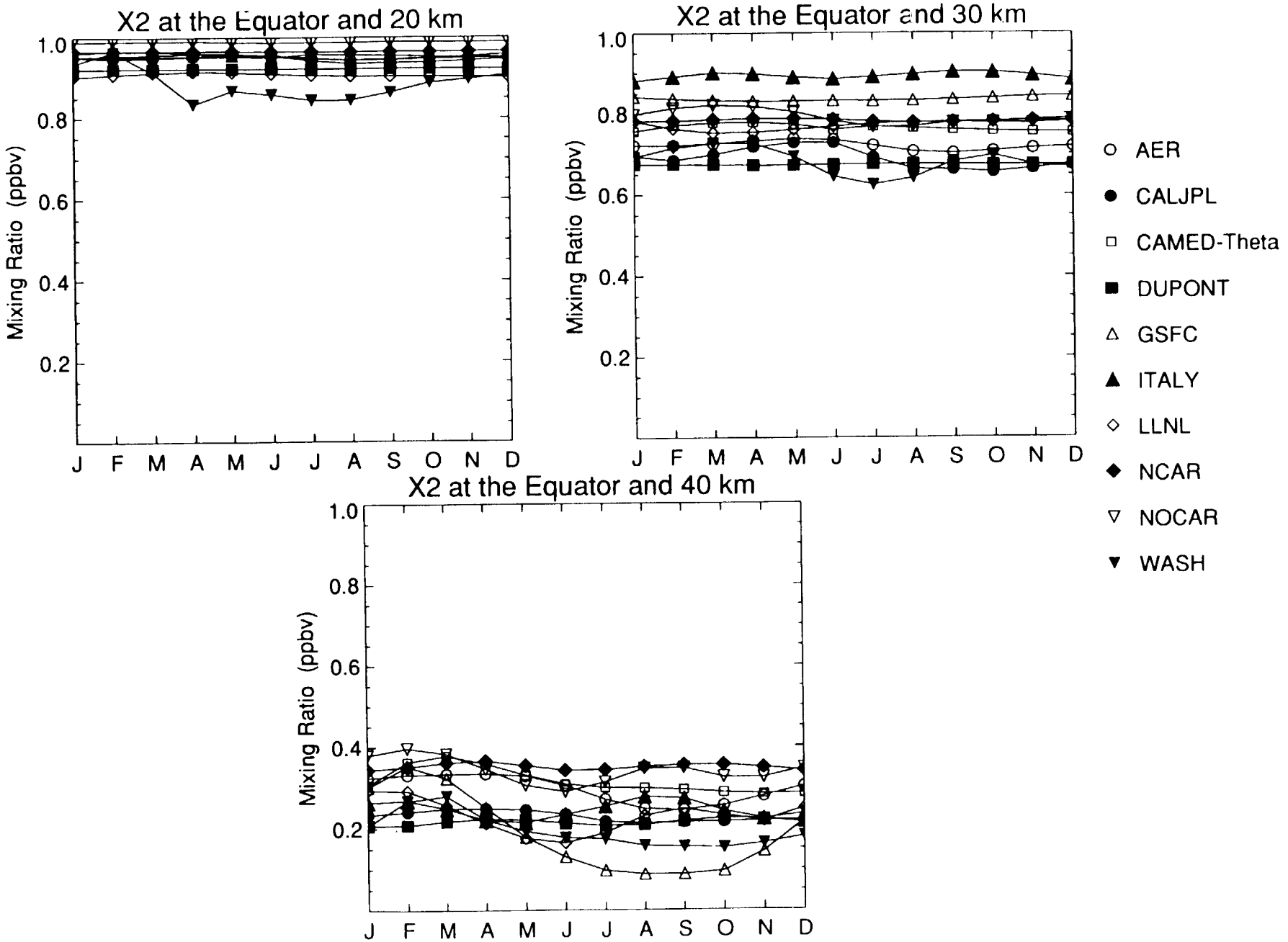
X2 at the Equator and 20 km
X2 at the Equator and 30 km
X2 at the Equator and 40 km
Mixing Ratio (ppbv)
1.0
0.8
0.6
0.4
0.2
J F M A M J J A S O N D
AER
CALJPL
CAMED-Theta
DUPONT
GSFC
ITALY
LLNL
NCAR
NOCAR
WASH

Figure O-12

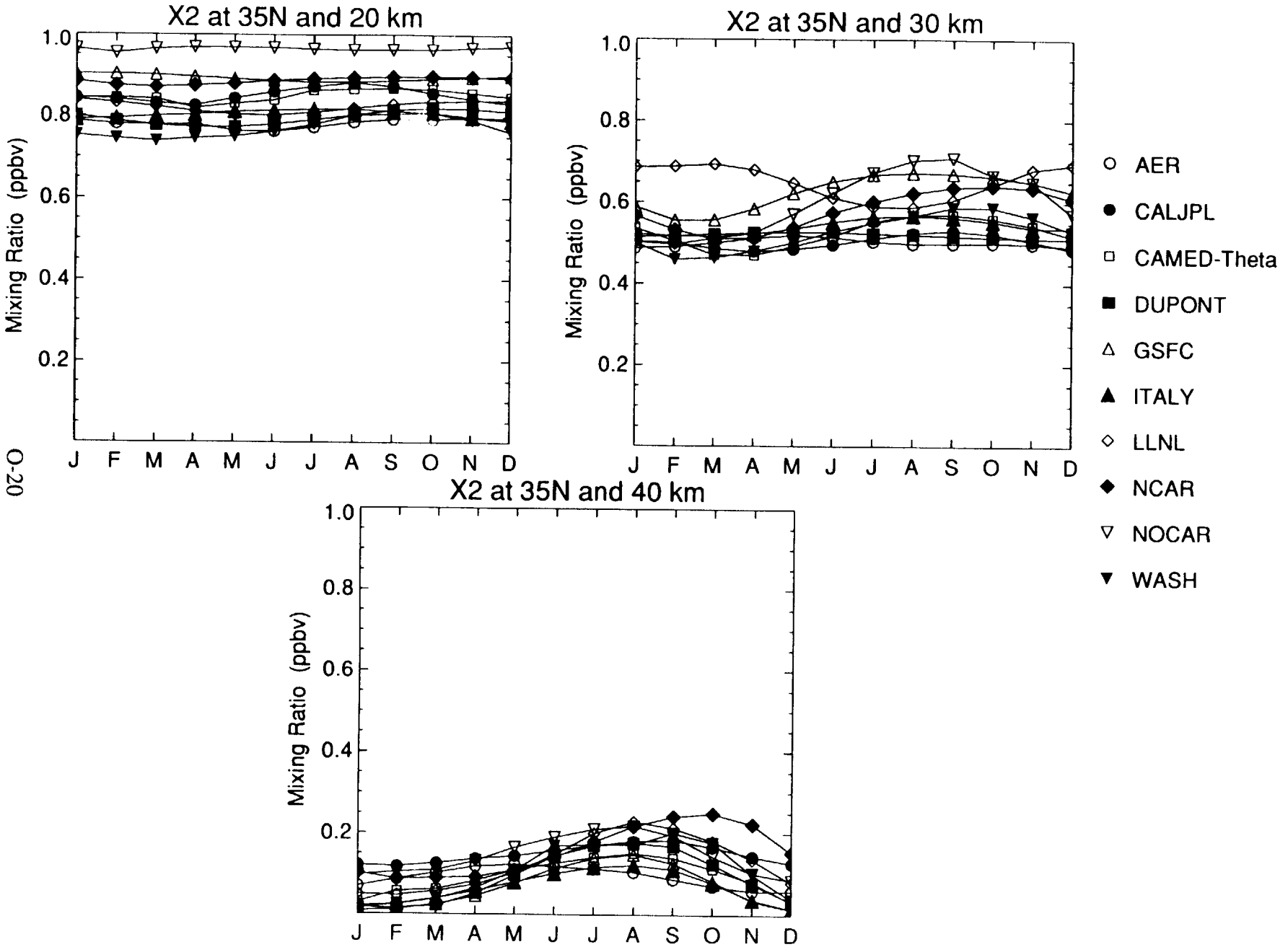

Figure O-12 (cont.)

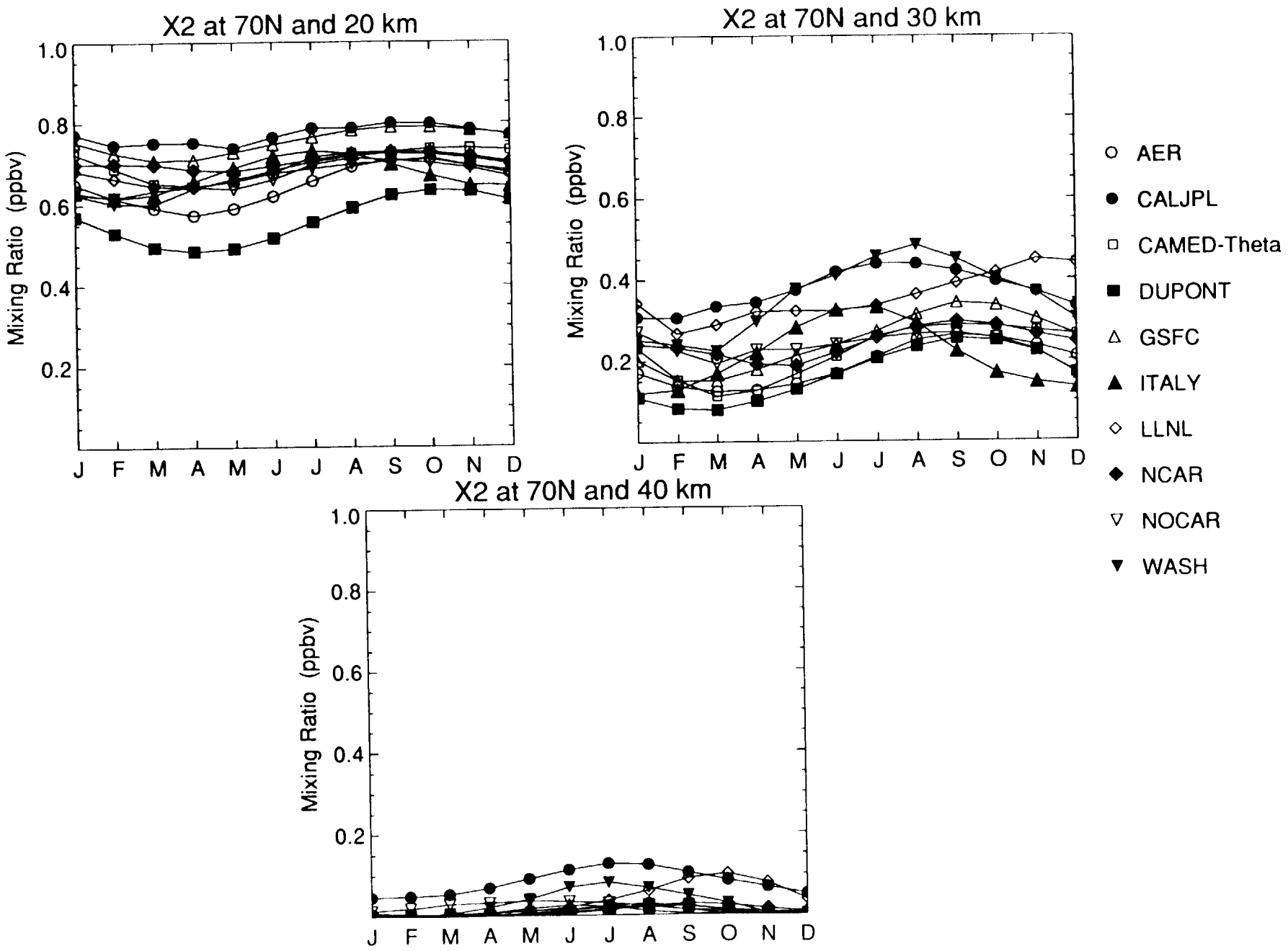

Figure O-12 (cont.)

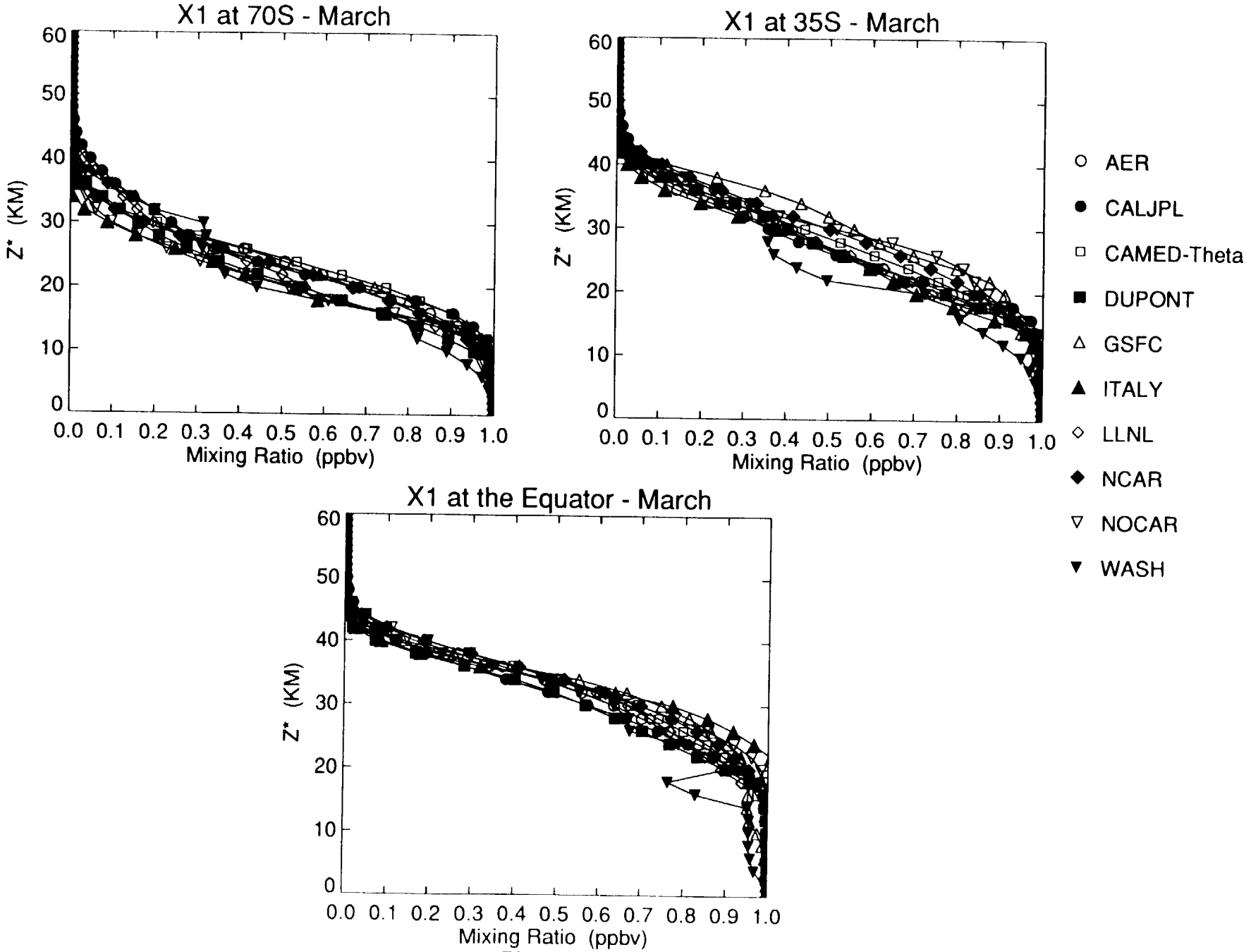
X1 at 70S - March
X1 at 35S - March
X1 at the Equator - March
Z* (KM)
Mixing Ratio (ppbv)
0 10 20 30 40 50 60
0.0 0.1 0.2 0.3 0.4 0.5 0.6 0.7 0.8 0.9 1.0
AER
CALJPL
CAMED-Theta
DUPONT
GSFC
ITALY
LLNL
NCAR
NOCAR
WASH

Figure O-13

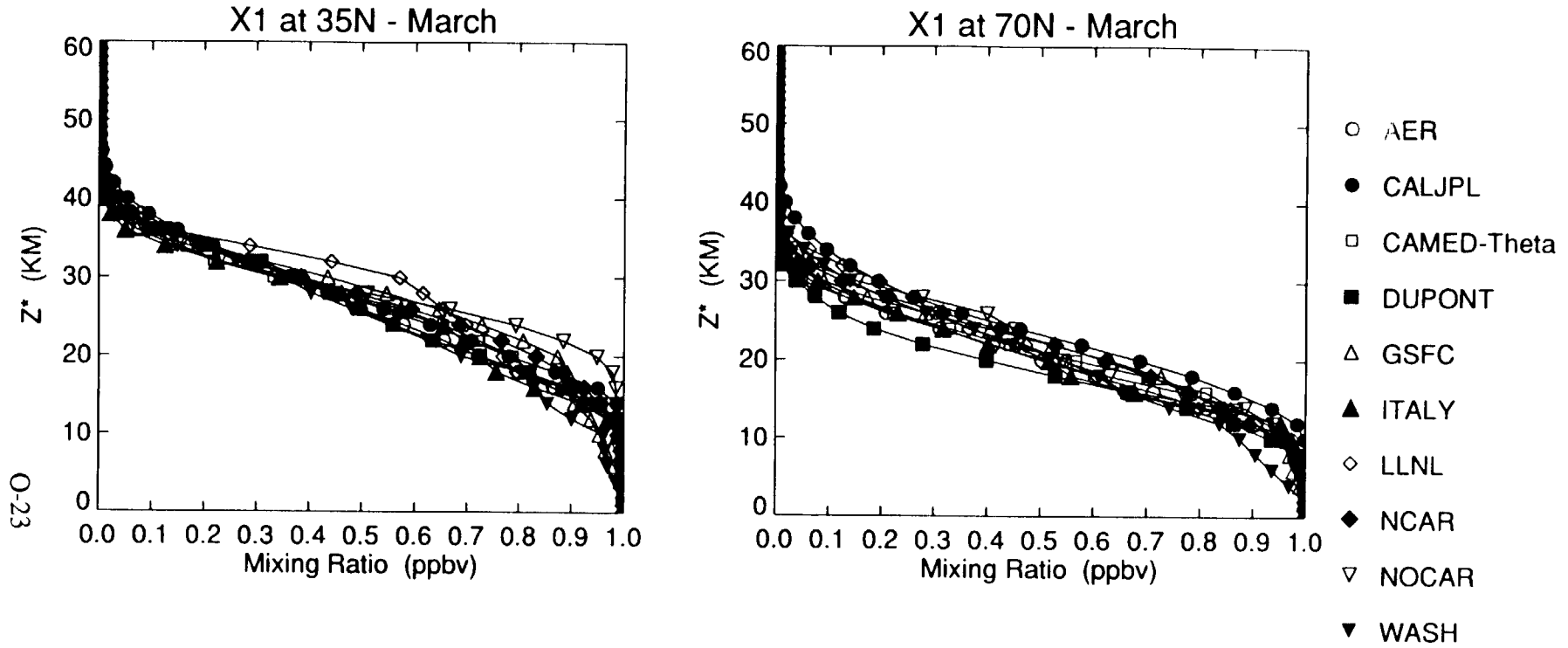

Figure O-13 (cont.)

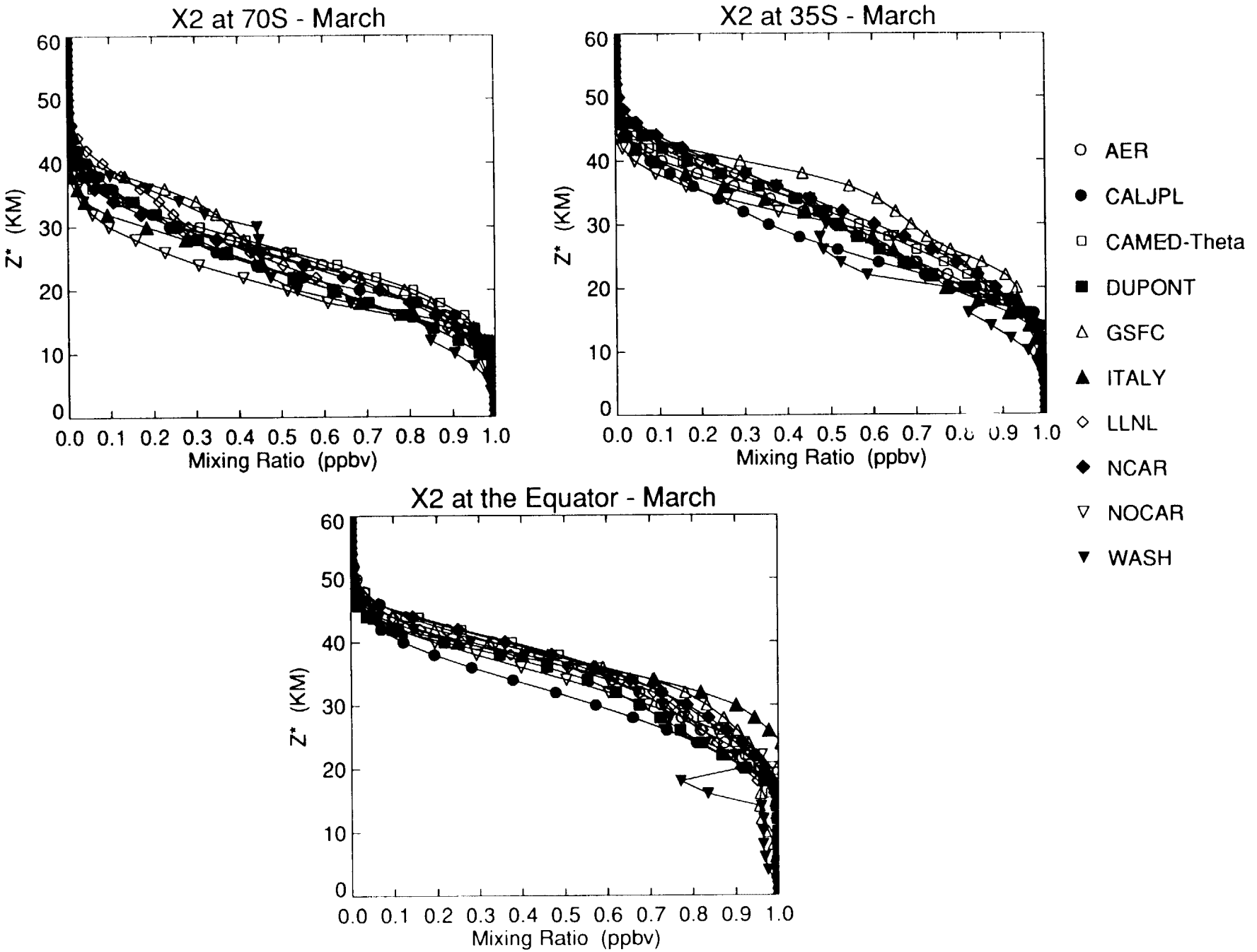
X2 at 70S - March
X2 at 35S - March
X2 at the Equator - March
Z* (KM)
Mixing Ratio (ppbv)
0 10 20 30 40 50 60
0.0 0.1 0.2 0.3 0.4 0.5 0.6 0.7 0.8 0.9 1.0
AER
CALJPL
CAMED-Theta
DUPONT
GSFC
ITALY
LLNL
NCAR
NOCAR
WASH

Figure O-14

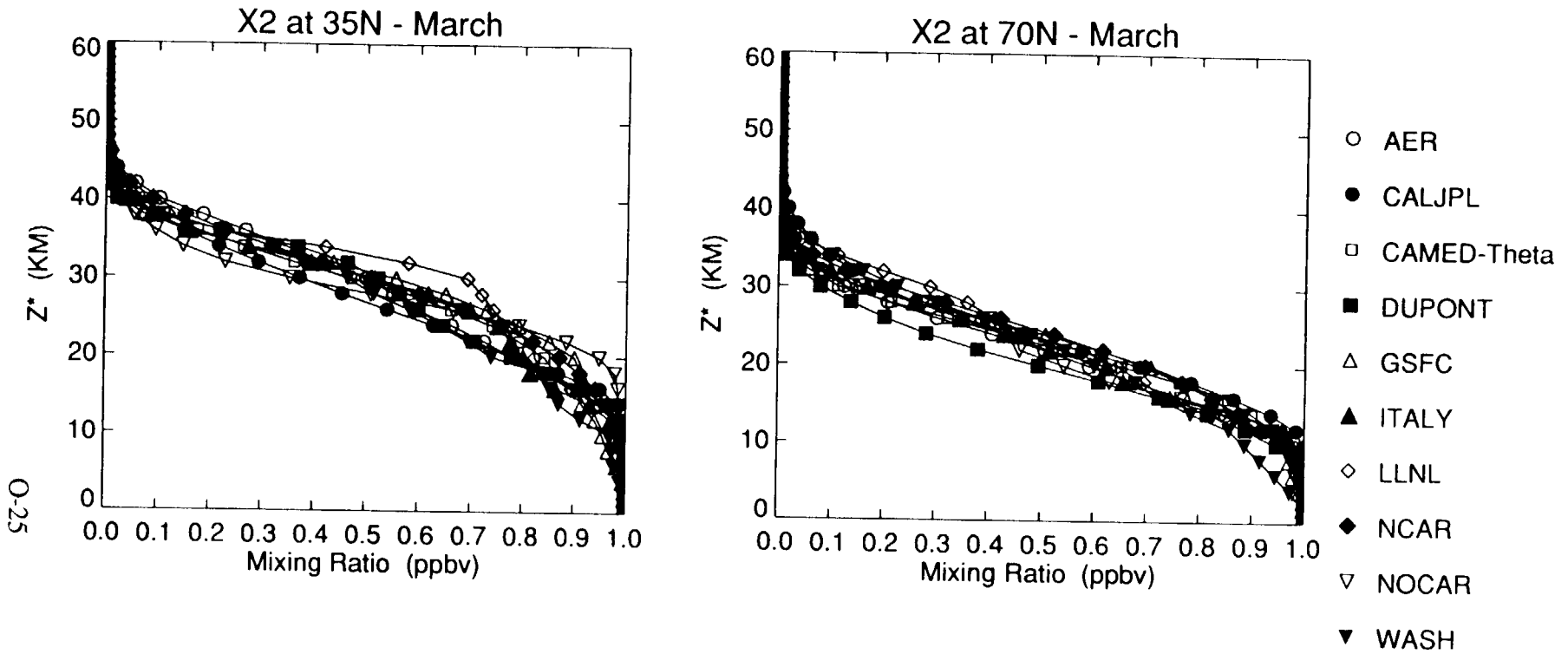

Figure O-14 (cont.)

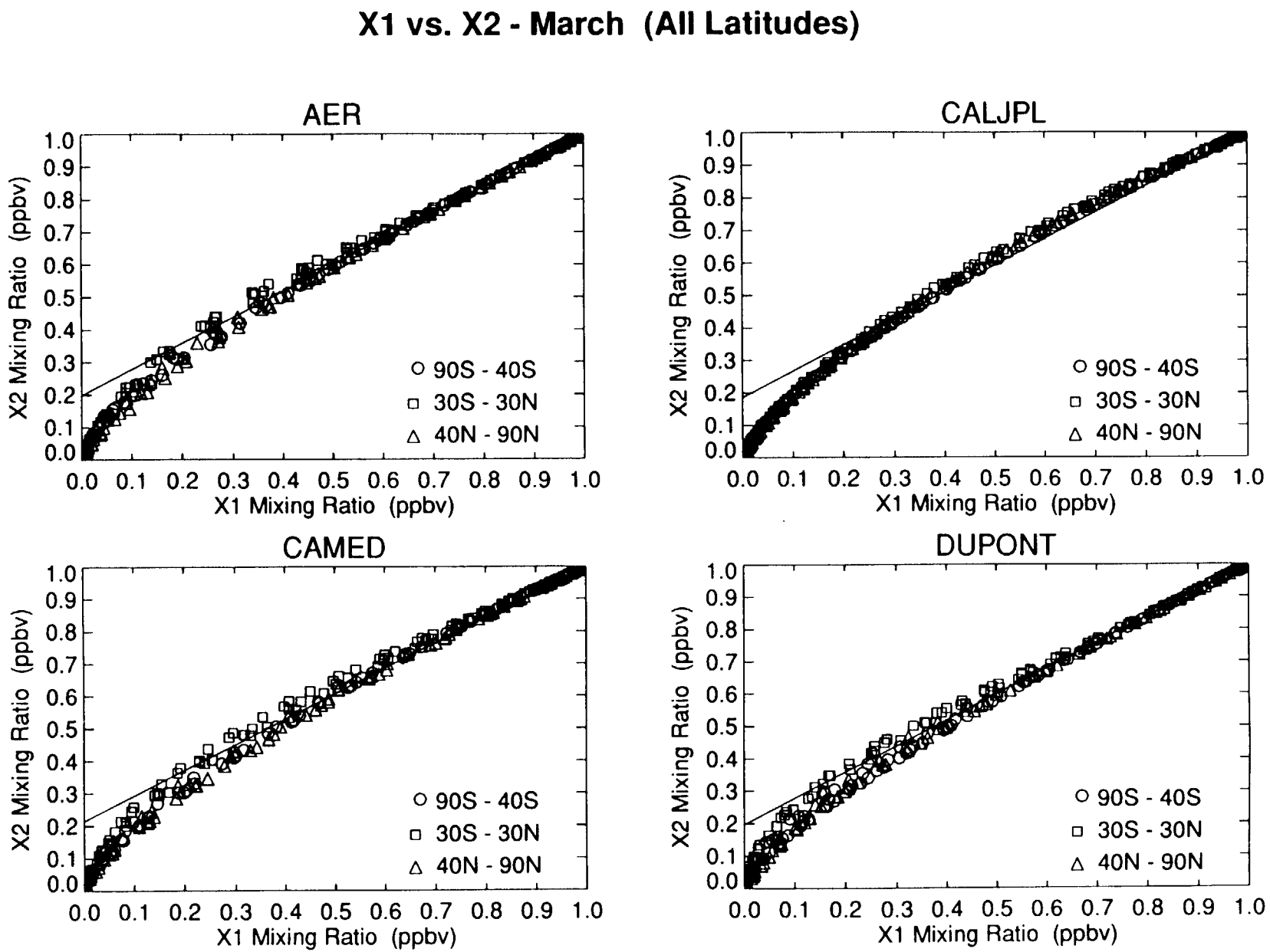
X1 vs. X2 - March (All Latitudes)
AER
CALJPL
CAMED
DUPONT
X2 Mixing Ratio (ppbv)
X1 Mixing Ratio (ppbv)
0.0 0.1 0.2 0.3 0.4 0.5 0.6 0.7 0.8 0.9 1.0
90S - 40S
30S - 30N
40N - 90N

Figure O-15

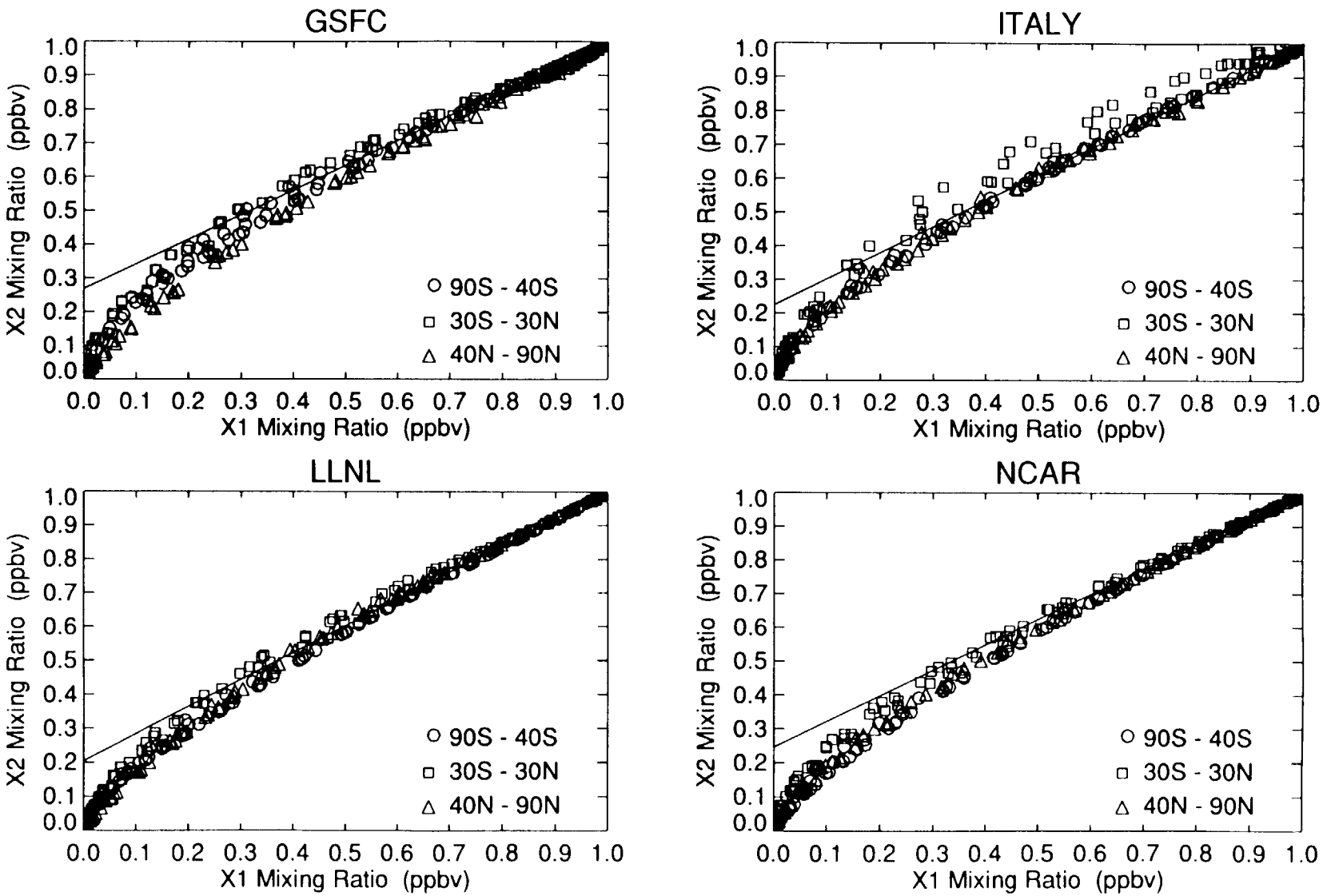

Figure O-15 (cont.)

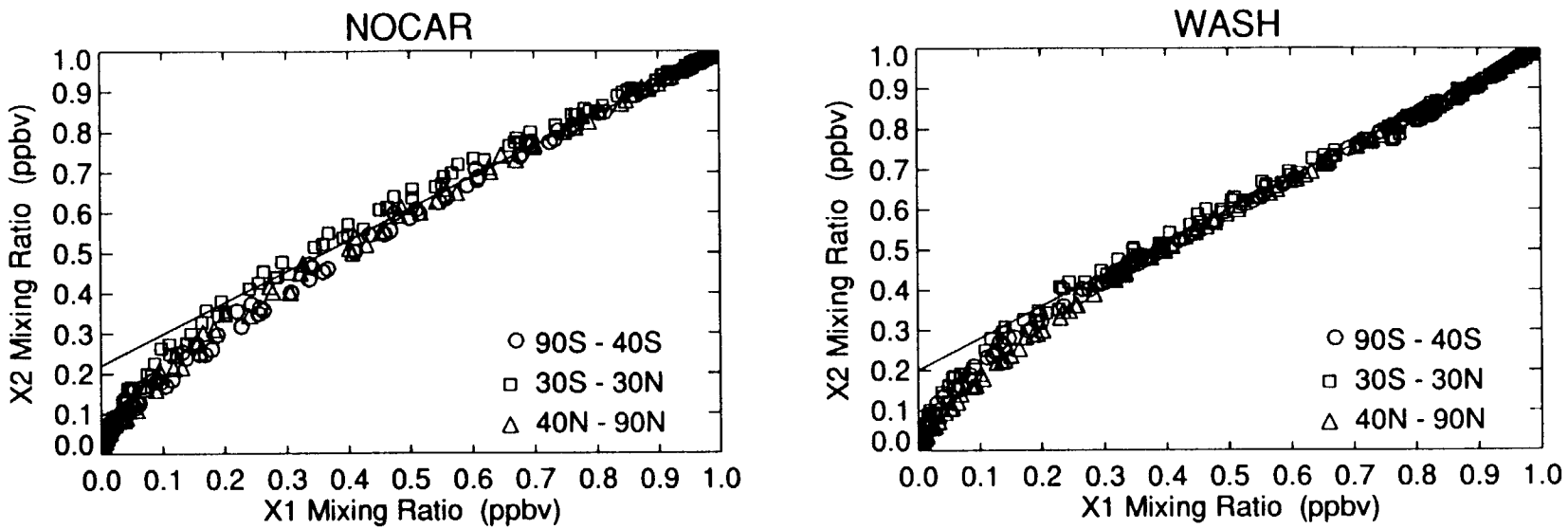

Figure O-15 (cont.)

W vs. X1 - March

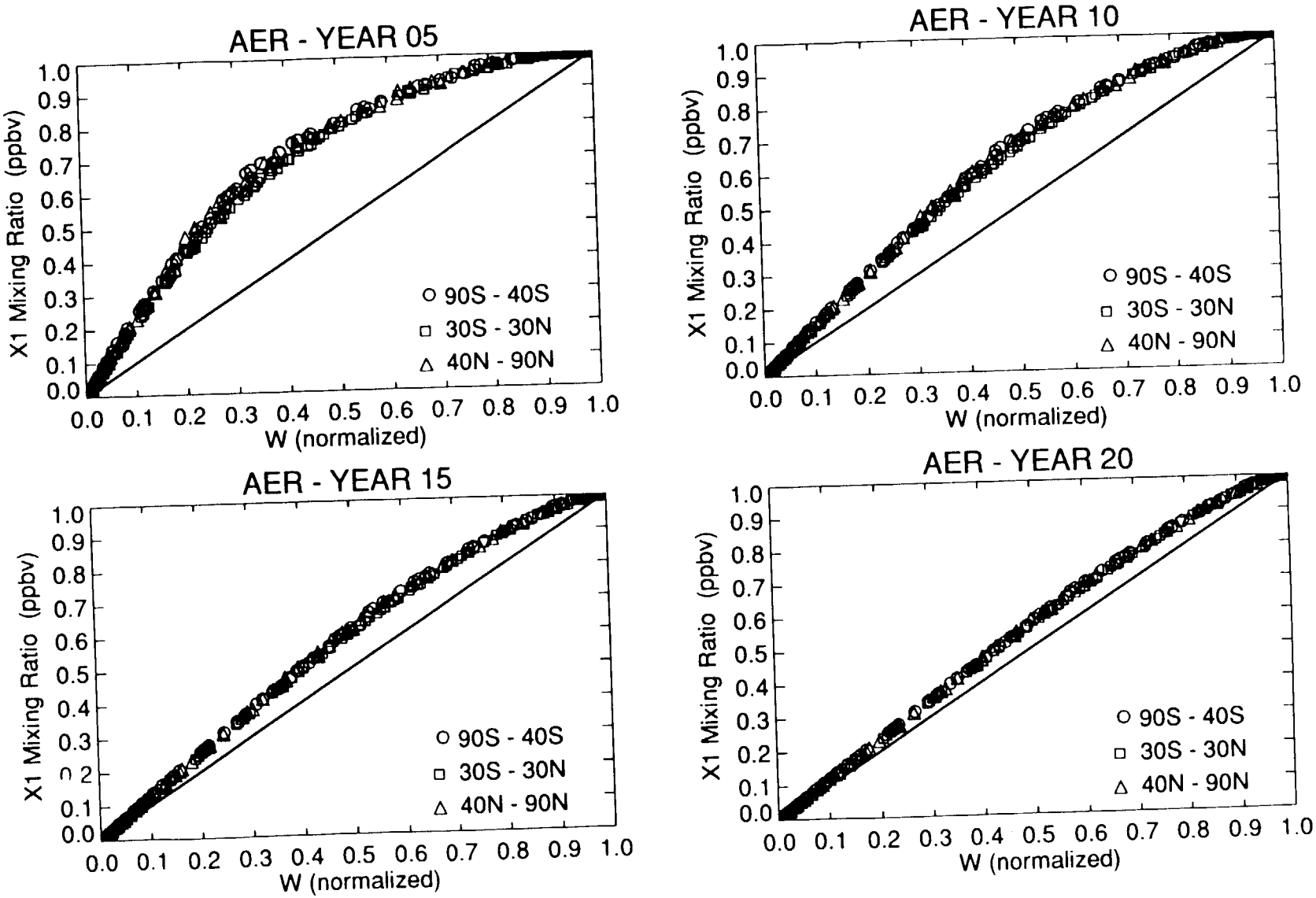

Figure O-16

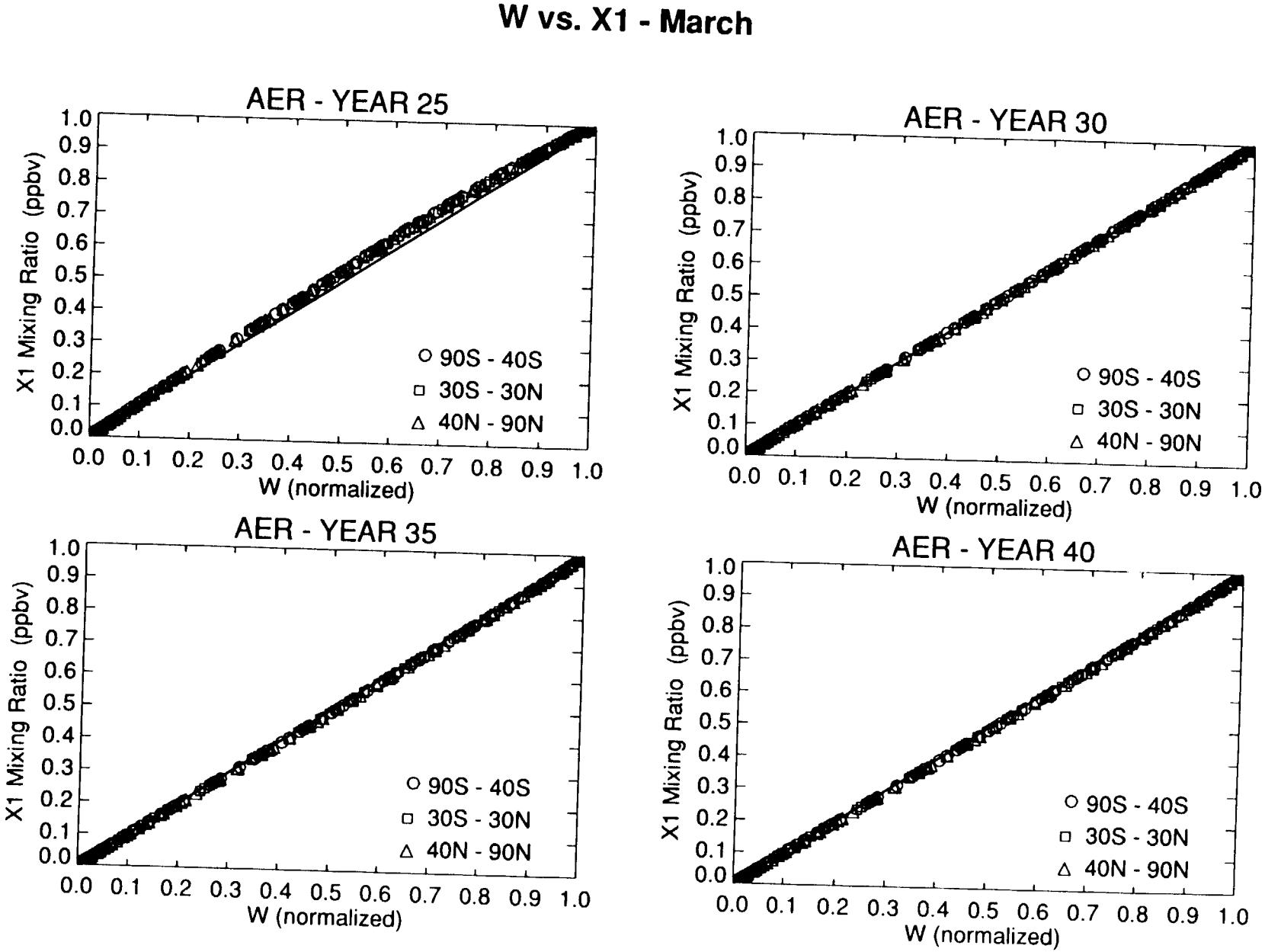

Figure O-16 (cont.)

W vs. X1 - March

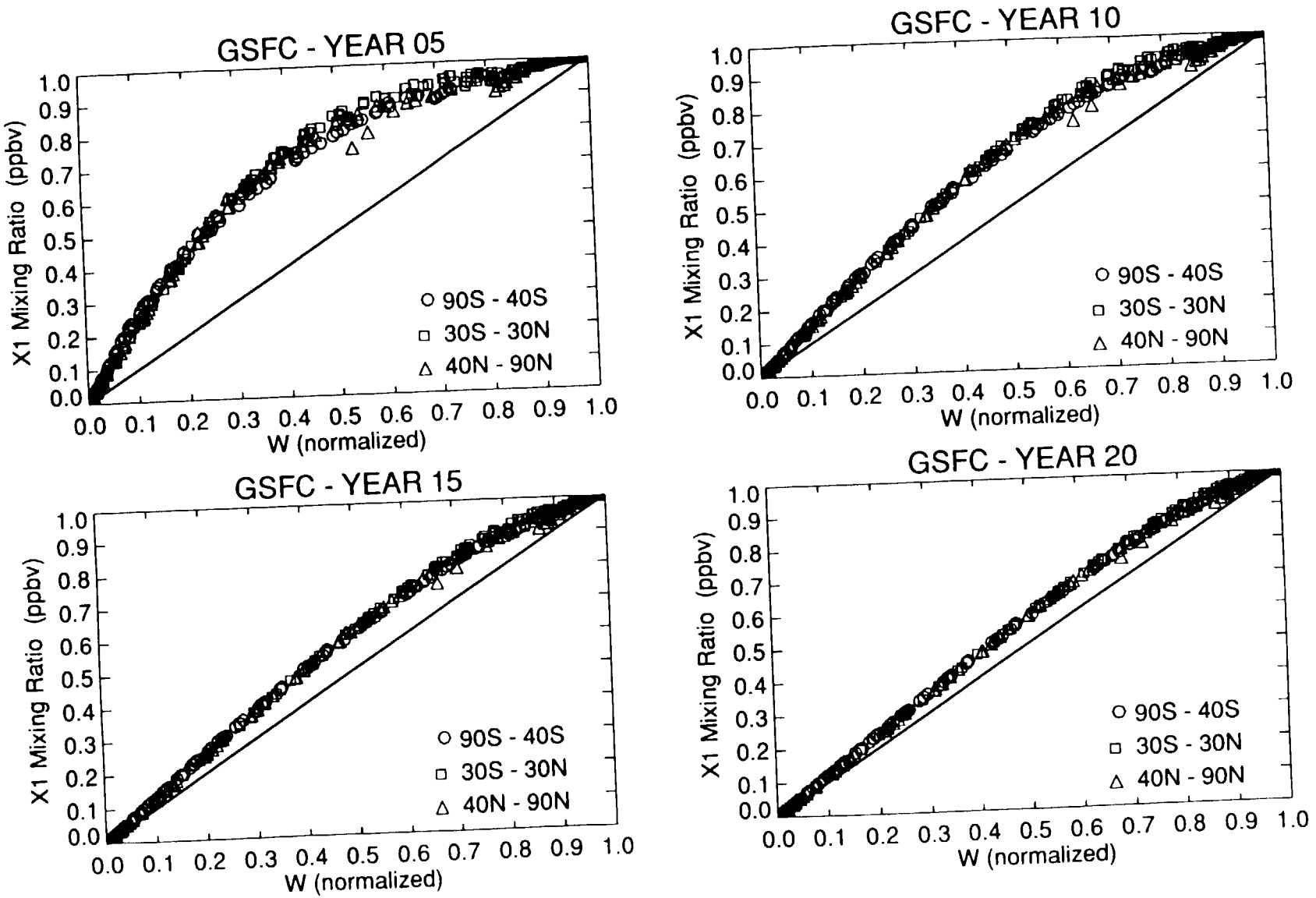

Figure O-17

W vs. X1 - March

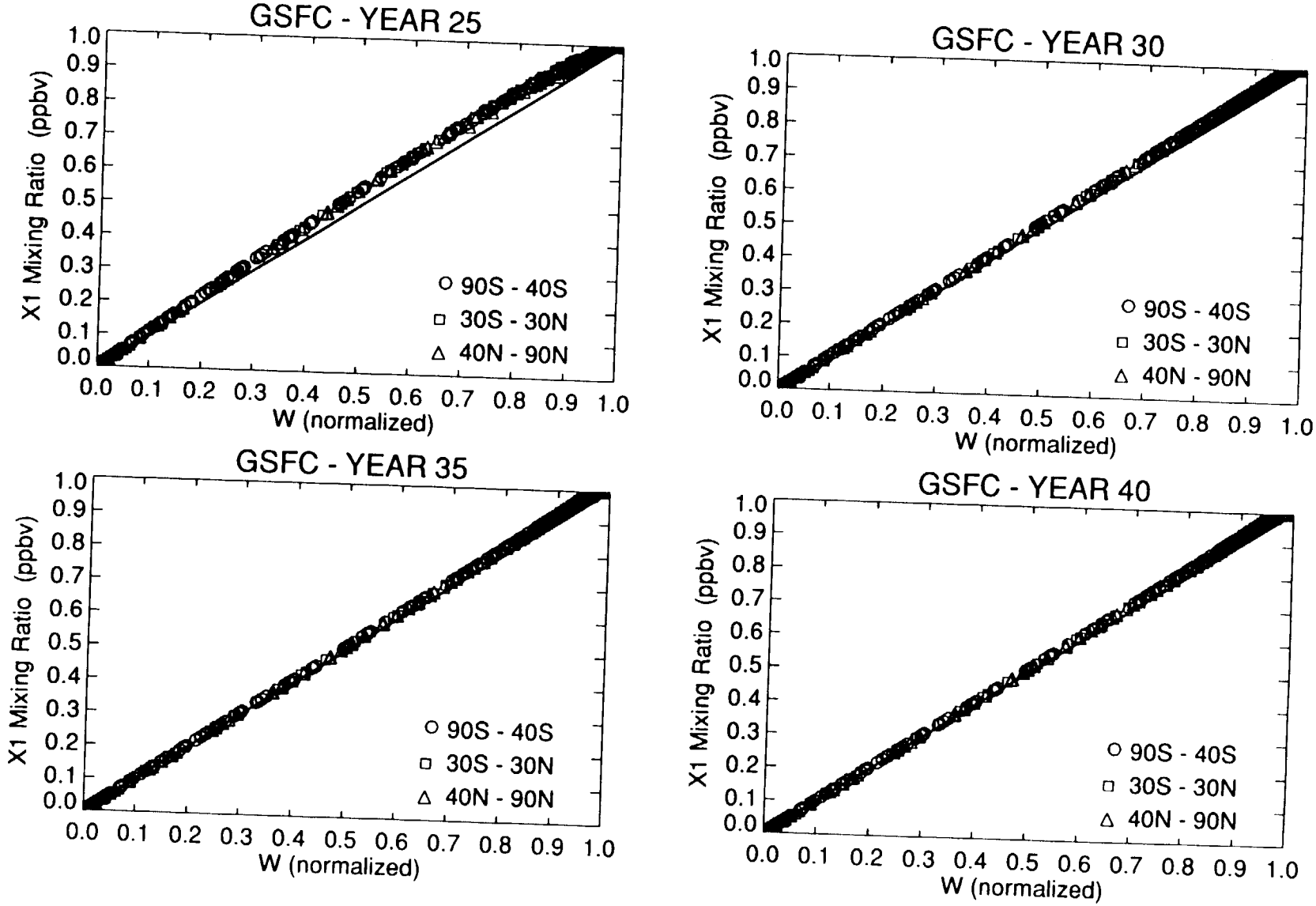

Figure O-17 (cont.)

W vs. X1 - March

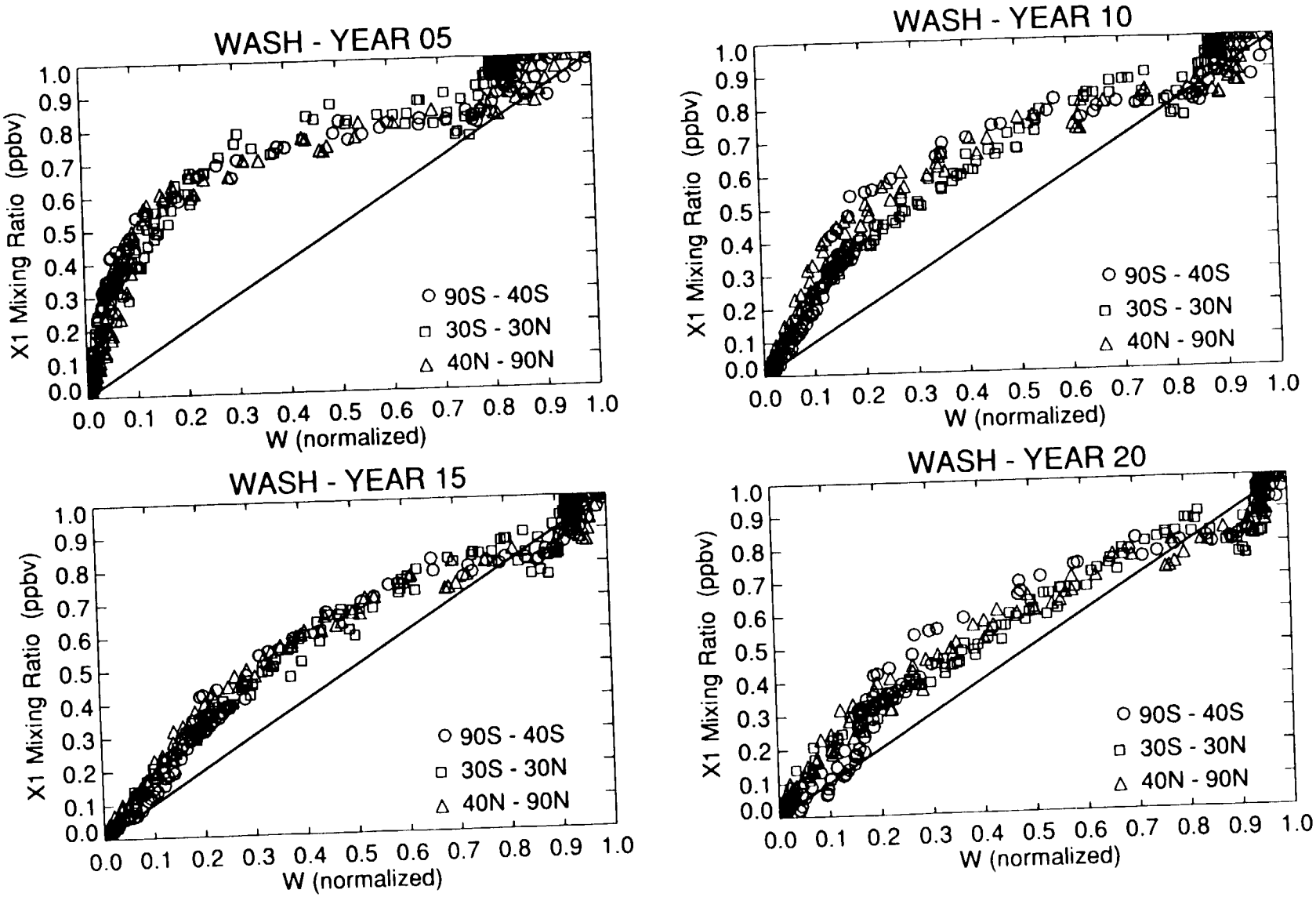

Figure O-18

W vs. X1 - March

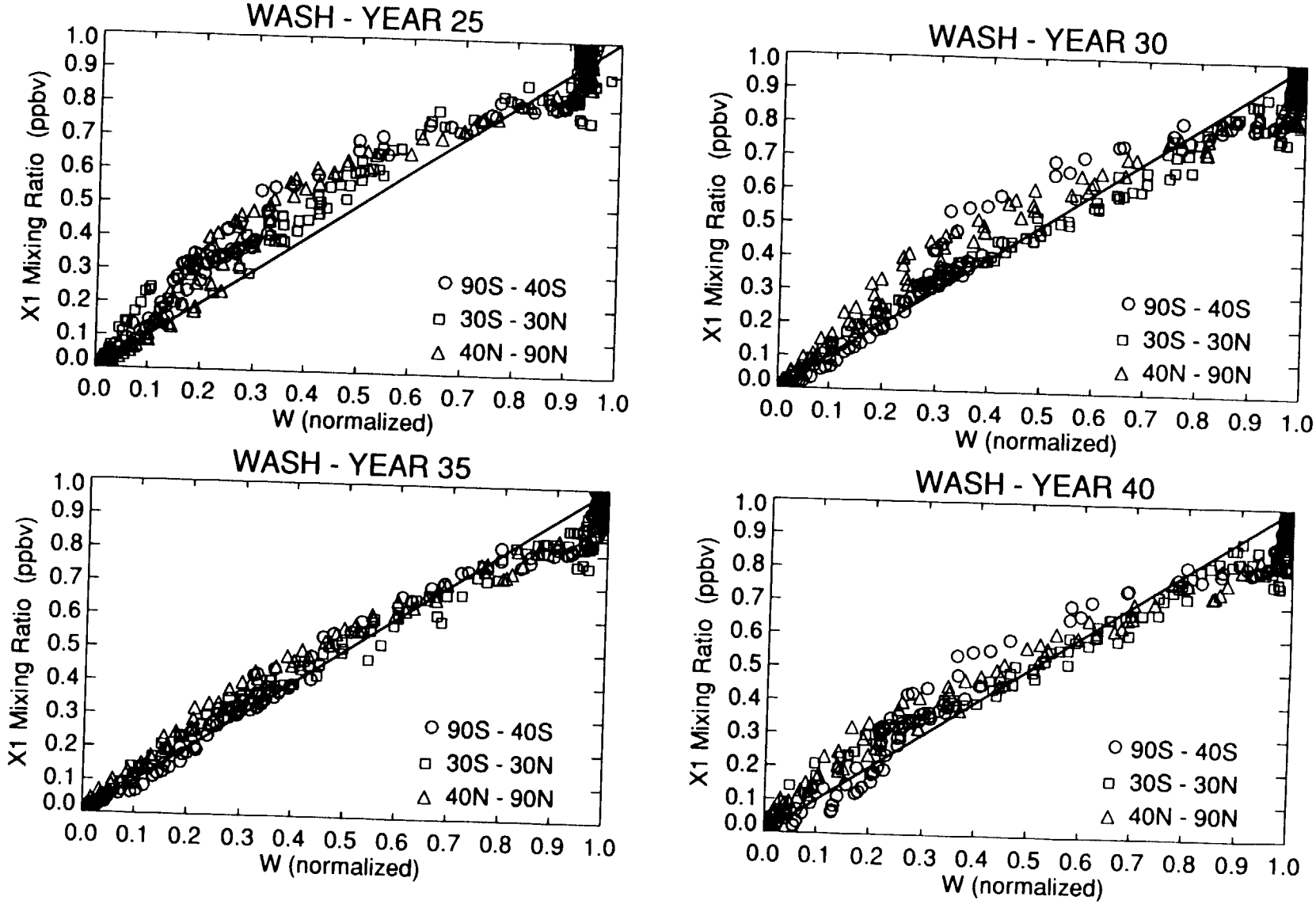

Figure O-18 (cont.)

NASA

Report Documentation Page

1. Report No.	2. Government Accession No.	3. Recipient's Catalog No.
NASA RP-1292, Vol. III		

4. Title and Subtitle

The Atmospheric Effects of Stratospheric Aircraft:
Report of the 1992 Models and Measurements Workshop
Volume III—Special Diagnostic Studies

5. Report Date
March 1993

6. Performing Organization Code

7. Author(s)
Michael J. Prather and Ellis E. Remsberg, Editors

8. Performing Organization Report No.

10. Work Unit No.

9. Performing Organization Name and Address
NASA Office of Space Science and Applications
Earth Science and Applications Division

11. Contract or Grant No.

13. Type of Report and Period Covered
Reference Publication

12. Sponsoring Agency Name and Address
National Aeronautics and Space Administration
Washington, DC 20546

14. Sponsoring Agency Code

15. Supplementary Notes

Prather: NASA Office of Space Science and Applications, Washington, D.C.;
Remsberg: Langley Research Center, Hampton, VA.

16. Abstract

This Workshop on Stratospheric Models and Measurements (M&M) marks a significant expansion in the history of model intercomparisons. It provides a foundation for establishing the credibility of stratospheric models used in environmental assessments of chlorofluorocarbons, aircraft emissions, and climate-chemistry interactions. The core of the M&M comparisons involves the selection of observations of the current stratosphere (i.e., within the last 15 years): these data are believed to be accurate and representative of certain aspects of stratospheric chemistry and dynamics that the models should be able to simulate.

17. Key Words (Suggested by Author(s))	18. Distribution Statement
The stratosphere; Observations; Chemical models; Dynamical models; Ozone	Unclassified - Unlimited Subject Category 45

19. Security Classif. (of this report)	20. Security Classif. (of this page)	21. No. of pages	22. Price
Unclassified	Unclassified	352	A16

NASA FORM 1626 OCT 86

NASA-Langley, 1993